UNIVERSITY OF TWENTE

ISBN: 978-90-365-4907-3
DOI: 10.3990/1.9789036549073

MODELLING PLOUGHING BY AN ELLIPTICAL ASPERITY THROUGH A ZINC COATED STEEL SHEET T. Mishra

MODELLING PLOUGHING BY AN ELLIPTICAL ASPERITY THROUGH A ZINC COATED STEEL SHEET

With application to modelling friction in deep-drawing

Tanmaya Mishra

MODELLING PLOUGHING BY AN ELLIPTICAL ASPERITY THROUGH A ZINC COATED STEEL SHEET

With application to modelling friction in deep-drawing

Tanmaya Mishra

Faculty of Engineering Technology,

Laboratory of Surface Technology and Tribology,

University of Twente

This research was carried out under project number S22.1.14520a in the framework of the Partnership Program of the Materials innovation institute M2i (www.m2i.nl) and the Technology Foundation TTW (www.stw.nl), which is part of the Netherlands Organization for Scientific Research (www.nwo.nl).

This dissertation has been approved by

Supervisors:
Prof.dr.ir. M.B. de Rooij
Prof.dr.ir. D.J. Schipper

Cover design: Tanmaya Mishra
Printed by: Gilde Print
Lay-out: Tanmaya Mishra
ISBN: 978-90-365-4907-3
DOI: 10.3990/1.9789036549073

MODELLING PLOUGHING BY AN ELLIPTICAL ASPERITY THROUGH A ZINC COATED STEEL SHEET

With application to modelling friction in deep-drawing

DISSERTATION

to obtain
the degree of doctor at the University of Twente,
on the authority of the rector magnificus,
Prof.dr. T.T.M. Palstra,
on account of the decision of the Doctorate Board,
to be publicly defended
on Wednesday 4 December 2019 at 14.45

by:

Tanmaya Mishra

born on 25 August 1989

in Bhubaneswar, India

Graduation Committee:

Chairman/Secretary:
Prof.dr. G.P.M.R. Dewulf

Supervisors:
Prof.dr.ir. M.B. de Rooij,
Prof.dr.ir. D.J. Schipper

Committee members:
Prof.dr.ir. M.B. de Rooij
Prof.dr. S. Luding
Prof.dr.ir. A.H. van den Boogaard
Prof.dr. C. Gachot
Prof.dr.ir. L. Nicola
Prof.dr.ir. D.J. Schipper

Dedicated to my late grandfather (Aja)
who instilled the scientific fervour in me

Summary

Modelling of friction in deep-drawing process is critical to the design to the product. Typically, the steel sheets used in deep-drawing are coated with a thin zinc layer by hot dip galvanization. The zinc coated steel sheets are further lubricated and provided with the required surface texture, amongst other things, to optimize the frictional stresses in a deep-drawing process. The friction in deep-drawing during loading and sliding of the tool against the sheet, in boundary lubrication regime, results from shearing of the interfacial layers, but also from ploughing of the flattened sheet surface by rigid tool asperities. The asperities on the surface of the tool have been mapped with elliptic bases of varying sizes and orientation relative to sliding direction. The current thesis aims to model the ploughing behaviour by an elliptical asperity sliding through a zinc coated steel sheet.

The friction in ploughing results from the plastic deformation of the sheet substrate and the shearing of the interface between the asperity and the substrate. These two factors are also part of a material point method (MPM)-based numerical ploughing model and a simplistic analytical ploughing model. Both the numerical and the analytical models have been extended to calculate the friction in ploughing of uncoated and zinc coated steel sheets by elliptical and spherical asperities of varying sizes, ellipticity ratios and orientation relative to the sliding direction. The analytical ploughing model has been developed for rigid-plastic material behaviour of the substrate and a constant interfacial frictional shear strength. In contrast, experimentally characterized material strength models, yield functions and interfacial friction models have been implemented in the MPM-based ploughing model.

An experimental characterization technique to measure the interfacial shear strength has been developed for unlubricated and lubricated, uncoated and zinc coated steel sheets at varying loads and sliding velocities using line contacts in linear sliding experiments. Also an experimental characterization technique to determine the yield criteria for the (anisotropic) temper rolled zinc coating on steel sheet has been developed using Knoop indentations. The method has also been applied on cold rolled steel sheet and validated using standard yield criteria. The experimentally characterized parameters for the interfacial friction model, the yield function and the yield criteria for the steel sheet and the zinc coating on steel sheet have been implemented in the MPM model to perform simulations of ploughing asperities with properties close to the reality.

Further ploughing experiments are performed using indenters with spherical tips of varying sizes and indenters with ellipsoidal tips with varying size and orientation relative to sliding

direction. Further, experiments have been performed with varying ploughing direction on unlubricated and lubricated steel sheets, lubricated zinc block and lubricated, temper rolled and unrolled zinc coated steel sheets under a range of applied loads. The developed MPM-based ploughing model is validated using experimental results such as the measured friction force and measured ploughing depth. The measured results are found to be in very good agreement with calculations. The MPM-based ploughing model results are also compared and shown to agree well with the analytical model results for simpler rigid-plastic material behaviour of the substrate.

The developed MPM-based ploughing model and the analytical models can therefore be used as robust tools in computing friction in single asperity ploughing. The models can be utilized to accurately model friction due to ploughing for tool sheet contacts in a deep-drawing processes. In this way, the models describing friction in deep-drawing processes can be improved.

Samenvatting

Modellering van wrijving in dieptrekprocessen is cruciaal voor het ontwerp van een diepgetrokken product met bijbehorend productieproces. Typisch worden de staalplaten die worden gebruikt bij dieptrekken bekleed met een dunne zinklaag door een proces zoals thermisch verzinken. De verzinkte staalplaten worden verder gesmeerd en voorzien van de vereiste oppervlaktetextuur, onder andere om de wrijving bij dieptrekken te optimaliseren. De wrijving bij het dieptrekken gedurende het contact tussen het gereedschap tegen de plaat in het grenssmeringsregime, is het gevolg van afschuiving in de contacten, maar ook van ploegeffecten van gereedschapsruwheidstoppen door het afgevlakte plaatoppervlak. In dit onderzoek worden de oneffenheden op het oppervlak van het gereedschap gemodelleerd met elliptische ruwheidstoppen van verschillende grootte en oriëntatie ten opzichte van de afschuifrichting. Het huidige proefschrift heeft als doel het ploeggedrag te modelleren van elliptische ruwheidstoppen die ploegen door een verzinkte staalplaat.

De wrijving bij het ploegen is het gevolg van de plastische vervorming van de plaat en de afschuiving van het grensvlak tussen de ruwheidstop en het substraat. Deze twee bijdragen aan de wrijvingskracht zijn te bepalen uit het ontwikkelde, op MPM (Material Point Method) gebaseerde model en een analytisch model voor een ploegende ruwheidstop. De ontwikkelde numerieke en analytische modellen zijn verder ontwikkeld om de wrijvingskrachten te berekenen bij het ploegen door niet verzinkte en verzinkte staalplaten middles elliptische en bolvormige ruwheidstoppen van verschillende afmetingen, elliptische verhoudingen en oriëntatie ten opzichte van de afschuifrichting. Het analytische ploegmodel is ontwikkeld voor het geval van rigid-plastisch materiaalgedrag in het substraat en een constante grensvlakwrijving (afschuifsterkte) op de interface. Experimenteel gekarakteriseerde modellen voor het vervormingsgedrag en afschuiving op het grensvlak zijn geïmplementeerd in het op MPM gebaseerde ploegmodel om een zo realistisch mogelijk model te maken.

Een experimentele methode om de afschuifsterkte van het grensvlak te meten is ontwikkeld voor niet-gesmeerde en gesmeerde, niet-gecoate en verzinkte staalplaten bij verschillende belastingen en glijsnelheden. Hiervoor zijn lijncontacten gebruikt in experimenten met een lineair beweging. Ook is een experimentele karakterisatietechniek voor het bepalen van het vloeigedrag voor de (anisotrope) zinkcoating op staalplaat ontwikkeld met behulp van Knoop-indentaties. Deze resultaten zijn gevalideerd met bekende resultaten van experimenten gedaan op koudgewalste staalplaat. De experimenteel bepaalde parameters voor het grensvlakwrijvingsmodel, de vloeifunctie en de vloeicriteria voor de staalplaat en de zinkcoating op staalplaat zijn vervolgens geïmplementeerd in het MPM-model.

Verdere ploegexperimenten worden uitgevoerd met bolvormige en elliptische indenters met verschillende groottes, oriëntatie ten opzichte van glijrichting en walsrichting op niet-gesmeerd en gesmeerd plaatmateriaal, een gesmeerd zinkblok en verschillende gecoate en niet gecoate soorten plaatmateriaal onder verschillende belastingen. Het ontwikkelde MPM-gebaseerde ploegmodel is gevalideerd met experimentele resultaten zoals de gemeten wrijvingskracht en ploegdiepte. Als deze resultaten worden vergeleken, dan wordt er een goede overeenstemming gevonden tussen model en experiment. De op MPM gebaseerde ploegmodelresultaten zijn ook vergeleken, en blijken goed overeen te komen, met de analytische modelresultaten. Voor deze resultaten is een eenvoudiger rigid-plastic materiaalgedrag van het substraat aangenomen.

Het ontwikkelde MPM-gebaseerde ploegmodel en de analytische modellen kunnen daarom worden gebruikt als robuuste modellen bij het berekenen van wrijving bij ploegen met één ruwheidstop. De modellen kunnen worden gebruikt om wrijving, inclusief het ploeggedrag, in het grenssmeringsregime te berekenen voor het contact tussen ene gereedschap en de plaat in een dieptrekproces. Op deze manier kunnen de wrijvingsmodellen voor dieptrekprocessen worden verbeterd.

Acknowledgements

As I am at the cusp of a memorable journey, I reminisce the enriching pursuit of my research and I acknowledge the invaluable contributions of so many people to the successful completion of my PhD.

To start with, I would like to thank my supervisor Prof. Matthijn de Rooij to have seen the potential and shown the confidence and patience in me as a PhD candidate. I would also like to express my gratitude for his constant guidance, sincere supervision, cordial mentoring and friendly nature. I have always ended up being invigorated and motivated after all our weekly meetings and impromptu short discussions. I would like to thank my promoter Prof. Dirk Schipper for his critical observations and indispensable suggestions on my research. I would also like to thank Dr. Javad Hazrati for our discussions, his guidance and corrections on my research.

I would like to express my heartfelt gratitude to ing. Erik de Vries for his immense help in setting up experiments and quick fixes to the issues in the laboratory. My gratefulness to ing. Nick Helthuis, Ms. Belinda Bruinink and ing. Walter Lette for their timely help in my research. I want to extend my gratitude to Dr. Jeroen van Beeck, Dr. Marco Appelman, Dr. Matthijs Toose and Dr. Carel ten Horn from TATA steel Europe and Dr. Jan Dirk Kamminga from M2i for their valuable inputs and suggestions in the progress meetings and help in specimen preparation. I would like to thank Dr. Georg Ganzenmüller for his help and our wonderful collaboration on the USER-SMD package for MPM.

A big thanks to my colleagues and friends for making my PhD journey so memorable and with whom I have shared so many fun experiences and from whom I have learnt a lot. I would like to thank my project mate Shyam, for our fruitful discussions and his support with my research. I would also like to thank my office mates, Mohammad, Xavi and Dennis for our discussions, for helping me with my problems and for maintaining a warm (for Xavi getting us the room heater), fun and friendly work environment. I would like to thank Melkamu and Dmitri for bringing back the Tribos spirit and memories into the cafeteria, canteen and laboratories at Twente. I would extend my gratitude to Shivam, Febin, Aydar, Michel, Ida, Pramod, Can, Leon and Pedro for the nice memories and work experience. Thanks to all my friends, for their support and all the memories: Poorya, Bharat, Balan, Keerti, Mehetab, Valon, Catur, Rana, Vicky, Siddharth, Rashmi, Tapan, Amit, Manish, Boity and Deepak. I thank my grandparents, uncles, aunts and cousins for motivating me for this remarkable journey.

Most importantly, I would have not come this far without the support and sacrifice of my parents. Their interest and pride in my research has always kept me driven. Their constant love, motivation and guidance is pricesless and cannot be described in words. Thanks to my dear sister Salona, for her support in writing and always giving me fresher perspectives to look at things. Last but certainly not the least, the support, encouragement and the immense love of my partner, my dearest wife Renata, has made me come through every obstacle. She has made me assured, calmer and has also helped me solve my worries with ease and grace. I am thankful to her, and for her.

To everyone who has thus contributed in one way or the other, your inputs and sacrifices in this journey will always be remembered and cherished.

Tanmaya Mishra, *Enschede*, *November* 2019

Contents

Appended papers

(A) T. Mishra, G.C. Ganzenmüller, M.B. de Rooij, M.P. Shisode and J. Hazrati, D.J. Schipper. Modelling of ploughing in a single-asperity sliding contact using material point method. Wear 2019; 418:180-90.
https://doi.org/10.1016/j.wear.2018.11.020.

(B) T. Mishra, M.B. de Rooij, M.P. Shisode, J. Hazrati and D.J. Schipper. An analytical model to study the effect of asperity geometry on forces in ploughing by an elliptical asperity. Tribology international 2019; 137:405-19.
https://doi.org/10.1016/j.triboint.2019.05.015.

(C) T. Mishra, M.B. de Rooij, M.P. Shisode, J. Hazrati and D.J. Schipper. A material point method based ploughing model to study the effect of asperity geometry on the ploughing behaviour of an elliptical asperity. (2019). Tribology international 2019; 142:106017
https://doi.org/10.1016/j.triboint.2019.106017

(D) T. Mishra, M.B. de Rooij, M.P. Shisode, J. Hazrati and D.J. Schipper. Characterization of interfacial shear strength and its effect on ploughing behaviour in single-asperity sliding. (2019). Wear 2019; 436-437:203042.
https://doi.org/10.1016/j.wear.2019.203042

(E) T. Mishra, M.B. de Rooij, M.P. Shisode, J. Hazrati and D.J. Schipper. Characterization of yield criteria for zinc coated steel sheets using Nano-indentation with Knoop indenter. (2019). Surfaces and coatings Technology .
https://doi.org/10.1016/j.surfcoat.2019.125110

(F) T. Mishra, M.B. de Rooij, M.P. Shisode, J. Hazrati and D.J. Schipper. Modelling of ploughing behaviour in soft metallic coatings using material point method. (2019). Submitted to Wear.

Nomenclature

The list below describes several symbols that will be later used within the part I of the thesis.

Abbreviations and acronyms

err	error
tol	tolerance
ALE	Arbitrary Lagrangian Eulerian
BL	Boundary lubrication
EBSD	Electron backscatter diffraction
EDT	Electron discharge texturing
EDX	Energy-dispersive X-ray spectroscopy
FEM	Finite element method
GIMPM	Generalized interpolation material point Method
HL	Hydrodynamic lubrication
KHN	Knoop hardness number
LAMMPS	Large-scale atomic/molecular massively parallel simulator
LBT	Laser beam texturing
MD	Molecular dynamics
MP	Mirror polished
MPM	Material point method
ND	Normal direction
OVITO	Open visualization tool
PATAT	Ploughing asperity tester at the University of Twente

RD	Rolling direction
SEM	Scanning electron microscope
SMD	Smooth mach dynamics
SP	Shine polished
SPH	Smooth particle hydrodynamics
TD	Transverse direction
TLSPH	Total lagrangian smooth particle hydrodynamics
UMT	Universal mechanical tester

Roman symbols: uppercase

$\bar{A}$	Ratio to real area of contact to nominal contact area	
ΔG	Activation energy	J
$\mathbb{C}$	Stiffness matrix	
$\mathbb{P}$	Matrix with anisotropy parameters	
J	Jacobian matrix	
S	Spherical coordinate system	
$\tilde{H}$	Ratio of hardness of the coating to hardness of the substrate	
A/A_c	Contact area of the asperity with substrate	μm^2
A_r	Real area of contact	μm^2
A_Δ	Area of the surface element	μm^2
A_{xy}	Projected area in xy-plane	μm^2
A_{xz}	Projected area in xz-plane	μm^2
A_{yz}	Projected area in yz-plane	μm^2
B_p	Factor in expression for coefficient of friction in ploughing by a 2D wedge	
B_p	Factor in expression for coefficient of friction in wedging by a 2D wedge	
C	Centre of the elliptic contact base	
C_p	Coefficient of contact pressure in relation to interfacial shear strength	
C_v	Coefficient of sliding velocity in relation to interfacial shear strength	
D_l	Length of the longer diagonal of the Knoop indenter	μm
D_p	Degree of penetration	

E	Elastic modulus	GPa
F	Total force acting on the sliding asperity	N
F_b	Force acting on the blank holder	kN
F_f	Friction (Lateral) force acting on the sliding asperity	N
F_n	Normal force (load) acting on the sliding asperity	N
F_p	Force acting on the punch	kN
G	Shear modulus	GPa
H	Hardness	MPa
I	Identity matrix	
I_0	First influence factor in a coated system	
I_1	Second influence factor in a coated system	
J_1	First stress invariant	
J_2	Second stress invariant	
K	Bulk Modulus	GPa
L	End point of contact in z axis	
L_x	Projected length on the x-axis	μm
M	Plastic flow separation point in contact plane	
N	Contact end point in contact plane in $+y$ axis	
O	Centre of the ellipsoidal asperity	
P	Hydrostatic pressure component	
P_0	Maximum contact pressure	GPa
P_{nom}	Nominal contact pressure	GPa
Q	Activation energy	Jm
R_0	Lankford coefficient along the rolling direction	
R_a	Mean surface roughness	μm
R_q	Root mean squared surface roughness	μm
R_{45}	Lankford coefficient at 45° the rolling direction	
R_{90}	Lankford coefficient along the transverse direction	
S	Contact end point in contact plane in $-y$ axis	
T	Temperature	K

T_0	Room/reference temperature	K
T_c	Contact temperature	K
T_m	Melting point temperature	K
U_1, U_2, U_3	Parameters for yield stress in tension in Hill's yield criteria	
V	Volume	μm^3
V_1, V_2, V_3	Parameters for yield stress in simple shear in Hill's yield criteria	
W_{np}	Interpolation function from node to particle	
W_{pn}	Interpolation function from particle to node	
X_x	Axis length of ellipsoid projected in x-axis	μm
Y_y	Axis length of ellipsoid projected in y-axis	μm
Z	Height of the ellipsoid in z-axis	μm

Roman symbols: lowercase

Δq	Heat generated	J
$\dot{t}$	Time	s
$\overset{*}{d}$	Distance between KHN-based points and yield locus in plane-stress plane	
$\widehat{SN}$	Arc SN: semi-elliptic contact boundary	
$\vec{n}$	Normal vector to the surface of the indenter in contact with the substrate	
$\vec{t}$	Tangent vector to the contacting surface of the indenter along plastic flow	
$\widehat{n}$	Unit normal to the surface of the indenter in contact with the substrate	
$\widehat{t}$	Unit tangent to the contacting surface of the indenter along plastic flow	
a	Major axis of base of elliptic asperity	μm
a_c	Contact radius for a (semi-)circular contact patch	μm
a_x	Major axis of elliptic contact patch in x-axis	μm
a_y	Major axis of elliptic contact patch in y-axis	μm
a_z	Reference contact radius for contact with an (semi-) elliptic contact patch	μm
b	Contact width for a (line) rectangular contact patch	μm
b_0	Initial guess for contact width b	μm
c	Height of the elliptic asperity	μm
c_p	Specific heat capacity	$J/kg.K$

d/d_p	Penetration/ploughing depth in the ploughed profile	μm
$d^{'}/d^{''}$	Modified/corrected ploughing depth	μm
d_e	Penetration depth in a perfectly elastic substrate	μm
d_g	Groove depth of the ploughed profile	μm
d_s	Length of the shorter diagonal of the Knoop indenter	μm
e_x	Ellipticity ratio of the asperity base in the x-axis	
e_y	Ellipticity ratio of the asperity base in the x-axis	
f/f_{hk}	Ratio of shear strength of the interfacial and shear strength of the bulk	
g	Strain hardening exponent (Bergström van Liempt model)	
h	Indentation depth in Nano-indentation	μm
h_{pu}	Pile-up height	μm
i	Orientation of the Knoop indenter	
j	Dynamic stress power (Bergström van Liempt model)	
k	Boltzmann constant	$8.617 \times 10^{-5}\, eVm$
l	Contact length in the (line) rectangular contact	μm
l_s	Sliding distance	mm
m	Slope of the (semi-)elliptic contact patch boundary	
m_s	mass scaling factor	
n	Strain hardening exponent	
n_p	Exponent of contact pressure in relation to interfacial shear strength	
n_T	Exponent of contact temperature in relation to interfacial shear strength	
n_v	Exponent of sliding in relation to interfacial shear strength	
o_g	Fitting factor for groove depth with asperity geometry	
o_{pu}	Fitting factor for change in pile-up height with asperity geometry	
p	Fitting factor for ploughing depth accounting for plastic flow change	
p_{pl}	Contact pressure on the asperity/indenter due to plastic deformation	MPa
q	Fitting factor for ploughing depth accounting plastic flow distribution	
r	Radius of the (spherical) indenter	μm
s_{ij}	Elastic compliance	$1/MPa$
t	Coating thickness	μm

u_a	Fitting factor for interfacial shear component increasing ploughing depth	
u_b	Fitting factor for interfacial shear component decreasing ploughing depth	
v/v_s	Sliding velocity	m/s
w	Fitting factor for ploughing depth accounting for interfacial shear strength	
x	x-coordinate(abscissa)/axis	
y	y-coordinate(ordinate)/axis	
z	z-coordinate axis (also rolling direction)	

Sub- and superscripts

T	Transpose of the matrix	
b/bl	boundary layer	
c	coating	
cs	coated substrate	
i/j	Direction or iteration $i/j = 1, 2, 3...$	
N	applied load	
p/pl	resulting from plastic deformation of the substrate	
s	substrate	
s/sh	resulting from shearing of the interface	
x	along x-axis	
y	along y-axis	
z	along z-axis	

Greek symbols

α	Orientation of the c axis of zinc crystal with respect to indentation direction	
$\bar{\sigma}$	Stress ratio in deviatoric plane or plane stress plane	
$\bar{\varepsilon}/\bar{\epsilon}$	Strain ratio in deviatoric plane or plane stress plane	
β	Angle of orientation of asperity relative to sliding direction in xy-plane	$^\circ$
β_0	Linear hardening parameter	
χ	Strain rate hardening coefficient (Johnson-Cook model)	
δ_{ij}	Kronecker delta	
$\dot{\epsilon_p}$	Plastic strain rate	1/s

$\dot{\varepsilon_0}$	Reference/initial strain rate	$1/s$
ϵ/ε	Total strain	
ϵ_d	Deviatoric strain	
ϵ_p	Plastic strain	
ϵ_v	Volumetric strain	
η	Dynamic viscosity of the lubricant	$mPa.s$
γ	Angle of attack at the asperity-substrate contact	$^\circ$
ι	Thermal softening exponent (Johnson-Cook model)	
κ	Shear strength of the bulk	MPa
κ_T	Thermal conductivity of the material	W/mK
Λ	Stiffness in nano-indentation	N/m
λ	Rate of the plastic multiplier in flow rule	
μ	Coefficient of friction	
ν	Poisson's ratio	
ω	Remobilization parameter	
Φ	Yield (criteria) function	
ϕ	Polar angle in spherical coordinates	$^\circ$
ψ_M	Angle subtended by a point on contact plane at the center O with z axis	$^\circ$
ρ	Material density	kg/m^3
σ	Total stress	MPa
$\sigma_d/\sigma^{'}/\sigma^d$	Deviatoric stress	MPa
σ_d^{trial}	Trial deviatoric stress	MPa
σ_f	Equivalent flow stress	MPa
σ_y	Yield stress (uniaxial)	MPa
σ_{V_0}	Maximum dynamic stress (Bergström van Liempt model)	MPa
σ_{y_0}	Initial yield stress	MPa
τ_{sh}	Shear strength of the interface	MPa
θ	Azimuthal angle in spherical coordinates	$^\circ$
υ	Penetration of the indenter's triangle into the MPM particle	μm
ε_0	Reference/initial strain	

φ	Transverse direction (polar angle in cylindrical coordinate)	$^{\circ}$
ϱ	Normal direction (radius in cylindrical coordinate)	μm
ξ	Strain hardening exponent (Johnson-Cook model)	
ζ	Strain hardening coefficient (Johnson-Cook model)	MPa
$d\sigma_m$	Stress increment parameter (Bergström van Liempt model)	MPa

Part I

The Thesis

Chapter 1

Introduction

This chapter introduces the industrial relevance and the motivation behind the current research. The previous works in understanding of processes in contributing to friction in deep-drawing have been summarized into the understanding of the modelling of friction in deep-drawing. The significance of a robust friction model in deep-drawing has been highlighted and relevance of micro-scale ploughing of an elliptical shaped asperity through a zinc-coated sheet leading to a friction model for deep-drawing has been pointed out.

1.1. Industrial background

Sheet metal forming processes have been increasingly used to manufacture complex geometries from metallic sheets by large scale deformation of sheet metal. Bending, deep-drawing and stretch-forming are common examples of sheet metal forming process differing in tooling requirements and material flow characteristics. The current thesis focuses on the deep-drawing process of cold rolled sheet metals commonly used in manufacturing of domestic appliances, automotive bodies as well as in packaging. A car door panel manufactured by a deep-drawing process is shown in figure 1.1a. With increasing demand for new product design, there is an increased need to have a feasible manufacturing system for the evolving products with reduced failure cost and lead time.

(a) Door panel (TATA Steel)

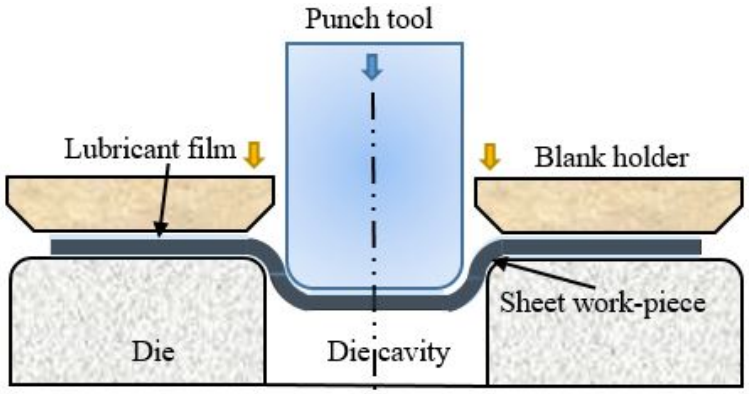

(b) Schematics of deep-drawing process

Figure 1.1: Deep-drawing product and process.

Cold rolled steel is commonly used as the work-piece in deep-drawing of automotive panels due to its availability, cost effectiveness and desired material properties. In deep-drawing of a sheet metal, the work-piece (sheet) is clamped between a blank holder and a die while the shape of the punch tool and the die is transferred into the blank as the punch tool presses into the cavity of the die as shown in figure 1.1b. The product quality in deep-drawing is assessed by checking the geometric accuracy of the product and the presence of wrinkles and scratches in the product.The friction forces resist the sliding between the tool and the work-piece and control the deformation of the work-piece in the sheet metal forming process. Sheet metal forming involves work-pieces with large surface area to volume ratio. Hence the frictional forces acting on the surface are very influential in the process, behaviour and product quality in deep-drawing.

The application of a zinc coating on steel sheets prior to deep-drawing has been very popular for the purpose of improving the durability of the product by increasing the corrosion-resistance and paintability of the product, see e.g. [1] and [2]. Typically, the deposition of the zinc coating on the steel sheets is done by (continuous) hot-dip galvanization and electro-galvanization processes [3]. During hot-dip galvanizing, depending on the requirements, the thickness of the zinc coating is controlled to be between 10-100 μm by help of air knives after the rolled sheet is passed through a molten zinc bath [4]. For deposition of thinner (1-10 μm) zinc coatings with smoother and shinier surface finish, the steel sheets are passed as a cathode through an electrolytic zinc bath with an metallic anode. The appearance, mechanical properties and

corrosion resistance of the zinc coated sheets can be controlled by the composition of the zinc coating. Annealing of galvanized sheets can be done to produce galvannealed steel containing inter-layers of iron-zinc intermetallics [5]. By controlling the amount of elements like magnesium and aluminum in the galvanizing zinc bath [6] also the properties of the coating can be changed significantly.

The use of advanced lubrication systems includes the use of pre-lubes, additives booster lubes and thin organic coatings (TOC). This results in a multi-layered system with a complex interfacial behaviour. Moreover, the surface texture of galvanized/galvannealed steel sheets is modified by (temper) rolling the sheets using roll mills. Shot blasting (SB), laser beam texturing (LBT) and electrical discharge texturing (EDT) are the commonly used methods for giving the desired texture to the rolls of a mill [7]. The texturing of the zinc coating along with the orientation of its crystals induces an anisotropy in the mechanical properties of the zinc coated sheet which also affects the frictional behaviour in deep-drawing. The surface texturing process, the resulting roughness and the micro-structure of the coating, the substrate and the tool result in a complex interplay. The properties of the surface will affect the deformation and frictional behaviour in deep-drawing and later, the paintability of the final product, see [8] and [9].

1.2. Modelling of friction in deep-drawing

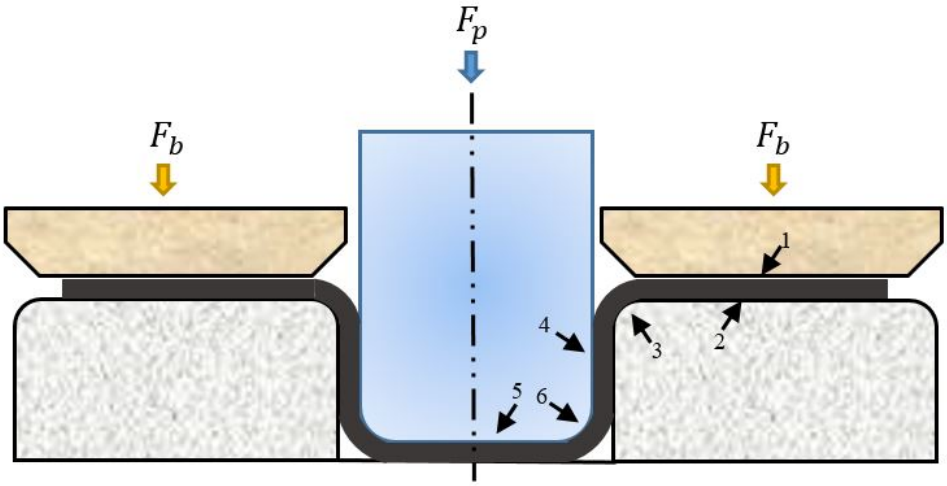

Figure 1.2: Critical contacting regions in deep-drawing [11].

Loading of the punch with a force of F_p presses the sheet (work-piece) held between the black holder and die, into the die cavity. The loading of the blank holder with a force of F_b, together with the force F_p results in a sliding contact between the black holder and the sheet, the die and the sheet and the punch tool and the sheet. Due to the nature of the process the operating conditions for contact between the tool and the work-piece in deep drawing vary along the whole sheet. Six regions have been specified on the sheet metal which are critical in determining the friction in deep-drawing [10], as shown in figure 1.2. The flange regions 1 and 2 mark the contact between the blank holder and the sheet and the die and the sheet. Region 1 and 2 experience tangential tensile stress and the contact pressure in these regions range between 1-50 MPa. The sheet metal slides along the blank holder and the die with a velocity ranging from 1-10 mm/s depending on the operational conditions and the location. The local conditions

depend on the punch force, the black holder force, the mechanical properties and the roughness of the contacting surfaces and lubricant. Depending on the operating conditions both boundary lubrication of mixed lubrication are possible in region 1 and 2. The die rounding region 3 and the punch rounding region 6 mark the contact between the sheet and the edge of the die and the contact between the sheet and the edge of the punch respectively. These regions experience severe stretching and bending resulting in circumferential compressive stress and radial tensile stress along with contact pressures ranging from 10-100 MPa. A high friction is required in region 3 and 6 for the sheet to follow the punch movement while a low friction in region 1 and 2 to prevent damage and fracture of the sheets. The contact between the punch flank and sheet marked as region 4 and the contact between the punch base and sheet is marked as region 5. These regions mostly experience stretching without any significant contact pressure and do not have a significant contribution to friction in deep-drawing.

The contact in deep-drawing at different scales is illustrated in figure 1.3. As the lubricated sheet is loaded with the punch tool and black holder, the sheet slides radially inward into the die cavity. As the sheet slides into the die cavity, it experiences resistance due to friction resulting in stretching with loading in normal and tangential direction. The loading of a section of the sheet in figure 1.3a pertaining to region 1 in figure 1.2 is zoomed in and shown in figure 1.3b. At the beginning of loading, the surface of the tool is relatively smooth compared to the surface of the work-piece. As the flat tool comes in contact with the asperities of the softer work-piece, it flattens the rough surface of the work-piece into plateaus and valleys as shown in figure 1.3c. The real area of contact between the tool and the sheet A_r at the end of normal loading is then calculated according to the available micro-contact models. As the sliding and stretching begins, the effect of bulk straining is included with normal loading in the calculation of the real area of contact. The lubricant in the valleys of the work-piece possibly generates potentially a hydrostatic pressure in response to the normal loading of the tool and hydrodynamic pressure in response to sliding of the tool. Also the hydrostatic and hydrodynamic pressures are included in the calculation of the real area of contact in the mixed lubrication (ML) model as explained in [12]. The section of the contact between the seemingly flat, smooth tool and the flattened sheet (plateaus) in figure 1.3c, given by the calculated area of contact at the meso-scale is zoomed in and shown in figure 1.3d. Now, the asperities of the rigid tool are in contact with the flattened plateaus of the sheet. In the presence of a lubricant, the asperities of the tool are separated from the surface of the sheet by a lubricant boundary layer. Loading and sliding of the work-piece now results in ploughing of the tool asperities through the soft sheet resulting in friction and possibly abrasive wear in boundary lubrication (BL) regime. The coefficient of friction in the boundary lubrication regime μ_{BL} is calculated based on a micro-ploughing model. The friction due to shearing of the lubricant film in the hydrodynamic lubrication regime μ_{FL} is calculated based on the hydrodynamic lubrication (FL) model. The fractional contact area $\bar{A}$ is given as the ratio between the real contact area and the nominal contact area of the tool and the work-piece. The coefficients of friction μ_{BL} and μ_{HL} are multiplied with the corresponding fractional contact areas $\bar{A}$ and $1 - \bar{A}$ and summed to calculate the total coefficient of friction μ at the macro-scale in equation 1.1.

$$\mu = \mu_{BL}\bar{A} + (1 - \bar{A})\mu_{HL} \tag{1.1}$$

1.3. Towards understanding of friction in deep-drawing.

Modelling of friction in a deep-drawing process has been the topic research over the last few decades. Considering deep-drawing as a lubricated process, both boundary lubrication, mixed

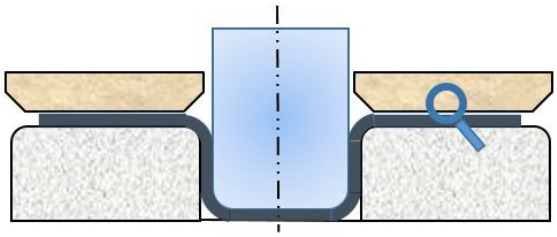

(a) Schematic of deep drawing at macro-scale.

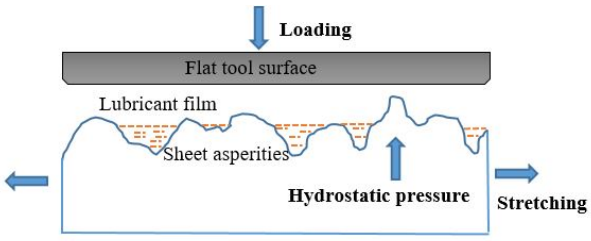

(b) Loading and stretching of contact.

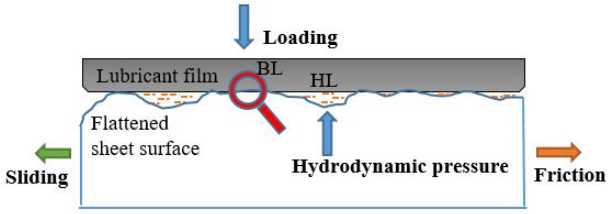

(c) Schematic of contact at meso-scale.

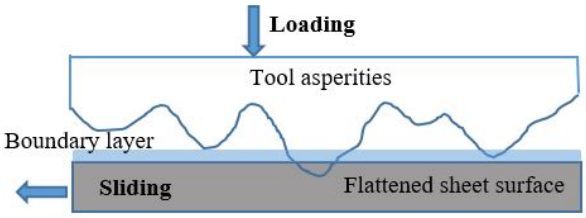

(d) Ploughing of micro-contacts.

Figure 1.3: Processes in deep-drawing at different scales

lubrication and full film lubrication regimes can be present in deep-drawing, depending on the contact and operating conditions [13]. To calculate the total friction force in deep-drawing, it is important to also model the contact between the tool and work-piece. Two important length-scales can be determined in a typical tool/sheet contact, namely the micro-and macro-scale. It is also important to identify the factors contributing to friction at the micro- and macro-contact scales in deep-drawing. Some of the initial work in understanding friction and lubrication in sheet metal forming was done by Wilson [14] who categorized the lubrication regimes occurring at various locations of a sheet metal during forming (deep-drawing) process into thin film, boundary and mixed lubrication. In these studies, the effect of surface roughness and lubricant film thickness over different regions of the sheet metal on the lubrication regime was highlighted.

Friction and contact in the boundary lubrication regime was further analyzed in [15] by modelling loading and flattening of wedge-shaped sheet asperities by a flat tool. The asperity deformation models in [15] and [16] used plane stress and plane strain approximations utilizing the upper-bound method to compute the real area of contact and effective hardness of the substrate. Friction models for boundary and the thin film lubrication regime, were coupled to finite element computation of nodal pressure and strains for sheet metal forming in [17]. The effect of bulk straining, loading and sliding on friction in sheet metals, both coated and uncoated and laminates with different tool roughness and lubricants was studied at the laboratory scale using a test set-up designed in [18]. With the help of the sheet metal forming experiments for various sheets materials and loading parameters, the effect of tool roughness and mechanical properties of the coated (galvanized and galvannealed) sheet was highlighted in [18]. For numerical simulation of forming processes, computational tool [19, 20, 21, 22] have been developed and continuously improved to model large deformations in deep-drawing process.

The effect of operating conditions on shearing of the interface and tool surface roughness (asperity geometry) on ploughing of the substrate in boundary lubrication was studied by [11]. Based on [15] and [16], [11] developed a contact model for calculating the real contact area for loading

of sheets having arbitrary shaped asperities by a flat tool. The contact model developed in [11], was extended in [23], by accounting for strain hardening and inter-asperity shearing during flattening and rising of asperities due to loading and bulk straining of the sheet. The resulting change in surface roughness during loading was calculated using energy and volume conservation laws. The contact model in [23] included summit based stochastic roughness parameters, which was earlier determined from the height of surface points.

The effect of various coatings on blank holder and punch-tools and sheet metals in deep-drawing was studied in [24]. The material behaviour of the coated tool and coated sheets has been characterized as an input parameter to model the contact between a coated tool and a coated sheet. In doing so, the work highlights the roughness properties of the tool where rigid asperities of the tool plough through the flattened plateaus on the sheet. The ploughing of the sheet combined with adhesion between the tool and sheet can result in wear due to material transfer (galling) [24] in the case of e.g. aluminum or zinc coated sheet material. The summit height distribution of the tool surface has been used and updated considering the material transfer. The contact between asperity summits on the surface of the tool and flattened sheet, has been mapped as a collection of elliptic contact patches with varying size and orientation as per the contact model of [25]. The contact patches have been characterized as a height matrix of pixels obtained from processing of the image observed under a digital microscope in [26]. Further understanding of the effect of tool roughness (asperity micro-geometry) in modelling of ploughing friction and wear can be found in the work done on the effect of the size and orientation relative to the sliding direction of an elliptic-paraboloid asperity on friction and wear volume in [27], [28] and [29]. Both [30] and [31] have focused on modelling the contact of a sliding rough tool through a flatted sheet and the resulting effect of asperity micro-geometry on abrasive wear. Later, in [32], the mapped geometry of the contacting asperity summits has been used to model friction and material transfer in ploughing of hexagonal-pyramid shaped asperities through a plastically deforming substrate.

The sliding between two surfaces loaded in boundary lubrication results in ploughing of the softer surface by the asperities of the harder surface. Friction forces and wear volumes in ploughing of a soft, smooth substrate (sheet) by rigid (tool) asperities has been modelled using slip line field theory by [33]. The friction in ploughing takes into account the resistance to sliding due to plastic deformation of the substrate and shearing of the interface as explained in [34]. The slip-line field solutions for friction have been extended to spherical asperities in [35] by using the interfacial shear strength and the ratio between the ploughing depth and contact radius, defined as 'degree of penetration'. In the work of [36] and [31], the 'degree of penetration' has also been modified for elliptical asperities and implemented in the calculation of friction in ploughing for various values of geometrical parameters of asperities mapped from the tool roughness. The effect of loading and reloading on the computing the contact and friction in sliding of a single-asperity has been modelled in [37] and extended to the calculation of contact and friction on macro-scale.

1.4. Optimizing friction in deep-drawing

The algorithm to model and optimize the friction in deep-drawing of zinc coated sheets has been laid out in figure 1.4. It can be seen that development of a micro-friction model is essential in modelling friction at a macro-scale in deep-drawing. Modelling friction at the micro-scale is done with the help of micro-scale ploughing model and contact model. Furthermore, the material behaviour and the interfacial shear strength are measured from experiments and fed

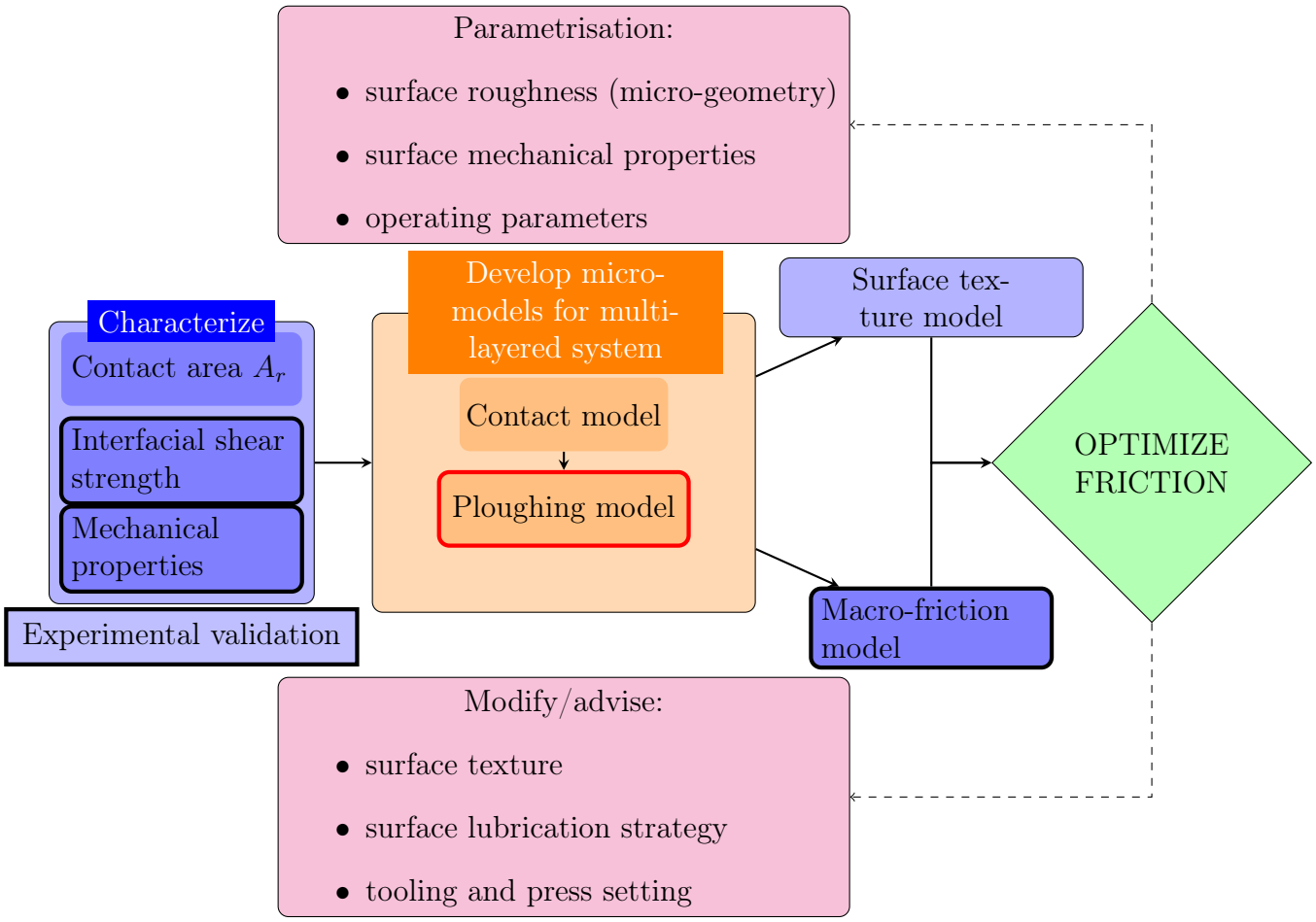

Figure 1.4: Layout of the approach towards modelling of friction in deep-drawing (highlighted steps are included in the current micro-scale ploughing model).

as input into the micro-friction model. The developed ploughing model will be validated with the ploughing experiments for different material and operating parameters. The friction force obtained from the ploughing model in combination with the contact model will be used to compute the over all friction force as per equation 1.1. The optimal friction is obtained by designing the surface texture to realize a certain desired friction level.

As shown in figure 1.4, a multi-scale friction modelling approach has been adapted. The research project has been divided into two parts. The current thesis work aims to build the friction model at micro-scale (see figure 1.3d) and characterize the relevant material behaviour at roughness scale. The coefficient of friction in the boundary lubrication regime μ_{BL}, mainly attributed to the ploughing of the flattened substrate surface by the rigid tool asperities, is modelled using a micro-ploughing model. The development of the macro-friction model and the contact model will be covered in the thesis work of another PhD student [38]. The friction in the full film lubrication regime, attributed to the hydrodynamic and hydrostatic effects of the lubricant film in the tool-sheet contact μ_{FL} will be modelled in the macro-friction model is not a part of the current research. The contact model calculating the ratio of real area of contact to total nominal contact area A_r between the tool and the sheet is also done at macro level and is also not a part of the current research. The current research focuses on development of the ploughing model for multi-layer system with the help of experimental characterization of the mechanical properties of the sheets and interfaces and validation of the model results, as encircled and highlighted in figure 1.4.

1.5. Problem definition

In order to have an efficient and flexible deep-drawing process, with the ability to manufacture new products, it is critical to have a numerical tool that can predict the required friction forces for the given product design. It is well-understood from section 1.3 that the friction force varies locally based on the contact conditions at different scales. The friction force in boundary lubrication results from ploughing of the tool asperities through the surface of the sheet metal as shown on micro-scale in 1.3. The geometry of the tool asperities have shown to affect the ploughing behaviour in the work of Bowden and Tabor [34] and Challen and Oxley [33]. The geometry of the tool asperities is mapped by modelling the tool-flattened sheet contact as shown in figure 1.5 and incorporated in the ploughing model for calculation of friction as given in figure 1.4.

The initial statistical contact models by [39] have characterized surface roughness using spherical asperities of varying sizes. However, the characterization of the contact between a hard, rough surface in contact with a smooth surface has been done by describing the contact as interacting contact patches in [25]. These contact patches have been described as a connected height matrix of pixels mapped from asperity image-processing as shown in figure 1.5. Based on the contact patch geometry and height distribution, the asperity geometry has been mapped as elliptic-paraboloid or ellipsoid of varying sizes and orientations in [26]. The contact between (anisotropic) rough surfaces have also been characterized using elliptic-paraboloids in [40]. The size of the elliptic base of the asperity is parameterized by the size of the major axis a and minor axis b of the elliptic contact patch. The orientation of the asperity is given by the angle β the major axis of the contact patch makes relative to the sliding velocity vector v_s. The height of the asperity, as well as the radii of curvature R_x and R_y are obtained from the height distribution of the connecting pixels [26].

The friction force acting on an asperity has been shown to be a function of the angle γ, which is the tangent of the asperity-substrate contact relative to the sliding velocity v_s [33], see figure 1.5. For three dimensional asperities, the angle γ is expressed in terms of the ratio of the penetration depth and contact length in the sliding direction i.e. the degree of penetration of the asperity [35]. Initial work on modelling the contact and wear for sliding of elliptic-paraboloid asperities through a metallic substrate in terms of their degree of penetration was done in Masen et al. [30] and [31]. The forces acting on an elliptic-paraboloid asperity sliding through a rigid-plastic substrate was computed by approximating a hexagonal pyramid to an elliptic-paraboloid shaped asperity in [28] and [32]. Here the friction forces acting on the face of the hexagonal pyramid computed from forces due to the contact pressure generating from the plastic deformation of the substrate and the force due to shearing of the interface.

Hence the development of a single-asperity ploughing model is critical to the modelling of friction in deep drawing. The available models for contact between tool and sheet have tool asperities characterized as elliptic-paraboloids with varying size and orientations. The developed ploughing model must include elliptic asperities to account for the anisotropy in the micro-geometry of the tool surface roughness. The ploughed sheets are zinc coated steel sheets. The zinc coating in the sheet is known to have anisotropic material behaviour resulting from the orientation of the zinc grains [41, 42] and temper rolling of the sheets with textured rolls prior to deep-drawing. Therefore, it is important to include anisotropic behaviour in the ploughing model for zinc coatings. As a starting point it can be summarized that, in order to compute

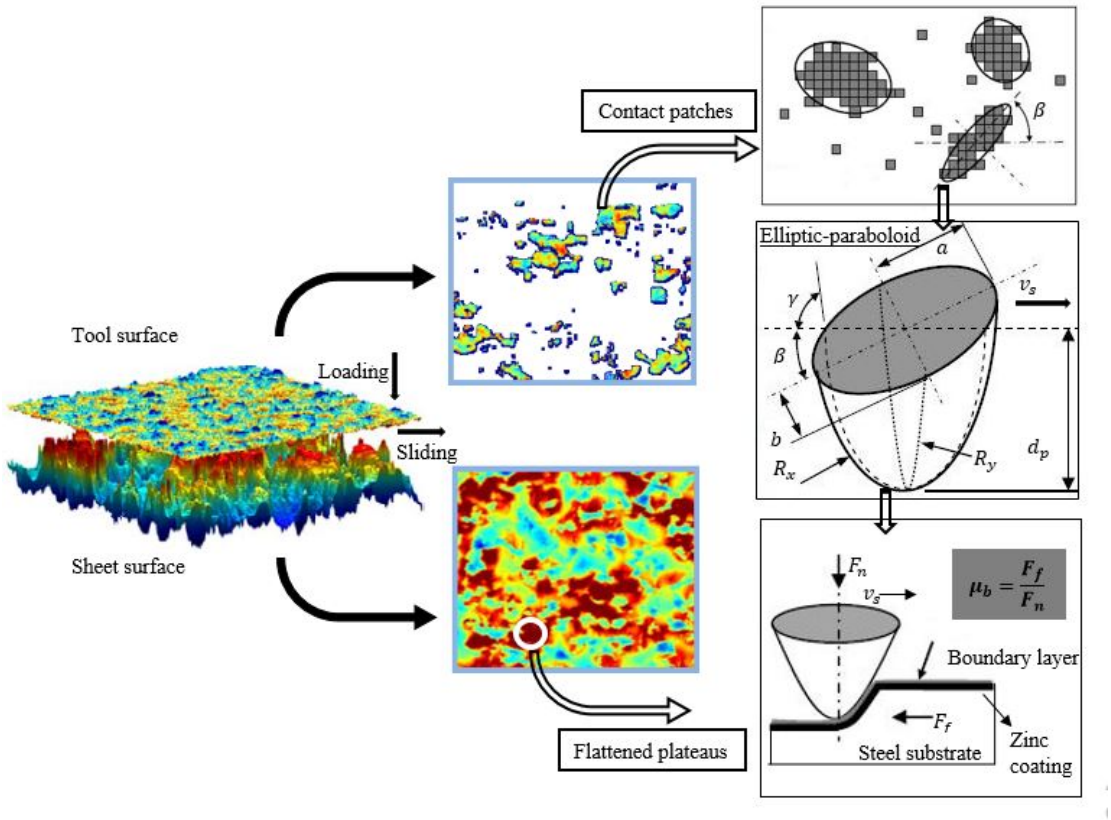

Figure 1.5: Ploughing by an elliptic-paraboloid shaped asperity resulting from loading and sliding of tool against sheet [29, 26].

the friction in boundary lubrication in deep-drawing the current research must:

- develop single-asperity ploughing model which,
- includes an elliptical asperity geometry where the asperities can have different orientations with respect to the sliding velocity vector and
- models anisotropic material behaviour in the zinc coating

1.6. Research scope

In can be concluded that it is critical to have a robust micro-ploughing model in order to model friction in deep-drawing. The development of a single asperity ploughing model is fundamental to develop a multi-asperity ploughing model. Hence, different aspects in single-asperity ploughing model are analyzed. Previous studies have shown that modelling of ploughing of hard tool asperities through a metallic sheet substrate is complex due to the large scale localized plastic deformation. Further, the shear strength of the interfacial boundary layer is important to model friction in ploughing. Taking into account the industrial background of the current work and the understanding of the friction in ploughing from section 1.2, the factors that have been identified to have possible influence on ploughing behaviour of a single asperity sliding through a coated metallic sheet are shown in figure 1.6 and listed as:

- Operating conditions: contact pressure, temperature and sliding velocity.

- Surface texture of the tool: length of the axes of the elliptical asperity, height of the asperity, angle of orientation of the asperity with respect to sliding velocity vector.
- Stiffness of the tool asperity.
- Adhesion between the tool and the (coated) substrate.
- Surface texture of the substrate: texture size, depth and orientation.
- Shear strength of the interfacial boundary layer.
- Stiffness of the (coated) substrate: elastic moduli, Poisson's ratios of the coating and the substrate.
- Yield properties of the (coated) substrate: yield strength, hardness of the coating and the substrate.
- Degree of anisotropy in the (coated) substrate: Anisotropic yield criteria constants (Longitudinal and transverse strain ratios), Anisotropic hardening constants, Stiffness matrix constants.
- Thickness of the coating in the coated substrate.

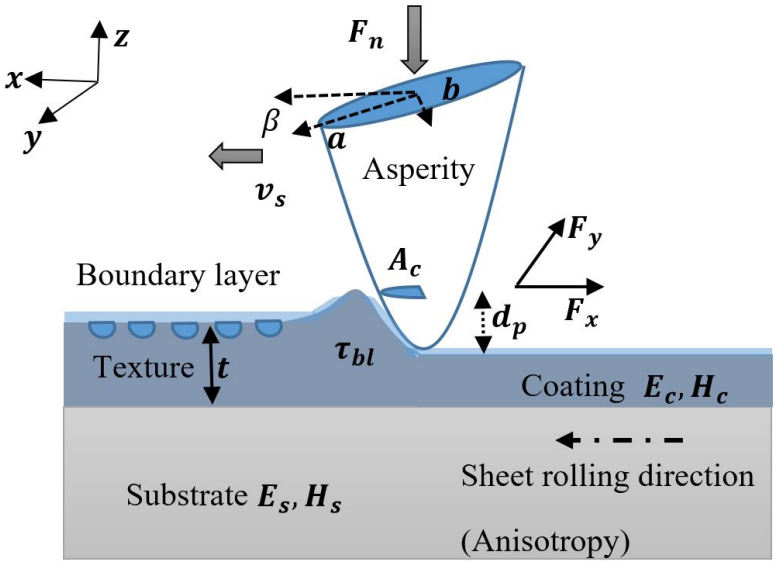

Figure 1.6: The tribological system in single-asperity sliding contact showing the factors affecting friction in ploughing.

Based on the defined problem, the industrial relevance and the possible factors affecting friction in ploughing, the scope of the current research includes the following goals:

- The development of a numerical model for an elliptical asperity ploughing through zinc coated steel sheets to compute friction forces and ploughed profile on the substrate.
- To validate the developed ploughing model with ploughing experiments using both zinc coated and uncoated steel sheets under varying loading conditions, interfacial shear strengths and asperity geometries.
- To analyze of effect of the aforementioned parameters in the tribological system (see figure 1.6) for a single-asperity sliding on the friction force and wear volume in ploughing.

1.7. Outline of the thesis

The thesis has been designed into the following chapters. Chapter 2, titled 'Theoretical background' provides and overview of the relevant literature on single-asperity ploughing models and the relevant material characterization for the development of the aimed ploughing model. The gaps in the available models and characterization methods are highlighted leading up to the setting of the objective and outline of the current research. The main body of the thesis is presented in Chapter 3, 4 and 5. Chapter 3, titled 'Development of single asperity ploughing models' explains the development of the Material Point Method (MPM) based numerical ploughing model. The chapter also explains steps in calculation of forces acting on an elliptical asperity sliding through a rigid-plastic substrate with the help of an analytical model. Chapter 4, titled 'Experimental procedure and characterization' explains preparation of tool and sheet specimens and experimental set-ups for both experimental characterization of test specimen and experimental validation of the numerical ploughing simulation. The characterization of the shear strength of the interfaces and the yield curve and yield function for both coated and uncoated sheets are further explained in chapter 4. The friction and wear results from the ploughing simulation are presented in chapter 5 titled 'Results and discussion'. The numerical results are validated with experiments for both zinc coated and uncoated steel sheets. The numerical results are also compared with the results obtained from the analytical model for an ideal (rigid-) plastic material model. Chapter 5 also highlights and discusses the effect of geometrical parameters of the asperity such as shape, size and orientation with respect to the sliding direction, interfacial shear strength, coating thickness and anisotropy on friction and wear in ploughing. Finally the main conclusions and recommendations for future research are given in chapter 6.

Chapter 2

Theoretical background

The relevant background on modelling of friction in ploughing has been summarized in the current chapter. Friction in ploughing has been attributed to the plastic deformation of the substrate and the shearing of the interface. To model the deformation of the substrate, the available studies on characterization of the material behaviour of the substrate has been highlighted. Likewise, the studies on measurement of the interfacial shear strength have been summarized to model the shearing of the interface. Both analytical and numerical models available to compute friction in ploughing have been studied. Based on the limitations and advantages of the available numerical and mathematical tools, the approach towards modelling ploughing will be motivated. The gaps in characterization techniques for material properties of zinc coated steel sheets and the shear strength of interfaces have also been highlighted while setting the objectives of the work done in the current dissertation. To reach the research aims, both numerical and analytical approaches are combined to model the ploughing behaviour of elliptical asperities. The combined approach will enable modelling a computationally efficient and physically accurate single-asperity ploughing model with the possibility to apply the model in a multi-asperity model.

2.1. Literature review: Single-asperity ploughing model

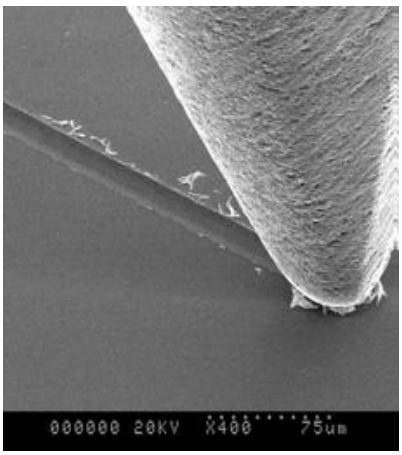

(a) Ploughing by a single-asperity as seen under SEM at 400x magnification [27].

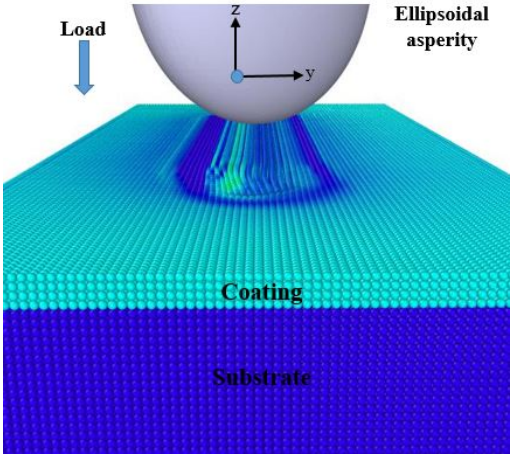

(b) Ploughing model by an elliptical asperity of a coated substrate.

Figure 2.1: Single-asperity ploughing.

Ploughing is defined as the displacement of substrate material from the path of an rigid, sliding asperity, without any actual removal of material, (see figure 2.1a). A ploughing model is critical to the understanding of friction and wear (deformation). The simulation of ploughing by an elliptical asperity through a coated substrate has been illustrated in figure 2.1b. In literature, both analytical models and numerical simulations have been developed to study the ploughing behaviour of rigid asperities on soft/smooth substrates. Generally, analytical methods provide fast solutions for the coefficient of friction and wear volume with simplified assumptions of ideal (elastic-plastic) material behaviour. Furthermore, by varying the geometrical parameters for a single asperity each asperity geometry in the analytical model can be taken as a unit event and be used to develop a multi-asperity ploughing model. However, real materials have complex mechanical and interfacial behaviour. Hence, numerical models are required to simulate ploughing of real materials and provide a deeper insight into the effects of different factors contributing to the friction and wear in single-asperity sliding. Generally, accounting for a more realistic representation of ploughing numerical models can result at high computational cost. The accuracy of the model in replicating ploughing behaviour should be tested by physical validation of the model results using the results obtained from laboratory or industrial scale experiments.

The friction F_f in sliding of a rigid asperity through a smooth deformable substrate has been attributed to the (1) force due to the contact stress resulting in deformation of the substrate F_{pl} and (2) force due to the shear stress at the interface F_{sh} [34] as shown in equation 2.1. In order to compute the force due to deformation of the substrate, it is important to characterize the material behaviour of the substrate. Likewise, in order to compute the force due to shearing of the interface, the interfacial shear strength must be determined. The characterization techniques for material behaviour and interfacial shear strength, specific to coated metals, available in the literature have been studied in the subsequent subsection 2.1.1 and 2.1.2. Also, the available analytical methods and numerical tools to model ploughing by a single-asperity in metallic substrates has been discussed in subsection 2.1.3 and 2.1.4. In choosing the numerical tools for the current research, the scope of the the discussed methods to model ploughing by

an elliptical asperity in an anisotropic-coated system has been focused.

$$\vec{F_f} = \vec{F_{pl}} + \vec{F_{sh}} \tag{2.1}$$

2.1.1. Material characterization

In sheet metal forming operations like deep-drawing, the steel sheets (work-pieces) are made by the process of cold rolling. Further, the steel sheets are hot dip-galvanized to provide them with zinc coating. Typically, the zinc-coated sheets are temper rolled (commonly called skin-passing) to provide them with the desired surface texture and flatness. The rolling process results in thickness reduction and directional strain hardening of the sheet metals. Rolling also introduces a deformation texture along the rolling, transverse and normal directions (orthogonal) which result in an induced anisotropy in the plastic deformation of the sheets (elastic deformation is negligible in sheet metal forming). The zinc grains in the coating are formed as pancakes of 100 μm size and 10 μm thick [41]. The difference in the size and amount of zinc along the thickness and surface plane could also be attributed to the anisotropy in the mechanical properties zinc coatings. Additional anisotropy is inherent to the zinc grains due to their *hcp* (hexagonal closed pack) crystal structure. The variation in their critical resolved shear stress (CRSS) in the slip and twinning systems of the *hcp* zinc crystal structure results in basal slip and twinning being the predominant deformation modes in zinc coating [43]. The preferential deformation mode and the dissimilar hardening of the slip systems result in anisotropy in elasticity, yielding and hardening in zinc [43, 44] .

Some of the initial work in characterizing the elastic moduli of zinc crystals was done in [42] by the use of both static (longitudinal tension test) and dynamic (composite oscillator method) methods. The elastic, shear and bulk moduli and the Poisson's ratio of zinc crystals were reviewed and listed in [45]. Later, the deformation properties of multi-crystalline zinc in zinc coated steel were studied with the help of a tensile test and EBSD (electron back-scatter diffraction) technique. The critical resolved shear stress (CRSS) and the hardening parameters for the different slip systems for the zinc coating were identified and the evolution of the CRSS with plastic slip was given by the hardening law in [43] and [44]. The deformation and damage modes of both the temper rolled and non-temper rolled zinc coating resulting from the dominant slip planes in the deformed and cracked grains were analyzed using FE calculations and EBSD in [43] and [46]. The interfacial fracture and the coating-substrate adhesion in zinc coatings was further analyzed for various grain sizes and grain orientations by experiments and FE calculations in [47] and [48]. A strain-hardening law, given in equation 2.2a and 2.2b, for the zinc coatings in [47] used averaged, nano-indentation based material parameters given in table 2.1 [41]. For the isotropic steel substrate, the Bergström-van Liempt material model (hardening law) can be used to compute the yield stress as a function of the strain, strain rate and working temperature [49].

$$\sigma = E\epsilon \quad \forall \epsilon \leq \epsilon_y \tag{2.2a}$$

$$\sigma = \sigma_y \Big(1 + \frac{E}{\sigma_y}(\epsilon - \epsilon_y)\Big)^n \quad \forall \epsilon > \epsilon_y \tag{2.2b}$$

The nano-indentation of the zinc coating was done for zinc grains with different indentation angles α_i (grain orientation) which is the angle between the indentation normal and c-axis of the hexagonal zinc grains as shown in figure 2.2a. The elastic modulus E_c and hardness H_c

Table 2.1: Macroscopic properties of the zinc coating in equation 2.2a and 2.2b [41, 50, 47].

Property	Value (range)
E_c	70 GPa
σ_y	75 MPa
n	0.14
H_c	1.1 GPa
ν_c	0.3

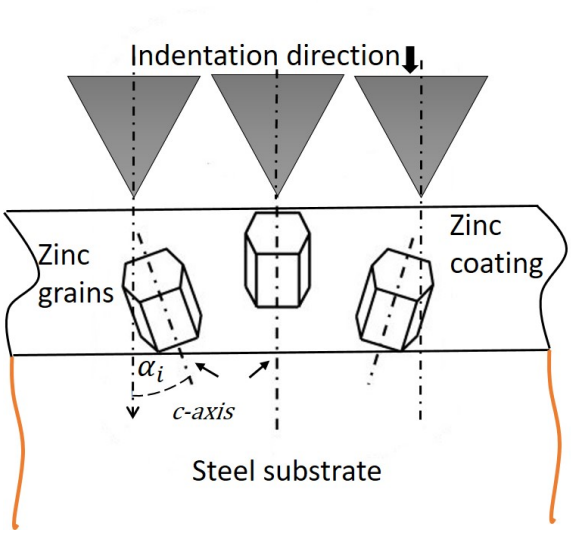

(a) Indentation of zinc grains at various α_i.

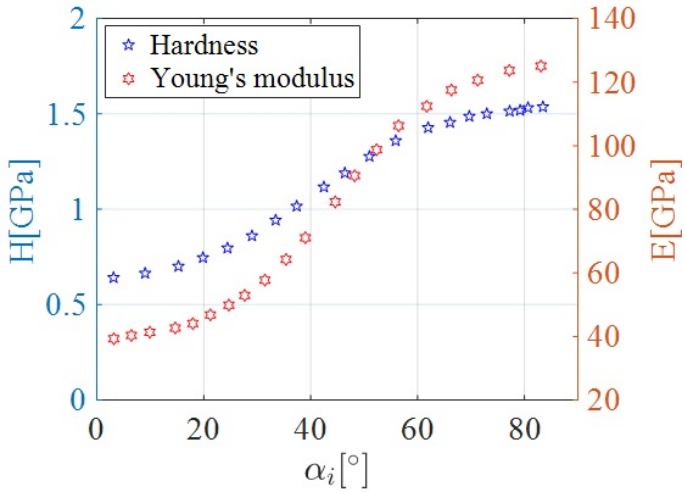

(b) Variation of hardness and elastic modulus with α_i [41].

Figure 2.2: Effect of orientation of zinc grain on elastic modulus and hardness.

of the zinc grains were plotted as a function of the orientation of the crystal as shown in 2.2b [41]. The variation in E_c and H_c with respect to α_i have been listed in table 2.2. Based on the relationship between the elastic modulus and the crystallographic orientation of the crystal, given in equation 2.3, the independent elastic compliance $s_{11}, s_{12}, s_{13}, s_{33}$ and s_{44} were obtained and listed in table 2.2. The elastic compliance can thus be used to obtain the Poisson's ratio and Young's moduli and hence the elasticity matrix of poly-crystalline zinc [41] and [50]. Using the elasticity matrix obtained by nano-indentation, the anisotropy in the elastic deformation in the zinc coating can be modelled by decomposition of total stress into hydrostatic and deviatoric components as shown in [51].

$$1/E_\alpha = s_{11}\sin^4\alpha + (2s_{13} + s_{44})\sin^2\alpha\cos^2\alpha + s_{33}\cos^4\alpha \tag{2.3}$$

Modelling of plastic deformation in a sheet requires knowledge of its yield criteria and hardening function. The initiation of yielding in a slip system is given by its CRSS which are summarized for zinc crystals in [44]. The evolution of CRSS with plastic slip is used to represent the hardening of the zinc in [44]. However, for large scale (anisotropic) plastic deformation occurring at both micro-(asperity ploughing) and macro-scale in deep-drawing, the yield criteria and hardening laws must be based on continuum plasticity rather than crystal plasticity as the deformation occurs over multiple grains in the coated sheet. In modelling the plastic deformation in an isotropic material, the von Mises yield criteria is commonly used. On the other hand, Hill's yield criteria [52] is used for modelling of plastic deformation of an anisotropic

Table 2.2: Variation in mechanical properties of zinc grain as a function of the angle of indentation α_i and elastic compliance based on equation 2.3 [41].

Elastic compliance	Value $[10^{-13} m^2/N]$
s_{11}	81.7
s_{12}	5.0
s_{13}	60.7
s_{33}	259
s_{44}	263
Property	**Value (range)**
α_i	$3^o - 84^o$
E	39 - 124 GPa
H	0.6 - 1.54 GPa
$\bar{\nu}$	0.23 - 0.34

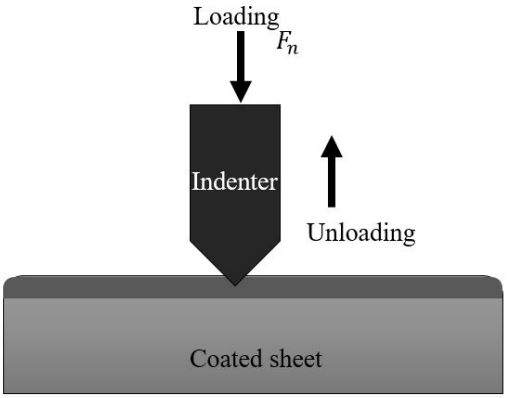

(a) Schematic of an indentation measurement.

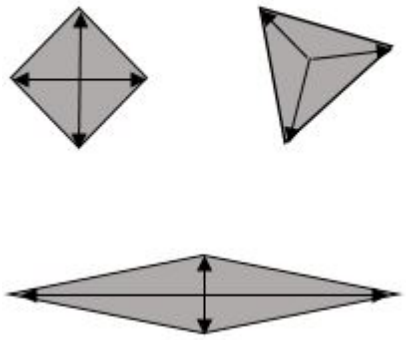

(b) Vickers (top-left), Berkovich (top-right) and Knoop (bottom) indentation marks showing diagonal lengths.

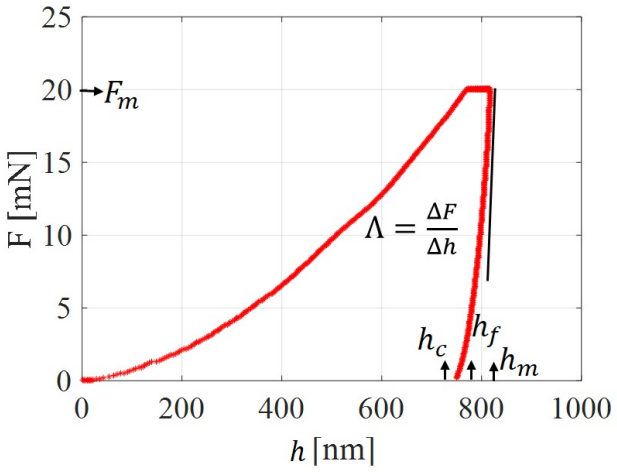

(c) Load-depth plot from nano-indentation.

Figure 2.3: Measurement of hardness using (Knoop) indentation.

material. Recently, the Vegter yield criterion [53] has also been used for plane stress situations in sheet metals. For determining the parameters of the anisotropic yield criteria, and hence the yield loci, uniaxial, equi-biaxial, pure shear and plane strain tests are typically performed on bulk specimens. However, determination of the anisotropic yield parameters for a coated

system using bulk loading tests is challenging due to the difficulty of separating the anisotropy in the thin film from the anisotropy in the substrate due to the large difference in properties of the coating and bulk material. Indentation based methods are generally able to measure the mechanical properties of the (coated) surfaces as shown in figure 2.3a. Nano-indentation based measurement have been able to calculate the stiffness and hardness of the materials from the load-depth curves as shown in figure 2.3c. The stiffness Λ is given as the slope of the unloading curve which extrapolates to the depth h_f. The maximum load F_m correspond to maximum depth h_m. The hardness is obtained from the maximum load and contact depth h_c. Nano-indentation in combination with orientation imaging microscopy (OIM) has been used to characterize the anisotropy in zinc crystals. The hardness and Young's modulus have been plotted for various crystallographic orientations on the surface of the zinc coating using nano-indentation measurements in [41] and [50]. The measurement of anisotropic plastic behaviour using micro-hardness indentations by indenters such as Vickers and Berkovich (see figure 2.3b) is challenging as the directionality in the material properties is averaged out by the symmetric geometry of the indenters. Hence, in characterizing the yield criteria of highly anisotropic sheet metals and alloys, the asymmetric Knoop indenter has been commonly used [54, 55, 56], although not at all for coatings or in a nano-indentation set-up.

In using the Knoop hardness number (KHN) to plot the yield curve of a specimen, it is assumed that the ratio of deviatoric stress resulting in plastic flow along the diagonals of the indenter is proportional to the ratio of lengths of the diagonals of the Knoop indenter [54]. By aligning either of the diagonal of the indenter along the orthogonal axis, i.e. rolling direction, transverse direction and normal directions, six Knoop indentations correspond to six points on the deviatoric stress plane. The KHN data has been used to plot the yield loci on the plane-stress plane by using strain and stress ratios derived using the Lévy-mises and the volume constancy equations. The KHN is equated with the equivalent yield stress in the yield criteria to obtain the coordinates on the plane-stress plane corresponding to the indentation in [55]. The KHN-based yield loci have been validated to good agreement with the conventional yield loci at 0.01 and 0.1 strain in [55] and [56] for various titanium and magnesium alloys respectively. Although KHN-based yield loci have also not been accurate for highly anisotropic materials that have a difference in compressive and tensile yield stresses at low strains [56], it has shown considerable agreement with the conventional bulk test-based yield loci for most materials [57, 58, 59]. Furthermore, the stress ratios for all six indentations were corrected by taking the degree of anisotropy into account [56]. Recently, a Knoop indenter has been used to perform depth-sensing nano-indentations on various materials, [60]. However, due to the axi-symmetric geometry of the indenter calculation of stiffness from the unloading curve using the Oliver and Pharr method [61] is challenging. The hardness is best calculated from the maximum depth in the load-depth curve or size of the indentation imprint as shown in figure 2.3b and 2.3c. Thus far the parameters of the anisotropic yield criteria have been best evaluated by Knoop indentation. However, an extension of the Knoop indentation technique to evaluate the yield criteria for anisotropic (zinc) coatings is not available in literature and has to be developed.

2.1.2. Interfacial shear strength characterization

In the presence of a lubricant at the interface, the lubricant molecules attaches itself to the metallic surface forming a boundary layer. At low contact pressure, for non-polar lubricants and inactive metallic surface, boundary layer is formed through physical adsorption of lubricant molecules to the surface due to Van der Walls interaction as shown in figure 2.4a. At high contact pressure, for polar lubricants and an activated metallic substrate, the (polar) functional

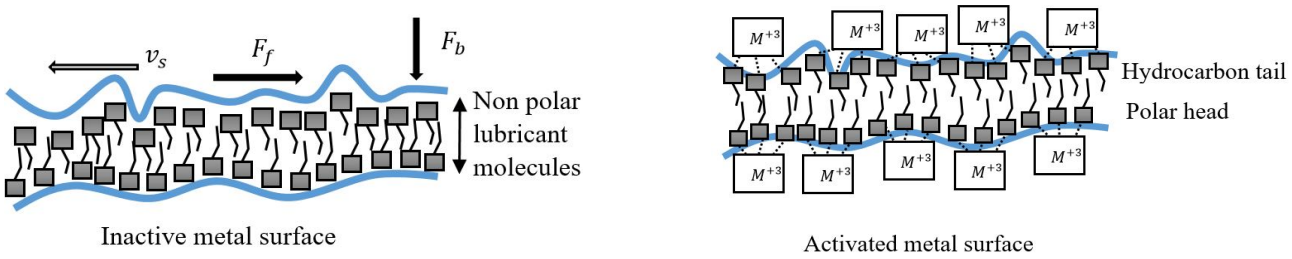

(a) Physical adsorption.

(b) Chemical adsorption.

Figure 2.4: Mechanisms for boundary layer formation [34].

group of the lubricant molecule attaches it self to the metallic ions on the surface to form the boundary layer through chemical reaction and adsorption as shown in figure 2.4b [62, 63, 64]. The tip of the lubricant molecule adsorbed on the substrate along with its long chain hydrocarbon tail form vertically adsorbed mono-layers at the interface called 'boundary layers' which prevent direct metal-to-metal contact. The shear strength of the boundary layers has been shown to depend on the contact pressure, sliding velocity and contact temperature [65]. The boundary layer shear strength has been expressed as the resistance to movement of dislocations in the Eyring's model [66] which is a function of the aforementioned parameters. By doing experiments to measure the boundary layer shear strength of lubricated (coated) glass and mica for varying loads, sliding velocity and temperature and fitting the expressions derived from [66], empirical relations of a boundary layer shear strength have been derived, in [65], [67] and [68].

The effect of contact pressure, sliding velocity, temperature and number of monolayers in the boundary layer on the boundary layer shear strength τ_b from various studies has been summarized in [11]. Power law relationships between the boundary layer shear strength and the nominal contact pressure and the boundary layer shear strength and the sliding velocity were proposed. Also the boundary layer shear strength has been expressed as an exponential function of the temperature. Combining all these relations, a general empirical-theoretical expression for τ_b as function of P, T and v_s is given in equation 2.4a in terms of constants $\tau_0, n_0, \bar{R}, Q$ and q. Here $\bar{R}$ is the ideal gas constant. By taking the anti-log on both sides, equation 2.4a can be deduced, see equation 2.4b. The boundary layer shear strength for metallic contact lubricated with stearic acid was studied in [69] using aluminum and gold coated glass. The boundary layer shear strength for deep-drawing steel sheet lubricated with forming oil was first measured using a lubricated line contact in [29] and expressed to be a power-law relationship with the nominal contact pressure (see equation 2.4c). The experimental techniques to measure the boundary layer shear strength of a metallic contact lubricated with forming oils for (zinc) coated sheets still remains unexplored.

$$\ln \tau_b = \tau_0 \ln v_s + \frac{Q}{\bar{R}T} + n_0 \ln P + q \tag{2.4a}$$

$$\tau_b = C P^{n_p} v_s^{n_v} \exp\left(\frac{Q}{\bar{R}T}\right) \tag{2.4b}$$

$$\tau_b = 0.96 P^{0.88} \tag{2.4c}$$

2.1.3. Analytical ploughing models

Ploughing friction has first been analyzed analytically in [34] where a spade, sphere and a cylinder were ploughed through a smooth metallic substrate. Later [33] proposed steady state solutions for the coefficient of friction and wear rate based on slip-line field theory for deformation of two-dimensional wedge shaped asperities as shown in figure 2.5. The abrasive wear due to deformation of the asperities was classified into the three regimes, i.e. ploughing, cutting and wedging. As further explained in [35], the material of the substrate was displaced from the sliding path/wear track of the rigid asperity in the ploughing wear mode, the material of the substrate was removed as chips in the cutting wear mode and the material of the substrate was lumped in front of the sliding asperity as wedges in the wedging wear mode with possible transfer to the surface of the asperity on unloading. The expressions for the coefficient of friction for two dimensional wedge shaped asperities were extended to three dimensional spherical asperities, as listed in equations 2.5a-2.5c. The coefficient of friction in cutting μ_C, wedging μ_W and ploughing μ_P is expressed as a function of the degree of penetration D_p of the asperity into the substrate and the interfacial friction factor f. The 'interfacial friction factor' is the ratio of the boundary layer shear strength τ_b to the bulk shear strength κ of the substrate. The 'degree of penetration', defined as the ratio of the depth of penetration to the contact length of the asperity sliding through the substrate, is a function of the asperity geometry (angle γ shown in figure 2.5).

$$\mu_C = \tan\gamma - \frac{\pi}{4} + \frac{\arccos f}{2} \tag{2.5a}$$

$$\mu_W = \frac{(1 - 2\sin A_w + \sqrt{1-f^2})\sin\gamma + f\cos\gamma}{(1 - 2\sin A_w + \sqrt{1-f^2})\cos\gamma - f\sin\gamma} \tag{2.5b}$$

$$\mu_P = \frac{B_p \sin\gamma + \cos(\arccos f - \gamma)}{B_p \cos\gamma + \sin(\arccos f - \gamma)} \tag{2.5c}$$

where, for 2D wedge-shaped asperities,

$$\tan\gamma = \frac{h}{a}$$

and for (3D) spherical asperities

$$\frac{1-\cos\gamma}{\sin\gamma} = \frac{d}{a} = D_p$$

$$f = \frac{\tau_b}{\kappa}$$

$$A_w = \gamma - \frac{\pi}{4} - \frac{\arccos f}{2} - 2\gamma - \arcsin\left(\frac{\sin\gamma}{\sqrt{1-f^2}}\right)$$

$$B_p = 1 + \frac{\pi}{2} + \arccos f - 2\gamma - 2\arcsin\left(\frac{\sin\gamma}{\sqrt{1-f^2}}\right)$$

Slip line field solutions for plane stress and plain strain boundary value problems for yielding of rigid-plastic solids have also been commonly used for modelling the coefficient of friction for two-dimensional geometries. Slip-lines have been constructed by use of chords in studying friction due to ploughing by curved surfaces in [70]. The method of generating slip line fields by chords and logarithmic curves has been further studied and adapted in experimental investigations of friction in circular and two dimensional cylindrical asperities in [71] and [72] respectively. Due

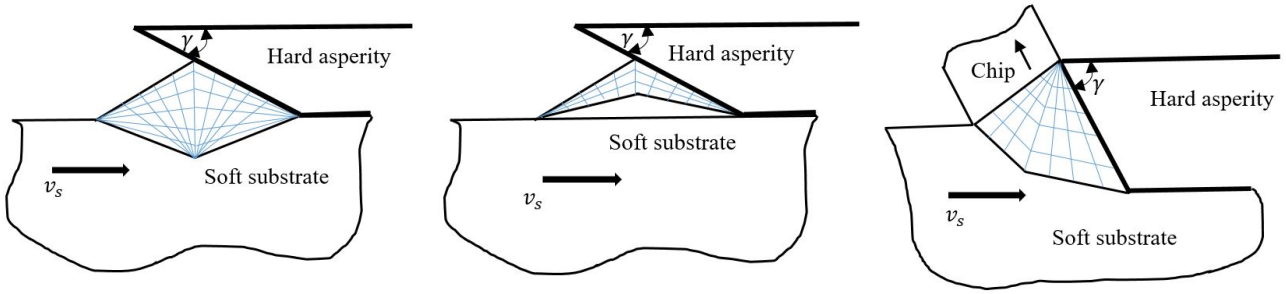

(a) Ploughing (b) Wedging (c) Cutting

Figure 2.5: Wear modes using slip-line field theory (blue lines: slip lines) [33].

to the limitation of slip-line field method in calculating friction for two-dimensional asperities only, upper-bound methods have been used to study ploughing by three-dimensional asperities. Upper-bound methods are based on minimization of the velocity field around the asperity resulting in minimization of work due to plastic deformation and interfacial friction. Upper bound methods have been used to estimate the force on pyramidal [73] and conical asperities [74] where the configuration of the plastic zone are known a priori. To capture pile-up of substrate material in ploughing, the shape of the pile-up has been determined on a rigorous basis while updating the upper bound solution in [75] and [76]. Although the effects of asperity geometry have been captured using pyramidal indenters with varying tip and side angles [28], prior estimation of plastic zone is challenging for a complex asperity geometry.

As studied in [39], [25] and [26], and shown in chapter 1, asperities in contact with a rough surface are represented by elliptical paraboloids of different sizes and orientations. The slip-line field theory and upper bound theory are limited in modelling of friction in ploughing by either two dimensional asperities or three dimensional pyramid and conical shape asperities. Upper bound models also need to approximate for the deformation and pile-up in the substrate prior to modelling friction. However, in using the theory given by Bowden and Tabor [34], shown in equation 2.1, the total friction acting on the face of an asperity is resolved into a friction force due to contact pressure from plastic deformation acting along the normal into the surface and friction force due to shearing of the interface acting tangent to the surface along the plastic flow. The plasticity theory has been successfully used to compute friction in ploughing by hexagonal pyramids [32] and spheres [77]. Hence, calculation of the friction forces as the product of contact area and contact stress and interfacial shear stress tensors seems effective in developing an analytical ploughing model.

2.1.4. Numerical ploughing models

Both mesh-based and mesh-less methods have been used to model ploughing in coated and uncoated systems. Among the available mesh-based methods to model ploughing, finite element (FE) methods have been preferred to model single-asperity sliding through both coated and uncoated substrates. 3D FE packages have also been used to study scratching of hard elastic coatings on metallic substrates [78, 79] and multi-layer polymeric coating-substrate systems [80, 81]. The FE models have focused on studying the pile-up by varying the material parameters of coating and the substrate such as Young's modulus, yield stress, hardening parameter and interfacial friction coefficient [82]. The selected FE packages have used methods such as adaptive re-meshing, element deletion and differential meshing to avoid element distortion due to large scale plastic deformation and wear and to reduce the computational cost of the simulation [83,

84, 85, 86, 79]. The FE-based ploughing models have typically used bi-linear-elastic plastic or the Johnson's Cook material model along with Columbic or Coulomb-type friction frictional contact at the interface [78] and [87]. To the author's knowledge, FE models have not been used for detailed study on ploughing behaviour in soft metallic coatings.

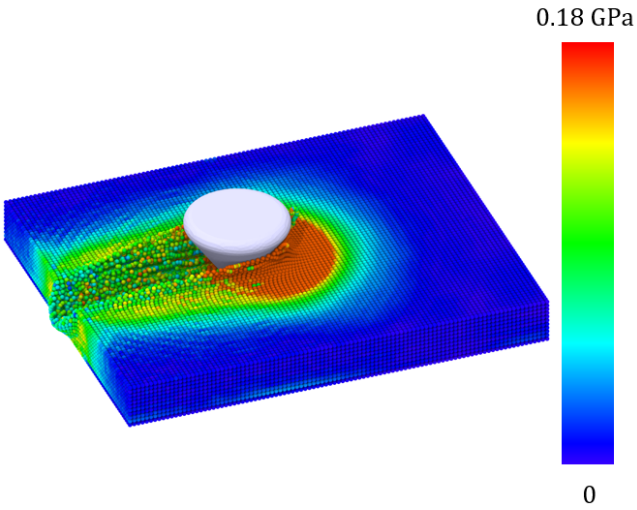

Figure 2.6: Modelling of ploughing using particle based method (showing stress in the substrate).[95]

In the recent years, particle based methods such as Molecular Dynamics (MD) have been used as numerical tool to study friction and wear in the sliding of a single asperity through the substrate at a nano-scale. Interfacial shear and plastic deformation of the substrate has been explained in MD by the help of movement of dislocations and voids [88]. The active slip systems and crystal surface orientations specific to pile-up in scratching of titanium and magnesium having a hcp crystal structure like zinc have been studied in [89]. MD simulations of scratching have been done using different asperity geometries ploughing through a smooth substrate in [88]. Also MD simulations of sliding of rough, coated and lubricated surfaces have been done in [90]. One of the critical steps in MD simulations is the choice of the correct interaction potential which is not straight forward. Furthermore in order to physically validate the MD simulations results attempts have been made to couple MD models with macro-scale models [91]. Typically particle base methods such as Smooth Particle Hydrodynamics (SPH) have been used in modelling of large arbitrary deformations in fluids. The use of SPH in modelling deformation in solids have dealt with numerical problems of rank deficiency and tensile instabilities. To model ploughing at the laboratory scale, the SPH forulation has been extended to a robust meshless Total Lagrangian formulation (TLSPH), although limited by the amount of substrate deformation [92]. TLSPH has been used in [93] and [94] where the constitutive material behaviour has been used to model frictionless scratching behaviour in metals. Hence an accurate experimental validation of the overall friction is absent in [93]. Figure 2.6 show the equivalent von-Mises stresses in ploughing using the particle based TLSPH method.

The use of hybrid numerical tools which combine mesh and particle based methods has helped to tackle the numerical problems in modelling of scratching. These methods often use an Arbitrary Lagrangian Eulerian (ALE) formulation which combines the features of pure Lagrangian analysis (in which the mesh follows the material) and Eulerian analysis (in which the mesh is fixed and the material flows though the mesh) [96]. Among them SPH has been used in

combination with FEM to model orthogonal cutting with varying damage criteria and particle density [97]. A Lagrangian FEM method, Particle FEM (PFEM) has been used with re-meshing to simulate formation of continuous chips in metal cutting processes [98]. Likewise the Material Point Method (MPM) is also a hybrid method which combines a background mesh as well as concepts of particle methods derived from the earlier Particle-In-Cell (PIC) techniques [99]. Historically MPM has been a popular numerical tool for modelling two-phase analysis and large scale deformation in soil penetration and structural collapses in geo-mechanics [100]. Recently the standard material point method has been generalized using a variational form and a Petrov–Galerkin discretization scheme resulting in the meshless Generalized Interpolation Material Point (GIMPM) method[101]. Both MPM and GIMPM have been recently used in machining applications like orthogonal cutting [102] and micro-milling [103]. Recent studies have presented GIMPM as a numerical tool in modelling large scale deformation [103].

The FE simulation of ploughing have dealt with numerical problems resulting from large scale, localized and dynamic plastic deformation. On the other hand, purely particle methods like MD models for ploughing at an atomistic scale have difficulty in accounting for the macro-scale factors of plastic deformation and shear and hence face the challenge of physical validation of numerical results. To successfully model friction in ploughing a numerical model must be adaptable to include the parameters affecting ploughing as discussed in chapter 1. However, GIMPM, a hybrid on particle and mesh based method uses the benefits of both techniques and has shown to model large scale deformation processes at a laboratory scale successfully. Moreover, GIMPM has been implemented as a user package in the open-source LAMMPS code [104]. The availability of GIMPM as an open source package (USER-SMD) combined with its modelling capabilities as discussed before encourages its implementation for ploughing simulations.

2.2. Research gap

Experimental techniques to characterize the boundary layer shear strength and material characteristics of the coated-substrate with varying operating parameters, critical to the design of the ploughing model, have not been fully explored in the available literature. Characterization of the soft zinc-coating with low thickness in the order of $10\mu m$ makes the characterization of coating related properties challenging. Bulk characterization methods for characterizing the yield properties sheet metals cannot be applied to coated sheets, while the micro-indentation based characterization coating on the cross-section is limited by the coating thickness. Nano-indentation techniques have been more effective in characterizing the variation in Young modulus and hardness with crystallographic orientation of anisotropic coatings. Knoop indentation hardness has also been used to evaluate the yield criteria mostly for uncoated anisotropic metals. However, a Knoop indenter based nano-indentation method has not been used so far to evaluate anisotropic yielding in coated sheets, although it has been used in bulk materials.

The current studies have shown that a robust ploughing model at micro-scale is key to modelling friction in deep-drawing. However, modelling of ploughing on micro-scale for metallic, coated contacts is complex and is affected by various aspects as shown in section 1.5. Moreover, the anisotropy in roughness and texture of tools and the substrate have shown to greatly affect the friction and wear in the sliding contact between a hard tool and a soft sheet substrate. The complex micro-geometry of the tool asperities, modelled as elliptic paraboloids, combined with the asymmetry in the resulting plastic flow makes development of an efficient multi-asperity model a challenging process. In this regard, analytical methods to compute friction and deformation

in ploughing by elliptical asperities with variable size and orientation with respect to sliding are not available. Currently, both numerical and analytical models to simulate ploughing by taking into account realistic material deformation and interfacial shear behaviour are absent. Firstly, analytical models to compute friction are limited to 2D wedges and cylinders using the slip-line field theory and simpler pyramidal and conical geometries using the upper bound theory. Secondly, the numerical simulation of ploughing using FE packages has been mostly limited to model small scale deformations and hence the use of simple bi-linear elastic-plastic material models and Coulomb friction law at the interface. Furthermore the MD simulations of ploughing are limited to nano-scale. Most of the numerical simulations of ploughing, both mesh-based FE methods, particle-based MD and TLSPH methods have not been able to accurately validate the friction and wear results with ploughing experiments. Although hybrid numerical tools such as the GIMP method has shown to be promising in modelling large scale plastic deformations including dynamic friction laws, their implementation to single-asperity ploughing still remains unexplored.

Hence it is important to take into account all the aforementioned factors in the chosen numerical ploughing model for a single-asperity. Based on the theoretical background of the available ploughing models, the effect of the following factors have yet not been fully considered in the calculation of friction and the ploughing behaviour:

- size and orientation of elliptical asperities with respect to the sliding direction.
- shear strength of the interface under various lubricating and operating conditions.
- anisotropy in the deformation of the zinc coating.
- zinc coating thickness.

2.3. Aim of the research

Based on the above research gaps obtained from the available literature survey and the problem definition for the proposed research, the following research objectives have been laid out:

- To build a numerical model to simulate the single-asperity ploughing behaviour for the tool-work-piece micro-contact (tool asperities sliding through the work-piece) in deep-drawing. The numerical model should consider the factors affecting friction and wear in ploughing behaviour listed in section 1.5. The designed ploughing model should include a zinc coated-substrate and take into account the effect of the boundary layer. The model should also include an elliptical asperity of varying size and orientation relative to the sliding direction, being able to adapt the characterized geometrical parameters of the ploughing asperity.
- To develop an analytical model for ploughing of an ideal (rigid-) plastic substrate by an elliptical asperity with varying size and orientation relative to the sliding direction. The analytical model in combination with the numerical model should be able to explain and account for the factors contributing to the friction in ploughing. The analytical model should be used to model one micro-contact in a multi-asperity contact for friction computations on macro-scale.
- To develop or adapt an experimental technique to measure interfacial shear strength for a lubricated boundary layer on an uncoated and coated surface.

- To develop or adapt an experimental technique to characterize the yield behaviour (yield criteria and coating hardness) for the zinc coating of a zinc coated steel sheet.

Although friction forces are considered, in the development of the aforementioned theory and ploughing model, abrasive wear resulting in the calculation of material removal is not part of the research.

2.4. Research outline

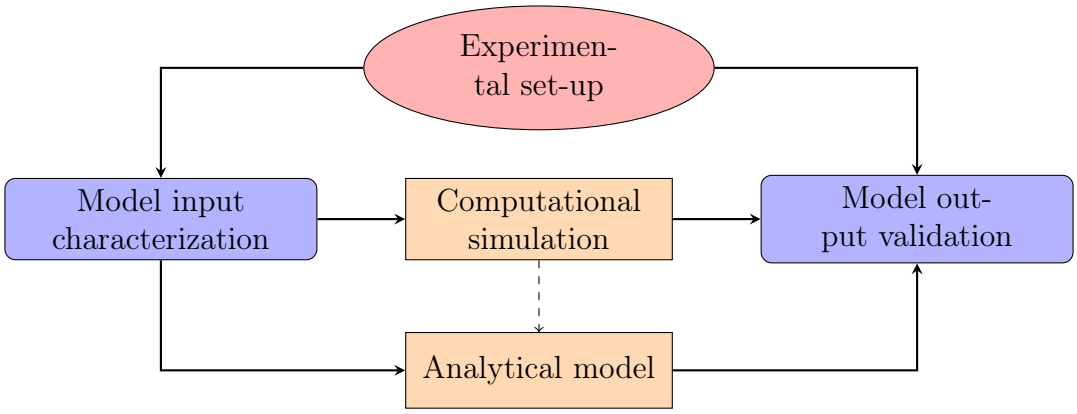

Figure 2.7: Flowchart of modelling single-asperity sliding.

The current research studies the sliding behaviour of a single-asperity through a substrate by numerical modelling and ploughing experiments. The study is done in a three-step procedure as listed in the flowchart in figure 2.7. The first step is model build-up which includes the development of a generalized interpolation material point method (GIMPM) based numerical model for simulating ploughing behaviour. Based on the observations from the numerical ploughing model, an analytical model to compute forces and wear in ploughing is developed with the aim to be implemented in a multi-asperity model. The numerical and analytical models will be able to model the ploughing behaviour of different ellipsoidal-shaped asperities under different orientations relative to the sliding direction. The numerical model has also been extended to incorporate experimentally derived interfacial shear strength relations and constitutive behaviour of steel substrates and zinc coatings taking into account the isotropic and anisotropic material deformation behaviour.

Chapter 3

Development of single-asperity ploughing models

This section describes the development of a numerical model, an analytical model and an experimental set up to study the ploughing behaviour of a single-asperity sliding through a substrate. The generalized interpolation material point (GIMP) method has been used to build a computational model of a single asperity sliding through a zinc coated substrate. The model does so by implementing the interfacial shear and material properties obtained experimentally. The measurement methods and results will be explained in chapter 4. The numerical model has been built to simulate single-asperity sliding behaviour for anisotropic material behaviour, elliptical asperity geometry, various substrate texture and lubricating conditions.

The developed numerical model will be further validated with ploughing experiments in chapter 5.The theory of friction in ploughing given by Bowden and Tabor [34] has been used to develop an analytical model for understanding the forces, deformation and wear in single-asperity sliding through a plastically deforming substrate. The analytical model has been built to be the basis of a friction model describing friction between a tool and a sheet surface, so a multi-asperity contact. The purpose of having an analytical model in combination with an experimentally validated numerical model for the single-asperity sliding is to build a robust tool to predict friction in deep-drawing process. The analytical model results are discussed in chapter 5 and compared with the numerical model results for ideal (elastic/plastic) material behaviour.

The contents of this chapter can be referred from the appended papers A [95], B [105], C [106] and F [107]. Further details on each section of the chapter can be seen in the following papers:

- Numerical simulation: Paper A [95], Paper C [106] and Paper F [107]
  - Paper A explains the build up of the numerical model.
  - Paper C and Paper F explain the implementation of ellipsoidal asperity geometry and coated substrate into the numerical model respectively.
- Analytical modelling: Paper B [105], Paper C [106] and Paper F [107]
  - Section 3.2.1-3.2.5: Paper B computes ploughing friction for a constant ploughing depth. Paper C takes into account the variation in pile-up to compute the ploughing friction by implementing the model in paper B.
  - Section 3.2.6-3.2.7: Ploughing model for coated substrates is explained in Paper F.

3.1. Numerical simulation

As discussed in chapter 2, the Generalized interpolation material point (GIMP) method has been chosen to model ploughing of the sheet by a rigid asperity. This section briefly discusses the fundamentals of the MPM-based ploughing model and elaborates on the modifications and extensions done in the model to simulate ploughing behaviour. The modifications done in the MPM model to include the effects of micro-geometry of the tool asperities, coating, anisotropic material model and a coated system have also been elaborated. The model parameters are listed in table 3.1. Further details on the development of the the numerical model can be found in [95], [106] and [107] (appended paper A, paper C and paper F).

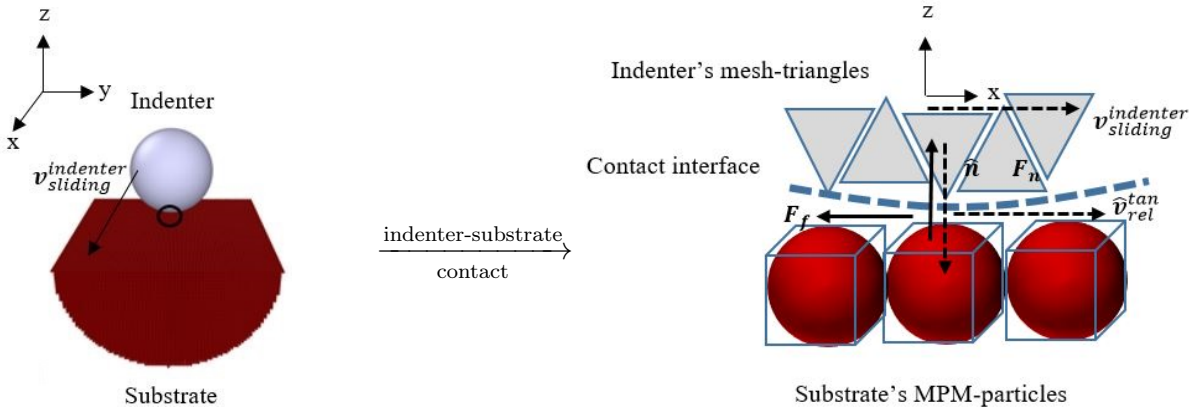

(a) Ploughing of MPM substrate by an indenter visualized in OVITO.

(b) Schematics of contact forces between indenters mesh triangle and substrates MPM particles.

Figure 3.1: MPM-based modelling of ploughing.

The GIMP method is commonly referred as material point method (MPM) and incorporates features of a particle and mesh based method. In a way it is similar to the arbitrary lagrangian and eulerian (ALE) method. Based on the more common, particle in cell (PIC) method, MPM uses an interpolation function to transfer information on history dependent variables between the nodes and the particles. The GIMP method has been implemented in the user-SMD (smooth mach dynamics) package of the open source molecular dynamics code, LAMMPS [104]. Two main code classes are key to modelling ploughing using MPM. The first class called 'MPM-linear pair style' class defines the algorithm for interaction between the particles in the substrate. The rigid indenter/asperity which is modelled as a STL file with triangular mesh elements. The modelled asperity is rigid and has no self-interaction. The triangular elements of the indenter interact with the MPM-particles in the substrate using 'Tri-smd pair style' class. The features of both the classes have been briefly explained in this section, for details see [95].

Here, revision 70 of the user-SMD package is used to model single-asperity sliding. A simulation domain of dimensions accommodating the asperity and the substrate was set with fixed boundaries in all axes except for the periodic boundaries in the sliding direction. A semi-cylindrical region was generated and filled with substrate particles, as shown in figure 3.1. A spherical indenter composed of a triangulated mesh was exported from the corresponding *.STL file where the nodes of each triangular element, grouped as a particle type were predefined. The indenter is run with constant load or depth depending on the simulation, as the model is able to simulate both load-controlled and depth-controlled scratch tests.

Table 3.1: MPM ploughing model parameters.

Parameters	Symbol	Values/expression
Rigid spherical indenter radius	R_i	0.2mm, 0.5mm and 1.5mm
Semi-cylindrical substrate radius	R_s	0.25mm
Sliding distance of indenter	l	0.6mm
Semi-cylindrical substrate length	l_s	$l + 2r_i$
Substrates MPM particle cell size	r_p	5, 10, 15 and 20 μm
Indenters triangulated mesh element size	r_t	5, 10 and 20 μm
Sliding velocity of indenter	v_s	0.1 mm/s
Mass scaling factor	m_s	1e6
Boundary conditions	$\mathfrak{p}, \mathfrak{f}, \mathfrak{f}$	periodic, fixed, fixed

For faster computations, parallel processors using the message passing interface (MPI) technique and spatial decomposition of the simulation domain were used on a Linux-based cluster consisting of 2 processors with 12 cores each to run the user-SMD code. In MPI simulation runs, the number of cores is also increased to reduce the net CPU time. A high-sliding velocity also leads to reduced simulation run time. However, for a fast moving indenter both the un-transmitted thermal stress (high Peclet number) and the stress waves reflected from the substrate boundary in previous time steps can interfere and cause large fluctuations in the stress generated. Although the sliding velocity can be varied within a given range for accurate results, it is kept optimal for fast and stable simulations. Like many mesh-based methods, MPM uses mass scaling to scale-up the mass of the particle that has the smallest time step, thereby increasing the time step size and reducing the total computational time. The mass scaling factor, has been optimized (m_s= 1e6 in current simulations) to achieve a low computational cost as well as stable and accurate results. Since the simulation results are resolution dependent, both the particle-size in the substrate and the element size in the indenter were reduced step wise from 20 to 5 μm to obtain accurate results independent of discretization effects by extrapolating the converging data at 0 resolution.

3.1.1. Asperity-substrate contact

The contact between the asperity and the substrate is modelled based on the penalty algorithm. As the asperity approaches the substrate the pair style detects the possibility of contact. For MPM particles whose point of contact falls within the projected area of the triangle and whose distance r from the triangle is less than their diameter, contact is detected. Once contact is detected, the contact force between the particle and the triangle is calculated by assuming the particle as an elastic cube being uni-axially compressed by the surface of the triangle.The contact force is calculated as the product of the contact stress and the contact area. The contact stress is given as the product of elastic modulus E and strain ϵ. For particle of radius r_c, penetration υ of the triangle is $r - r_c$. The strain ϵ is given as υ/r_c. The contact area A_c per particle-triangle contact is given as $4r_c^2$. The elastic modulus is modified to $E^{'}$ by multiplying E with $1 - \epsilon^2$ to account for large penetration. The contact force acts along the direction of the line joining the center of the contacting triangle and particle cell into the contact plane given by unit vector $\hat{n}$. Taking all the above expression into account, the contact force for the contact between a triangular element of the asperity and MPM particle in the substrate is given in equation 3.1.

$$\vec{F_n} = -4E^{'}(r - r_c)r\hat{n} \tag{3.1}$$

The contacting triangles and particles experience a tangential force due to shearing of the contacting interface. The friction force due to interfacial shear acts on the triangle in the direction opposite to the relative tangential velocity of the triangle with respect to the MPM particle given as unit vector $\hat{t}$. The interfacial friction force is given as the product of the interfacial shear stress τ_b and the contact area A_c. The interfacial shear strength is calculated based on two methods. In the first method, the interfacial shear strength is calculated as a power law function of the operational parameters such as nominal contact pressure P_{nom}, sliding velocity v_s and contact temperature T_c as given in equation 3.2c. In the second method the boundary layer shear strength is given as a fraction f_{hk} of the bulk shear strength κ of the substrate in equation 3.2b. For perfectly plastically deforming substrate the bulk shear strength is assumed to be equal to $\kappa = \sigma_y/\sqrt{3}$ [108] where σ_y is the uniaxial yield strength of the substrate. The coefficients C_p, C_v and C_T and exponents n_p n_v and n_T in the boundary layer shear stress equation are found by fitting the experimental results as further explained in chapter 4.

$$\vec{F_t} = -4\tau_b r^2 \hat{t} \tag{3.2a}$$

$$\tau_b = f_{hk}\kappa \tag{3.2b}$$

$$\tau_b = C_p P_{nom}^{n_p} C_v v_s^{n_v} C_T \exp -\left(\frac{n_T}{T_c}\right) \tag{3.2c}$$

3.1.2. MPM particle-particle interaction

The particles interact with an auxiliary background mesh grid by the help of an interpolation function W. W is a compact function as it interacts with the nearby nodes up to a distance of twice the mesh node spacing. It is given by a dyadic product of one-dimensional cubic B-splines. The information about mass, velocity, stress, external forces, thermal energy, volume, and deformation gradient are stored with the particle at the beginning of each time step. The properties evolve as per the modified stress update last (MUSL) scheme as shown in figure 3.2.

The mass, heat, velocity and external forces of the particle are first interpolated to the nearby nodes using interpolation function W at time $\dot{t}$ using mass, energy and momentum conservation laws. The forces in the grid are computed from the product of particle stress, volume and particle to node interpolation function W_{pn}. The heat rate in the grid is given as the product of thermal conduction coefficient and spatial second derivative of heat distribution at nearby nodes. From the forces and heat rate computed at the grid node the velocities and heat for time $\dot{t} + \Delta\dot{t}$ at the node are time integrated using Euler forward update. The velocity, acceleration and heat of the particles are now interpolated back using the node to particle interpolation function W_{np}. The update of the velocity of the particle is done using two ways, one of which is the pure PIC (particle in cell) update using the interpolation function, while the other is the pure FLIP (fluid implicit particle method) which uses the acceleration of the particle at time $\dot{t}$. The MPM-linear pair style uses a combination of both these methods using a parameter with a value of 0.99 in order to avoid strong dissipation and numerical noise which are inherent to the PIC and FLIP method respectively. The position of the particles is updated in the next time step from the updated particle velocities. The updated velocities of the particles are again interpolated to the grid using W_{pn} . The velocity gradient of the particle locations is computed from the gradient of the grid velocity of grid and interpolation function W_{pn}.The velocity gradient of the particle is then used to update the deformation gradient. The determinant of the updated deformation gradient is used to update the particle volume. The particle strain

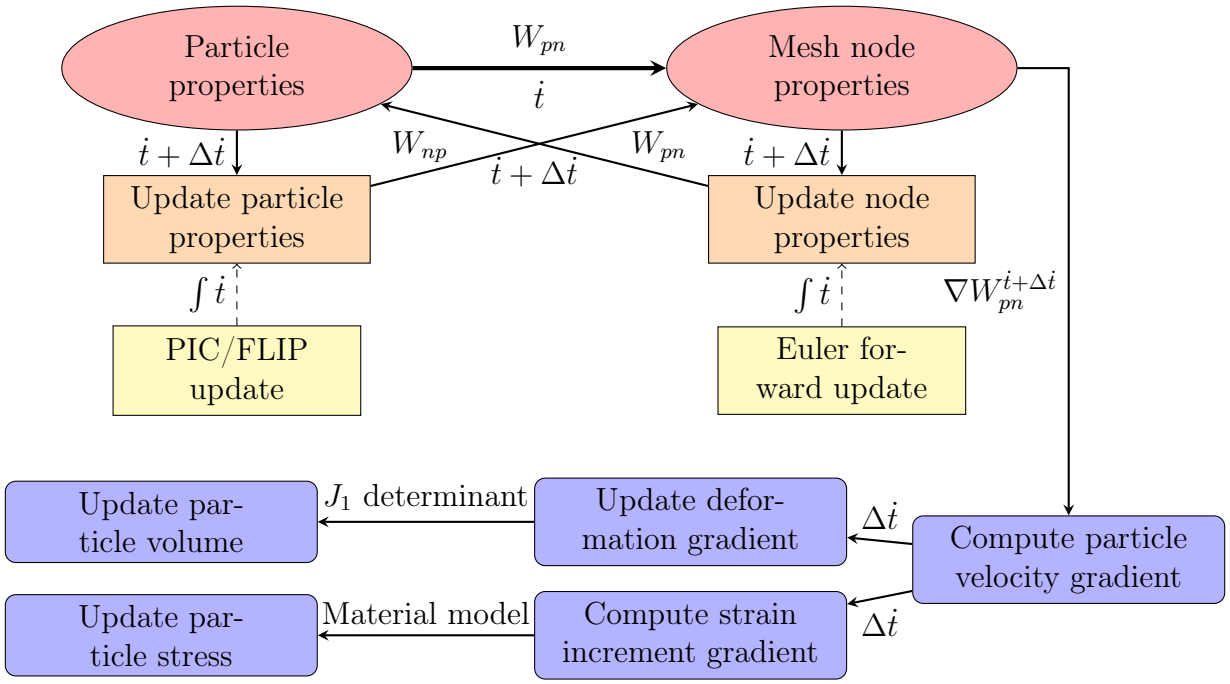

Figure 3.2: Flowchart for the MUSL algorithm used in GIMPM.

increment is also computed at from the updated velocity gradient for time step $\Delta\dot{t}$. Finally the particle stress is updated from the particle strain using the material constitutive laws.

3.1.3. MPM-material model

The constitutive laws describing the stress strain relationship, comprises of a material model which computes the deviatoric and hydrostatic components of stress based on deviatoric and hydrostatic strains/deformations respectively. The stress tensor can be decomposed into independent volumetric and deviatoric components for an isotropic material as given in equation 3.4. However, the decomposition of the total stress into volumetric and deviatoric stress is not independent of the corresponding volumetric and deviatoric strains in an anisotropic material. Several studies have been done to explain the stress-strain relationship and decomposition for anisotropic materials (orthotropic) [109, 51, 110, 111]. The total stress tensor σ_n is given as the sum of the hydrostatic stress tensor $-PI$ (P is the hydrostatic pressure computed using the equation of state model and I is the second order identity tensor) and the deviatoric stress tensor σ_d, as given in equation 3.4. A linear equation of state is used to relate the change in volume $\epsilon_v = J_1 - 1$ to the hydrostatic pressure using the bulk modulus as shown in equation 3.5. The deviatoric stress tensor σ_d is computed from the product of devaitoric strain tensor ϵ_d and shear modulus G.

$$\{\sigma\} = [\mathbb{C}]\{\epsilon\} \tag{3.3}$$

$$\sigma_n = -PI + \sigma_d \tag{3.4}$$

$$P = K(J_1 - 1) \tag{3.5}$$

The deviatoric strain tensor is the computed difference between the total strain tensor ϵ and volumetric strain tensor, $\epsilon_v = J_1 - 1$. The deviatoric stress is computed using the plasticity algorithm termed as 'radial return' [112] for plastically deforming material. The second deviatoric

stress invariant J_2 is calculated from the norm of the matrix-vector product of the transpose of the trial deviatoric stress $\sigma_d^{trial\mathsf{T}}$ vector, the anisotropy matrix $\mathbb{P}$ and the trial deviatoric stress as per the Hill's yield criteria [52] as given in equation 3.6. The Hill's constants U_1, U_2, U_3, V_1, V_2 and V_3 comprising the anisotropy matrix $\mathbb{P}$ will be characterized experimentally for both the zinc coating and an uncoated steel sheet to study the anisotropic yielding behaviour (see chapter 4). The second deviatoric stress invariant for isotropic materials is calculated from the norm of the trial deviatoric stress in the von Mises yield criterion.

$$\begin{aligned}\Phi = U_1\big(\sigma_{d22} - \sigma_{d33}\big)^2 + U_2\big(\sigma_{d33} - \sigma_{d11}\big)^2 + U_3\big(\sigma_{d22} - \sigma_{d33}\big)^2 \\ + 2V_1\sigma_{d23}^2 + 2V_2\sigma_{d31}^2 + 2V_3\sigma_{d12}^2 - \sigma_f^2\end{aligned} \tag{3.6}$$

Yielding occurs if the equivalent flow stress $\sqrt{3J_2}$ exceeds the tensile yield strength of the material σ_y. If the yield condition is satisfied, the material model updates the plastic strain increment and deviatoric stress for the next time step. The updated deviatoric stress is used to calculate the the increment of un-rotated deviatoric stress $\Delta\sigma_d$ which is then used in the elastic trial update in the next time step. Likewise the updated strain increment is used to calculate the plastic strain in the next time step. If the yield criteria is not satisfied, the material still has purely elastic deformation as a result of which there is zero plastic strain increment and the trial deviatoric stress is taken as the deviatoric strain at the next time step given as:

$$\sigma_d^{trial} = \sigma_d^{\dot{t}} + 2G\Delta\epsilon_d \tag{3.7}$$

The plastic strain computed in the 'radial return' plasticity algorithm is used to model the yield strength of the substrate (MPM particles) using the yield functions. The yield stress is calculated based on the yield function from the plastic strain increment in the time step. For comparing the results of the analytical model, rigid-plastic material behaviour is incorporated in the MPM ploughing simulations. Assuming, adiabatic conditions, the heat generated Δq due to plastic deformation results in a temperature change ΔT which is calculated as $\Delta T = \Delta q/mc_p$ using the specific heat capacity c_p and the mass of the particle $m = \rho V$ (material density ρ and cell volume V). The heat transfer is calculated using thermal conductivity κ_t. The material parameters for calculation of temperature change is given in table 3.2.

Table 3.2: Material model rigid–plastic parameters for analytical validation.

Parameters	Symbols	Values
Substrate and indenter material (steel) density	ρ_s	7850 kg/m^3
Substrate and indenter specific heat capacity	c_{p_s}	502 J/kgK
Substrate and indenter thermal conductivity	κ_{t_s}	50 W/mK
Coating material (zinc) density	ρ_c	7140 kg/m^3
Coating specific heat capacity	c_{p_c}	377 J/kgK
Coating thermal conductivity	κ_{t_c}	116 W/mK
Poisson's ratio of the substrate	ν_s	0.3
Initial yield stress of the substrate	σ_{y_0}	150 MPa
Hardness of the substrate	H_s	$3\sigma_{y_0}$

A constant yield strength σ_y is taken for rigid-plastic (no elastic recovery) material behaviour. The analytical model developed in the section 3.2 will use the rigid-plastic material behaviour to compute the friction in ploughing. For rigid-plastic materials, the interfacial shear strength

Table 3.3: Model parameters for rigid–plastic coated system used in analytical validation.

Parameters	Symbols	Values
Elastic modulus of the substrate	E_s	210 GPa
Poissons ratio (coating and substrate)	ν	0.3
Elastic modulus of the coating	E_c	80 GPa
Reference hardness of the coating	H_{c_0}	225/450 MPa
Reference hardness of the substrate	H_{s_0}	450/900 MPa
Reference coating thickness	t_0	25 MPa
Relative hardness of coating	$\tilde{H}$	0.1-10
Thickness of coating	t	0-200 μm
Interfacial shear stress	τ_{sh}	$H/3\sqrt{3}$ [113, 24]

can be given as a fraction f of the bulk shear strength κ in equation 3.2b. The bulk shear strength κ is given as $H/3\sqrt{3}$ where H is the hardness of the substrate [113, 24]. In a coated system, the hardness of the coating H_c will be varied relative to the hardness of the substrate H_s along with its thickness t to study its effect on ploughing friction and ploughing depth. Table 3.3 lists the parameters for rigid-plastic material that will be used in the analytical model for a coated system.

In the current thesis, the yield strength is computed from the physically based isothermal Bergström van Liempt hardening relation [49]. The hardening relation has been modified by Vegter for sheet metals used in deep-drawing [114] where the yield strength σ_y^{BL} is given in equation 3.8a as the sum of the static-work, strain hardening stress σ_{wh} and dynamic stress σ_{dyn}. The dynamic stress includes both the strain-rate and the thermal effects as shown in the equation 3.8a. The hardening model includes for interaction processes between dislocations in cell structures including the changing shape of dislocation structures. The Bergström van Liempt (BL) material strength model is based on strain ε, strain rate $\dot{\varepsilon}$ and temperature T and is used for the steel substrate whose parameters are listed in chapter 4. The parameters of the Bergström-van Liempt material model for DX56 steel are listed in table 3.4. The yield strength of the zinc coating is calculated by a work hardening model similar to the Swift (S) strain hardening relationship given in equation 3.8b. The yield strength is computed by the work hardening exponent n, elastic modulus, E and initial yield strength σ_{y_0} which are listed from literature [47] in table 3.6. The yield strength of the bulk zinc is calculated using the Johnson-Cook material model. The Johnson-Cook material model also accounts for the strain ε, strain-rate $\dot{\varepsilon}$ and thermal (temperature) T effects as shown in equation 3.8c.

$$\sigma_y^{BL} = \sigma_{wh} + \sigma_{dyn} = \sigma_{f_0} + d\sigma_m\Big(\beta_0(\varepsilon+\varepsilon_0) + \Big(1 - \exp\big(-\omega(\varepsilon+\varepsilon_0)\big)\Big)^g\Big) + \sigma_{v_0}\left(1 + \frac{kT}{\Delta G_0}\ln\frac{\dot{\varepsilon}}{\dot{\varepsilon}_0}\right)^j \tag{3.8a}$$

$$\sigma_y^S = \sigma_{y_0}\Big(1 + \frac{E}{\sigma_{y_0}}(\varepsilon - \varepsilon_0)\Big)^n \tag{3.8b}$$

$$\sigma_y^{JC} = \big(\sigma_{f_0} + \zeta\varepsilon^\xi\big)\left(1 + \chi\ln\frac{\dot{\varepsilon}}{\dot{\varepsilon}_0}\right)\left(1 - \Big(\frac{T - T_0}{T_m - T_0}\Big)^\iota\right) \tag{3.8c}$$

Table 3.4: Bergström-van Liempt material model parameters for DX56 steel.

Parameters	Symbols	Values
Initial static stress	σ_{f_0}	82.988 MPa
Stress increment parameter	$d\sigma_m$	279.436 MPa
Linear hardening parameter	β_0	0.482
Remobilization parameter	ω	6.690
Strain hardening exponent	g	0.5
Initial strain	ε_0	0.005
Initial strain rate	$\dot{\varepsilon_0}$	$10^{-8}s^{-1}$
Maximum dynamic stress	σ_{v_0}	1000 MPa
Dynamic stress power	j	3.182
Activation energy	ΔG_0	0.8
Boltzmanns constant	k	8.617 $\times 10^{-5} eV$

Table 3.5: Johnson-Cook material model for pure zinc block [115].

Parameters	Symbols	Values
Initial yield stress	σ_{y_0}	82.51 MPa
Strain hardening constant	ζ	288.34 MPa
Linear Strain hardening exponent	ξ	0.1786
Strain rate hardening constant	χ	0.0202
Reference strain rate	$\dot{\varepsilon_0}$	$1s^{-1}$
Reference temperature	T_0	$298K$
Melting point of zinc	T_m	$693K$
Thermal softening constant	ι	0.843

Table 3.6: Material model for $10\mu m$ thick zinc coating on steel substrate [116, 41].

Parameters	Symbols	Values
Initial yield stress	σ_{y_0}	85 MPa
Strain hardening exponent	n	0.14
Young's modulus	E	80 GPa

The parameters for the yield function given in equations 3.8a, 3.8b and 3.8c for steel, zinc coating and are listed in table 3.4, 2.1 and 3.5 respectively. The USER-SMD class 'smd-material-model' gives the possibility of incorporating different yield criteria and material models in the GIMP code. For anisotropic material behaviour, a suitable model needs to be implemented. Material models such as the strain, strain rate and temperature dependent Johnson-Cook material model are already present in the GIMP package.

3.2. Analytical modelling

An analytical model has also been developed with the aim to gain a deeper understanding of the single asperity ploughing behaviour and to represent the numerical model results. The analytical model focuses on computing the ploughing forces acting on the elliptical asperity. The model will also aim to predict the ploughed profile of the uncoated substrate. The general concepts of the model have been described further in [105], [106] and [107] (appended paper B, paper C and paper F).

The total force acting on a ellipsoidal asperity ploughing through a substrate can be decomposed as the sum of the force due to contact pressure on the deforming substrate and the force due to shearing of the asperity-substrate interface acting on each surface element. The contact pressure p_{pl} is generated due to the plastic deformation of the substrate and is assumed to be equal to the hardness H of the substrate. The shearing of the interface results in an interfacial shear strength τ_{sh}. Both the stress components act on the total contact area A_c. The force due to plastic deformation acts in normal direction $\hat{n}$ into the asperity, while the force due to interfacial shear acts along the tangent $\hat{t}$ along the direction of relative plastic flow of the substrate with respect to the asperity. The total force acting on the asperity is given as $\vec{F}$ in equation 3.9.

$$\vec{F} = p_{pl} A_c \hat{\mathrm{n}} + \tau_{sh} A_c \hat{\mathrm{t}} \tag{3.9}$$

3.2.1. Calculation of surface unit vectors

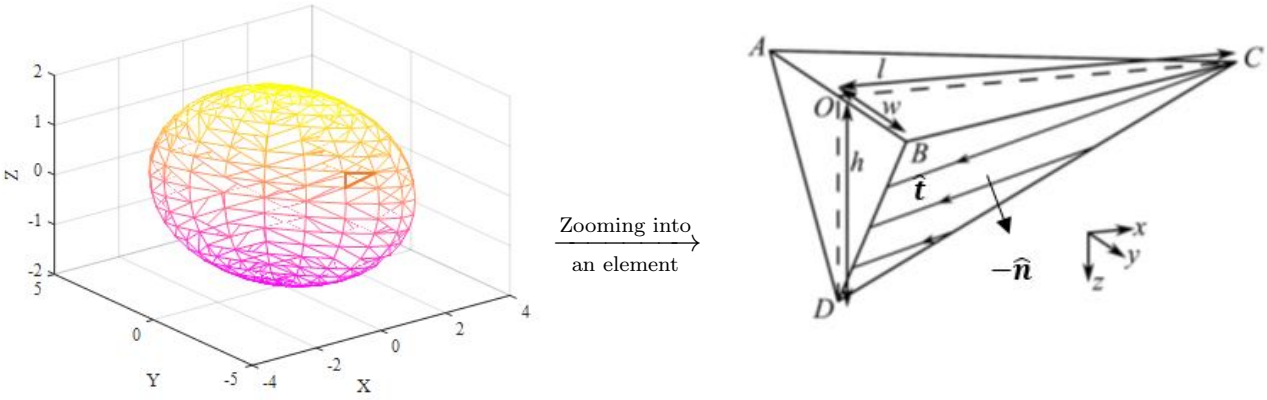

(a) Discretization of the surface of the ellipsoidal asperity into triangular elements.

(b) Tetrahedral element OBCD along unit normal $\hat{n}$ and unit tangent vector $\hat{t}$.

Figure 3.3: Analysis of the forces acting on a elemental area of an ellipsoidal asperity [28].

To compute the forces acting on an ellipsoidal asperity ploughing through a rigid plastic substrate, the surface of the asperity is divided into infinitesimally small triangular elements as shown in 3.3a. The discretization of the surface is equivalent to meshing the surface with triangular elements. The tetrahedral element $OBCD$ has side-lengths of l, w and h from vertex O to base triangle ΔBCD as shown in 3.3b. Taking the center of the ellipsoid as the origin of the Cartesian coordinate system, the sides OC, OB and OD are orthogonal to each other and along the x, y and z respectively. The points B, C and D are given in the Cartesian coordinate space as $(0, w, 0)$, $(l, 0, 0)$ and $(0, 0, h)$ respectively. The normal vector $\vec{n}_{\Delta BCD}$ into the surface element ΔBCD is given as the cross product of its two sides $\vec{BC}$ and $\vec{BD}$ as given in equation

3.10a. The unit normal vector $\hat{\mathrm{n}}$ is obtained by dividing the normal vector $\vec{n}_{\Delta BCD}$ with its magnitude and is expressed in terms of the ratio of projected area of ΔBCD in the xz, yz and xy planes with the total area of ΔBCD expressed as A_{xz}, A_{yz}, A_{xy} and A_Δ respectively in equation 3.10b.

$$\vec{\mathrm{n}}_{\Delta BCD} = \vec{BC} \times \vec{BD} = -wh\hat{\mathrm{i}} - lh\hat{\mathrm{j}} - wl\hat{\mathrm{k}} \tag{3.10a}$$

$$\hat{\mathrm{n}} = \frac{\vec{\mathrm{n}}_{\Delta BCD}}{\mid n_{\Delta BCD} \mid} = \frac{-wh\hat{\mathrm{i}} - lh\hat{\mathrm{j}} - wl\hat{\mathrm{k}}}{\sqrt{(wh)^2 + (lh)^2 + (wl)^2}} = -\frac{A_{yz}}{A_\Delta}\hat{\mathrm{i}} - \frac{A_{xz}}{A_\Delta}\hat{\mathrm{j}} - \frac{A_{xy}}{A_\Delta}\hat{\mathrm{k}} \tag{3.10b}$$

The relative velocity $\vec{x}$, of an tetrahedral element of an ellipsoidal asperity sliding in the x direction with velocity v is given in the Cartesian coordinate as $l\hat{i}$. The tangent vector $\vec{t}_{\Delta BCD}$ to ΔBCD is given by minimizing the inner product $\vec{x}.\vec{t}_{\Delta BCD}$ in the plane described by $\vec{x}$ and $\vec{n}_{\Delta BCD}$. Thus the tangent vector to the elemental ΔBCD is given as the double cross product of $\vec{x}$ and $\vec{n}_{\Delta BCD}$ and $\vec{n}_{\Delta BCD}$ in equation 3.11a. Likewise the unit tangent vector $\hat{\mathrm{t}}$ is obtained by dividing the normal vector $\vec{t}_{\Delta BCD}$ with its magnitude and is expressed in terms of the ratio of function of projected areas of ΔBCD in the xz, yz and xy planes with the total area of ΔBCD in equation 3.11b. The expressions for unit tangent and unit normal vectors for the surface element remains unchanged for all orientations of the element with respect to the center of the ellipsoid and for surface elements with higher sided-polygon base [28].

$$\vec{t}_{\Delta BCD} = (\vec{\mathrm{x}} \times \vec{n}_{\Delta BCD}) \times \vec{n}_{\Delta BCD} = -l((lw)^2 + (lh)^2)\hat{i} + w(lh)^2\hat{j} + h(lw)^2\hat{k} \tag{3.11a}$$

$$\hat{\mathrm{t}} = \frac{\vec{\mathrm{t}}_{\Delta BCD}}{\mid t_{\Delta BCD} \mid} = \frac{-((lw)^2 + (lh)^2)\hat{i} + (hw)(lh)\hat{j} + (wh)(lw)\hat{k}}{\sqrt{(lw)^2 + (lh)^2}\sqrt{(lw)^2 + (lh)^2 + (wh)^2}} \tag{3.11b}$$

$$\hat{\mathrm{t}} = -\frac{\sqrt{A_{xy}^2 + A_{yz}^2}}{A_\Delta}\hat{\mathrm{j}} + \frac{A_{xz}A_{yz}}{A_\Delta\sqrt{A_{xy}^2 + A_{yz}^2}}\hat{\mathrm{j}} + \frac{A_{xy}A_{yz}}{A_\Delta\sqrt{A_{xy}^2 + A_{yz}^2}}\hat{\mathrm{k}} \tag{3.11c}$$

3.2.2. Calculation of the elemental projected area

The geometry of an ellipsoidal asperity sliding through the substrate along the x direction is defined by its major axis a and minor axis b for the central elliptic base in the xy (sliding) plane. The height of the ellipsoidal asperity is given by the other axis c in the z direction. The orientation of the ellipsoid in the sliding plane is given by the angle β between its major axis and the global x axis. The spherical coordinates of a point are given by the its radial distance r from the origin, its polar angle ϕ from the zenith direction and the azimuth angle θ of its orthogonal projection on the plane through the origin and perpendicular to the zenith. The points on the surface of an ellipsoid (asperity) are given in the spherical coordinates system in equation 3.12a. For the rotation of the ellipsoidal asperity by an angle β, the points on the ellipsoid are given by multiplying the points for the x and y coordinates with the rotation matrix R, given in equation 3.12b. The points on the rotated ellipsoidal asperity in the spherical coordinate system are given in 3.12c.

$$[x, y, z] = [a\cos\theta\sin\phi, b\sin\theta\sin\phi, c\cos\phi] \quad \forall\theta \in [0, 2\pi]; \phi \in [0, \pi] \tag{3.12a}$$

$$\begin{pmatrix} x_r & y_r & z_r \end{pmatrix} = \begin{pmatrix} x & y & z \end{pmatrix} \times \begin{pmatrix} \cos\beta & -\sin\beta & 0 \\ \sin\beta & \cos\beta & 0 \\ 0 & 0 & 1 \end{pmatrix} \tag{3.12b}$$

$$[x_r, y_r, z_r] = [(a\cos\theta\cos\beta - b\sin\theta\sin\beta)\sin\phi, (a\cos\theta\sin\beta + b\sin\theta\cos\beta)\sin\phi, c\cos\phi]$$
$$\forall\theta \in [0, 2\pi]; \phi \in [0, \pi]; \beta \in [-\pi/2, \pi/2] \tag{3.12c}$$

For mathematical convenience, the expressions for the unit normal and the unit tangent vector given in equation 3.11a and 3.11b are now expressed in the spherical coordinate system. In order to calculate the expressions for the elemental area and its projections in spherical coordinate system the Jacobian determinant $J_{\mathrm{C}}^{\mathrm{S}} = \det \mid \partial \mathrm{C}/\partial \mathrm{S} \mid$ is used to transform the Cartesian coordinate system C(x,y,z) to the spherical coordinate system S(θ,ϕ,r). The expressions for the projected areas of an tetrahedral element in the xy, yz and zx planes are given as A_{xy}, A_{yz} and A_{xz} in the spherical coordinate system in equations 3.13a -3.13c respectively. The unit normal and the unit tangent vectors are now expressed in equations 3.14a and 3.14b respectively, terms of the projected area in the spherical coordinate system by applying the Jacobian (determinant) transformation on both the numerator and denominator terms in equation 3.11a and 3.11b.

$$dA_{xz} = dxdz = J_{xz}^{\phi\theta} d\phi d\theta = l(\theta,\phi) d\phi d\theta \tag{3.13a}$$

$$dA_{yz} = dydz = J_{yz}^{\phi\theta} d\phi d\theta = m(\theta,\phi) d\phi d\theta \tag{3.13b}$$

$$dA_{xy} = dxdy = J_{xy}^{\phi\theta} d\phi d\theta = n(\phi) d\phi d\theta \tag{3.13c}$$

$$\hat{n} = \frac{-m(\theta,\phi)d\phi d\theta}{dA_{\Delta}(r,\theta,\phi)}\hat{i} - \frac{l(\theta,\phi)d\phi d\theta}{dA_{\Delta}(r,\theta,\phi)}\hat{j} - \frac{n(\phi)d\phi d\theta}{dA_{\Delta}(r,\theta,\phi)}\hat{k} \tag{3.14a}$$

$$\hat{t} = \frac{-f(\theta,\phi)d\phi d\theta}{dA_{\Delta}(r,\theta,\phi)}\hat{i} - \frac{g(\theta,\phi)d\phi d\theta}{dA_{\Delta}(r,\theta,\phi)}\hat{j} - \frac{h(\theta\phi)d\phi d\theta}{dA_{\Delta}(r,\theta,\phi)}\hat{k} \tag{3.14b}$$

where,

$$J_{AB}^{CD} = \det \begin{vmatrix} \frac{dA}{dC} & \frac{dA}{dD} \\ \frac{dB}{dC} & \frac{dB}{dD} \end{vmatrix}$$

$$l(\theta,\phi) = c(a\sin\theta\cos\beta + b\cos\theta\sin\beta)(\sin\phi)^2$$

$$m(\theta,\phi) = c(a\sin\theta\sin\beta - b\cos\theta\cos\beta)(\sin\phi)^2$$

$$n(\phi) = \frac{ab}{2}\sin 2\phi$$

$$f(\theta,\phi) = \sqrt{(n(\phi))^2 + (l(\theta,\phi))^2}$$

$$g(\theta,\phi) = \frac{l(\theta,\phi)m(\theta,\phi)}{f(\theta,\phi)}$$

$$h(\theta,\phi) = \frac{n(\phi)m(\theta,\phi)}{f(\theta,\phi)}$$

3.2.3. Calculation of boundaries of contact/plastic flow

As the ellipsoidal asperity ploughs through the rigid-plastic substrate with sliding velocity v_s in the x direction, the mean penetration of the asperity in the substrate is given by ploughing depth d. Assuming the initial ploughing depth is constant over the contact patch, the boundaries of the contact are obtained. The initial contact patch in the sliding plane is shown to be semi-elliptic for a rigid-plastic substrate with no elastic recovery. The deformation behaviour of the rigid-plastic substrate is assumed to be viscoplastic resulting in plastic flow of the deformed substrate around the sliding asperity. The plastic flow of the deformed substrate around the sliding asperity is illustrated in figure 3.4a. In order to calculate the total force acting on an asperity due to plastic deformation of the substrate and the interfacial shear, the discrete force components acting on the surface elements of the asperity in contact with the substrate must be integrated over the contact boundary, i.e limits of the contact region.

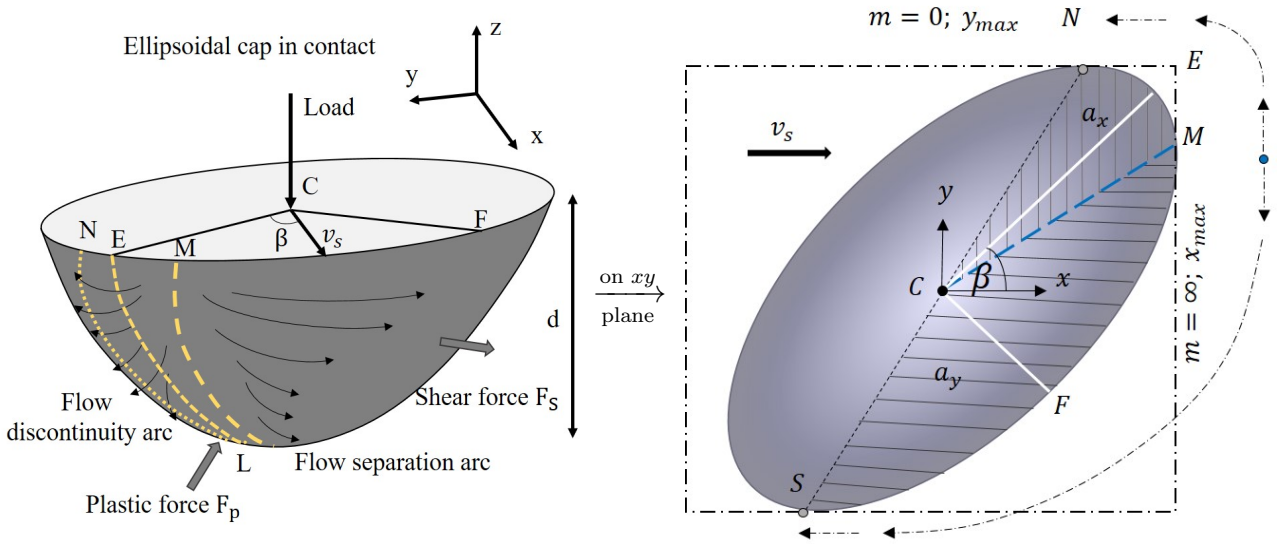

(a) Schematic of an ellipsoidal asperity.

(b) Projection of the asperity on the xy plane.

Figure 3.4: Schematic of an ellipsoidal asperity sliding through a rigid-plastic substrate oriented at an angle β with the sliding velocity v_s in x direction and its projection in the horizontal sliding (xy plane). The section with horizontal and vertical shades have plastic flow component in -y and +y directions respectively. The green dots are the separation point of plastic flow or first contact while the red dots are the end point of plastic flow/contact. The dashed black arrows show the direction of plastic flow. The dashed green lines/arcs mark the separation of plastic flow and the dashed blue lines/arcs mark the end of contact. The dashed red/orange lines mark the bounding box.

As the ellipsoidal asperity slides through the rigid-plastic substrate in the x direction oriented at an angle β, the deformed substrate comes in contact with the ellipsoidal cap as shown in figure 3.4. The projection of the ellipsoidal cap in the sliding xy plane is encapsulated by a rectangular bounding box at a given point of time whose sides are tangential to the semi-elliptic patch. This is done to derive the coordinates of boundaries of plastic flow of the substrate around the asperity. As explained in previous section the plastic flow of the substrate is in the direction opposite to sliding velocity following the curvature of the asperity. The contact/ plastic flow is initiated in a point on the semi-elliptic contact patch $NMSC$ at the point corresponding with maximum abscissa (x_{max}), since the sliding direction is along x axis. The maximum abscissa corresponds to point M which also corresponds to the point on the vertical side of the bounding box with infinite slope ($m = \infty$). As the plastic flow of the substrate follows the curvature of the asperity, the deformed substrate in contact with the asperity flows in $+y$ and $-y$ direction after the plastic flow separation at point M. As the plastic flow continues along the elliptic arcs $\overset{\frown}{MN}$ and $\overset{\frown}{MS}$ in the $+y$ and $-y$ direction the contact/plastic flow is terminated in the points corresponding to maximum ordinate (y_max), as there is no elastic-recovery. The maximum ordinate corresponds to the points N and S which also corresponds to the point on the vertical side of the bounding box with zero slope ($m = 0$). In the absence of elastic recovery the contact/plastic flow in the z direction also terminates at point L which corresponds to the point on the asperity with minimum z coordinate. Consequently the arc of separation of plastic flow on the ellipsoidal cap is given by $\overset{\frown}{LM}$ and the arcs of discontinuity/bounds of contact/plastic flow are given by $\overset{\frown}{LN}$, $\overset{\frown}{LS}$ and $\overset{\frown}{SN}$.

The center of the ellipsoidal asperity is taken as the origin of the coordinate system. In order to obtain the coordinates of the points (bounds of contact) L, M, N and S in the xy plane, the equation of the contacting (semi-)ellipse in the contact plane, i.e. $px^2 + qy^2 + rxy + t = 0$ is solved for its intersection with the bounding box. The equation of the ellipse results in one solution for its intersection with the bounding box, tangential to the ellipse. Hence the determinant of the quadratic equations is zero taking $x = x_{max}$ for point M and $y = y_{max}$ for point N. The equation of the contacting ellipse rotated by an angle β in the sliding plane with major axis a_x and minor axis a_y is given in equation 3.15e. Solving the two quadratic equations for a unique (single) solution resulting from equation 3.15e taking y and x coordinates as y_{max} and x_{max} for the intersection of the bounding box and the ellipse, the x and y coordinates are given for points N, M and S. The z coordinates of points N, M and S are obtained from their ploughing depth d_N, d_M and d_S relative to point L i.e. the separation of the corresponding points from the center of the asperity.

$$L(x, y, z) = (0, 0, -c) \tag{3.15a}$$

$$N(x, y, z) = \left(-\frac{r}{2p} N_y, \sqrt{\frac{pt}{(r/2)^2 - pq}}, -(c - d_N) \right) \tag{3.15b}$$

$$M(x, y, z) = \left(\sqrt{\frac{qt}{(r/2)^2 - pq}}, -\frac{r}{2q} M_x, -(c - d_M) \right) \tag{3.15c}$$

$$S(x, y, z) = \left(\frac{r}{2p} N_y, -\sqrt{\frac{pt}{(r/2)^2 - pq}}, -(c - d_S) \right) \tag{3.15d}$$

$$px^2 + qy^2 + rxy + t = 0 \tag{3.15e}$$

where,

$$p = [(a_y \cos\beta)^2 + (a_x \sin\beta)^2]$$
$$q = [(a_x \cos\beta)^2 + (a_y \sin\beta)^2]$$
$$r = (a_x^2 - a_y^2) \sin 2\beta$$
$$t = a_x^2 a_y^2$$

The coordinates of the points N, M, S and L in the spherical coordinates system are obtained by equating the x, y and z coordinates of N, M, S and L given in equations 3.15a-3.15d to that given in equation 3.12c. The azimuthal angles θ_M and θ_N are obtained equating the ratio of the x coordinate and the y coordinate of points M and N obtained in equations 3.15b and 3.15c with their corresponding expressions in spherical coordinates in equation 3.12c. The azimuthal angle θ_S is the of the angle θ_N. The polar angles ϕ_M, ϕ_S, ϕ_L and ϕ_N are obtained by equating the z coordinates of points M, S, L and N with the expression for the z coordinate in spherical coordinate system in equation 3.12c. Since all the points lie on the surface of the asperity, their radial coordinate is the reference radius of the ellipsoidal asperity r. Hence the coordinates of boundaries of the ploughed profile is obtained with equations 3.16a-3.16d. The expression for the ploughing depths at points M, S and N will be derived in subsection 3.2.4.

$$L(\theta, \phi, r) = (0, 0, r) \tag{3.16a}$$

$$N(\theta, \phi, r) = \left(\arctan\left(\frac{a}{b}\frac{N_y \cos\beta - N_x \sin\beta}{N_y \sin\beta + N_x \cos\beta}\right), \arctan\left(1 - \frac{d_N}{c}\right), r \right) \tag{3.16b}$$

$$M(\theta, \phi, r) = \left(\arctan\left(\frac{a}{b}\frac{M_y \cos\beta - M_x \sin\beta}{M_y \sin\beta + M_x \cos\beta}\right), \arctan\left(1 - \frac{d_M}{c}\right), r \right) \tag{3.16c}$$

$$S(\theta, \phi, r) = \left(\theta_N - \pi, \arctan\left(1 - \frac{d_S}{c}\right), r \right) \tag{3.16d}$$

3.2.4. Calculation of ploughed profile

The ploughing depth of an asperity sliding through a deforming substrate is computed by equating the applied load to the reaction force due to the contact stress underneath the substrate. For a plastically deforming substrate, the normal stress is given as hardness H of the substrate. The contact area A of an ellipsoidal asperity bearing the load F is obtained from equation 3.17a and corresponds to the frontal half of the elliptical contact area for the case of an indentation. The contact area is expressed in terms of the reference contact length a_z. The ploughing depth d of the asperity is obtained from the reference contact length and the ellipticity ratios of the asperity as given in equation 3.17b.

$$F = HA = \pi a_x a_y / 2 = \pi e_x e_y a_z^2 / 2 \tag{3.17a}$$

$$d = r - \sqrt{r^2 - a_z^2} = r - \sqrt{r^2 - \frac{2F}{\pi H e_x e_y}} \tag{3.17b}$$

However, the skewness in the shape of an ellipsoidal asperity and the resulting asymmetry in plastic flow around it results in variation in ploughing depth along the contact profile of the asperity. The variation in plastic flow is seen as the change in pile-up height h_{pu} and groove depth d_g whose sum is taken as the total ploughing depth d_p. These variations in pile-up height and groove depth are obtained from the ploughed profile of the substrate obtained in the MPM-based ploughing simulations of ellipsoidal asperity and input in the analytical model. The analytical model incorporates the variations in ploughed profile for varying indenter size and orientations with respect to sliding directions by using fitting factors p, q and w which are further explained in this subsection. Therefore, the ploughed profile around the ellipsoidal asperity is calculated by calibrating the ploughing depth over the contacting region based on inputs from the numerical model. Ploughing is assumed to be a dynamic, plastic event where the initial deformation of the substrate is followed by the subsequent shearing of the interface.

3.2.4.1. Variation in ploughing depth due to shape of the asperity

Pile-up height of the deformed substrate around the ellipsoidal asperity is affected by the slope of the asperity in the sliding (xy and xz) planes and projected area in the (yz) plane perpendicular to sliding. For rotation of an ellipsoidal asperity, with its major axis along the x axis, the projected length L_y and the projected area A_{yz} increases with angle β as shown in figure 3.5a. The increase in A_{yz} increases the resistance to plastic flow in the x direction resulting in an increased pile-up of the deformed substrate in front of the sliding asperity as shown in figures 3.6a and 3.6b. The increase in pile-up height is further assisted by the increase

in slope of the ellipsoidal asperity in the xz plane with a decrease in projected length L_x with increase in angle β as shown in figure 3.5b. The 'sharpness of the asperity', i.e. radius of curvature in the xy plane decreases with rotation of the asperity as shown in figure 3.5b. This results in a higher resistance to plastic deformation and separation of plastic flow around the asperity and hence a higher pile-up height. Since the total applied load on the asperity is shared by the deformed substrate in the pile-up material and under the ploughed groove, an increase in pile-up height results in a decrease in the groove depth as shown in figures 3.6a and 3.6b.

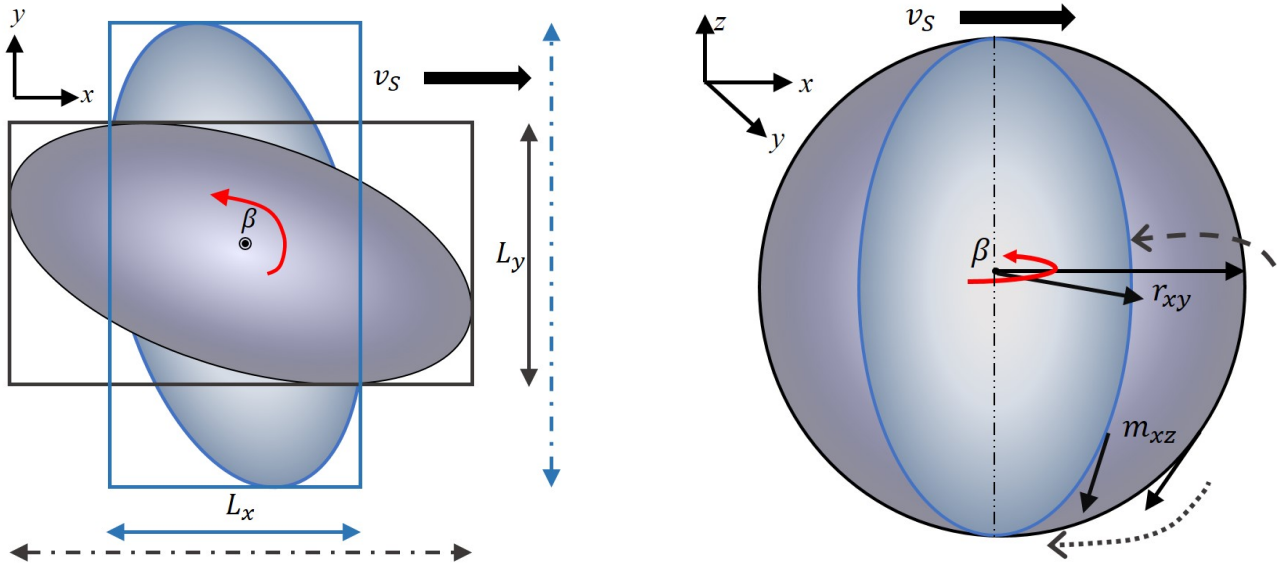

(a) Projection of the contact in the xy plane.

(b) Projection of the ellipsoid in the xz plane.

Figure 3.5: Projection of ellipsoidal contact region in the xy plane with projected lengths of the major axis in x and y axis for two asperity orientations β_1 (blue) and β_2 (grey) in the xz plane showing effect of asperity shape on direction of plastic flow. The slope in the xz plane m_{xz}, curvature in the xy plane $1/r_{xy}$ and the direction of plastic flow around the asperity in xy plane (dashed arrow) and under the asperity in xz plane (dotted arrow) is shown.

So the pile up height h_{pu} is proportional to L_y/L_x. As the pile-up height does not follow the profile of the asperity, the average pile-up height is expressed by fitting the power l to L_y/L_x in equation 3.18a. Likewise the average groove depth is given by fitting the power n to L_y/L_x. The total ploughing depth d in equation 3.17b is calibrated to the ploughing depth $d^{'}$ by accounting for the variations in pile-up height and groove depth due to the shape of the asperity as given in equation 3.18a. The total ploughing depth is now given by fitting the power p to L_y/L_x. The projected lengths L_y and L_x are given by $2y_N$ and $2x_M$ as seen from figure 3.6. So the mean ploughing depth $d^{'}$ is obtained from the initial ploughing depth d by multiplying it with y_N/x_M fitted with power p as expressed in equation 3.18b.

$$d^{'} = h_{pu} + d_g = d\left(\frac{L_y}{L_x}\right)^{o_{pu}} + d\left(\frac{L_x}{L_y}\right)^{o_g} \quad \forall o_{pu}, o_g \epsilon [0,1] \tag{3.18a}$$

$$d^{'} = d\left(\frac{L_y}{L_x}\right)^{p} = \left(\frac{y_N}{x_M}\right)^{p} \quad \forall p \epsilon [-1,1] \tag{3.18b}$$

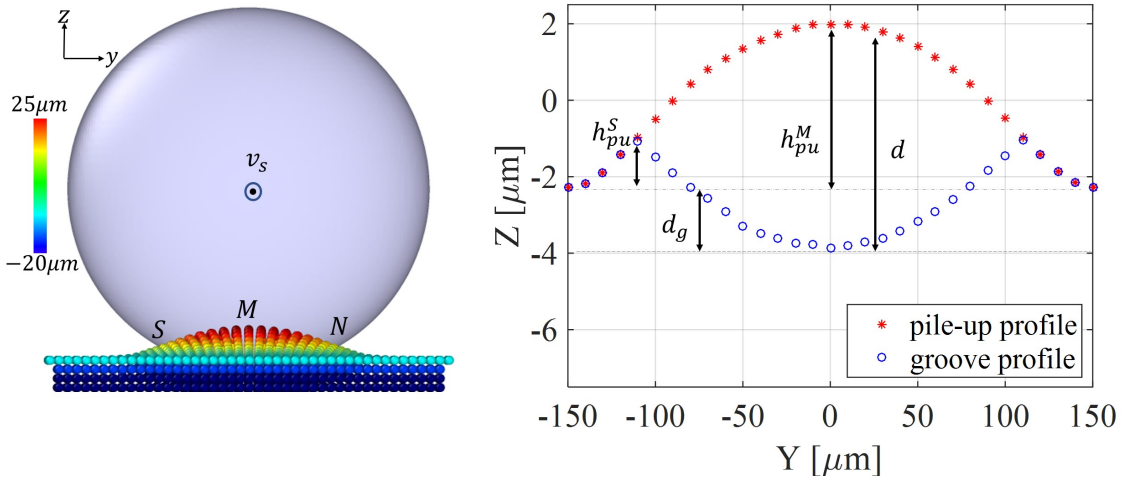

(a) Projection of the ellipsoid in the yz plane at $\beta = 0°$ orientation.

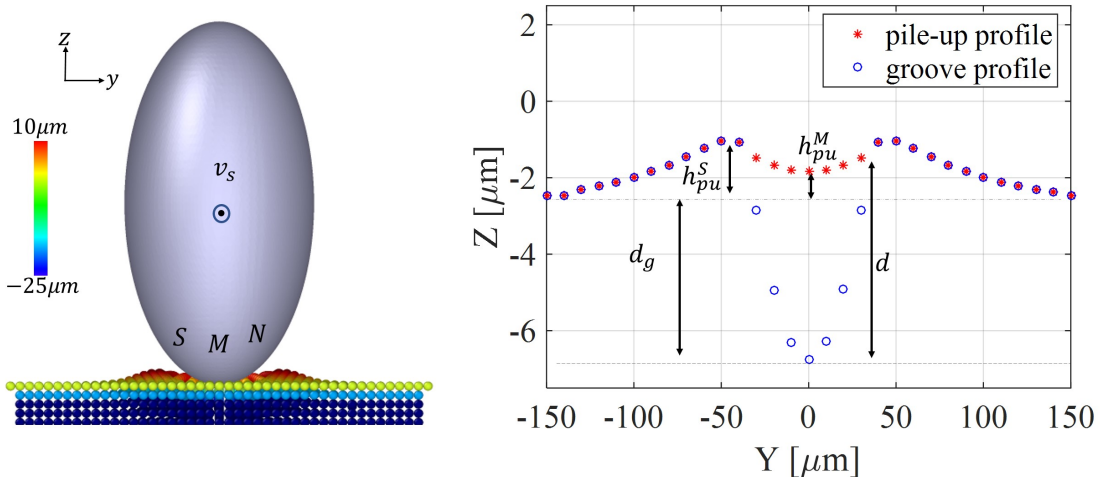

(b) Projection of the ellipsoid in the yz plane at $\beta = 90°$ orientation..

Figure 3.6: The projection of the ploughing ellipsoid (a) in the yz plane showing effect of orientation $\beta = 0°$ and (b) $\beta = 90°$ on the ploughed profile. The corresponding ploughed profile is scaled down and plotted on the right showing groove depth d_g and pile-up height h_{pu} at points M and S where the dotted black line is undeformed surface height. The encircled dot points out of the plane.

3.2.4.2. Variation of the ploughing depth due to orientation of the asperity

The asymmetry in the shape of the ellipsoidal due to its orientation angle ($\beta\epsilon(0^o - 90^o)$) results in asymmetry in plastic plow around the asperity which causes a difference in ploughing depth on either sides of the ploughed profile in $+y$ and $-y$ direction. This difference in ploughing depth d^* is expressed by fitting the factor q to the ratio of the difference in projected contact lengths of elliptic arcs $\overset{\frown}{MN}$ and $\overset{\frown}{MS}$, given by $2x_N$ (see figure 3.7b), to the un-rotated contact length a_x along the x axis. Since the increase in plastic flow on one side of the asperity results in the decrease in plastic flow on the other side of the asperity, the ploughing depths at point N and S are given by $d^{'} - d^*$ and $d^{'} + d^*$ respectively in equations 3.19a and 3.19b. The ploughing depth at point M is given as the sum of reference ploughing depth at point N d_N and additional pile-up height at point M h_M as shown in 3.7a. The additional height h_M is obtained from the similar triangles $\Delta NSS^{'}$ and $\Delta NMM^{'}$ formed by the additional pile-up heights $SS^{'}$ and $MM^{'}$

and projected contact lengths SN and MN in the y direction as shown in figure 3.7a. The projected contact lengths SN and MN are given as $2y_N$ and $y_N - y_M$ while the additional pile-up height at S is given as $d_S - d_N$. By equating the ratios of the contact lengths and additional pile up heights at M and S the additional height h_M is given as $(y_N - y_M)(d_S - d_N)/2y_N$. The ploughing depth at point of separation of plastic flow d_M is given in equation 3.19c.

$$d_N = d'\left(1 - q\frac{x_N}{a_x}\right) \tag{3.19a}$$

$$d_S = d'\left(1 + q\frac{x_N}{a_x}\right) \tag{3.19b}$$

$$d_M = d'\left(1 - 2q\frac{x_N}{a_x}\frac{y_M}{y_N}\right) \tag{3.19c}$$

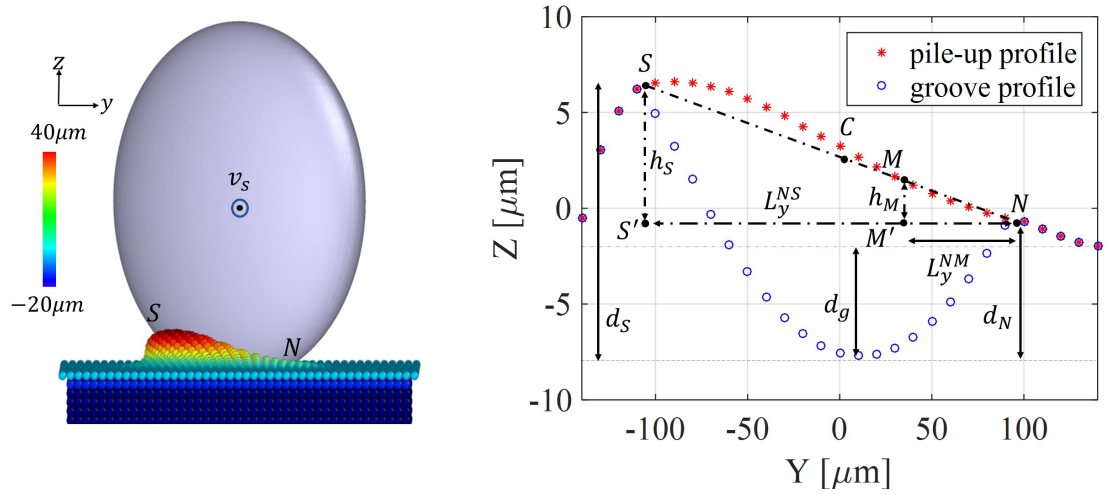

(a) Projection of the ellipsoid in the yz plane.

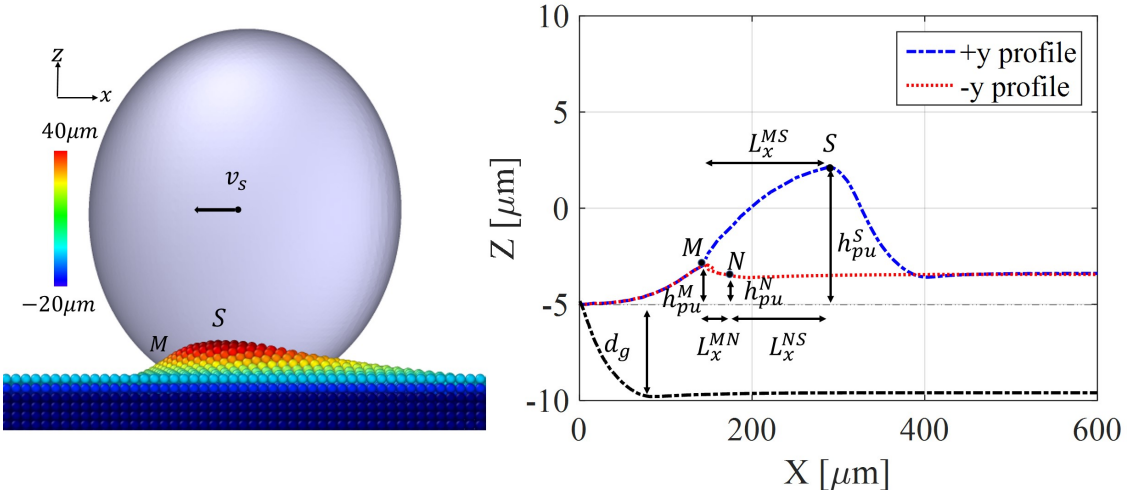

(b) Projection of the ellipsoid in the xz plane.

Figure 3.7: The projection of the ploughing ellipsoid at $\beta = 45°$ orientation on the (a) yz plane and (b) the xz plane showing the effect of orientation of ploughed profile. The corresponding ploughed profile is scaled down and plotted on the right showing the asymmetry is distribution of ploughing depth due to orientation. The projected contact length, pile-up height and ploughing depth at points M, S and N are also shown.

3.2.4.3. Variation in ploughing depth due to interfacial shear

The applied force in equation 3.17a is balanced only by the contact pressure due to plastic deformation. However, as the asperity slides through the substrate the vertical z component of the force due to interfacial shear F_z^{sh} also contributes to balancing the applied load along with the force due to plastic deformation F_z^{pl}. The force F_z^{sh} acts on the substrate in the direction opposite to that of plastic flow at the interface. On one hand, the force F_z^{sh} restricts the plastic flow of the deformed substrate and tends to reduce the ploughing depth. On the other hand the forces F_z^{sh} and F_z^{pl} in opposite directions on the elements of deforming substrate resulting in a bi-axial tensile state.This assists the deformation of the substrate and increases the ploughing depth. Taking the contrasting effects of the interfacial shear the reaction force due to interfacial shear F_z^{sh} has been corrected by the fitting factors u_a and u_b. The final ploughing depth $d^{''}$ is then given by the equation 3.20.

$$d^{''} = r - \sqrt{r^2 - 2\frac{F_z^{pl} - u_a F_z^{sh} + u_b F_z^{sh}}{\pi H e_x e_y}} \tag{3.20}$$

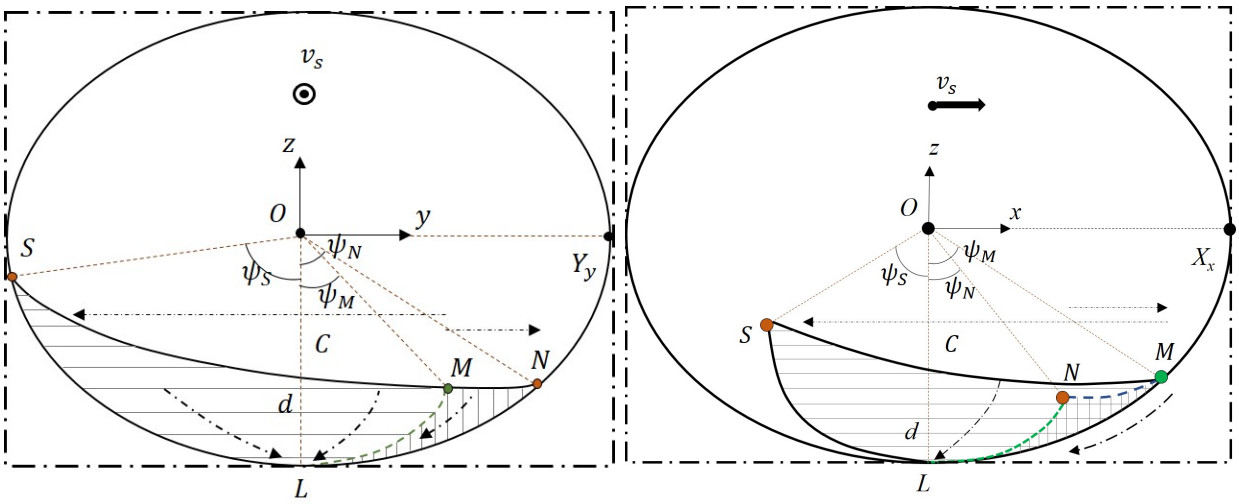

(a) Projection of ellipsoidal asperity in yz plane (b) Projection of ellipsoidal asperity in xz plane

Figure 3.8: Projection of the ellipsoidal asperity in the vertical yz and xz planes showing the contact region with plastic flow in the $+y$ direction shown by vertical lines and in the $-y$ direction shown by horizontal lines. The green arcs LS, LN and LM show the boundaries of plastic flow. The angle ψ_M, ψ_N and ψ_S show the angle subtended by the points M, S and N at the center of the ellipsoid O with the z axis.

3.2.5. Calculation of the total force components

The components of the total force acting the the ellipsoidal asperity sliding through the rigid-plastic substrate is given along the Cartesian coordinates F_x, F_y and F_z. These components of the total force are further resolved into the force due to plastic deformation of the substrate F^{pl} and force due to shearing of the interface F^{sh} as given in equation 3.9. The components of elemental forces are calculated using the expressions for the unit normal and unit tangent vectors in equations 3.10b and 3.11c in section 3.2.1 which are expressed in terms of the elemental projected areas. The unit normal and unit tangent given in the spherical coordinates in section 3.2.2 are integrated over the boundaries of contacting region given in section 3.2.3 to obtain the components of total force.

In order to obtain the components of force acting on the asperity, the total contact area between the asperity and the substrate resulting in the corresponding component of plastic flow is calculated. The asperity-substrate contacting region can be given as the sum of the ellipsoidal cap with horizontal base at N and the ellipsoidal segment between S and N. The area of such an ellipsoidal segment is approximated as half the area of the ellipsoidal band, which is the surface of the asperity bounded by horizontal planes intersecting at S and N. In calculating the total force due to ploughing and shearing in the x and z direction the integration of elemental forces is done over the ellipsoidal cap with base at N and the ellipsoidal segment between S and N as shown in figure 3.8a and given in equations 3.21a, 3.21c, 3.21d and 3.21f. In calculating the total force due to ploughing and shearing in the y direction, the component of force in the -y axis F_{-y} is subtracted from the component in the $+y$ axis F_{+y}. F_{+y} is calculated by integrating over the region bound by the elliptic cap with base plane at M and elliptic segment between S and M, while F_{-y} is calculated by integrating over the region bound by the elliptic cap with base plane at N and elliptic segment between N and M as shown in figure 3.8b and in equations 3.21b and 3.21e. The friction force in the x and y directions is calculated by summing the respectively components of F_{pl} and F_{sh}. The total magnitude of friction force is $\sqrt{F_x^2 + F_y^2}$.

$$F_x^{pl} = p_{pl} \oint_{N,L}^{S} dA_\Delta \, \hat{n}\,\hat{i} \approx p_{pl}\left(\int_0^{\phi_N} \int_{\theta_N}^{\theta_S} \mid m(\theta,\phi) \mid \, d\theta d\phi + \frac{1}{2} \int_{\phi_N}^{\phi_S} \int_{\theta_N}^{\theta_S} \mid m(\theta,\phi) \mid \, d\theta d\phi \right)$$
$$\Rightarrow F_x^{pl} \approx \frac{p_{pl} c}{2} \big(\cos\phi_N \sin\phi_N - \phi_S + \cos\phi_S \sin\phi_N - \phi_N \big) \big(a \cos\theta_N \sin\beta + b \sin\theta_N \cos\beta \big) \tag{3.21a}$$

$$F_y^{pl} = p_{pl}\left(\oint_{M,L}^{S} dA_\Delta - \oint_{N,L}^{M} dA_\Delta \right) \hat{n}\,\hat{j} \approx p_{pl}\left(\int_0^{\phi_M} \int_{\theta_S}^{\theta_M} \mid l(\theta,\phi) \mid \, d\theta d\phi + \right.$$
$$\left. \frac{1}{2} \int_{\phi_M}^{\phi_S} \int_{\theta_S}^{\theta_M} \mid l(\theta,\phi) \mid \, d\theta d\phi - \int_0^{\phi_M} \int_{\theta_M}^{\theta_N} \mid l(\theta,\phi) \mid \, d\theta d\phi + \frac{1}{2} \int_{\phi_N}^{\phi_M} \int_{\theta_M}^{\theta_N} \mid l(\theta,\phi) \mid \, d\theta d\phi \right)$$
$$\Rightarrow F_x^{pl} \approx \frac{p_{pl} c}{2} \Big(\big(\phi_S - \phi_N \big) + 2\phi_M - \cos\phi_S \sin\phi_S + \cos\phi_N \sin\phi_N - 2\cos\phi_M \sin\phi_M \Big)$$
$$\Big(a \cos\theta_N \cos\beta - b \sin\theta_N \sin\beta \Big) \tag{3.21b}$$

$$F_z^{pl} = p_{pl} \oint_{N,L}^{S} dA_\Delta \, \hat{n}\,\hat{k} \approx p_{pl} \int_0^{\phi_N} \int_{\theta_N}^{\theta_S} \mid n(\phi) \mid \, d\theta d\phi + \frac{1}{2} p_{pl} \int_{\phi_N}^{\phi_S} \int_{\theta_N}^{\theta_S} \mid n(\phi) \mid \, d\theta d\phi \tag{3.21c}$$
$$\Rightarrow F_x^{pl} \approx \frac{\pi}{8} p_{pl} a b \big(2 - \cos 2\phi_S - \cos 2\phi_N \big)$$

$$F_x^{sh} = \tau_{sh} \oint_{N,L}^{S} dA_\Delta \, \hat{t}\,\hat{i} \approx \tau_{sh} \int_0^{\phi_N} \int_{\theta_N}^{\theta_S} \mid f(\theta,\phi) \mid \, d\theta d\phi + \frac{1}{2} \tau_{sh} \int_{\phi_N}^{\phi_S} \int_{\theta_N}^{\theta_S} \mid f(\theta,\phi) \mid \, d\theta d\phi \tag{3.21d}$$

$$F_y^{sh} = \tau_{sh}\left(\oint_{M,L}^{S} dA_\Delta - \oint_{N,L}^{M} dA_\Delta \right) \hat{t}\,\hat{j} \approx \tau_{sh}\left(\int_0^{\phi_M} \int_{\theta_S}^{\theta_M} \mid g(\theta,\phi) \mid \, d\theta d\phi + \right.$$
$$\left. \frac{1}{2} \int_{\phi_M}^{\phi_S} \int_{\theta_S}^{\theta_M} \mid g(\theta,\phi) \mid \, d\theta d\phi - \int_0^{\phi_M} \int_{\theta_M}^{\theta_N} \mid g(\theta,\phi) \mid \, d\theta d\phi + \frac{1}{2} \int_{\phi_N}^{\phi_M} \int_{\theta_M}^{\theta_N} \mid g(\theta,\phi) \mid \, d\theta d\phi \right) \tag{3.21e}$$

$$F_z^{sh} = \tau_{sh} \oint_{N,L}^{S} dA_\Delta \, \hat{t}\,\hat{k} \approx \tau_{sh} \int_0^{\phi_N} \int_{\theta_N}^{\theta_S} \mid h(\phi) \mid \, d\theta d\phi + \frac{1}{2} \tau_{sh} \int_{\phi_N}^{\phi_S} \int_{\theta_N}^{\theta_S} \mid h(\phi) \mid \, d\theta d\phi \tag{3.21f}$$

3.2.6. Calculation of contact area in ploughing of a coated substrate

An analytical model is developed to calculate the coefficient of friction in coated systems as a function of the hardness of the coating relative to the substrate and the coating thickness. The analytical model is based on the concept of load sharing in a coated system in contact with a rigid-counter face, given in [117], [118], and [119]. Rigid-plastic material behaviour is chosen for the coated system. The analytical model will consist of a contact model to compute the contact area between the asperity sliding through the coated substrate. Using the calculated contact area and the hardness of the coating, substrate and the coated system the ploughing friction will be calculated. The analytical model will be used to understand the factor contributing to ploughing friction and to compare and explain the results obtained from the numerical (MPM) ploughing model and ploughing experiments on coated systems respectively. Further details can be found in paper F [107].

The response to loading (indentation) of a coated system is determined from its effective hardness H_{cs} [117]. The effective hardness of a coated system H_{cs} is given by combining the hardness of the substrate (H_s) and the hardness of the coating (H_c) typically by using some rule of mixtures. Typically H_{cs} is obtained as a function of coating thickness t from the indentation response to a spherical indenter. For thin, soft coatings on hard substrates the effective hardness is given using equation 3.22 [3]. The value $k_1 = 125$ was obtained by experimentally fitting the indentation response of spheres of various radii r on a coated substrate, where $H_{cs} \approx H_c$ for values of $t/r \geq 0.04$ [3].

$$H_{cs} = H_s + (H_s - H_c) \exp\left(- k_1 \frac{t}{r} \right) \tag{3.22}$$

A rigid spherical indenter sliding through a rigid-plastic coated system could result in two contacting conditions. In the first case, the spherical indenter is only in contact with the coating, i.e. the ploughing depth d_p is less than the coating thickness t. In the second case, the spherical indenter is in contact with both the coating and the substrate, i.e. the ploughing depth is more than the coating thickness. For a spherical indenter of radius r, ploughing through the coated substrate, the contact radius is taken as a. Considering the frontal half of the indenter in contact during ploughing only through the coating in rigid-plastic coated-substrate (see figure 3.9a), the horizontal projection $A_{xy} = A_{sh}$ of the total contact area is given in equation 3.23a. By equating the applied load F_n with the contact pressure P_{pl} over the horizontal projection of the contact area A_{sh} is obtained. For normal loading of a plastically deforming coated substrate, the contact pressure P_{pl} equals the effective indentation hardness H_{cs} of the coated system. The ploughing depth d_p for a spherical indenter of radius r is obtained from its contact radius as given in equation 3.23b The (vertical) cross-sectional contact area $A_{yz} = A_{pl}$ for a spherical indenter ploughing in x direction is given as the area of the segment formed by the intersection of the contact plane on the indenters mid yz-plane and is expressed in equation 3.23c (see figure 3.9b).

$$A_{sh} = \frac{\pi a^2}{2} = \frac{F_n}{H_{cs}} \tag{3.23a}$$

$$d_p = r - \sqrt{r^2 - a^2} \tag{3.23b}$$

$$A_{pl} = r^2 - \arctan \frac{a}{r - d_p} \tag{3.23c}$$

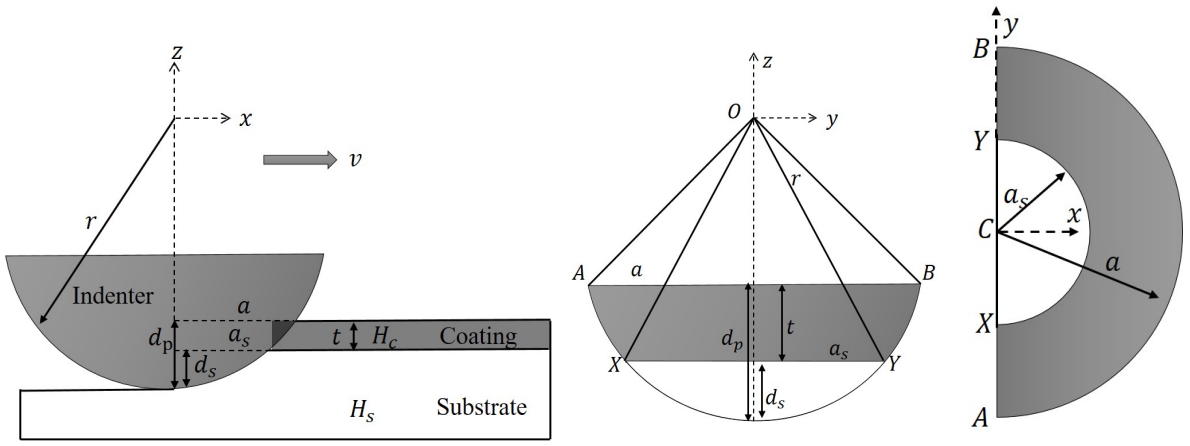

(a) Projection in xz plane.

(b) Projection in yz plane.

(c) Projection in xy plane.

Figure 3.9: Schematic of a spherical indenter of radius r ploughing through a rigid-plastic coated substrate, with coating thickness t, coating hardness H_c, substrate hardness H_s and its projection in xz, yz, xy planes.

Figure 3.9 shows the case of a rigid spherical indenter ploughing through both the coating and the substrate. The total ploughing depth d_p is given as the sum of ploughing depth in the substrate d_s and ploughing depth in the coating d_c. In this case, $d_p > t$, resulting in $d_c = t$. The applied normal load F_n is now carried by both the coating and the substrate over the total contact area $A_{sh} = A_{sh_c} + A_{sh_c}$ where A_{sh_s} is the contact area of the substrate and A_{sh_c} is the contact area of the coating, (seen figure 3.9c). It is assumed that the contact pressure generated in the coating equals the effective hardness of the coated system H_{cs}, while the contact pressure in the substrate equals hardness of the substrate H_s. The contact area of the coating with the indenter A_{sh_c} (the area of the annular semi-circle in figure 3.9c) is given in equation 3.24a in terms of the ploughing depth in the substrate d_s, indenter radius r and coating thickness t (using equation 3.23b for $d_p = d_s + t$). By equating the applied load to the contact pressure in the contact area with the coating and the substrate in equation 3.24b and substituting expression of A_{sh_c} from equation 3.24a, the expression of d_s is given by solving the resulting quadratic equation in equation 3.24c. The horizontal and vertical projections of the contact area with the substrate A_{sh_s} and A_{pl_s} can be computed using equation 3.24d and 3.24e. The total horizontal projection A_{pl} of the indenter with the coated substrate is now given by substituting $d_p = d_s + t$ in equation 3.23c. The vertical projection of contact area of the indenter with the coating A_{pl_c} is given in equation 3.24f is given as the difference between A_{pl} and A_{pl_s} as shown in figure 3.9b.

$$A_{sh_c} = A_{sh} - A_{sh_c} \implies A_{sh_c} = 0.5\pi t(2(r - d_s) - t) \tag{3.24a}$$

$$F_n = H_s A_{sh_s} + H_{cs} A_{sh_c} \tag{3.24b}$$

$$d_s = -\frac{B + \sqrt{B^2 - 4AC}}{2A} \tag{3.24c}$$

$$\forall A = 0.5\pi H_s, B = \pi(H_{cs}t - H_s r), C = F_n - 0.5\pi t(2r - t)H_{cs}$$

$$A_{sh_s} = 0.5\pi(r^2 - (r - d_s)^2) \tag{3.24d}$$

$$A_{pl_s} = r^2 - \arctan\frac{a}{r - d_s} \tag{3.24e}$$

$$A_{pl_c} = A_{pl} - A_{pl_s} \tag{3.24f}$$

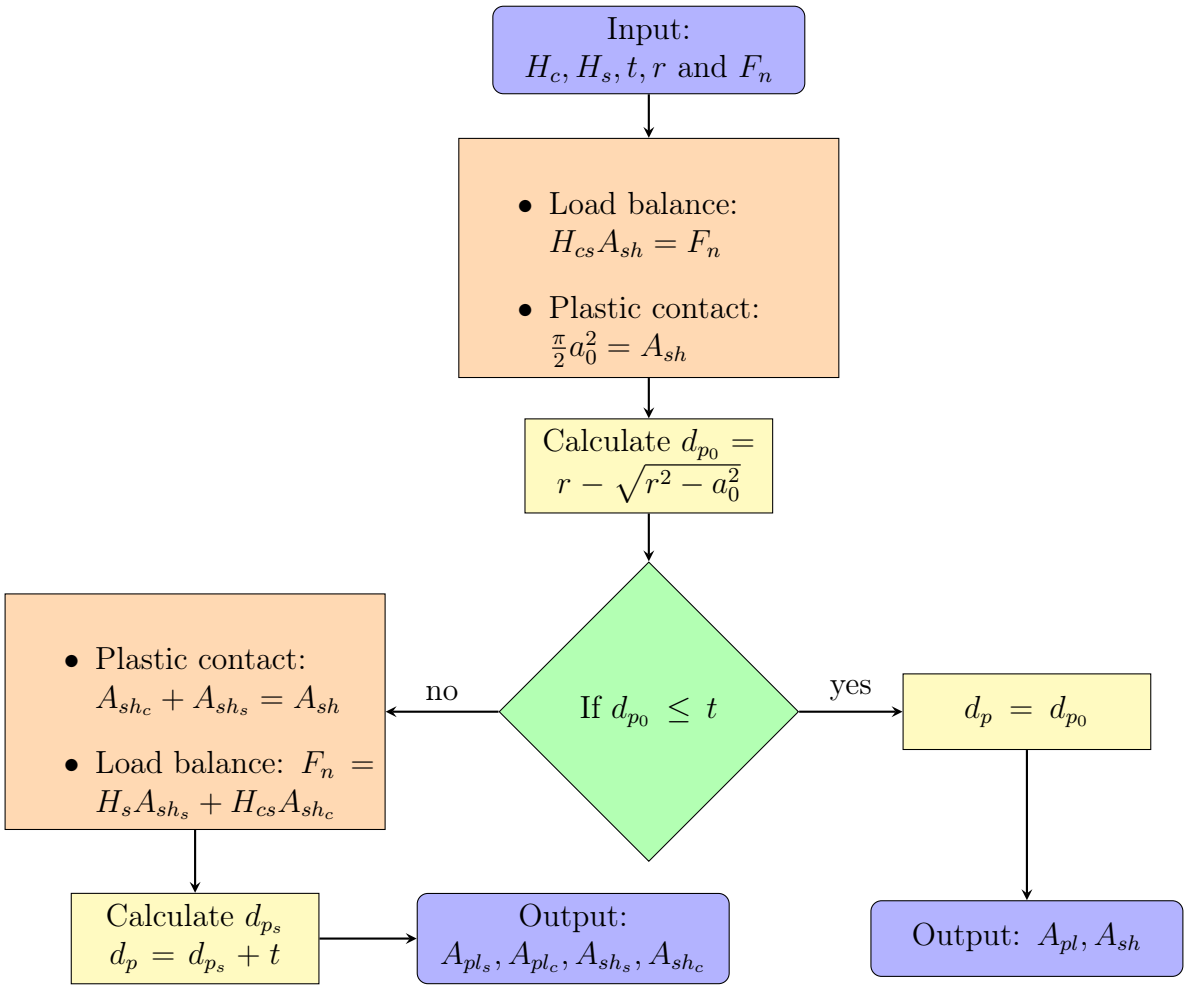

Figure 3.10: Algorithm to calculate the projected contact areas in the horizontal xy plane A_{sh} and vertical xz plane A_{pl} for a rigid-sphere ploughing through a rigid plastic coated system in x direction.

An algorithm to compute the projection of contact area of the indenter sliding through a coated substrate is shown in figure 3.10. The algorithm accounts for both the cases of contact between the indenter and the coated substrate, i.e. indenter with the coating and the indenter with both the coating and the substrate. An initial prediction of the ploughing depth of the spherical indenter is made by equating the applied load with the effective indentation hardness H_{cs}. The ploughing depth is compared with the coating thickness to categorize the contact condition among the two cases described above. Following the set of equations 3.23a-3.23c and equations3.24a-3.24f the algorithm computes the contact areas for each of the cases.

3.2.7. Calculation of ploughing friction components in coated system

The ploughing friction is calculated as the sum of the friction force due to plastic deformation of the ploughed specimen and the friction force due to shearing of the interface [34]. The friction force F_f acting on a spherical asperity ploughing through a specimen is given in equation 3.25a. The friction force due to ploughing is given as the product of the contact pressure due to the plastic deformation of the substrate P_{pl} and the area of the ploughed cross section A_{pl}. The friction force due to shearing of the interface is given as the product of the interfacial shear strength τ_{sh} and the contact area between the indenter and the specimen at the surface A_{sh}. The overall coefficient of friction μ is calculated using equation 3.25b.

$$F_f = F_{pl} + F_{sh} = P_{pl}A_{pl} + \tau_{sh}A_{sh} \tag{3.25a}$$

$$\mu = \frac{F_f}{F_n} = \frac{F_p l + F_s h}{F_n} = \mu_{pl} + \mu_{sh} \tag{3.25b}$$

$$\mu_{pl} = \frac{F_{pl}}{F_n} = \frac{H_s A_{pl_s} + H_c A_{pl_c}}{F_n} \tag{3.25c}$$

$$\mu_{sh} = \frac{F_{sh}}{F_n} = \frac{f_s H_s A_{sh_s} + f_c H_c A_{sh_c}}{3\sqrt{3}F_n} \tag{3.25d}$$

In ploughing through an rigid-plastic coated substrate, the stress acting on the ploughed cross section p_{pl}, is taken as the hardness of the coating H_c or hardness of the substrate H_s. The coefficient of friction due to plastic deformation of the coated system μ_{pl} is obtained using equation 3.25c, where the friction force due to ploughing is shared by the vertical projected areas of the coating A_{pl_c} and the substrate A_{pl_s}.The shear stress at the indenter-coating interface and the indenter-substrate interface is taken as fractions f_c and f_s of the maximum shear strength of the coating τ_{sh_c} and the substrate τ_{sh_s} respectively. Typically for uncontaminated surfaces, $f = 1$. For a rigid-plastic material, its shear strength τ_{sh} is given as a factor $1/k_0$ of its hardness H. Typically for metals $k_0 = 3\sqrt{3}$ [113] and [24]. The interfacial friction is due to shearing of the substrate and the coating is given the shear stress $f_s\tau_{sh_s}$ and $f_c\tau_{sh_c}$ distributed over the horizontal projected areas A_{sh_s} and A_{sh_c} respectively. The coefficient of friction due to shearing of the interface μ_{sh} in a coated system is given in equations 3.25d. If $d_p < t$, the coefficient of friction is given by substituting $A_{pl_s} = 0$ and $A_{sh_s} = 0$ in equation 3.25c and 3.25d respectively. The results obtained from the analytical ploughing model for a coated substrate are given in Paper F[107].

3.3. Summary

A Material point method based, numerical ploughing model has been developed in this section. The section summarises the material models and the contact (friction) models in the building of the MPM based ploughing model. An analytical model to compute the ploughed profile and ploughing forces has also been developed. The analytical model has incorporated the changes in pile-up for various asperity geometries from the MPM ploughing model to accurately calculate the ploughed profile and hence the ploughing friction. Both the models can compute the ploughed profile and ploughing friction for both on uncoated and coated substrate ploughed by ellipsoidal asperities with varying sizes, ellipticity rations and orientation relative to sliding direction.

Chapter 4

Experimental procedure and characterization

Experiments have been done to serve two objectives. The first objective is to characterize the required properties of the specimen to input into the numerical and analytical model. The second objective is to reproduce the single-asperity sliding behaviour for validating and comparing the results with that of the numerical and analytical model. The section describes the experimental set-ups such as the linear friction tester and nano-indenter used for measurement of the friction force and elastic and plastic properties of the coating and the substrate. The specimens are then analyzed using different microscopy techniques. The preparation of the tools and sheets for the experiments are also explained.

The interfacial shear strength is measured for both zinc coated steel and uncoated steel sheets which are covered with a stable oxide film or with boundary layers using two different forming oils. The measured interfacial shear strength is plotted as a function of contact pressure and sliding velocity. An algorithm is designed to measure the effective indentation hardness and elastic modulus of the zinc coated sheets in combination with indentation experiments. The yield locus for an uncoated steel sheet is plotted based on the Knoop hardness data and compared with the yield locus obtained from standard bulk test. The Knoop hardness data is further utilized to plot the yield locus of the zinc coating.

The chapter has been categorized into two sections. In the first section the experimental set ups used in the experimental validation and characterization are explained. The second section explained the characterization procedure and the characterized material properties. The contents of this chapter can be referred from the following appended papers:

- Experimental procedure:
  - Ploughing set-up and experiments: Paper A [95], Paper C [106] and Paper F[107].
  - Indentation set-up: Paper E [120]
- Experimental characterization:
  - Hardness and Young's modulus of the coated system: Paper D [121]
  - Interfacial shear strength: Paper D [121]
  - Yield criterion and yield function: Paper E [120]

4.1. Experimental procedure

The experimental set-ups are chosen and the experimental methods are designed to serve a two fold purpose. One is to characterize the properties of the lubricant boundary layer, substrate material and the tool and substrate surface in order to provide input values to the ploughing model. The second is to simulate ploughing at a laboratory scale and validate the characterized friction and wear profiles for different parameters with the results of the numerical model. The experimental set-ups consist of a line contact shear test set-up, a scratch test set-up, an indentation set up and different imaging/microscopy set up all of which will be described in this section. Further details on the experimental characterization procedure and results can be referred to [121] and [107] (appended paper D and E).

4.1.1. Materials

The materials for the ploughing experiments will be categorized into tools interacting with a sheet metal substrate. The tools used are the cylindrical rollers for sliding, the diamond indenters and the pins for ploughing. Cylindrical rollers with a logarithmic profile were used in a line contact set-up for measurement of the interfacial shear strength. The Knoop indenter has been used in the micro-hardness tester and the Nano-indentation tester over a varied range of loads. The measurements from indentations of varying sizes has been used to the study effect of indentation size of measured surface properties such as hardness. Berkovich and Vickers indenters have also been used for reference indentation measurements and to compute the average indentation hardness. The ploughing experiments were performed using pins with various tip geometries representing the micro-geometry of the tool-asperities in deep-drawing. Elliptical pins and spherical pin have been used to replicate the size and orientation relative to sliding direction for tool asperities. Pins with ellipsoidal tips of varying size, ellipticity ratio have been designed as further explained below. Spherical balls have also also mounted on pin tips and used for experimental validation of the numerical model.

The substrate was designed from the sheet used as work-piece in deep-drawing. The steel sheet was coated with a layer of zinc deposited by the process of continuous hot-dip galvanization. The sheet was drawn into a molten zinc bath with traces of aluminum. As the sheet was drawn out of the zinc bath, the excess zinc was removed from the substrate using air-knives thus controlling the coating thickness on the steel sheet. The sheet metals are polished to the required roughness in order to avoid any unwanted roughness effects during characterization and experimental validation. The lubricants used in deep-drawing process is applied on the steel sheet prior to the ploughing experiments.

4.1.1.1. Sliding tools

A cylindrical roller with a logarithmic profile is used to measure the interfacial shear strength by loading and sliding the cylinder over its curved surface as shown in figure 4.1b, resulting more or less in a line contact with the substrate. Without any edge profile in the cylinder, the discontinuity of contact results in increase in contact pressure and singularity of contact pressure at the edge of the line contact. Logarithmic crowning at the edges of the cylindrical rollers is shown to reduce the concentration of contact pressure at the edge of the roller [122].

For several ploughing experiments, spherical balls are mounted on top of cylindrical holders (see figure 4.1a). The top of the holders are designed to be able to hold balls of various

(a) Pin, spherical ball of 3mm dia. at tip.

(b) Pin, logarithmic crowned roller of 10mm dia.

Figure 4.1: Image of the pin tips/tools used in the Linear friction tester.

Table 4.1: Measured axes lengths and roughness values of ellipsoidal pins.

Pin name	a [μm]	b [μm]	R_a [μm]	R_q [μm]
A1	1000±55.8	375±24.1	0.83	0.43
A2	833.3±21.8	300±1	0.82	0.48
A3	666.7±32.4	250±6.9	0.77	0.12
B1	250±12.2	500±10.3	0.84	0.15
B2	333.3±2.2	500±4.3	0.72	0.91
B3	417.5±10	500±5.5	1.01	0.33
B4	500±4	500±5.5	0.63	0.53
B5	600±11.2	500±6.7	0.71	0.54
B6	750±7.1	500±7.2	1.38	0.58
B7	1000±32	500±7.3	0.97	0.53
C	2000±153.6	500±10.4	0.60	0.192

diameters ranging from 0.3-3mm. The balls are made of chrome steel termed AISI 52100 (100CrMn6) and are mounted on the top of the holder by using industrial glue which prevents any possible movement of the ball with respect to the holder. The spherical balls have highly precise diameters and mean surface roughness of 0.025 μm. Typically spherical balls of 1mm and 3mm diameter are used in the ploughing experiments for validation of the results obtained from numerical simulations. Pins with smaller tip diameters of 0.1 and 0.2mm were made by grinding and polishing a hardened conical tip pin with base radius of 6mm.

The ellipsoidal pin tips are made out of D2 tool steel (DIN 1.2379) cylinders which are heat treated to a hardness of 62±2 HRC (746HV or 7.32GPa). The base of the heat-treated cylinder then undergoes the process of grinding followed by high precision milling and polishing to obtain the designed ellipsoidal shape at the tip with the required roughness as shown in figure 4.2a. The process has been used to design 11 different ellipsoidal pin-tips as listed in table 4.1. The length of one axis of the base of the ellipsoidal tip is increased while the length of the other

(a) View of the tip (b) View of the base

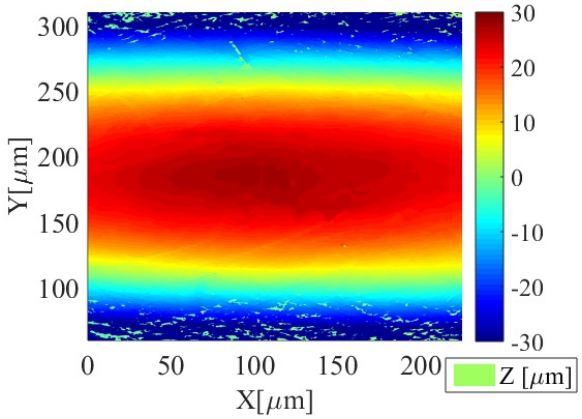

(c) Height distribution of the pin tip

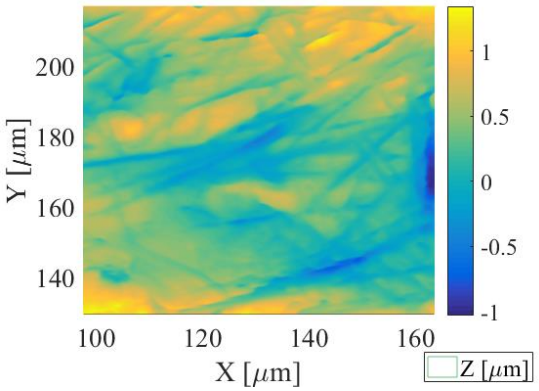

(d) Surface roughness of the pin tip

Figure 4.2: Image of the ellipsoidal pin ($a = 1mm, b = 0.25mm$) with distribution of tip height and roughness as seen under the confocal microscope at 50x magnification.

axis is kept constant for 7 pins named B1-B7. In 3 other pins namely A1-A3, the length of the axis of the base of the ellipsoid is changed such that the length of the other changes as the reciprocal of the first axis. A large ellipsoidal pin C with axis length of 2mm was also designed. The reference radius (axis length or height) of the ellipsoidal pin was taken as 0.5mm. The ellipsoidal pins A1-A3 and C were marked by lines with angular separation of 15° while the markings are made along the major and minor axes of pins B1-B7 at the edge of the base as shown in figure 4.2b. This allows a defined angle between the ploughing asperity and the sliding velocity vector. As an example, the geometry of the pin tip with length of its axis $a = 1mm$ and $b = 0.25mm$ is shown in figure 4.2c. The roughness of the pin tip is obtained by removing the designed shape of the pin tip from the measured surface heights and is shown in 4.2d. It can be seen from table 4.1 and figure 4.2c and 4.2d that the geometry of pin tips are within the 10% of the design tolerance while the mean surface roughness R_a and root-mean-square roughness R_q is in the range of 0.6-1.4μm and 0.1-0.9μm respectively.

4.1.1.2. Substrate specimen

Ploughing experiments are performed on both coated and uncoated sheets. The (uncoated) substrate is made up of cold rolled deep-drawing DX56 steel sheet. The steel sheet is coated with zinc coating with an amount varying from 100-275 g/m^2 which corresponds to a coating

thickness of 7-25μm. The zinc coated steel sheets DX56 Z100/275 EDT are then temper rolled using EDT (electrical discharge texturing) roll mills to give them with required surface texturing. Due to the prior rolling processes, the sheets have an initial surface roughness ranging from 1-2μm as shown in 4.3a. For characterization of the properties of the sheets and for performing ploughing experiments the effects of roughness on the substrate should be minimized. Hence the surface and the cross-section of both the coated and uncoated sheets were polished to a mean surface roughness of 0.05 μm.

Hot mounting of the sheets on 50mm Bakelite discs were done after laser cutting them to the required size of 32.5mm $\times$ 32.5mm using a hot mounting machine, prior. The powdered Bakelite's resin was put on top of the cut sheets and pressurized at a load of $1kN$ at a temperature of 180^oC for 7 minutes and then cooled to room temperature by water for 7 minutes. Similarly, the sheets were cut both along the rolling as well as in the transverse direction into rectangular specimens of $15mm$ length and $5mm$ width. For indentation experiments, the cross-section of the sheets were hot mounted on a 25mm Bakelite's disc with the support of rings.

The polishing of the hot mounted-sheets was done using "Struers" automatic/polishing machine. Initially, grinding of the steel sheet was done using a 220P grade sandpaper with 68μm size silicon carbide particles at 25N load at 150 rpm for 3 minutes to remove any unevenness and waviness, resulting in flat sheets. The lapping of the steel specimens was then done using 9 μm size diamond suspension for at 40 N load for 5 minutes. At this stage the steel sheet is polished to a mean surface roughness of 0.03μm as shown in figure 4.3b. This will result in a 'shine-polished' specimen with a stable layer of metallic oxide on its surface. Further polishing of the steel sheet can be done using diamond suspension of 3μm particle size at an applied load of 20N at 150 rpm for 4 minutes. The final polishing step uses silica suspension of particles size 0.04μm at a load of 15N at 150 rpm for 3 minutes. All these polishing steps results in a 'mirror-polished steel' sheet of 0.005μm mean surface roughness. The mirror-polished specimen can be also used to study the micro-structure of the steel sheet as shown in figure 4.3c.

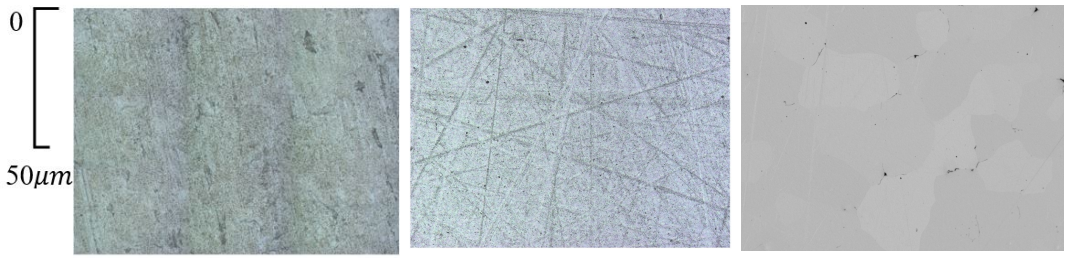

(a) Before polishing (b) After shine polishing (c) After mirror polishing

Figure 4.3: Image of the steel sheet at various stages in polishing as seen with an optical microscope at 50x magnification.

The zinc coated sheets were polished by using water less suspension as the softness of zinc and its reaction with water can leave the coatings with scratches, discolored or even etched. Two separate procedures were followed for the polishing of the surface and cross sections of the zinc coated sheets. Firstly, grinding of the mounted cross-section of the sheets was done using 320P grade sandpaper for 2 minutes with 46 μm silicon carbide particles at 30N load and 300 rpm. Then the lapping of the flattened cross-section of the sheets was done using diamond suspension with particle size 9 μm at 30N load, 150rpm for 4 minutes. The fine polishing of the

cross section of the sheets consisted of water-less steps using yellow, alcohol-based lubricants. Firstly, the cross section was polished with a poly-crystalline diamond slurry suspension of $3\mu m$ particle size and the lubricant at 25N load, 150rpm for 4 minutes. Then a diamond slurry suspension of $1\mu m$ was used with the lubricant at 20N load and 150 rpm for 4 minutes. Finally the cross-section of the sheets was polished using de-agglomerated gamma alumina powder of 0.05 μm particle size mixed with ethanol denatured with iso-propyl alcohol at 15N and 150rpm for 2 minutes. The fine polished steps were repeated for polishing of the surface of the coating surface as grinding of the coating removed the zinc from the sheet. All the specimens were cleaned using industrial ethanol in an ultra-sonic bath at the end and within each step and heated in vacuum oven to remove any dirt before storing the samples in a dehumidifying chamber.

4.1.1.3. Indenters

Indentation techniques are commonly used to characterize the material behaviour of coated specimens. Typically Vickers indenters are used for micro-hardness measurement studies. Vickers indenters have a square pyramidal base with an included angle of 136° between plane faces of the indenter tip as shown in figure 4.4a. Berkovich indenters have a three-sided pyramid geometry with a total included angle of 142.3° (see figure 4.4b) and have the same projected area to depth ratio as Vickers indenter. Berkovich tips are commonly used in nano-indenters as the tip is better defined for a three sided pyramid than for a four sided pyramid.

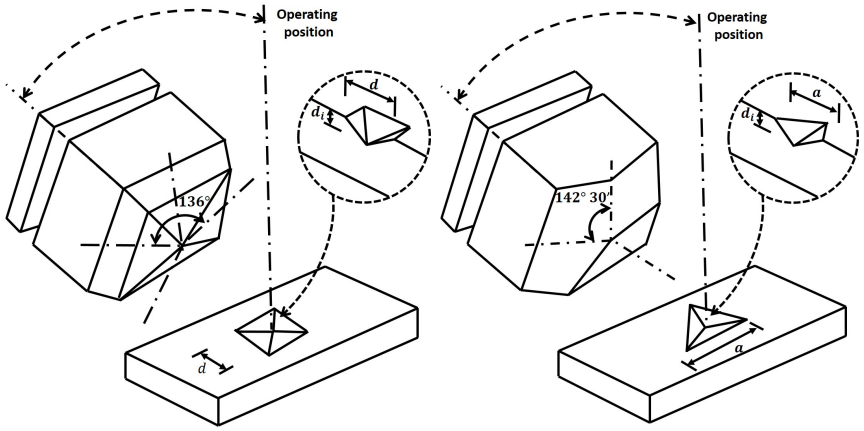

(a) Vickers indenter (b) Berkovich indenter

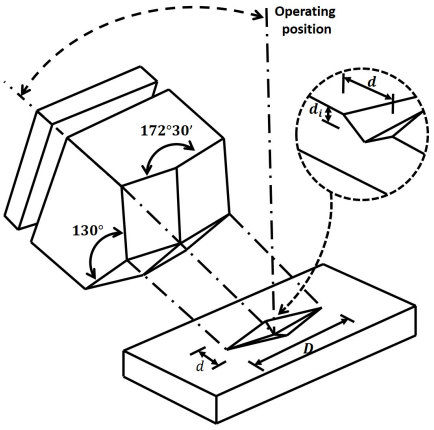

(c) Knoop indenter

Figure 4.4: Geometry of pyramidal indenters and their corresponding indentation marks.

A Knoop indenter is a pyramidal shaped indenter with a rectangular base and a tip with ratio of the diagonals equal to 7:1. This results in an angle of 172.5° between the faces including the long diagonal and angle of 130° between faces including the short diagonal as shown in figure 4.4c. The depth of the indentation is approximated to be $1/30^{th}$ of the long diagonal of the imprint of the indent. As the Knoop indenter is relatively blunt, it cause a lot of plastic deformation at low indentation depth. Hence, Knoop indenters have been used to measure hardness of brittle materials and thin coating films. Also, due to the long slender geometry of the indenter resulting in its asymmetric shape, the Knoop indentation has been used to measure the properties of the coating cross-section and also measure the direction dependent properties of materials. By aligning the diagonals of the Knoop indenter with the direction of anisotropy of the material, the yield loci of the material has been plotted from the Knoop hardness number (KHN) [54].

4.1.2. Methods

This section deals with the various set ups for characterization of the specimens, ploughing experiments and analysis of the characterized and ploughed profile of the specimens. The characterization of the sheets is done by indentation set ups at both micro and nano scales. The ploughing experiments are done using a linear friction tester with 2-D and 3-D load cells namely PATAT (ploughing asperity tester at Twente) and Bruker's UMT-2 (Universal Mechanical Tester) respectively. In all cases, the experiments were repeated three times to check the repeatability and variation in results. The ploughed profile and the indentation marks are analyzed using various microscopes. Confocal microscopes are used to analyze the surface height data, while optical and scanning electron microscopes are used to image and analyze the profile at high magnification. Scanning electron microscope in combination with Energy-dispersive X-ray spectroscopy (EDX) as well as Electron back-scatter diffraction (EBSD) is used to study the chemical composition of the specimen and the orientation of the crystals, grains and presence of phases in the prepared sheets.

4.1.2.1. Ploughing set-ups

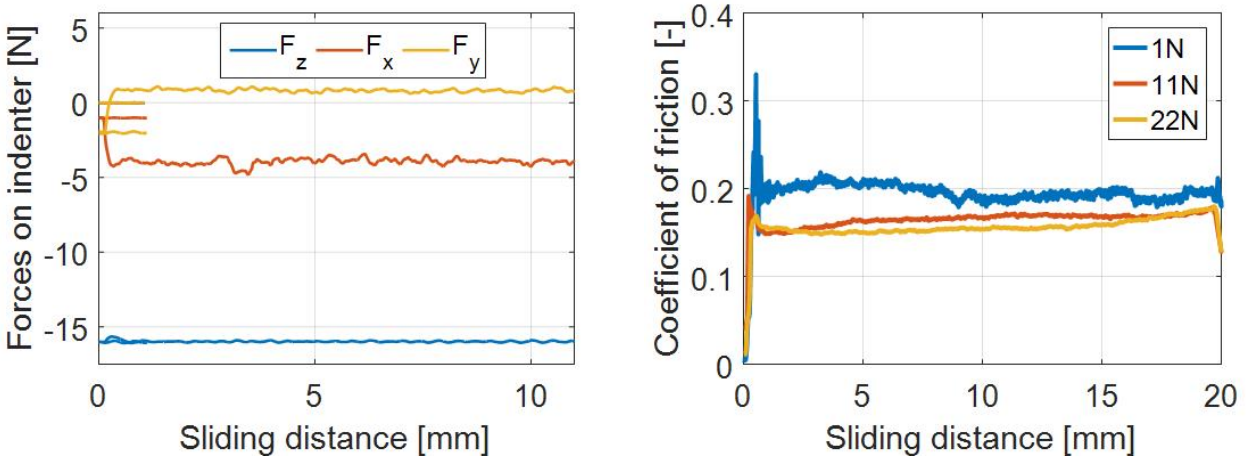

(a) Forces acting on the pin: UMT-2 (b) Coefficient of friction at various loads: PATAT

Figure 4.5: Friction and coefficient friction plots vs sliding distance.

An experimental ploughing set-up consists of a mechanism to load and slide the pin through a clamped substrate. The ploughing set-up should also include a device for measurement of

friction forces in the sliding plane. The available ploughing set-up, namely PATAT measures friction only in the sliding direction. However, for pins with (asymmetric) ellipsoidal tips, friction forces acts on the sliding pin both in the sliding direction and perpendicular to the sliding direction. Hence a ploughing experimental set up is designed using the available UMT-2 using a 3D load sensor as explained further in the section below. The measured friction force is taken as the mean of the steady-state section of the friction signal as shown in forces acting on the pin in figure 4.5a. Similarly the plot for the coefficient of friction is obtained by dividing the friction force at a given point by the corresponding normal load as shown in figure 4.5b. The mean coefficient of friction and friction force is computed in the steady state for a sliding distance of 0.6 times the total siding distance. This avoids the initial friction and tail end of the sliding measurements as seen in figure 4.5.

Linear friction tester A: PATAT

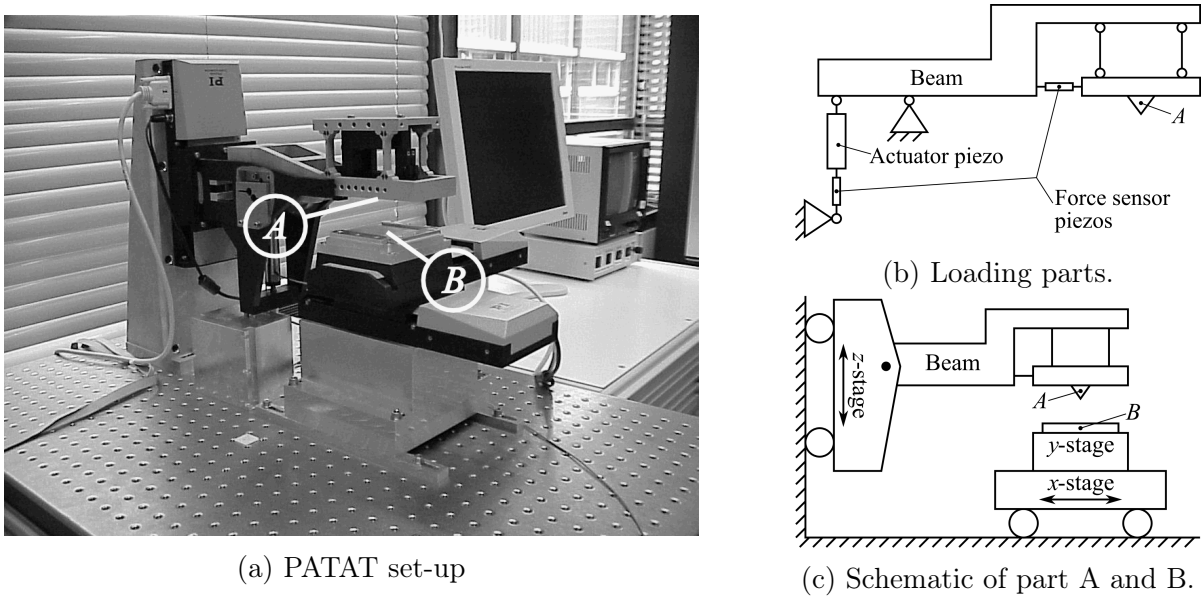

(a) PATAT set-up

(b) Loading parts.

(c) Schematic of part A and B.

Figure 4.6: Image of the linear friction tester A, PATAT, for boundary shear characterization and ploughing experiments showing schematics of loading tip A and sliding part B [28, 95].

The linear friction tester A, namely PATAT (Ploughing Asperity Tester At Twente) was also used for the characterization of boundary layer shear strength and experimental validation of the friction during ploughing for the case of coated and uncoated sheets and pins with spherical tips. The PATAT consisted mainly of two working parts, namely the loading part A and the sliding part B as shown in figure 4.6 and 4.6a. The sliding part B consists of a XY linear positioning stage driven separately by actuators as shown in figure 4.6c. A horizontal beam supports the loading tip and moves the z-stage using a linear and piezo-actuator for coarse and fine displacement respectively while applying the normal load. The normal load is applied using a force controlled piezo-actuator, connected to a PID (proportional integral derivative) control loop feedback system so the system can operate load controlled. The friction forces are measured by a piezo-sensor along the loading tip as shown in figure 4.6b.

Linear friction tester B: UMT2

The Bruker UMT-2 (Universal Mechanical Tester) tribometer was used to carry out the ploughing experiments using pins with ellipsoidal tips. The tribometer has been adapted to be a

(a) UMT-2 set-up

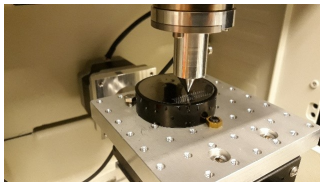

(b) Loading tip

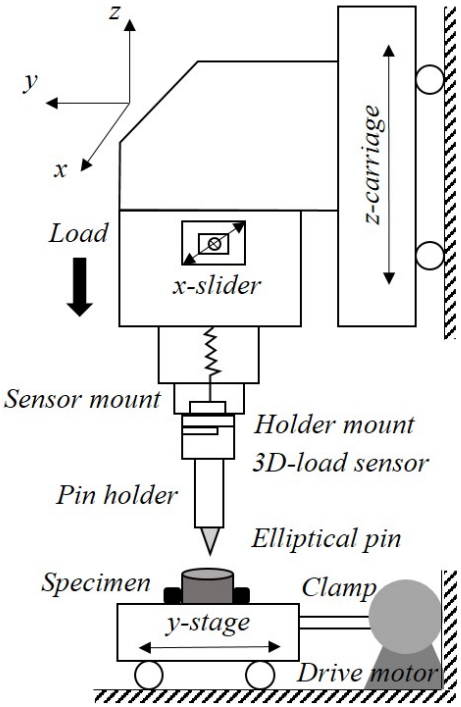

(c) Schematic of UMT-2

Figure 4.7: Linear friction tester B image for ploughing experiments using ellipsoidal-tip pins.

scratch test set-up as shown in figure 4.7. The UMT-2 scratch set-up consisted of three stages for motion in all three directions. The (ellipsoidal) indenter was mounted on the z-carriage. The z-carriage was also used to adjust the height of the ellipsoidal pin while also applying the given load on the contact. The pin was slid along the x axis using the x-slider. The xy-stage was used to mount the specimen to be tested and also used as the main actuator for the ploughing experiments. The z-carriage, x-slider and y-stage were moved using a stepper motor drive by translating rotational into a linear motion using a lead screw and guide rails. The y-stage consisted of an eccentric screw which was used to clamp the disc specimen to the two fixed screws on the stage. The y-stage was connected to the motor using a lead screw of 2 mm pitch.

The load applied on the pin and the friction in both x and y direction were measured using the ATI F/T mini 40 (3D) load sensor with a load range of 0-60 N and 0.01 N resolution in the z-axis and a load range of 0-20 N and 0.05N resolution in the x- and y-axis. In this way, the force components involved in ploughing with an elliptical indenter can be measured. The 3D load sensor was connected to the pin holder using a mount and to the upper drive stage using a suspension block as shown in figure 4.7c. The suspension block with its spring plates helped in adjusting for possible shock loads. The pin holder consisted of a hole with inner diameter the same as that of the base of the pin and a marking along the x-axis, i.e. direction of x-slider to adjust the orientation of the ellipsoidal pin. Load controlled tests were performed at 7N and 16N normal loads for the different pin sizes and orientation along the sliding direction.

4.1.2.2. Indentation set-up

The Anton Paar Nano-indentation tester (NHT^3) has been used to perform indentation based characterization of the uncoated DC04 steel and zinc coated steel specimen. The indentation

of both the coated and the uncoated sheets are performed using a nano-indentation set-up as shown in figure 4.8. The nano-indenter uses depth-sensing indentation where the applied load and the penetration depth of the indenter into the specimen are recorded and used to determine the mechanical properties of the test specimen [123]. The penetration depth is constantly measured in the nano-indentation set-up by a changing displacement sensor which is typically an inductance or a capacitive sensor with sub nm resolution. The normal force on the indenter is continuously controlled by a feedback loop. The force is applied during indentation by a piezo-electric actuator with a feedback control. In the current work, the Nano-indentation tester can apply a load up to a maximum force of 500 mN at a resolution of 0.02 μN and a maximum penetration depth of 200 μm at a resolution of 0.01 nm. An anti-vibration table is provided for the Nano-indentation tester which is placed in the laboratory with the least external vibration. The Nano-indentation tester used, has a noise floor value of $\pm$ 0.5 μN for load controlled indentation which indicates the maximum resolution with which noise is precisely measured [124].

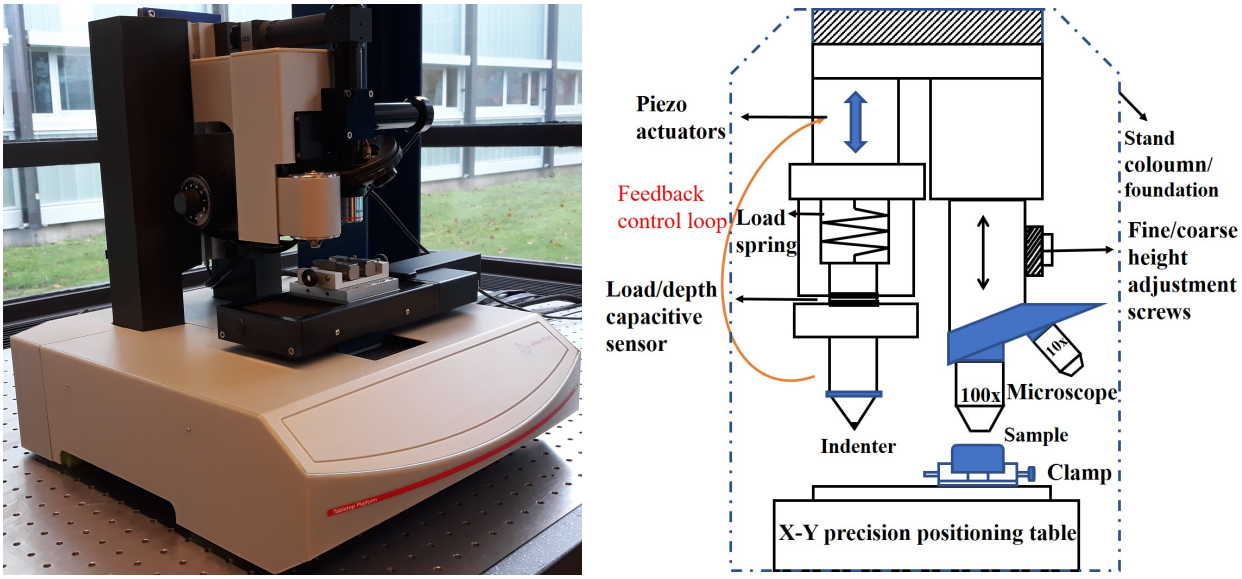

(a) The nano-indentation set-up.

(b) Schematic of the Nano-indentation setup.

Figure 4.8: Nano-indentation using a Knoop indenter.

The shape function of the indenter gives the projected area of the indentation at the contact depth h_c and is approximated by fitting a polynomial function to the experimentally calibrated data. The shape function takes into account the curvature of the indenter tip in the measurement of the projected contact area. By indenting the calibrated fused silica specimen and curve-fitting the experimental data as shown in figure 4.9a the shape function of the Knoop indenter in nano-indentation was obtained in equation 4.1. The curve fit was implemented in the calibration file of the nano-indenter for Knoop indentation.

$$A_c(h_c) = 97.77h_c^2 + 5.57 \times 10^{-6}h_c + 5 \times 10^{-14} \tag{4.1}$$

In depth sensing nano-indentation technique [61], the hardness and the elastic modulus of the specimen are measured using the loading and unloading curves as shown in figure 4.10b. During loading the load is increased to the set maximum load F_m for a time duration of 30s. At the maximum load F_m the load is kept constant for a dwell time duration of 10s to avoid creep

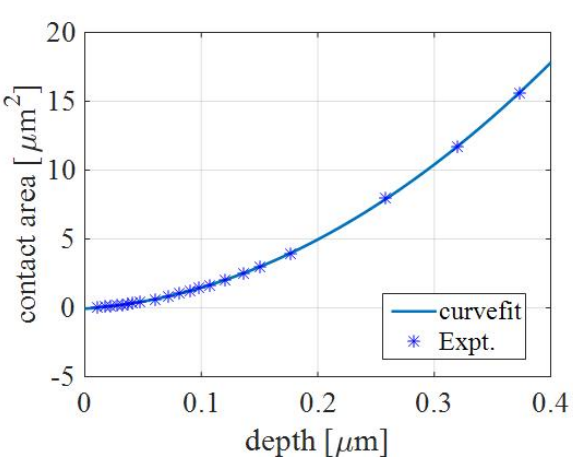

(a) Curve-fit of Knoop indenter shape function.

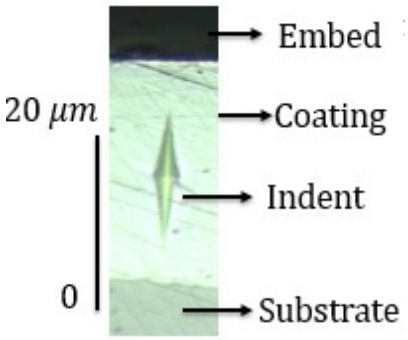

(b) Knoop indent on coated cross-section.

Figure 4.9: Calibration of Knoop indenter for nano-indentation.

effects. The unloading is done at a similar rate as loading for a duration of $30s$. The loading and unloading sequence and the corresponding penetration depth is plotted in figure 4.10a. The hardness of the specimen is measured from the ratio of the applied load to the indentation area A_c which corresponds to the maximum penetration depth h_m as given in equation 4.2a for Knoop indenter. The unloading of the indenter is followed by elastic recovery of the substrate. The stiffness of the substrate can be given as the slope of the unloading curve in figure 4.10b. The constant c_i (figure 4.10b depends on the indenter geometry. The residual elastic modulus of the indenter substrate system E_r is calculated by 4.2b. The elastic modulus of the substrate is calculated using the given value of elastic modulus of the diamond indenter in equation 4.2c.

$$H = \frac{F_m}{A_c} \; \forall A_c = 65.44h^2 \tag{4.2a}$$

$$E_r = \frac{\sqrt{\pi}}{2} \frac{\Lambda}{\sqrt{A_c}} \; \forall \Lambda = \frac{dF}{dh} \tag{4.2b}$$

$$\frac{1}{E_r} = \frac{1-\nu_i^2}{E_i} + \frac{1-\nu_s^2}{E_s} \tag{4.2c}$$

The hardness and the elastic modulus can also be measured from the geometry of the indent. The Knoop hardness is given using the length of the longer diagonal D of the indentation imprint by equation 4.3a. The elastic modulus of the specimen can also be obtained using the ratio of final (recovered) diagonal lengths of the Knoop indent from equation 4.3b [125].

$$KHN = \frac{Load(F_m)}{Indent\ area(mm^2)} = 139.54 \frac{F_m}{D_l^2} MPa = 14.23 \frac{F_m}{D_l^2} \frac{kgf}{mm^2} \tag{4.3a}$$

$$\frac{d_s}{D_l} = \frac{1}{7.114} - \frac{0.45KHN}{E} \tag{4.3b}$$

It can be deduced from figure 4.11 and 4.12 that the size of the grains is typically in the order of the size of the Knoop indent (see figure 4.9b). If the grain size is larger than the indentation size, then the grain size and orientation has a major effect on the properties obtained from the indentation [41]. Hence larger loads are chosen for Nano-indentation keeping in mind the coating thickness for zinc coated specimens. Furthermore, multiple indentations (20-50 in

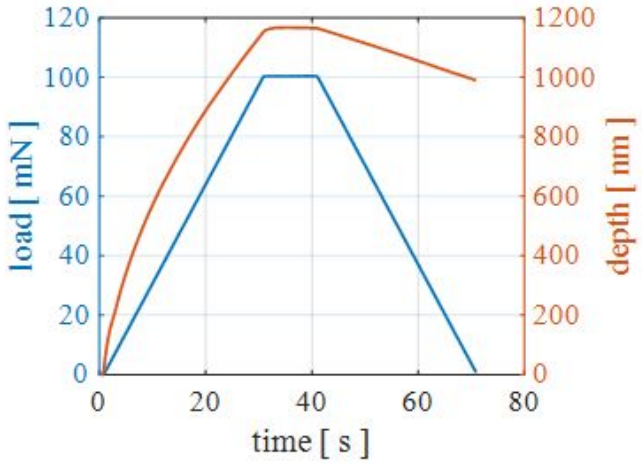

(a) Load vs time plot and penetration depth vs time plot.

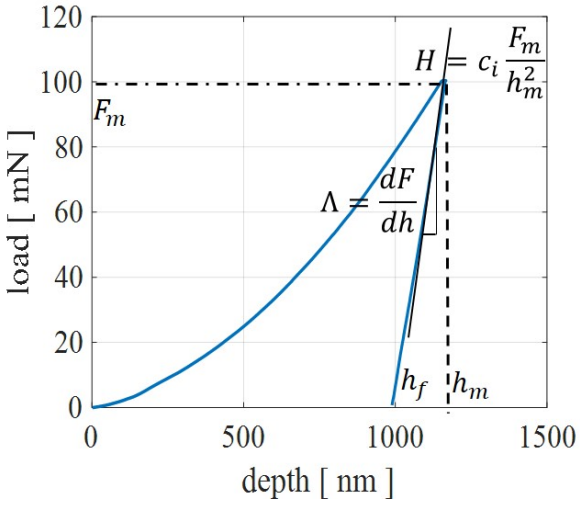

(b) Hardness and stiffness from load-depth plot.

Figure 4.10: Measurement of material properties from nano-indentation.

number) have been performed as a matrix spread out over a region of the specimen and the average of the data obtained from the indentations is taken. This helps in averaging the effect of local grain orientation and size of the data obtained from the Knoop indentation.

4.1.2.3. Confocal and electron microscopes

The surface profile of the ploughed surface and the pins are checked for calculating the wear volume, ploughing depth and any possible material transfer to the surface of the pin. The confocal microscope illuminates a section of the surface by focusing laser light and detecting back the emitted signal, while cutting off out of focus signals using a pinhole. The height distribution in the surface is viewed in 3D by using a raster scan where several optical planes are scanned and stacked using a suitable microscopy deconvolution software (z-stack). Figure 4.11 shows the height profile of the surface of a polished zinc coated sheet obtained by confocal microscopy at 150x magnification.

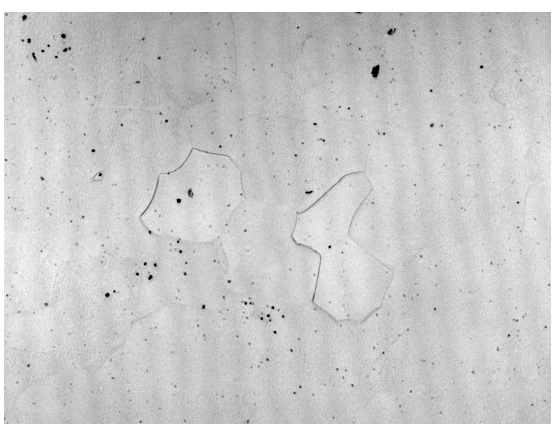

(a) GI sheet under optical microscope

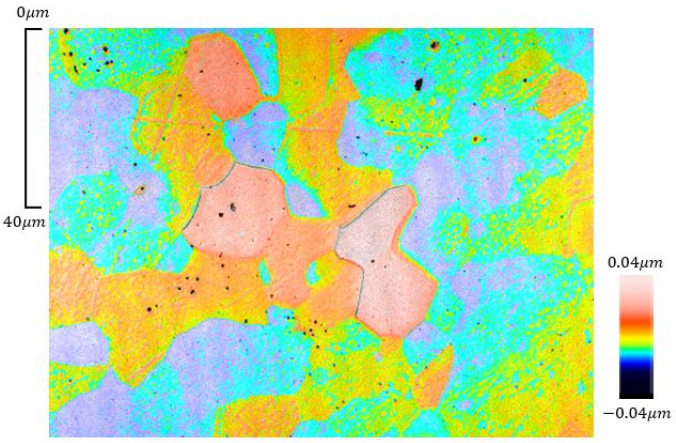

(b) Confocal image showing surface height profile

Figure 4.11: Image of polished GI sheet surface seen at 150x magnification.

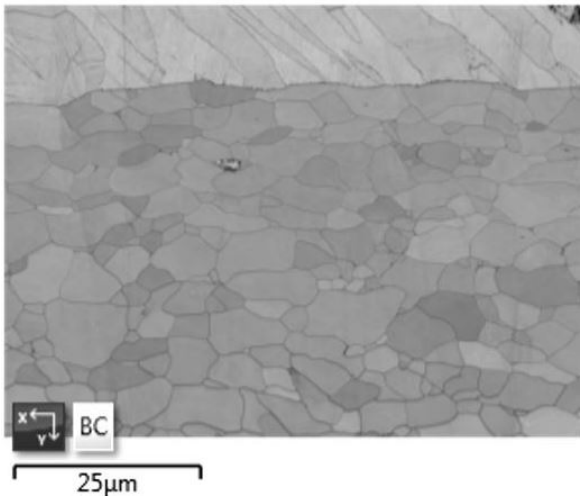

(a) Cross-section of rolled GI sheet in SEM.

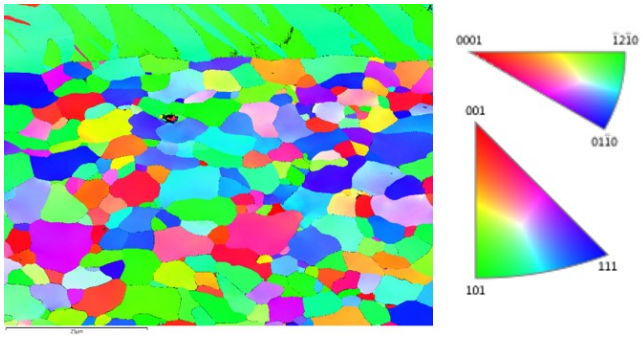

(b) Inverse pole figure-Z (EBSD).

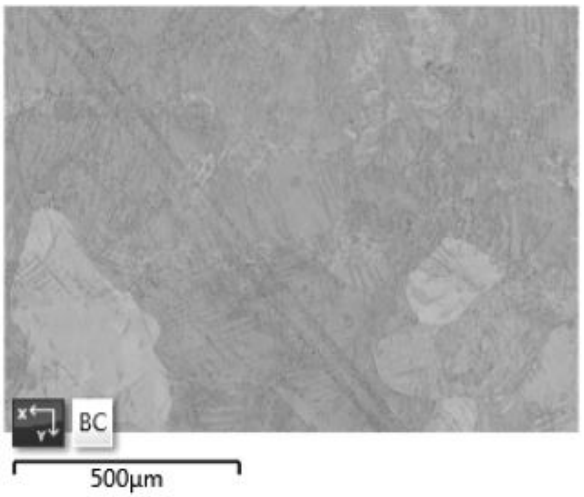

(c) Surface of rolled GI sheet in SEM.

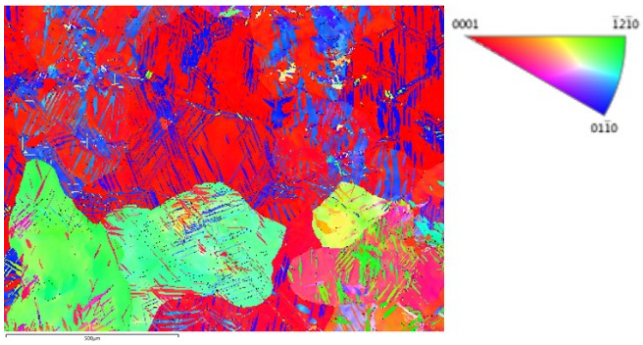

(d) Inverse pole figure-Z (EBSD).

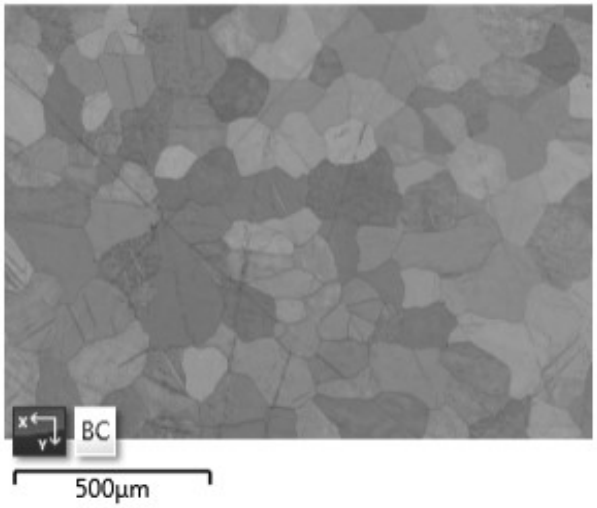

(e) Surface of unrolled GI sheet in SEM.

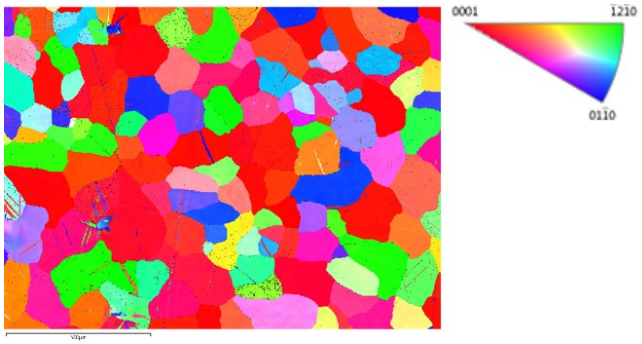

(f) Inverse pole figure-Z (EBSD).

Figure 4.12: Measurement of grain orientation and structure from EBSD SEM analysis of cross-section and surface of (rolled and unrolled) zinc coated steel sheet.

In many experiments SEM was used to study the micro-structure and composition of the specimens. The emitted X-ray is characteristic to the atomic composition of the specimen and can be analyzed in Energy-dispersive X-ray spectroscopy (EDX) was used to analyze the composition of the zinc coated sheets. By orienting the specimen at an angle of 70° to the electron beam, the electrons are diffracted by the atomic layers in the crystalline materials, which is the basis of Electron backscatter diffraction (EBSD). The diffracted electrons are detected on a phosphor screen and the electron backscatter patterns are studied to obtain information about the crystal/grain structure, orientation and phase of the zinc and steel in the zinc coated sheets [126]. The Inverse pole figures (IPF) showing the orientation and size of the grains of the zinc coating and the steel substrate are shown in figure 4.12.

Figure 4.12a shows the cross-section of the zinc coated steel sheets cut along the rolling direction. The zinc grains are present as columns and orient along the rolling direction in figure 4.12b. The grain size of the iron in the substrate is much smaller at around 10-20μm as seen from figure 4.12a. The grains in the substrate are are randomly oriented body centred cubic crystals. The surface of the rolled zinc coating is shown in figure 4.12c. The average grain size of the zinc coating can be estimated to be around 100-200μm. It can be seen that the zinc grains are aligned as pancakes with a thickness of 20μm. The zinc grains are mostly oriented along their (*hcp* hexagonal closed packed crystal) c axis almost normal to the sheet plane. However certain grains can be seen elongated and aligned along the rolling direction in the inverse pole figure 4.12d. Multiple pyramidal slips and twins can be seen throughout the grain matrix as well. In case of the surface of unrolled zinc coating on steel sheet, shown in figure 4.12e, the alignment of the zinc grains with their c axis normal to the sheet plane is less as compared to the rolled zinc coating (see figure 4.12f). Furthermore, the zinc grains are not elongated and are devoid of slips and twins in unrolled zinc coating. Hence the rolling process clearly has an effect on the deformation texture in the sheet resulting in the anisotropic behaviour of the zinc coating.

4.2. Experimental characterization

The characterization experiments of the properties of the experimental specimens, coated and uncoated steel sheets and lubricants have been divided into three sections. The first section deals with the individual hardness and elastic modulus of the coating and the substrate and effective hardness and Young's modulus of the coated system. Further details about interfacial shear strength characterization is explained in paper D [121]. The second section deals with the interfacial shear strength of the lubricant boundary layers and oxide layers formed at the interface of the zinc coated and uncoated steel sheets and the pins at various contact pressure and sliding velocities. The final section plots the anisotropic yield criteria for the zinc coating based on Knoop indentation experiments. Also the measured parameters for the yield function of the zinc coating and the substrate will be discussed. Further details about anisotropic yield loci characterization is explained in paper E [120].

4.2.1. Hardness and Young's modulus of the coated system

In loading a coated surface, the effective hardness and stiffness of the sheet determines its deformation behaviour. The effective Young's modulus and stiffness of the zinc coated system is obtained based on the indentation behaviour of the zinc coating. The effective Young's modulus is used to determine the line contact width of a cylindrical roller loaded on the zinc coated sheet. The hardness of the zinc coated sheet H_{cs} is measured by equation 4.4 using the

substrate hardness H_s, coating hardness H_c, coating thickness t and indenter radius r [117].

$$H_{cs} = H_s + (H_s - H_c)\exp\left(-125\frac{t}{r}\right) \tag{4.4}$$

The reduced Young's modulus in the tool-sheet contact E^* is defined in equation 4.5a by the Youngs modulus and the Poisson's ratio of the coated system E_{cs} and ν_{cs}, and that of the indenter tool E_{in} and ν_{in} respectively (equation 4.5b). The reduced elastic modulus of the coated system with n layers of coating is calculated from the Young's modulus and Poisson's ratio of each layer and two influence factors I_0 and I_1 as per equation 4.5c [127]. The influence factors I_0 and I_1 are calculated in equations 4.5d and 4.5e respectively with $i = 1$ as the bottom layer and $i = n$ as the top layer. The equations use the relative coating thickness $\bar{t}_i$, the ratio of the total layer thickness up to layer i $(t_1, t_2, ..., t)$ and the contact radius a and the mean Poisson's ratio of all layers $\bar{\nu}$ in equations 4.5f and 4.5g respectively [127, 128]. For zinc coated steel with one coating layer and taking the same Poisson's ratio of zinc and steel the effective Young's modulus of the zinc coated steel is given as E_{cs} in equation 4.5h [128].

$$b = \sqrt{\frac{4F_n r}{\pi l E^*}} \tag{4.5a}$$

$$\frac{1}{E^*} = \frac{1-\nu_{cs}^2}{E_{cs}} + \frac{1-\nu_{in}^2}{E_{in}} \tag{4.5b}$$

$$\frac{1-\nu_{cs}^2}{E_{cs}} = \frac{1-\nu_s - \sum_{i=1}^{n-1} I_1(\nu_i - \nu_{i+1}) - I_1(\nu_n - \nu_s)}{\frac{E_s}{1+\nu_s} + \sum_{i=1}^{n-1} I_0\left(\frac{E_i}{1+\nu_i} - \frac{E_i}{1+\nu_{i+1}}\right) + I_0\left(\frac{E_n}{1+\nu_n} - \frac{E_s}{1+\nu_s}\right)} \tag{4.5c}$$

$$I_0 = \frac{2}{\pi}\arctan\bar{t}_i + \frac{\left((1-2\bar{\nu})\bar{t}_i \ln\frac{1+\bar{t}_i^2}{\bar{t}_i^2} + \frac{\bar{t}_i^2}{1+\bar{t}_i^2}\right)}{2\pi(1-\bar{\nu})} \tag{4.5d}$$

$$I_1 = \frac{2}{\pi}\arctan\bar{t}_i + \frac{\bar{t}_i}{\pi}\ln\frac{1+\bar{t}_i^2}{\bar{t}_i^2} \tag{4.5e}$$

$$\bar{t}_i = \sum_{k=1}^{i}\frac{t_k}{b} \tag{4.5f}$$

$$\bar{\nu} = \frac{1}{n}\sum_{i=1}^{n}\nu_i \tag{4.5g}$$

$$E_{cs} = E_c + (E_c - E_s)I_0 \;\forall n = 1, \nu_c = \nu_s \tag{4.5h}$$

The expressions for the influence factors used to compute the effective Young's modulus use the contact length b in the indentation (expression of relative coating thickness in 4.5f). As the effective Young's modulus is used to compute the contact width of the line contact, an optimization algorithm, shown in figure 4.14, is developed to compute E_{cs} using equation 4.5h for zinc coated steel. The hardness of the bulk zinc, zinc coating and the steel sheets were measured using indentation experiments. The hardness and Young's modulus of the zinc coating are taken as $0.5GPa$ and $70GPa$ while that for the steel substrate is taken as $1.4GPa$ and $210GPa$ respectively, making zinc coated steel a soft, ductile coating on a hard, stiff substrate. Hence as the thickness of the coating increases the effective hardness and Young's modulus (stiffness) of the coated system tends towards that of the zinc coating as shown in figure 4.13a. The effective Young's modulus of the zinc coated system is plotted against the coating thickness for a range of applied loads in figure 4.13b. The stiffness of the coated system tends

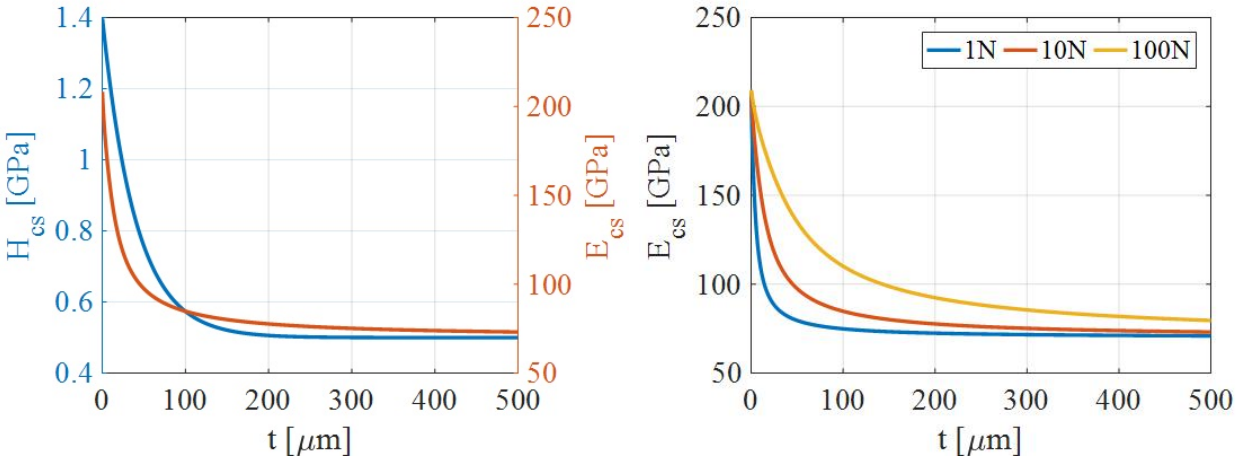

(a) H_{cs} and E_{cs} vs t (b) E_{cs} vs t and F_n

Figure 4.13: The effect of coating thickness t on effective hardness H_{cs} and Youngs modulus E_{cs} of a coated system and (b) the effect of applied load on E_{cs} obtained using equation 4.5a and equation 4.4 and material data from table 4.2.

to be closer to the substrate than the coating at a higher applied load, i.e. higher penetration depth. The effective Youngs modulus E_{cs} ranges between 92.5-135.1 GPa and the effective hardness H_{cs} is 1.046 GPa is obtained from equation 4.5h and 4.4 respectively for the given zinc coating thickness of $20\mu m$ and applied load of 1 to $16N$. The layer hardness for the zinc coating is obtained using indentation to be 800.1 MPa with standard deviation of 18.8 MPa.

4.2.2. Interfacial shear strength

The shear strength of the interface is calculated from the linear sliding experiments using the logarithmic profiled cylinder. The experiments are designed such that the friction force measured is purely attributed to shearing of the interface. The interfacial shear strength τ_b is given as the ratio between the measured friction force F_f and the contact area A.

The contact area in the line contact between the cylindrical roller and (zinc-coated) sheet is measured for a range of loads such that the resulting nominal contact pressure is kept below the yield strength ($\sigma_{cs} = H_{cs}/\sqrt{3}$ [113]) of the zinc coated steel. The contact area for the logarithmic profiled cylindrical roller (uncrowned) of length l with semi-contact width b is given as $A_c = 2bl$. The contact width is calculated from the effective Young's modulus of the pin-substrate contact E^* using the algorithm in figure 4.14. In order to compute the contact width in a line contact for the case of a cylindrical roller in contact with a flat surface, using the effective elastic modulus of the coated system, an initial guess for the contact width b_0, is used to calculate the line contact width b. The calculated contact width b is then corrected by adding the difference $\mid b - b_0 \mid$ and used as the new value to recalculate b. The steps are iterated until the difference $\mid b - b_0 \mid$ is minimized below a given tolerance of $tol = 0.001\mu m$ as shown by the algorithm in figure 4.14. The algorithm calculates the line contact area for a single layer of (hot dip galvanized) zinc-coated steel sheet using the effective Youngs modulus E_{cs} computed by the equation 4.5h, deduced from equation 4.5c for $n = 1$ and $\nu_s = \nu_c$. The contact width measured using the analytical method in the algorithm agrees well with that obtained from the FE (finite element) method as shown in table 4.3. The maximum contact pressure P_0 is measured from the nominal contact pressure in equation 4.6. The material parameters for the

specimens used in the interfacial shear strength characterization experiments are listed in table 4.2.

$$P_0 = \frac{4}{\pi} P_{nom} \; \forall P_{nom} = \frac{F_n}{2bl} \tag{4.6}$$

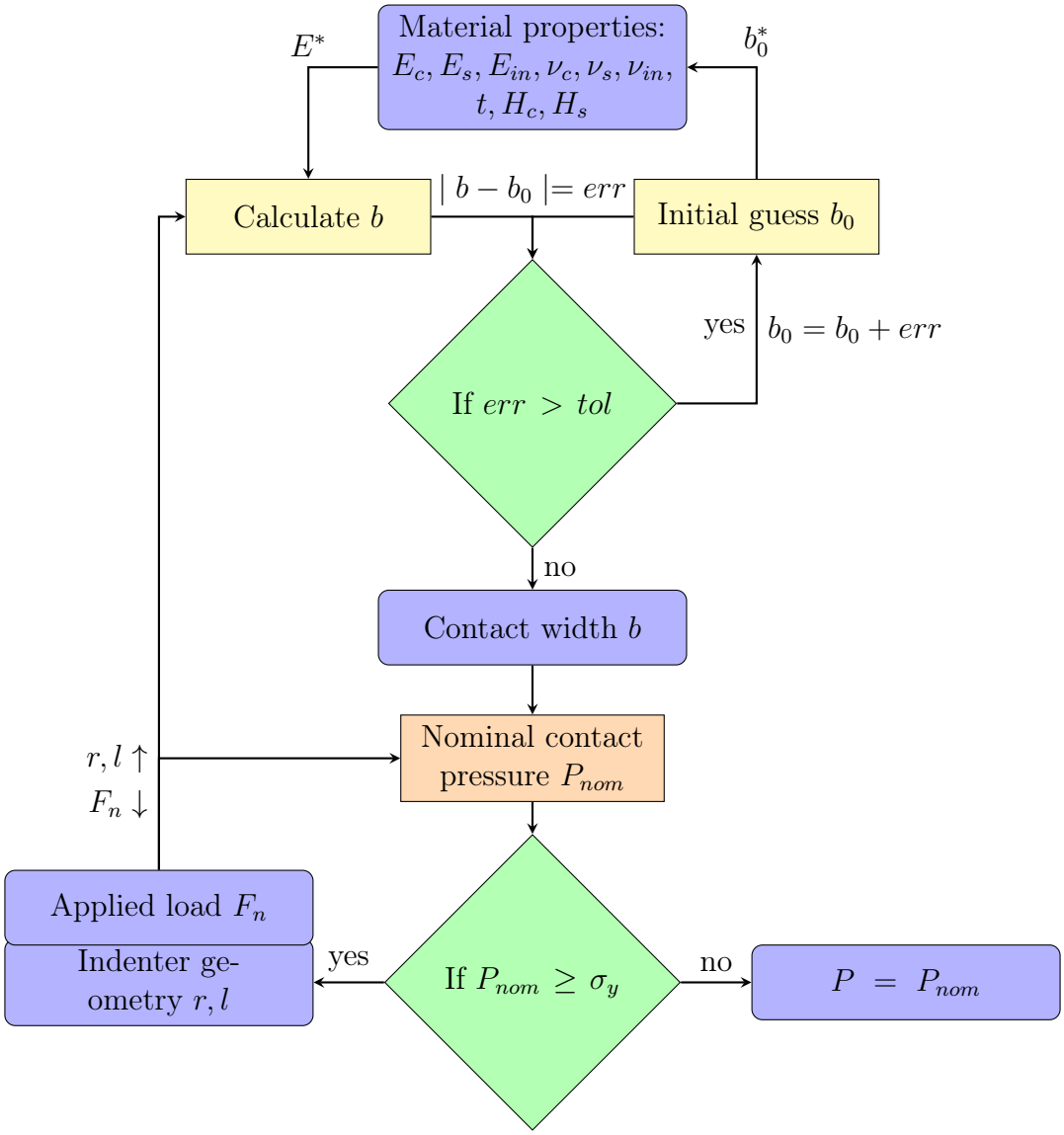

Figure 4.14: Flow chart to calculate contact width and contact pressure in coated systems.

The coefficient of friction vs sliding distance, obtained for different loads, is plotted in figure 4.15a. The mean friction force is calculated for the sliding length of 14mm in the middle of total sliding distance of 20mm. The coefficient of friction due to shearing of the boundary layer decreases with increasing load. The steady state friction force is obtained after multiple traverses as shown in the steadying of the average coefficient of friction after initial decline due to running-in with each traverse in figure 4.15b. The average steady state friction forces measured from the sliding experiments is divided by the computed Hertzian contact area to obtain the boundary layer shear strength τ.

The mean coefficient of friction for the shear experiments is plotted against various sliding velocities in figure 4.16. It can be seen that the boundary layer shear strength is not greatly affected

Table 4.2: Material parameters for interfacial shear strength characterization

Parameters	Substrate	Coating	Tool/Pin
Geometry	Circular sheet of thickness 1 mm and dia. 50mm	Circular sheet of thickness 1 mm and dia. 50mm	Cylinder/roller with logarithmic crowning
Radius at center of roller	–	–	5mm
Uncrowned contact length of the roller	–	–	5mm
Total length of the roller	–	–	10mm
Material	DX56 steel	Zinc coated DX56 / Galvanized steel	AISI 52100 bearing steel
Coating thickness	0	20 μm	0
Young's modulus	210 GPa	70 GPa [47]	210 GPa
Hardness	1.4 GPa	0.5 GPa [28]	8.2 GPa
Poissons ratio	0.3	0.3	0.3
Lubricant A	Viscosity $\eta_{40°C}$	Lubricant B	$\eta_{40°C}$
Quaker FERROCOAT N6130	23 $mPas$	Fuchs Anticorit PLS100T	90 $mPas$

Table 4.3: Contact width and contact pressure for line contact on zinc coating

Load F_n	Contact width b -analytical (μm)	Contact width b -FEA (μm)	Contact pressure- analytical $P_{nom}[MPa]$
1	8.44	11.8	23.7
2	11.68	13	34.4
4	16.01	17.2	30.3
7	20.06	23	68.3
11	25.32	28.8	87.3
16	30.02	34.2	106.7

by the change in sliding velocity. The boundary layer shear strength, for the Quaker lubricant marginally increases with sliding velocity while that for the Anticorit lubricant marginally decreases with sliding velocity, as shown in figure 4.16a and 4.16b respectively. For experiments done with the Quaker lubricant, the effect of shear strain rate, i.e. for boundary layer thickness seems to dominate, as a result of which τ^Q increases with sliding velocity. For experiments done with the Anticorit lubricant, the visco-elastic effect, i.e. for sliding distance d, seems to dominate, as a result of which τ^A decreases with sliding velocity. The effect of visco-elastic retardation due to compression and strain rate was first accounted for in the measurement of boundary layer shear stress in the work of Briscoe and Tabor [67], where for high sliding

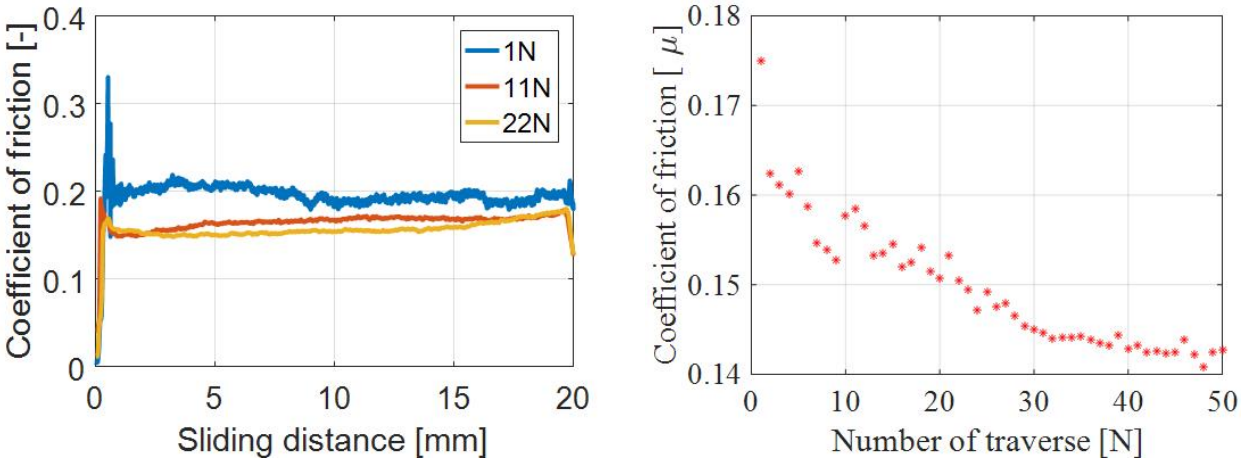

(a) Coefficient of friction for various normal loads. (b) Running-in, friction with each traverse at 16N.

Figure 4.15: Friction measurements with the linear sliding friction tester.

velocity, the visco-elastic term diminishes while for low sliding velocity the strain rate term diminishes. In the visco-elastic effect (the response time to compression/contact pressure), the effect contact pressure $\bar{P} \propto P/\exp v_s/a$ in response to application to normal stress (contact radius a) reduces with v_s as a result of which τ^A decreases with v_s [67]. The relationship between the interfacial shear strength and sliding velocity obtained by performing these experiments is given in equation 4.7a and 4.7b for both the lubricants. Each experiment has been performed (repeated) three times.

$$\tau_I^Q = 13.13 \times 10^7 v_s^{0.018} \tag{4.7a}$$

$$\tau_I^A = 9.32 \times 10^6 v_s^{-0.053} \tag{4.7b}$$

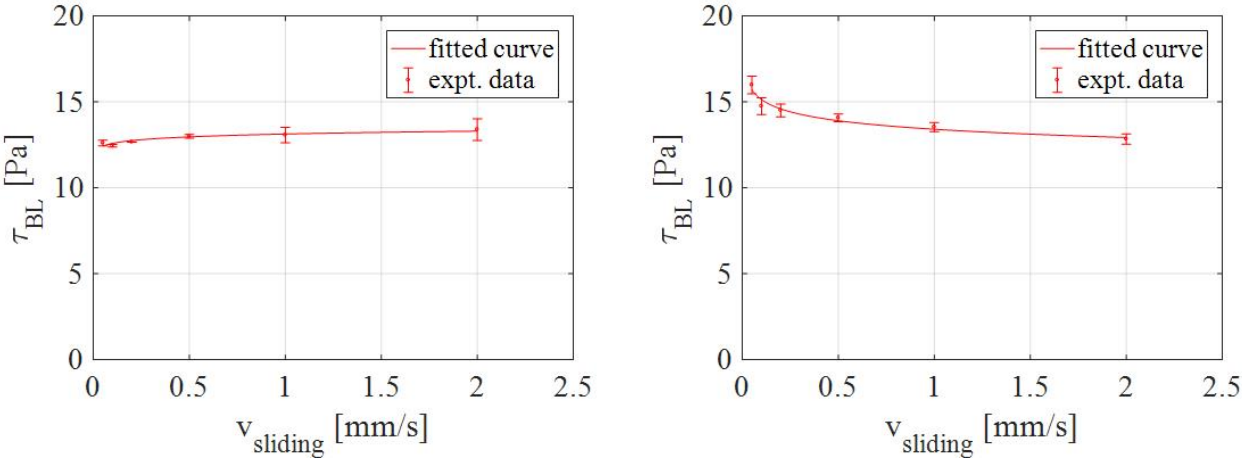

(a) Quaker Ferrocoat N136. (b) Fuchs Anticorit PLS100T.

Figure 4.16: Boundary layer shear strength vs sliding velocity plots for DX56 lubricated sheet.

The characterization of the boundary layer shear strength for Quaker Ferrocoat N136 and Fuchs Anticorit PLS100T lubricated and unlubricated DX56 steel sheets with varying contact pressures was done using the linear sliding friction experimental set-up, shown in figure 4.6. Figure 4.17 shows the variation of boundary layer shear strength with (applied load) nominal contact

pressures for both lubricated and unlubricated steel sheets. As explained in the literature [65], a higher contact pressure increases the potential barrier for the shearing of the boundary layers, thereby increasing the interfacial shear strength. It can be seen from figure 4.17 that the rate of increase in boundary layer shear strength decreases with change in the nominal contact pressure. Hence, the boundary layer shear strength (at constant sliding velocity and temperatures) has been plotted against the contact pressures by fitting the experimental data with the power law relation (based on equation 2.4b) in equations 4.8a-4.8c. Both the lubricants have interaction with the surface, generating boundary layers with different shear strength. The shear strength of the Quaker lubricated interface is lower than that of the Anticorit lubricated interface. The shear strength of the unlubricated interface has been measured for experiments with stable friction behaviour where galling is absent. The absence of a lubricant boundary layer results in a high shear strength of the interface, see figure 4.17b.

$$\tau_I^Q = 1.34 P_{nom}^{0.88} \tag{4.8a}$$

$$\tau_I^A = 0.64 P_{nom}^{0.93} \tag{4.8b}$$

$$\tau_I^U = 2.05 P_{nom}^{0.88} \tag{4.8c}$$

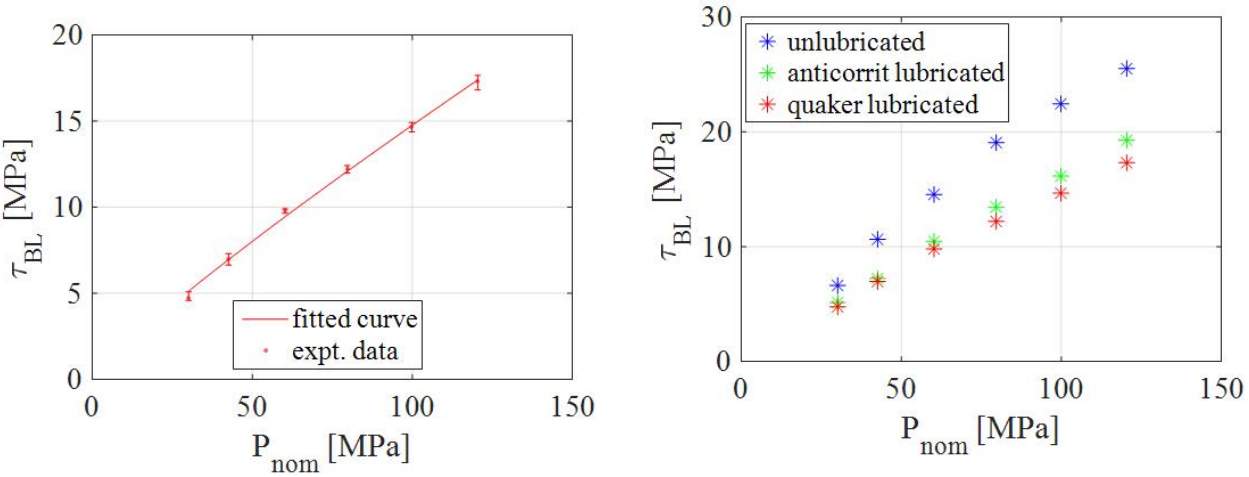

(a) Quaker Ferrocoat N136.

(b) Comparison of interfacial shear with both lubricated and unlubricated sheet-sliding pin interfaces.

Figure 4.17: Curve fit boundary layer shear strength vs nominal contact pressure plot for Quaker Ferrocoat N136 on DX56 sheet; comparison with Fuchs Anticorit PLS100T, unlubricated case.

The characterization of the boundary layer shear strength for experiments done with zinc coated DX-56 steel was also carried out using sheets lubricated with Quaker and Anticorit lubricants. The unlubricated shear experiments done with zinc coated steel were avoided as steel pins sliding through zinc coated sheets have shown a higher affinity for material transfer and resulted in galling. The mean friction forces obtained from the shear experiments were divided by the contact area calculated for the coated system in section 4.2.1. The boundary layer shear strength was plotted against applied nominal pressure for experiments done with lubricated GI sheets (at constant temperature and velocity) and fitted with power law expressions derived in equation 2.4b in figure 4.18. The expressions for both the lubricants for the case of zinc coated sheets are given in equation 4.9a and 4.9b:

$$\tau_{GI}^Q = 0.32 P_{nom}^{0.95} \tag{4.9a}$$

$$\tau_{GI}^A = 7.34 P_{nom}^{0.78} \tag{4.9b}$$

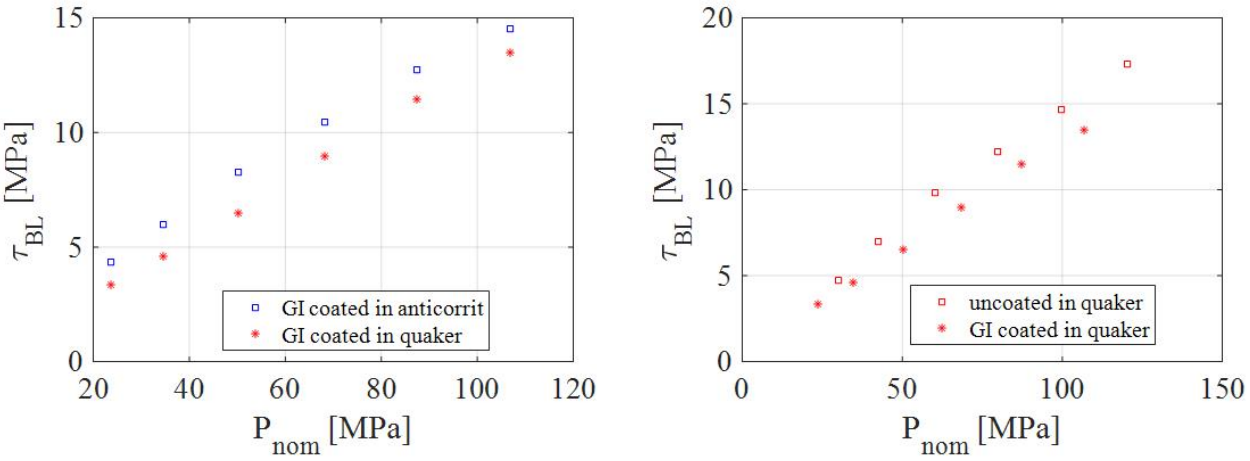

(a) Comparison of interfacial shear with various lubricants on zinc coated steel sheet.

(b) Comparison of interfacial shear with zinc coated and uncoated steel sheet.

Figure 4.18: Comparison of boundary layer shear strength vs contact pressure plots for lubricated steel and zinc-coated sheets (Quaker Ferrocoat N136, Fuchs Anticorit PLS100T).

4.2.3. Yield criterion and yield function

For indentations with the longer diagonal of the Knoop indenters base, along and perpendicular to the axes of anisotropy, the strain ratio $\bar{\epsilon}$ follows from the ratio of the length of the diagonals and is equal to 7. Following Levy-Mises equations for isotropic, ideal plastic materials, the strain ratio equals the deviatoric stress ($\sigma^{'}$) ratio. In order to plot the yield locus in the deviatoric plane, the points corresponding to the KHN for each of the six indentations namely $i_a, i_b, i_c, i_d, i_e, i_f$ lie on lines with the slope equal to the deviatoric stress ratio $\bar{\sigma}$ as shown in equation 4.10 [54] (In the deviatoric plane the rolling direction is given as z, transverse direction as φ and normal direction as ϱ). In the deviatoric stress plane, the position of the point on the line for the particular indentation is equal to its KHN. Using volume constancy, the net strain increment $d\varepsilon_r + d\varepsilon + d\varepsilon_z = 0$. Then all six strain ratios are given as elements of vector $\bar{\varepsilon}$ in equation 4.11 [55].

$$\bar{\sigma}_{i_a} = \frac{\sigma_z^{'}}{\sigma_\varphi^{'}} = 7;\ \bar{\sigma}_{i_b} = \frac{\sigma_z^{'}}{\sigma_\varphi^{'}} = \frac{1}{7};\ \bar{\sigma}_{i_c} = \frac{\sigma_\varphi^{'}}{\sigma_\varrho^{'}} = 7;\ \bar{\sigma}_{i_d} = \frac{\sigma_\varphi^{'}}{\sigma_\varrho^{'}} = \frac{1}{7};\ \bar{\sigma}_{i_e} = \frac{\sigma_\varrho^{'}}{\sigma_z^{'}} = 7;\ \bar{\sigma}_{i_f} = \frac{\sigma_\varrho^{'}}{\sigma_z^{'}} = \frac{1}{7}; \tag{4.10}$$

$$\bar{\varepsilon} = \left[\frac{d\epsilon_z}{d\epsilon_\varphi} = \bar{\epsilon};\ \frac{d\epsilon_\varphi}{d\epsilon_z} = \frac{1}{\bar{\epsilon}};\ \frac{d\epsilon_\varphi}{d\epsilon_\varrho} = \frac{-1}{1+\bar{\epsilon}};\ \frac{d\epsilon_\varrho}{d\epsilon_\varphi} = -1+\bar{\epsilon};\ \frac{d\epsilon_\varrho}{d\epsilon_z} = -\frac{1+\bar{\epsilon}}{\bar{\epsilon}};\ \frac{d\epsilon_z}{d\epsilon_\varrho} = -\frac{\bar{\epsilon}}{1+\bar{\epsilon}}\right] \tag{4.11}$$

In plane stress $\sigma_3 = 0$, the yield locus Φ is described by a family of ellipses in the $\sigma_1 - \sigma_2$ principal stress plane in equations 4.12a and 4.12b. The curvature of the yield locus between two points is obtained from the normality-flow rule which states that the plastic strain-increment vector is normal to the yield locus, $d\varepsilon = \lambda \partial\Phi/\partial\sigma$ (λ is the rate of the plastic multiplier). The stress ratio is corrected and expressed in terms of strain ratios R_0, R_{90} and $\bar{\varepsilon}$ in equation 4.12c and 4.12d (R_0 and R_{90} are known as Lankford coefficients). The KHN is taken in kg/mm^2 units and equated to the equivalent yield stress for Hosford yield criteria as given in [55]. This method has been commonly used to plot the yield locus based on Knoop hardness number in plane stress plane in [55, 57, 56]. Following the previous works, equating KHN to the equivalent yield

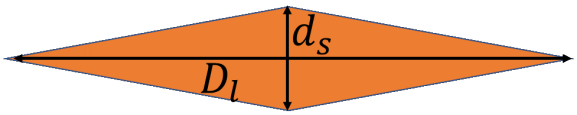

(a) The geometry of a Knoop indent. Lengths of short diagonal d_s and long diagonal D_l.

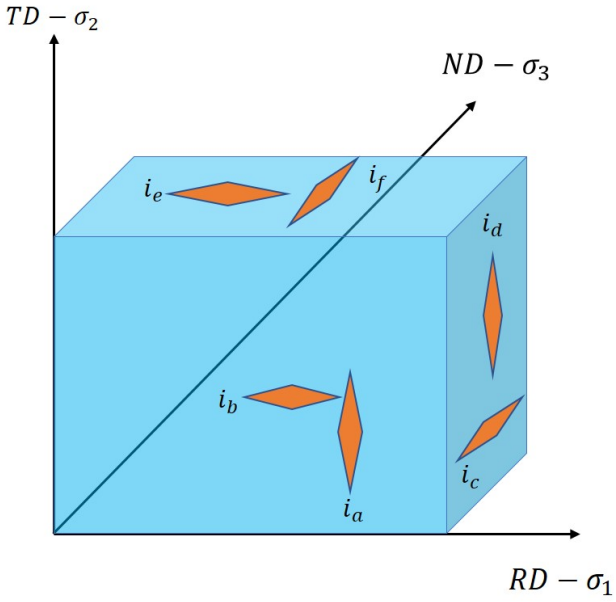

(b) The orientation of six Knoop indentations i_a, i_b, i_c, i_d, i_e and i_f with D_l and d_s along RD (rolling direction) ,TD (transverse direction) and ND (normal direction).

Figure 4.19: 6 orientations for Knoop indentations.

stress σ_y for anisotropic Hill's 48 yield criteria [52], the coordinates of points corresponding to KHN of each indentation Khn_i and its stress ratio $\bar{\sigma}_i$ ($i\epsilon[i_a, i_b, i_c, i_d, i_e, i_f]$) are given in the $\sigma_1 - \sigma_2$ plane in equation 4.13 by taking σ_1 and σ_2 as common factor out of the right hand side of equation 4.12b. The six indentations namely i_a, i_b, i_c, i_d, i_e and i_f correspond to the diagonals of the Knoop indenters are oriented along the principal coordinate direction which are also aligned along the axes of anisotropy: RD (rolling direction),TD (transverse direction) and ND(normal direction) as shown in figure 4.19.

$$\Phi = \sigma_1^2 - \frac{2R_0}{R_0+1}\sigma_1\sigma_2 + \frac{R_0(R_{90}+1)}{R_{90}(R_0+1)}\sigma_2^2 - \sigma_y^2 \tag{4.12a}$$

$$KHN_i \sim \sqrt{\sigma_1^2 - \frac{2R_0}{R_0+1}\sigma_1\sigma_2 + \frac{R_0(R_{90}+1}{R_{90}(R_0+1)}\sigma_2^2} \tag{4.12b}$$

$$\bar{\varepsilon} = \frac{d\varepsilon_1}{d\varepsilon_2} = \frac{\frac{d\Phi_1}{d\sigma_1}}{\frac{d\Phi_2}{d\sigma_2}} = \frac{2\sigma_1 - \frac{2R_0}{R_0+1}\sigma_2}{\frac{2R_0(R_{90}+1)}{R_{90}(R_0+1)}\sigma_2 - \frac{2R_0}{R_0+1}\sigma_1} \tag{4.12c}$$

$$\bar{\sigma} = \frac{\sigma_1}{\sigma_2} = \frac{R_0}{R_{90}}\frac{\bar{\epsilon}R_{90} + 1 + R_{90}}{\bar{\epsilon}R_0 + R_0 + \bar{\epsilon}} \tag{4.12d}$$

$$\sigma_1 \sim \frac{KHN_i}{\sqrt{C_2 - C_1\bar{\sigma}_i + \bar{\sigma}_i^2}}\ ,\ \sigma_2 \sim \frac{\bar{\sigma}_i KHN}{\sqrt{C_2 - C_1\bar{\sigma}_i + \bar{\sigma}_i^2}}\ \forall C_1 = \frac{2R}{R+1}\ ,\ C_2 = \frac{R(P+1)}{P(R+1)} \tag{4.13}$$

To further analyze the data, an algorithm to plot the yield locus from the KHN data (table 4.4) and calculate R_0, R_{90} and σ_y has been developed (see paper E [120]). Initially, points are plotted on the deviatoric plane in figure 4.22 from KHN, using $\bar{\sigma}$ from equation 4.10 ($\bar{\sigma} = \bar{\varepsilon}$)

and 4.12b ($R_0 = R_{90} = 1$) respectively. However, the yield locus obtained in the deviatoric plane or for that matter in the plane-stress plane with an isotropic assumption of $R_0 = R_{90} = 1$ is not accurate for anisotropic material. Also, typically sheet metal processes have used plane stress assumptions in expressing anisotropic material behaviour. Hence, an algorithm has been developed to optimize the value of R_0 and R_{90} and use the optimized values to plot the yield locus in the plane-stress plane. The algorithm minimized the distance $\overset{*}{d}$ between the points plotted on the plane-stress plane using KHN-data and the yield locus plotted on the plane stress plane using the chosen values of R_0, R_{90} and σ_y.

Hence, the initial KHN-data points are plotted on the plane-stress plane by taking initial values of $R_0 = R_{90} = 1$. The yield locus is solved for the plotted points from which values of R, P and σ_y are obtained. The values of R_0 and R_{90} are used to correct $\bar{\sigma}$ and re-plot the yield locus until the difference in the distance between iterated KHN-data points and the yield loci from the values of modified R_0, R_{90} and σ_y is below tolerance. The optimized KHN-yield locus is plotted on the plane-stress plane in figure 4.23 and its R_0, R_{90} and σ_y are listed in table 4.4 and compared with those obtained from the bulk loading tests of DC04 steel. The close agreement in both the methods sets the possibility of using Knoop (Nano-)indentation with the developed algorithm given in figure 4.20 to characterize the yield locus for thin, zinc coatings in galvanized steel sheets [120].

Table 4.4: Knoop hardness data and the yield loci parameters for DC04 steel [129].

KHN_i	Value [GPa]	Yield loci parameters	Value
KHN_{i_a}	118.25	R_0^{bulk}	1.93
KHN_{i_b}	115.1	R_{90}^{bulk}	2.21
KHN_{i_c}	177.35	${\sigma_y}^{bulk}$	157.8 MPa
KHN_{i_d}	167.4	R_0^{KHN}	1.80
KHN_{i_e}	136.55	R_{90}^{KHN}	2.34
KHN_{i_f}	141.35	${\sigma_y}^{KHN}$	168.5 MPa

Multiple indentations have been done, shown as an indentation matrix in figure 4.21b. The size of the Knoop indentation have been measured by observing them under the confocal microscope. The length of the long diagonal D_l, short diagonal d_s and indentation depth h of the Knoop indent mark is measured from the height profile of the indent as shown in figure 4.21a.

Table 4.5: Knoop hardness data and the yield loci parameters for Zinc coating steel.

KHN_i	Value [GPa]	Yield loci parameters	Value
KHN_{i_a}	51.04	R_0^{bulk}	–
KHN_{i_b}	59.77	R_{90}^{bulk}	–
KHN_{i_c}	66.16	σ_y [47]	50-110 MPa
KHN_{i_d}	37.23	R_0^{KHN}	0.45
KHN_{i_e}	53.67	R_{90}^{KHN}	1.56
KHN_{i_f}	78.28	$\sigma_{y_{KHN}}$	57.7-81.7 MPa

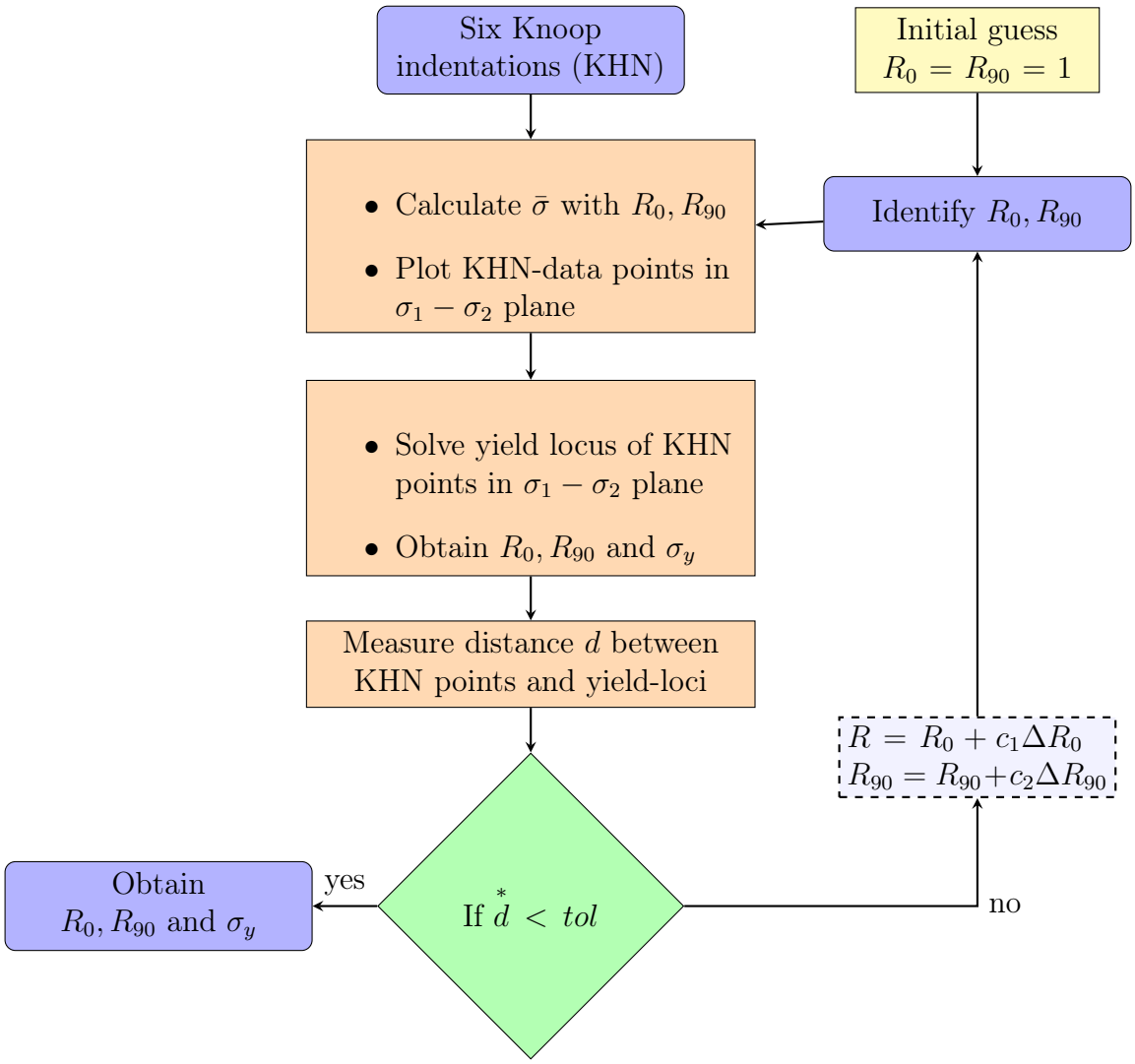

Figure 4.20: Flowchart showing the optimization algorithm to obtain values of R_0, R_{90} and σ_y.

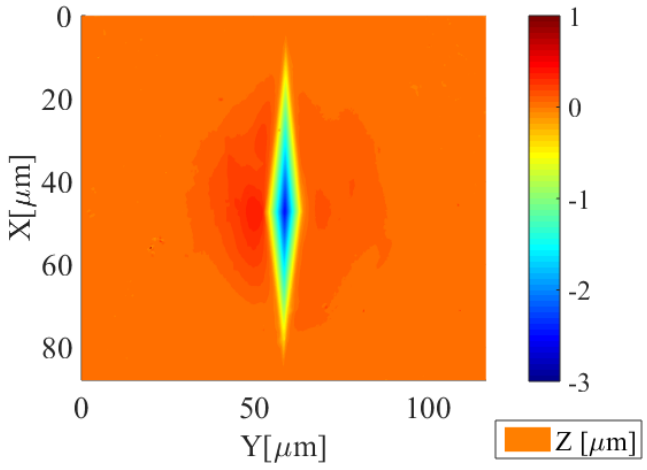

(a) The height profile and size of the Knoop indent on DC04 steel at 50g load.

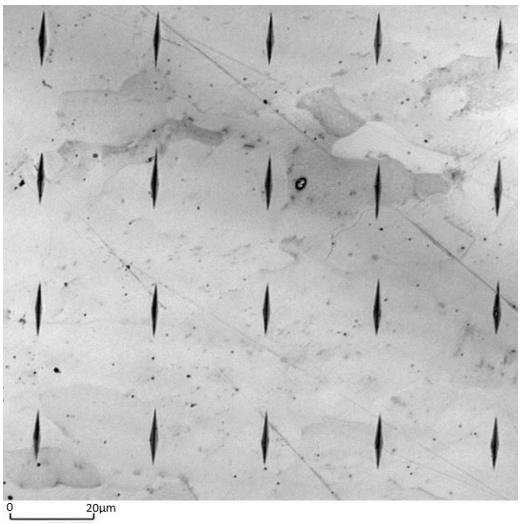

(b) Image of matrix of Knoop indents on DC04 steel at 20 mN load.

Figure 4.21: Measurement of indent size from nano-indentation of DC04 steel.

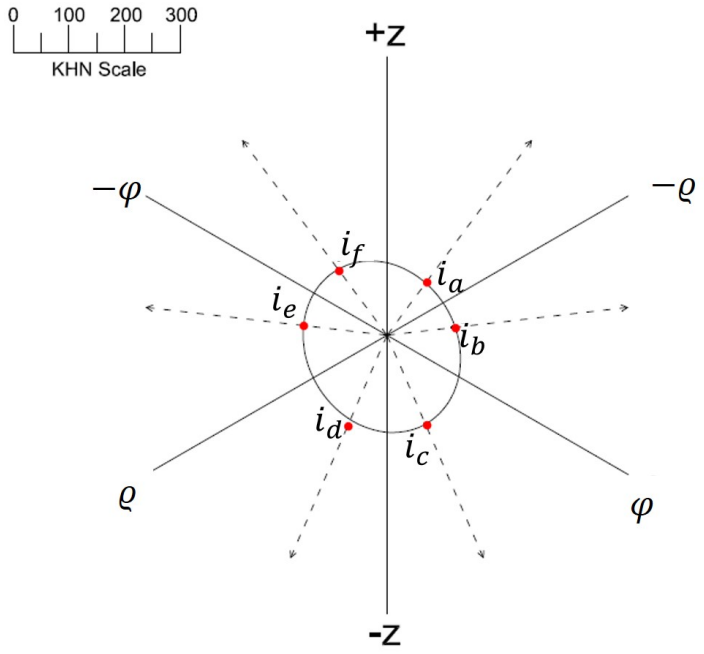

Figure 4.22: Yield locus for DC04 steel sheet in the deviatoric plane in the rolling direction z, transverse direction φ and normal direction ϱ with KHN scale in kgf/mm^2.

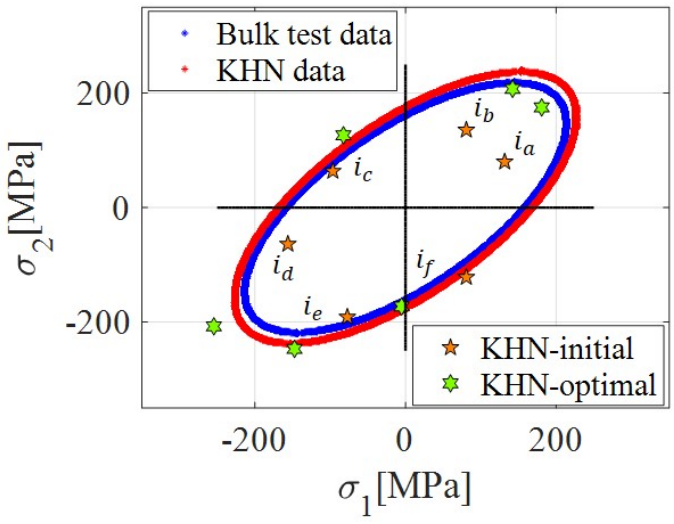

Figure 4.23: The yield loci obtained from KHN data on the plane-stress plane optimized for anisotropy and compared with that obtained bulk tests on DC04 steel sheet.

Multiple indentation have also been performed on the cross-section of the zinc coating as shown in figure 4.24a. The indentation load is limited to 50mN in order to keep the indentation size within the coating thickness of 20 μm as shown in figure 4.24b. The average value of the measurements of the indents are taken to reduce the local effects of anisotropy due to grain size and orientation.

Having validated the yield locus obtained from the Knoop indentations of DC04 steel sheet with that obtained from the bulk tests, the Knoop indentation characterization technique of yield locus has been extended to the zinc coating on steel sheets. The KHN data has been taken for 6 Knoop indentations in table 4.5. The points are plotted on the plane stress $\sigma_1 - \sigma_2$

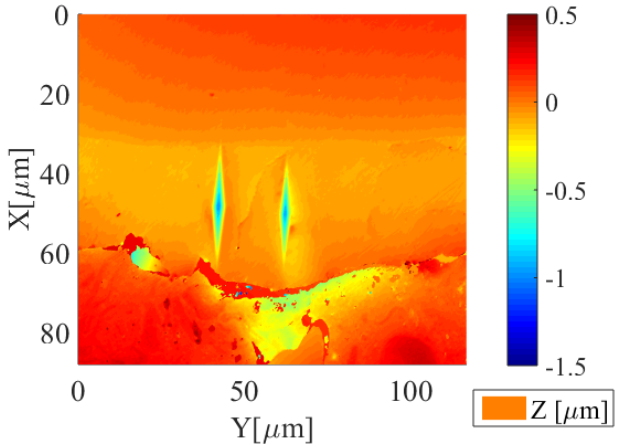

(a) The height profile and size of the Knoop indent on zinc coating cross-section at 50mN load.

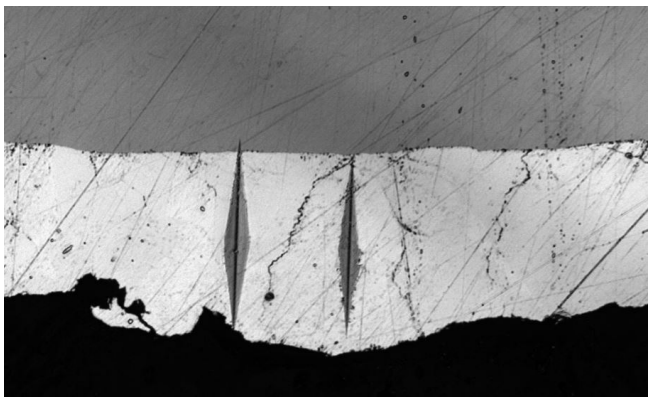

(b) Image of matrix of Knoop indents on cross-section of the zinc coating at 50 mN load

Figure 4.24: Measurement of indent size from nano-indentation of zinc coating on steel.

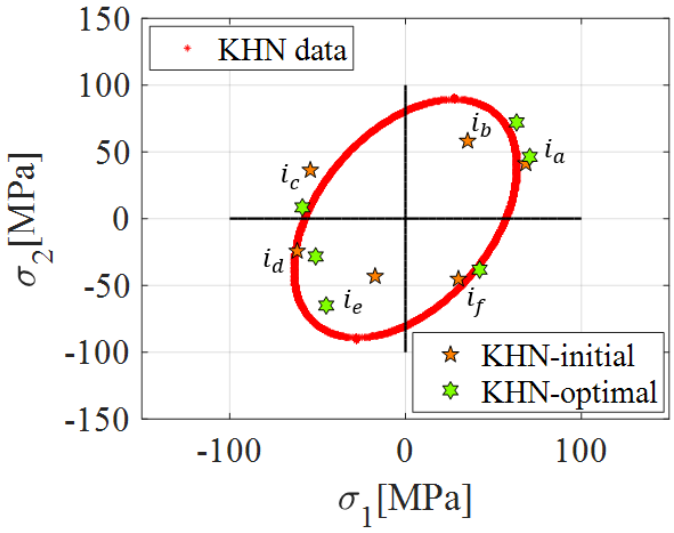

Figure 4.25: The yield locus obtained from KHN data on the plane-stress plane optimized for anisotropy for zinc coating on steel sheet.

plane. taking initial values of $R_0 = R_{90} = 1$. The values of R_0, R_{90} and σ_y are then varied (increased/decreased) using constants c_1, c_2 as shown in the algorithm in figure 4.20. The distance d between the measured KHN-data points on the plane stress plane and the yield locus based on R_0, R_{90} and σ_y is computed. The values of R_0, R_{90} are accepted for values of $\overset{*}{d}$ below a given tolerance tol. Finally the optimized yield locus for the zinc coating on the steel sheet is plotted by optimizing the KHN-data points in figure 4.25.

The parameters for the Hill's quadratic yield criteria [52] can be calculated from the Lankford coefficients (R_0, R_{90} values) obtained from the KHN based yield locus of the DC04 steel sheet and the zinc coating on the steel sheets. The Hill's quadratic yield criteria is given in equation 3.6 in terms of constants U_1, U_2, U_3, V_1, V_2 and V_3. The Lankford constants are defined for a sheet metal as the ratio of the strain ϵ_{φ_r} in the plane of loading at the angle of orientation φ_r with respect to the rolling direction to the strain out of the plane ϵ_z. The relationship between

the three Lankford coefficients R_0, R_{90} and R_{45} and the parameters of the Hill's quadratic yield constants are given in equation 4.14a. By expressing the Hills quadratic yield criteria in plane-stress plane in terms of both the Hill's constants $U_1, U_2, ..., V_3$ (taking σ_{13}, σ_{23} and $\sigma_{33} = 0$ in equation 3.6 in chapter 3 section 3.1.3.) and the Lankford coefficients as given in equations 4.14b and 4.14c, the relationship between the Hill's constants and the Lankford coefficients are in equation 4.14d. Solving equation 4.14a and 4.14d, and assuming planar anisotropy the parameters for the Hill's quadratic yield criteria for both DC04 steel sheet and zinc are listed in table 4.6. The value of R_{45}=1.44 is given for DC04 steel but no such value is obtained for the zinc coating. Hence, the constants of the shear stress in the Hills quadratic equation in equation 4.14d are taken N=1.5, M=1.5 and L1.5 for the zinc coating.

$$R_0 = \frac{U_3}{U_2} = \frac{d\epsilon_{\varphi=0^\circ}}{d\epsilon_z}; R_{90} = \frac{U_3}{U_1} = \frac{d\epsilon_{\varphi=90^\circ}}{d\epsilon_z}; R_{45} = \frac{U_3}{U_1 + U_2} - \frac{1}{2} = \frac{d\epsilon_{\varphi=45^\circ}}{d\epsilon_z} \tag{4.14a}$$

$$2\Phi(\sigma_{ij}) = (U_2 + U_3)\sigma_{11}^2 - 2U_3\sigma_{11}\sigma_{22} + (U_1 + U_3)\sigma_{22}^2 + 2V_3\sigma_{12}^2 = 1 \tag{4.14b}$$

$$f(\sigma_{ij}) = \sigma_{11}^2 - \frac{2R_0}{R_0 + 1}\sigma_{11}\sigma_{22} + \frac{R_0(R_{90} + 1)}{R_{90}(R_0 + 1)}\sigma_{22}^2 + \frac{(R_0 + R_{90})(2R_{45} + 1)}{R_{90}(R_0 + 1)}\sigma_{12}^2 = 1 \tag{4.14c}$$

$$U_1 = \frac{R_0}{R_{90}(R_0 + 1)}; U_2 = \frac{1}{R_0 + 1}; U_3 = \frac{R_0}{R_0 + 1}, V_3 = \frac{R_0 + R_{90}}{R_{90}(R_0 + 1)}\Big(R_{45} + \frac{1}{2}\Big); V_2 = \frac{3}{2}; V_1 = \frac{3}{2} \tag{4.14d}$$

Table 4.6: Parameters for Hill's quadratic yield criteria for DC04 steel and zinc coating [129].

Hill's 48	DC04 Steel	Zinc coating
U_1	0.298	0.2
U_2	0.341	0.69
U_3	0.659	0.31
V_3	1.274	1.5
V_1	1.5	1.5
V_2	1.5	1.5

4.3. Summary

The experimental set-up and specimens used in characterization of the material properties and ploughing behaviour of uncoated and zinc coated steel sheets have been described in this chapter. To summarize the methods to determine the interfacial shear strength and the yield locus of uncoated steel sheet and zinc coating on steel sheet have been elaborated in this chapter. Firstly, an experimental characterization technique to measure the boundary layer shear strength of uncoated and zinc coated steel substrate with varying applied load and sliding velocities has been developed. Secondly, a combined numerical and experimental method to plot the anisotropic yield locus based on Knoop indentation has been developed. The yield parameters are optimized to plot the best fit yield locus from the KHN data. The method has been implemented to plot the yield locus for DC04 steel sheet and validated against bulk tests. The method has been extended to plot the yield locus of the zinc coating on steel sheet. The Knoop indentation based method has been used effectively to compute the parameters of the anisotropic Hill's quadratic yield criteria (for coated systems) which has been typically calculated by bulk tensile tests. The parameters for the Hill's 48 yield criteria for the zinc coating, i.e. U_1, U_2, U_3, V_1, V_2 and V_3 are calculated using the Knoop-indentation method in

table 4.6 have been implemented in the equation 3.6 (Hill's 48 yield criteria) in chapter 3, section 3.1.3 for building the anisotropic material model. The anisotropic material model is used in ploughing simulations of the rolled zinc coated sheets in chapter 5 [120].

Chapter 5

Results and discussion

In this chapter, results will be shown for the developed model being the components of the coefficient of friction, depths of the ploughed profile and the wear mode. The results will be discussed in terms of the effect of the model parameters (see section 1.5) such as asperity geometry, interfacial shear strength, anisotropy and thickness of the zinc coating and applied loads. The numerical results have been compared with the analytical results for ideal (rigid-) plastic and elastic material behaviour. The numerical results have also been validated with the results obtained from the ploughing experiments and will be shown to be in good agreement. The results will illustrate the limitations and possibilities of the MPM based model to simulate the ploughing behaviour of an elliptical single-asperity sliding through both coated and uncoated substrates with anisotropic material behaviour.

The chapter will provide an overview of the results obtained from the appended papers A [95], B [105], C [106], D [121], and F [107]. This will include results from the developed numerical(MPM) model in chapter 3 section 3.1, the analytical model described in chapter 4 section 3.2., and the experiments performed using the experimental set-ups described in chapter 4 section 4.1. The input to the numerical MPM model will be given from the characterized material properties given in chapter 4 section 4.2 and the data listed in tables 3.6, 3.4 and 3.5. Some experimental results on the effect of (ellipsoidal) asperity geometry and material anisotropy on friction in ploughing of (temper-rolled) lubricated zinc coated steel sheets will also be presented.

The results will be presented, categorized into two sections. The first section will deal with the coefficient of friction results regarding the friction forces in ploughing obtained from the analytical and numerical models and the ploughing experiments. The second section will deal with the ploughing depth results regarding the ploughed profile as obtained from the analytical and numerical model and the ploughing experiments. Each section is divided into subsection on the results specific to the ploughing of uncoated steel and zinc coated steel sheets. The results presented in this section are categorised and are referred to the appended papers as given below:

- Ploughing depth
  - Ploughed profile in uncoated steel sheet: Paper A[95], C[106], and D [121]
    - Comparison of the the simulated profile depth with the analytical model: Paper A[95] and C[106]
    - Comparison of the simulated profile depth with ploughing experiments: Paper A[95] and D[121]
  - Ploughed profile in zinc-coated steel sheet: Paper F[107]
- Friction force
  - Friction in ploughing of uncoated substrates: Paper A[95], C[106], and D [121]
    - Comparison of the simulated friction force with the analytical model: Paper A[95] and C[106]
    - Comparison of the simulated friction force with ploughing experiments: Paper A[95] and D[121]
  - Friction in ploughing of zinc-coated substrates: Paper F[107]

5.1. Ploughed profile

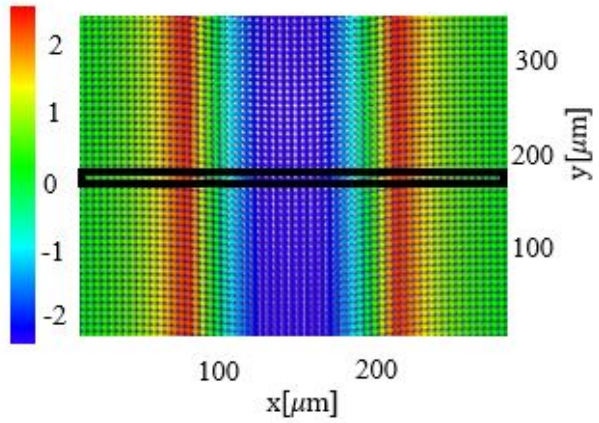

(a) Surface height of ploughed profile (MPM simulations) Highlighted region for ploughed cross-section.

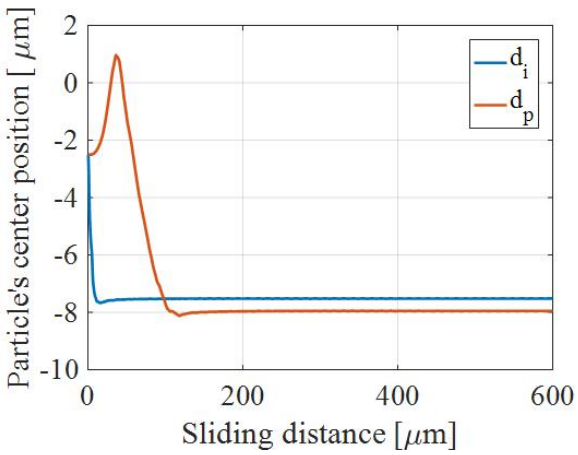

(b) Average position of the particle group under the indenter for duration of sliding.

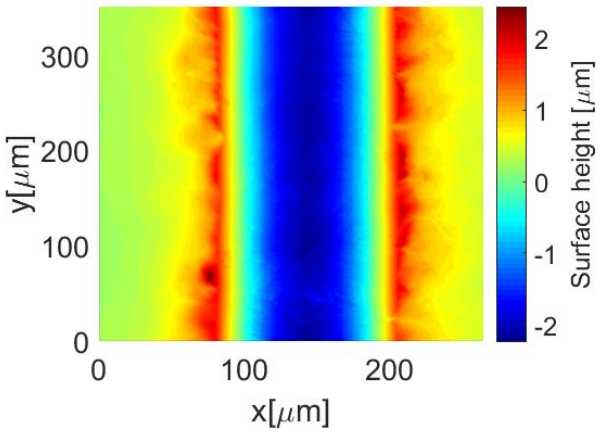

(c) Surface height of ploughed profile obtained from ploughing experiments.

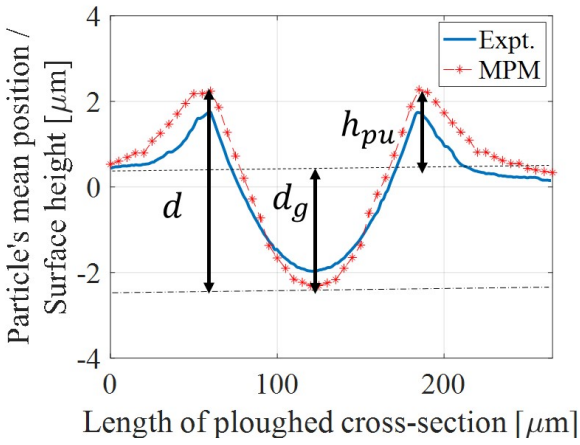

(d) Comparison of the profile of the ploughed cross section from experiments and simulation.

Figure 5.1: Ploughed track for a lubricated-7N load controlled scratch test using a 1mm indenter in 1: linear sliding friction tester as seen using confocal microscope 50x magnifications 2: MPM simulation ($5\mu m$ particle resolution) showing position of particle group at center of ploughed profile over sliding distance (duration) and the profiles of the ploughed cross-sections obtained from MPM-ploughing model and ploughing experiments. The results ofor ploughing on uncoated substrate can be refereed to paper A [95], paper B [106] and paper D [121].

The ploughing depth of the wear track is computed for the analytical model, MPM-simulations and the ploughing experiments. The analytical model computes the ploughing depth of the points on the contact boundary by the equations 3.19a-3.19c in section 3.1.4. The MPM-based ploughing simulation selects groups of particles in the cross section of the surface of the substrate perpendicular to the sliding direction as shown in figure 5.1a. The final average position of the group of particles is measured at the end of the simulations and the profile of the cross-section on the wear track is mapped out as shown in figure 5.1b. The ploughed wear track is observed under the confocal microscope at 50x resolution for the surface height profile as shown in 5.1c. The height of the cross-section of both the plough profiles obtained from the MPM-simulation and ploughing experiments, when compared, are in good agreement, see figure 5.1d.

5.1.1. Ploughed profile in uncoated substrates

The ploughing depth is measured from the simulated ploughed profile of an uncoated DX56 steel substrate ploughed using spherical and ellipsoidal indenters. The ploughing depth obtained from the simulated ploughed profile is compared with the ploughing depth obtained using the analytical model in section 3.2 and using ploughing experiments. The results shown below can be referred to paper A [95], paper C [106] and paper D [121].

5.1.1.1. Comparison of the the simulated profile depth with the analytical model

For validation purposes, the penetration/ploughing depths obtained by the MPM-model and the analytical model are compared with each other for a range of applied loads on substrates with perfectly elastic and perfectly plastic material behaviour [95, 106]. The penetration depth for the contact length a by a spherical indenter of radius r is given as $d = a^2/r$. In the MPM-model, the penetration depth of the spherical indenter is computed by the difference in the position of the centre of mass of particle-group on the surface of the substrate which are deformed from their reference position as the sliding-indenter comes in contact with them. For a perfectly elastic substrate the penetration depth is obtained from the expression for Hertzian point contact and given as d_e in equation 5.1a. For the ploughing of a rigid-plastic substrate with a spherical indenter the ploughing depth d_p is given using the load balance from equation 3.17a and expressed in equation 5.1b.

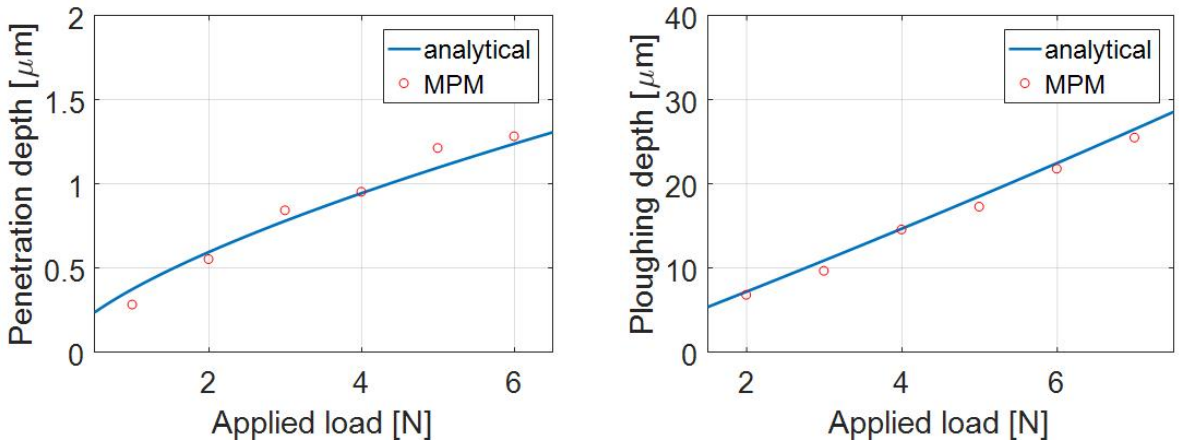

(a) Perfectly elastic substrate (b) Perfectly (rigid-) plastic substrate.

Figure 5.2: Penetration/ploughing depths vs applied loads for ploughing through a perfect elastic and a rigid-plastic substrate.

In order to study the ploughed profile, and compare the results to the numerically simulated ploughing depths, a section of the substrate material surface was chosen as shown in figure 5.1a. The section comprised of different regions with size of a unit particle volume and the average position of each of the region was plotted as a function of the sliding distance. Figure 5.1b shows the average position of the particle in the region under the central axis of the asperity in the sliding direction over the whole sliding distance, shown as black mark in figure 5.1b. The ploughing depth d_p is calculated as the sum of the pile-up height and groove depth (see figure 5.1d) in the ploughed profile. The ploughed profile is obtained from the final average position of the particles in the ploughed cross section as shown in figure 5.1b and 5.1d. It can be seen

from figure 5.2a and 5.2b that the depth of penetration/ploughing obtained from the MPM simulations agrees well with the analytical results for the given range of loads.

$$d_e = \left(\frac{9F^2 r(1-\nu^2)^2}{16E^2}\right)^{\frac{1}{3}} \tag{5.1a}$$

$$d_p = \frac{2F}{\pi H r} \tag{5.1b}$$

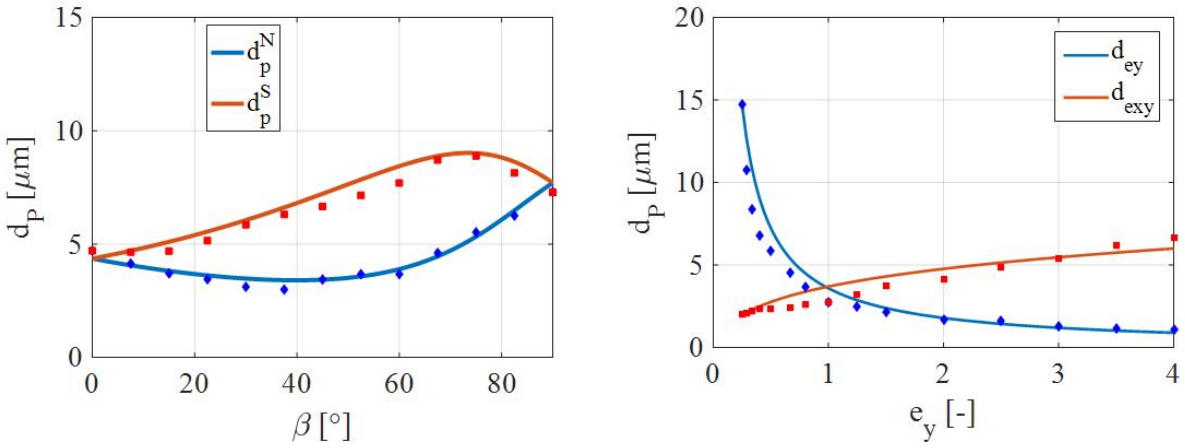

(a) Effect of orientation on ploughing depth

(b) Effect of size on ploughing depth.

Figure 5.3: Comparison of MPM-ploughing model results with analytical model results (section 3.2.4) for a ploughing of a rigid-plastic substrate by an ellipsoidal asperities with (a) axes size $a = 100\mu m, b = 200\mu m, c = 200\mu m$ and (b) ellipticity ratio e_y changing such that e_x=1 and $e_x e_y$=1 at an applied load of 1N. (marks: MPM model, line: analytical model).

Following equation 3.17b (section 3.2), the ploughing depth is independent of the orientation and size of the asperity and is assumed constant over the ploughed profile. However, the developed model has accounted for the plastic and shear flow behaviour to develop fitting factors to compute the ploughing depth as a function of asperity orientation. Figure 5.3 shows the ploughing depth obtained from the analytical and numerical model for various orientation, size and ellipticity ratio of the ellipsoidal asperity. In figure 5.3a we consider ploughing by an elliptical asperity with its major axes $b = 200\mu m$ (minor axis $a = 100\mu m$) perpendicular to the sliding direction. The pile-up height in front of the given asperity decreases with increase in β from 0° to 90° due to decrease in the projected area in yz-plane (see section 3.2.4). The decrease in the pile-up height of the ploughed profile with β corresponds to the increase in the groove depth to balance the load shared by the piled-up substrate in front of the asperity (see section 3.2.4). The groove depth dominates the fraction in the total ploughing depth for an elliptical asperity. The depth of the final ploughed track increases for an increase in β from 0° and 90° as shown in figure 5.3a.

The asymmetric separation of flow due to asymmetry in the ploughing asperity results in a variable ploughing depth on either ends of the ploughed track (points S and N shown in figure 3.7 and 3.8 in chapter 3, section 3.2), as given in figure 5.3a. The change in asperity orientation from 0° and 90° results in an rapid divergence in ploughing depths d_p^N and d_p^S on either side of ploughed wear track followed by their steady convergence as shown in figure 5.3a. This behaviour is explained by the variation in distribution of piled-up substrate material in front of

the asperity to its periphery with β, as shown in section 3.2.4 using equations 3.19a and 3.19b. The ploughing depths for the ellipsoidal asperity increase with a decrease in e_y only following load balance and plastic flow correction as shown in figure 5.3b. However the ploughing depth increases with e_y, which increases as reciprocal of e_x, due to increase in the resistance to plastic flow. The numerical ploughing depth d_p does agree fairly well with the analytical ploughing depths.

5.1.1.2. Comparison of the simulated profile depth with ploughing experiments

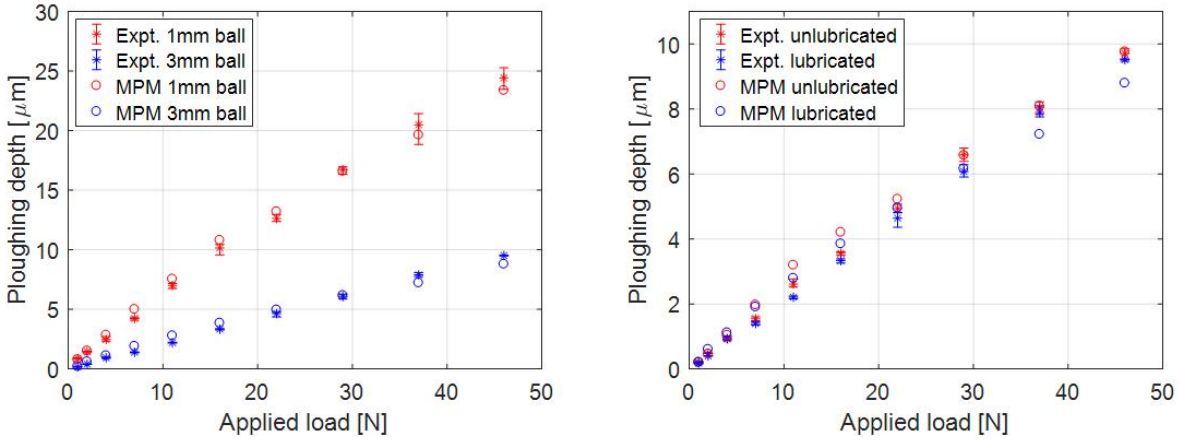

(a) Effect of r and F_n on ploughing depth

(b) Effect of τ and F_n on ploughing depth

Figure 5.4: Ploughing depths for load controlled test carried out with indenters of diameter 1mm and 3mm on lubricated and unlubricated steel sheet with the linear sliding friction tester and MPM-ploughing model that includes the Bergström-van Liempt material model parameters given in table 3.4 and interfacial shear stress model given in equations 4.8a and 4.8c.

Initial experimental validation of ploughing depth obtained from the MPM ploughing model was done using ploughing experiments using pins with spherical balls at their tips [95, 121]. The applied loads were varied from 1-46 N while 1mm and 3mm spherical ball diameters were used at the pin tips for ploughing on a DX56 steel sheet lubricated with 'Quaker' oil. The applied loads were chosen such that ploughing was the sole wear mode where the material was displaced from the groove into the piled-up ridges as the indenter slid through the substrate, thereby avoiding the generation of any wear debris. As no material was removed or detached from the substrate, both the material under the ploughed groove and in the piled-up ridge supported the applied load during the ploughing of the steel substrate. In another case the ploughing experiments were performed using a 3mm diameter spherical ball for ploughing on the steel sheet with a stable oxide layer prepared by shine polishing (see section 4.1.1.2) in the absence of any lubricant. The ploughed profile obtained from the experiment and the MPM simulations are compared as shown in figure 5.1d. The ploughing depth was calculated as the sum of the pile-up hieght h_{pu} and groove depth d_g. The total ploughing depths calculated from the ploughing experiments and the MPM model were plotted in figure 5.4a for two indenters of different radii over a range of loads. The MPM model can be seen to accurately compute the ploughing depths for an asperity sliding through the steel substrate.

The ploughing depths obtained from the MPM-based ploughing simulations for ploughing of lubricated and unlubricated steel substrate by a 3mm diameter indenter have been validated against ploughing experiments in figure 5.4b. The ploughing simulation results agree well

with the experimental results for the given range of loads both in lubricated and unlubricated conditions. It can be seen that the increase in interfacial shear strength, in the absence of a lubricant, increases the deformation of the substrate and hence the ploughing depth. The force on the substrate due to interfacial shear acts in the opposite direction, $-F_z^s h$ (see section 3.2.4.3 and 3.2.5). Thus a component of the force acts on the substrate in the $+z$ axis due to interfacial shear and a component of force acts on the substrate in the $-z$ axis due to plastic compressive pressure. Hence, the forces acting on the asperity-substrate contact due to interfacial shear and plastic deformation result in a bi-axial tension on the deforming substrate elements. Such a stress-state caused faster yielding and increases the ploughing depth to maintain load balance.

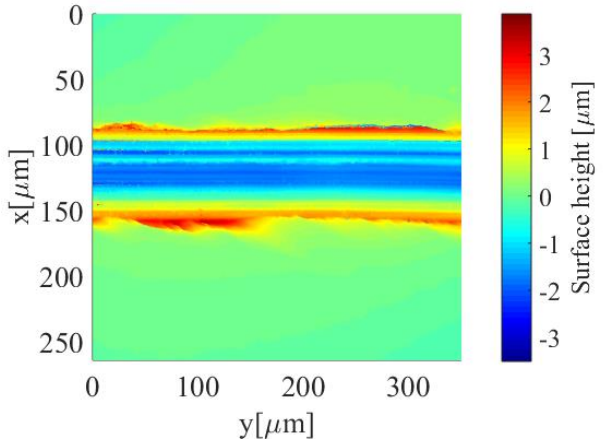

(a) Ploughed track (Experimental) for asperity $\beta = 0°$.

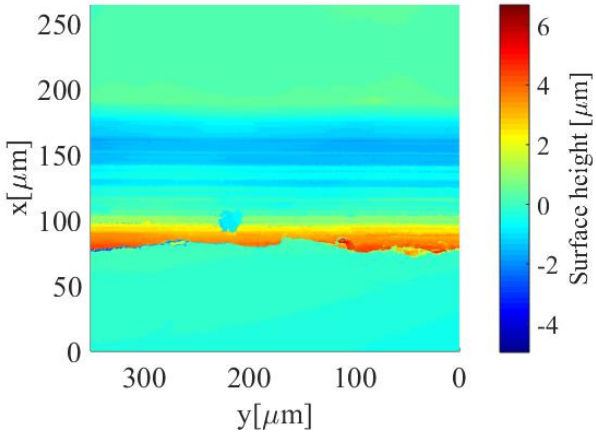

(b) Ploughed track (Experimental) for asperity $\beta = 30°$.

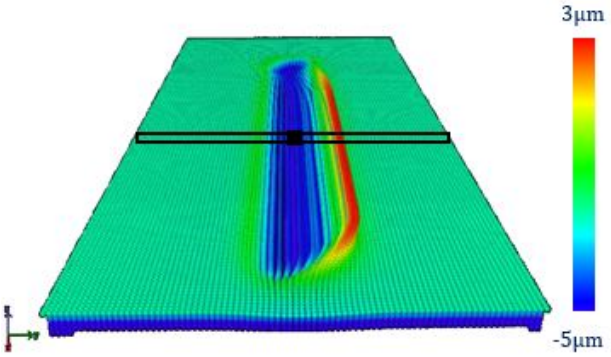

(c) Ploughed track (MPM simulation) for asperity $\beta = 0°$.

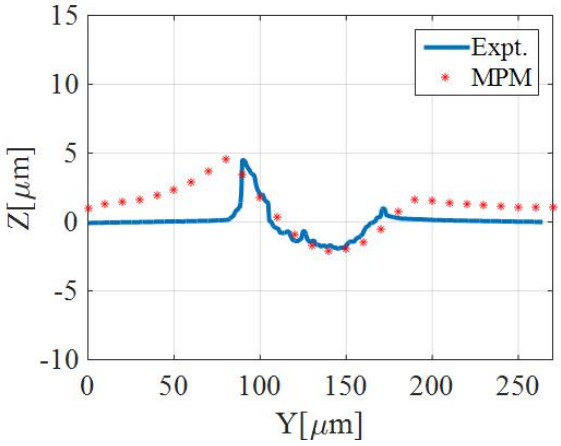

(d) Comparison of ploughed cross-section (Expt. vs MPM) for asperity $\beta = 0°$.

Figure 5.5: Confocal image at 50x magnification of the ploughed track showing surface height distribution of a substrate ploughed by a load of 7N using an ellipsoidal asperity of axes size $a = 1000\mu m, b = 250\mu m$ orientated at angle with respect to sliding direction (a) $\beta = 0°$, (b) $\beta = 30°$ obtained from experiments and (c) MPM simulation (highlighting ploughed cross-section) and (d) comparison of ploughed cross-section from experiments and MPM simulations using material parameters from table 3.4 and interfacial friction model in equation 4.8a.

The ploughing depth d was obtained as the sum of the maximum groove depth, d_g and the maximum pile-up height h_{pu} on either side of the ploughed wear track for both the experiments

as well as the simulations. The ploughing depth on the $+y$ axis was given as d_{+y} and on the $-y$ axis was termed as d_{-y}. The ploughed track that was observed under the confocal microscope for experiments done at different orientations for a ellipsoidal asperity with an ellipticity ratio e_{xy} of 4 are shown in figure 5.5. It can be clearly seen particularly in figure 5.5a that for an orientation of 0° (and 90°), the ploughing depths on either side of the wear track are more or less similar. Any possible difference in the ploughing depth can be due to the sliding misalignment in clamping the ellipsoidal pin mark with the pin holder marking to set the require orientations of 0° and 90°. When the ellipsoid is oriented at an angle of for e.g. 30° there is a difference in the ploughing height on either side of the ploughed wear track as seen in figure 5.5b. This behaviour has also been seen in the MPM simulation of ploughing by the ellipsoidal asperity of the same size as oriented at an angle of 30° as seen in figure 5.5c. Comparison of the ploughed profile by taking a cross-section on the ploughing track as shown in figure 5.5d results in good agreement between the MPM-model and ploughing experiments.

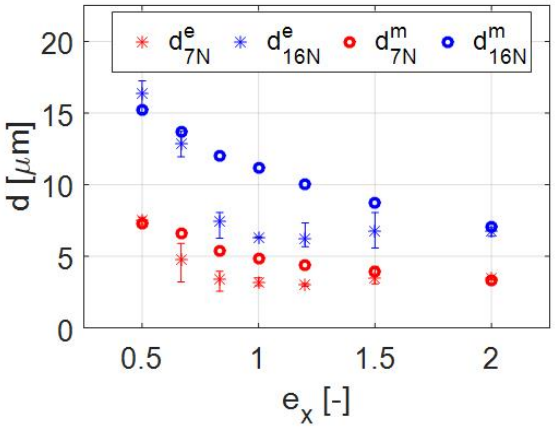

(a) Effect of asperity's ellipticity ratio e_x and load F_n on ploughing depth

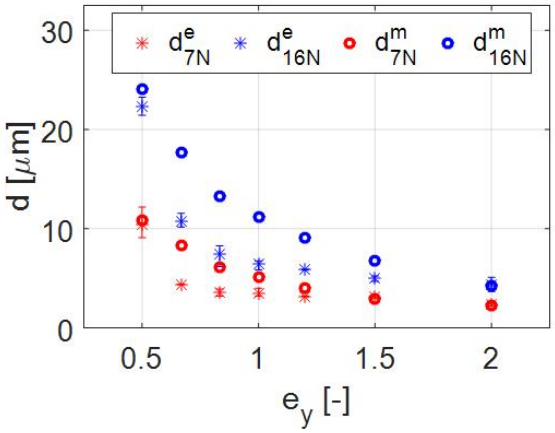

(b) Effect of asperity's ellipticity ratio e_x and load F_n on ploughing depth.

Figure 5.6: Comparison of ploughing depth d for applied loads of 7N and 16N (subscript) obtained from MPM-based ploughing simulation (superscript: m) and ploughing experiments (superscript: e) for varying ellipticity ratio along the (a) x- axis (sliding direction) and (b) y-axis .

The total ploughing depths obtained from ploughing experiments and simulation has been plotted as a function of the ellipsoid size in x and y direction for applied loads of 7N and 16N as shown in figure 5.6 [106]. It can be seen in figure 5.6a that the ploughing depth decreases with increase in size of the ellipsoidal indenter as also follows from the load balance given in equations 3.17a and 3.17b. The ploughing depths for pins with e_y between 0.5 to 1 is higher as compared to the pins with e_x between 0.5 to 1 as shown in figure 5.6. This follows from equation 3.18a and 3.18b where a smaller axes size in y-direction results in a lower resistance to plastic flow, and hence a higher penetration of the pin into the substrate. However, both the numerical and experimental ploughing depths decrease as e_x and e_y increase from 1 to 2, the experimental ploughing depth in fact increases as the ellipticity ratio e_x increases from 1 to 2. The increase in ploughing depth could be due to misalignment of the ellipsoidal pins in the vertical plane which results in deeper penetration of the pin into the substrate. As discussed previously, an ellipsoidal pin with its major axis in the sliding direction is sensitive to misalignment in the x or y axis. The increase in ploughing depth for larger pins in figure 5.6a also explains the increase in their corresponding coefficient of friction as shown in figure 5.17a.

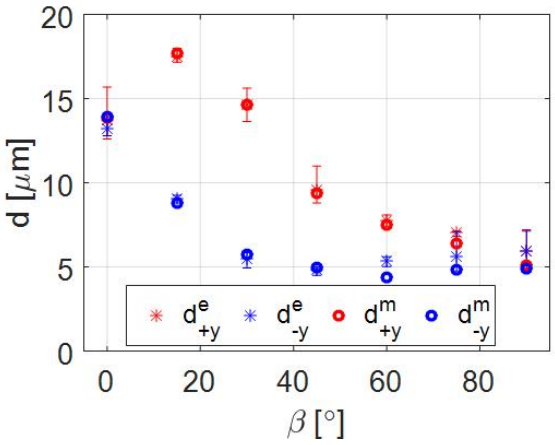

(a) Size of ellipsoidal pin $a = 1000\mu m, b = 250\mu m$ Load $= 16N$

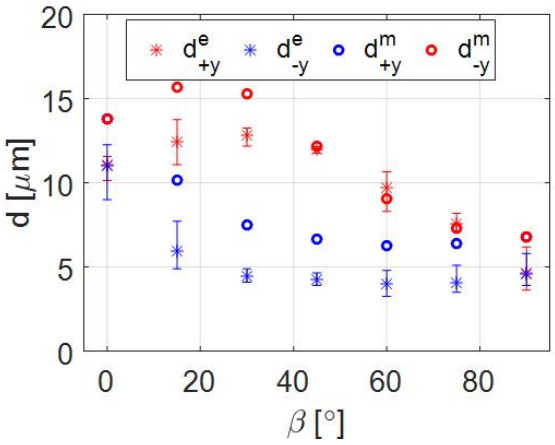

(b) Size of ellipsoidal pin $a = 833\mu m, b = 300\mu m$ Load $= 16N$

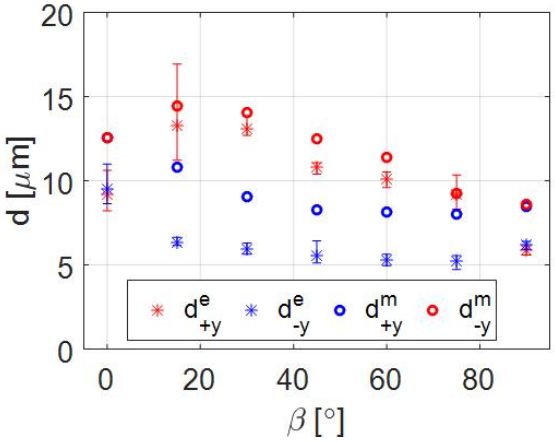

(c) Size of ellipsoidal pin $a = 667\mu m, b = 375\mu m$ Load $= 16N$

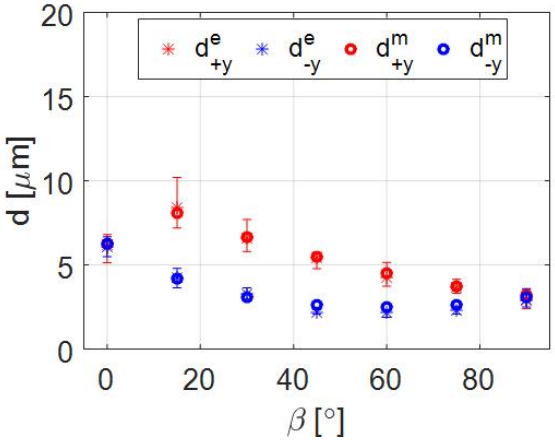

(d) Size of ellipsoidal pin $a = 1000\mu m, b = 250\mu m$ Load $= 7N$

Figure 5.7: Comparison of ploughing depths d along the periphery at $+y$ and $-y$ axis (subscript) obtained from MPM-based ploughing simulation (superscript: m) and ploughing experiments (superscript: e) for varying angle of ellipsoid orientation β

It can also be seen that the ploughing depths for the ellipsoidal pins in experiments are smaller than those obtained from the simulations. The difference in penetration can be attributed to the relatively high surface roughness of the pins as listed in table 4.1. To compare the effect of roughness on penetration, when a highly polished reference spherical ball of 0.5mm radius was used instead of pin B4 of radius 0.5mm which was made by milling method (roughness $R_a = 0.6\mu m$, see table 4.1), the ploughing depth obtained was about 1.5 2 times higher. The effect of roughness is mostly prominent for ellipsoids with low ellipticity ratio and large size where the geometry of the ellipsoid doesnt allow for deeper penetration and the surface roughness affects the ploughing depths. However, for high ellipticity ratio the numerical and the experimental wear profile compare very well as shown in figure 5.5d. The ploughing depth obtained from experiments and simulations for either side of the ploughed track are plotted for applied loads of 7N using ellipsoidal pins of ellipticity ratios 4, 2.8 and 1.8 and applied load of 16N for ellipticity ratio 4 as shown in figure 5.7. It can be seen from figure 5.7a and 5.7d that for high ellipticity ratio of 4, the ploughing depths obtained on the $+y$ and $-y$ axis of the ploughed tracks are in good agreement for both experiments and simulation for both applied loads of 7N and 16N. However, as the ellipticity ratio decreases and the ellipsoidal pin is closer to a

spherical shape, the roughness effects sets in and the experimental ploughing depths decreases on either side of the ploughed track (see [106]). This results in experimental ploughing depth being lower as compared to the simulated ploughing depth for ellipsoidal pins with ellipticity ratio of 1.8 and 2.8 at 16N load as shown in figure 5.7b and 5.7c. Details can be seen in paper C [106].

5.1.2. Ploughed profile in coated substrates

The ploughing depth is measured from the simulated ploughed profile of (zinc) coated (steel) substrates ploughed using spherical indenters. The ploughing depth obtained from the simulated ploughed profile is compared with the ploughing depth obtained using the analytical model in section 3.2 and using ploughing experiments. The results in this presented below are referred from paper F [107].

5.1.2.1. Comparison of the simulated profile depth with the analytical model

In this section, the ploughing depths obtained from the theory given in chapter 3, section 3.2.6 have been plotted and compared with those obtained using the MPM simulations for rigid-plastic coated-substrate. The effects of relative hardness of the coating with respect to the substrate $\tilde{H}$ and the coating thickness t on the coefficient of friction and the ploughing depths has been studied. The material parameters used in the MPM-simulations of the rigid-plastic coated-substrates to be compared with the analytical model are listed in table 3.3. The ploughing depth and coefficient of friction are obtained for the MPM simulations utilize a 0.4mm diameter indenter at 3N load. A coating thickness of $t = 25\mu m$ is used in the first study where the relative hardness of the coating $\tilde{H}$ is varied from 0.1 to 10 and the interfacial shear strength constant or taken as a factor of hardness of the coating and substrate. In the first case, the interfacial shear strength of the coating τ_c and the substrate τ_s is kept constant at H_0/k_0 where $H_0 = 450MPa$ and $k_0 = 3\sqrt{3}$. In the second case, the interfacial shear strength of the coating and the substrate is taken as per $\tau = H/k_0$ where $H = H_s$ for the substrate and $H = H_c$ for the coating. In the second study, the coating thickness is varied from $0\mu m$ for uncoated substrate to $200\mu m$, where coating material is the bulk. The relative coating hardness is varied for two different cases. In first case, $\tilde{H} = 0.5$ ($H_c = 450MPa, H_s = 900MPa$) and in the second case, $\tilde{H} = 2$ ($H_s = 900MPa, H_c = 450MPa$).

The total ploughing depth obtained from the ploughing simulations is compared with that obtained by the analytical model in figure 5.8 using equations 3.23b and 3.23b in chapter 3, section 3.2.6. It can be seen that, the ploughing depths obtained by the analytical model agree well for those obtained from the ploughing simulations for both studies [107].

In the first study, where the relative hardness $\tilde{H}$ is varied from 0.1 to 10, the ploughing depths obtained using the analytical model and the MPM simulations decrease with $\tilde{H}$ and are shown to agree for $\tilde{H} \geq 0.5$ in figure 5.8a. For low values of $\tilde{H}$ (coating hardness), the ploughing depths obtained from the MPM model slightly exceed those calculated by the analytical model. Also for low values of $\tilde{H}$, the indenter penetrates more into the coating and the simulated ploughing depths exceed the coating thickness resulting in the wear of the coating material in the corresponding MPM ploughing simulations but not in the analytical model which assumes only ploughing.

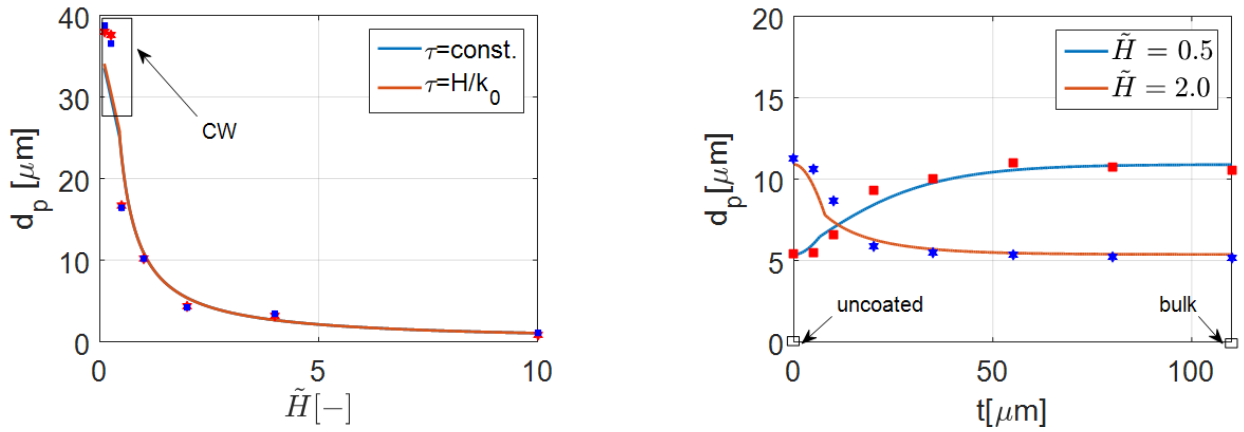

(a) Effect of $\tilde{H}$ on d_p.

(b) Effect of t on d_p.

Figure 5.8: Ploughing of rigid-plastic substrate by 0.4 mm diameter ball at 3N load. (a) Effect of relative coating hardness ($t = 25\mu m$) on the total ploughing depth with a constant interfacial shear and with interfacial shear $\tau = H/k_0$. (b) Effect of coating thickness on the total ploughing depth for a hard coating ($\tilde{H} = 2$) and a soft coating ($\tilde{H} = 0.5$). ($r = 200\mu m, k_1 = 12.5$) (Marks: MPM model, Lines: Analytical model). CW: Coating wear/degradation.

In the second study, the total ploughing depths for a hard coating ($\tilde{H} = 2$) and for a soft coating ($\tilde{H} = 0.5$) are studied as a function of the coating thickness t as shown in figure 5.8b. The ploughing depths obtained from the MPM ploughing simulations agree well with those obtained from the analytical model. The ploughing depth for the soft coated system increases with coating thickness, as the effective hardness of the soft coated system decreases with the increase in coating thickness. Consequently, the ploughing depth for the hard coated system decreases with coating thickness as the effective hardness increases with the coating thickness (equation 3.23b). The slope of the ploughing depth plots changes at a coating thickness $t_c = 5.75\mu m$ for the soft coating and $t_c = 4.3\mu m$ for the hard coating where $d_p = t$ after which increase in t results in transition of the contact of the indenter from both the substrate and the coating to the coating only. So, the ploughing depths are calculated accurately by MPM for all cases [107].

5.1.2.2. Comparison of the simulated profile depth with ploughing experiments

The total ploughing depths obtained from the uncoated steel sheet [95] and the zinc block lubricated by Quaker lubricant and ploughed by a 1mm diameter ball were compared and found to be in good agreement from figure 5.9a. The zinc block having lower yield stress compared to the DX56 steel sheet (see figure 10a) resulted in a higher ploughing depth for all the loads. The ploughing depth for the zinc blocks also increased faster than that of the DX56 steel sheets due to the lower strain hardening of the zinc block at high loads compared to the DX56 steel sheet (see figure 10, table 3.4 and table 3.5). Having validated the ploughing depth for bulk zinc and steel, the numerically calculated ploughing depths will be also validated using zinc coated steel sheet [95].

The total ploughing depth obtained from the ploughing experiments and simulations with the zinc coated steel sheet for a load range of 1-46N was compared for spherical indenters of 1mm and 3mm diameter and found to agree well as shown in figure 5.9b. The larger 3mm diameter indenter penetrates less compared to the 1mm indenter owing to its larger contact area to carry the applied load.

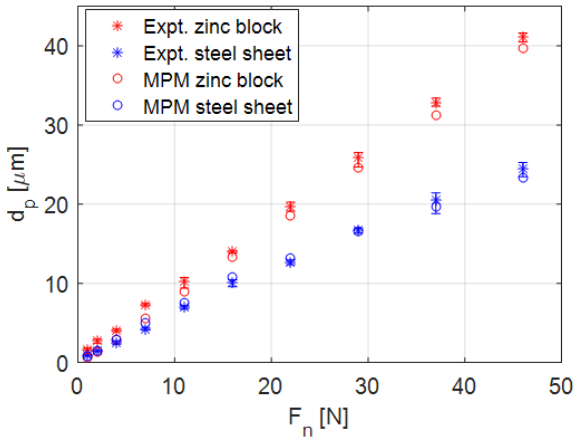

(a) Effect of F_n and substrate type (zinc/steel) on ploughing friction

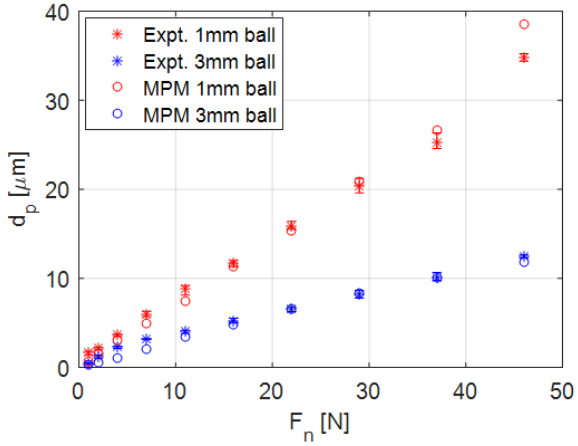

(b) Effect of F_n and r (zinc coated steel sheet) on ploughing friction

Figure 5.9: Comparison of the ploughing obtained from MPM model and ploughing experiments on Quaker lubricated zinc block, 15 μm zinc coated sheet and DX56 steel sheet by 1mm and 3mm diameter balls. Material model parameters given in tables 3.6, 3.4, 4.5b and interfacial friction model in equation 4.8a and 4.9a for zinc (coating) and steel.

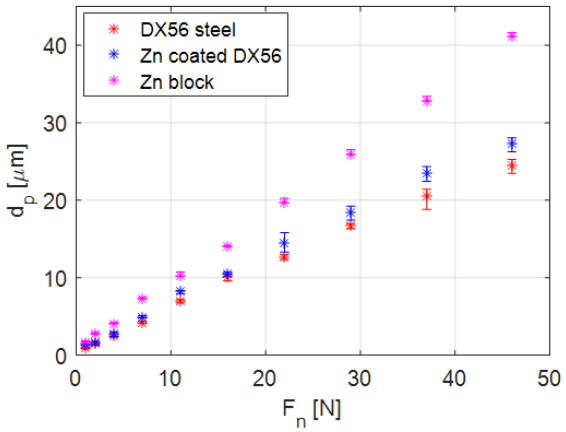

(a) Effect of F_n and substrate type: bulk/coated substrate on ploughing friction.

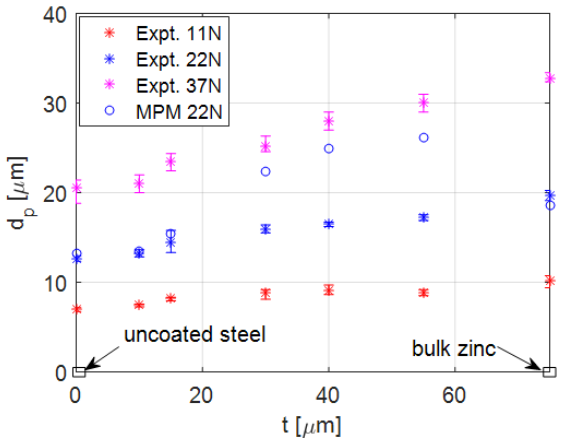

(b) Effect of F_n and t (zinc coating thickness) on ploughing friction.

Figure 5.10: Comparison of the total ploughing depths obtained from MPM model and ploughing experiments on Quaker lubricated zinc block, 15 μm zinc coated sheet and DX56 steel sheet by 1mm diameter balls and on various zinc coating thickness.

The differences in the ploughing depths obtained from experiments with steel sheet, zinc coated steel sheet and the zinc block are summarized over loads ranging from 1-46N in figure 5.10a. As the thickness of the zinc coating is increased from 10 to 15, 30, 40 and 55μm, the ploughing depths are also shown to increase for three different loads in figure 5.10b. The increase in ploughing depth with coating thickness is due to the decrease in the effective hardness for the soft zinc coated system with increase in coating thickness (as per equation 3.22 [117]). The rate of increase in ploughing depth with respect to the coating thickness increases with increase in the applied load. The MPM simulations have a larger increase in ploughing depth compared to that of the experiments with coating thickness above 30μm, as shown in figure 5.10b. The lower penetration depths obtained from the ploughing experiments for large coating thickness

can be explained by the unpolished rougher surface of thicker zinc coatings which is in contrast with the thinner zinc coatings. Further the yield strength of the zinc coating used in the MPM simulations is measured by nano indentation for a coating thickness of $10\mu m$ [41]. For higher coating thickness, the size of the zinc grains could have significant effects in the measured yield strength and hardness. As the thickness of the coating decreases, deformation during indentation is localized with the plastic flow being restricted by the substrate [130]. This could lead to a lower yield strength and hence effective hardness for thinner zinc coatings.

5.2. Friction force

In this section, the components of friction acting on a ploughing asperity will be shown with the normal load being applied in the z direction and sliding in the x direction as shown in figure 5.11. For an ellipsoidal indenter, the axes sizes are taken as a, b and c. The ellipticity ratios are $e_x = a/c$ and $e_y = b/c$. The orientation relative to sliding direction is β. Load controlled ploughing simulations and experiments were carried under a constant load. Some results are shown in figure 5.12a. Depth-controlled ploughing simulations have also been carried out for comparison with analytical models. During the sliding of the indenter through a rigid-plastic substrate, the material in contact with the frontal half of the indenter is permanently deformed and lose contact with the rear half of the indenter as the indenter slides over it.

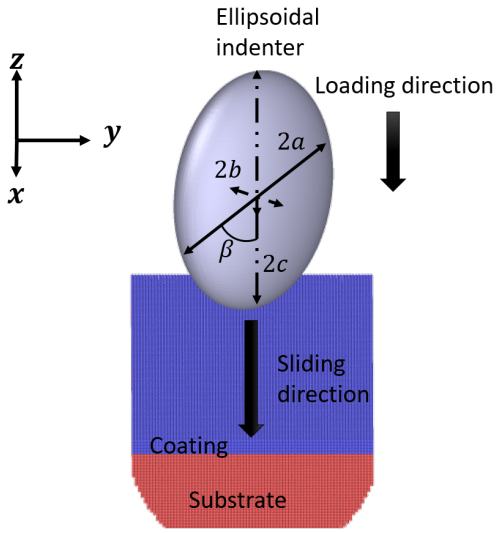

Figure 5.11: An ellipsoidal asperity ploughing through a coated substrate with its axes sizes a, b and c and orientation β relative to sliding direction. The loading direction and sliding direction are also shown.

During the depth-controlled ploughing of a rigid- plastic substrate, as the contact area is halved (frontal part of indenter in contact), the reaction force F_z is halved in order to maintain the contact pressure as shown in figure 5.12b. The coefficient of friction obtained from the MPM ploughing simulations has been compared with the values obtained from the analytical model and the ploughing experiments. The forces acting on the sliding asperity have been divided by the applied load to obtain the coefficient of friction. The coefficient of friction obtained from the analytical model has been compared with the numerical model for ideal (rigid-) plastic material behaviour. Likewise the coefficient of friction obtained from the ploughing experiments has been compared with the values obtained from the numerical simulations for zinc coated and uncoated DX56 steel sheet.The results will be shown below.

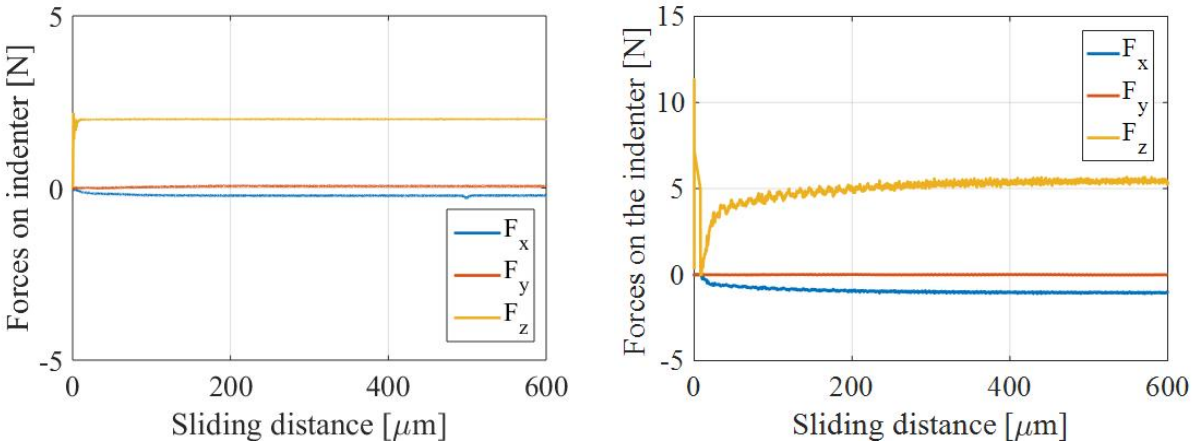

(a) Load controlled ploughing (b) Depth controlled ploughing

Figure 5.12: Forces acting on the asperity in x, y and z directions for load controlled ploughing simulations.

5.2.1. Friction in ploughing of uncoated substrates

The friction force in ploughing of uncoated steel substrate is measured from the MPM based ploughing model (shown in chapter 3 section 3.1 and compared with the results from the analytical model in chapter 3 section 3.2 and the experimental results using the experimental set-up explained in chapter 4, section 4.1. The material parameters for the steel substrate are given in table 3.4 and interfacial friction model used is given in equation 4.8a and 4.8c for the MPM ploughing simulation of an uncoated DX56 steel substrate. The results described below are referred from paper A [95], paper C [106] and paper D [121].

5.2.1.1. Comparison of the simulated friction force with the analytical model

Initial load controlled ploughing simulations have been done in a rigid-plastic substrate in the absence of interfacial shear strength ($\tau_{sh} = 0$) [95]. The coefficient of friction is obtained as the ratio of the tangential force in the x direction and the applied load in the z direction. The tangential force in the x direction is measured from the contact pressure due to plastic deformation of the substrate over the vertical projected area A_{yz}. The applied load F_n is balanced by the horizontal projected area A_{xy} and the pressure resulting in plastic deformation of the substrate, which is given by its indentation hardness H. The friction coefficient for a spherical asperity sliding through a frictionless rigid-plastic substrate is thus determined by equation 5.2a. In the presence of an interfacial shear τ_{sh}, the forces F^{pl} and F^{sh} act on a spherical asperity in x and z directions due to the plastic deformation pressure p_{pl} and due to interfacial shear as given in equations 5.2b- 5.2e [77]. The MPM-ploughing simulations have shown good agreement with the friction forces and coefficient of friction obtained for both analytical models with and without friction/shear at the interface as shown in figures 5.13b and 5.13a respectively (see paper B [105]).

$$\mu = \frac{F_f}{F_n} = \frac{F_{pl}}{F_n} = \frac{HA_{yz}}{HA_{xy}} = \frac{2}{\pi}\left(\left(\frac{r}{a}\right)^2 \phi_C - \sec\phi_C\right) \forall \phi_C = \arctan\left(\frac{a}{r-d}\right) \tag{5.2a}$$

$$F_x^{pl} = -P_{pl} r^2 (\phi_C - \sin\phi_C \cos\phi_C) \tag{5.2b}$$

$$F_x^{sh} = -2\tau_{sh} r^2 \int_0^{\pi/2} \int_0^{\phi_C} \sin\phi \sqrt{\sin^2\theta + \cos^2\theta}\, d\phi d\theta \tag{5.2c}$$

$$F_z^{pl} = \frac{\pi}{2} p_{pl} r^2 (\sin\phi_C)^2 \tag{5.2d}$$

$$F_z^{sh} = -\tau_{sh} r^2 \left(\sin\phi_C - (\cos\phi_C)^2 \ln(\sec\phi_C - \tan\phi_C)\right) \tag{5.2e}$$

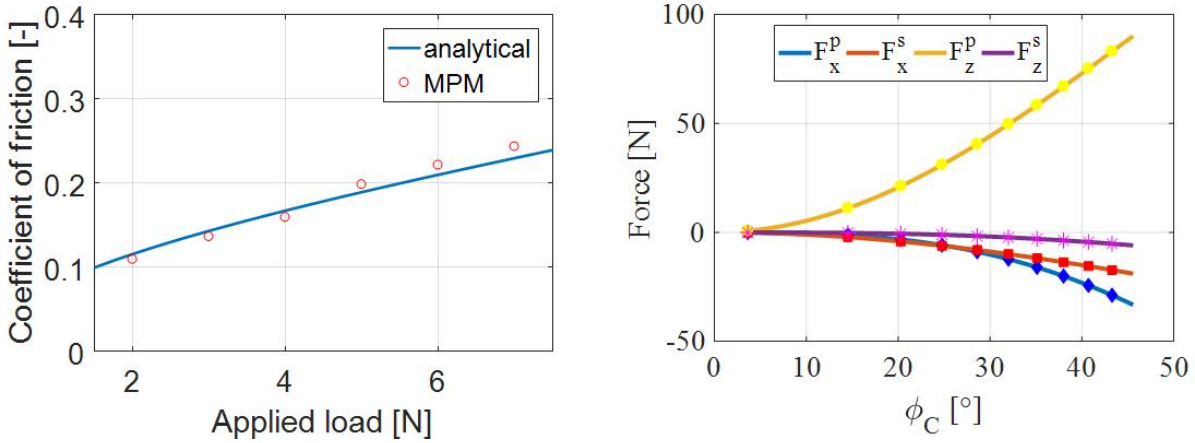

(a) Load controlled ploughing validation.

(b) Depth controlled ploughing validation.

Figure 5.13: Validation of simulated friction forces using MPM acting on a spherical asperity ploughing through a rigid-plastic substrate with analytical models using equations (5.2a-5.2e) [77]. Model parameters refereed from table 3.2.

The coefficient of friction plot due to plastic deformation and interfacial shear was resolved into the components in the x and y axis and plotted for different axis size and load in figure 5.14. The coefficient of friction in x-direction due to plastic deformation μ_x^p increased with β from 0° to 90° due to increase in projected area along the plane perpendicular to the x-axis as shown in equation 3.21a. The coefficient of friction in the y-axis due to plastic deformation μ_y^p increases to its maximum at 30° due to the difference in the net projected area perpendicular to the y-axis for positive plastic flow from equation 3.21b and is 0 at 0° and 90° due to the symmetry of the ellipsoid along the x-axis. The coefficient of friction due to interfacial shear along x and y axis, i.e. μ_x^s and μ_y^s remain constant and close to zero respectively. Following equations 3.21c and 3.21d, the projected area in the horizontal plane dominates μ_x^s while the net projected area perpendicular to the x-axis for net positive shear flow dominates μ_y^s. The coefficient of friction decreases for all of its components as the ellipticity ratio is reduced close to unity as shown in figure 5.15a. This is because both the projected area for net plastic and shear flow are reduced and the ploughing depth reduces with the major axis of the ellipsoid. A higher applied load increases the ploughing depth and magnifies the effect of asperity orientation on coefficient of friction components as shown in figure 5.15b. For an ellipsoidal asperity with major axis perpendicular to the sliding direction, the trends in the coefficient of friction are reversed as shown in figure 5.14b. The asymmetric pile-up of substrate material around the ellipsoidal asperity due to the asperity shape and orientation results in variable ploughing depth across

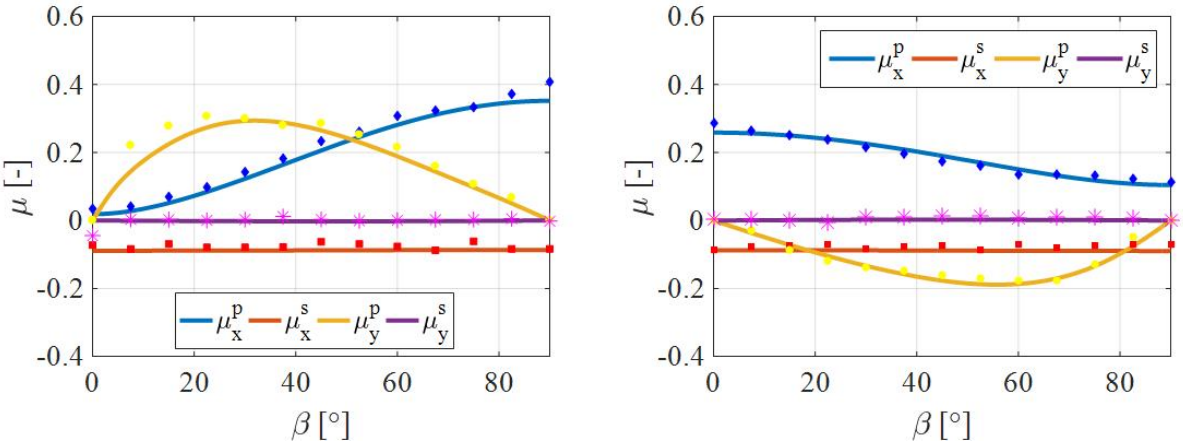

(a) a=500μm, b=80μm, c=200μm. (b) a=100μm, b=200μm, c=200μm.

Figure 5.14: Effect of orientation on forces acting on an ellipsoidal asperity with axes size a, b and c. The markers represents the coefficient of friction obtained using MPM simulations while the lines are obtained from the analytical model using equation set 3.21a-3.21f. Model parameters given in table 3.2.

the ploughed profile. The results obtained from the numerical ploughing simulation for a rigid plastic substrate are in good agreement with those obtained from the analytical model, taking into account the modified ploughed profile including pile-up as discussed in chapter 3, section 3.2.4.

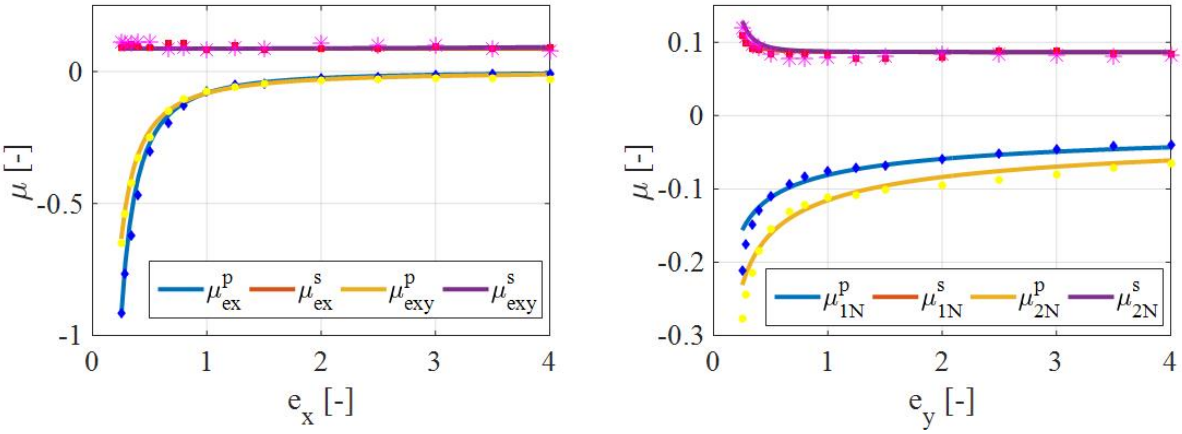

(a) e_x varies; $e_y = 1$ and $e_x e_y = 1$ for 1N load. (b) e_y varies; $e_x = 1$ for 1N and 2N loads.

Figure 5.15: Effect of asperity size and load on forces acting on ellipsoidal asperity of reference size c 200 μm. The markers represents the coefficient of friction obtained using MPM simulations while the lines are obtained from the analytical model using equation set 3.20. Model parameters listed in table 3.2.

The effect of asperity size and applied load on the coefficient of friction due to plastic deformation and interfacial shear has been shown for three different cases in figure 5.15. For the case where the ellipticity ratio e_x is increased while keeping e_y as 1, the coefficient of friction due to ploughing decreases. This is because the ploughing depth decreases with increase in asperity size to maintain the same contact area for a given load. However if the ellipticity ratio e_x is

increased such that $e_x = 1/e_y$, the coefficient of friction due to plastic deformation decreases due to the decrease in projected area perpendicular to the sliding direction. The depth also increases with e_x as explained in 4.1.2., which combined with the change in projected area results in the friction plots in figure 5.15a. In the third case, as the ellipticity ratio e_y increases keeping e_x as 1, the ploughing depth decreases while the projected area perpendicular to the sliding direction increases. This decreases the coefficient of friction due to plastic deformation with increase in e_y, although at a lower rate compared to the previous two cases. The coefficient of friction due to plastic deformation increases with load while that due to interfacial shear remains mostly constant as shown in figure 5.15b. However for low values of e_y, μ^s increases with e_y due to the faster increase in projected area perpendicular to the x-axis due to an increase in ploughing depth. The analytical model shows good agreement with the numerical model except for small e_y, where cutting effects the numerically determined friction force, while analytical model assumes ploughing.

5.2.1.2. Comparison of the simulated friction force with ploughing experiments

Ploughing experiments were performed on uncoated DX56 steel sheet lubricated with 'Quaker' forming oil using pins with a spherical ball in the linear sliding friction tester PATAT. Spherical balls of 1mm and 3mm diameter were used for ploughing experiments and simulations. Loads ranging from 1N to 46N were applied during sliding of the spherical balls and the coefficient of friction was calculated with a set of 3 experiments. The ploughing simulations were performed with substrate particle and indenter triangle(mesh) sizes of 5, 10 and 20 μm. The simulation results were converged to mesh/particle size of 0 μm, independent of particle/mesh resolution and the extrapolated coefficient of friction was compared with that obtained from ploughing experiments. The coefficient of friction obtained from the MPM-based ploughing simulation agreed very well with the values obtained from the experiments for both the indenter sizes and load ranges as shown in figure 5.16a.

The coefficient of friction obtained for ploughing with 1mm balls was higher than for 3mm balls (see figure 5.16a) as the smaller size of the indenter resulted in higher penetration depth (see figure 5.4a) [95]. The coefficient of friction increases at a higher rate with respect to the applied load for the smaller size indenter. A higher ploughing depth resulted in a larger asperity-substrate contact area which causes higher plastic deformation of the substrate and shearing of the interface. The smaller asperity (indenter) size also resulted in higher strain rates which cause higher hardening of the substrate. This results in a higher hardness of the substrate and hence a faster increase in the coefficient of friction with increase in applied load.

The shear strength of the interface will also increase by changing the interfacial condition, for example equation 4.8a to equation 4.8c when changing from the Quaker forming lubricant to unlubricated sheet with a stable oxide film [121]. The absence of a lubricant resulted in an increase in shear strength. The relationship between the interfacial shear strength and applied nominal contact pressure (load) given in equation 4.8a and 4.8c was adopted into the MPM-based ploughing model. Ploughing experiments were also performed on the unlubricated uncoated DX56 steel specimen prepared as described in section 4.1.1.2. The coefficient of friction results obtained from the MPM-simulations showed good agreement with the values obtained from the unlubricated experiments as well for most of the loads ranging from 4-29N. At higher loads the wear mode in the sliding asperity was predominantly wedging wear (shown as WW in figure 5.16b) which resulted in transfer of substrate material onto the surface of the indenter as lumps. This caused an increase in friction coefficient in the experiments compared

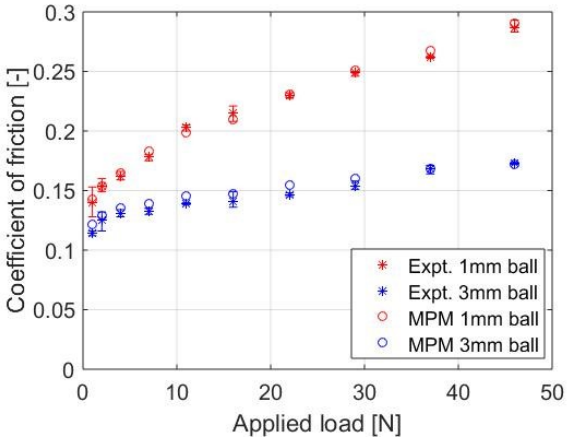

(a) Effect of r and F_n on ploughing friction.

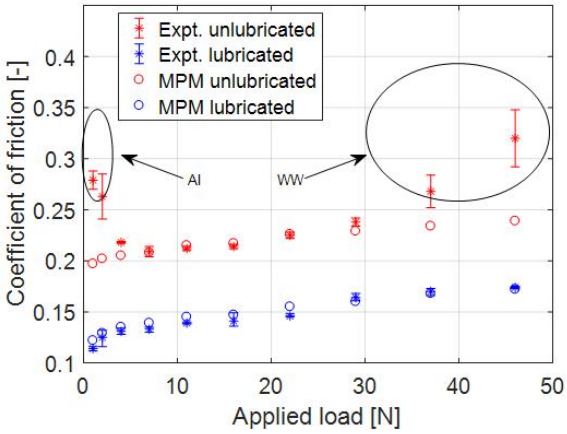

(b) Effect of τ on ploughing friction.

Figure 5.16: Validation of friction forces acting on a spherical asperity ploughing through a steel substrate with experiments. (WW:Wedging wear/Galling, AI:Asperity Interaction). Material model parameters listed in table 3.4 and interfacial friction models are obtained from equations 4.8a and 4.8c.

to the simulations as shown in figure 5.16b [121]. The friction at lower loads increases in unlubricated tests due to the interlocking of the asperities (AI Asperity interlocking in 5.16b) of the rough substrate with the asperities on the indenter.

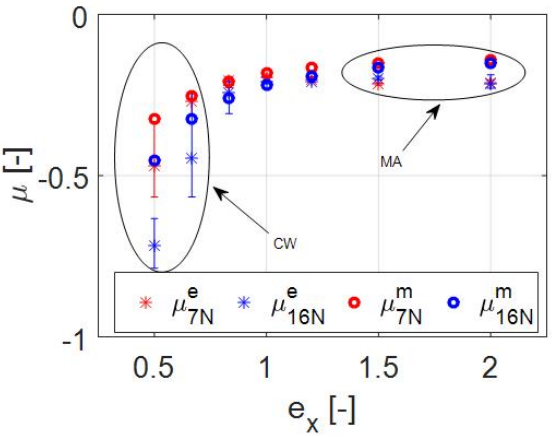

(a) Effect of e_x and F_n on ploughing friction.

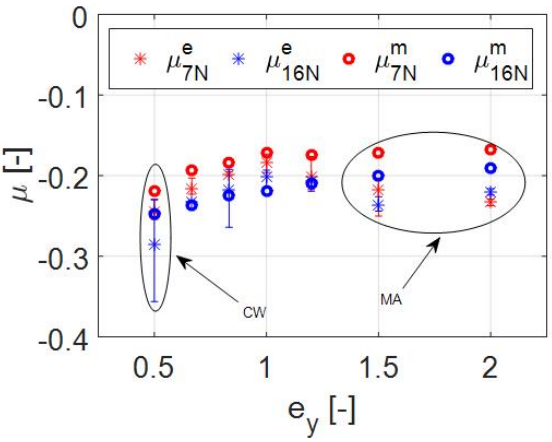

(b) Effect of e_y and F_n on ploughing friction.

Figure 5.17: Comparison of coefficient of friction μ for applied loads of 7N and 16N (subscript) obtained from MPM-based ploughing simulation (superscript: m) and ploughing experiments (superscript: e) for varying ellipticity ratio along the (a) x- axis (sliding direction) and (b) y-axis. (CW: cutting wear, MA: misalignment). The ploughing model uses material parameters from table 3.4 and interfacial friction model in equation 4.8a.

The effect of asperity geometry on the ploughing behaviour in single-asperity sliding was studied using the ellipsoidal shaped indenters as designed in section 4.1.1.1. Ploughing experiments were performed in the UMT-2 based linear sliding tester designed with the 3D force sensor at loads of 7N and 16N as described in section 4.1.2. Figure 5.17a shows the variation in coefficient of friction with the increase in the size of the axis of the ellipsoidal pin in the direction of sliding.

The penetration of the pin into the substrate has been shown to increase with a decrease in size of the indenter. This results in higher ploughing friction for a smaller size of the asperity. Furthermore the increase in the size of the asperity axis in the sliding direction results in an increase of the groove depth of the asperity as explained in section 3.1.4. A lower axis size along the sliding direction also increases the pile-up height and angle of attack in the deforming substrate. This results in a transition of the wear mode from ploughing to cutting in the ploughing experiments. Hence the experiments result in a higher friction force compared to the simulations for smaller ellipticity ratio e_x in sliding direction. For a less skewed indenter, with ellipticity ratio closer to unity the MPM-simulations have shown good agreement to the ploughing experiments as can be seen in figures 5.17a and 5.17b.For a larger ellipticity ratio, the coefficient of friction results are highly sensitive to the orientation of the ellipsoidal pin with respect to both loading and sliding direction. Hence we see an increase in coefficient of friction for pins with a large axis size along and perpendicular to the direction of sliding in figures 5.17a and 5.17b.

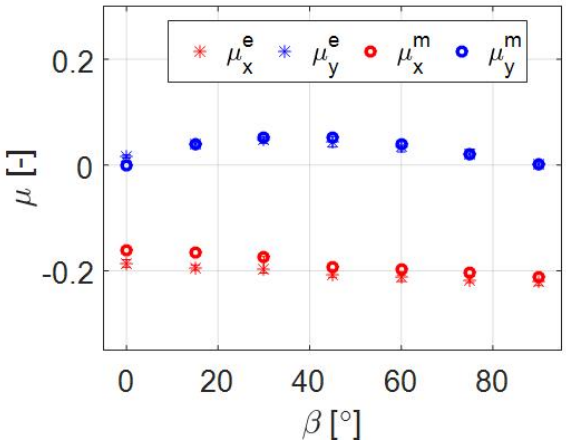

(a) Effect of β on μ for $e_x/e_y = 1.78$, 7N load.

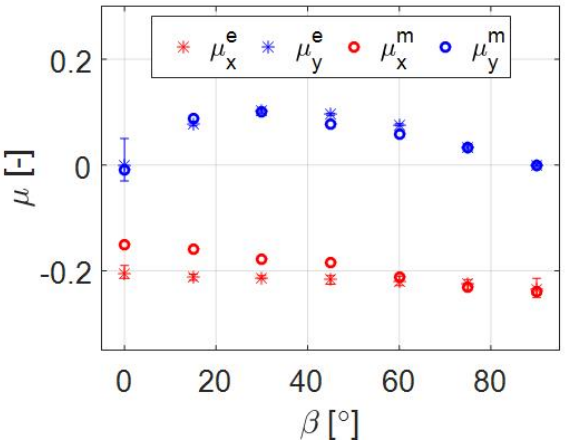

(b) Effect of β on μ for $e_x/e_y = 2.78$, 7N load.

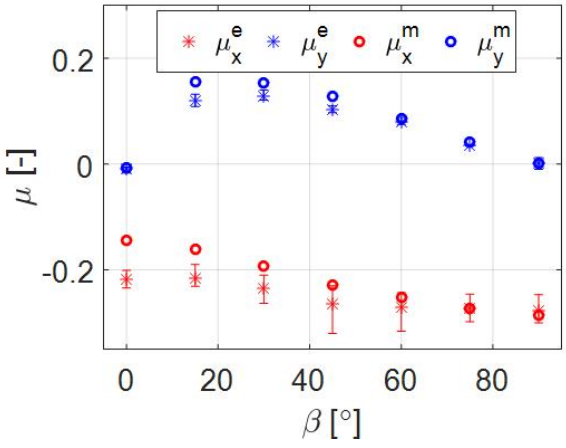

(c) Effect of β on μ for $e_x/e_y = 4$, 7N load.

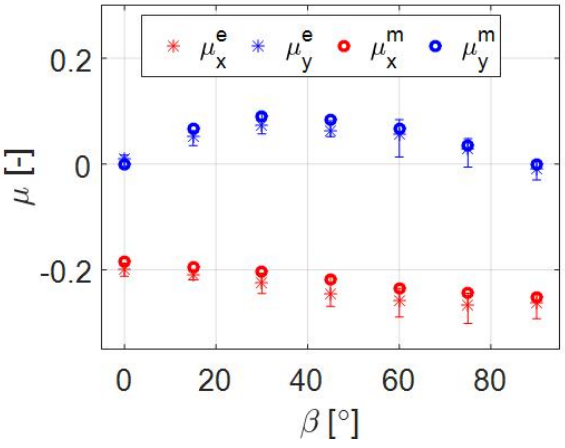

(d) Effect of β on μ for $e_x/e_y = 1.78$, 16N load.

Figure 5.18: Validation of friction forces acting on an ellipsoidal asperity ploughing through a steel substrate with varying orientation and shape. MPM-based ploughing model (superscript:m) Ploughing experiment (superscript:e). The ploughing model uses material parameters from table 3.4 and interfacial friction model in equation 4.8a.

The coefficient of friction was studied as a function of the angle of orientation with respect to the sliding direction β for ellipsoidal pins with varying ellipticity ratio and applied load [106]. The ellipticity ratio of the axes e_x/e_y in the sliding plane was varied from 1.78 to 4 such that the product $e_x e_y$ was 1 and the coefficient of friction was plotted in figures 5.18a, 5.18b and 5.18c respectively. A load of 7N was applied to avoid any cutting effects and maintain ploughing wear. The load was changed to 16N for an ellipticity ratio of 1.8 and the coefficient of friction was plotted in figure 5.18d. For a lower ellipticity ratio of 1.8 the coefficient of friction plots both in the x and y axis 7N and 16N are shown in figure 5.18a and 5.18d. However, as the ellipticity ratio of the pins was increased to 2.8 and 4, the coefficient of friction plots both in x and y axis obtained from the ploughing experiments slightly exceeded those obtained from the numerical simulations for lower β values. The spread in values of the measured coefficient of friction can be attributed to the high sensitivity of the friction force with respect to misalignment for highly skewed and long indenters. A small forward tilt along the indenter in the x and y axis could lead to an increase in the friction force experienced by the indenter in the experiments. Although theoretically the coefficient of friction for angle $\beta = 0°$ should reduce with increasing ellipticity ratio due to a decrease in projected area in the sliding x direction, the observed increase in friction with increasing ellipticity ratio could be explained due to a minor misalignment and subsequent increase in contact area and friction due to interfacial shear.

Friction and wear (deformation of the substrate) in single-asperity ploughing experiments is also shown to be affected by the interaction of the micro-asperities on the rough tool surface and the misalignment of the ellipsoidal pins which increases the contact area and resulting penetration of the pin into the substrate. Details are given in paper C [106].

5.2.2. Friction in ploughing of coated substrates

The friction force in ploughing of uncoated steel substrate is measured from the MPM based ploughing model (shown in chapter 3, section 3.1 and compared with the results obtained from the analytical model in chapter 3, section 3.2 and the ploughing experiments using the set-up explained in chapter 4, section 4.1.2. The material parameters for the bulk zinc are given in table 3.5 and for the zinc coating in table 2.1. The interfacial friction model used is given in equation 4.9a for the MPM ploughing simulation of zinc coated DX56 steel sheet and equation 4.8a for uncoated DX56 steel sheet. The details of the work can be referred to paper F [107]

5.2.2.1. Comparison of the simulated friction force with the analytical models

The coefficient of friction μ, obtained from the MPM ploughing simulations is compared with the coefficient of friction obtained by the analytical model using equations 3.25b-3.25d in section 3.2 which combines components of μ for plastic deformation μ_{pl} and interfacial shear μ_{sh} for a coated substrate. The results are shown to agree well in both the case studies in figure 5.19. The calculated coefficient of friction plotted against $\tilde{H}$ for a constant interfacial shear stress, in figure 5.19a shows good agreement with the simulated coefficient of friction. The ploughing depth at $\tilde{H} = 0.46$ corresponds to the coating thickness $t = 25\mu m$ (see figure 5.8a). Hence, for MPM simulations at lower$\tilde{H}$ and $d_p > t$, there is coating damage. The coating wear is not captured by the analytical model in chapter 3, section 3.2.7, resulting in the difference in friction computed by the MPM model and the analytical ploughing model. For the case with constant interfacial shear in the coating and the substrate $\tau_{sh_c} = \tau_{sh_s}$, the ploughing depth d_p and consequently projected contact areas A_{pl} and A_{sh} decrease with $\tilde{H}$, thereby decreasing μ_{pl} and μ_{sh}. However in the case where interfacial stress is a function of the hardness of the coating and the substrate $\tau_{sh} = H/k_0$, the friction due to interfacial shear $F_{sh} = \tau_{sh_c} A_{sh}$,

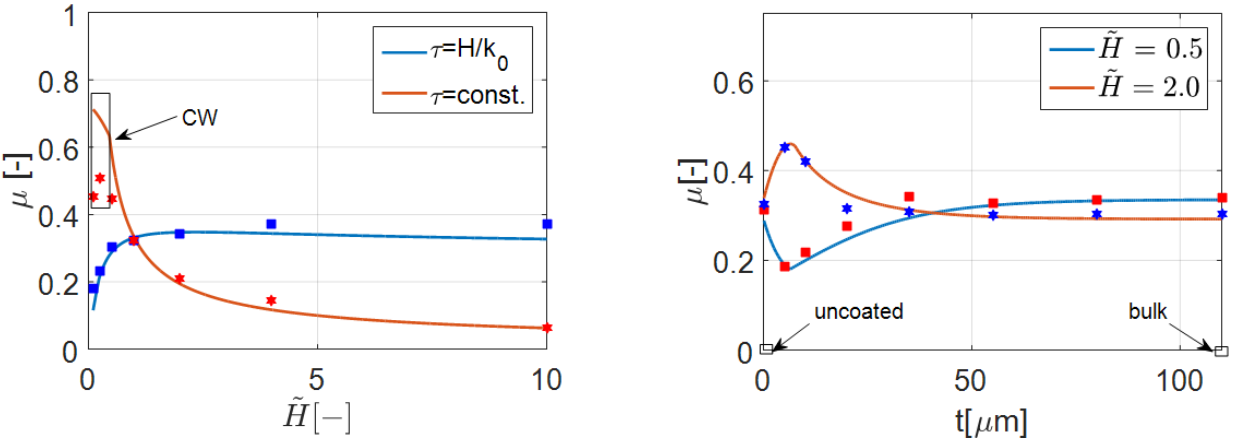

(a) Effect of $\tilde{H}$ on μ.

(b) Effect of t on μ.

Figure 5.19: Ploughing of rigid-plastic substrate by 0.4 mm diameter ball at 3N load. (a) Effect of relative coating hardness ($t = 25\mu m$) on the overall coefficient of friction with a constant interfacial shear and with interfacial shear $\tau = H/k_0$. (b) Effect of coating thickness on the overall coefficient of friction for a hard coating ($\tilde{H} = 2$) and a soft coating ($\tilde{H} = 0.5$). ($r = 200\mu m, k_1 = 12.5$) (Marks: MPM model, Lines: Analytical model). CW: Coating wear/degradation.

increases with $H_c(\tilde{H})$, in spite of the decrease in A_{pl} and A_{sh}. Therefore the total coefficient of friction increases with $\tilde{H}$ as shown in figure 5.19a.

The coefficient of friction has been plotted as a function of the coating thickness t for a hard coating ($\tilde{H} = 2$) and a soft coating ($\tilde{H} = 0.5$) in figure 5.19b. The coefficient of friction obtained from the MPM simulations agrees well with the values obtained from the analytical model. For a low coating thickness, the indenter is in contact with both the coating and the substrate. In figure 5.19b, μ is shown to initially increase and then decrease with t for the hard coating. The initial increase in μ corresponds to the increase in contact area due to increase in the thickness of the hard coating which thereby requires a higher friction force to shear and deform. However, once the indenter is in contact with only the hard coating ($t > 7.8\mu m$), the coefficient of friction plot follows the ploughing depth plot given in figure 5.8b, and decreases with increase in t (H_{cs}) for the hard coating. Using the same reasoning, the coefficient of friction first decreases and then increases ($t > 6.5\mu m$) with coating thickness for a soft coating. A fitting factor of $k_1 = 12.5$ is used to calculate H_{cs} for $r = 0.2mm$ in equation 3.22 [117] as the substrate used in MPM model($200\mu m$ thick keeps affecting H_{cs} for thickness coatings as well.

5.2.2.2. Comparison of the simulated friction force with the ploughing experiments

The coefficient of friction is obtained for the MPM ploughing simulations on the zinc block and the DX56 steel substrate lubricated with Quaker oil by a 1mm diameter ball is shown in figure 5.20a. The results are in good agreement over the load range of 1-46N. The coefficient of friction for ploughing of the zinc block is slightly higher than for the DX56 steel sheet for most of the load range. The higher coefficient of friction results from the larger plastic deformation of the bulk zinc during ploughing as can be seen from the higher ploughing depths for the bulk zinc in figure. However, in spite of a large difference in ploughing depths between bulk

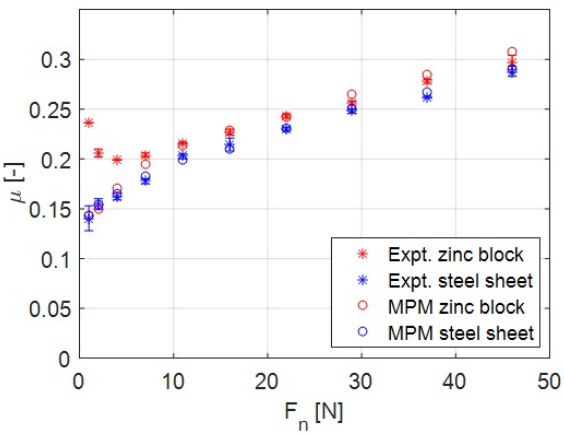

(a) Effect of normal load F_n and substrate (zinc block and steel sheet) on ploughing friction

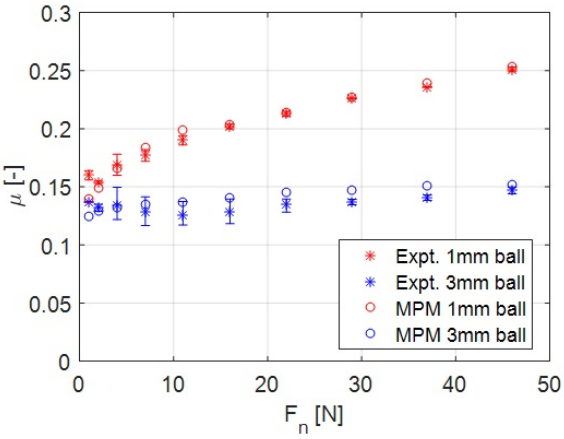

(b) Effect of normal load F_n and indenter radius r (zinc coated steel sheet) on ploughing friction

Figure 5.20: Comparison of the coefficient of friction obtained from MPM model and ploughing experiments on Quaker lubricated zinc block, 15 μm zinc coated sheet and DX56 steel sheet by 1mm and 3mm diameter balls. Material model parameters given in tables 2.1, 3.4, 4.5b and interfacial friction model in equation 4.8a and 4.9a for zinc (coating) and steel.

zinc and steel sheet, resulting in a large ploughing component of coefficient of friction μ_{pl}, the difference in overall coefficient of friction is minimized for ploughing of the zinc block and steel sheet. This is due to the large contribution of the coefficient of friction due to interfacial shear μ_{sh} to the overall μ (as shown in paper D) [121]. As the boundary layer shear strength τ_{bl} lubricated zinc is also lower than that of the lubricated steel sheet as seen from figure 4.18b, this reduces the overall coefficient of friction. The coefficient of friction at lower loads is higher for the ploughing experiments compared to the MPM simulation due to the possible asperity interlocking of the surface at low penetration depths [107].

The mean coefficient of friction obtained from both ploughing experiments and MPM simulations was plotted over a range of loads (1-46N) for spherical indenters of 1mm and 3mm diameters sliding over zinc coated steel sheet in figure 5.20b. The coefficient of friction obtained from the MPM ploughing model is very close to those obtained from the ploughing experiments. The coefficient of friction obtained for ploughing with a 1mm diameter ball increases steadily with the applied load range of 1-46N. However, as the size of the indenter is increased to 3mm, the coefficient of friction drops significantly. The increase in indenter size reduces the penetration of the indenter into the coating required to balance the applied load. The effective hardness of the coated system in response to penetration by a larger indenter is also higher as shown in figure 4.13a [117]. Furthermore, the increase in indenter size also increases the relative contribution of interfacial shear strength to the coefficient of friction as shown in [121]. Consequently, the coefficient of friction due to interfacial shear reduces with increase in applied load. Hence, for large indenters, although the coefficient of friction due to ploughing increases with load, the large contribution of the decreasing coefficient of friction due to interfacial shear results in a slight increase and almost a constant coefficient of friction over all coefficient of friction over the range of applied loads. See also paper F [107] for further details.

The presence of zinc coating on the steel substrate results in a reduced coefficient of friction in ploughing as compared to both the zinc block and the steel substrate (see figure 5.20). This is because the presence of hard steel substrate underneath the zinc reduces the ploughing depth in

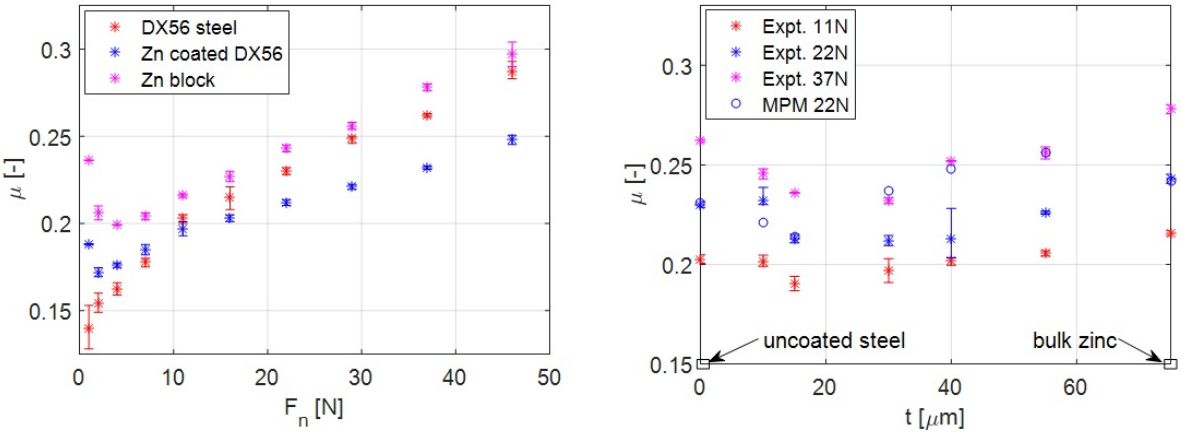

(a) Effect of normal load F_n and substrate (zinc block, zinc coating and steel sheet) on ploughing friction.

(b) Effect of normal load F_n and coating thickness t (zinc coated steel sheet) on ploughing friction.

Figure 5.21: Comparison of the coefficient of friction μ on Quaker lubricated zinc block, zinc coated sheet and DX56 steel sheet by 1mm diameter balls and the effect of coating thickness or μ obtained from MPM model and ploughing experiments.

the zinc coating compared to bulk zinc (see figure 5.9a) and hence the component of coefficient of friction due to plastic deformation μ_{pl}. Furthermore, the interfacial shear strength of the Quaker lubricant on zinc coating is lower as compared to that on DX56 steel substrate as shown in figure 4.18b. As interfacial shear has a major contribution to the overall coefficient of friction for large indenters [121], the lower boundary layer shear strength of the zinc coating combined with its deformation due to ploughing results a lower coefficient of friction compared to bulk zinc and steel. For low loads however, both the bulk zinc and the zinc coating have high coefficient of friction due to possible asperity interlocking. The surface roughness in a coating also increases the coefficient of friction in experiments compared to the ploughing of perfectly smooth surfaces in the MPM simulations [118].

The effect of coating thickness on the overall coefficient of friction for the (soft) zinc coating on the steel substrate is shown in figure 5.21b. The coefficient of friction was measured from ploughing experiments on zinc coatings with coating thickness of 10, 15, 30, 40 and 55 μm for 11, 22 and 37N loads. Also, MPM simulations for the same coating thickness at 22N load have been performed. The coefficient of friction decreases with an increase in coating thickness up to $15\mu m$. The change in coefficient of friction with zinc coating thickness matches the approximate theoretical relation between the coefficient of friction and the coating thickness for soft coatings shown in figure 5.19b. The relationship between the coating thickness and the coefficient of friction for a soft coating on a hard substrate can be derived from equation 3.25b in chapter 3, section 3.2.6. A higher coefficient of friction for thicker coatings, obtained with the MPM simulation could be explained due to the increase in ploughing depth for the MPM simulations (see figure 5.10b).

Effect of anisotropy in zinc coating and asperity geometry on ploughing friction

Experiments were also done to evaluate the effect of the orientation of the direction of anisotropy in the zinc coating relative to the sliding direction on the coefficient of friction. Two different zinc coated sheets with a coating thickness of 7 μm (Z100: 100 g/m^2 of zinc on steel sheet) and 20 μm (Z275: 275 g/m^2 of zinc on steel sheet) were ploughed using a ball of 1mm diameter. It can be seen from figure 5.22 that in both the zinc coatings, a higher coefficient of friction was obtained while sliding along the rolling direction (RD) than transverse to the rolling direction (TD).This can be explained by the lower yield stress and hence the decreased hardness of the zinc grains in the rolling direction as shown in the yield locus of the zinc coating in figure 4.25 (table 4.5) in chapter 4, section 4.2.3. The friction due to plastic deformation of the coating in rolling direction increases with decrease in hardness of the coating along the rolling direction. The substrate for the Z275 coating was harder than the substrate of the Z100 coating. The Z275 coating, owing to a harder substrate has higher effective hardness and hence a lesser ploughing depth which results in a lower coefficient of friction for the range of loads compared to the Z100 zinc coating. The decrease in friction with increase in coating thickness in 5.22 follows the figures 5.19b and 5.21b. The rolling process induced anisotropy in the deformation of the zinc coating definitely seem to affect the friction in ploughing of a zinc coated steel sheet.

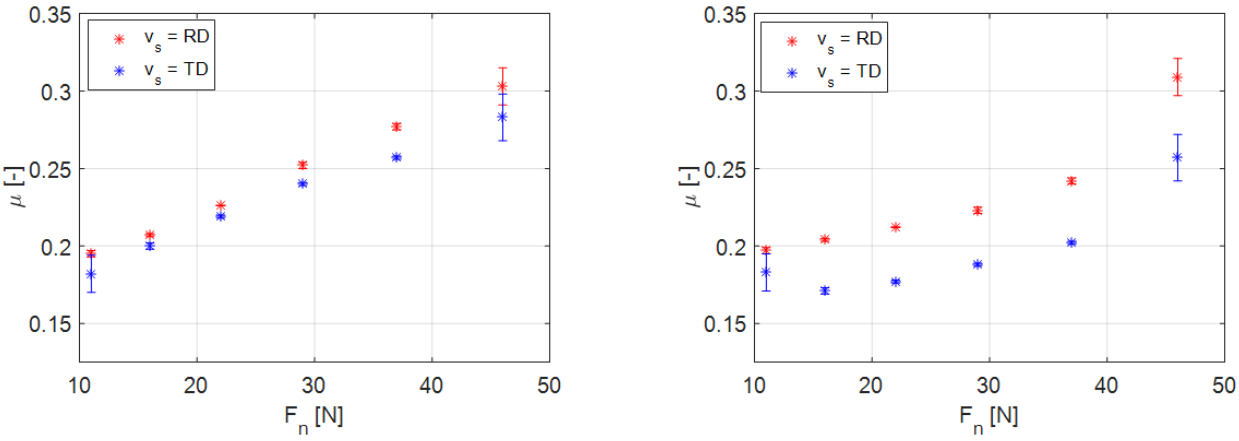

(a) Z100 zinc coating with $t = 7\mu m$.

(b) Z275 zinc coating with $t = 20\mu m$.

Figure 5.22: Effect of orientation of axis of anisotropy relative to sliding direction v_s on coefficient of friction. Sliding velocity v_s is along rolling direction (RD) and transverse to rolling direction (TD) at different loads ploughing unpolished rolled zinc coated sheets of two different zinc coating thicknesses.

Initial experiments were also performed using ellipsoidal pins of axis sizes $a = 833\mu m, b = 333\mu m$, $c = 500\mu m$ and $a = 1000\mu m, b = 250\mu m, c = 500\mu m$ such that ellipticity ratios $e_x/e_y = 2.8$ and $e_x/e_y = 4$. The components of friction in the x and y direction obtained from ploughing experiments done using ellipsoidal pin having ellipticity ratio $e_x/e_y = 2.8$ at 16N load on uncoated steel and zinc coated steel substrate are compared in figure 5.23a. The components of ploughing friction obtained for the zinc coated steel sheet are lower that those obtained for the uncoated steel sheet. The difference in the x component of ploughing friction is maximised as β approaches 90°. The increase in projected contact area with β increases the resistance to plastic flow around the indenter. This increases the pile-up and therefore decreases the groove depth (section 3.2.4). The decrease in groove depth reduces the restriction to flow of a soft coating on the hard substrate under the indenter. Similarly, the difference in pile-up heights

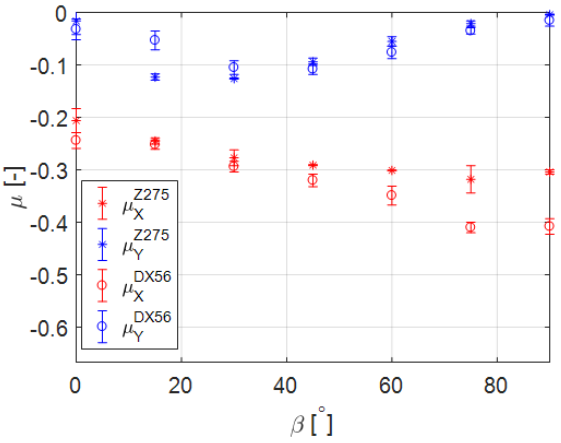

(a) μ vs β for Z275 zinc coating compared with steel for asperity with $e_x/e_y = 2.8$ at 16N load.

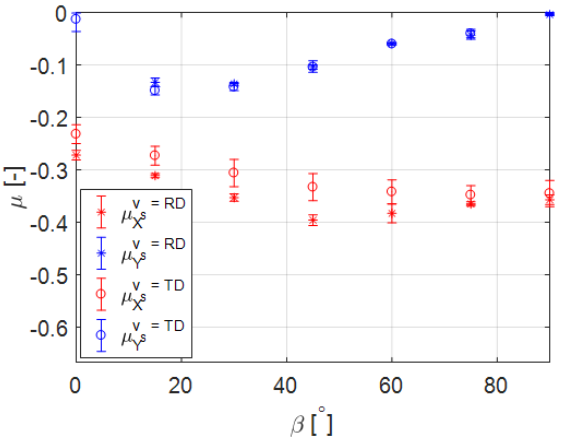

(b) μ vs β for v_s along RD and along TD for asperity with $e_x/e_y = 4$ at 16N load.

Figure 5.23: Effect of orientation of an ellipsoidal asperity on components of coefficient of friction along x and y direction with change is substrate (uncoated steel and 20μm thick zinc coated steel) and change in orientation of axis of anisotropy (RD/TD) relative to sliding direction v_s.

on the periphery of the asperity is maximum for $\beta = 30°$ resulting in the difference in the y component of ploughing friction between zinc coating and uncoated steel. The components of coefficient of friction are plotted against orientation β of ellipsoidal asperity having ellipticity ratio $e_x/e_y = 4$ at 16N load for orientation of axis of anisotropy (RD and TD) of the Z275 zinc coating with respect to the sliding velocity v_s in figure 5.23b. The x component of the coefficient of friction is higher for sliding along the rolling direction in the zinc coating. The y component of the coefficient of friction is slightly higher for sliding along the transverse direction in the zinc coating. The higher friction force components F_{f_x} and F_{f_y} in rolling direction and in transverse direction respectively is in agreement with the lower hardness ($H_c = 3\sigma_y$) of the zinc coating in rolling direction. The yield strength of the anisotropic zinc coating in the TD is higher than the RD (see yield locus of the zinc coating in figure 4.25 in chapter 4, section 4.2.3).

5.3. Summary

The numerical MPM model developed in this research has shown very good agreement with the analytical model for uncoated and coated substrates with for rigid-plastic material behaviour and also with ploughing experiments for both uncoated steel and zinc coated substrates. The validation of the friction results obtained from the MPM-based model is shown to be limited to the ploughing wear mode only. The formation of wedges and chips in front of the asperity resulting from the wedging and cutting wear modes results in unstable and high friction forces which cannot be captured by the current MPM-model. However, both the developed analytical model and the MPM model can be used to compute friction and the ploughed profile in ploughing for a range of operating conditions (loads) for elliptical asperities ploughing on coated substrates. The MPM model can use the material model given in section 3.1.3 to model plastic deformation in ploughing of the anisotropic zinc coating and validate the experimental results plotted for ploughing of anisotropic zinc coatings by ellipsoidal asperities.

Chapter 6

Conclusion and recommendations

Based on the discussed results in the chapter 5, and the objectives set for the research in chapter 2, a set of conclusions have been drawn in the current chapter. The conclusion highlights the key findings of the research and the limitations and scope of the developed ploughing model. Based on this, recommendations have been made in the context of extending the developed model to include the factors left out from the research scope in the current thesis. Also applications of the developed ploughing model to other aspects related to modelling friction and wear in the deep-drawing process have been recommended.

6.1. Conclusions

The material point method has been used to calculate friction forces and ploughing depth in simulating single-asperity sliding on metallic substrate. The model has been validated successfully using both elastic as well as pure plastic material behaviour with available single asperity sliding friction theories. Also results obtained using more complex material and friction laws have been compared with experimental data and found to be in good agreement with the experimental results.

In the context of building and validating the MPM-based ploughing model, it is important to note that the aim is to model only the ploughing behaviour of a single asperity sliding through a steel substrate. The MPM based model incorporates features of both mesh and particle-based numerical methods to model the complex ploughing behaviour. With respect to material choice, zinc coated DX56 steel and Quaker Ferrocoat N136 lubricant are commonly used in forming process for making automotive bodies and metallic packaging. Moreover, the ploughing model can be further validated with similar metallic substrates given the physical models and their parameters for calculating material strength and interfacial shear stress. The current work sets the platform to further extend the model to compute friction and wear in multi-asperity ploughing. However, unlike ploughing, for modelling other abrasive and adhesive wear modes which involves generation of wear debris and material removal, further work has to be done on the damage and adhesion models which is not in the scope of the current thesis.

An analytical model to study the effect of geometry of an elliptic-paraboloid and ellipsoid shaped asperity ploughing through a rigid-plastic substrate has been developed. The model calculates the components of force acting on the asperity, resolved in the three Cartesian coordinates, due to the plastic deformation of the substrate and interfacial shear at the contact. The effects of asperity orientation with sliding direction and axes sizes have been studied and discussed separately and simultaneously for both load and depth controlled ploughing. The model has also been verified with similar versions of analytical models for elliptic-paraboloid shaped asperities available in the literature [32], [28] and spherical asperity available in [77]. The analytical model computes forces acting on an asperity ploughing through a rigid plastic substrate where there is no material removal from the substrate.

The developed analytical model has been used to study and evaluate the variation in components of total force (friction) along the coordinate axes, acting on elliptic-paraboloid asperities with varying sizes, ellipticity ratios and orientations. An elliptic-paraboloid asperity with given geometrical parameters of reference axis size c, ellipticity ratios (e_x, e_y), orientation β and penetration/contact depth d can be used to describe the contact of single asperity present on a rough surface. The asperities in the contact of an (anisotropic) rough tool surface with a smooth, soft substrate can be mapped as a combination of differently shaped and differently oriented elliptic contact patches [77] and [32]. In this way, the contact between a hard/rough and a soft/smooth surface can be analyzed by describing asperities by a set of (ellipsoids) elliptic paraboloids, where the forces and ploughing depth can be calculated by applying the theory developed for a single asperity.

An analytical model to compute the ploughed profile and forces in ploughing by ellipsoidal asperities of varying size, ellipticity ratio and orientation has been extended and compared to the numerical model for a rigid-plastic substrate. The effect of asymmetry in asperity

geometry on the ploughing depths and ploughing friction has been discussed through results of the numerical model. The MPM-based ploughing model has been further validated with ploughing experiments using ellipsoidal pins on lubricated steel sheets. The results are in good agreement for most asperity geometries. The comparison between the analytical model, simulations and experiments have been made for both the forces involved in ploughing as well as the profile of the ploughed track. A good agreement has been found between the approaches. The deviation in the experimental and numerical results are described through roughness and alignment effects.

An experimental method to characterize the interfacial shear strength of lubricated and unlubricated contacts (coated and uncoated) has been developed. The interfacial shear strength has been fitted with empirical relations to express it as a function of contact pressure and sliding velocity. The fitted relations have been successfully implemented in the MPM-based ploughing model and the results have been validated against ploughing experiments to good agreement. The MPM-based ploughing model has been further used to understand the effect of interfacial shear strength on the friction and wear behaviour of single asperity sliding through a steel substrate. The Bowden and Tabor [34] relationship for friction in sliding contacts has been show to hold for large indenters at large applied loads as shown in chapter 5 [121]. In these cases, the contribution of the friction due to interfacial shear strength and plastic deformation to the total friction force and the ploughing depth is shown to be independent and additive. For long elliptical indenters and low loads the contribution of shear and the contribution of plastic deformation to the overall friction force are not independent and additive. An experimental study on the transition from ploughing to wedging wear mode has been carried out by varying the interfacial shear strength and the transition has been explained using the wear mode diagram for spherical indenters [35].

The coating thickness, substrate material properties and applied load have been varied to study their effect on the ploughing friction and ploughing depth and an analytical model which is then validated using the MPM based-ploughing model. The ploughing behaviour of a zinc coating on a steel substrate has been modelled and validated to good agreement using the MPM based ploughing model and ploughing experiments. The developed analytical model also seems to predict the effect of the coating thickness and substrate hardness on the coefficient of friction and ploughing depth. It can be concluded that ploughing friction in a coated system is a function of the material properties (flow/yield curve) of the coating and the substrate, the shear strength of the indenter-coating interface and the coating thickness.

Based on the ploughing experiments on a rolled zinc coated steel sheet, where the zinc coating is characterized in terms of anisotropic parameters, the direction of axes of anisotropy relative to the sliding of the indenter affects the plastic deformation behaviour of the ploughed coating. To summarize, the geometrical parameters of the ellipsoidal asperity such as size, ellipticity ratio, orientation relative to sliding direction and the properties of the (coated) substrate such as thickness of the coating, hardness of the coating and the substrate, flow curves of the coating and the substrate and the interfacial shear strength of the boundary layer on the (coated-) substrate all affect friction in ploughing. The developed numerical and analytical models have shown to capture these effects in the theoretical results very well when comparing with the ploughing experiments.

6.2. Recommendations for future research

The factors affecting ploughing behaviour listed in chapter 1 have been studied using the ploughing models developed in the current thesis. Based on the gaps in the results achieved, the following recommendations have been made for possible future research. The recommendation have been categorized into three categories based on their application.

6.2.1. For further model development

- Thus far the material point method has successfully modelled ploughing behaviour of coated and uncoated specimen. However, MPM has not been used to model friction and wear in wear regimes involving material removal. For this a robust damage model is needed. The inclusion of a damage model in MPM to simulate material removal and failure would account for formation of chips and wear particles during sliding of a single-asperity through a metallic substrate. Ploughing experiments could also be performed with elliptical asperities for asperity sizes and orientations resulting and in cutting conditions. Linear sliding experiments can be used to validate the cutting wear modelled using the MPM model.

- The developed MPM-based ploughing model should be compared with other numerical tools, either particle or mesh based or hybrid, which have simulated or would be able to simulate ploughing. This could highlight the modelling accuracy, capabilities and computational speed of numerical ploughing models including the generalized interpolation material point method.

- The transfer of substrate material to the surface of the pin has been observed as lumps formed in front of the sliding pin grew and adhered to the surface of the pin on unloading. This phenomenon termed 'galling' has been commonly observed in micro-contacts in deep-drawing. Galling results in severe wear of the sheet metal by changing the micro-geometry of the tool which is highly unwanted. By modelling adhesion between the asperity and the substrate and damage of the substrate in plastic deformation, the material transfer can be modelled to simulate galling in single-asperity ploughing. Indentation tests could be performed on clean surfaces using steel pins on unlubricated zinc coated and uncoated steel sheets at low loads to validate the adhesion model leading to material transfer.

- The MPM model can also be used to study the flattening of asperities of various geometries (elliptic asperities with varying size and orientation). MPM can also be used to study and model the contact between the elliptical asperities sliding against each other and the resulting deformation and wear. This can be used to understand contact between a deforming asperity and a rigid-flat substrate and the interaction between two deforming asperities which is critical to contact modelling in many mechanical processes and processes involving two-body wear and contact between rough surfaces.

6.2.2. For study of new materials

- Electrical discharge texturing of the rolling mill has been used to generate the texture on the surface of the zinc coating. Such texturing results in semi-deterministic stochastic texture on the zinc coating. The current model has modelled ploughing through flatted zinc coated sheets by considering the anisotropy induced by rolling using EDT textured roll. The effect of deterministic surface texture on the surface of the zinc coating and

uncoated steel sheet, obtained by laser texturing or by using laser textured roll, on the ploughing behaviour, friction and wear can also be studied using the MPM-based ploughing model and validated using ploughing experiments. The effect of texturing process, texture geometry, packing density and size can also be varied to study their effect on friction and wear.

- Although galvanized iron(zinc-coated steel) has been commonly used in automotive industry for manufacturing of automotive panels, new materials are constantly being developed and tested for their friction and wear behaviour in deep drawing. The galvanized steel is further annealed to diffuse iron into the zinc coating resulting in a multi-layered coating which consists of various iron-zinc intermetallics. Magnesium has also been used in the zinc bath to include magnesium in the zinc coating to improve the corrosion resistance of the deep-drawn product. Aluminum has also been tried in automotive industry to manufacture parts, although extensively in aerospace industry. Often aluminum is anodised resulting in a brittle harder layer of aluminum oxide which prevents further corrosion of aluminum. By characterizing the material and interfacial shear behaviour and (brittle) failure and damage of such materials and coatings, the MPM-based ploughing model can be extended to model friction and wear in ploughing of multi-layered coating and hard coatings on softer substrate.

- Likewise the current thesis has studied the shear behaviour of common forming oils such as 'Quaker' and 'Anticorrit' at room temperature. The shear strength of booster lubes and other lubricants can also be characterized as a function of temperature, pressure and sliding velocity and incorporated in the MPM-model to study their friction in ploughing of sheets lubricated with such lubricants at higher temperature.

6.2.3. For exploring new parameters

- The anisotropy of the zinc coating is also affected by the crystallographic orientations of the zinc grains in the coating. The yield behaviour of each grain combined with the adhesion between the zinc-steel inter-layer contributes to the friction due to plastic deformation. The deformation behaviour of the zinc grains can also be modelled in the MPM code by allocating the properties of each grain to the group of particles defined as the zinc grains. Like wise nano-indentation can be done at the granular level to characterize the yield criteria of each zinc grain.

- Finally the anisotropy in the micro-geometry of the tool asperities and the anisotropy in the mechanical properties of the substrate can be combined to study their effect on the ploughing behaviour of the elliptical asperity sliding through the zinc-coated sheet. The orientation of the elliptical asperity can be varied relative to the rolling direction in the zinc coating combined with the sliding direction can be varied to study its effect on the plastic deformation behaviour and hence the ploughing friction. The thickness of the coating can be varied in combination with the anisotropy of the pin and the sheet to affect the ploughing behaviour in the single-asperity sliding.

- Typically in sliding micro-contacts of rough surfaces, multiple hard asperities plough through the soft substrate. This results in interaction between two asperities where the ploughed groove created by one asperity is later ploughed again by another asperity with a higher asperity height. Ploughing by an asperity on the substrate adjacent to the ploughed groove also affects the friction and wear in the current ploughing asperity. The

MPM-based ploughing model can be used to study the effects of simultaneous ploughing by multiple asperities with varied location on the same substrate, resulting in subsequent interaction of asperities and their ploughed wear tracks.

- The analytical model developed to compute the friction and ploughed profile in sliding of elliptical asperities can be extended to compute wear by elliptical asperities. The wear volume in abrasive wear has been characterized by the ratio of the difference in area of the piled-up ridge and groove and the area of the groove. By computing the depth of the groove for different asperity geometry and characterizing the degree of wear as a degree of penetration the wear volume can be modelled as a function of the asperity geometry. An accurate characterization of the material deformation behaviour (hardness) can also be incorporated in the analytical wear model to compare the computed wear volume with that obtained by experiments by sliding elliptical pins on steel sheets. The analytical model can also be fit to material properties of coated sheets to do simplified friction computations in ploughing.

Bibliography

[1] X.B. Zhang. "Finite element modeling of deep drawing of coated sheet". In: Advanced Materials Research 430-432 (2012), pp. 1302–1305. DOI: 10.4028/www.scientific.net/AMR.430-432.1302.

[2] L. Wang, T. Zhou, and Y. Huang. "Zinc coating failure analysis and sheet formability during hot-dip galvanized sheet stamping". In: Key Engineering Materials 575-576 (2014), pp. 510–514. DOI: 10.4028/www.scientific.net/KEM.575-576.510.

[3] American Galvanizers Association. Zinc Coatings: A Comparative Analysis of Process and Performance Characteristics. https://galvanizeit.org/uploads/publications/Zinc_Coatings.pdf. Accessed: 2019-05-07. July 2011.

[4] Y. Zhang, Q. Cui, f. Shao, J.S. Wang, and H.Y. Zhao. "Influence of air-knife wiping on coating thickness in hot-dip galvanizing". In: Journal of Iron and Steel Research International 19.6 (2012), pp. 70–78. DOI: 10.1016/S1006-706X(12)60130-7.

[5] L.G. Garza and C. Vantyne. "Friction and formability of galvannealed interstitial free sheet steel". In: Journal of Materials Processing Technology 187-188 (2007), pp. 164–168. DOI: 10.1016/j.jmatprotec.2006.11.062.

[6] N. Van Landschoot, C. Dane, R. Bleeker, and M. Vlot. "Zinc-Magnesium Coated Hot Dip Galvanised Steel". In: ATZ Worldwide 115.4 (2013), pp. 4–8. DOI: 10.1007/s38311-013-0036-4.

[7] J. Simão, D.K. Aspinwall, M.L.H. Wise, and M.F.El-Menshawy. "Mill roll texturing using EDT". In: Journal of Materials Processing Technology 45.1-4 (1994), pp. 207–214. DOI: 10.1016/0924-0136(94)90342-5.

[8] K. Brörmann, I. Barel, M. Urbakh, and R. Bennewitz. "Friction on a microstructured elastomer surface". In: Tribology Letters 50.1 (2013), pp. 3–15. DOI: 10.1007/s11249-012-0044-3.

[9] R. Zhou, J. Cao, Q.J. Wang, F. Meng, K. Zimowski, and Z.C. Xia. "Effect of EDT surface texturing on tribological behavior of aluminum sheet". In: Journal of Materials Processing Technology 211.10 (2011), pp. 1643–1649. DOI: 10.1016/j.jmatprotec.2011.05.004.

[10] J.A. Schey. Tribology in Metalworking: Friction, Lubrication and Wear. Metals Park, OH: American Society for Metals, 1983. ISBN: 0871701553.

[11] A. Westeneng. "Modelling of contact and friction in deep drawing process". PhD thesis. University of Twente, The Netherlands, 2001. ISBN: 90-365-1549-1.

[12] D.K.Karupannasamy, J.Hol, M.B.de Rooij, T.Meinders, and D.J.Schipper. "Modelling mixed lubrication for deep drawing processes". In: Wear 294-295 (2012), pp. 296–304. DOI: 10.1016/j.wear.2012.06.006.

[13] R. Stribeck. "Die wesentlichen Eigenschaften der Gleit- und Rollenlager [Characteristics of Plain and Roller Bearings]". In: Zeitschrift des Vereines Deutscher Ingenieure 46.38 (1902), pp. 1432–1438.

[14] W.R.D. Wilson. "Friction and Lubrication in Sheet Metal Forming". In: Mechanics of Sheet Metal Forming. Ed. by D.P. Koistinen and N.M. Wang. Boston, MA: Springer, 1978, pp. 157–177. ISBN: 978-1-4613-2880-3.

[15] W.R.D. Wilson and S. Sheu. "Real area of contact and boundary friction in metal forming". In: International Journal of Mechanical Sciences 30.7 (1988), pp. 475–489. DOI: 10.1016/0020-7403(88)90002-1.

[16] M.P.F. Sutcliffe. "Surface asperity deformation in metal forming processes". In: International Journal of Mechanical Sciences 30.11 (1988), pp. 847–868. DOI: 10.1016/0020-7403(88)90010-0.

[17] W.R.D. Wilson, T.C. Hsu, and X-B. Huang. "A Realistic Friction Model for Computer Simulation of Sheet Metal Forming Processes". In: Journal of Engineering for Industry 117.2 (1995), pp. 202–209. DOI: 10.1115/1.2803295.

[18] R. ter Haar. "Friction in sheet metal forming, the influence of (local) contact conditions and deformation". PhD thesis. University of Twente, The Netherlands, 1996. ISBN: 90-9009296-X.

[19] J. Huetink. "Analysis of Metal Forming Processes Based on a Combined Eulerian-Lagrangian Finite Element Formulation". In: Numerical Methods in Industrial Forming Processes. Ed. by J. F. T. Pittman. Ann Arbor, MI: Pineridge Press, 1982, pp. 501–509. ISBN: 0906674204.

[20] M. Bapinar and M. Akkök. "Modeling and Simulation of Friction in Deep Drawing". In: Journal of Tribology 138.2 (2015), (021104)1–7. DOI: 10.1115/1.4031671.

[21] E. Evin, M. Tomá, and M. Výrostek. "Benchmarking of friction models used in the simulation of deep-drawing". In: Annals of faculty engineering Hunedoara-International Journal of Engineering 10.2 (2012), pp. 129–134. ISSN: 1584 2665.

[22] F. Stachowicz and T. Trzepieciski. "Modelling of friction anisotropy of deep-drawing sheet in ABAQUS/EXPLICIT". In: Archives of Foundry Engineering 10 (2010), pp. 47–52.

[23] J. Hol. "Multi-scale friction modeling for sheet metal forming". PhD thesis. University of Twente, The Netherlands, 2013. ISBN: 978-90-77172-98-8.

[24] M.B de Rooij. "Tribological aspects of unlubricated deep-drawing process". PhD thesis. University of Twente, The Netherlands, 1998. ISBN: 90-3651218-2.

[25] P. Nayak. "Random Process Model of Rough Surfaces in Plastic Contact". In: Wear 26 (1973), pp. 305–333. DOI: 10.1016/0043-1648(73)90185-3.

[26] X. Ma, M.B. de Rooij, and D.J. Schipper. "A load dependent friction model for fully plastic contact conditions". In: Wear 269.11-12 (2010), pp. 790–796. DOI: 10.1016/j.wear.2010.08.005.

[27] M. Masen. "Abrasive tool wear in metal forming process". PhD thesis. University of Twente, The Netherlands, 2004. ISBN: 90-365-2061-4.

[28] G. van der Linde. "Predicting galling behaviour in deep-drawing processes". PhD thesis. University of Twente, The Netherlands, 2011. ISBN: 978-90-365-3284-6.

[29] D.K. Karupannasamy. "Friction modelling on multiple scales for deep-drawing processes". PhD thesis. University of Twente, The Netherlands, 2013. ISBN: 978-94-91909-01-6.

[30] M.A.Masen and M.B.de Rooij. "Micro-contact based modelling of abrasive wear". In: Wear 256.6 (2004), pp. 639–646. DOI: 10.1016/j.wear.2003.10.006.

[31] M.A.Masen, M.B.de Rooij, and D.J.Schipper. "Micro-contact based modelling of abrasive wear". In: Wear 258.1-4 (2005), pp. 339–348. DOI: 10.1016/j.wear.2004.09.009.

[32] M.B. de Rooij, G. van der Linde, and D.J. Schipper. "Modelling material transfer on a single asperity scale". In: Wear 307.1-2 (2013), pp. 198–208. DOI: 10.1016/j.wear.2013.09.006.

[33] J.M. Challen and P.L.B. Oxley. "An explanation of the different regimes of friction and wear using asperity deformation models". In: Wear 53.2 (1979), pp. 229–248. DOI: 10.1016/0043-1648(79)90080-2.

[34] F.P. Bowden, A.J.W. Moore, and D. Tabor. "The Ploughing and Adhesion of Sliding Metals". In: Journal of Applied Physics 14.2 (1943), pp. 80–91. DOI: 10.1063/1.1714954.

[35] K.Hokkirigawa and K.Kato. "An experimental and theoretical investigation of ploughing, cutting and wedge formation during abrasive wear". In: Tribology International 21.1 (1988), pp. 51–57. DOI: 10.1016/0301-679X(88)90128-4.

[36] D.K.Karupannasamy, M.B.de Rooij, and D.J.Schipper. "Multi-scale friction modelling for rough contacts under sliding conditions". In: Wear 308.1-2 (2013), pp. 222–231. DOI: 10.1016/j.wear.2013.09.012.

[37] D.K.Karupannasamy, J.Hol, M.B.de Rooij, T.Meinders, and D.J.Schipper. "A friction model for loading and reloading effects in deep drawing processes". In: Wear 318.1-2 (2014), pp. 27–39. DOI: 10.1016/j.wear.2014.06.011.

[38] M. Shisode, J. Hazrati, T. Mishra, M.B. de Rooij, and T. van den Boogaard. "Multi-Scale Contact Modeling of Coated Steels for Sheet Metal Forming Applications". In: Key Engineering Materials 767.6 (2018), pp. 223–231. DOI: 10.4028/www.scientific.net/KEM.767.223.

[39] J.A. Greenwood and J.B.P. Williamson. "Contact of nominally flat surfaces". In: Proceedings of the Royal Society of London, Series A, Mathematical and Physical sciences 295 (1966), pp. 300–319. DOI: 10.1098/rspa.1966.0242.

[40] A.W. Bush, R.D. Gibson, and T.R. Thomas. "The elastic contact of a rough surface". In: Wear 35.1 (1975), pp. 87–111. DOI: 10.1016/0043-1648(75)90145-3.

[41] Y.T. Pei, G.M. Song, W.G. Sloof, and J.Th.M. De Hosson. "A methodology to determine anisotropy effects in non-cubic coatings". In: Surface and Coatings Technology 201.16-17 (2007), pp. 6911–6916. DOI: 10.1016/j.surfcoat.2006.11.044.

[42] C.A. Wert and E.P.T. Tyndall. "Elasticity of Zinc Crystals". In: Journal of Applied Physics 20.6 (1949), pp. 587–589. DOI: 10.1063/1.1698431.

[43] R. Parisot, S. Forest, A. Pineau, F. Grillon, X. Demonet, and J.M. Mataigne. "Deformation and Damage Mechanisms of Zinc Coatings on Hot-Dip Galvanized Steel Sheets: Part I. Deformation Modes". In: Metallurgical and Materials Transactions A 35.3 (2004), pp. 797–811. DOI: 10.1007/s11661-004-0007-x.

[44] R. Parisot, S. Forest, A.F. Gourgues, A. Pineau, and D. Mareuse. "Modeling the mechanical behavior of a multicrystalline zinc coating on a hot-dip galvanized steel sheet". In: Computational Materials Science 19.1-4 (2000), pp. 189–204. DOI: 10.1016/S0927-0256(00)00155-5.

[45] H. M. Ledbetter. "Elastic properties of zinc: A compilation and a review". In: Journal of Physical and Chemical Reference Data 6.4 (1977), pp. 1181–1203. DOI: 10.1063/1.555564.

[46] R. Parisot, S. Forest, A. Pineau, F. Grillon, X. Demonet, and J.M. Mataigne. "Deformation and Damage Mechanisms of Zinc Coatings on Hot-Dip Galvanized Steel Sheets: Part II. Damage Modes". In: Metallurgical and Materials Transactions A 35.3 (2004), pp. 813–823. DOI: 10.1007/s11661-004-0008-9.

[47] G.M. Song, W.G. Sloof, Y.T. Pei, and J. Th. M. De Hosson. "Interface fracture behavior of zinc coatings on steel: Experiments and finite element calculations". In: International Journal of Materials Research 201.7 (2006), pp. 4311–4316. DOI: 10.1016/j.surfcoat.2006.08.046.

[48] G. M. Song, W. G. Sloof, T. Vystavel, and J. Th. M. De Hosson. "Interface Microstructure and Adhesion of Zinc Coatings on TRIP Steels". In: Materials Science Forum 539-543 (2007), pp. 1104–1109. DOI: 10.4028/www.scientific.net/MSF.539-543.1104.

[49] P. van Liempt. "Work hardening and sub structural geometry of metals". In: Journal of Materials Processing Technology 45.1-4 (1994), pp. 459–464. DOI: 10.1016/0924-0136(94)90382-4.

[50] R.R. Tohid and S.J. Bull. "Getting accurate nanoindentation data from time-dependent and microstructural effects of zinc". In: International Journal of Materials Research 98.5 (2007), pp. 353–359. DOI: 10.3139/146.101477.

[51] C.E. Anderson., P.A. Cox, G.R. Johnson, and P.J. Maudlin. "A constitutive formulation for anisotropic materials suitable for wave propagation computer programsII". In: Computational Mechanics 15.3 (1994), pp. 201–223. DOI: 10.1007/BF00375030.

[52] R. Hill. "A theory of the yielding and plastic flow of anisotropic metals". In: Proceedings of the Royal Society of London A: Mathematical and Physical Sciences 193.1033 (1948), pp. 281–297. DOI: 10.1098/rspa.1948.0045.

[53] H. Vegter and A.H. van den Boogaard. "A plane stress yield function for anisotropic sheet material by interpolation of biaxial stress states". In: International Journal of Plasticity 22.3 (2006), pp. 557–580. DOI: 10.1016/j.ijplas.2005.04.009.

[54] R.G. Wheeler and D.R. Ireland. "Multiaxial plastic flow of Zircaloy2 determined from hardness data". In: Electrochemical Technology 4.7-8 (1966), pp. 313–317.

[55] D. Lee, F.S. Jabara, and W.A. Backofen. "The Knoop-hardness yield loci for two titanium alloys". In: Transaction of the Metallurgical Society of AIME 239.9 (1967), pp. 1476–1478.

[56] B.C. Wonsiewicz and W.W. Wilkening. "A comparison of conventional and Knoop hardness yield loci for magnesium and magnesium alloys". In: Trans. of the Metallurgical Society of AIME 245.6 (1969), pp. 1313–1319.

[57] M.F. Amateau and W.D. Hanna. "Comparison of First Quadrant Yield Loci for Ti-6AI-4V With Those Predicted by Knoop Hardness Measurements". In: Metallurgical Transactions A 6.2 (1975), pp. 417–419. DOI: 10.1007/BF02667299.

[58] D. Lee and W.A. Backofen. “Yielding and plastic deformation in textured sheet of titanium and its alloys”. In: Transaction of the Metallurgical Society of AIME 236.12 (1966), pp. 1696–1704.

[59] K.L. Murty and I. Charit. “Texture development and anisotropic deformation of zircaloys”. In: Progress in Nuclear Energy 48.4 (2006), pp. 325–359. DOI: 10.1016/j.pnucene.2005.09.011.

[60] L. Riester, P.J. Blau, E. Lara-Curzio, and K. Breder. “Nanoindentation with a Knoop indenter”. In: Thin Solid Films 377-378 (2000), pp. 635–639. DOI: 10.1016/S0040-6090(00)01298-0.

[61] W.C. Oliver and G.M. Pharr. “An improved technique for determining hardness and elastic modulus using load and displacement sensing indentation experiments”. In: Journal of Materials Research 7.6 (1992), pp. 1564–1583. DOI: 10.1557/JMR.1992.1564.

[62] F. P. Bowden and L. Leben. “The friction of lubricated metals”. In: Philosophical Transaction of the Royal Society of London A. Mathematical and Physical Sciences 239.799 (1940), pp. 1–27. DOI: 10.1098/rsta.1940.0007.

[63] D. Godfrey. “Boundary Lubrication”. In: Interdisciplinary Approach to Friction and Wear. Ed. by P.M. Ku. Washington, DC: NASA SP-181, 1968, pp. 335–384.

[64] S.Jahanmir and M.Beltzer. “Effect of additive molecular structure on friction coefficient and adsorption”. In: Journal of Tribology 108.1 (1986), pp. 109–116. DOI: 10.1115/1.3261129.

[65] B.J. Briscoes and D.C.B Evans. “The shear properties of Langmuir-Blodgett layers”. In: Proceedings of the Royal Society London A 380.1779 (1982), pp. 389–407. DOI: 10.1098/rspa.1982.0048.

[66] H. Eyring. “Viscosity, plasticity and diffusion as examples of absolute reaction rates”. In: Journal of Chemical Physics 4.283 (1936), pp. 283–291. DOI: 10.1063/1.1749836.

[67] B.J. Briscoe and D. Tabor. “Rheology of thin organic films”. In: ASLE Transactions 17.3 (1973), pp. 158–165. DOI: 10.1080/05698197408981452.

[68] K.J. Chugg and M.M. Chaudhri. “Boundary lubrication and shear properties of thin solid films of dioctadecyl dimethyl ammonium chloride (TA 100)”. In: Journal of Physics D: Applied Physics 26 (1993), pp. 1993–2000. DOI: 10.1088/0022-3727/26/11/023.

[69] R.S. Timsit and C.V. Pelow. “Shear strength and tribological properties of stearic acid films - Part I: on glass and aluminium-coated glass”. In: J. Tribology 114.1 (1992), pp. 150–158. DOI: 10.1115/1.2920854.

[70] J. Challen and P. Oxley. “Slip-line fields for explaining the mechanics of polishing and related processes”. In: Journal mechanical engineering science 26.6-8 (1983), pp. 403–418. DOI: 10.1016/0020-7403(84)90030-4.

[71] J.D. Bressan and J.A. Williams. “Mathematical slip-line field solutions for ploughing a hard particle over a softer material”. In: Wear 267.86-88 (2009), pp. 1865–1872. DOI: 10.1016/j.wear.2009.03.008.

[72] M. Busquet and A. Torrance. “A numerical slip-line field for the sliding cylinder problem”. In: Wear 241 (2000), pp. 403–418. DOI: 10.1016/S0043-1648(00)00360-4.

[73] M. DeVathire, F. Delamare, and E. Felder. “An upper bound model of ploughing by a pyramidal indenter”. In: Wear 66 (1981), pp. 51–64. DOI: 10.1016/0043-1648(81)90032-6.

[74] T. Abildgaard. “Prediction of the force components acting on a ploughing cone by means of three-dimensional upper bound theory”. In: Advanced technology of plasticity : proceedings of the First International Conference on Technology of Plasticity. Ed. by International Conference on Technology of Plasticity. Vol. 1. Tokyo: The Japan Society for Technology of Plasticity, 1984, pp. 121–126.

[75] A. Azarkhin and O. Richmond. “A model of ploughing by a pyramidal indenter-upper bound method for stress-free method”. In: Wear 157 (1992), pp. 409–418. DOI: 10.1016/0043-1648(92)90077-L.

[76] A. Azarkhin and M.L. Devenpeck. “Enhanced model of a plowing asperity”. In: Wear 206 (1997), pp. 147–155. DOI: 10.1016/S0043-1648(96)07502-3.

[77] N. Tayebi, T.F. Conry, and A.A. Polycarpou. “Determination of hardness from nanoscratch experiments: Corrections for interfacial shear stress and elastic recovery”. In: Journal of Materials Research 18.9 (2003), pp. 2150–2162. DOI: 10.1557/JMR.2003.0301.

[78] K. Holmberg, A. Laukkanen, H. Ronkainen, K. Wallin, S. Varjus, and J. Koskinen. “Tribological contact analysis of a rigid ball sliding on a hard coated surface Part I: modelling stresses and strains”. In: Surface and Coatings Technology 200.12-13 (2006), pp. 3793–3809. DOI: 10.1016/j.surfcoat.2005.03.040.

[79] G. Kermouchea, N. Aleksya, J.L. Loubet, and J.M. Bergheaua. “Finite element modelling of the scratch response of a coated time-dependent solid”. In: Wear 267.11 (2009), pp. 1945–1953. DOI: 10.1016/j.wear.2009.05.005.

[80] M. M. Hossain, S. Xiao, H. J. Sue, and M. Kotaki. “Scratch behavior of multilayer polymeric coating systems”. In: Materials and Design 128 (2017), pp. 143–149. DOI: 10.1016/j.matdes.2017.05.012.

[81] H. Jiang, R. Browning, J. D. Whitcomb, M. Ito, M. Shimouse, T. A. Chang, and H.-J. Sue. “Mechanical Modeling of Scratch Behavior of Polymeric Coatings on Hard and Soft Substrates”. In: Tribology Letters 37.2 (2010), pp. 159–167. DOI: 10.1007/s11249-009-9505-8.

[82] A. Vedaei-Sabegh, S. R. Ahmadi, and B. Gholamzadeh. “Investigation of pile-up during a rigid ball sliding on coated surface based on elasticplastic analysis”. In: Surface and Coatings Technology 251 (2014), pp. 283–292. DOI: 10.1016/j.surfcoat.2014.04.040.

[83] F. Elwasli, F. Zemzemi, A. Mkaddem, S. Mzali, and S. Mezlini. “A 3D multi-scratch test model for characterizing material removal regimes in 5083-Al alloy”. In: Materials and Design 87 (2015), pp. 352–362. DOI: 10.1016/j.matdes.2015.07.121.

[84] G. Subhash and W. Zhang. “Investigation of the overall friction coefficient in the single-pass scratch test”. In: Wear 252.1-2 (2002), pp. 123–134. DOI: 10.1016/S0043-1648(01)00852-3.

[85] J.L. Bucaille, E. Felder, and G. Hochstetter. “Mechanical analysis of the scratch test on elastic and perfectly plastic materials with the three-dimensional finite element modelling”. In: Wear 249.5-6 (2001), pp. 422–432. DOI: 10.1016/S0043-1648(01)00538-5.

[86] M. Woldman, E. Van Der Heide, T. Tinga, and M.A. Masen. “A Finite Element Approach to Modeling Abrasive Wear Modes”. In: Tribology transactions 60.4 (2017), pp. 711–718. DOI: 10.1080/10402004.2016.1206647.

[87] D.A. Doman, D.A.R. Bauer, and A. Warkentin. "Experimentally validated finite element model of the rubbing and ploughing phases in scratch tests". In: Proceedings of the Institution of Mechanical Engineers, Part B: Journal of Engineering Manufacture 223.12 (2009), pp. 1519–1527. DOI: 10.1243/09544054JEM1520.

[88] Y. Gao, C. Lu, N.N. Huynh, G. Michal, H.T. Zhu, and A.K. Tieu. "Molecular dynamics simulation of effect of indenter shape on Nano scratch of Ni". In: Wear 267.11 (2009), pp. 1998–2002. DOI: 10.1016/j.wear.2009.06.024.

[89] I.A. Alhafez and H.M. Urbassek. "Scratching of hcp metals: A molecular-dynamics study". In: Computational Materials Science 113.2 (2016), pp. 187–197. DOI: 10.1016/j.commatsci.2015.11.038.

[90] X. Zheng, H. Zhu, A.K. Tieu, and B. Kosasih. "A molecular dynamics simulation of 3D rough lubricated contact". In: Tribology International 67 (2013), pp. 217–221. DOI: 10.1016/j.triboint.2013.07.015.

[91] S. Solhjoo and A.I. Vakis. "Single asperity nanocontacts: comparison between molecular dynamics simulations and continuum mechanics models". In: Computational Materials Science 99 (2015), pp. 209–220. DOI: 10.1016/j.commatsci.2014.12.010.

[92] G.C. Ganzenmüller. "An hourglass control algorithm for Lagrangian Smooth Particle Hydrodynamics". In: Computer Methods in Applied Mechanics and Engineering 286 (2015), pp. 87–106. DOI: 10.1016/j.cma.2014.12.005.

[93] S. Leroch, M. Varga, S.J. Eder, A. Vernes, M. Ripolla, and G.C. Ganzenmüller. "Smooth particle hydrodynamics simulation of damage induced by a spherical indenter scratching a visco-plastic material". In: International Journal of Solids and Structures 81 (2016), pp. 188–202. DOI: 10.1016/j.ijsolstr.2015.11.025.

[94] M. Varga, S. Leroch, S.J. Eder, and M.R. Ripoll. "Meshless microscale simulation of wear mechanisms in scratch testing". In: Wear 376377.B (2017), pp. 1122–1129. DOI: 10.1016/j.wear.2016.11.023.

[95] T. Mishra, G. C. Ganzenmüller, M.B. de Rooij, M.P. Shisode, J. Hazrati, and D.J. Schipper. "Modelling of ploughing in a single-asperity sliding contact using material point method". In: Wear 418-419 (2019), pp. 180–190. DOI: 10.1016/j.wear.2018.11.020.

[96] J. Donéa, A. Huerta, Ponthot J-Ph, and A.R. Ferran. "Arbitrary Lagrangian-Eulerian Methods". In: Encyclopaedia of Computational Mechanics. Ed. by E. Stein, R. De Borst, and T.J.R. Hughes. New Jersey, United States: Wiley and sons, 2004. Chap. 14, pp. 413–437. DOI: 10.1002/0470091355.ecm009.

[97] B. Takabi, M. Tajdari, and B.L. Tai. "Numerical study of smoothed particle hydrodynamics method in orthogonal cutting simulations Effects of damage criteria and particle density". In: Journal of Manufacturing Processes 30 (2017), pp. 523–531. DOI: 10.1016/j.jmapro.2017.10.020.

[98] J.M. Rodríguez, J.M. Carbonell, J.C. Cante, and J. Oliver. "Continuous chip formation in metal cutting processes using the Particle Finite Element Method (PFEM)". In: International Journal of Solids and Structures 120 (2017), pp. 81–102. DOI: 10.1016/j.ijsolstr.2017.04.030.

[99] D. Sulsky, Z. Chen, and H.L. Schreyer. "A particle method for history-dependent materials". In: Computer Methods in Applied Mechanics and Engineering 118.1-2 (1994), pp. 179–186. DOI: 10.1016/0045-7825(94)90112-0.

[100] I. Jassim, D. Stolle, and P. Vermeer. "Two-phase dynamic analysis by material point method". In: International Journal for Numerical and Analytical Methods in Geomechanics 37.15 (2013), pp. 2502–2522. DOI: 10.1002/nag.2146.

[101] S. Bardenhagen and E. Kober. "The Generalized interpolation material point method". In: Computer Modeling in Engineering and Sciences 5.6 (2004), pp. 477–495. DOI: 10.3970/cmes.2004.005.477.

[102] J.A. Nairn. "Numerical simulation of orthogonal cutting using the material point method". In: Engineering Fracture Mechanics 149 (2015), pp. 262–275. DOI: 10.1016/j.engfracmech.2015.07.014.

[103] S. Leroch, S.J. Edera, G. Ganzenmüller, L.J.S. Murilloc, and M.R. Rodríguez. "Development and validation of a meshless 3D material point method for simulating the micromilling process". In: Journal of Materials Processing Technology 262 (2018), pp. 449–458. DOI: 10.1002/nag.2146.

[104] S. Plimpton. "Fast parallel algorithms for short-range molecular dynamics". In: Journal of Computational Physics 117.1 (1995), pp. 1–19. DOI: 10.1006/jcph.1995.1039.

[105] T. Mishra, M.B de Rooij, M.P. Shisode, J. Hazrati, and D.J. Schipper. "An analytical model to study the effect of asperity geometry on forces in ploughing by an elliptical asperity". In: Tribology International 137 (2019), pp. 405–419. DOI: 10.1016/j.triboint.2019.05.015.

[106] T. Mishra, M.B de Rooij, M.P. Shisode, J. Hazrati, and D.J. Schipper. "A material point method based ploughing model to study the effect of asperity geometry on the ploughing behaviour of an elliptical asperity". In: Tribology international 142 (2020), p. 106017. DOI: 10.1016/j.triboint.106017.

[107] T. Mishra, M.B de Rooij, M.P. Shisode, J. Hazrati, and D.J. Schipper. "Modelling of ploughing behaviour in soft metallic coatings using material point method". In: Wear (2019).

[108] F.P. Bowden and D. Tabor. The friction and lubrication of solids. Clarendon Press, Oxford, UK, 1964. ISBN: 9780198507772.

[109] P.E. ODonoghue, C.E. Anderson, G.J. Friesenhahn, C.H. Parr, and Dirk J. Schipper. "A Constitutive Formulation for Anisotropic Materials Suitable for Wave Propagation Computer Programs". In: Journal of Composite Materials 26.13 (1992), pp. 1860–1884. DOI: 10.1177/002199839202601301.

[110] Steven Segletes. Deviatoric constitutive relationship for anisotropic materials. Tech. rep. BRL-TD-2825. Aberdeen proving ground, Maryland: US army ballistic research laboratory, June 1987.

[111] Carlos A.Felippa and Eugenio Oñate. "Stress, strain and energy splittings for anisotropic elastic solids under volumetric constraints". In: Computers and Structures 81.13 (2003), pp. 1343–1357. DOI: 10.1016/S0045-7949(03)00060-9.

[112] R.D. Krieg and D.B. Krieg. "Accuracies of numerical solution methods for the elastic-perfectly plastic model". In: Journal of Pressure Vessel Technology 99.4 (1977), pp. 510–515. DOI: 10.1115/1.3454568.

[113] D. Tabor. The hardness of metals. Oxford university press, London, UK, 2000. ISBN: 9780198507765.

[114] H. Vegter. "On the plastic behaviour of steel during sheet forming". PhD thesis. University of Twente, The Netherlands, 1991. ISBN: 9789090043739.

[115] P.E. Senseny, J.Duffy, and R.H. Hawley. "Experiments on strain rate history and temperature effects during the plastic deformation of close-packed metals". In: Journal of Applied Mechanics 45.1 (1978), pp. 60–66. DOI: 10.1115/1.3424274.

[116] G.M. Song, J.Th.M. De Hosson, W.G. Sloof, and Y.T. Pei. "Evaluation of interface adhesion of hot-dipped zinc coating on TRIP steel with tensile testing and finite element calculation". In: WIT Trans. Eng. Sci 91 (2015), pp. 3–14. DOI: 10.2495/SECM150011.

[117] J. Halling and R.D. Arnell. "Ceramic Coating in the war on wear". In: Wear 100.1-3 (1984), pp. 367–380. DOI: 10.1016/0043-1648(84)90022-X.

[118] J. Halling and M. A. Sherbiney. "The role of surface topography in the friction of soft metallic films". In: Tribology 1978. Materials Performance and Conservation ImechE, Proc. Conf, Swansea, Wales. Apr. 1978, pp. 131–134. ISBN: 0852984006.

[119] W.R.Chang. "An elastic-plastic contact model for a rough surface with an ion-plated soft metallic coating". In: Wear 212.2 (1997), pp. 229–237. DOI: 10.1016/S0043-1648(97)00148-8.

[120] T. Mishra, M.B de Rooij, M.P. Shisode, J. Hazrati, and D.J. Schipper. "Characterization of anisotropic yield criteria for zinc coated steel sheets using nano indentation with Knoop indenter". In: Surfaces and coatings technology (2019), p. 121150. DOI: 10.1016/j.surfcoat.2019.125110.

[121] T. Mishra, M.B de Rooij, M.P. Shisode, J. Hazrati, and D.J. Schipper. "Characterization of interfacial shear strength and its effect on ploughing behaviour in single-asperity sliding". In: Wear 436-437 (2019), p. 203042. DOI: 10.1016/j.wear.2019.203042.

[122] H. Fujiwara and T. Kawase. "Logarithmic Profile of Rollers in Roller Bearing and Optimization of the Profile". In: Transactions of the Japan Society of Mechanical Engineers Series C 72.721 (2006), pp. 3022–3029. DOI: 10.1299/kikaic.72.3022.

[123] A.C. Fischer-Cripps. "Depth-Sensing Indentation Testing". In: Introduction to Contact Mechanics. Mechanical Engineering Series. 2nd ed. Boston, MA: Springer, 2007. Chap. 11, pp. 189–199. DOI: 10.1007/978-0-387-68188-7_11.

[124] A.C. Fischer-Cripps. "Nanoindentation Test Instruments". In: Nanoindentation. Springer, New York, NY, 2004, pp. 178–194. DOI: 10.1007/978-0-387-22462-6_9.

[125] P.J. Blau. The Lab Handbook of Microindentation Hardness Testing. Section 4.2, Oak Ridge, TN 2000, Sect. 5.2: Blue Rock Technical Publications, Dec. 1999, pp. 4.5–5.1.

[126] B.J Inkson. "Scanning electron microscopy (SEM) and transmission electron microscopy (TEM) for materials characterization". In: Materials characterization using nondestructive evaluation (NDE) methods. Elsevier, 2016, pp. 17–43. DOI: 10.1016/B978-0-08-100040-3.00002-X.

[127] H. Gao, C.H. Chiu, and J. Lee. "Elastic contact versus indentation modelling of multilayered materials". In: International Journal of Solids and Structures 29.20 (1992), pp. 2471–2492. DOI: 10.1016/0020-7683(92)90004-D.

[128] M.V. Swain and J. Mencík. "Mechanical property characterization of thin films using spherical tipped indenters". In: Thin Solid Films 253.1-2 (1994), pp. 204–211. DOI: 10.1016/0040-6090(94)90321-2.

[129] Y.G. An, E. Atzema, M. Workel, H. Vegter, L. Elliott, and J. Moerman. "Comparison of Yield loci measured with mechanical tests and calculated from crystal plasticity for steel sheets." In: 1st International Conference on Super-high Strength Steels, Rome, Italy. 2005.

[130] N. Panich and Y. Sun. “Effect of penetration depth on indentation response of soft coatings on hard substrates: a finite element analysis.” In: Surface and Coatings Technology 182.2-3 (2004), pp. 342–350. DOI: 10.1016/j.surfcoat.2003.07.002.

Part II

Appended Papers

Paper A

Modelling of ploughing in a single-asperity sliding contact using material point method

Tanmaya Mishra[1*], Georg C. Ganzenmüller[3], Matthijn de Rooij[1], Meghshyam Shisode[2], Javad Hazrati[2], and Dirk J. Schipper[1]

[1]Surface Technology and Tribology, Faculty of Engineering Technology, University of Twente, 7500 AE Enschede, the Netherlands
[2]Nonlinear Solid Mechanics, Faculty of Engineering Technology, University of Twente, 7500 AE Enschede, the Netherlands
[3]Department of Sustainable Systems Engineering, Albert-Ludwig University of Freiburg, D-79110 Freiburg, Germany

Abstract

Loading and sliding of a rigid asperity over a substrate results in friction due to shearing of the contact interface and deformation of the substrate. In this article, we introduce the Material Point Method (MPM) based numerical tool to study friction during ploughing of a soft-smooth metallic sheet by a rigid-spherical asperity. The numerical model incorporates a dislocation based physical model for substrate material deformation and interfacial shear strength at the asperity- substrate contact. Initially, the numerical output has been validated using results obtained from the analytical models available in the literature for single-asperity sliding. Finally, the depth of the ploughed wear profile and the overall coefficient of friction obtained from the numerical simulations has been compared with the data obtained from the ploughing experiments and are shown to be in good agreement. Hence, the developed MPM model can be established as a robust tool to model ploughing in a single-asperity sliding contact.

Keywords: Friction model, Boundary layer, Asperity sliding, Ploughing, Material Point Method

1 Introduction

Loading and sliding of a hard, sharp-tipped asperity against a softer and smooth substrate, thereby leading to wear, is termed scratching. At the macro-scale, scratch tests can be performed under controlled conditions to characterize the material and tribological behaviour of the substrate specimen. Generally, the contribution to friction can be divided into two components: friction is required to overcome forces resulting from (1) the plastic deformation by ploughing of the asperity and (2) shearing of the boundary layer at the asperity- substrate contact interface [1]. These two components of friction in single-asperity sliding, referred to as ploughing friction and the shear contribution to friction, have been studied, modelled and experimentally validated in this work.

First of all, a friction force is required to overcome the shear strength of the adhesive junctions formed at the contacting metallic interface. In the presence of a lubricant in a sliding contact, a boundary layer is formed either by adsorption of lubricant molecules on the substrate's surface or by bonding of lubricant's polar functional groups to an activated, metallic surface [1] and [2]. The interfacial shear strength and hence the friction in the presence of the lubricated boundary layer is considerably less than an unlubricated contact due to frequent formation of adhesive junctions in a direct asperity contact. An asperity with a small curvature, sliding on an ideally smooth-lubricated surface, tends to deform the substrate only elastically under low loads due to the relatively low pressure. Hence, in this situation the friction only results from the shearing of the boundary layer. The boundary layer shear strength of lubricant monolayers deposited on smooth surfaces has been determined to be a function of the contact pressure, contact temperature and the sliding velocity [3]. The interfacial shear strength has been also modelled as the resistance to discrete molecular movement using Eyring's model [4]. By fitting Eyring's expressions for shear strength to experimental plots, expressions have been obtained between the boundary layer shear strength and contact pressure, temperature and sliding velocity [5], [3] and [6].

The effect of asperity geometry and surface roughness on ploughing friction has been previously explained using asperity deformation models. Initially, Challen and Oxley used the theory proposed by Green to derive the steady state solutions for the coefficient of friction and the wear rate for a wedge shaped single-asperity [7] and [8]. The various regimes of friction and abrasive wear obtained in Challen et al. [7] were experimentally characterized as ploughing, wedging and cutting for sliding of a spherical asperity using a wear mode diagram [9]. Such a wear mode diagram maps the wear regimes as a function of the degree of penetration of the asperity into the substrate and the boundary layer shear strength at the asperity-substrate interface. Ploughing is defined as the wear mode in which the substrate material is displaced from the path of the sliding asperity. Unlike ploughing, cutting involves removal of substrate material, in the form of chips, while wedging involves piling up and adhesion of the damaged substrate material in front of the asperity tip. In the current study, the focus is on the ploughing wear.

The analytical models for the single-asperity sliding assume ideally elastic or plastic material behaviour in contrast to realistic material behaviour which might work harden and thermally soften while deforming. To model friction in the sliding of an asperity on a lubricated-metal surface, numerical models are more flexible than analytical models as there are less limitations in terms of geometry and material behaviour. This study investigates and selectively uses one of the available numerical models to estimate friction in sliding of an asperity. Traditionally,

mesh-based finite element methods (FEM) have been preferred to model single asperity sliding in scratch tests. In modelling a highly dynamic and large scale deformation problem such as scratching, the selected explicit FE packages have used adaptive re-meshing, element deletion and differential meshing to deal with problems of element distortion and high computational cost [10, 11, 12, 13]. Ploughing models in the commercial FE packages have mostly used time-independent bilinear elastic-linearly hardening and Johnson-Cook material models and Columbic frictional contact at the interface [14] and [15].

Hence, particle-based atomistic methods such as Molecular Dynamics (MD), have been extensively used to study friction and wear in single-asperity sliding through substrate at an atomistic/nano scale. MD explains the interfacial shear and the substrate plastic deformation on a molecular scale. Thus MD is also used to model effect of the asperity geometry along with complex phenomena of ploughing in lubricated, rough and coated contacts [16] and [17]. However, it is still challenging to upscale the MD models for physical validation by coupling them with macro-scale models [18]. The selection of interaction potentials, paramount in accurate model design up, is also debatable with MD models.

To enable the use of constitutive material behaviour, which is experimentally accessible, meshless numerical methods are available. The most common method is Smooth Particle Hydrodynamics (SPH), which allows for the modelling of arbitrarily high deformations of fluids, but is neither robust nor accurate for solid material behaviour. An extension of this method to the Total Lagrangian formulation resolves these issues, but limits the amount of deformation that can be accurately modelled [19]. The Total Lagrangian SPH formulation (TLSPH) to has been used to model scratching behaviour in metals using the Johnson-Cook material model. For that particular study, an accurate experimental validation has not been possible due to the absence of a friction law in the numerical model [20].

A robust numerical method capable of accurately modelling friction in single-asperity sliding needs to incorporate both a realistic material model as well as a realistic interfacial boundary layer shear stress model. Such a numerical model preferably can simulate friction in single-asperity sliding on a metal surface at a macro-scale and be compared to experiments. To this end, we base our study on the Material Point Method (MPM) [21], which is a hybrid method that combines both a background mesh as well as meshless concepts and can accurately model both solid and fluid behaviour, i.e., plastic flow. MPM has been used as a tool for two phase dynamic analysis and modelling large deformation phenomena such as micro-milling [22], soil penetration and structural collapses in geo-mechanics [23]. Here, a newly developed Generalised Interpolation Material Point Method (GIMPM) [24] has been used to model single-asperity sliding. Initially, the GIMPM-based single-asperity sliding model will be validated by comparing the deformation, stresses and ploughing friction output with the theoretical models. The model incorporates both an interfacial shear model to compute friction due to shearing of the boundary layer and the Bergström-van Liempt material model [25] to compute friction due to deformation of the substrate. Finally, the numerical friction and ploughing depth results are validated using experiments.

2 Computational method

GIMPM is a hybrid mesh/particle method which incorporates aspects similar to the Arbitrary Lagrangian and Eulerian (ALE) method [26]. It is based on the original Material Point Method

(MPM) method, which itself is based on the Particle In Cell (PIC) method. All of these methods use an auxilliary background of mesh cells to solve for the spatial gradients near the particles which determine the rates of mass, density, and energy. An interpolation function transfers information between the mesh-nodes and the particles as the material properties evolve with time. While PIC use Dirac Delta functions for this transfer, MPM uses linear functions, and GIMPM employs polynomials of higher order with smooth derivatives, enabling a more accurate computation of the gradients. We used the GIMPM implementation in the user-SMD (Smooth Mach Dynamics) package of an open source standard molecular dynamics code, namely LAMMPS [27]. LAMMPS operates by defining the interaction for each combination of particle types by a certain pair style-based class. The particles in the substrate interact with each other by 'MPM linear'-based pair style following the laws of conservation (explained in section 2.1). The indenter elements have no self-interaction to maintain a rigid boundary condition. However, the indenter mesh elements interact with the substrate MPM particles according to the 'tri surface'-based pair style (explained in section 2.2).

Here, revision 70 of the user-SMD package is used to model single-asperity sliding. A simulation domain of dimensions accommodating the asperity and the substrate was set with fixed boundaries in all axes except for the periodic boundaries in the sliding axis. A semi-cylindrical region was generated and filled with substrate particles, as shown in figure 2a. A spherical indenter composed of triangulated mesh was exported from the corresponding *.STL file where the nodes of each triangular element, grouped as a particle type were predefined. The indenter is run with constant load or depth providing the opportunity to model both load-controlled and depth-controlled scratch tests. The model parameters are listed in Table 1.

For faster computations, parallel processors using the message passing interface (MPI) technique and spatial decomposition of the simulation domain were used on a Linux-based cluster consisting of 2 processors with 12 cores each to run the user-SMD code. In MPI simulation runs, the number of cores is also increased to reduce the net CPU time. A high-sliding velocity also leads to reduced simulation run time. However, for a fast moving indenter both the un-transmitted thermal stress (high Peclet number) and the stress waves reflected from the substrate boundary in previous time steps can interfere and cause large fluctuations in the stress generated. Although the sliding velocity can be varied within a given range for accurate results, it is kept optimal for fast and stable simulations. As in the Courant–Friedrichs–Lewy (CFL) condition, the stable time step δt, for an explicit time integration is the smallest time step for particles of mass density ρ, bulk modulus K and cell size l_0, as given in equation 1[28]:

Like many mesh-based methods using CFL time step criteria, MPM uses mass scaling to scale-up the mass of the particle that has the smallest time step, thereby increasing the time step size and reducing the total computational time. The mass scaling factor, m_s has been optimized $m_s = 1e6$ in current simulations) to achieve a low computational cost as well as stable and accurate results.

Since the simulation results are resolution dependent, both the particle-size in the substrate and the element size in the indenter were reduced stepwise from 20 to 5 μm to obtain accurate results independent of discretization effects by extrapolating the converging data at 0 resolution. As we reduce the triangulated element size in the indenter, we approximate it to a sphere from a polyhedron. As we reduce the particle resolution, the number of particles in the substrate

increases according to the power of cube. Hence a higher number of iterations are required per time step to complete the total run time. The number of iteration per time step per processor i in LAMMPS simulations is related to the number of particles N at particle resolution l_0 and processors P. The total number of iterations/the CPU time I_t is the ratio between i and time step δt.

$$\delta t \leq \frac{l_0}{c} = \frac{l_0}{\sqrt{\frac{K}{\rho}}} = \frac{m_s}{\sqrt{l_0}} \tag{1}$$

$$i \propto \frac{N}{P} = \frac{1}{l_0^3 P} \tag{2}$$

$$I_t = \frac{i}{\delta t} = \frac{1}{m_s P l_0^{2.5}} \tag{3}$$

Table 1: MPM ploughing model parameters.

Parameters	Symbol	Values/expression
Rigid spherical indenter radius	R_i	0.2mm, 0.5mm and 1.5mm
Semi-cylindrical substrate radius	R_s	0.25mm
Sliding distance of indenter	l	0.6mm
Semi-cylindrical substrate length	l_s	$l + 2r_i$
Substrates MPM particle cell size	r_p	5, 10, 15 and 20 μm
Indenters triangulated mesh element size	r_t	5, 10 and 20 μm
Sliding velocity of indenter	v_s	0.1 mm/s
Mass scaling factor	m_s	1e6
Boundary conditions	$\mathfrak{p}, \mathfrak{f}, \mathfrak{f}$	periodic, fixed, fixed

2.1 MPM particles interaction pair style

MPM particles interact through an interpolation function, W which transfers information between grid and particles. W is of compact support and can only interact with nearby nodes up to a distance $2h$ where h is the mesh node spacing. W is given by the dyadic product of 1-D, cubic B-splines [29].

At the beginning of each time step, information about the velocity, stress, external forces, deformation gradient, thermal energy and volume is located with the particle. These properties then evolve according to the Modified Stress Update Last (MUSL) scheme. First the particle's mass, velocity and heat are interpolated to the nearby nodes using the interpolation function and laws of conservation of mass, momentum and energy. Now the grid forces are computed from the divergence of particle's stress fields from nearby nodes. The heat rate is computed from the product of the thermal conductivity and the second derivative of the heat distribution. Then the grid velocity and heat are updated for the next time steps and then interpolated back to the particle. Simultaneously, the particle's acceleration is computed from the particle's mass and grid forces using the interpolation function. Now, the particle's position is updated by using a combination of pure PIC and FLIP (Fluid Implicit Particle) update to simultaneously obtain increased numerical stability and decreased dissipation. A FLIP update ratio of 0.99 is used in the current MPM simulations. Then grid masses and velocities are again updated using the interpolation function at the new time step. The velocity gradient at the particle

locations is computed as cross product of the nodal velocity and divergence of interpolation function. Finally, from the velocity gradient, the deformation gradient and strain increment are computed and updated respectively. From the updated deformation gradient, the simulation volume is updated. At last the stresses are computed from the strain increment using the defined material constitutive laws [29] and [24].

The MPM simulations rely on a material model/constitutive law to compute stresses and displacements in particles. The material model comprises of both hydrostatic and deviatoric stress components, corresponding to volumetric and shear deformations respectively. The volumetric deformation tensor and hydrostatic stress tensor $-pI$ (where, I is the second order identity tensor and p is the pressure) are related by the equation of state model, while shear deformation tensor ε_d and the stress deviator tensor σ_d are related by the material strength model. Thus the stress tensor σ_n is expressed as:

$$\sigma_n = -pI + \sigma_d \tag{4}$$

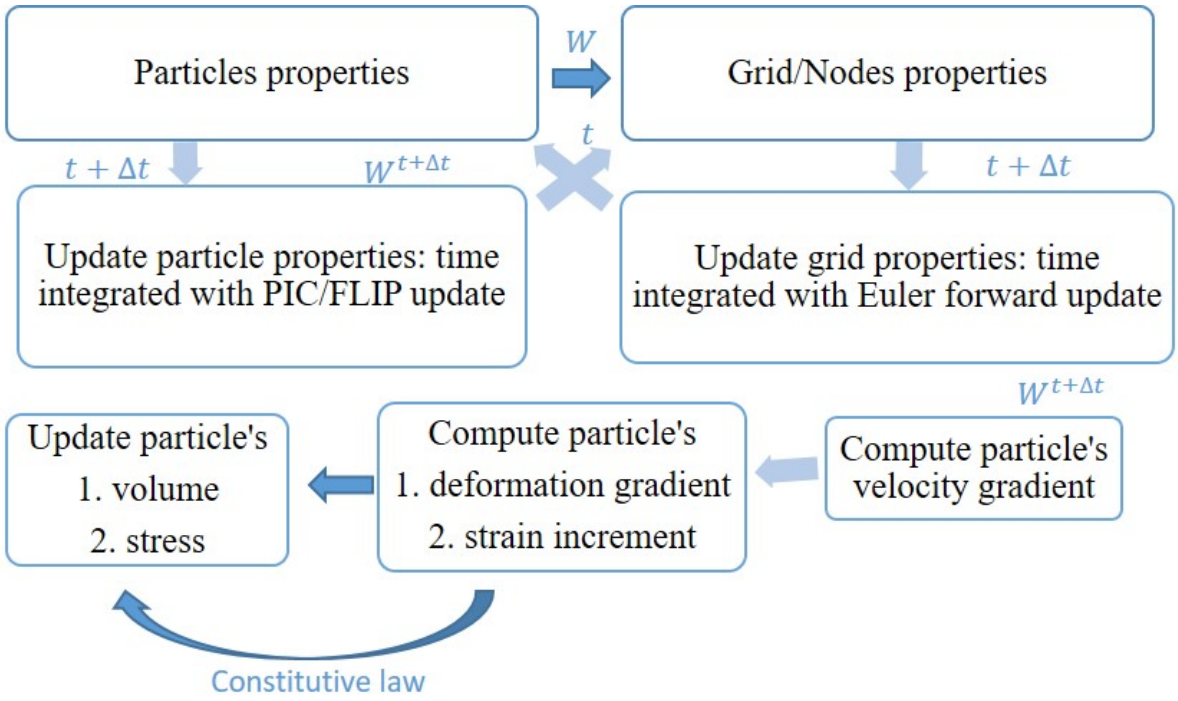

Figure 1: Schematic of the GIMPM MUSL algorithm.

For the current work, we have employed a linear equation of state to compute pressure from the volumetric deformation as shown in equation 5.1. For elastic materials the deviatoric stress is computed directly as per equation 5.1. However, for plastically deforming materials, the deviatoric stress is computed from a trial stress deviator using a history-dependent strength model as shown in equation 5.2. This plasticity algorithm is termed as 'radial return'. An elastic trial update is performed to the stress deviator now, at each time step where the second invariant of the trial deviatoric stress is now computed and compared with the von-Mises yield stress computed from the chosen material strength model. As long as the second invariant of the trial stress remains less than or equal to the yield stress, the trial yield stress is accepted as the new deviatoric stress. However, otherwise a new deviatoric stress is scaled back to the

yield surface along with the new plastic strain incremented at the given time step [29] and [24].

$$\sigma_n^{elastic} = K\mu I + 2G\Delta\varepsilon_d \tag{5.1}$$
$$\sigma_n^{trial} = \sigma_d^t + 2G\Delta\varepsilon_d \tag{5.2}$$

where $\mu = J - 1$, with J being the determinant of the deformation gradient, K is the bulk modulus and G is the shear modulus of the material modelled, $\Delta\varepsilon_d$ is the deviatoric strain increment, σ_d^{trial} is the deviatoric trail stress and σ_d^t is the deviatoric stress at time t. The material model parameters for linear elastic-perfect plastic material models used in the analytical validation of MPM are listed in Table 2.

The current yield stress is computed from the physically based isothermal Bergström van Liempt hardening relation [25]. The relation was modified by Vegter for sheet metal forming processes [30], leading to the following formulation where the yield strength σ_y^{BL} is decomposed into a static-work/strain hardening stress σ_{wh} and dynamic stress σ_{dyn} which takes into account the strain-rate and the thermal effects as shown in equation 3. This flow stress model has been included in the current MPM numerical set up to account for the interaction processes between dislocations in cell structures including the changing shape of dislocation structures. It is expressed as:

$$\sigma_y^{BL} = \sigma_{wh} + \sigma_{dyn} = \sigma_{f_0} + d\sigma_m\left(\beta_0(\varepsilon+\varepsilon_0) + \left(1 - \exp\big(-\omega(\varepsilon+\varepsilon_0)\big)\right)^g\right) + \sigma_{v_0}\left(1 + \frac{kT}{\Delta G_0}\ln\frac{\dot{\varepsilon}}{\dot{\varepsilon}_0}\right)^j \tag{6}$$

Table 2: MPM material model (linear elastic –perfect plastic) parameters for analytical validation.

Parameters	Symbols	Values
Substrate and indenter material (steel) density	ρ_s	7850 kg/m^3
Substrate and indenter specific heat capacity	c_{p_s}	502 J/kgK
Substrate and indenter thermal conductivity	κ_{t_s}	50 W/mK
Coating material (zinc) density	ρ_c	7140 kg/m^3
Coating specific heat capacity	c_{p_c}	377 J/kgK
Coating thermal conductivity	κ_{t_c}	116 W/mK
Poisson's ratio of the substrate	ν_s	0.3
Initial yield stress of the substrate	σ_{y_0}	150 MPa
Hardness of the substrate	H_s	$3\sigma_{y_0}$

The Bergström van Liempt material model constants are listed in Table 3 with their characterized values obtained for the DX56 steel sheet. The model parameters ε, $\dot{\varepsilon}$ and T represent the strain, strain rate and working temperature respectively. Besides this, the user-SMD package also has provisions for various material strength models (e.g. Johnson-Cook flow stress model) and equation of state models (e.g. Mie–Gruneisen equation of state) [29].

Table 3: Bergström-van Liempt material model parameters for DX56 steel.

Parameters	Symbols	Values
Initial static stress	σ_{f_0}	82.988 MPa
Stress increment parameter	$d\sigma_m$	279.436 MPa
Linear hardening parameter	β_0	0.482
Remobilization parameter	ω	6.690
Strain hardening exponent	g	0.5
Initial strain	ε_0	0.005
Initial strain rate	$\dot{\varepsilon_0}$	$10^{-8}s^{-1}$
Maximum dynamic stress	σ_{v_0}	1000 MPa
Dynamic stress power	j	3.182
Activation energy	ΔG_0	0.8
Boltzmanns constant	k	8.617 $\times 10^{-5} eV$

2.2 Indenter triangle and surface MPM particles interaction pair style

In this work, a contact model/pair style is developed to effectively compute the shear stress of the lubricated contact interface of the asperity ploughing through the substrate. The contact between the triangulated mesh of the indenter and the MPM particles in the substrate determines the forces during sliding of the indenter through the substrate. The pair style first detects the possibility of contact in MPM particle. It computes the shortest distance between triangle-particle centres, r. If the distance computed is less than the diameter of the particle/cell and the point of contact lies inside the projected area of the specific triangle, contact/penetration of the indenter into the substrate is determined and the contact forces are computed according to the contact model.

The contact model uses the penalty method algorithm to compute the repulsive contact force based on the penetration across the point of contact. The contact force acts in the direction normal to the contact plane, with unit normal vector $\hat{\boldsymbol{n}}_{\boldsymbol{n}}$. The particles are assumed to be elastic-cubic cells of size equalling twice the particle radius, r_c. The contact is taken to be that of an elastic cube in uniaxial compression with an elastic modulus, E. The strain in the particle penetrated by depth $\delta = r - r_c$, is given by $\epsilon = \delta / r_c$. The magnitude of the repulsive force F is computed as the product of the contact stress, $\sigma_c = E\epsilon$ and the contact area, $A_c = 4r_c^2$. A non-linearity factor $E^{'} = E(1 - \epsilon^2)$, correcting for the stiffness resulting from penetration, is multiplied by the repulsive force to prevent interpenetration for highly dynamic simulations. Hence, the contact force acts on the triangular element of the indenter penetrating the substrate MPM particles in the direction opposite to the normal to triangles contact plane (negative sign) and is expressed as:

$$F_n = \sigma_c A_c = -4E(r - r_c)r_c \tag{7.1}$$

$$\vec{\boldsymbol{F}}_{\boldsymbol{n}} = -4E^{'}(r - r_c)r\hat{\boldsymbol{n}}_{\boldsymbol{n}} \tag{7.2}$$

The friction force acting on the indenter's triangle from the substrate particles due to boundary shear strength at the interface between indenter and substrate is given as the product of τ, the shear strength at the interfacial boundary between the indenter and the substrate and A_c, the contact area for each particle-triangle interaction and $\hat{\boldsymbol{n}}_{\boldsymbol{t}}$, the unit vector along the direction of relative tangential velocity of the triangle with respect to the particle. The relative velocity, $\vec{\boldsymbol{v}}_{\boldsymbol{rel}}$

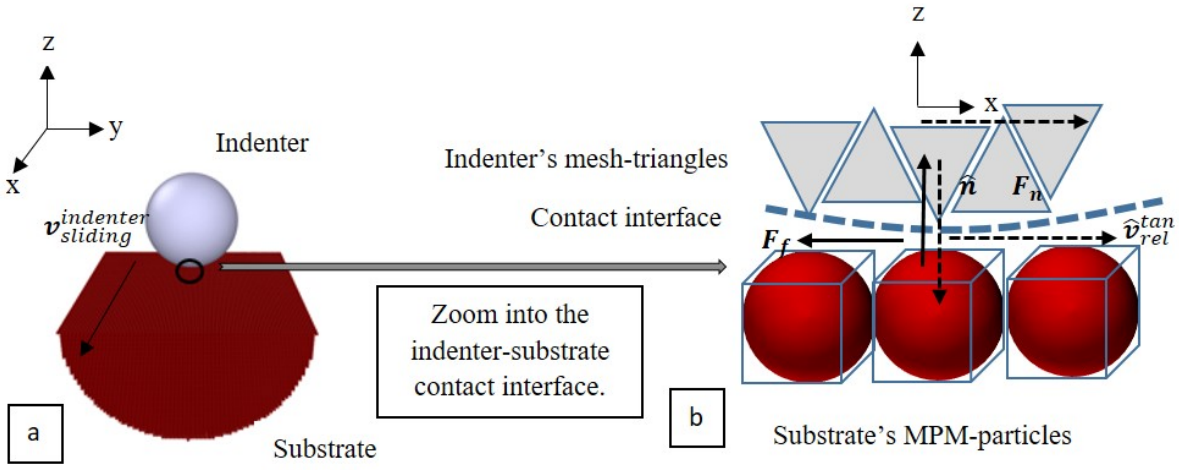

Figure 2: (a) OVITO Visualization of ploughing of MPM substrate with an STL surface [31]. (b) Schematics of contact forces between indenter's mesh triangle and substrate's MPM particles.

of a triangle with velocity $\vec{\boldsymbol{v}}_{\boldsymbol{tri}}$, with respect to a particle with velocity $\vec{\boldsymbol{v}}_{\boldsymbol{particle}}$, is calculated as the sum of the relative tangential velocity, $\vec{\boldsymbol{v}}_{\boldsymbol{tan}}$ and relative normal velocity, $\vec{\boldsymbol{n}}_{\boldsymbol{norm}}$.

$$\vec{\boldsymbol{F}}_{\boldsymbol{f}} = -4\tau A_c \hat{\boldsymbol{n}}_{\boldsymbol{t}} \tag{8.1}$$

$$\vec{\boldsymbol{v}}_{\boldsymbol{rel}} = \vec{\boldsymbol{v}}_{\boldsymbol{particle}} - \vec{\boldsymbol{v}}_{\boldsymbol{tri}} = \vec{\boldsymbol{v}}_{\boldsymbol{tan}} + \vec{\boldsymbol{v}}_{\boldsymbol{norm}} = \vec{\boldsymbol{v}}_{\boldsymbol{tan}} + (\boldsymbol{v}_{\boldsymbol{rel}} \cdot \hat{\boldsymbol{n}}_{\boldsymbol{n}})\hat{\boldsymbol{n}}_{\boldsymbol{n}} \tag{8.2}$$

$$\vec{\boldsymbol{v}}_{\boldsymbol{tan}} = v_{tan}\hat{\boldsymbol{n}}_{\boldsymbol{t}} = \vec{\boldsymbol{v}}_{\boldsymbol{rel}} - (v_{rel} \cdot \hat{\boldsymbol{n}}_{\boldsymbol{n}})\hat{\boldsymbol{n}}_{\boldsymbol{n}} \tag{8.3}$$

where the unit vector normal to contact plane,$\hat{\boldsymbol{n}}_{\boldsymbol{n}}$ is expressed as the ratio between the distance vector, $\vec{r}$ and its magnitude, $\vec{\boldsymbol{n}}_n = \vec{\boldsymbol{r}}/\|\boldsymbol{r}\|$ and the unit vector tangential to the contact plane $\hat{\boldsymbol{n}}_{\boldsymbol{n}}$ is expressed as the ratio between the tangential velocity vector and its magnitude, $\hat{\boldsymbol{n}}_{\boldsymbol{t}} = \vec{\boldsymbol{v}}_{\boldsymbol{tan}}/\|\boldsymbol{v}_{\boldsymbol{tan}}\|$. The magnitude of any vector is computed by the norm function expressed as $\|\boldsymbol{vector}\|$ The net force on the particles $\vec{\boldsymbol{F}}_{\boldsymbol{P}}$, acts opposite to the net force on triangles $\vec{\boldsymbol{F}}_{\boldsymbol{T}}$, as shown in figure 2, is expressed by:

$$\vec{\boldsymbol{F}}_{\boldsymbol{T}} = \vec{\boldsymbol{F}}_{\boldsymbol{n}} + \vec{\boldsymbol{F}}_{\boldsymbol{f}} = -\vec{\boldsymbol{F}}_{\boldsymbol{P}} \tag{9}$$

The total contact area between the indenter and substrate is given as the sum of individual particle- triangle contact area (N particles in contacts)

$$A_{Total} = \sum_{i=1}^{N} A_c^i = 4Nr_c^2 \tag{10}$$

The boundary layer shear strength of the contact interface can be computed using one of the two models that have been developed using experimental characterization and fitting. The first model computes the boundary layer shear strength as a function of contact pressure, temperature and sliding velocity. The second function takes the boundary-layer shear strength as a fraction (interfacial friction factor) of the bulk shear strength and the real contact area as a fraction of the nominal contact area, A_c. The interfacial shear stress model parameters have been determined experimentally as explained in section 3.

Interfacial shear stress model 1

A power-law expression for boundary-layer shear stress as a function of the nominal pressure P_c, sliding velocity v_s and the contact temperature T_c has been implemented in the triangles-particles interaction pair style as equation 11.1.

where C_p is the pressure constant,C_T is the temperature constant, C_v is the velocity constant, n_p is the pressure exponent, n_v is the velocity exponent and n_T is the temperature exponent. The C's and n's are experimentally fit factors. Most shear strength-pressure relations obtained from the literature include complex power law relations. For example, the shear strength between stearic acid and calcium stearate on glass, or calcium carbonate and dodecane on glass, is a sum of more than one pressure term combined in various constants and exponents [32]. To include multiple pressure terms in the 1^{st} interfacial shear stress model, the interfacial shear strength-pressure relation in equation 11.1 is expressed as:

$$\tau = C_p P_c^{n_p} C_v v_s^{n_v} C_T \exp -\frac{n_T}{T_c} \tag{11.1}$$

$$C_p P_c^{n_p} = \left(\left(C_{p_1} P_{nom}^{n_{p1}} \right)^{n_{p11}} + C_{p12} \left(\left(C_{p_2} P_{nom}^{n_{p2}} \right)^{n_{p22}} + C_{p123} \left(C_{p_3} P_{nom}^{n_{p3}} \right)^{n_{p33}} \right)^{n_{p23}} \right)^{n_{p123}} \tag{11.2}$$

where $P_{nom} = F_n/A_c$, is the nominal pressure obtained between each indenter's triangle and MPM particle in contact. The coefficients and exponents in the equation 11.2 can be arranged to obtain a simplistic Columbic friction law as well. In the equation 11.1, the contact temperature is obtained from the simulations for sliding as the wall temperature of indenter T_c. The relative tangential velocity of the indenter's triangle with respect to the MPM particle in contact v_{tan}, is taken locally as v_s. The coefficients C_p, C_v and C_T and exponents n_p, n_v and n_T can be obtained through experiments in a linear sliding friction test by varying the contact pressure, sliding velocity and temperature [33].

$$\vec{\boldsymbol{F}}_{\boldsymbol{f}} = -f\kappa r_a A_c \hat{\boldsymbol{n}}_{\boldsymbol{t}} \ \forall r_a, f\epsilon[0,1] \tag{12}$$

Interfacial shear stress model 2

A second interfacial shear stress model is developed to compute the boundary layer shear strength in a partial contact considering the roughness of the interface [33]. The interfacial shear strength, τ varies from 0 for a frictionless contact to κ, the shear strength of the bulk for a perfectly uncontaminated surface. The ratio of the interfacial shear strength to bulk shear strength is the interfacial friction factor, $f = \tau/\kappa$. The real contact area for contact of a rough surface $A_r = r_a A_c$, is a fraction r_a of the nominal contact area, A_c. The friction force in the 2^{nd} interfacial shear stress model is expressed as:

3 Experimental procedure

The experimental procedure consists of experimental characterization for the MPM model inputs and experimental validation of the MPM model results. First, the constitutive behaviour of the steel substrate has been characterized for the material model and listed in Table 3. Secondly, the boundary layer shear strength of the lubricant on the steel substrate has been characterized for the interfacial shear stress model. Finally, the numerical results of MPM single-asperity sliding model were validated with ploughing experiments.

3.1 Boundary shear strength characterization

The boundary layer shear strength characterization of 'Quaker Ferrocoat N136' lubricated-DX56 steel interface with varying contact pressure was done using a linear sliding friction test set-up as shown in figure 4. The experimental procedure and the test set-up parameters has been described in the thesis of Karupannasamy [33] and applied in the boundary shear characterization experiments for verifying the repeatability and reproducibility previously obtained results. Figure 3 shows the friction plots for various test loads and the computed boundary layer shear strength of the lubricated contact as a function of the contact as obtained from the experiments. The current MPM model uses the 1^{st} interfacial shear stress model computes the boundary layer shear strength τ_{BL}, as a function of nominal contact pressure with coefficient $C = 1.34$ and exponent $n = 0.88$ expressed in [33] as:

$$\tau_{BL} = 1.34 P_{nom}^{0.88} \tag{13}$$

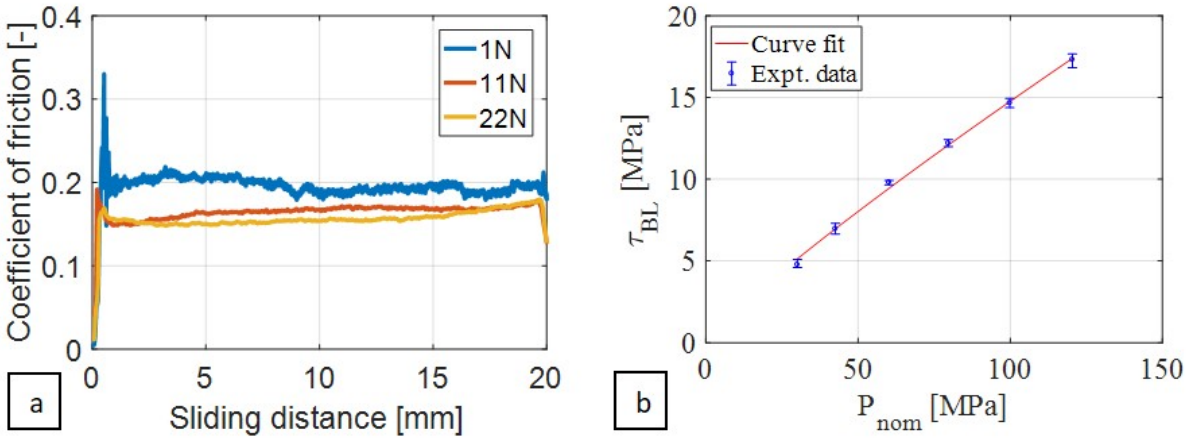

Figure 3: (a).Friction measurements with the linear sliding friction tester for various normal loads F_n= 1,11 and 22N. (b) Boundary layer shear strength measurements for lubricated line contact.

3.2 Ploughing experiments

The ploughing experiments on the 'Quaker Ferrocoat N136' lubricated DX56 steel sheet were done using the linear friction tester with 3 repetitions, as shown in figure 4. The linear friction tester consists of a XY linear positioning stage driven separately by actuators as shown in figure 4B. A horizontal beam supports the loading tip and moves the Z-stage using a linear and piezo actuator for coarse and fine displacement respectively while applying the normal load. The normal load is applied using a force controlled piezo actuator, connected to a PID control loop feedback system so the system can operate load controlled. The friction forces are measured by a piezo sensor along the loading tip as shown in figure 4A. An example of the friction signal divided by the normal load is shown in figure 3a, the coefficient of friction as a function of the sliding distance.

A spherical bearing ball of 1mm and 3mm diameter has been used as indenters. Different loads, ranging from 1-50 N, were applied on these balls to perform load controlled ploughing experiments. The plots for forces on the indenter were obtained from the linear sliding tester

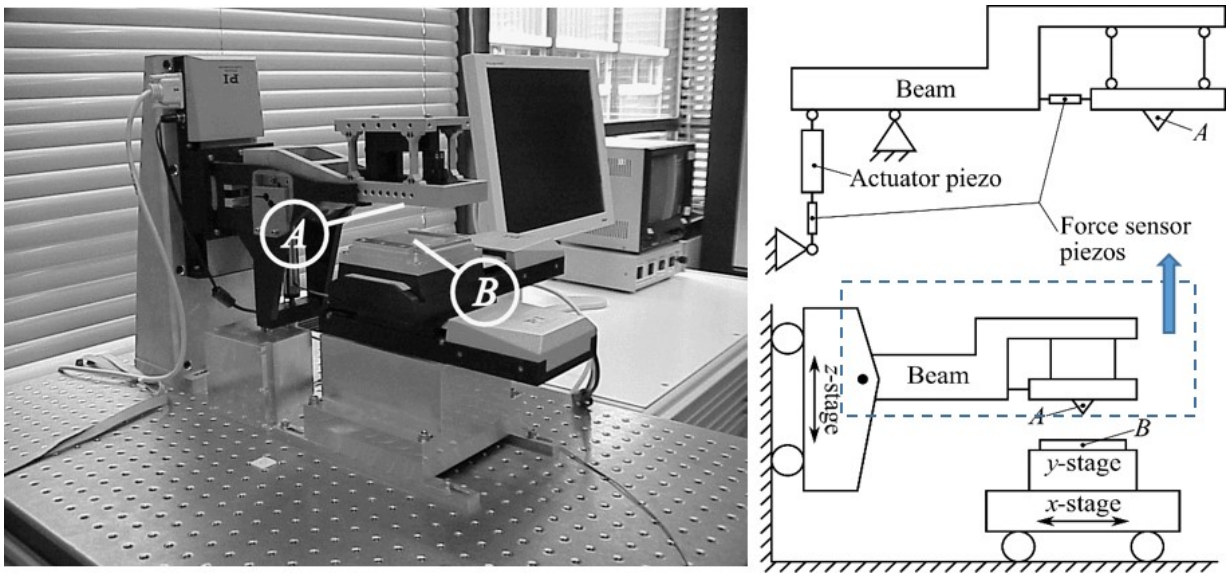

Figure 4: Linear friction tester for boundary shear characterization and ploughing experiments with schematic of (A) loading tool tip and (B) substrate test specimen.

and the average coefficient of friction for the steady state was obtained for all test loads. The wear track was studied under both optical and confocal microscopes to measure the wear track.

4 Results and discussion

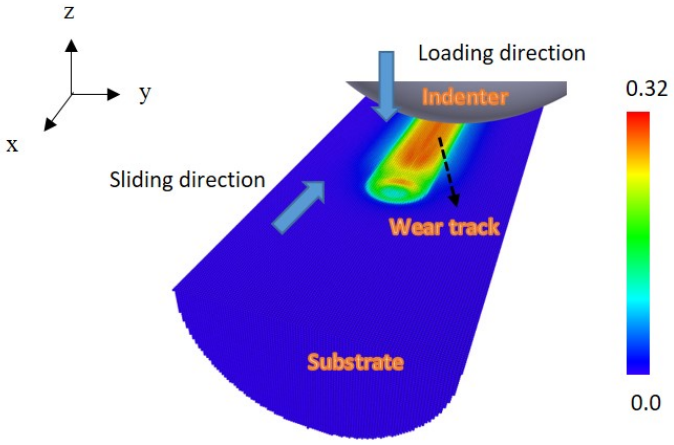

Figure 5: MPM simulation of an indenter ploughing through a substrate representing plastic strain.

The MPM-simulation of single-asperity ploughing a substrate was performed for the purpose of model validation in two steps. The analytical validation was included to compare the numerical model results with the corresponding results from available theoretical expressions. Also the MPM simulation results have been compared to experimental data. In the coordinate system used in the simulation, sliding/ploughing (subscript 'p') occurs along positive x-axis and loading (subscript 'i') occurs along negative z- axis as shown in figure 5. The MPM ploughing model parameters used have been listed in tables 1, 2 and 3.

4.1 Analytical validation of MPM method

Initial MPM simulations of single-asperity sliding were performed with frictionless contact on a substrate with ideal, perfectly elastic and elastic-perfectly plastic material behaviour. An indenter of radius 0.2 mm was used to plough through the given substrate. The simulations were performed for particle and triangle resolutions ranging from 20-5μm in order to do a convergence study on the model results. The friction force and penetration depth resulting from the MPM simulation showed linear convergence and a linear regression analysis was done to extrapolate the result at zero particle size. The spatial grid convergence study is typically done to obtain results independent of particle/grid size [34].

4.1.1 Validation with perfectly elastic material behaviour

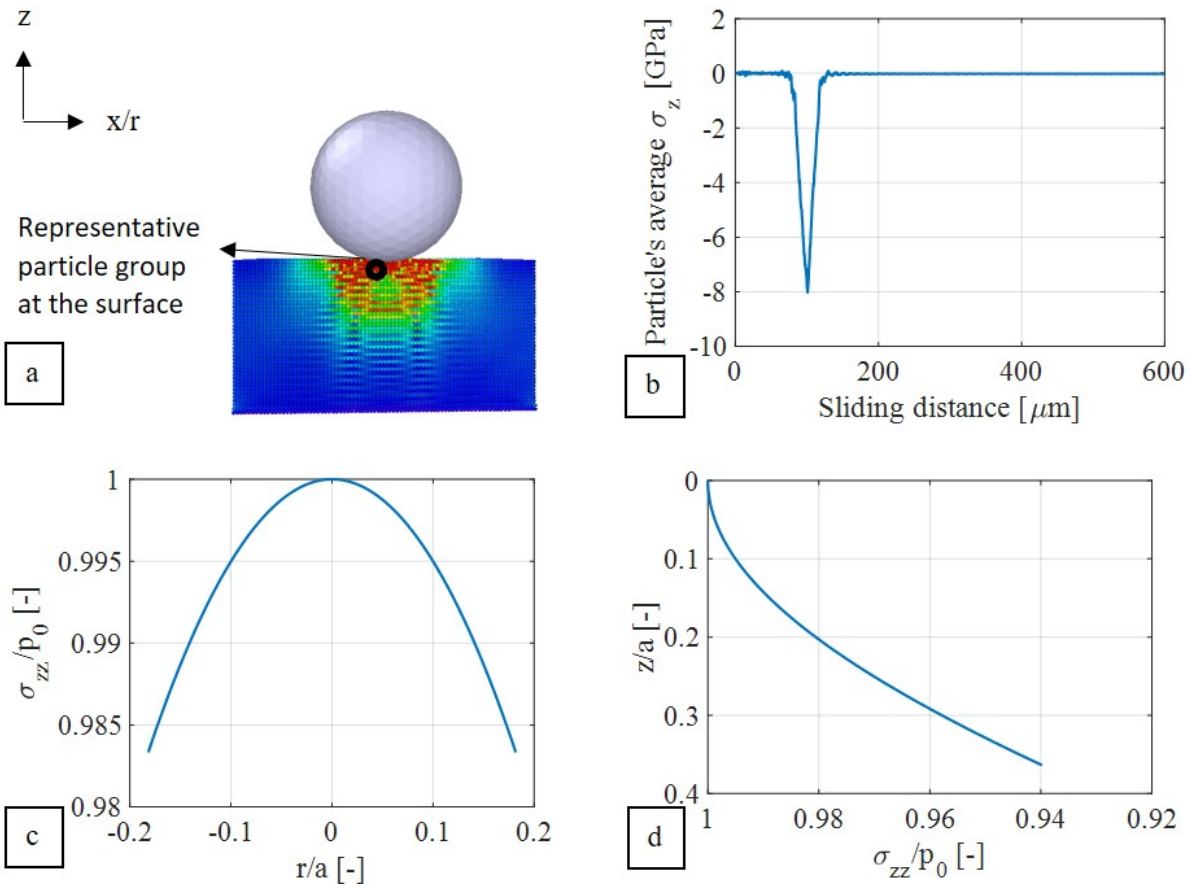

Figure 6: (a) Cauchy stresses developed in the substrate with particle of size 5 μm (encircled in black) for an applied load of 6N, (b) averaged, z-component of per-particle stress tensor and sub-surface stress σ_{zz} variation along (c) radial direction and (d) depth normalized by the maximum Hertzian contact pressure p_0 and plotted against distance from point of contact normalized by contact width a.

First, for ploughing under elastic conditions, the penetration depths and mean contact stress generated in the MPM model for a range of applied loads were compared to that obtained using Hertzian point contact equations and Hamilton's equations for stresses beneath a sliding spherical contact respectively [35]. To compute the MPM results such as Cauchy stresses and penetration, a representative volume of a particle on the surface of the substrate along the ploughing track, was grouped and defined, as shown in figure 6a. The particle-group's

properties such as the average stress history and the position of centre of mass are mapped during run time. For example, figure 6b shows the component of the symmetric Cauchy stress tensor in z direction σ_{zz}, averaged for the selected group of particles.

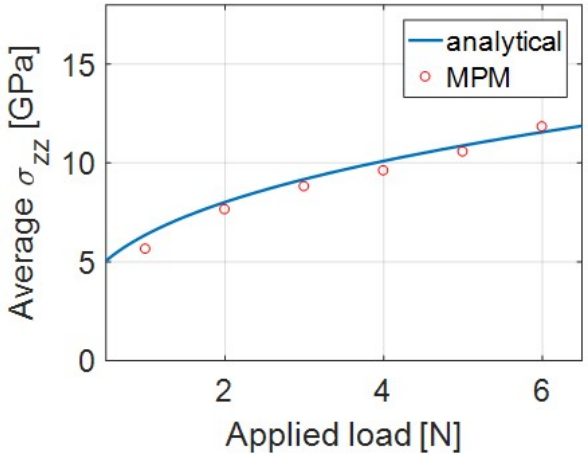

Figure 7: Mean Cauchy stress in z axis vs applied loads for sliding through perfectly elastic substrate.

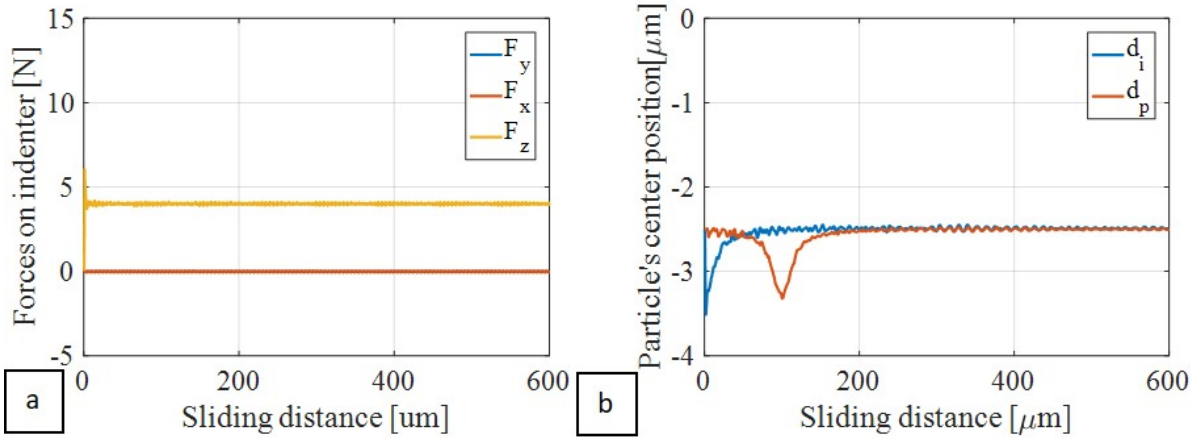

Figure 8: (a) Forces acting on the indenter sliding through an elastic substrate and (b) position of the centre of mass of the particle-group located on the surface along the MPM-simulated wear track.

Since the stresses obtained from MPM are defined per-particle and averaged for the region occupied by the particle-group, the contact pressure (magnitude of contact stress in z-direction) obtained from the Hertzian elastic point contact must be averaged over the same volume as that occupied by the particle-group for the sake of accurate comparison. The contact width a_e and the maximum contact pressure p_0 with a load F for a Hertzian point contact are expressed in equation 14.1 and 14.2 respectively. To obtain the mean contact pressure, the variation of stress field σ_{zz} in the radial plane (x-y plane) $\sigma_{zz}\ (r) = \sigma_{zz}\ (x) = \sigma_{zz}\ (y)$ and depth (-z-axis) $\sigma_{zz}(z)$, as shown in figure 6c and d, are averaged for a particle/cell volume of size r_p, as expressed in equation 14.3. The simulated, average σ_{zz}-per-particle is then compared with the averaged stress field σ_{zz} for a range of indentation loads. From figure 7, a near perfect agreement between the average stress σ_{zz} results from the MPM model and the Hertzian based analytical method of Hamilton [35] for loading of a perfectly elastic substrate is observed.

In the case of frictionless ploughing of a perfectly elastic material both the model and theory calculate zero friction forces due to lack of plastic deformation and complete elastic recovery of the substrate. The numerical model shows the expected elastic recovery of the elastic substrate and the corresponding zero friction forces in figure 8a and b as the position of the centre of mass of the selected particle ($r_p = 5\mu m$) is restored to its original position after the passage of the indenter. The penetration depth of the spherical indenter is computed by the difference in the position of the centre of mass of particle-group on the surface of the substrate which are elastically deformed from their reference position as the sliding-indenter comes in contact with them. The simulated penetration depth of the indenter is then plotted against a range of applied loads and compared with the penetration depth in the case of an elastic Hertzian point contact obtained as $d_i = a_e^2/R_i$, as shown in figure 9, with good agreement.

$$a_e = \sqrt[3]{3FR_i(1-\nu^2)/4E} \tag{14.1}$$

$$p_0 = 3F/(2\pi a_e^2) \tag{14.2}$$

$$\sigma_{zz-perParticle} = p_{mean} = \frac{\int_0^{r_p}\int_{-0.5r_p}^{0.5r_p}\int_{-0.5r_p}^{0.5r_p}\sigma_{zz}\,(x)\,dx\,(y)\,(z)dydz}{\int_0^{r_p}\int_{-0.5r_p}^{0.5r_p}\int_{-0.5r_p}^{0.5r_p}dxdydz} \tag{14.3}$$

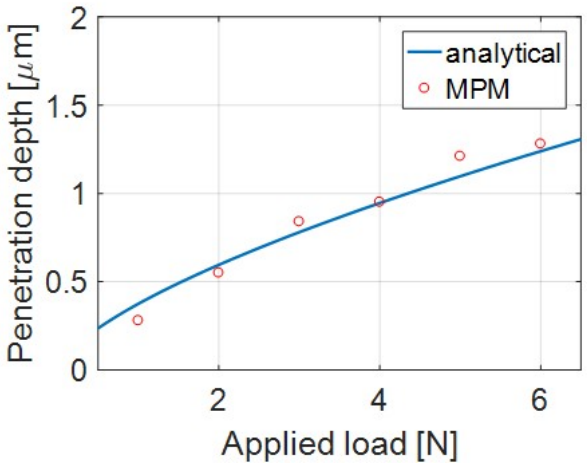

Figure 9: Penetration depths vs applied loads for sliding through perfectly elastic substrate.

4.1.2 Validation with perfectly plastic material behaviour

Similarly, for ploughing of an perfectly plastic substrate, the ploughing depth obtained from the MPM model for ploughing through a perfect-plastic substrate has been also verified with that obtained by balancing the load F applied by the rigid spherical indenter to the reaction force due to the permanent plastic deformation (hardness, H) of the substrate over the sliding contact area A_p. Expressing A_p using the contact width a_p and expressing the penetration depth $d = a_p^2/R_i$, we have the relation:

$$F = HA_p \tag{15.1}$$

$$A_p = \pi a_p^2/2 \tag{15.2}$$

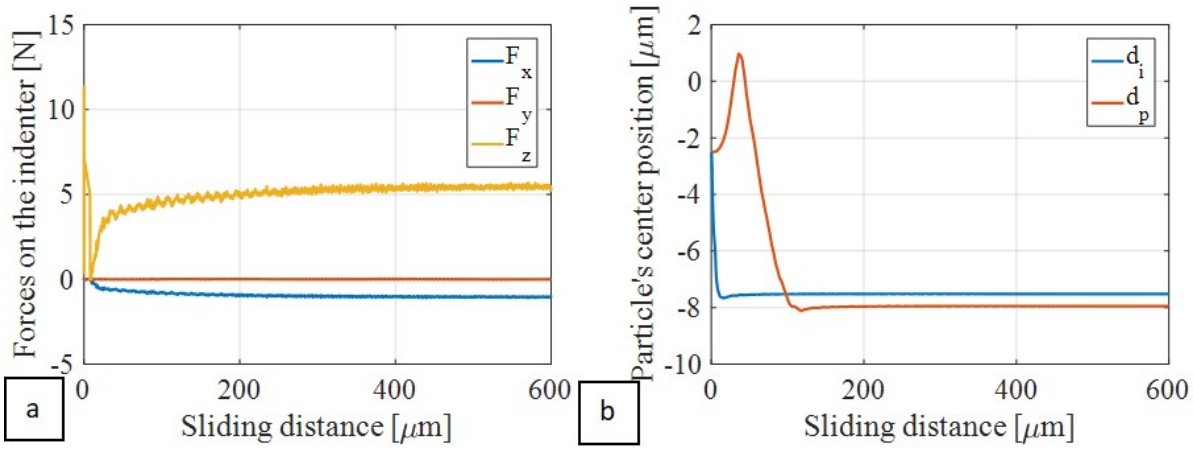

Figure 10: (a)Forces on the indenter for depth controlled ploughing and (b)sliding depths (position of the centre of mass of the particle-group at the surface of the substrate) for load controlled ploughing.

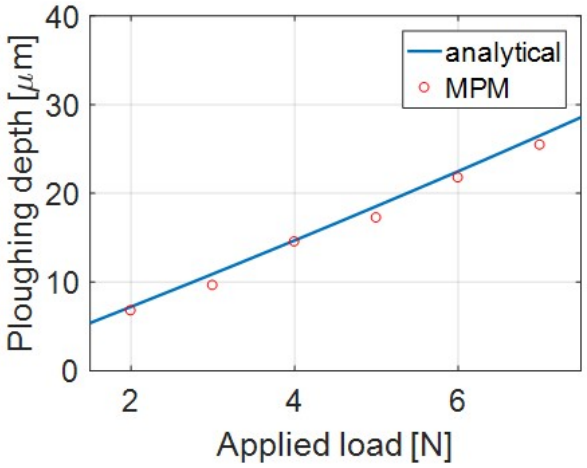

Figure 11: Ploughing depths vs app loads for ploughing through perfectly plastic substrate.

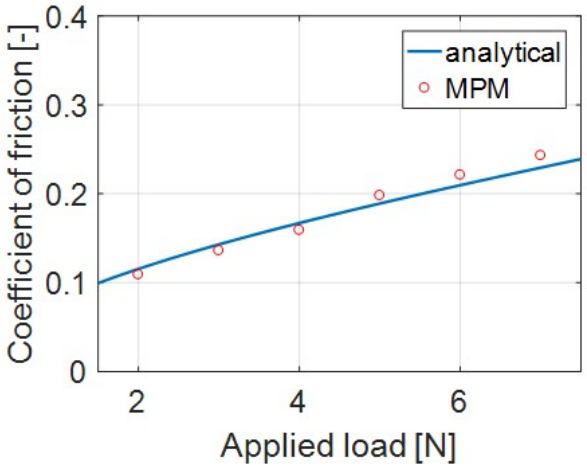

Figure 12: Friction coefficient vs ploughing depths in for perfectly plastic substrate.

During the sliding of the indenter over a perfectly plastic substrate the particles in contact with the frontal half of the indenter are permanently deformed and lose contact with the rear half of the indenter as the indenter slides over it. In order to balance the load applied on the indenter with this reduction in contact area, the depth of ploughing doubles as compared to the depth of indentation. Correspondingly, during a depth-controlled ploughing of a perfect plastic substrate the reaction force is halved during ploughing in order to follow load balance. Both of these effects due to load balancing were observed in the ploughing simulation of perfect plastic substrate as shown in figure 10a and b. The ploughing depths obtained from MPM model over a range of applied loads show good agreement with the analytical results as shown in figure 11.

In order to obtain the coefficient of friction for frictionless ploughing of a perfectly plastic substrate, the work of Tabor was referred [1]. As the material behaviour is rigid-plastic, both the tangential force f and normal force F on the substrate result in a pressure both in the tangential direction, p_t and normal direction p both equal to hardness H. Since there is no shear strength at the interface, the overall friction coefficient μ, is given as the ratio of the vertical and horizontal projection of the contact area between the spherical indenter and rigid-plastic substrate, represented as A_v and A_p respectively. A_p is computed from equation 15 while A_v can be computed as a the area of the segment formed by the intersection of the contact plane on the spherical indenter 'mid yz-plane' and is expressed as:

$$\mu = f/F = HA_v/HA_p = A_v/A_p \tag{16.1}$$

$$A_v = R_i^2\theta - a_p(R_i - d_p) \tag{16.2}$$

where $\theta = \arctan a_p/(R_i - d_p)$ is half angle subtended by the contact line at the indenter's centre. On plotting the coefficient of friction resulting from the MPM simulation against that obtained from equation 16, good agreement between both results were obtained, as shown in figure 12.

4.2 Experimental validation of sliding asperity friction and wear

For experimental validation of the MPM model of ploughing through DX56 steel sheet, indenters of diameter 1 mm and 3 mm were chosen. The Bergström van Liempt material model and the friction model based on 'Interfacial shear stress model 1' for the Quaker lubricated boundary layer on steel given in equation 6 and 13 respectively were included in the MPM-model. A convergence study was performed from the data obtained from the ploughing simulation at particle resolutions of 5, 10 and 20 μm and triangulated element sizes of 5, 10 and 20 μm. The result at zero resolution was extrapolated using the convergence order obtained from the convergence study. Because of the effect of particle resolution on the forces both due to the plastic deformation and the boundary layer shear, the results for varying particle resolution converged non linearly, with a convergence order varying from 0.5 to 2.

A section of the ploughed track on the DX56 steel sheet specimen, tested using a 1mm diameter spherical indenter under an applied load of 7N, was observed using the confocal microscope and the digital optical microscope at 50X magnification, and shown in figure 13a and b. The presence of pile-up and cracks at the edge of the ploughed track obtained from the experiments typical to ploughing of plastically deforming substrate can be seen in figure 13a and b. The ploughed profile of the simulated substrate with $5\mu m$ particles was also visualized using the OVITO software and shown in figure 13c with the same colour scale as the images of the ploughed profile from the confocal microscope. Further, the profile of the ploughed cross section

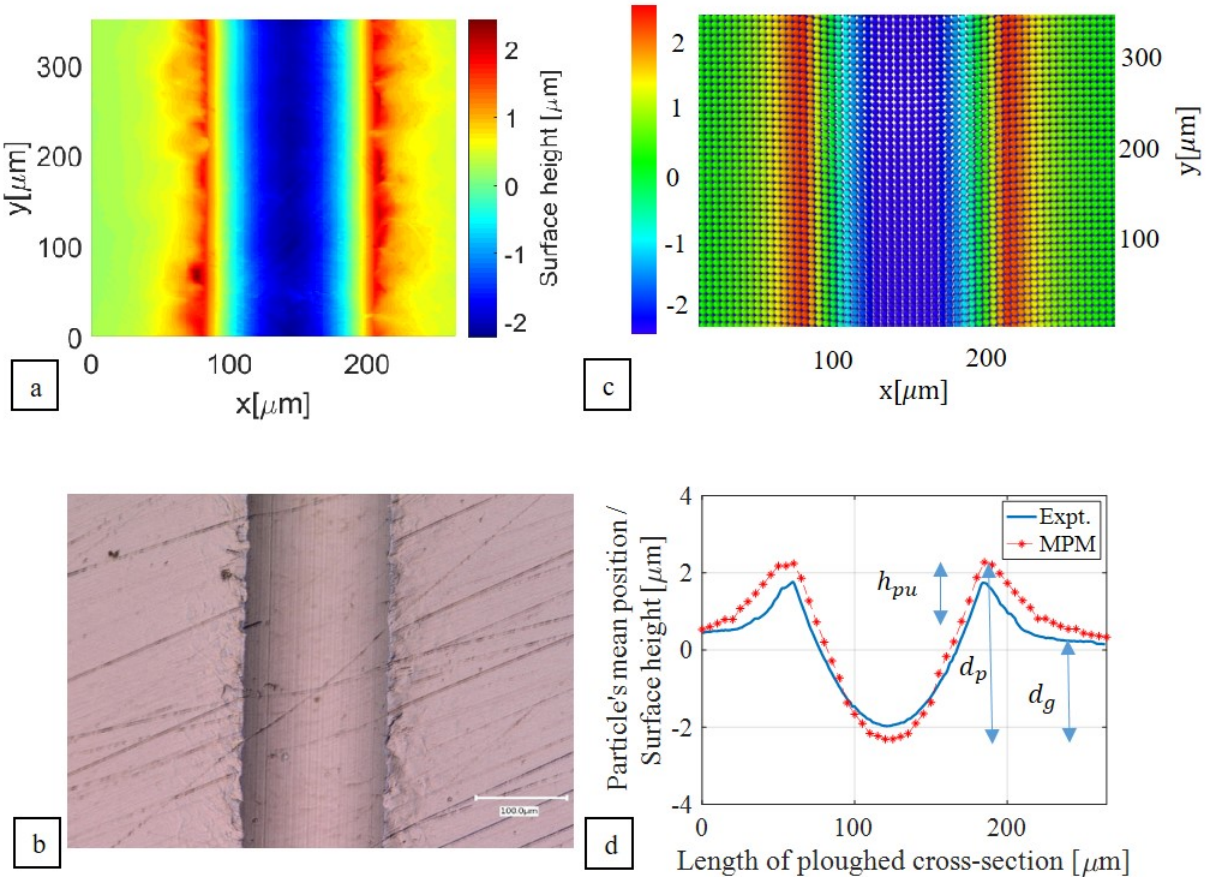

Figure 13: Ploughed track for a lubricated-7N load controlled scratch test using a 1mm indenter in 1: linear sliding friction tester as seen using (a) confocal microscope, (b) digital optical microscope at 50x magnifications (c) 2: MPM simulation ($5\mu m$ particle resolution) and (d) the profiles of the ploughed cross-sections obtained from MPM-ploughing model and ploughing experiment.

obtained from the experiments were compared with that obtained from the MPM simulations, and seen to be in good agreement, as shown in figure 13d. The substrate-material, removed from the groove by the sliding asperity, is displaced into to the piled-up ridge at the edge of the ploughed track resulting in zero wear volume.

As shown in figure 13d, the total ploughing depth d_p, was obtained as the sum of the pile-up height h_{pu} and the groove depth d_g of the ploughed track, both of which were calculated with respect to the mean surface height of the undeformed DX56 steel's surface and mean position of the particles on the surface prior to ploughing experiments and simulations respectively. The total ploughing depths calculated from the ploughing experiments and the MPM model were plotted in figure 14 for two indenters of different radii over a range of loads. The MPM model can be seen to correctly compute the ploughing depths for an asperity sliding through the steel substrate. The test loads were chosen such that ploughing was the sole wear mode where the material was displaced from the groove into the piled-up ridges as the indenter slid through the substrate, thereby avoiding the generation of any wear debris. As no material was removed or detached from the substrate, both the material under the ploughed groove and in the piled-up ridge supported the applied load during the ploughing of the steel substrate.

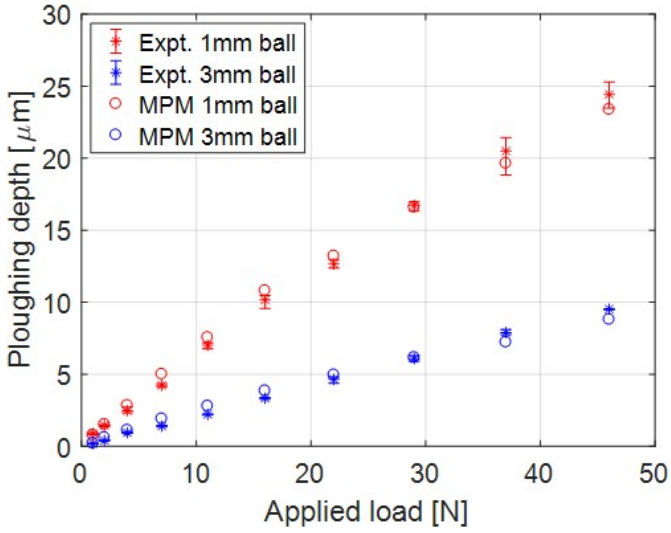

Figure 14: Ploughing depths for load controlled tests carried out with indenters of diameter 1mm and 3mm on lubricated steel sheet with the linear sliding friction tester and MPM-ploughing model that includes the Bergström-van Liempt material model and interfacial shear stress model 1.

The friction plots obtained from both experiments and simulation of a given particle resolution are plotted in figure 15a and b respectively. The ratio of the net friction forces on the indenter to the range of applied loads, obtained from the experiments and the extrapolated MPM simulation results were compared for the purpose of validation as coefficient of friction plots as shown in figure 16. The measured and calculated coefficient of friction are very close for different loads and indenter radii. It can be seen that the MPM model accurately predicts friction forces in ploughing through the steel sheet.

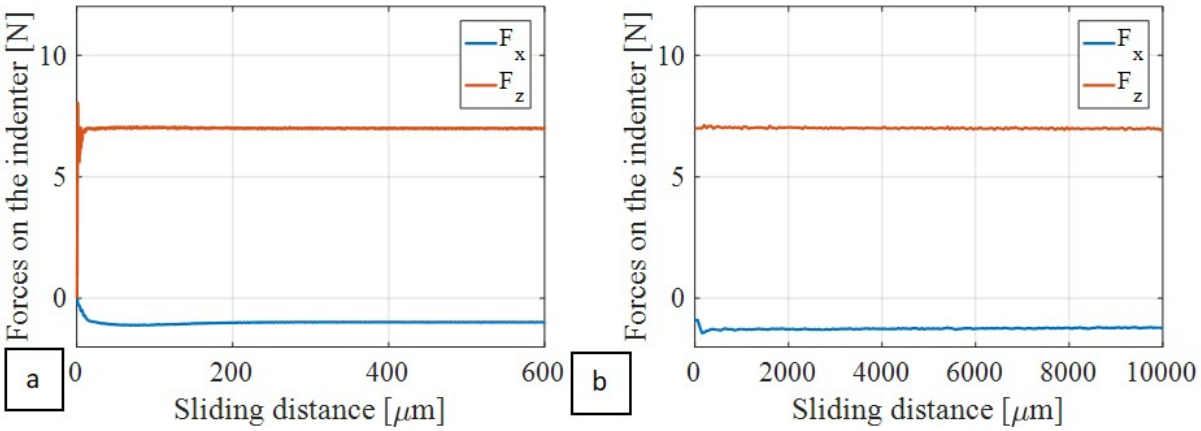

Figure 15: Forces acting on a 1mm diameter indenter for a lubricated-7N load controlled scratch test obtained from (a) linear sliding friction tests and (b) MPM simulation ($5\mu m$ particle resolution).

In the context of building and validating the MPM-based ploughing model, it is important to note that the aim is to model only the ploughing behaviour of a single asperity sliding through a steel substrate. The MPM based model incorporates features of both mesh and particle-based numerical methods to model the complex ploughing behaviour. The test

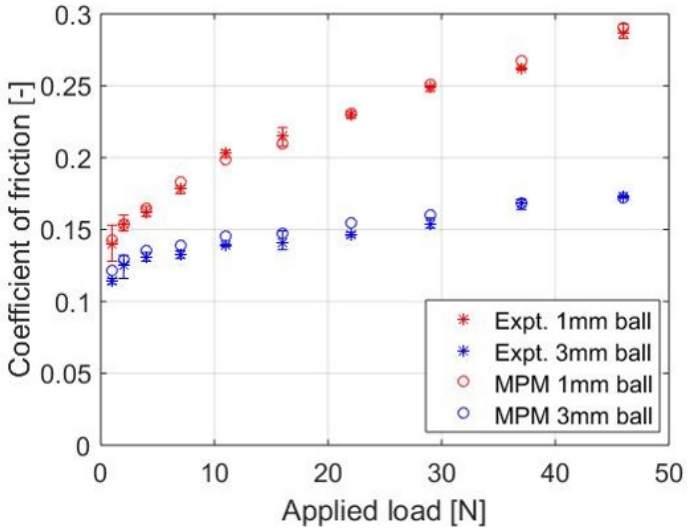

Figure 16: Coefficient of friction for load controlled test carried out with indenters of diameter 1mm and 3mm on lubricated steel sheet with the linear sliding friction tester and MPM-ploughing model that includes the Bergström-van Liempt material model and interfacial shear stress model 1.

materials, DX56 steel and Quaker Ferrocoat N136 lubricant are commonly used in forming process for making automotive bodies and metallic packaging. Moreover, the ploughing model can be further validated with similar metallic substrates given the physical models and their parameters for calculating material strength and interfacial shear stress. The current work sets the platform to further extend the model to compute friction and wear in multi-asperity ploughing. However, unlike ploughing, for modelling other abrasive and adhesive wear modes which involves generation of wear debris and material removal, further work has to be done on the damage and adhesion models which is not in the scope of the current paper.

5 Conclusion

The Material point method has been used to calculate friction forces and ploughing depth in simulating single-asperity sliding on metallic substrate. The model has been validated successfully using both elastic as well as pure plastic material behaviour with available single asperity sliding friction theories. Also results obtained using more complex material and friction laws have been compared with experimental data and found to be in good agreement to the experimental results.

Acknowledgments

This research was carried out under project number S22.1.14520a in the framework of the Partnership Program of the Materials innovation institute M2i (www.m2i.nl) and the Technology Foundation TTW (www.stw.nl), which is part of the Netherlands Organization for Scientific Research (www.nwo.nl). The authors would like to greatly acknowledge Dr.ir. Jeroen van Beeck from Tata Steel Europe R&D for his technical guidance and provision of Bergström-van Liempt material model parameters for DX56 steel.

Bibliography

[1] F.P. Bowden, A.J.W. Moore, and D. Tabor. "The Ploughing and Adhesion of Sliding Metals". In: Journal of Applied Physics 14 (1943), p. 80. DOI: 10.1063/1.1714954.

[2] E. Rabinowicz and D. Tabor. "Metallic transfer between sliding metals: an auto radiographic study." In: Proceedings of the Royal Society A: Mathematical, Physical and Engineering Sciences 208 (1951), pp. 455–475. DOI: 10.1098/rspa.1951.0174.

[3] B.J. Briscoes and D.C.B. Evans. "The shear properties of Langmuir-Blodgett layers". In: Proceedings of the Royal Society A: Mathematical, Physical and Engineering Sciences 380 (1982), pp. 389–407. DOI: 10.1098/rspa.1982.0048.

[4] H. Eyring. "Viscosity, plasticity and diffusion as examples of absolute reaction rates". In: The Journal of Chemical Physics 4 (1936), pp. 283–291. DOI: 10.1063/1.1749836.

[5] K.J. Chugg and M.M. Chaudhri. "Boundary lubrication and shear properties of thin solid films of dioctadecyl dimethyl ammonium chloride (TA 100)". In: Journal of Physics D: Applied Physics 26 (1993), pp. 1993–2000. DOI: 10.1088/0022-3727/26/11/023.

[6] R.S. Timsit and C.V. Pelow. "Shear strength and tribological properties of Stearic acid films - Part I: On glass and aluminium-coated glass". In: Journal of Tribology 114 (1992), pp. 150–158. DOI: 10.1115/1.2920854.

[7] J. Challen and P. Oxley. "An explanation of different friction and wear using asperity deformation models". In: Wear 53 (1979), pp. 229–243. DOI: 10.1016/0043-1648(79)90080-2.

[8] A.P. Green. "The plastic yielding of metal junctions due to combined shear and pressure". In: Journal of the Mechanics and Physics of Solids 2 (1954), pp. 197–211. DOI: 10.1016/0022-5096(54)90025-3.

[9] K. Hokkirigawa and K. Kato. "An experimental and theoretical investigation of ploughing, cutting and wedge formation during abrasive wear". In: Tribology International 21 (1988), pp. 51–57. DOI: 10.1016/0301-679X(88)90128-4.

[10] G. Subhash and W. Zhang. "Investigation of the overall friction coefficient in the single-pass scratch test". In: Wear 252 (2002), pp. 123–134. DOI: 10.1016/S0043-1648(01)00852-3.

[11] J.L. Bucaille, E. Felder, and G. Hochstetter. "Mechanical analysis of the scratch test on elastic and perfectly plastic materials with the three-dimensional finite element modelling". In: Wear 249 (2001), pp. 422–432. DOI: 10.1016/S0043-1648(01)00538-5.

[12] G. Kermouchea, N. Aleksya, J.L. Loubet, and J.M. Bergheaua. "Finite element modelling of the scratch response of a coated time-dependent solid". In: Wear 267 (2009), pp. 1945–1953. DOI: 10.1016/j.wear.2009.05.005.

[13] F. Elwasli, F. Zemzemi, A. Mkaddem, S. Mzali, and S. Mezlini. "A 3D multi-scratch test model for characterizing material removal regimes in 5083-Al alloy". In: Materials and Design 87 (2015), pp. 352–362. DOI: 10.1016/j.matdes.2015.07.121.

[14] D.A. Doman, D.A.R. Bauer, and A. Warkentin. "Experimentally validated finite element model of the rubbing and ploughing phases in scratch tests". In: Proceedings of the Institution of Mechanical Engineers B: Journal of Engineering Manufacture 223 (2009), pp. 1519–1527. DOI: 10.1243/09544054JEM1520.

[15] K. Holmberg, A. Laukkanen, H. Ronkainen, K. Wallin, S. Varjus, and J. Koskinen. "Tribological contact analysis of a rigid ball sliding on a hard coated surface Part I: Modelling stresses and strains". In: Surface and Coatings Technology 200 (2006), pp. 3793–3809. DOI: 10.1016/j.surfcoat.2005.03.040.

[16] Y. Gao, C. Lu, N.N. Huynh, G. Michal, H.T. Zhu, and A.K. Tieu. "Molecular dynamics simulation of effect of indenter shape on Nano scratch of Ni". In: Wear 267 (2009), pp. 1998–2002. DOI: 10.1016/j.wear.2009.06.024.

[17] X. Zheng, H. Zhu, A.K. Tieu, and B. Kosasih. "A molecular dynamics simulation of 3D rough lubricated contact". In: Tribology International 67 (2013), pp. 217–221. DOI: 10.1016/j.triboint.2013.07.015.

[18] S. Solhjoo, A.I. Vakis, A.K. Tieu, and B. Kosasih. "Single asperity nanocontacts: Comparison between molecular dynamics simulations and continuum mechanics models". In: Computational Materials Science 99 (2015), pp. 209–220. DOI: 10.1016/j.commatsci.2014.12.010.

[19] G.C. Ganzenmüller. "An hourglass control algorithm for Lagrangian Smooth Particle Hydrodynamics". In: Computer Methods in Applied Mechanics and Engineering 286 (2015), pp. 87–106. DOI: 10.1016/j.cma.2014.12.005.

[20] S. Leroch, M. Varga, S.J. Eder, A. Vernes, M. Ripolla, and G.C. Ganzenmüller. "Smooth particle hydrodynamics simulation of damage induced by a spherical indenter scratching a visco-plastic material". In: International Journal of Solids and Structures 81 (2016), pp. 188–202. DOI: 10.1016/j.ijsolstr.2015.11.025.

[21] D. Sulsky, Z. Chen, and H.L. Schreyer. "A Particle Method for History-Dependent Materials". In: Computer Methods in Applied Mechanics and Engineering 118 (1994), pp. 179–186. DOI: 10.1016/0045-7825(94)00033-6.

[22] S. Leroch, S.J. Edera, G.C. Ganzenmüller, L.J.S. Murilloc, and M.R. Rodríguez. "Development and validation of a meshless 3D material point method for simulating the micro-milling process". In: Journal of Materials Processing Technology 262 (2018), pp. 449–458. DOI: 10.1016/j.jmatprotec.2018.07.013.

[23] I. Jassim, D. Stolle, and P. Vermeer. "Two-phase dynamic analysis by material point method". In: International Journal for Numerical and Analytical Methods in Geomechanics 37 (2013), pp. 2502–2522. DOI: 10.1002/nag.2146.

[24] S. Bardenhagen and E. Kober. "The Generalized Interpolation Material Point Method". In: Computer Modelling in Engineering and Sciences 5 (2004), pp. 477–495. DOI: 10.3970/cmes.2004.005.477.

[25] P. van Liempt. "Work hardening and sub structural geometry of metals". In: Journal of Materials Processing Technology 45 (1994), pp. 459–464. DOI: 10.1016/0924-0136(94)90382-4.

[26] J. Donea, A. Huerta, J-Ph Ponthot, and A.R. Ferran. "Arbitrary Lagrangian-Eulerian Methods". In: Encyclopaedia of Computational Mechanics. John Wiley & Sons, 2004, pp. 1–23. DOI: 10.1002/0470091355.ecm009.

[27] S. Plimpton. “Fast parallel algorithms for short-range molecular dynamics”. In: Journal of Computational Physics 117 (1995), pp. 1–19. DOI: 10.1006/jcph.1995.1039.

[28] R. Courant, K.O. Fredrichs, and H. Lewy. “Uber die Differenzengleichungen der Mathematischen Physiks”. In: Mathematische Annalen 100 (1928), pp. 32–74. DOI: 10.1007/BF01448839.

[29] J.A. Nairn. “Material Point Method Calculations with Explicit Cracks”. In: Computer Modelling in Engineering and Sciences 4 (2003), pp. 649–663. DOI: 10.3970/cmes.2003.004.649.

[30] H. Vegter. “On the plastic behaviour of steel during sheet forming”. PhD thesis. University of Twente, The Netherlands, 1991. ISBN: 9789090043739.

[31] A. Stukowski. “Visualization and analysis of atomistic simulation data with OVITO - the Open Visualization Tool”. In: Modelling and Simulation in Materials Science and Engineering 18 (2010), p. 015012. DOI: 10.1088/0965-0393/18/1/015012.

[32] A. Westeneng. “Modelling of contact and friction in deep drawing process”. PhD thesis. University of Twente, The Netherlands, 2001. ISBN: 90-365-1549-1.

[33] D.K. Karupannasamy. “Friction modelling on multiple scales for deep-drawing processes”. PhD thesis. University of Twente, The Netherlands, 2013. ISBN: 978-94-91909-01-6.

[34] P.J. Roache. “Perspective: A method for uniform reporting of grid refinement studies”. In: Journal of Fluids Engineering 116 (1994), pp. 405–413. DOI: 10.1115/1.2910291.

[35] G.M. Hamilton. “Explicit Equations for the Stresses beneath a Sliding Spherical Contact”. In: Proceedings of the Institution of Mechanical Engineers C: Journal of Mechanical Engineering Science 197 (1983), pp. 53–59. DOI: 10.1243/PIME_PROC_1983_197_076_02.

Paper B

An analytical model to study the effect of asperity geometry on forces in ploughing by an elliptical asperity

Tanmaya Mishra[1*], Matthijn de Rooij[1], Meghshyam Shisode[2], Javad Hazrati[2], and Dirk J. Schipper[1]

[1]Surface Technology and Tribology, Faculty of Engineering Technology, University of Twente, 7500 AE Enschede, the Netherlands
[2]Nonlinear Solid Mechanics, Faculty of Engineering Technology, University of Twente, 7500 AE Enschede, the Netherlands

Abstract

An analytical ploughing model is used to compute the forces on a rigid, elliptical, i.e. ellipsoid and elliptic-paraboloid shaped, asperity sliding through a rigid-plastic substrate as a function of its axes size, ellipticity ratio and sliding orientation. The normal force due to the plastic deformation of the substrate and the tangential force due to the shearing of the asperity-substrate interface are calculated from the surface normal vector and the tangent vector along the direction of plastic flow. The elemental forces are integrated over the boundaries of the asperity-substrate contact to obtain the individual force components. In this way, an analytical model to study the effect of asperity geometry on ploughing forces has been developed and compared with the available theories.

Keywords: Friction modelling, Elliptical asperity, Asperity geometry, Ploughing.

Nomenclature of symbols

$OBCD$	Tetrahedral element on elliptic asperity	α	Rotation angle of $OBCD/ABCDEF$
$ABC-DEF$	Hexagonal pyramid: approx. elliptic-paraboloid	β	Angle of orientation of asperity relative to sliding direction in xy -plane
ΔBCD	Triangle (Δ) BCD: base of OBCD	γ	Sector angle subtended by $\widehat{SL}$ at O
$\widehat{SN}$	Arc $\widehat{SN}$: semi-elliptic contact bound	θ	Azimuthal angle: spherical coordinates
A_c	Asperity to substrate contact area	ϕ	Polar angle: spherical coordinates
$A_{\text{-}}$	Area of the surface element	φ	Azimuthal angle: cylindrical coordinates
A_{xy}	Projected area in xy-plane	ρ	Axial distance: cylindrical coordinates
A_{xz}	Projected area in xz-plane	κ	Shear strength of the substrate (bulk)
A_{yz}	Projected area in yz-plane	τ_{sh}	Shear strength of the interface
C	Centre of the elliptic contact base	σ_y	Uniaxial yield stress
$\boldsymbol{C}$	Cartesian coordinate system: (x, y, z)	μ	Force on asperity to applied load ratio
H	Hardness of the rigid-plastic substrate	a	Major axis of base of elliptic asperity
$\boldsymbol{F}$	Total force vector acting on the sliding asperity	a_x	Major axis of elliptic contact patch in x-axis
$F^{p/pl}$	Force on the asperity due to plastic deformation	a_y	Minor axis of elliptic contact patch in y-axis
F_f	Lateral force acting on the asperity	a_z	Reference contact radius
$F^{s/sh}$	Force on the asperity due to interfacial shear	b	Minor axis of base of elliptic asperity
$F_{x/y/z}$	Force in the x, y or z direction	c	Height of the elliptic asperity
$\boldsymbol{J}$	Jacobian transformation matrix	d	Penetration/ploughing depth of the asperity
L	End point of contact in z axis	e_x	Ellipticity ratio of asperity in x-axis
N	Contact end point in contact plane in $+y$ axis	e_y	Ellipticity ratio of asperity in y-axis
$\boldsymbol{N}$	Normal force acting on the asperity	f	Interfacial to bulk shear strength ratio
M	Plastic flow separation point in contact plane	h	Height of $OBCD/ABCDEF$
Mu	Ratio of interfacial shear strength and hardness	l	Length of $OBCD/ABCDEF$
O	Centre of the ellipsoidal asperity	m	Slope of a point on contact plane
$\boldsymbol{P}$	Polar/cylindrical coordinate system: $P(\varphi,\ u, \rho)$	$\widehat{\boldsymbol{n}}$	Unit normal vector to the surface element
$\boldsymbol{R}$	Rotation matrix	p_{pl}	Contact pressure due to plastic deformation
R	Reference radius of the asperity	r	Radius distance spherical coordinates
$\boldsymbol{S}$	Spherical coordinate system: $S(r, \theta, \phi)$	$\widehat{\boldsymbol{t}}$	Unit tangent vector to the surface element
S	Contact endpoint in xy plane, $-y$ axis	u	Height in cylindrical coordinates
X_x	Projected major axis length in x-axis	v_s	Sliding velocity
Y_y	Projected major axis length in y-axis	w	Width of $OBCD/ABCDEF$

1 Introduction

Analytical models to calculate friction due to ploughing of a plastically deforming substrate by a rigid asperity have been studied extensively [1], [2], [3], [4] and [5]. Traditionally, friction and wear during sliding of rigid asperities have been investigated by the use of plasticity, slip-line field and (upper) bounding theorems, where asperities are represented by geometrical forms in two dimensions such as wedges and cylinders and in three dimensions such as cones, pyramids and spheres.

The forces experienced by a rigid asperity ploughing through a rigid-plastic substrate (having negligible elastic deformation) are attributed to the plastic deformation of the substrate and the shearing of the adhesive junctions at the interface, see also Bowden et al. [6]. Their use of different indenter shapes to highlight the contribution of plastic deformation and interfacial shear on friction, emphasizes the effect of asperity-geometry on forces acting on the asperity. Based on the work done in [6], the forces acting on an asperity sliding through a rigid-plastic substrate is calculated from both the contact pressure due to deformation of the substrate and shear stress at the interface over the total contact area. This concept has been used by Moore to compute friction in ploughing by cylindrical, spherical and conical asperities [7]. Goddard and Wilman also derived expressions for the coefficient of friction due to ploughing and adhesion for spheres, cones and triangular-and square pyramids sliding through rigid-plastic substrates [1]. In Tayabi et al., the pressure due to plastic flow acting into the contact surface and the shear stress components acting tangential to the intersection of the contact surface with the meridional and latitudinal planes were used to calculate the forces acting along the sliding and loading directions on a spherical asperity in a nano-scratch test [8].

The slip-line field theory has been used to give an exact solution based on plane strain and plane stress boundary value problems for yielding of the junctions connecting rigid-plastic solids [9]. First suggested by Green, the slip-line field theory has been used by Challen and Oxley to derive the expressions for abrasive wear and friction in sliding of wedge-shaped asperities [2]. They further extended their work to predict friction and wear for rigid cylinders abrading softer work-pieces by approximating curved contacting surfaces using chord(s) to construct slip-line fields representing plastic deformation [10]. Their results were later adapted and compared with experiments using cylindrical asperities [11]. Later, slip-line fields generated from a family of logarithmic curves were also proposed to obtain solutions for ploughing by a hard circular particle [12], the results were in good agreement with [11]. Further, Hokkirigawa and Kato experimentally investigated the relations for the coefficient of friction in different wear regimes, mentioned in [13]. In their study using spherical asperities, the abrasive wear modes were mapped as a function of the 'degree of penetration' (ratio of penetration depth and contact length) and the interfacial shear strength [13], thereby reiterating the effect of asperity-geometry on friction in sliding. Both slip-line field and upper bound theories have been used to study ploughing [4], [5] and [14] and asperity deformation [15], [16] and [17].

However, the slip-line field theory has only been used in two dimensional problems with rigid-plastic materials. Hence the upper bound theorem has been used to analyse ploughing by three dimensional asperities, assuming the moving blocks of deformed rigid-plastic, incompressible material resulting in discontinuities in the tangential components of flow velocities at the contact interfaces. The true velocity field minimizes the rate of work due to plastic deformation and interfacial friction. This helps to estimate the forces on the asperity, planes of discontinuity and strain in the substrate. The upper bound ploughing models, applied mostly for pyramidal [18]

and conical asperities [19], require the configuration of the plastic zones to be known a priori. Hence, the upper bound method has been extended to model ploughing by a pyramidal asperity for stress free surfaces where the shape of the plastic zone (pile-up) has been determined on a rigorous basis with the rigid block scheme [20]. The pile-up shape has been incrementally updated while repeating the work minimization steps to obtain a steady state solution [20] and [21]. By defining the angle subtended by the adjacent faces containing the pyramid tip as the front and side angles of the pyramid-shaped asperity and using the upper bound theorem, van der Linde has plotted the effect of asperity geometry on both the deformation power of the asperity and wear modes [3]. Nevertheless, estimating the plastic-zone and rigid blocks in building upper bound ploughing models adds to the complexity in many other asperity geometries.

The ploughing friction coefficient have been evaluated for conical nano-indenters with blunt spherical tips in Lafaye et al. [22] by taking the friction due to plastic deformation of the substrate and shearing of the interface into account. The elastic recovery of the plastically deforming substrate has been included in calculating the contact area for both ductile and brittle substrates in [22] and [23]. However, both in pyramidal and cone-shaped asperities, studied previously, a differentiable curvature is absent which is not usually true. Moreover, a constant 'degree of penetration' with varying penetration depths for a pyramidal or a conical asperity leads to an unclear distinction between the change in wear regimes with varying loads.

In characterizing asperities for statistical contact model, spherical geometries have traditionally been used [24]. To improve statistical characterization, Nayak has characterized asperity summits as contact patches with varying shapes and orientations in the random process model for rough surfaces [25]. Using the random process model, the shape of the asperities in elastic contacts were first approximated as elliptic paraboloids in [26]. Elliptic-paraboloid shape asperities have also been used to account for the contact of anisotropic rough surfaces as summarized by McCool in [27]. Until recently, the contact patches were described as a connected height matrix of pixels mapped from asperity image-processing [28]. Using the volume and area of the identified contact patches, the contact cross section and curvature in the asperities were characterized as elliptic and parabolic in shape respectively [29]. Hence, an elliptic-paraboloid geometry (elliptic cross-section and parabolic shape) has been chosen to give a more realistic description and control of the asperity's shape as compared to a pyramid, sphere or cone.

Modelling of ploughing using an elliptic-paraboloid asperity also gives us the possibility to model multi-asperity contact and friction in anisotropic surfaces with varying asperity geometries. The contact between rough surface [25] modelled as (elliptic) paraboloids [26] have been used to study frictionless elastic contacts in [30] and the role of surface tension in elastic contacts in [31]. The parabolic asperity geometry has also been used in lateral contact modelling to study shear behaviour in anisotropic rough surfaces by introducing orientation angles in elastic-plastic contact of interacting asperities in [32] and [33]. Thus far the statistical contact models described in [25] and [28] have not been used to fully explore the ploughing of rigid elliptic-paraboloid shaped asperities in plastically deforming substrates.

Some initial work has also been done in modelling contact and wear using elliptic-paraboloid asperity in ploughing through elastic-plastic substrates in [34] and [35], where the wear volume has been expressed using the size and orientation of the asperity. In order to account for realistic

asperity geometries, van der Linde simplified elliptic-paraboloid shaped asperities into pyramid-shaped asperities [3]. The base of the pyramid is approximated as a hexagon, being oriented at an angle between 0 and 90^0 along the sliding direction or a parallelogram, if oriented along or perpendicular to the sliding direction to give the best fit to an elliptic base. The dimensions of the original ellipse were scaled to the dimensions of the hexagon using a scaling factor. The components of friction forces in x and y directions were obtained by resolving the forces due to the plastic pressure and the shear stress along the surface normal vector and the tangent vector along the direction of flow for the contacting planes of the hexagonal pyramid [36] and [29]. However, the hexagonal-pyramid approximation of an ellipsoid loses its accuracy for high ellipticity ratios. Moreover, the behaviour of the asperity varies from that of a real asperity due to its non-differentiable geometry.

It can be summarized that an analytical model to calculate forces acting on an elliptic-paraboloid shaped-asperity is absent in the literature. Hence, the current work presents a comprehensive analytical model to calculate the forces acting on an asperity with an elliptic base, i.e. ellipsoidal and elliptic-paraboloid shape asperities sliding through a rigid-plastic substrate. The forces are calculated as the result of stresses on an elemental contact area due to plastic deformation of the substrate and shearing of the interface along the unit normal to the surface of the asperity and tangent to the direction of plastic flow of the substrate relative to the asperity respectively. The elemental forces are then integrated over the boundaries of the plastic flow for the total contact area to give the components of the total forces. Results for both ellipsoid and elliptic-paraboloid asperities have been compared for a reasonable range of ploughing depths. The results obtained from the developed analytical model were compared with that from Tayabi et al. [8], for a spherical asperity, and with that obtained from van der Linde [3] and [29] for a hexagonal pyramid approximation of an elliptic-paraboloid shape asperity. Further, the ellipticity ratio, axes sizes and orientation of the asperity have been varied to highlight their effects on forces on the asperity. The model-based understanding of the effect of asperity geometry on friction would aid in developing a robust multi-asperity ploughing model.

2 Calculation of forces on a single-elliptical asperity

The forces acting on a rigid asperity ploughing through a rigid-plastic substrate is contributed by the contact pressure due to the plastic deformation of the substrate and by the shear stress due to the shearing of the interface [6]. The contact pressure acts along the normal into the contact surface with a unit normal vector $\widehat{\boldsymbol{n}}$, while the interfacial shear stress acts tangentially along the contact surface in the direction of plastic flow with a unit tangent vector $\widehat{\boldsymbol{t}}$. The total force vector $\boldsymbol{F}$, due to the plastic pressure p_{pl} and the interfacial shear stress τ_{sh} acting over the contact area A_c, can be expressed as,

$$\vec{F} = p_{pl} A_c \hat{n} + \tau_{sh} A_c \hat{t} \tag{1}$$

2.1 Calculation of the surface unit vectors

The surface of an ellipsoidal asperity can be discretized into infinitesimally small triangular elements. Polygonal surface elements, which are a combination of triangles, also yield the same results as triangular elements. The surface discretization also corresponds to the meshing of the ellipsoidal surfaces in numerical ploughing methods, as shown in figure 1a. Figure 1b shows a pyramidal (tetrahedral) solid element ABCD with the triangulated surface element ΔBCD

centred at O. The pyramidal element OBCD with the triangular base ΔBCD has dimensions of l, w and h along x, y and z axes in the Cartesian coordinates.

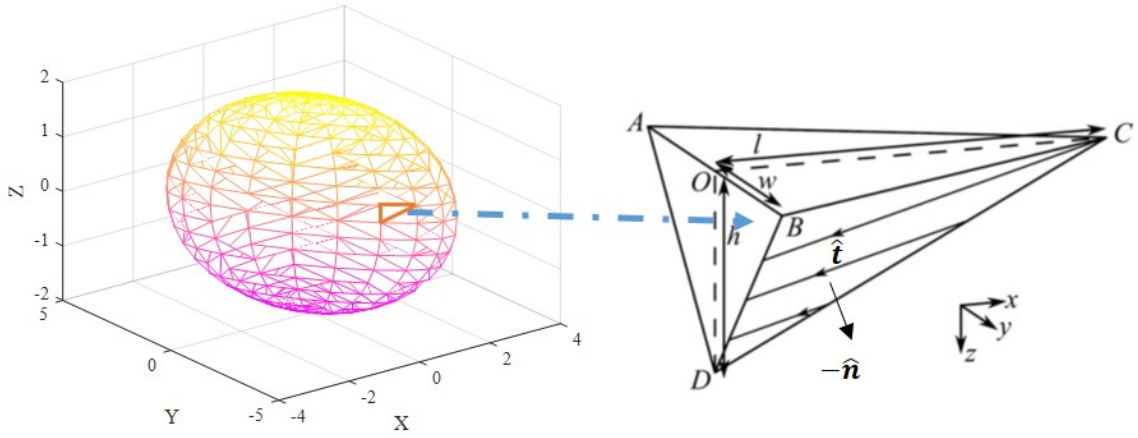

Figure 1: (a) Schematic of the triangulated ellipsoidal asperity mesh and (b) the dimensions of a pyramidal element with the triangular surface unit normal and tangent vectors in the cartesian coordinate system [36].

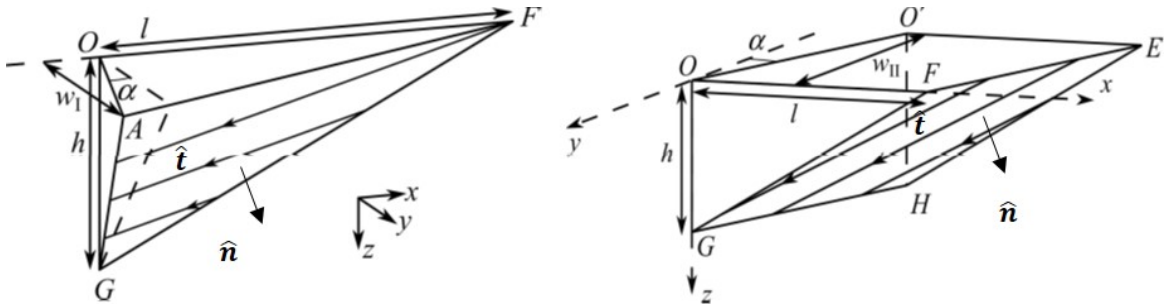

Figure 2: The dimensions of (a) an oblique pyramidal element and (b) an oblique prism with its unit normal and tangent vectors to its surface in the Cartesian coordinate system [3].

Correspondingly, the coordinates B, C and D of ΔBCD are $(0,\ w,\ 0)$, $(l,\ 0,\ 0)$ and $(0,\ 0,\ h)$ respectively. The normal vector into the plane containing ΔBCD is given by the cross product of its sides $\overrightarrow{BC}$ and $\overrightarrow{BD}$, given as $l\hat{i} - w\hat{j}$ and $-w\hat{j} + h\hat{k}$ respectively in equation 2.1 [36]. Here $\hat{i}$, $\hat{j}$ and $\hat{k}$ are the unit vectors along x, y and z axes respectively. The unit normal vector $\hat{\boldsymbol{n}}$ is obtained by dividing the normal vector by its magnitude (equation 2.2) with the negative sign on its components indicating the inward direction, into plane of ΔBDC. The area of ΔBCD is half of the magnitude of the cross product of its two sides, i.e. $A_{\Delta BCD} = \left|\overrightarrow{BC} \times \overrightarrow{BD}\right| /2$. The projected areas of ΔBCD in the yz, xz and xy planes are the areas of ΔOBD, ΔOCD and ΔOBC, i.e. $wh/2$, $lh/2$ and $lw/2$ respectively. $\hat{\boldsymbol{n}}$ is expressed as function of the projected areas in equation 2.3.

$$\vec{n}_{\Delta BCD} = \vec{BC} \times \vec{BD} = -wh\hat{\mathrm{i}} - lh\hat{\mathrm{j}} - wl\hat{\mathrm{k}} \tag{2.1}$$

$$\hat{n} = \frac{\vec{\mathrm{n}}_{\Delta BCD}}{|\ n_{\Delta BCD}\ |} = \frac{-wh\hat{\mathrm{i}} - lh\hat{\mathrm{j}} - wl\hat{\mathrm{k}}}{\sqrt{(wh)^2 + (lh)^2 + (wl)^2}} \tag{2.2}$$

$$\hat{n} = -\frac{A_{yz}}{A_\Delta}\hat{\mathrm{i}} - \frac{A_{xz}}{A_\Delta}\hat{\mathrm{j}} - \frac{A_{xy}}{A_\Delta}\hat{\mathrm{k}} \tag{2.3}$$

For the ellipsoidal asperity sliding with a velocity $\boldsymbol{v}$ in the x direction, the relative velocity in the far field is directed in the x direction, $\boldsymbol{x}$ i.e. $(l,\ 0,\ 0)$. The vector $\boldsymbol{t_{\Delta BCD}}$ is the tangent to ΔBDC as close as possible to plastic flow on the interface. As mentioned in [36], in order to obtain $\boldsymbol{t_{\Delta BCD}}$, the inner product $\boldsymbol{x}.\boldsymbol{t_{\Delta BCD}}$ has to be minimized. Hence, $\boldsymbol{t_{\Delta BCD}}$ has to be in the plane described by vectors $\boldsymbol{x}$ and $\boldsymbol{n}_{\Delta BCD}$. So $\boldsymbol{t_{\Delta BCD}}$ is given as the double cross product of $\boldsymbol{x}$ and $\boldsymbol{n}_{\Delta BCD}$ and $\boldsymbol{n}_{\Delta BCD}$ in equation 3.1. Furthermore the unit tangent vector $\widehat{\boldsymbol{t}}$ is obtained by dividing $\boldsymbol{t_{\Delta BCD}}$ with its magnitude, as given in equation 3.2. The unit tangent vector is further expressed as a function of the triangular element's contact area, $A_{\Delta BCD}$ and its projected areas A_{xz}, A_{yz} and A_{xy} in the xz, yz and xy coordinate planes respectively in equation 3.3.

$$\begin{aligned}
&\vec{t}_{\Delta BCD} = (\vec{\mathrm{x}} \times \vec{n}_{\Delta BCD}) \times \vec{n}_{\Delta BCD} = \\
&(l\hat{i} \times -(wh\hat{i} + lh\hat{j} + lw\hat{k})) \times -(wh\hat{i} + lh\hat{j} + lw\hat{k}) \\
&= (l^2 w\hat{j} - l^2 h\hat{k}) \times -(wh\hat{i} + lh\hat{j} + lw\hat{k}) \\
&= -l((lw)^2 + (lh)^2)\hat{i} + w(lh)^2\hat{j} + h(lw)^2\hat{k}
\end{aligned} \tag{3.1}$$

$$\begin{aligned}
\hat{\mathrm{t}} &= \frac{\vec{\mathrm{t}}_{\Delta BCD}}{\mid t_{\Delta BCD} \mid} = \frac{-(l(l^2w^2 + (l^2h^2)\hat{i} + l^2h^2w\hat{j} + l^2w^2h\hat{k}}{\sqrt{l^4(w^2+h^2}\sqrt{(lw)^2 + (lh)^2 + (wh)^2}} \\
&= \frac{-((lw)^2 + (lh)^2)\hat{i} + (hw)(lh)\hat{j} + (wh)(lw)\hat{k}}{\sqrt{(lw)^2 + (lh)^2}\sqrt{(lw)^2 + (lh)^2 + (wh)^2}}
\end{aligned} \tag{3.2}$$

$$\hat{\mathrm{t}} = -\frac{\sqrt{A_{xy}^2 + A_{yz}^2}}{A_\Delta}\hat{\mathrm{j}} + \frac{A_{xz}A_{yz}}{A_\Delta\sqrt{A_{xy}^2 + A_{yz}^2}}\hat{\mathrm{j}} + \frac{A_{xy}A_{yz}}{A_\Delta\sqrt{A_{xy}^2 + A_{yz}^2}}\hat{\mathrm{k}} \tag{3.3}$$

Similarly, for an oblique pyramid or prism, where the surface elemental triangle or parallelogram has been rotated by an angle α in the xy coordinate plane, the expressions for $\widehat{\boldsymbol{t}}$ and $\widehat{\boldsymbol{n}}$ can be reduced into those as given in equation 2.3 and 3.3. The x coordinate l for point C (figure 1b), when rotated by angle α, changes to $l + w_I tan\alpha$ for point F in the oblique pyramid OAGF as shown in figure 2a. Similarly, the x coordinate l of point C, changes to $l + w_{II} tan\alpha$ for point F in the oblique prism O'OEF as shown in figure 2b. The area of the surface parallelogram element $EFGH$ in the oblique prism is given as $A_{EFGH} = \left|\overrightarrow{FE} \times \overrightarrow{FG}\right| = \left|\left(w_{II} tan\alpha\widehat{\boldsymbol{i}} + w_{II}\widehat{\boldsymbol{j}}\right) \times (-l\widehat{\boldsymbol{i}} + h\widehat{\boldsymbol{k}})\ \right|$ [3].

2.2 Calculation of the elemental area and its projections

The equation of an un-rotated ellipsoid centred at the origin in Cartesian coordinate system, with axes sizes a, b and c along the x, y and z direction is given in equation 4.1. Its ellipticity ratios are $e_x = a/c$ and $e_y = b/c$ along the x and y direction respectively. Because of mathematical simplicity, the ellipsoid has been expressed in the spherical coordinate system for further calculations. The points on the ellipsoid are now written as a function of spherical parameters such as radial distance r, azimuthal angle θ and polar angle ϕ in equation 4.2. The radial distance equals the ellipsoid's axis size along the z axis, $c = r$. Hence, the axis sizes in the x and y directions are written as $a = re_x$ and $b = re_y$. For an ellipsoidal asperity oriented at an angle β with the sliding (x) direction in the sliding (xy) plane, the points on the ellipsoid are also rotated by an angle β. The rotated points on the surface of the ellipsoidal asperity are given in equation 4.3 by multiplying the rotation matrix $\boldsymbol{R}$ to the x and y coordinates of the ellipsoid as given in equation 4.2.

$$\frac{x^2}{a^2}+\frac{y^2}{b^2}+\frac{z^2}{c^2}=1 \tag{4.1}$$

$$x=a\cos\theta\sin\phi;\ y=b\sin\theta\sin\phi;\ z=c\cos\phi \tag{4.2}$$

$$\begin{bmatrix}x_r\\y_r\end{bmatrix}=\boldsymbol{R}\begin{bmatrix}x\\y\end{bmatrix}\forall\boldsymbol{R}=\begin{bmatrix}\cos\beta & -\sin\beta\\ \sin\beta & \cos\beta\end{bmatrix};\ z_r=z=c\cos\phi$$
$$x_r=(a\cos\theta\cos\beta-b\sin\theta\sin\beta)\sin\phi; \tag{4.3}$$
$$y_r=(a\cos\theta\sin\beta+b\sin\theta\cos\beta)\sin\phi$$

In order to compute $\widehat{\boldsymbol{n}}$ and $\widehat{\boldsymbol{t}}$ in the spherical coordinate system, the projections of the elemental contact area in the xz, yz and xy planes are also calculated in the spherical coordinate system. Subsequently a coordinate transformation is done on the expressions derived in the Cartesian coordinate system $\boldsymbol{C(x,y,z)}$ to the spherical coordinate system $\boldsymbol{S(\theta,\ \phi,\ r)}$ using the Jacobian determinant, $\boldsymbol{J_C^S}=det\,|\partial\boldsymbol{C}/\partial\boldsymbol{S}|$ as the conversion factor. This gives us the elemental projected areas of the surface of the ellipsoidal asperity: dA_{xy}, dA_{xz} and dA_{yz} in terms of variables θ and ϕ (r and β being constants) in equations 5.1, 5.2 and 5.3 respectively. After the Jacobian transformation, the components of $\widehat{\boldsymbol{n}}$ and $\widehat{\boldsymbol{t}}$ and are expressed as the functions of θ and ϕ in equation 5.4 and 5.5 respectively. The Jacobian transformation has been applied on each individual terms in equation 2.3 and 3.3 or equivalently applying the Jacobian on the whole expression of each component. The terms of functions of θ and ϕ given in equation 5.1-5.5 are expressed in equation 6.1-6.6.

$$dA_{xy}=dxdy=\boldsymbol{J_{xy}^{\theta\phi}}d\theta d\phi=n(\phi)d\theta d\phi\ ;\ \boldsymbol{J_{xy}^{\theta\phi}}=det\begin{vmatrix}\frac{\partial x_r}{\partial\theta} & \frac{\partial x_r}{\partial\phi}\\ \frac{\partial y_r}{\partial\theta} & \frac{\partial y_r}{\partial\phi}\end{vmatrix} \tag{5.1}$$

$$dA_{xz}=dxdz=\boldsymbol{J_{xz}^{\theta\phi}}d\theta d\phi=l(\theta,\phi)d\theta d\phi;\ \boldsymbol{J_{xz}^{\theta\phi}}=det\begin{vmatrix}\frac{\partial x_r}{\partial\theta} & \frac{\partial x_r}{\partial\phi}\\ \frac{\partial z_r}{\partial\theta} & \frac{\partial z_r}{\partial\phi}\end{vmatrix} \tag{5.2}$$

$$dA_{yz}=dydz=\boldsymbol{J_{yz}^{\theta\phi}}d\theta d\phi=m\,(\theta,\phi)\,d\theta d\phi;\ \boldsymbol{J_{yz}^{\theta\phi}}=det\begin{vmatrix}\frac{\partial y_r}{\partial\theta} & \frac{\partial y_r}{\partial\phi}\\ \frac{\partial z_r}{\partial\theta} & \frac{\partial z_r}{\partial\phi}\end{vmatrix} \tag{5.3}$$

$$\begin{aligned}\boldsymbol{J_{\theta,\phi}}\hat{n}&=-\frac{\boldsymbol{J_{\theta,\phi}dA_{yz}}\widehat{\boldsymbol{i}}}{\boldsymbol{J_{\theta,\phi}dA_{\Delta}}}-\frac{\boldsymbol{J_{\theta,\phi}dA_{xz}}\widehat{\boldsymbol{j}}}{\boldsymbol{J_{\theta,\phi}dA_{\Delta}}}-\frac{\boldsymbol{J_{\theta,\phi}dA_{xy}}\widehat{\boldsymbol{k}}}{\boldsymbol{J_{\theta,\phi}dA_{\Delta}}}\\&=-\frac{(m\,(\theta,\phi)\,d\theta d\phi\ \widehat{\boldsymbol{i}}+l\,(\theta,\phi)\,d\theta d\phi\ \widehat{\boldsymbol{j}}+n\,(\theta,\phi)\,d\theta d\phi\ \widehat{\boldsymbol{k}})}{dA_{\Delta}(\theta,\ \phi)}\end{aligned} \tag{5.4}$$

$$\begin{aligned}\boldsymbol{J_{\theta,\phi}}\widehat{\boldsymbol{t}}&=-\frac{\sqrt{\boldsymbol{J_{\theta,\phi}^2dA_{xy}^2}+\boldsymbol{J_{\theta,\phi}^2dA_{xz}^2}}}{\boldsymbol{J_{\theta,\phi}dA_{\Delta}}}\widehat{\boldsymbol{i}}+\frac{\boldsymbol{J_{\theta,\phi}^2dA_{xz}dA_{yz}}}{\boldsymbol{J_{\theta,\phi}dA_{\Delta}}\sqrt{\boldsymbol{J_{\theta,\phi}^2dA_{xy}^2}+\boldsymbol{J_{\theta,\phi}^2dA_{xz}^2}}}\widehat{\boldsymbol{j}}+\\&\frac{\boldsymbol{J_{\theta,\phi}^2A_{xy}A_{yz}}}{\boldsymbol{J_{\theta,\phi}dA_{\Delta}}\sqrt{\boldsymbol{J_{\theta,\phi}^2dA_{xy}^2}+\boldsymbol{J_{\theta,\phi}^2dA_{xz}^2}}}\widehat{\boldsymbol{k}}\\&=\frac{(-f\,(\theta,\phi)\,d\theta d\phi\ \widehat{\boldsymbol{i}}+g\,(\theta,\phi)\,d\theta d\phi\ \widehat{\boldsymbol{j}}+h\,(\theta,\phi)\,d\theta d\phi\ \widehat{\boldsymbol{k}})}{dA_{\Delta}(\theta,\ \phi)}\end{aligned} \tag{5.5}$$

where,

$$l(\theta,\phi) = c\,(a\sin\theta\,\cos\beta\; + b\cos\theta\,\sin\beta\,)\sin^2\phi \tag{6.1}$$

$$m(\theta,\phi) = c\,(a\sin\theta\,\sin\beta\; - b\cos\theta\,\cos\beta\,)\sin^2\phi \tag{6.2}$$

$$n(\phi) = -\frac{ab}{2}\sin 2\phi \tag{6.3}$$

$$f(\theta,\phi) = \sqrt{n(\phi)^2 + l(\theta,\phi)^2} = \sqrt{\left(-\frac{ab}{2}\sin 2\phi\;\right)^2 + \left(c\,(a\sin\theta\,\cos\beta\; + b\cos\theta\,\sin\beta\,)\sin^2\phi\,\right)^2} \tag{6.4}$$

$$\begin{aligned} g(\theta,\phi) &= \frac{l(\theta,\phi)\,m(\theta,\;\phi)}{f(\theta,\phi)} \\ &= \frac{\left(c\,(a\sin\theta\,\cos\beta\; + b\cos\theta\,\sin\beta\,)\sin^2\phi\,\right)\left(c\,(a\sin\theta\,\sin\beta\; - b\cos\theta\,\cos\beta\,)\sin^2\phi\,\right)}{\sqrt{\left(-\frac{ab}{2}\sin 2\phi\,\right)^2 + \left(c\,(a\sin\theta\,\cos\beta\; + b\cos\theta\,\sin\beta\,)\sin^2\phi\,\right)^2}} \end{aligned} \tag{6.5}$$

$$h(\theta,\phi) = \frac{n(\phi)\,m(\theta,\;\phi)}{f(\theta,\phi)} = \frac{\left(-\frac{ab}{2}\sin 2\phi\,\right)\left(c\,(a\sin\theta\,\sin\beta\; - b\cos\theta\,\cos\beta\,)\sin^2\phi\,\right)}{\sqrt{\left(-\frac{ab}{2}\sin 2\phi\,\right)^2 + \left(c\,(a\sin\theta\,\cos\beta\; + b\cos\theta\,\sin\beta\,)\sin^2\phi\,\right)^2}} \tag{6.6}$$

2.3 Calculating the boundaries for plastic contact/flow

For an ellipsoidal asperity (see figure 3a) indenting into substrate at a given depth d, oriented at an angle β with respect to the sliding direction i.e. x axis, the surface in contact with the substrate is an ellipsoidal cap. As the asperity starts ploughing through the plastically deforming substrate, contact is lost from the rear half of the asperity as the deformed substrate is unable to recover elastically. The semi-elliptic segment $NCSM$ shown in figure 3d, is the contact cross-section in the xy plane. Along with the ellipsoid, the elliptic cross- section is also rotated by β and is bounded by a box such that point M represents the maximum $+x$ coordinate and points N and S represent the maximum $+y$ and $-y$ coordinates respectively. So the tangents to the elliptic cross-section, i.e. the bounding box's lines have slopes $m = \infty$ at M and $m = 0$ at N and S.

As the asperity ploughs through the substrate in the $+x$ direction, the contact first happens at the maximum $+x$ coordinate (abscissa) of the contacting ellipse, i.e. at M. The substrate in contact is then plastically deformed and the contact and thus the plastic flow moves along the slope of the contacting ellipse (in the xy plane) until it reaches the point of maximum ordinate at slope $m = 0$ i.e. N and S, where it loses contact with the asperity. Hence the flow occurs in $+y$ direction in the sector NCM and in $-y$ direction in the sector MCS as shown by the dashed arrows in figure 3d. Correspondingly, the y component of force in the corresponding sector due to plastic flow pressure is along $\hat{\boldsymbol{n}}\hat{j}$. The separation in plastic flow direction can also be seen in the xz and yz projection of the ellipsoidal asperity, shown as segment $SLMN$ in figure 3b and 3c. The flow separation line CM in figure 3d follows from point M on the contact plane to the contact depth at point L along an elliptic arc $\overset{\frown}{ML}$, as shown in figure 3b and 3c. In the same figures, elliptic arcs $\overset{\frown}{SL}$ and $\overset{\frown}{NL}$ represent the contact separation curves on the ellipsoidal asperity projected in the xz and yz planes.

Therefore the spherical coordinates of the points $N,\ M,\ S$ and L are obtained by solving the intersection of the bounding box's lines with the elliptic contact patch in the xy plane. The

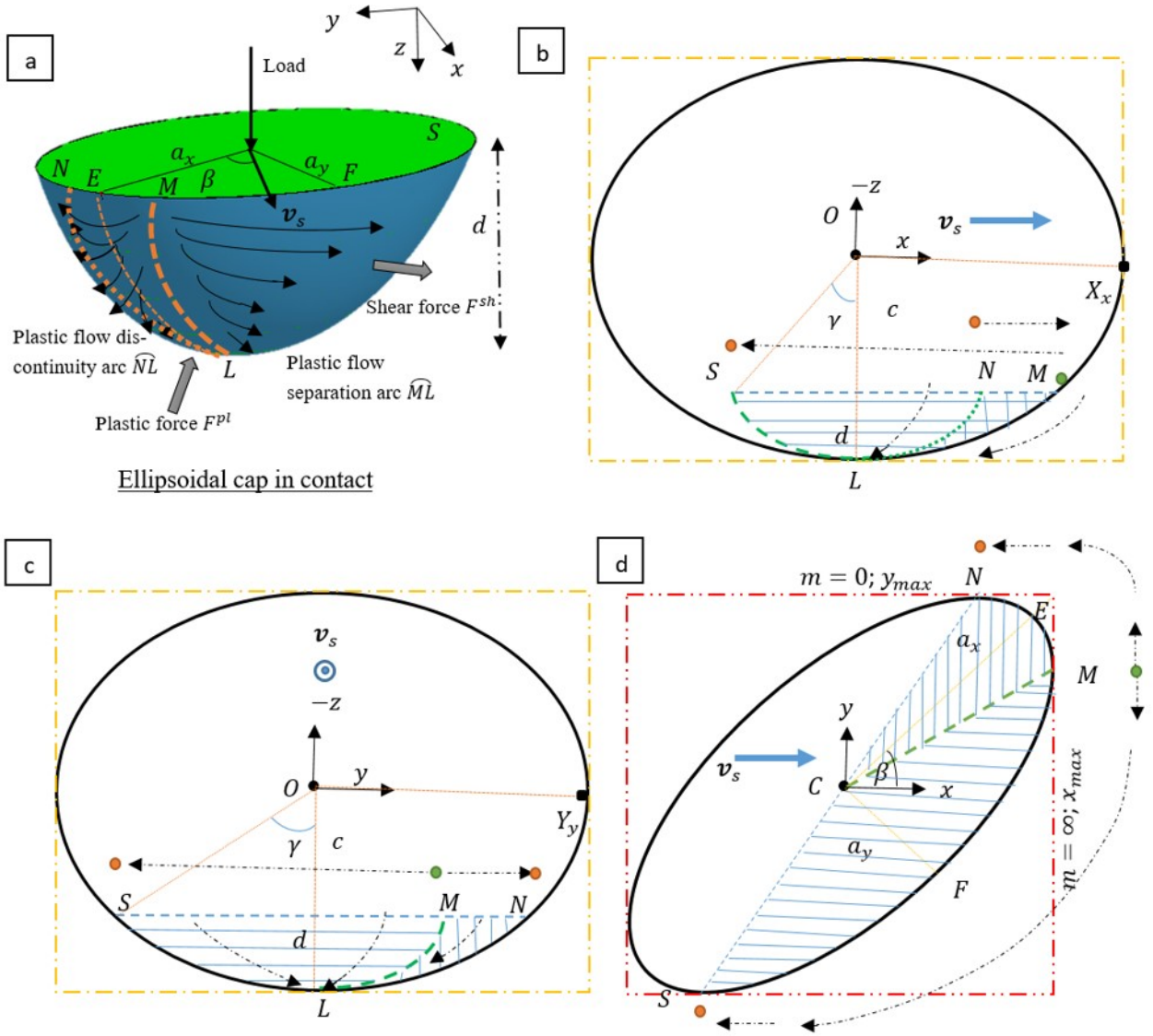

Figure 3: (a) Schematic of an ellipsoidal asperity sliding through a rigid-plastic substrate at a velocity $\boldsymbol{v_s}$, oriented at an angle β with the sliding $(+x)$ direction and its projections in the (b) xz, (c) yz and (d) xy planes. The shaded sections represent the contact regions. The section with horizontal and vertical shades have plastic flow component in $-y$ and $+y$ directions respectively. The green dots are the separation point of plastic flow or first contact while the red dots are the end point of plastic flow/contact. The dashed black arrows show the direction of plastic flow. The dashed green lines/arcs mark the separation of plastic flow and the dashed blue lines/arcs mark the end of contact. The dashed red/orange lines mark the bounding box.

length of the axes of the contact ellipse, while un-rotated, along x and y axis are derived from the ploughing depth d. The coordinates of points E and F, located at the axes' edge of the un-rotated ellipsoid, are given as $(a_x, 0,\ c-d)$ and $(0,\ a_y,\ c-d)$. Substituting them in equation 4.1, we obtain size of the axes of the contacting ellipse in x and y direction as a_x and a_y in equation 7.1. The equation of the contacting ellipse, rotated by β, is obtained by multiplying the rotation matrix $\boldsymbol{R}$ for $-\beta$ with the x and y coordinates of the equation of ellipse (set $z = 0$ for equation 4.1), resulting in equation 7.2. Expanding and rearranging equation 7.2, a quadratic equation can be obtained in two variables, x and y in equation 7.3 [37].

The coordinates of N and M are obtained by solving the intersection of the two lines of the bounding box: $N\,(y = y_{max})$ and $M\,(x = x_{max})$ with equation 7.3. This gives us two quadratic equations in one variable x and y for solving x and y coordinates of N and M respectively as, shown in equation 7.4. Solving for one solution (intersection point), i.e. determinant $B^2 - 4AC = 0$, gives the coordinates N_y and M_x. Subsequently the coordinates N_x and M_y are obtained by solving the quadratic equation as $-B/2A$. The resulting coordinates of N and M are listed as $N\,(x, y)$ and $M\,(x, y)$ in equation 7.4 [37]. In order to express points N, M, S and L in the spherical coordinate system, their x and y coordinates are expressed using equation 4.3 and equated with equation 7.5. The azimuthal angles θ_M and θ_N for point S, M and N are computed in equation 7.6 by dividing the x and y coordinates of both M and N, expressed using equation 4.3. Point S being diametrically opposite to N has $\theta_S = \theta_N - \pi$ Since S, M and N are on the same xy contact plane (same z coordinate), they have the same polar angle ϕ_C. Using equation 4.3, polar angle ϕ_C for $z = c - d = c\mathrm{cos}\phi_C$, is obtained for S, M and N. Point L, being on the z axis, has $\phi_L = 0$.

$$a_y = e_y\sqrt{2cd - d^2};\ a_x = e_x\sqrt{2cd - d^2} \tag{7.1}$$

$$\frac{(x\mathrm{cos}\beta\ + y\mathrm{sin}\beta\ )^2}{a_x^2} + \frac{(y\mathrm{cos}\beta\ - x\mathrm{sin}\beta\ )^2}{a_y^2} = 1 \tag{7.2}$$

$$\begin{aligned}&\left[(a_y\mathrm{cos}\beta\ )^2 + (a_x\mathrm{sin}\beta\ )^2\right] x^2 + \left[(a_y\mathrm{sin}\beta\ )^2 + (a_x\mathrm{cos}\beta\ )^2\right] y^2 + \left[\left(a_y^2 - a_x^2\right)\mathrm{sin}2\beta\ \right] xy - a_x^2a_y^2 = 0\\ &\Rightarrow px^2 + qy^2 + rxy + t = 0;\\ &p = (a_y\mathrm{cos}\beta\ )^2 + (a_x\mathrm{sin}\beta\ )^2;\ q = (a_y\mathrm{sin}\beta\ )^2 +\ (a_x\mathrm{cos}\beta\ )^2;\ r = \left(a_y^2 - a_x^2\right)\mathrm{sin}2\beta\ ;\ t =\ -a_x^2a_y^2\end{aligned} \tag{7.3}$$

$$\begin{aligned}&N\,(x, y) \Rightarrow Ax^2 + Bx + C = 0\ \ (y = y_{max})\,;\ A = p,\ B = ry_{max},\ C = qy_{max}^2 + t\\ &M(x, y) \Rightarrow Ay^2 + By + C = 0\ (x = x_{max}); A = q,\ B = rx_{max},\ C = px_{max}^2 + t\end{aligned} \tag{7.4}$$

$$N\,(x, y) = \left(-\frac{r}{2p}N_y,\ \sqrt{\frac{pt}{\frac{r}{4}^2 - pq}}\right)\ , M\,(x, y) = \left(\sqrt{\frac{qt}{\frac{r}{4}^2 - pq}}, -\ \frac{r}{2q}M_x\right), \tag{7.5}$$

$$\begin{aligned}&S\,(x, y) = -N\,(x, y)\,, L\,(z) = -c\\ &N\,(\theta, \phi) = \left(\mathrm{arctan}\left(\frac{a}{b}\frac{\frac{N_y}{N_x}\mathrm{cos}\beta\ - \mathrm{sin}\beta}{\frac{N_y}{N_x}\mathrm{sin}\beta + \mathrm{cos}\beta}\right), \phi_C\right), M\,(\theta, \phi) = \left(\mathrm{arctan}\left(\frac{a}{b}\frac{\frac{M_y}{M_x}\mathrm{cos}\beta - \mathrm{sin}\beta}{\frac{M_y}{M_x}\mathrm{sin}\beta + \mathrm{cos}\beta}\right), \phi_C\right)\\ &S\,(\theta, \phi) = (\theta_N - \pi, \phi_C)\,, L\,(\phi) = 0;\ \phi_C = \mathrm{arccos}\left(1 - \frac{d}{c}\right)\end{aligned} \tag{7.6}$$

2.4 Calculating the total projected areas and total contact area

The projected areas of the rotated ellipsoidal cap in contact with the substrate in the xy, yz and xz planes are given as the area of the elliptic segments $SMNL$, SNL and SML (see figure 3d, 3c and 3b respectively) in the equations 8.2, 8.3 and 8.4 respectively. The area of an elliptic segment is obtained by subtracting the area of the triangle ΔONS from the area of the sector (ONS), formed by the chord NS arc SLN of the projected contact with the centre respectively. The points on the central xy plane of the rotated ellipsoid with maximum x coordinate and maximum y coordinate are given as $X\,(x, y)$ and $Y\,(x, y)$. The points $(0,\ c)$, $(X_x,\ 0)$ and $(Y_y,\ 0)$ form the end points of the projected ellipse's axes in the corresponding xz and yz planes They are obtained the same way as $M(x, y)$ and $N(x, y)$, i.e. by the intersection of the ellipse in the central xy plane with the bounding box's lines. X is the

point for maximum abscissa while Y is the point for maximum ordinate on the central rotated ellipse. The coordinates of the points X and Y, X_x, X_y and Y_x and Y_y, are shown in figure 3b and 3c. Based on the area of the sector for the reference circle given as $\omega r_C^2/2$, the area of the sector for the projected ellipse is obtained by scaling the sides of the circle r_C and its central angle ω to that of the projected ellipse with sides a and b and central angle γ (figure 3b and 3c), given as $A_{elliptic\ sector} = \frac{ab}{2}\text{arctan}\left(\frac{a}{b}\text{tan}\,\gamma\right)$.

The total contact area of the ellipsoidal asperity is calculated by integrating an elemental surface area over the contact boundaries. The position vector $\boldsymbol{r}$ for any point on the surface of the ellipsoidal asperity is given by equation 9.1 in the spherical coordinates (equation 4.3). Taking the cross product of the partial differential of $\boldsymbol{r}$ over the spherical coordinates which vary on the surface, i.e. θ and ϕ, we get the expression for the elemental surface area vector in equation 9.2. Taking the magnitude of the surface area vector we obtain the integrand/elemental area in equation 9.3. The elemental area is integrated from 0 to π, over $d\theta$ and 0 to ϕ_C, over $d\phi$. On expanding the integral we obtain an expression which can be summed over smaller weights, using the Gauss-Chebyshev integration scheme, as given in equation 9.4 [38] and [39].

$$Y(x,y) = \left(-\frac{R}{2P}Y_y,\ \sqrt{\frac{PT}{\frac{R}{4}^2 - PQ}}\right); X(x,y) = \left(\sqrt{\frac{QT}{\frac{R}{4}^2 - PQ}}, -\frac{R}{2Q}X_x\right); \tag{8.1}$$

$$P = (b\text{cos}\beta\ )^2 + (a\text{sin}\beta\ )^2;\ Q = (b\text{sin}\beta\ )^2 + (a\text{cos}\beta\ )^2;\ R = \left(a^2 - b^2\right)\text{sin}2\beta\ ; T = -a^2b^2$$

$$A_{yz} = A_{SMNL} = A_{OSN} - A_{\Delta ONS}$$

$$A_{OSN} = 2\left(\frac{1}{2}Y_y c\ \text{arctan}\left(\frac{N_y}{c-d}\frac{Y_y}{c}\right)\right); A_{\Delta ONS} = 2\left(\frac{1}{2}N_y(c-d)\right) \tag{8.2}$$

$$A_{xz} = A_{SNL} = A_{OSN} - A_{\Delta ONS}$$

$$A_{OSN} = 2\left(\frac{1}{2}Y_x c\ \text{arctan}\left(\frac{N_x}{c-d}\frac{Y_x}{c}\right)\right); A_{\Delta ONS} = 2\left(\frac{1}{2}N_x(c-d)\right) \tag{8.3}$$

$$A_{xy} = \pi a_x a_y/2 \tag{8.4}$$

$$\boldsymbol{r} = x\hat{\boldsymbol{i}} + y\hat{\boldsymbol{j}} + z\hat{\boldsymbol{k}} = a\text{cos}\theta\ \text{sin}\phi\ \hat{\boldsymbol{i}} + b\text{sin}\theta\ \text{sin}\phi\ \hat{\boldsymbol{j}} + c\text{cos}\phi\ \hat{\boldsymbol{k}} \tag{9.1}$$

$$d\boldsymbol{A_\Delta} = \frac{\partial \boldsymbol{r}}{\partial(\theta,\phi)} = \frac{\partial \boldsymbol{r}}{\partial\theta}d\theta \times \frac{\partial \boldsymbol{r}}{\partial\phi}d\phi = \left(bc\text{cos}\theta\text{sin}\phi\ \ \hat{\boldsymbol{i}} + ca\text{sin}\theta\ \text{sin}\phi\ \hat{\boldsymbol{j}} + ab\text{cos}\phi\ \hat{\boldsymbol{k}}\right)\text{sin}\phi\ d\theta d\phi \tag{9.2}$$

$$A_C = \oint_0^{\pi,\phi_C} dA_\Delta = 2bc\int_0^{\frac{\pi}{2}}\sqrt{B(\theta)}\left(\int_H^1\sqrt{1+F(\theta)u^2}du\right)d\theta = \frac{ab}{2}\int_{-1}^{1}\frac{f(v)}{\sqrt{1-v^2}}dv = \frac{ab}{2}\sum_{i=1}^{n} w_i f(x_i)$$

$$u = \text{cos}\phi\ ,\ v = \text{sin}\theta\ ,\ H = \text{cos}\phi_C\ ; w_i = \frac{\pi}{i},\ x_i = \text{cos}\left(\frac{2i-1}{2n}\pi\right)\ = t$$

$$B(t) = 1 - \left(1 - \frac{a^2}{b^2}\right)t^2;\ F(t) = \frac{a^2}{c^2}\left(\frac{1}{B(t)}\right); G(t) = \sqrt{H^2 + (1-H^2)\frac{c^2}{a^2}B(t)}$$

$$f(t) = 1 - HG(t) + \frac{c}{a}\sqrt{\frac{B(t)}{F(t)}}\text{arcsinh}\left(\frac{a}{c}\sqrt{\frac{F(t)}{B(t)}}(G(t) - H)\right) \tag{9.3}$$

2.5 Integrating the total forces

To compute the total force acting on an ellipsoidal asperity ploughing through the substrate at a ploughing depth d or under an applied load N, the force acting on each elemental area is integrated over the boundaries of contact area of the ellipsoidal asperity. Mathematically this can be expressed as the product of the contact pressure/shear stress and surface integral of the contact area over the flow boundaries. The limits of integration correspond to angular coordinates of the asperity along the positive x, y and z axis. Both the ploughing force due to the deformation pressure of the perfectly plastic substrate acting along the surface normal vector and the ploughing force due to shearing of the interface acting along the surface tangent vector along plastic flow have three components in x, y and z axes. The individual components and the total force in the 3 Cartesian coordinate axes are given in equation 10.1-10.7.

$$F_x^{pl} = p_{pl} \oint_{S,L}^{N} dA_\Delta \widehat{\boldsymbol{n}}.\widehat{\boldsymbol{i}} = p_{pl} \int_0^{\phi_C} \int_{\theta_S}^{\theta_N} |m(\theta,\phi)|\, d\theta d\phi \tag{10.1}$$

$$\Rightarrow F_x^{pl} = p_{pl} c(\phi_C - cos\phi_C\ sin\phi_C\ )(a\cos\theta_N\ \sin\beta + b\sin\theta_N\ \cos\beta)$$

$$F_y^{pl} = p_{pl} \left(\oint_{S,L}^{M} dA_\Delta - \oint_{N,L}^{M} dA_\Delta \right) \widehat{\boldsymbol{n}}.\widehat{\boldsymbol{j}}$$

$$= p_{pl} \left(\int_0^{\phi_C} \int_{\theta_S}^{\theta_M} |l(\theta,\phi)|\, d\theta d\phi - \int_0^{\phi_C} \int_{\theta_N}^{\theta_M} |l(\theta,\phi)|\, d\theta d\phi \right) \tag{10.2}$$

$$\Rightarrow F_y^{pl} = p_{pl} c\,(\phi_C - \cos\phi_C\ \sin\phi_C\ )\,(a\cos\theta_N\ \cos\beta - b\sin\theta_N\ \sin\beta)$$

$$F_z^{pl} = p_{pl} \oint_{S,L}^{N} dA_\Delta \widehat{\boldsymbol{n}}.\widehat{\boldsymbol{k}} = p_{pl} \int_0^{\phi_C} \int_{\theta_S}^{\theta_N} |n\,(\phi)|\, d\theta d\phi \tag{10.3}$$

$$\Rightarrow F_z^{pl} = \pi ab\,(1 - \cos\,(2\phi_C)\ )\,/4$$

$$F_x^{sh} = -\tau_{sh} \oint_{S,L}^{N} dA_\Delta \widehat{\boldsymbol{t}}.\widehat{\boldsymbol{i}} = -\tau_{sh} \int_0^{\phi_C} \int_{\theta_S}^{\theta_N} |f\,(\theta,\phi)|\, d\theta d\phi \tag{10.4}$$

$$F_y^{sh} = -\tau_{sh} \left(\oint_{S,L}^{M} dA_\Delta - \oint_{M,L}^{N} dA_\Delta \right) \widehat{\boldsymbol{t}}.\widehat{\boldsymbol{j}}$$

$$= -\tau_{pl} \left(\int_0^{\phi_C} \int_{\theta_S}^{\theta_M} |g(\theta,\phi)|\, d\theta d\phi - \int_0^{\phi_C} \int_{\theta_M}^{\theta_N} |g(\theta,\phi)|\, d\theta d\phi \right) \tag{10.5}$$

$$F_z^{sh} = -\tau_{sh} \oint_{S,L}^{N} dA_\Delta \widehat{\boldsymbol{t}}.\widehat{\boldsymbol{k}} = -\tau_{sh} \int_0^{\phi_C} \int_{\theta_S}^{\theta_N} |h\,(\theta,\phi)|\, d\theta d\phi \tag{10.6}$$

$$F_x = F_x^{pl} + F_x^{sh}; F_y = F_y^{pl} - F_y^{sh}; F_z = F_z^{pl} + F_z^{sh}; F = \sqrt{F_x^2 + F_y^2 + F_z^2} \tag{10.7}$$

2.6 Forces acting on an elliptic-paraboloid shape asperity

Next to the ellipsoidal asperity analysed above, here an elliptic-paraboloid shaped asperity will also be discussed as it is used in models in [3], [28] and [35]. An elliptic-paraboloid shaped asperity centred at the origin in Cartesian coordinate system, with the elliptic base located at a height c whose axes size are given as a and b along the x and y direction, is expressed in equation 11.1 and shown in figure 4. Its ellipticity ratios are $e_x = a/\rho$ and $e_y = b/\rho$ along the x and y direction respectively where ρ is the reference radius of the base (axial distance). Because of mathematical simplicity, the elliptic-paraboloid has been expressed in the polar coordinate system for further calculations. The points on the elliptic-paraboloid are now written as a function of spherical parameters such as height parameter $u = z/c$ and azimuthal angle φ

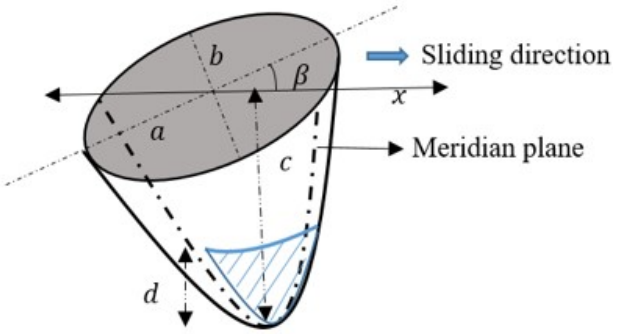

Figure 4: An elliptic-paraboloid shape asperity, with base axes of size a and b and height c, oriented at an angle β w.r.t. sliding direction x and ploughing depth h (contact region marked with lines) [28]

in equation 11.2. Like the ellipsoidal asperity, the points on an elliptic-paraboloid asperity oriented at an angle β with the sliding (x) direction in the sliding (xy) plane are obtained by multiplying the rotation matrix $\boldsymbol{R}$ to the x and y coordinates of the elliptic-paraboloid as given in equation 11.2 and 11.3.

$$\frac{x^2}{a^2} + \frac{y^2}{b^2} = \frac{z}{c} \tag{11.1}$$

$$x = a\sqrt{u}\cos\varphi \;\; ; y = b\sqrt{u}\sin\varphi \; ; z = cu \forall\; \varphi\epsilon\,[0,\; 2\pi]\; and u\epsilon\,[0,1] \tag{11.2}$$

$$x_r \; = (a\cos\varphi\; \cos\beta - b\sin\varphi\; \sin\beta\;)\sqrt{u};\; y_r = \;(a\cos\varphi\; \sin\beta\; + b\sin\varphi\; \cos\beta\;)\sqrt{u};\; z_r = cu \tag{11.3}$$

$$l\,(\varphi, u) = c\,(a\sin\varphi\; \cos\beta\; + b\cos\varphi\; \sin\beta\;)\;\sqrt{u} \tag{12.1}$$

$$m\,(\varphi, u) = c\,(a\sin\varphi\; \sin\beta\; - b\cos\varphi\; \cos\beta\;)\sqrt{u} \tag{12.2}$$

$$n = -\frac{ab}{2} \tag{12.3}$$

$$f\,(\varphi, u) = \sqrt{n^2 + l(\varphi, u)^2} = \sqrt{\left(-\frac{ab}{2}\right)^2 + \left(c\,(a\sin\varphi\; \cos\beta\; + b\cos\varphi\; \sin\beta\;)\sqrt{u}\;\right)^2} \tag{12.4}$$

$$g\,(\varphi, u) = \frac{l\,(\theta, u) * m\,(\theta, u)}{f\,(\theta, u)} = \frac{(c\,(a\sin\varphi\; \cos\beta\; + b\cos\varphi\; \sin\beta\;)\sqrt{u}\;)\,(c\,(a\sin\varphi\; \sin\beta\; - b\cos\varphi\; \cos\beta\;)\sqrt{u}\;)}{\sqrt{\left(-\frac{ab}{2}\right)^2 + (c\,(a\sin\varphi\; \cos\beta\; + b\cos\varphi\; \sin\beta\;)\sqrt{u}\;)^2}} \tag{12.5}$$

$$h\,(\varphi, u) = \frac{n(\theta, u) * m\,(\theta,\; u)}{f\,(\theta, u)} = \frac{\left(-\frac{ab}{2}\right)(c\,(a\sin\varphi\; \sin\beta\; - b\cos\varphi\; \cos\beta\;)\sqrt{u}\;)}{\sqrt{\left(-\frac{ab}{2}\right)^2 + (c\,(a\sin\varphi\; \cos\beta\; + b\cos\varphi\; \sin\beta\;)\sqrt{u}\;)^2}} \tag{12.6}$$

Likewise the projected areas in the xy, yz and zx planes are done by a coordinate transformation on the expressions derived in the Cartesian coordinate system $\boldsymbol{C(x, y, z)}$ to the polar (cylindrical) coordinate system $\boldsymbol{P(\varphi,\, u, \rho)}$ using the Jacobian, $\boldsymbol{J_C^P = det\,|\partial C/\partial P|}$. The Jacobian transformation of the projection of the elemental areas dA_{xy}, dA_{xz} and dA_{yz} in given terms of functions of the variables φ and u (β being constant) which are listed in the equation 12.1-12.6 respectively (similar to equation 6.1-6.6).

Integrating the total forces over the contact boundaries which have coordinates N and S for end points of plastic flow and M for the point of flow separation the in the elliptic contact plane we obtain the components of the total forces as given in equation 13.1 - 13.6. They are defined in the same way as given section 2.3 with same height $z = h$, i.e. $u_C = h/c$ and the azimuthal angle φ corresponding to N, M and S given by φ_M, φ_N and φ_S and the point L with $\varphi_L = 0$ and $u = 0$. h also corresponds to the ploughing depth.

$$\begin{aligned} F_x^{pl} &= p_{pl} \oint_{S,L}^{N} dA_\Delta \widehat{\boldsymbol{n}}.\widehat{\boldsymbol{i}} = p_{pl} \int_0^{u_C} \int_{\varphi_S}^{\varphi_N} |l(\theta,u)|\, d\theta du \\ \Rightarrow F_x^{pl} &= p_{pl} \left(\frac{4}{3}c\right) \left(\frac{h}{c}\right)^{\frac{3}{2}} (a\cos\varphi_N \sin\beta + b\sin\varphi_N \cos\beta) \end{aligned} \tag{13.1}$$

$$\begin{aligned} F_y^{pl} &= p_{pl} \left(\oint_{S,L}^{M} dA_\Delta - \oint_{N,L}^{M} dA_\Delta \right) \widehat{\boldsymbol{n}}.\widehat{\boldsymbol{j}} \\ &= p_{pl} \left(\int_0^{u_C} \int_{\varphi_S}^{\varphi_M} |m(\theta,u)|\, d\varphi du - \int_0^{u_C} \int_{\varphi_N}^{\varphi_M} |m(\theta,u)|\, d\varphi du \right) \\ \Rightarrow F_y^{pl} &= p_{pl} \left(\frac{4}{3}c\right) \left(\frac{h}{c}\right)^{\frac{3}{2}} (a\cos\varphi_N \cos\beta - b\sin\varphi_N \sin\beta) \end{aligned} \tag{13.2}$$

$$F_z^{pl} = p_{pl} \oint_{S,L}^{N} dA_\Delta \widehat{\boldsymbol{n}}.\widehat{\boldsymbol{k}} = p_{pl} \int_0^{u_C} \int_{\varphi_S}^{\varphi_N} |n|\, d\varphi du \Longrightarrow F_z^{pl} = \frac{\pi abh}{2c} \tag{13.3}$$

$$F_x^{sh} = -\tau_{sh} \oint_{S,L}^{N} dA_\Delta \widehat{\boldsymbol{t}}.\widehat{\boldsymbol{i}} = -\tau_{sh} \int_0^{u_C} \int_{\theta_S}^{\theta_N} |f(\varphi,u)|\, d\varphi du \tag{13.4}$$

$$\begin{aligned} F_y^{sh} &= -\tau_{sh} \left(\oint_{S,L}^{M} dA_\Delta - \oint_{M,L}^{N} dA_\Delta \right) \widehat{\boldsymbol{t}}.\widehat{\boldsymbol{j}} \\ &= -\tau_{pl} \left(\int_0^{u_C} \int_{\theta_S}^{\theta_M} |g(\varphi,u)|\, d\varphi du - \int_0^{u_C} \int_{\theta_M}^{\theta_N} |g(\varphi,u)|\, d\varphi du \right) \end{aligned} \tag{13.5}$$

$$F_z^{sh} = -\tau_{sh} \oint_{S,L}^{N} dA_\Delta \widehat{\boldsymbol{t}}.\widehat{\boldsymbol{k}} = -\tau_{sh} \int_0^{u_C} \int_{\varphi_S}^{\varphi_N} |h(\varphi,u)|\, d\varphi du \tag{13.6}$$

3 Results and discussion

Forces due to ploughing are calculated for the cases of both constant load as well as constant ploughing depth. The components of the forces obtained from equation 10 and 13 are normalized by $F_z^{pl} = p_{pl} A_{xy}$ which remains constant $\forall\beta$ as the projected area in the xy plane A_{xy} remains constant $\forall\beta$. The five force ratios are represented as $\mu_x^p = F_x^{pl}/F_z^{pl}$, $\mu_x^s = F_x^{sh}/F_z^{pl}$, $\mu_y^p = F_y^{pl}/F_z^{pl}$, $\mu_y^p = F_y^{sh}/F_z^{p}$ and $\mu_z^s = F_z^{sh}/F_z^{pl}$. The sign of μ represents the direction on the corresponding Cartesian coordinate axis. The angle made by the major/minor axis with respect to the sliding direction, $\beta\epsilon\left[0,\ 90^0\right]$ for all possible orientations. The ploughing depth d for load controlled ploughing is found from the contact radius $a_z = A_{xy}/\pi e_x e_y$ of the reference sphere for the ellipsoid as $d = r - \sqrt{r^2 - a_z^2}$.

The shear strength of the contact interface, τ_{sh} varies from 0 for a frictionless contact to the shear strength of the bulk, κ for an perfectly uncontaminated surface. The ratio of the interfacial shear strength to bulk shear strength is the interfacial friction factor, $f = \tau_{sh}/\kappa$, $f\epsilon[0,\ 1]$. According to Tresca and von Mises failure criterion, a metal fails in pure shear when the shear stress, exceeds its shear strength which is **½** or $1/\sqrt{3}$ times the uniaxial yield strength, σ_y

respectively. Now as per Tabor, the hardness H of most plastically deforming metals is 2.8 *to* 3 times their σ_y [40]. Expressing shear strength as a function of hardness, we have $\kappa = H/3\sqrt{3}$ and $f = 3\sqrt{3}\mathbf{Mu}$, $\mathbf{Mu} = \tau_{sh}/H$. For $\mathbf{Mu}\in(0$ to $1)$, $f \in (0$ to $0.18)$. In the results presented below, a rigid-plastic substrate in a dry, uncontaminated and perfectly smooth contact with the asperity is assumed. Thus we have $p_{pl} = H$ and $\tau_{sh} = H/3\sqrt{3}$ [3]. The hardness is $H = 450MPa$.

3.1 Depth controlled ploughing results comparison

Initial comparisons on the forces acting on the asperities as a function of asperity size and orientation are drawn between both the studied geometries of elliptic-paraboloid and ellipsoid using results from depth controlled ploughing. Further comparisons are drawn using the depth controlled ploughing results for elliptic-paraboloid shaped asperity approximated as hexagonal pyramids in de Rooij et al [29] and [3]and ellipsoid shaped asperity approximated as spherical asperity in Conry et al. [8] where both the current and the compared models use plasticity theory to obtain the forces acting on the asperity. The following comparisons have been done to validate the results of the analytical model before further explaining the results in section 3.2 using load controlled ploughing.

Comparison of ellipsoid with elliptic-paraboloid shape asperity.

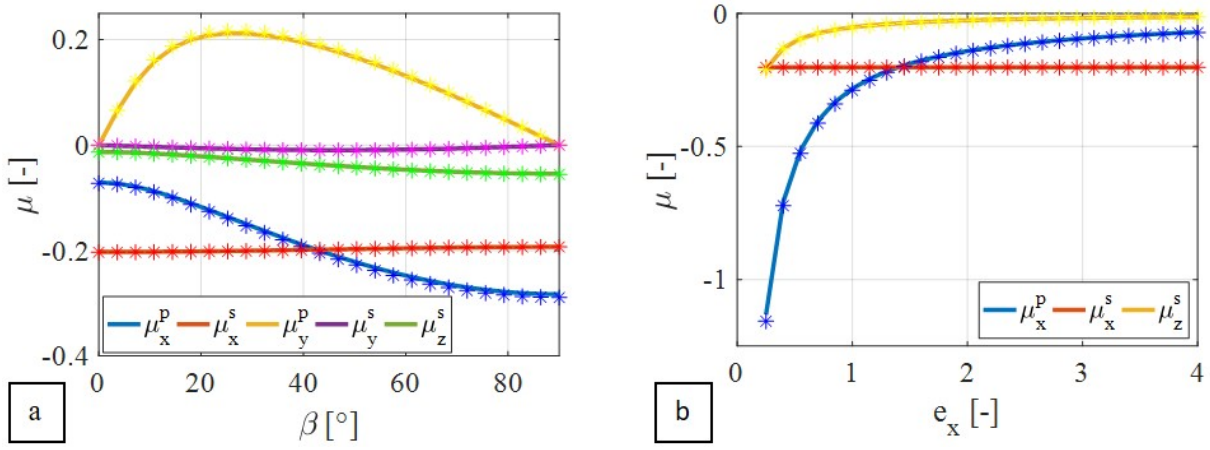

Figure 5: Variation of forces normalized with force acting in the z direction, μ with (a) angle of orientation β (b) and contact axis size in $x-$ sliding direction due to ploughing of an elliptic-paraboloid shape asperity and ellipsoid shape asperity (shown with markers of same colour) with reference radius $c = 500\ \mu m$, both having same contact size and ploughing depth of $100\mu m$.

The variation of forces acting on a elliptic-paraboloid shaped asperity sliding through a rigid plastic has been resolved in all three axis and normalized with the force in z-direction is given in figure 5. Figure 5 also compares the forces obtained for an ellipsoid with the same ploughing depth and contact axis size and shows near perfect match for both the geometries. This results from the parabolic approximation of the spherical contact radius (reference radius R) $a = \sqrt{2Rd - d^2} \approx \sqrt{2Rd}$, for smaller ploughing depths d. It must be noted that the $d = 100\mu m$ in figure 5 is in the very high and of comparable order to the asperity reference size $R = 500\mu m$. As the ploughing depth approaches the reference radius of the ellipsoidal

asperity or its ellipticity ratio increase to a very high value, the forces on it deviates from that of the elliptic-paraboloid. However, for most physical ploughing depths and ellipticity ratios, both elliptic-paraboloid and ellipsoid shaped asperities have the same variation in forces with orientation and size of the asperity.

To compute the forces acting on an elliptic-paraboloid shape asperity ploughing at a given depth, the length of the axes of the contact patch a_x and a_y and the orientation in the sliding plane β must be defined. Mathematically, an ellipsoid requires an additional parameter, the reference radius to define its geometry compared to the elliptic-paraboloid in computing forces in ploughing. Further, due to the closed surface geometry, the penetration depth for an ellipsoid is restricted to its axes size in z direction unlike elliptic-paraboloid in case of real asperities. The variation in the forces with size and orientation of the asperity shown in figure 5 are further explained in section 3.2. The study in section 3.2, on the effect of asperity size and orientation have been considered similar for both the geometries mentioned above.

3.2 Comparison with ploughing by a spherical asperity

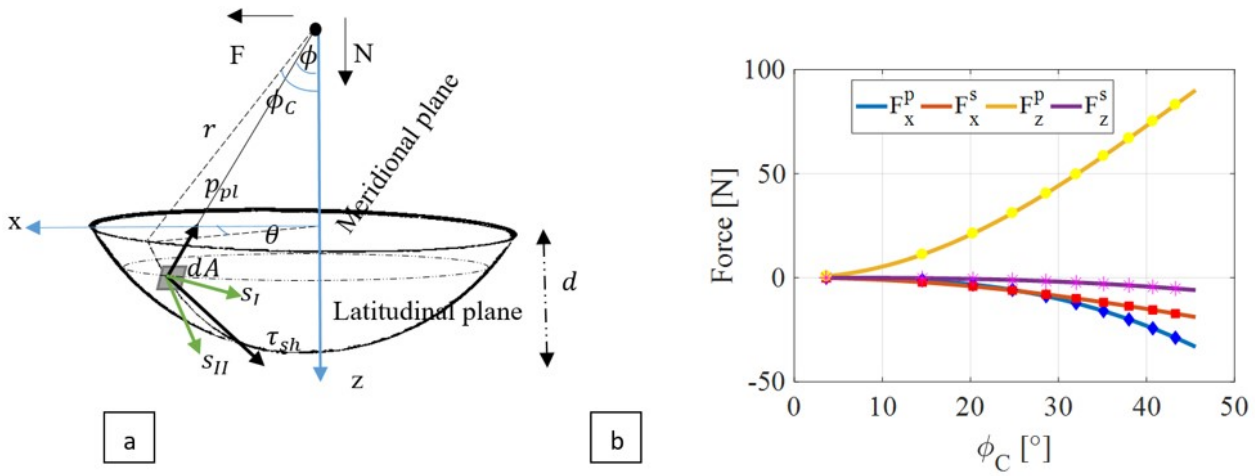

Figure 6: Forces on a spherical asperity (of diameter 1 mm) ploughing through a rigid plastic substrate (a) shown as a schematic of resolution of forces along x and z axis (b) plotted against angle contact angle ϕ_c (indentation depth) shown by solid line for current model and dots for results from Conry et al. [8].

The analytical model for a spherical asperity ploughing through a substrate, given in [8] computes the total force on the asperity by integrating the force on an elemental area of the sphere with radius r as shown in figure 6a. As mentioned in Conry et al. [8], the ploughing component of the lateral force (F_f) necessary to maintain sliding of an elemental surface area $dA = r^2 \sin\phi \; d\phi d\theta$ is given as $dF^p_x = p_{pl} \sin\phi \; \cos\theta \; dA$ while that of the ploughing component the normal force ($\boldsymbol{N}$) necessary to maintain the load balance is given as $dF^p_z = p_{pl} \cos\phi \; dA$. The shear component of the lateral force is given as $dF^s_x = (s_I \, |\sin\theta \, | + s_{II} \cos\theta \; \cos\phi \;)dA$ and that of the normal force is given as $dF^s_z = (s_{II} \sin\phi \;)dA$, where s_I and s_{II} are the shear components along the tangent to the intersection between the latitude plane and the sphere and the tangent to the intersection of meridional plane and sphere respectively. The components of τ_{sh} which acts opposite to the direction of relative tangential surface velocity at the elemental area, is given by equation 14.5. The elemental forces were integrated over the surface of the sphere in contact with the plastically deforming substrate (frontal half) with

ploughing depth d, i.e. $\theta\epsilon(-\pi/2, \pi/2)$ and $\phi\epsilon(0, \phi_C)$, where $\phi_C = \arccos(1 - d/r)$. The components of total force in the x and z axes are given in equation 14.1-14.4.

The results obtained from equation 14 are plotted in the figure 6b against that obtained by simplifying an ellipsoidal asperity into a sphere ($e_x = 1,\ e_y = 1,\ c = r$) for varying penetration depths d and hence angles ϕ_C. It can be seen that all the components of the forces due to plastic deformation of the substrate and interfacial shear along lateral and normal directions gives a perfect fit with the results obtained from [8].

$$F_x^p = -p_{pl} r^2 \left(\phi_C - \sin\phi_C \cos\phi_C\right) \tag{14.1}$$

$$F_x^s = -2\tau_{sh} r^2 \int_0^{\frac{\pi}{2}} \int_0^{\phi_C} \sin\phi \sqrt{\sin^2\theta + \cos^2\theta \cos^2\phi}\, d\phi d\theta \tag{14.2}$$

$$F_z^p = \frac{\pi}{2} p_{pl} r^2 (\sin\phi_C)^2 \tag{14.3}$$

$$F_z^s = -\tau_{sh} r^2 \left(\sin\phi_C - (\cos\phi_C)^2 \ln\left(\sec\phi_C - \tan\phi_C\right)\right) \tag{14.4}$$

$$\begin{aligned} s_I &= \frac{\tau_{sh} |\sin\theta|}{\sqrt{(\sin\theta)^2 + (\cos\theta \cos\phi)^2}} \\ s_{II} &= \frac{\tau_{sh} \cos\theta \cos\phi}{\sqrt{(\sin\theta)^2 + (\cos\theta \cos\phi)^2}} \end{aligned} \tag{14.5}$$

3.3 Comparison with ploughing by a hexagonal-pyramidal asperity

In the work by de Rooij et al. [19], the hexagonal pyramidal shaped asperity was divided into three sections consisting of two pyramids with a triangular base and a prism/ pyramid with a rectangular base, as shown in figure 7a and b. The base of the triangles of the constituting hexagonal base is given as l, while the their altitude are given as w_I and w_{III}. The distance between the sides central parallelogram section of the hexagon is given as w_{II}. The height of the pyramid is given as h. The hexagon is now scaled into an ellipse oriented at an angle β along the sliding direction as shown in figure 7c. The dimensions $l,\ w_I$ and w_{III} of the hexagonal asperity are then scaled into an ellipse using the scaling factor, c as given in equation 15.1 The friction forces (along the sliding plane) on the hexagonal-pyramidal asperity oriented at an angle α to the sliding direction, ploughing through a rigid substrate is given in equation 15.2 -15.5 by combining the forces on the individual sections $I,\ II$ and III.

Van der Linde [3] and de Rooij [29] used the description above to calculate ploughing forces on a single asperity. In order to compare the results from [3] and [29] with the current model, the ploughing depth h and axes sizes of the elliptic contact patch of the asperity a and b are chosen as $h/b = 0.1$ and 0.25 and $a/b = 1.5$ and 10 respectively. It can be seen from figure 8 that the results from the current model and from [3] and [29] mostly match. The coefficient of friction due to the plastic flow pressure of the substrate in the sliding x direction matches in both the models. However, the maximum coefficient of friction in the y direction, for asperities with high ellipticity ratios, in case of de Rooij et al. [29] is higher than that obtained from the current model (see figure 8c and d). The higher maxima in coefficient of friction for results obtained from [29] and [3] could be explained due to the higher asymmetry in case of the hexagonal pyramid scaled to an elliptic-paraboloid with a high ellipticity ratio. Similarly the coefficient of friction due to shearing in the x direction is lower than the results obtained by van der Linde [3] as compared to the current model due to possible reduction in horizontal projection of contact

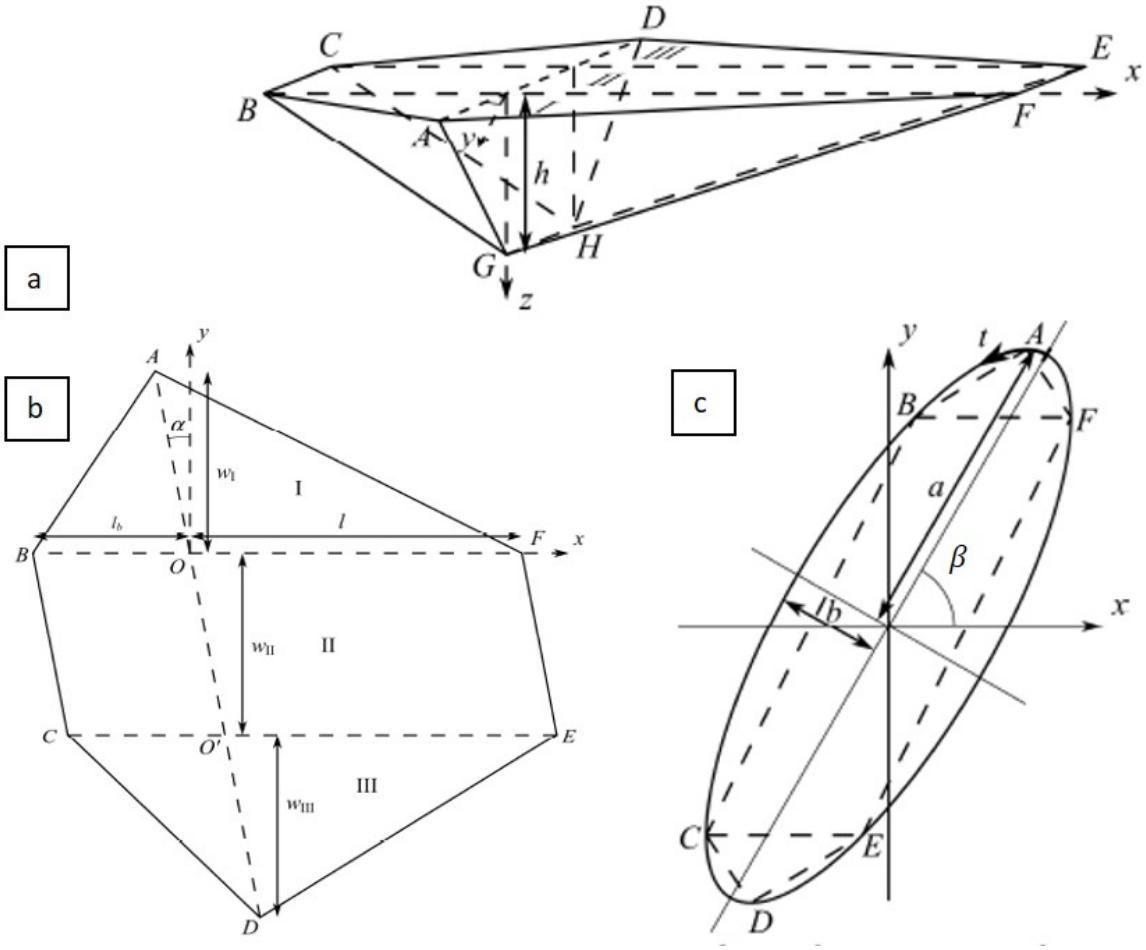

Figure 7: (a) A hexagonal-pyramidal asperity with (b) dimensions of a hexagon base oriented at an angle α to y axis and its fitting to an (c) elliptic base of an asperity oriented at angle β with respect to x axis [29].

area A_{xy} in the hexagonal approximation of the ellipse. The vertical projected shape for van der Linde's model changes with β from a triangle to a trapezoid (figure 7a) diverging from the elliptic approximation of the surface height for the current model and thus leads to a difference in A_{xz} and A_{yz} between the two models and so between the force components.

$$c_{scale} = -lw_{II} + \frac{\sqrt{l^2 w_{II}^2 + \pi abl\,(w_I + w_{III})}}{l\,(w_I + w_{III})} \tag{15.1}$$

$$F_x^p = -p_{pl} h \left(\frac{1}{2} w_I + w_{II} + \frac{1}{2} w_{III} \right) \tag{15.2}$$

$$F_x^s = -\frac{\tau_{sh}}{2} \left(\sqrt{(w_I l)^2 + h^2 (l + w_I \tan\alpha\ )^2} + 2w_{II} \sqrt{l^2 + h^2 \tan\alpha} + \sqrt{(w_{III} l)^2 + h^2 (l - w_{III} \tan\alpha)^2} \right) \tag{15.3}$$

$$F_y^p = -p_{pl} h \tan\alpha \ \left(\frac{1}{2} w_I + w_{II} + \frac{1}{2} w_{III} \right) \tag{15.4}$$

$$F_y^s = \tau_{sh} h^2 \left(\frac{0.5 w_I\,(l + w_I \tan\alpha\ )}{\sqrt{(w_I l)^2 + h^2 (l + w_I \tan\alpha\ )^2}} + \frac{w_{II} \tan\alpha}{\sqrt{l^2 + (h \tan\alpha\ )^2}} - \frac{0.5 w_{III}\,(l - w_{III} \tan\alpha\ )}{\sqrt{(w_{III} l)^2 + h^2 (l - w_{III} \tan\alpha\ )^2}} \right) \tag{15.5}$$

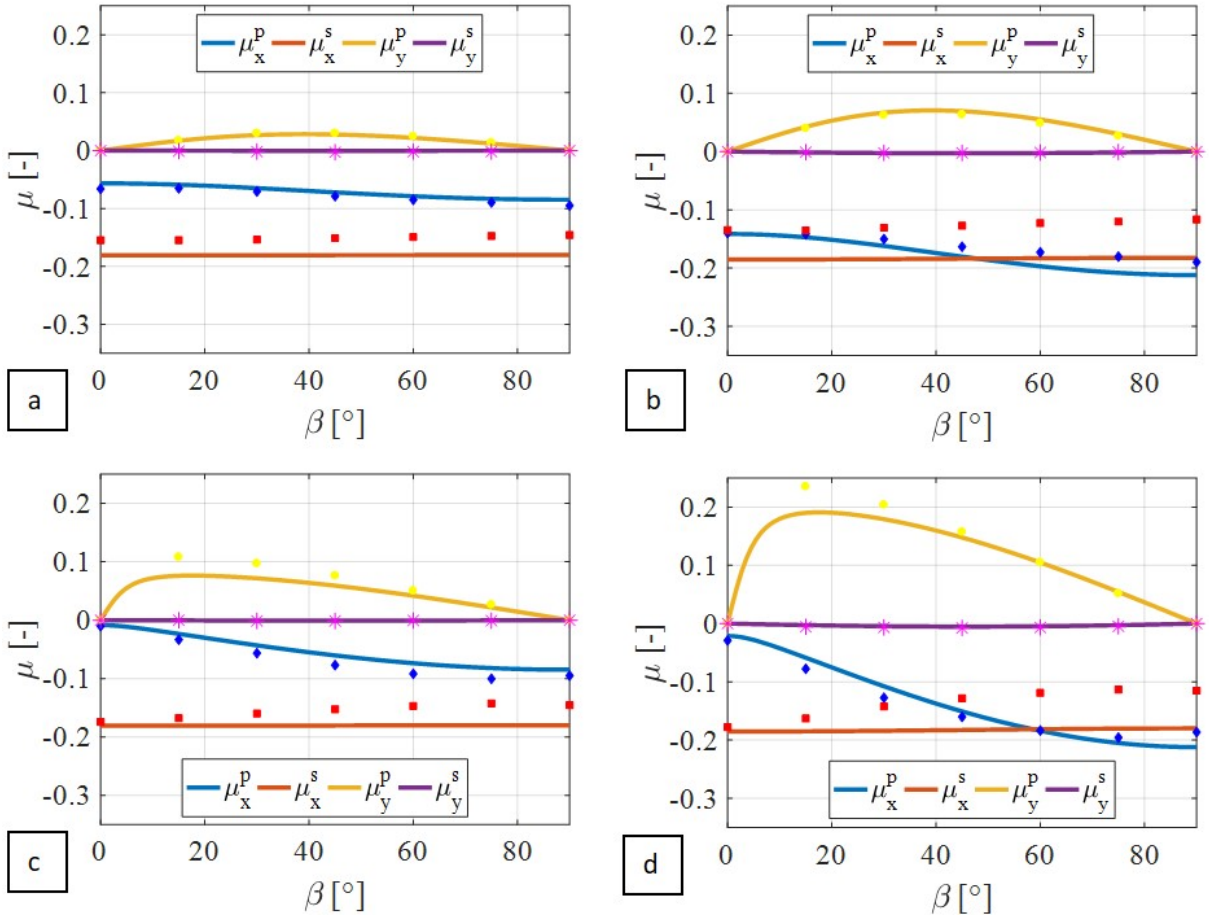

Figure 8: Comparison between the friction coefficients as a function of asperity orientation β obtained from depth controlled friction model (including interfacial friction factor $f = 0.18$) (solid lines) and van der Linde model [3] and [29] (dots of same colour) for (a) $a/b = 1.5$ and $h/b = 0.1$ (b) $a/b = 1.5$ and $h/b = 0.25$ (c) $a/b = 10$ and $h/b = 0.1$ and (d) $a/b = 10$ and $h/b = 0.25$.

3.4 Load controlled ploughing results discussion

The effect of asperity size, shape and orientation on the forces acting on an asperity ploughing through a rigid-plastic substrate is shown separately and simultaneously in this section. Concluding from section 3.1.1, the results are valid both for elliptic-paraboloid and ellipsoid asperities at the given applied loads.

3.4.1 Variation with angle of orientation, β

The effect of asperity orientation β on the forces due to ploughing is shown in figure 9 for different axes sizes in the sliding direction, a. The component of the force on the asperity due to plastic flow pressure is always opposite to the component of its applied load in the given direction. Hence, for $e_x > 1$, F_x^{pl} is in $-x$ direction and F_y^{pl} is in $+y$ direction. It can be seen that the direction of the force due to plastic flow changes direction in y direction as a reduces and $a < b$, i.e. $e_x < 1$. The point of separation of the plastic flow, for $\beta \in (0°,\ 90°)$ has $-y$ coordinate for $e_x < 1$ and moves to $+y$ coordinate for $e_x > 1$. Force component F_x^{pl} increases with the projected area in the yz plane A_{yz}. Thus, F_x^{pl} increases with β for $e_x > 1$ while it decreases with β for $e_x < 1$. The maximum $F_y^{pl}$is for $\beta \in (0°,\ 45°)$ for $e_x > 1$ and maxima

shifts from 45^0 to 0^0 as e_x increases. The exact opposite happens for $e_x < 1$ as e_x decreases. $F_y^{pl} = 0$ at $\beta = 0°$ and $90°$ due to symmetry of asperity w.r.t. x axis.

The forces due to the interfacial shear stress in x and y direction doesn't vary as much with β as the forces due to the plastic pressure. As shown in figure 9, μ_x^{sh} varies around $0.2 \approx 1/3\sqrt{3} = \tau/H$ as the major component of the force F_x^{sh} comes from the interfacial shear on A_{xy} resulting in $\mu_x^{sh} \approx \tau/H$. However, F_x^{sh} marginally decreases or increases with β for $e_x > 1$ and $e_x < 1$ respectively. This is because of the corresponding change in A_{xz} with β as seen from equation 3.3 and 6.4. The contribution of A_{xz} to F_x^{sh} is lower compared to that of A_{xy} for smaller depths d and e_x closer to unity as $A_{xz} < A_{xy}$. However, as d increases and e_x diverges from unity i.e. $e_x \gg 1,\ e_x \ll 1$, change in A_{xz} dominates equation 6.4 and F_x^{sh}varies more with β as seen in figure 8a. Force F_y^{sh} diminishes at $\beta = 0^0$ and $\beta = 90^0$ orientation due to symmetry of plastic flow on the xz plane. For $\beta \in (0°,\ 90°)$ and e_x closer to unity F_y^{sh} has a negligible contribution to F_y. For larger e_x, i.e. $e_x \gg 1$, F_y^{sh} becomes more predominant and has a maxima for $\beta \in (45°,\ 90°)$ which shifts from $45°$ to $0°$ as $e_x > 1$ increases. The exact opposite happens for $e_x \ll 1$ as e_x decreases. Force F_z^{sh} increases in a similar fashion to F_x^{pl}, because in both cases A_{yz} increases (equation 3.2 and 3.3). The direction of force due to interfacial shear stress is always in the opposite direction of the relative tangential velocity of the asperity with the plastic flow in the substrate. Hence for $e_x > 1$, F_x^{sh} is in $-x$ direction, F_y^{sh} is in $-y$ direction and F_z^{sh} is in $-z$ direction. The direction of F_y^{sh} reverses for $e_x < 1$.

The components of forces for an ellipsoidal asperity with varying shape i.e. increasing e_x while keeping a constant cross sectional area with $e_x e_y = 1$ is shown in figure 10. The forces vary similarly as to the case shown in figure 9c and 9d for $e_x > 1$. The change of the components of forces for the 3 axes are more pronounced compared to cases with increase in size in only one direction (e_x) due to the increased asymmetry of the asperity since in case of $e_x e_y = 1$ by the simultaneous increase in e_x and decreases in e_y. Thus it can be concluded from figure 10 that smaller asperity size leads to the larger normalized forces due to higher penetration depth. Also from figure 10 it can be seen that the effect of β on the forces acting on the asperity becomes more pronounced for higher ellipticity ratio (asymmetry).

3.4.2 Variation with axes sizes (ellipticity ratios) e_x and e_y

An ellipsoidal asperity with one of their axis along the sliding direction are axisymmetric with respect to the plastic flow in the xz plane due to which, $F_y^{pl} = 0$ and $F_y^{sh} = 0$. Four cases have been considered for such asperities where the size of each axis in the sliding plane xy is increased individually, simultaneously and reciprocally from $e \in (1/4,\ 4)$. The ploughing depth d, decreases for ellipsoidal asperities where the axis size is increased individually. The decrease in d with increase in e_x reduces A_{yz}, thereby reducing F_y^{pl}(see figure 11a and 11b). In case of an increase in e_y, the decrease in ploughing depth is nullified by an increase in A_{yz}. Thus, F_x^{pl} decreases with increase in e_y at a lower rate as compared to increase in e_x. The force F_x^{sh} decreases marginally with an increase in e_x as the reduction in ploughing depth and increase in a_x nullifies the change in A_{xz} and A_{xy} with e_x. However, with increase in e_y, the penetration depth decreases, with constant a_x and thus A_{xz} decrease and hence F_x^{sh} decreases rapidly with e_y for lower e_y. On the other hand, F_z^{sh} decreases rapidly with e_x as it is predominantly a function of A_{yz} which decreases with ploughing depth. The decrease in F_z^{sh} with e_y is lower compared to e_x as the decrease in ploughing depth is nullified by the increase in a_y resulting in constant A_{yz}.

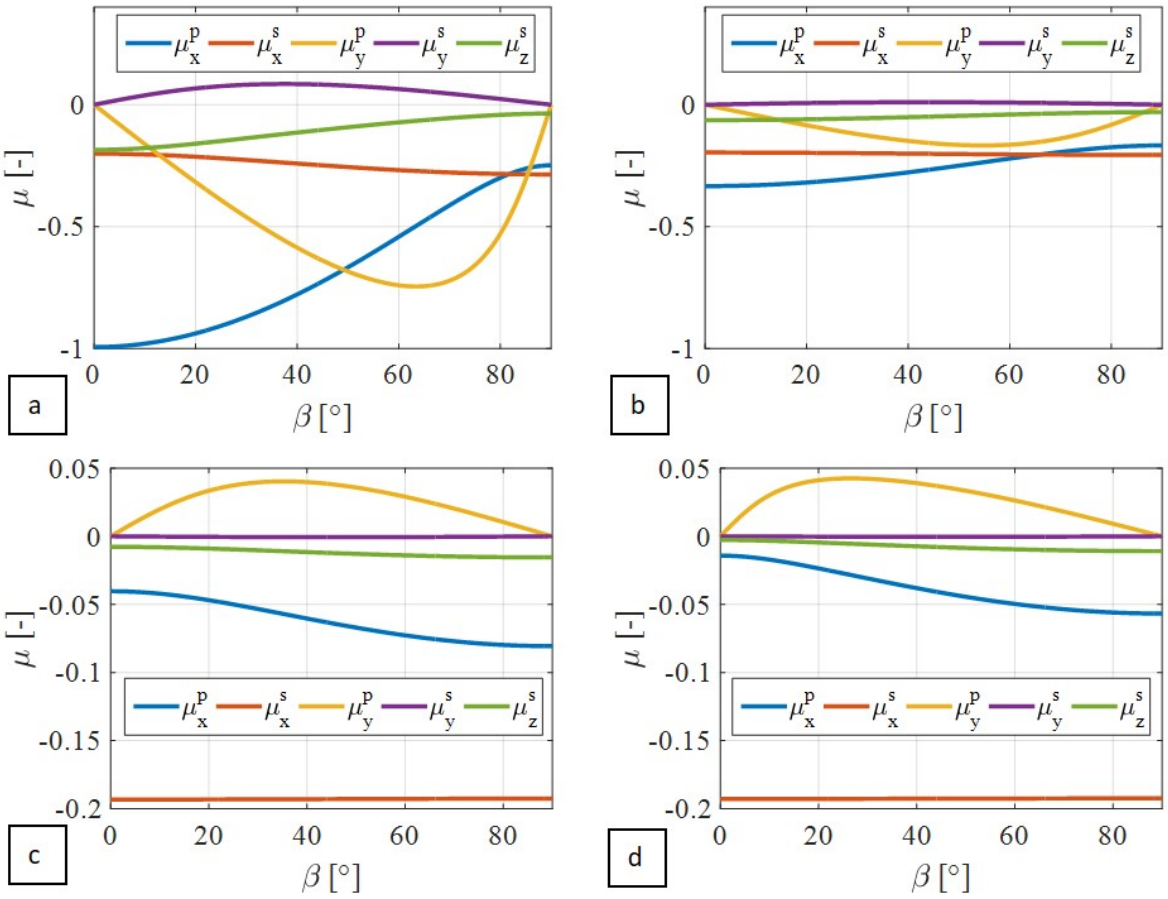

Figure 9: Variation of forces, normalized with normal load, μ with angle of orientation β due to ploughing of an ellipsoidal asperity with $c = 200\ \mu m$ under an applied load $2N$ with the axes size in $x-$ sliding direction (a) $e_x = 0.25$, (b) $e_x = 0.5$, (c) $e_x = 2$ and (d) $e_x = 4$, and $e_y = 1$.

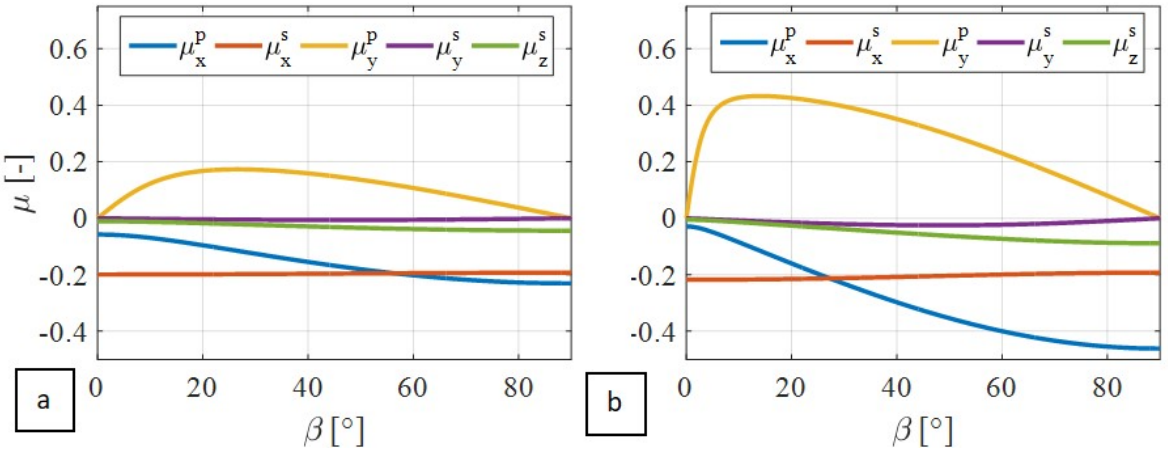

Figure 10: Variation of forces, normalized with normal load, μ with angle of orientation β due to ploughing of an ellipsoidal asperity with $c = 200\ \mu m$ under an applied load $2N$ with the axes size in $x-$ sliding direction as a reciprocal of the axes size in $y-$direction $e_x e_y = 1$ (a) $e_x = 2$ and (b) $e_x = 4$.

The effect of simultaneous increase in e_x and e_y results in the combination of effects of individual increase in e_x and e_y and hence magnification of the components of forces with respect to axis

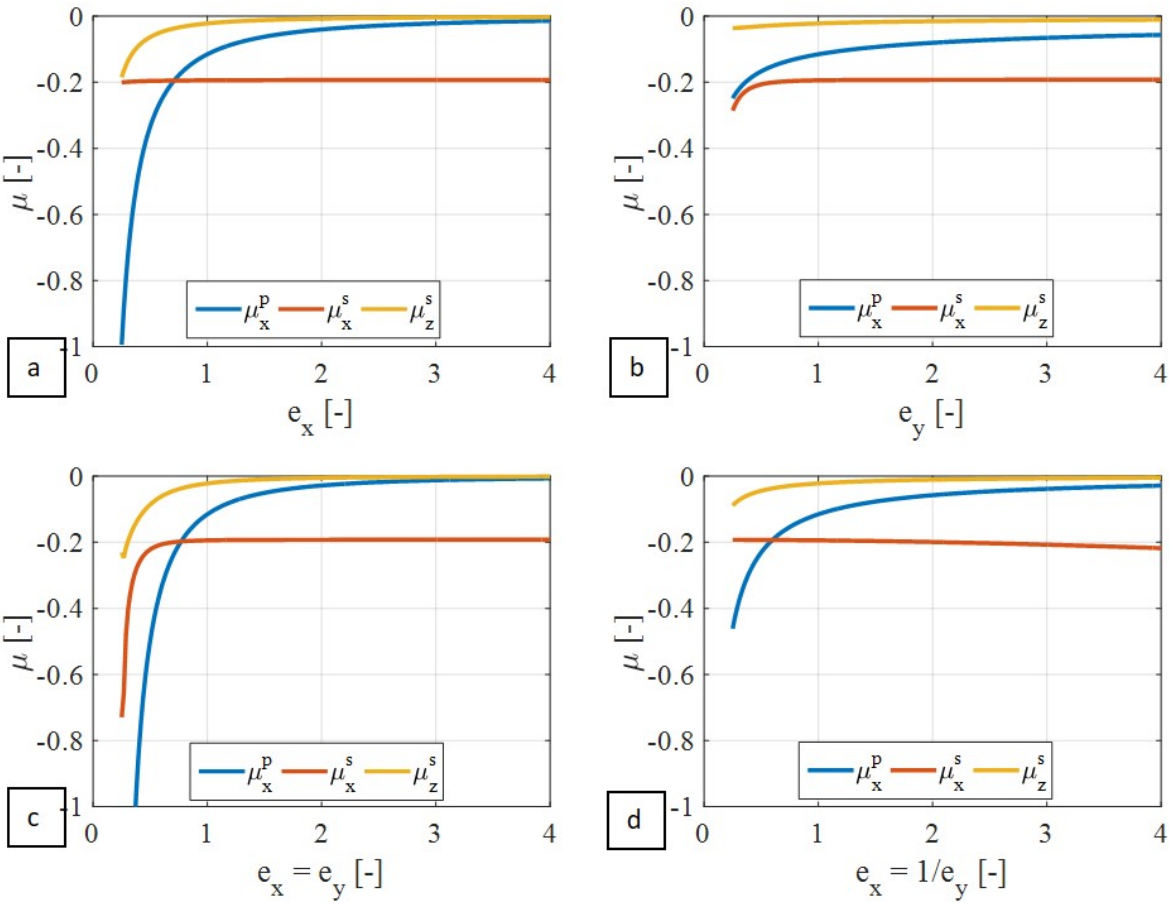

Figure 11: Variation of forces, normalized with normal load, μ with axis size due to ploughing of an ellipsoidal asperity oriented along the $x-$ sliding direction with $c = 200\ \mu m$ under an applied load $2N$ where axis size increases in (a) x direction only (b) y direction only (c) x direction as reciprocal of y direction and (d) both x and y direction.

sizes (see figure 11c). In the case of ellipsoidal asperity where one axis (e_x) increases while the other (e_y) decreases as its reciprocal, A_{xy} and hence d remains constant with e_x. The force F_x^{pl} decreases with increase in e_x due to the decrease in e_y and hence A_{yz}. Following equation 3.3, F_x^{sh} increases with e_x due to increase in A_{xz}. Similarly, the force component F_z^{sh} decreases with e_x due to the increase in e_y and hence A_{yz}. Unlike the previous cases where the increase in ellipsoid size was coupled with decrease in d to change the projected areas and forces, for $e_x e_y = 1$ the forces and the projected areas vary with the axes size only (constant d).

3.4.3 Variation with angle of orientation and axis size

It can be seen from the contour plots in figure 12 that both the normalized forces are symmetric, although in different magnitude, along the line $e_x = 1$, as variation of normalized forces for rotation of an ellipsoid with initial $e_x > 1$ from $\beta = 0°$ to $90°$ is the same as that for the rotation of the ellipsoid with $e_x = 1/e_y < 1$ from $\beta = -90°$ to $0°$. The maxima for F_x^{pl} and F_z^{sh}, both of which are functions of A_{yz} (equation 3.3) is obtained at $\beta = 90°$ for $e_x > 1$ and at $\beta = 0°$ for $e_x < 1$, as shown in figure 12a and 12e. On the contrary, the maxima for F_x^{sh}, which is a function of A_{xz} (equation 3.3) is obtained at $\beta = 0°$ for $e_x > 1$ and at $\beta = 90°$ for $e_x < 1$, as shown in figure 12c. The maxima for F_y^{pl} shifts towards $0°$ with an increase in ellipticity ratio, as shown in figure 12b. F_y^{sh} acts opposite to the direction of F_p^{sh} resulting from plastic pressure, and thus along the shear flow. So, the maxima for F_y^{pl} shifts towards $90°$ with an

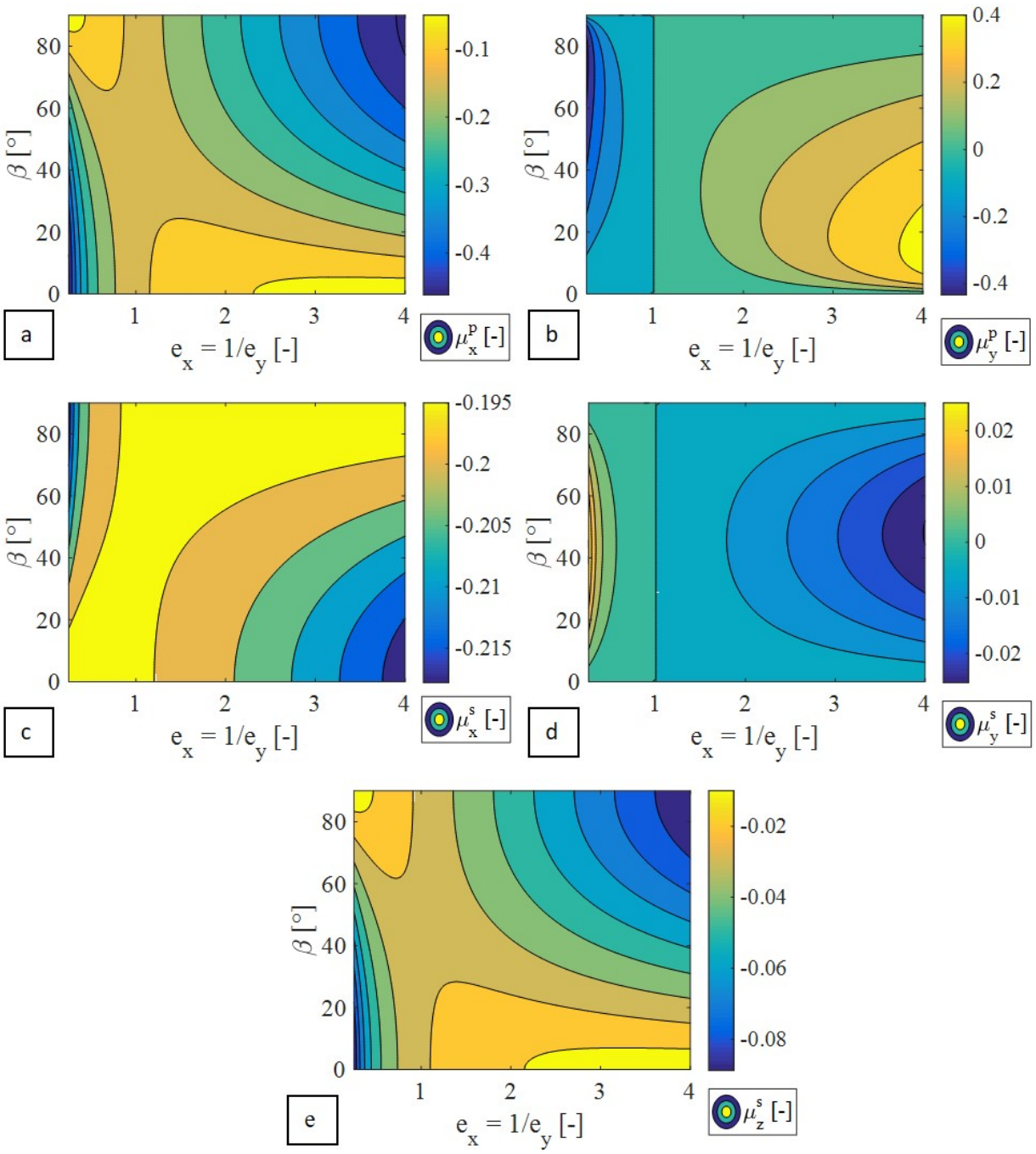

Figure 12: Contour plots represent components of normalized force μ due to plastic pressure in (a) x and, (b) y axes and due to interfacial shearing in (c) x, (d) y and (e) z axes plotted against axis size ($e_x e_y = 1$) and angle of orientation β along the $x-$ sliding direction with $c = 200\ \mu m$ under an applied load $2N$.

increase in ellipticity ratio, although with much lower rate compared to F_y^{sh}, as shown in figure 12d. Further, the change in all the forces increases w.r.t. β as e_x diverges from unity, leading to more asymmetry.

The developed analytical model has been used to study and evaluate the variation in components of total force (friction) along the coordinate axes, acting on elliptic-paraboloid asperities with varying sizes, ellipticity ratios and orientations. An elliptic-paraboloid asperity

with given geometrical parameters of reference axis size c, ellipticity ratios (e_x, e_y), orientation β and penetration/contact depth d can be used to describe the contact of single asperity summit on a rough surface. The asperities in the contact of an (anisotropic) rough tool surface with a smooth, soft substrate can be mapped as a combination of differently shaped and differently oriented elliptic contact patches [28] and [26]. In this way, the contact between a hard/rough and a smooth/soft surface can be analysed by describing asperities by a set of (ellipsoids) elliptic paraboloids, where the forces and scratch depth can be calculated by applying the theory developed to a single asperity.

4 Conclusion

An analytical model to study the effect of geometry of an elliptic-paraboloid and ellipsoid shaped asperity ploughing through a rigid-plastic substrate has been developed. The model has calculated the components of force acting on the asperity, resolved in the three Cartesian coordinates axis, due to the plastic deformation of the substrate and interfacial shear at the contact. The effects of asperity orientation with sliding direction and axes sizes have been studied and discussed separately and simultaneously for both load and depth controlled ploughing. The model has also been verified with similar versions of analytical models for elliptic-paraboloid shaped asperities available in the literature [3], [29] and spherical asperity available in [8]. The analytical model is suitable to compute forces acting on an asperity ploughing through a rigid plastic substrate where there is no material removal from the substrate.

Acknowledgment

This research was carried out under project number S22.1.14520a in the framework of the Partnership Program of the Materials innovation institute M2i (www.m2i.nl) and the Technology Foundation TTW (www.stw.nl), which is part of the Netherlands Organization for Scientific Research (www.nwo.nl).

Bibliography

[1] J. Goddard and H. Wilman. "A theory of friction and wear during the abrasion of metals". In: Wear 5 (1962), pp. 114–135. DOI: 10.1016/0043-1648(62)90235-1.

[2] J.M. Challen and P.L.B. Oxley. "An explanation of the different regimes of friction and wear using asperity deformation models". In: Wear 2 (1979), pp. 229–243. DOI: 10.1016/0043-1648(79)90080-2.

[3] G. Van der Linde. "Predicting galling behaviour in deep drawing processes". PhD thesis. University of Twente, The Netherlands, 2011. ISBN: 978-90-365-3284-6.

[4] J.A. Williams. "Analytical models of scratch hardness". In: Tribology International 29 (1996), pp. 675–694. DOI: 10.1016/0301-679X(96)00014-X.

[5] J.A. Williams. "Wear modelling: Analytical, computational and mapping: A continuum mechanics approach". In: Wear 225-229 (1999), pp. 1–17. DOI: 10.1016/S0043-1648(99)00060-5.

[6] F.P. Bowden, A.J.W. Moore, and D. Tabor. "The Ploughing and Adhesion of Sliding Metals". In: Journal of Applied Physics 14 (1943), pp. 80–91. DOI: 10.1063/1.1714954.

[7] DF. Moore. "Friction of Metals". In: Principles and applications of Tribology. Pergamon Press, Oxford, UK, 1975, pp. 33–60. DOI: 10.1016/C2013-0-02605-9.

[8] N. Tayebi, T.F. Conry, and A.A. Polycarpou. "Determination of hardness from nanoscratch experiments: Corrections for interfacial shear stress and elastic recovery". In: Journal of Materials Research 18 (2003), pp. 2150–2162. DOI: 10.1557/JMR.2003.0301.

[9] A.P. Green. "The plastic yielding of metal junctions due to combined shear and pressure". In: Journal of the Mechanics and Physics of Solids 2 (1954), pp. 197–211. DOI: 10.1016/0022-5096(54)90025-3.

[10] J.M. Challen and P.L.B. Oxley. "Slip-line fields for explaining the mechanics of polishing and related processes". In: International Journal of Mechanical Sciences 26 (1984), pp. 403–418. DOI: 10.1016/0020-7403(84)90030-4.

[11] M. Busquet M and A.Torrance. "A numerical slipline field for the sliding cylinder problem". In: Wear 241 (2000), pp. 86–98. DOI: 10.1016/S0043-1648(00)00360-4.

[12] J.D. Bressan and J.A. Williams. "Mathematical slip-line field solutions for ploughing a hard particle over a softer material". In: Wear 267 (2009), pp. 1865–1872. DOI: 10.1016/j.wear.2009.03.008.

[13] K. Hokkirigawa and K. Kato. "An Experimental and Theoretical Investigation of Plowing, Cutting and Wedge Formation during Abrasive Wear". In: Tribology International 21 (1988), pp. 51–57. DOI: 10.1016/0301-679X(88)90128-4.

[14] K. Komvopoulos, N. Saka, and N.P. Suh. "Plowing Friction in Dry and Lubricated Metal Sliding". In: Journal of Tribology 108 (1986), pp. 301–312. DOI: 10.1115/1.3261181.

[15] A.A. Torrance. “The influence of surface deformation on mechanical wear”. In: Wear 200 (1996), pp. 45–54. DOI: 10.1016/S0043-1648(96)07280-8.

[16] L.A. Mitchell and M.D. Rowe. “Influence of Asperity Deformation Mode on Gas Leakage between Contacting Surfaces”. In: Journal of Mechanical Engineering Sciences 11 (1969), pp. 534–549. DOI: 10.1016/0020-7403(84)90030-4.

[17] M.P.F Sutcliffe. “Surface asperity deformation in metal forming processes”. In: International Journal of Mechanical Sciences 30 (1988), pp. 847–868. DOI: 10.1016/0020-7403(88)90010-0.

[18] M. De Vathaire, F. Delamare, and E. Felder. “An upper bound model of ploughing by a pyramidal indenter”. In: Wear 66 (1981), pp. 55–64. DOI: 10.1016/0043-1648(81)90032-6.

[19] T. Abildgaard. “Prediction of the force components acting on a ploughing cone by means of three-dimensional upper bound theory”. In: Advanced Technology of Plasticity 1 (1984). Retrieved from www.scopus.com, pp. 121–126.

[20] A. Azarkhin and O. Richmond. “A model of ploughing by a pyramidal indenter - upper bound method for stress-free surfaces”. In: Wear 157 (1992), pp. 409–418. DOI: 10.1016/0043-1648(92)90077-L.

[21] A. Azarkhin and M.L. Devenpeck. “Enhanced model of a plowing asperity”. In: Wear 206 (1997), pp. 147–155. DOI: 10.1016/S0043-1648(96)07502-3.

[22] S. Lafaye and M. Troyon. “On the friction behaviour in nanoscratch testing”. In: Wear 261 (2006), pp. 905–913. DOI: 10.1016/j.wear.2006.01.036.

[23] A.H. Carreon and P.D. Funkenbusch. “Material specific nano-scratch ploughing friction coefficient”. In: Tribology International 126 (2018), pp. 363–375. DOI: 10.1016/j.triboint.2018.05.027.

[24] J.A. Greenwood and J.P. Williamson. “Contact of nominally flat surfaces”. In: Proceedings of the royal society of London. Series A. Mathematical and physical sciences 295 (1966), pp. 300–319. DOI: 10.1098/rspa.1966.0242.

[25] P.R. Nayak. “Random process model of rough surfaces in plastic contact”. In: Wear 26 (1973), pp. 305–333. DOI: 10.1016/0043-1648(73)90185-3.

[26] A.W. Bush, R.D. Gibson, and T.R. Thomas. “The elastic contact of a rough surface”. In: Wear 35 (1975), pp. 87–111. DOI: 10.1016/0043-1648(75)90145-3.

[27] J.I. McCool. “Comparison of models for the contact of rough surfaces”. In: Wear 107 (1986), pp. 37–60. DOI: 10.1016/0043-1648(86)90045-1.

[28] X. Ma, M.B. de Rooij, and D.J. Schipper. “A load dependent friction model for fully plastic contact conditions”. In: Wear 269 (2010), pp. 790–796. DOI: 10.1016/j.wear.2010.08.005.

[29] M.B. De Rooij, G. van der Linde, and D.J. Schipper. “Modelling material transfer on a single asperity scale”. In: Wear 307 (2013), pp. 198–208. DOI: 10.1016/j.wear.2013.09.006.

[30] Y. Waddad, V. Magnier, P. Dufrénoy, and G. De Saxcé. “A multiscale method for frictionless contact mechanics of rough surfaces”. In: Tribology International 96 (2016), pp. 109–121. DOI: 10.1016/j.triboint.2015.12.023.

[31] W. Yuan, J. Long, Y. Ding, and G. Wang. “tatistical contact model of rough surfaces: The role of surface tension”. In: International Journal of Solids and Structures 138 (2018), pp. 217–223. DOI: 10.1016/j.ijsolstr.2018.01.014.

[32] Z. Gao, W. Fu, W. Wang, W. Kang, and Y. Liu. "The study of anisotropic rough surfaces contact considering lateral contact and interaction between asperities". In: Tribology International 126 (2018), pp. 270–282. DOI: 10.1016/j.triboint.2018.01.056.

[33] A. Misra and S. Huang. "Effect of loading induced anisotropy on the shear behaviour of rough interfaces". In: Tribology International 44 (2011), pp. 627–634. DOI: 10.1016/j.triboint.2010.12.010.

[34] M.A. Masen and M.B. de Rooij. "Abrasive wear between rough surfaces in deep drawing". In: Wear 256 (2004), pp. 639–646. DOI: 10.1016/j.wear.2003.10.006.

[35] M.A. Masen, M.B. de Rooij, and D.J. Schipper. "Micro-contact based modelling of abrasive wear". In: Wear 258 (2005), pp. 339–348. DOI: 10.1016/j.wear.2004.09.009.

[36] G. van der Linde, M.B. de Rooij, and D.J. Schipper. "Stability criteria for a pyramidal shaped asperity ploughing through a plastically deforming substrate". In: Wear 300 (2013), pp. 96–104. DOI: 10.1016/j.wear.2013.01.119.

[37] M.C. Hendricks. "Rotated Ellipses and Their Intersections with Lines". accessed 13 January 2019 from http://quickcalcbasic.com/ellipse%20line%20intersection.pdf. PhD thesis. -, 2012.

[38] S.R. Keller. "On the Surface Area of the Ellipsoid". In: Mathematics of Computation 33 (1979), pp. 310–314. DOI: 10.1090/S0025-5718-1979-0514826-4.

[39] D. Poelaert, J. Schniewind, and F. Janssens. "Surface Area and Curvature of the general Ellipsoid". In: arXiv preprint arXiv:1104.5145 (2011). e-print arXiv:1104.5145, [math.CA] arXiv.org/abs/1104,5145.

[40] D. Tabor. The hardness of metals. Oxford University Press, London, 1951. ISBN: 0-521-29183-6.

Paper C

A material point method based ploughing model to study the effect of asperity geometry on the ploughing behaviour of an elliptical asperity

Tanmaya Mishra[1*], Matthijn de Rooij[1], Meghshyam Shisode[2], Javad Hazrati[2], and Dirk J. Schipper[1]

[1]Surface Technology and Tribology, Faculty of Engineering Technology, University of Twente, 7500 AE Enschede, the Netherlands
[2]Nonlinear Solid Mechanics, Faculty of Engineering Technology, University of Twente, 7500 AE Enschede, the Netherlands

Abstract

A material point method (MPM)-based numerical model has been used to study the effect of asperity size and orientation relative to sliding direction on the ploughing behaviour of a rigid, ellipsoidal asperity. Based on the simulated ploughing behaviour, an analytical model has been extended to calculate the ploughing depths over the wear track and compute the forces acting over the contacting surface of an ellipsoidal asperity sliding through a rigid-plastic substrate. The analytical model results have been compared with the MPM model results. The MPM model results are also validated to be in good agreement with the friction forces and ploughing depths measured from the ploughing experiments on lubricated steel sheets with ellipsoidal indenters up to certain sizes and orientations.

Keywords: Friction modelling, Ellipsoidal asperity, Ploughing, Multi-asperity.

Nomenclature of symbols

A	Contact area of the asperity with substrate	a	Major axis of base of elliptic asperity
A_Δ	Area of the surface element	$a_d \pm a_m$	Designed axes length ± avg. deviation
A_{xy}	Projected area in xy-plane	a_x	Major axis of elliptic contact patch in x-axis
A_{xz}	Projected area in xz-plane	a_y	Minor axis of elliptic contact patch in y-axis
A_{yz}	Projected area in yz-plane	a_z	Reference contact radius
C	Centre of the elliptic contact base	b	Minor axis of base of elliptic asperity
$\boldsymbol{C}$	Cartesian coordinate system: (x, y, z)	c	Height of the elliptic asperity
C_p	Coefficient: Interfacial shear-pressure relation	d/d_p	Penetration/ploughing depth of the asperity
H	Hardness of the rigid-plastic substrate	d_g	Groove depth
$\boldsymbol{F}$	Total force vector acting on the sliding asperity	d_0	Ploughing depth in front of the asperity along the x axis
F^p	Force on the asperity due to plastic deformation	d_{+y}	Ploughing depth at the periphery of the asperity on the $+y$ axis (i.e. point N)
F^s	Force on the asperity due to interfacial shear	d_{-y}	Ploughing depth at the periphery of the asperity on the $-y$ axis (i.e. point S)
$F_{x/y/z}$	Force in the x, y or z direction	d_S	Total ploughing depth at point S.
$\boldsymbol{I}$	Identity matrix	e_x	Ellipticity ratio of asperity in x-axis
$\boldsymbol{J}$	Jacobian transformation matrix	e_y	Ellipticity ratio of asperity base in y-axis
K	Bulk modulus	f	Ratio of interfacial and bulk shear strength
L	End point of contact in z axis	h_{pu}	Pile-up height
L_x^{SN}	Projected length of arc SN in the x axis	l	Ratio of ref. pile-up height and groove depth
M	Plastic flow separation point in contact plane	m	Slope of a point on contact plane
$\boldsymbol{N}$	Normal force acting on the asperity	n	Fitting factor to calculate pile-up height

Nomenclature of symbols

N	Contact end point in contact plane in $+y$ axis	o	Fitting factor to calculate groove depth
O	Centre of the ellipsoidal asperity	n_p	Exponent: Interfacial shear-pressure relation
R_a	Mean surface roughness	p	Fitting factor to calculate ploughing depth
R_q	Root mean squared surface roughness	p_{pl}	Contact pressure due to plastic deformation
$\boldsymbol{S}$	Spherical coordinate system: $S(r, \theta, \phi)$	q	Fitting factor for distribution of ploughing depth at either sides of asperity's periphery
S	Contact end point in contact plane in $-y$ axis	r	Reference radius of the asperity
$\widehat{SN}$	Arc ($\frown$) SN: semi-elliptic contact boundary	u	1^{st} fitting factor for interfacial shear force
T	Temperature	v_s	Sliding velocity
X_x	Axis length of ellipsoid projected in x-axis	v	2^{nd} fitting factor for interfacial shear force
Y_y	Axis length of ellipsoid projected in y-axis	w	Fitting factor for net interfacial shear force
β	Angle of orientation of asperity in xy-plane	α	Volumetric deformation
γ	Sector angle subtended by arc $\widehat{SL}$ at O	τ_{sh}	Shear strength of the interface
θ	Azimuthal angle in spherical coordinates	σ_{hyd}	Hydrostatic (volumetric) stress
ϕ	Polar angle in spherical coordinates	σ_y^{BL}	Yield stress by Bergström van Liempt model
κ	Shear strength of the substrate (bulk)	σ_y	Uniaxial yield stress
μ	Ratio of force on asperity and applied load	ε	Plastic strain
δ	Separation between asperity and substrate.	$\dot{\varepsilon}$	Plastic strain rate

1 Introduction

The geometry of an asperity plays a significant role in determining the forces acting on it while sliding through a substrate. Thus, a wide range of asperity geometries ranging from two dimensional wedges and cylinders [1] and [2] to three dimensional pyramids (with square and hexagonal bases) and spheres have been analysed in terms of frictional forces while ploughing through a substrate. Mathematical models have provided a great deal of support in understanding the effects of asperity geometry on friction during sliding. Both analytical and numerical models have been used to simulate the ploughing behaviour of a rigid-asperity sliding through a substrate [3], [4] and [5]. The friction in a system of two surfaces sliding relative to each other has been attributed to the plastic deformation of the asperities on the surface of the contacting bodies and shearing of the contact interface [6]. In sliding of an asperity through a substrate, ploughing is defined as displacing material from the sliding path of the asperity, without involving any actual material removal.

Some of the initial work on the effect of asperity geometry on the friction force was done by Bowden and Tabor [6], by analysing a spade, a cylinder and a sphere-shaped steel tool when ploughing through a metallic surface. Challen and Oxley [1] computed steady state solutions for the coefficient of friction for a two dimensional wedge shaped asperity sliding against a soft substrate based on Green's slip-line field theory [7]. Hokkirigawa and Kato [8] mapped the friction and wear in sliding of a spherical asperity as a function of 'degree of penetration', defined as the ratio of penetration depth and contact length and 'interfacial friction factor' defined as the ratio of interfacial shear strength and shear strength of the substrate. They modified the expressions for coefficient of friction by correcting the degree of penetration for three-dimensional, spherical asperities using an experimental fitting factor. The spherical asperity geometry was also assumed by most statistical contact models in modelling contacting surfaces [9]. Such an assumption is useful only in describing isotropic surfaces but cannot be easily extended to model anisotropic surfaces with variable asperity geometries. According to [10] and [11], anisotropic rough surfaces can be best described by elliptical asperities, with the contact being mapped as a set of elliptic patches. In order to compute friction using a multi-asperity model, it is important to model contacting asperities as ellipsoids and elliptic paraboloids based on the asperity height distribution and contact mapping [10], [12] and [13].

Initial work to build analytical ploughing models [14] for calculating forces acting on an elliptical asperity while sliding through a substrate was done by van der Linde [4] and [15], where a hexagonal pyramid was approximated by an elliptic-paraboloid shaped asperity. The net force acting on the contacting faces of the hexagonal-pyramid shaped asperity was calculated from the force due to the contact pressure, acting along the normal direction into the asperity's surface and the force due to the interfacial shear, acting along the tangent to the asperity's surface in the direction of plastic flow. The total force, calculated using the material properties and the unit vectors, was resolved in three dimensions. This approach was extended and used to calculate the forces acting on ellipsoidal and elliptic paraboloid shaped asperities, ploughing through a rigid-plastic substrate (having negligible elastic deformation) [16]. The forces acting on the asperity were shown to be a function of its axes length, ellipticity ratio and orientation with respect to the sliding direction. The ploughing forces calculated from the elliptical asperities with reduced geometrical parameters were compared with simpler analytical models for spherical [3] and hexagonal-pyramidal [5] asperities and were shown to be in close agreement.

Analytical models, in spite of being simple and fast cannot be applied to real materials due to their complex deformation and shear behaviour. Typically, numerical simulations of single-asperity sliding have been done using finite element (FE) method [17] and [18] and molecular dynamics (MD) [19], [20] and [21]. However, FE simulations have found modelling of large scale local plastic deformation in ploughing challenging [22] and [23]. In the available commercial FE codes, element deletion and adaptive re-meshing techniques are commonly used to model ploughing using simpler bilinear elastic-plastic material behaviour [24]. Typically, Coulomb friction is used to model interfacial friction in these FE models [25] and [26]. These in overall hinder the accuracy of the FE models and particularly increase the computational time. Variations to the standard FE such as crystal plasticity FE methods [27] and MD [19] have been used to model scratch at a nano-scale on single crystal substrate. Hence, particle methods such as MD have dealt with challenges of scaling and selection of interatomic potentials for modelling ploughing at small length scales [28], [29] and [30]. Particle based methods such as smooth particle hydrodynamics (SPH) have also been used to model ploughing, although without proper experimental validation [31]. Recently, the material point method (MPM) has been successfully implemented to develop a ploughing model which has been validated for the coefficient of friction and deformation results using ploughing experiments [32].

From the available literature it can be seen that neither analytical nor numerical models to compute the deformation and friction in an elliptical asperity sliding through a metallic substrate are available. Further, physical validation of the model and an extended study on the effect of asperity geometry on the ploughing behaviour has not been done using elliptical (ellipsoids and elliptic paraboloids with an elliptical central cross-section/base in the sliding plane) indenters.

In this regard, the current work extends the analytical model, introduced in [16], to compute the ploughed profile and ploughing forces on an elliptical asperity sliding through a rigid-plastic substrate (with negligible elastic deformation). The present work accounts for the asymmetry in plastic flow and interfacial shear with varying size and orientation of the asperity to compute the ploughing depth and the total force over the contacting region of an ellipsoidal asperity. Both the ploughing depth and the coefficient of friction obtained from the extended analytical model are compared with the MPM-based model [32], for ploughing of a rigid-plastic substrate by ellipsoidal asperities of varying size, orientation and applied load. Furthermore, ploughing experiments have also been performed using elliptical pins with varying size, orientation and applied load on a lubricated steel sheet. Also the ploughing depths and coefficient of friction from the MPM-based ploughing model are compared and validated with the results of the ploughing experiments.

2 Calculating ploughed profile and ploughing forces

Previously an analytical model to compute the forces in ploughing of a rigid-plastic substrate by an elliptical asperity was introduced in Mishra et al. [16]. The model decomposed the net force acting on the asperity into the force due to contact pressure and interfacial shear stress (see Figure 1a). As shown in Figure 1a, the contact pressure due to plastic deformation acted along the normal direction into the surface while the shear force acted tangential to the surface along the direction of plastic flow. The surface was divided into infinitesimal small (tetrahedral) elements and their normal vector and the tangential flow vector were calculated.

The expressions for the projected area of the surface of the tetrahedral element on the Cartesian coordinate planes were derived and also expressed in the spherical coordinates. The boundaries of the asperity-substrate contact and separation of plastic flow into positive and negative components were obtained from the points on the elliptic contact patch with zero and infinite slopes m respectively, (see Figure 1b). As shown in Figure 1b, for the contact patch centred at C on the sliding plane, points N and S mark the end of the asperity-substrate contact while point M indicates the point of separation of plastic flow into $+y$ and $-y$ components. The x and y coordinates of N, S and M are given using the contact lengths $CE = a_x$, $CF = a_y$ and angle of orientation β in equation 1. The component of force in the x, y and z axes, acting on a surface-element is expressed as the product of the elemental area and the (deformation and interfacial shear) stress along the x, y and z component of the unit vector corresponding to the stress. The total force due to deformation and interfacial shear in x, y and z axes are obtained by integrating the elemental forces over the contact and flow boundaries. The ploughing forces in [23] were calculated by assuming constant ploughing depth over the elliptic contact plane.

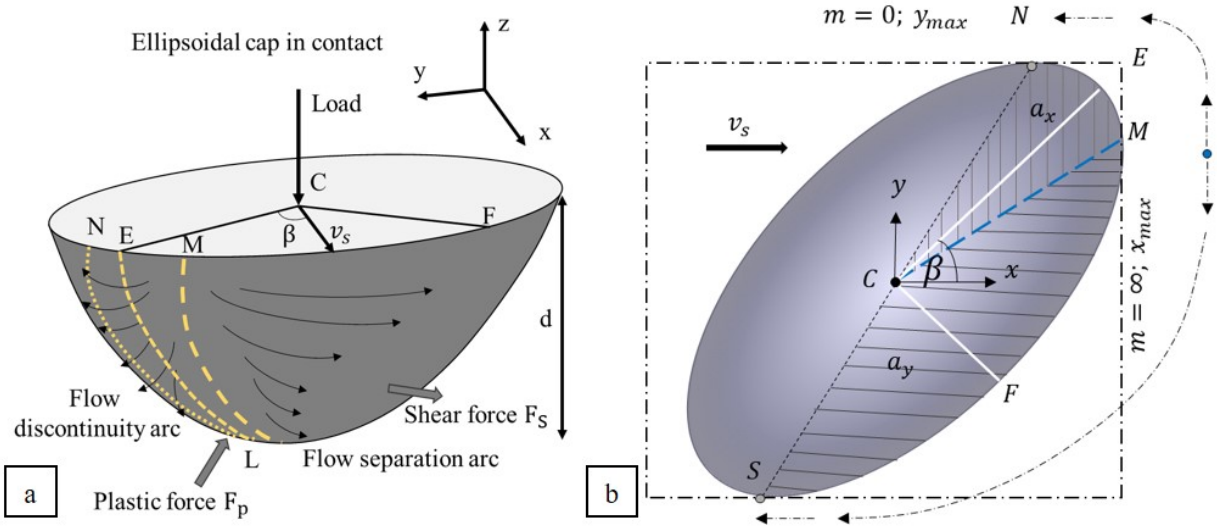

Figure 1: (a) Forces acting on an ellipsoidal cap ploughing through a plastically deforming substrate at an orientation β with respect to x axis [16] and (b) projection of the asperity-substrate contact region on the xy-plane. Horizontal lines show region with plastic flow in $-y$ direction and vertical lines show region with plastic flow in the $+y$ direction. The red box bounds the contact patch with zero and infinite slopes.

The current model builds on the findings of the analytical model in [16] and extends it to compute the depth profile and the forces in ploughing by an ellipsoidal asperity. It uses insights of the MPM-based ploughing simulations of ellipsoidal asperities to study and develop theoretical understanding of the effect of asperity geometry on the ploughed profile. Using the applied load, the model computes the initial ploughing depth of the substrate. (The ploughing depth is then calculated over the ploughed profile using fitting terms obtained from the ratios of the projected contact lengths, such as p, q and w which are further explained in section 2.1.1 and 2.1.2. These factors account for the additional pile-up or sink-in due to the asymmetric distribution of the plastic flow separated around the (arc $\overset{\frown}{LM}$) asperity in the $+y$ and $-y$ directions, conservation of the distributed plastic flow and resistance or assistance to

the plastic flow/deformation due to interfacial shear.)

$$y_N = \sqrt{\frac{it}{\frac{s}{4}^2 - ij}},\ \ x_N = -\frac{s}{2i}y_N; x_M = \sqrt{\frac{jt}{\frac{s}{4}^2 - ij}},\ y_M = -\frac{s}{2j}x_M; x_S = -x_N;\ y_S = -x_N \quad (1)$$
$$\forall\ i = (a_y \mathrm{cos}\beta)^2 + (a_x \mathrm{sin}\beta)^2;\ j = (a_y \mathrm{sin}\beta)^2 + (a_x \mathrm{cos}\beta)^2;\ s = \left(a_y^2 - a_x^2\right)\mathrm{sin}2\beta;\ t = -a_x^2 a_y^2$$

2.1 Calculation of ploughed profile

The ploughing depth for a load F applied by a rigid asperity on a plastically deforming substrate is given by balancing the applied load on contact area A with the stress underneath the asperity, i.e. hardness of the deforming substrate H as shown in equation 2.1. In this analysis, an ellipsoidal asperity with its axes along the x, y and z axis, slides in the xy plane with axis length r along the z direction. Thus its other axes lengths are $e_x r$ and $e_y r$, where e_x and e_y are the ellipticity ratios along the x and y direction respectively. The reference contact length is taken as a_z, where the contact length along the x and y axis is given as a_x and a_y. For a rigid-plastic substrate, the frontal half of the asperity is only in contact with the substrate during ploughing, and hence the contact area at a fixed depth is halved as shown in equation 2.1. The penetration depth d is then computed as the difference between the height of the asperity $c = r$, and the separation δ of the centre of the asperity from the surface of the un-deformed substrate $\delta = \sqrt{r^2 - a_z^2}$, as shown in equation 2.2.

$$HA = F;\ A = \pi a_x a_y/2 = \pi e_x e_y a_z^2/2 \quad (2.1)$$

$$d = r - \sqrt{r^2 - a_z^2} = r - \sqrt{r^2 - \frac{2F}{\pi H e_x e_y}} \quad (2.2)$$

However, the ploughing depth for an ellipsoidal asperity oriented at an angle to the sliding direction cannot be calculated directly from equation 2.2. Due to the skewness and asymmetry in the ellipsoidal asperity oriented along the sliding direction, the plastic flow due to deformation and interfacial shear is altered. Hence, the ploughing depth over the ellipsoidal asperity-substrate contact region is modified and calculated using fitting factors accounting for variations in the plastic flow. Ploughing is considered as a dynamic, visco-plastic event where the initial deformation of the substrate is followed by subsequent shearing and plastic flow of the deformed substrate. Here, the ploughing depth d is calculated as the sum of the pile-up height h_{pu} and the groove depth d_g over the ploughed profile, as shown in Figure 2b and 2c. The pile-up height h_{pu_0} and the groove depth d_{g_0}in measuring the total ploughing depth d for the spherical asperity ($e_x = e_y = 1$) are taken as the reference values in modifying the ploughing depth (pile-up height and groove depth) due to plastic deformation for an ellipsoidal asperity. The ratio of $h_{pu_0}$and d is taken as l.

2.1.1 Change in ploughing depth due to plastic deformation

Piling-up of deformed substrate in front of the asperity significantly affects the ploughing depth and forces. Here, the effect of asperity geometry on pile-up height will be discussed in terms of slope of asperity in the sliding (xy and xz) planes and projected area in the (yz) plane perpendicular to sliding. As an ellipsoidal asperity, with its major axis in the sliding direction (x-axis), is rotated in the sliding plane (see Figure 2a), the projected length of its major axis in x-direction, L_x decreases while that in y-axis, L_y increases. Firstly, the contact area projected in the yz-plane increases with increase in L_y resulting in increasing the resistance to plastic flow in the x-direction (see Figure 2c and 2d). This results in increased deformation of the substrate

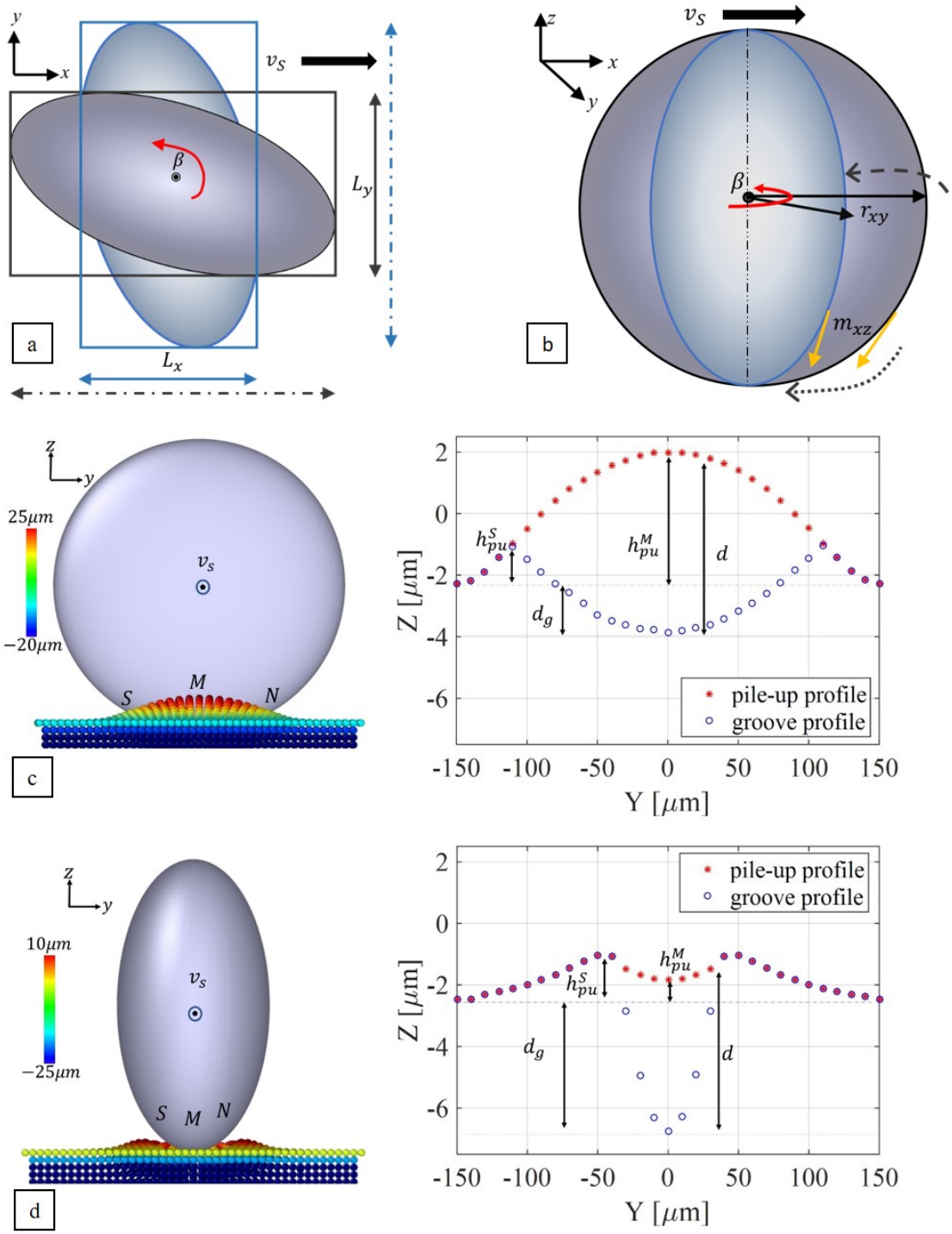

Figure 2: Projection of ellipsoidal contact region (a) in the xy plane with projected lengths of the major axis L_x and L_y in x and y axis for two asperity orientations β_1 (blue) and β_2 (grey); (b) in the xz plane showing the slope in the xz plane m_{xz} (shown using orange arrow), curvature in the xy plane $1/r_{xy}$ (r_{xy} shown using black arrow) and the direction of plastic flow around the asperity in xy plane (dashed arrow) and under the asperity in xz plane (dotted arrow). (c) Projection of the ellipsoidal asperity in the yz plane showing effect of orientation $\beta = 0°$ and (d) $\beta = 90°$ on the ploughed profile. The corresponding ploughed profile is scaled down and plotted on the right showing groove depth d_g and pile-up height h_{pu} at points M and S where the dotted black line is undeformed surface height. The encircled dot points out of the plane.

and its piling up in front of the asperity. Secondly, the slope of the asperity-substrate contact in the xz-plane decreases with increase in L_x. This results in decreasing the pile-up height due to the ease of plastic flow of the piled up substrate under the asperity, which follows its slope in the xz plane (see in Figure 2b). Finally, the sharpness of the asperity tip in the sliding direction, i.e. the change of slope of the elliptic contact profile in the xy-plane increases with increase in L_x and decreases with increase in L_y (see in Figure 2b). A sharp asperity tip assists the deformation of the substrate and the distribution of plastic flow of the piled up substrate around the asperity. A sharp asperity tip thus, reduces pile-up of the substrate. Thus, the total pile-up height h_{pu} is taken proportional to L_y/L_x i.e. the ratio of y and x-coordinates of points N and M respectively. In equation 3.1 h_{pu} is given by fitting power n to y_N/x_M.

As the asperity continues to plough through the substrate, the piled up material in front of the asperity shares the applied load with the material in the groove. To maintain load balance following equation 2.1, higher pile-up height results in lower groove depth d_g (see Figure 2c and d). Hence, the groove depth is proportional to L_x/L_y (see Figure 2c and 2d). Similarly, in equation 3.2, d_g is given by fitting power o to x_M/y_N. The height of the piled up substrate varies across the ploughed profile from the tip of the asperity to its edges (see Figure 2c and 2d). Unlike, the groove depth, the distribution of pile- up material does not follow the shape of the asperity. Hence, the average of the pile-up height of all contacting points is taken here as h_{pu}.

The mean ploughing depth d' for contacting points on the xy-plane, is taken as the sum of groove depth d_g and average pile-up height h_{pu}, and is given in equation 3.3 by fitting power p to y_N/x_M. The ploughed profile consists of the pile-up both in front of the asperity and in its periphery and the ploughed groove. The piled-up substrate in front of the asperity dominates the ploughed profile during ploughing. Hence, p is taken as a positive fraction in equation 3.3 in calculating the forces acting on the asperity during ploughing. The deformed substrate is subsequently distributed over the contacting surface as the asperity slides over a given section of the substrate, therefore, the pile-up subsides. Now the groove depth and pile-up on side of the asperity are only accounted in measuring the final ploughing depth where, p is taken as a positive or negative fraction in equation 3.3 depending on the measurement point (asperity periphery/front).

$$h_{pu} = h_{pu0}\left(\frac{L_y}{L_x}\right)^m = ld\left(\frac{y_N}{x_M}\right)^n \tag{3.1}$$

$$d_g = d_{g0}\left(\frac{L_x}{L_y}\right)^n = (1-l)\,d\left(\frac{x_M}{y_N}\right)^o \;\forall\; o \in [0,1] \tag{3.2}$$

$$d^{'} = h_{pu} + d_g = d\left(\frac{y_N}{x_M}\right)^p \forall\; p \in [-1,1] \tag{3.3}$$

The asymmetry in a rotated ellipsoidal asperity results in asymmetric plastic flow. This also results variations in ploughing depths on either sides of the asperity (see Figure 3a). The difference in the plastic flow in $+y$ and $-y$ axis (see Figure 1) is proportional to the difference in resistance to plastic flow in $+y$ and $-y$ axis in the xz plane. The difference in resistance to plastic flow is expressed as difference in the projected contact lengths of arcs MS and MN in the x-axis as shown in equation 4.1 (see Figure 3b). Thus the change in ploughing depth d^* at the periphery of the asperity, along the y-axis is taken proportional to the ratio of the projected contact length NS in x-axis $2x_N$ to the un-rotated contact length along x axis $2a_x$.

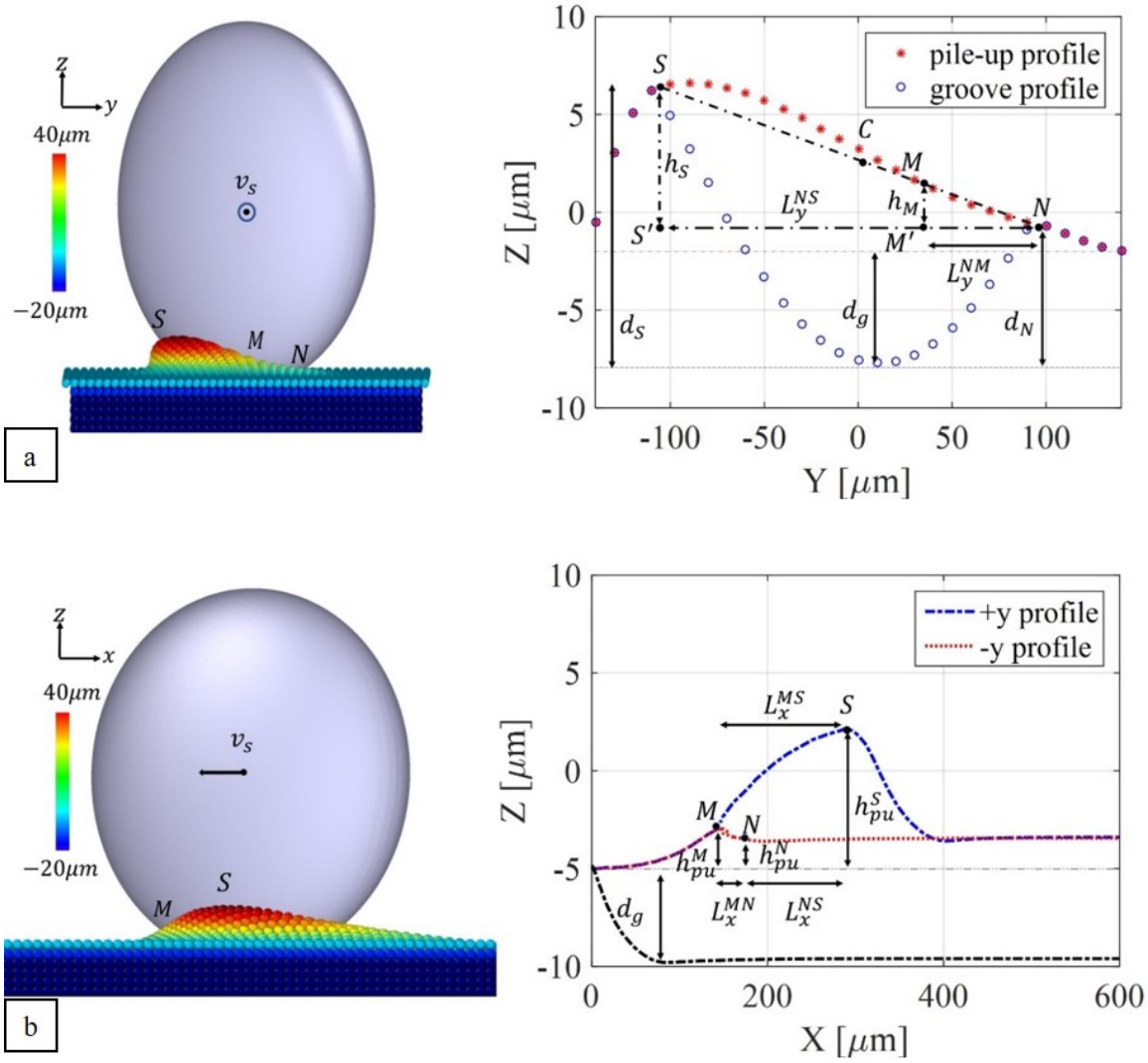

Figure 3: The projection of the ploughing ellipsoid at $\beta = 45°$ orientation on the (a) yz plane and (b) the xz plane showing the effect of orientation of ploughed profile. The corresponding ploughed profile is scaled down and plotted on the right showing the asymmetry is distribution of ploughing depth due to orientation. The projected contact length, pile-up height and ploughing depth at points M, S and N are also shown.

Fitting coefficient q, $d^* = d^{'} q x_N / a_x$. Following volume conservation, the increase in pile-up on one side of the asperity results in an equivalent decrease in pile-up on other side. This results in a ploughing depth of $d^{'} + d^*$ at point S and a ploughing depth of $d^{'} - d^*$ at point N as shown in 4.2 and 4.3.

The pile-up height at a given point of the contact plane with respect to the point N is proportional to the ratio of the its projected contact length from N to the total project contact length of NS in y direction. The projected profile of the pile-up in the yz plane is approximated as triangle $\Delta NSS'$ as shown in Figure 3a. The arc of flow separation $M'M$ forms triangle $\Delta NMM'$ at point N which is similar to $\Delta NSS'$. By using the proportionality rule for length of sides of similar triangles L_y^{MN} and L_y^{SN}, the relative pile-up height of point M with respect to point N h_M, is obtained as shown in equation 4.4 (see Figure 3a). The total ploughing depth at the point M is calculated in equation 4.5 as the sum of h_M and total ploughing depth d_N at reference point N.

$$L_x^{MS} - L_x^{MN} = L_x^{NS} = x_N - x_S = 2x_N \tag{4.1}$$

$$d_S = \left(1 + q\frac{x_N}{a_x}\right) d^{'} \tag{4.2}$$

$$d_N = \left(1 - q\frac{x_N}{a_x}\right) d^{'} \tag{4.3}$$

$$\frac{h_M}{h_S} = \frac{L_y^{MN}}{L_y^{SN}} \Rightarrow \frac{h_M}{d_S - d_N} = \frac{\left(L_y^{CN} - 2L_y^{CM}\right)}{L_y^{SN}} \Rightarrow \frac{h_M}{d_S - d_N} = \frac{(y_N - y_M)}{2y_N} \tag{4.4}$$

$$d_M = d_N + h_M = d_N + \left(\frac{1}{2} - \frac{y_M}{y_N}\right)(d_S - d_N) = \left(1 - 2q\frac{x_N}{a_x}\frac{y_M}{y_N}\right) d^{'} \tag{4.5}$$

2.1.2 Change in ploughing depth due to interfacial shear

The applied normal force in equation 2.1 is taken as the force responsible for deformation of the substrate before sliding starts. As sliding begins, an additional force F_z^{sh} acts on the asperity along the z- axis due to the shearing of the interface. The force on the asperity due to interfacial shear acts in the direction opposite to the relative velocity of the asperity with respect to the deforming substrate at the interface. The corresponding force on the substrate due to interfacial shear acts in the opposite direction, $-F_z^{sh}$. Thus a component of the force acts on the substrate in the $+z$ axis due to interfacial shear and a component of force acts on the substrate in the $-z$ axis due to plastic compressive pressure. On one hand, the force due to interfacial shear by its nature, restricts plastic flow around the contacting asperity which then decreases the ploughing depth. On the other hand, the forces acting on the asperity-substrate contact due to interfacial shear and plastic deformation result in a bi-axial tension on the deforming substrate elements. Such a stress-state caused faster yielding and increases the ploughing depth to maintain load balance. These ploughing depth derived in equation 2.2 is modified using F_z^{sh} by multiplying factors u and v which take into account factors for reducing or increasing plastic deformation. Combining both the factors u and v to a single factor w for including the effect of interfacial shear force, the final ploughing depth $d^{''}$ is given in equation 5.

$$d^{''} = r - \sqrt{r^2 - a_z^2} = r - \sqrt{r^2 - 2\frac{F_z^{pl} - uF_z^{sh} + vF_z^{sh}}{\pi H e_x e_y}} = r - \sqrt{r^2 - 2\frac{F_z^{pl} - wF_z^{sh}}{\pi H e_x e_y}} \tag{5}$$

2.2 Calculation of ploughing forces

The forces acting on the ellipsoidal asperity ploughing through the rigid-plastic substrate is calculated based on the method developed in [16]. The surface of the asperity in contact is divided into infinitesimal elements whose projected areas on the 3 Cartesian planes are calculated and expressed in spherical coordinate axes. The coordinates of the boundaries of contact of the asperity with the substrate is calculated based on the modified ploughing depths derived in section 2.1. The components of forces in the 3 axis due to plastic deformation and interfacial shear are now integrated over the modified contact boundaries to obtain the corresponding components of the total force.

2.2.1 Calculation of the projected areas.

The projected contact area between the ellipsoidal asperity and the substrate is corrected due to the correction in the ploughing depths. The projected area along the xy, yz and yz planes

are calculated by taking an small elemental area on the contact surface and resolving it in x, y and z direction. The elemental projected contact areas are then transformed from the Cartesian coordinate system $\boldsymbol{C(x, y, z)}$ into the spherical coordinate system $\boldsymbol{S(\theta, \phi, r)}$ using the Jacobian determinant $= \det|\partial \boldsymbol{C}/\partial \boldsymbol{S}|$. This gives us the expressions for the elemental projected areas dA_{xy}, dA_{xz} and dA_{yz} in terms of variables θ and ϕ as spherical coordinates (azimuthal angle and polar angles) and constants r and β (angle of orientation).

$$dA_{xy} = n(\phi)\, d\theta d\phi \;;\; n(\phi) = -\frac{ab}{2}\sin 2\phi \tag{6.1}$$

$$dA_{xz} = l(\theta, \phi)\, d\theta d\phi;\; l(\theta, \phi) = c\,(a\sin\theta\,\cos\beta\; + b\cos\theta\,\sin\beta\,)\sin^2\phi \tag{6.2}$$

$$dA_{yz} = m(\theta, \phi)\, d\theta d\phi;\; m(\theta, \phi) = c\,(a\sin\theta\,\sin\beta\; - b\cos\theta\,\cos\beta\,)\sin^2\phi \tag{6.3}$$

Integrating the expressions 6.1-6.3, we obtain the projections of the total contact area between the asperity and the substrate in the xy, yz and zx planes. Now the limits of the integration are found by obtaining the boundaries of contact. For an ellipsoid ploughing through the substrate at an angle β with respect to sliding direction x, the contact is divided into two regions with positive plastic flow and negative plastic flow, where the component of relative plastic flow velocity is along $+y$ and $-y$ directions respectively. The separation of plastic flow occurs at the point on the asperity surface where the slope is infinite in the sliding plane. The termination of plastic flow occurs on either side of the asperity where the slope is zero in the sliding plane as shown in Figure 1b. The flow separation curve is shown as arc LM, while the arcs consisting the boundaries of plastic flow are shown by curves SN, LN and LS in the Figure 1a.

The coordinates of the point N, M and S change as the ploughing depths are modified. However, in spherical coordinates this change is reflected only as a change in the polar angles ϕ of the points. The azimuthal angle θ and the radial distance of the points remain the same as they lie on the surface and maintain a slope of either zero or infinity. Hence the coordinates of the points S, M, N and L are given in set of equations 7.1-7.3 in spherical coordinates. The detailed derivation can be found in [16].

$$\theta_N = \arctan\left(\frac{a}{b}\frac{\frac{N_y}{N_x}\cos\beta\; - \sin\beta}{\frac{N_y}{N_x}\sin\beta\; + \cos\beta}\right), \phi_N = \arccos\left(1 - \frac{d_N}{c}\right) \tag{7.1}$$

$$\theta_M = \arctan\left(\frac{a}{b}\frac{\frac{M_y}{M_x}\cos\beta\; - \sin\beta}{\frac{M_y}{M_x}\sin\beta\; + \cos\beta}\right),\; \phi_M = \arccos\left(1 - \frac{d_M}{c}\right) \tag{7.2}$$

$$\theta_S = \theta_N - \pi, \phi_S = \arccos\left(1 - \frac{d_S}{c}\right);\theta_L = 0,\; \phi_L = 0 \tag{7.3}$$

2.2.2 Calculation of the total force components

Now the components of the forces acting on the asperity along Cartesian coordinate axes are calculated from the expressions of the unit normal and unit tangent. The unit vector expressions are functions of integrand of the corrected projected areas, $n(\phi)$, $l(\theta, \phi)$ and $m(\theta, \phi)$ given in equation 6.1-6.3 as derived in [16]. The limits of integration are taken from equations 7.1-7.3. Integrating the total projected area responsible for net positive plastic flow the total components of force due to plastic deformation are obtained in equation 8.1-8.3 as F_x^p, $F_y^p$and F_z^p. Similarly, the total components of force due to interfacial shear are given as F_x^s, $F_y^s$and F_z^s using integrands $f(\theta, \phi)$, $g(\theta, \phi)$ and $h(\theta, \phi)$ in equation 8.4-8.6.

The asperity-substrate contacting region can be given as the sum of the ellipsoidal cap with horizontal base at N and the ellipsoidal segment between S and N. The area of such an ellipsoidal segment is approximated as half the area of the ellipsoidal band, which is the surface of the asperity bounded by horizontal planes intersecting at S and N. In calculating the total force due to ploughing and shearing in the x and z direction the integration of elemental forces is done over the ellipsoidal cap with base at N and the ellipsoidal segment between S and N as shown in Figure 4a and given in equations 8.1, 8.3, 8.4 and 8.6. In calculating the total force due to ploughing and shearing in the y direction, the component of force in the $-y$ axis F_{-y} is subtracted from the component in the $+y$ axis F_{+y}. F_{+y} is calculated by integrating over the region bound by the elliptic cap with base plane at M and elliptic segment between S and M, while F_{-y} is calculated by integrating over the region bound by the elliptic cap with base plane at N and elliptic segment between N and M as shown in Figure 4b and given in equation 8.2 and 8.5.

$$F_x^p = p_{pl} \oint_{N,L}^{S} dA_\Delta \widehat{\boldsymbol{n}}.\widehat{\boldsymbol{i}} \approx p_{pl} \int_0^{\phi_N} \int_{\theta_N}^{\theta_S} |m(\theta,\phi)|\, d\theta d\phi + \frac{1}{2} p_{pl} \int_{\phi_N}^{\phi_S} \int_{\theta_N}^{\theta_S} |m(\theta,\phi)|\, d\theta d\phi$$
$$\Rightarrow F_x^{pl} \approx -\frac{1}{2} p_{pl} c\,(\phi_S - cos\phi_N sin\phi_N + \phi_N - \cos\phi_S \sin\phi_S\ )\,(a\cos\theta_N \sin\beta + b\sin\theta_N \cos\beta) \tag{8.1}$$

$$F_y^p = p_{pl} \left(\oint_{M,L}^{S} dA_\Delta - \oint_{N,L}^{M} dA_\Delta \right) \widehat{\boldsymbol{n}}.\widehat{\boldsymbol{j}}$$
$$\approx p_{pl} \int_0^{\phi_M} \int_{\theta_S}^{\theta_M} |l(\theta,\phi)|\, d\theta d\phi + \frac{p_{pl}}{2} \int_{\phi_M}^{\phi_S} \int_{\theta_S}^{\theta_M} |l(\theta,\phi)|\, d\theta d\phi$$
$$- p_{pl} \left(\int_0^{\phi_M} \int_{\theta_M}^{\theta_N} |l(\theta,\phi)|\, d\theta d\phi - \frac{1}{2} \int_{\phi_N}^{\phi_M} \int_{\theta_M}^{\theta_N} |l(\theta,\phi)|\, d\theta d\phi \right) \tag{8.2}$$
$$\Rightarrow F_y^{pl} \approx \frac{1}{2} p_{pl} c\,((\phi_S - \phi_N)\ + 2\phi_M - \cos\phi_S\ \sin\phi_S\ + \cos\phi_N\ \sin\phi_N\ - 2\cos\phi_M\ \sin\phi_M\ )$$
$$(a\cos\theta_N\ \cos\beta\ - b\sin\theta_N\ \sin\beta\ )$$

$$F_z^p = p_{pl} \oint_{S,L}^{N} dA_\Delta \widehat{\boldsymbol{n}}.\widehat{\boldsymbol{k}} \approx p_{pl} \int_0^{\phi_N} \int_{\theta_S}^{\theta_N} |n(\phi)|\, d\theta d\phi + \frac{1}{2} p_{pl} \int_{\phi_N}^{\phi_S} \int_{\theta_S}^{\theta_N} |n(\phi)|\, d\theta d\phi$$
$$\Rightarrow F_z^{pl} \approx \pi p_{pl} ab\,(2 - \cos(2\phi_S)\ - \cos(2\phi_N)\ )/8 \tag{8.3}$$

$$F_x^s = -\tau_{sh} \oint_{S,L}^{N} dA_\Delta \widehat{\boldsymbol{t}}.\widehat{\boldsymbol{i}} = -\tau_{sh} \int_0^{\phi_N} \int_{\theta_N}^{\theta_S} |f(\theta,\phi)|\, d\theta d\phi - \frac{1}{2} \tau_{sh} \int_{\phi_N}^{\phi_S} \int_{\theta_N}^{\theta_S} |f(\theta,\phi)|\, d\theta d\phi$$
$$\forall\ f(\theta,\phi) = \sqrt{n(\phi)^2 + l(\theta,\phi)^2} \tag{8.4}$$

$$F_y^s = -\tau_{sh} \left(\oint_{S,L}^{M} dA_\Delta - \oint_{M,L}^{N} dA_\Delta \right) \widehat{\boldsymbol{t}}.\widehat{\boldsymbol{j}} = -\tau_{sh} \int_0^{\phi_M} \int_{\theta_S}^{\theta_M} |g(\theta,\phi)|\, d\theta d\phi -$$
$$\frac{\tau_{sh}}{2} \int_{\phi_M}^{\phi_S} \int_{\theta_S}^{\theta_M} |g(\theta,\phi)|\, d\theta d\phi + \tau_{sh} \left(\int_0^{\phi_M} \int_{\theta_M}^{\theta_N} |g(\theta,\phi)|\, d\theta d\phi - \frac{1}{2} \int_{\phi_N}^{\phi_M} \int_{\theta_M}^{\theta_N} |g(\theta,\phi)|\, d\theta d\phi \right)$$
$$\forall\ g(\theta,\phi) = \frac{l(\theta,\phi) * m(\theta,\phi)}{f(\theta,\phi)},\ h(\theta,\phi) = \frac{n(\phi) * m(\theta,\phi)}{f(\theta,\phi)} \tag{8.5}$$

$$F_z^s = -\tau_{sh} \oint_{S,L}^{N} dA_\Delta \widehat{\boldsymbol{t}}.\widehat{\boldsymbol{k}} = \tau_{sh} \int_0^{\phi_C} \int_{\theta_S}^{\theta_N} |h(\theta,\phi)|\, d\theta d\phi \tag{8.6}$$

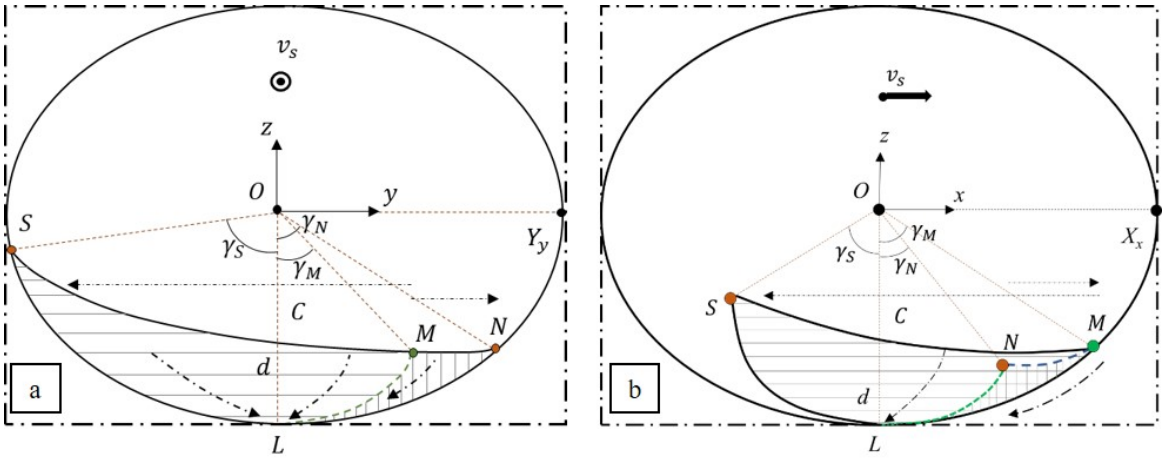

Figure 4: Projection of a ploughing ellipsoid with modified ploughed profile in the (a) yz plane and (b) the xz plane showing contact region with plastic flow in the $+y$ direction shown by vertical lines and $-y$ direction shown by vertical lines. Angles γ_M, γ_S and γ_N are subtended by the points M, S and N at the centre of the ellipsoid O with the z axis. C is the centre of the contacting region (semi-ellipse) in xy plane.

3 Numerical model and experimental setup

Both numerical calculations and experimental tests were conducted up for ploughing ellipsoidal pins using the same geometrical parameters. Simulations were also done using the numerical model to compare the results obtained from the modified analytical model using the same geometrical parameters for the ellipsoidal asperities. The axis size r of the ellipsoidal asperity is taken as 0.2 mm for comparison with the analytical model and 0.5 mm for comparison with experiments. The size of the ellipsoid are changed for both analytical and experimental studies involving cases where only one axis size is varied either along or perpendicular to the sliding direction or both axes sizes are varied such that $e_x e_y = 1$. For experimental studies, as listed also in table 4 in the first case, ellipticity ratios e_x are 1/2, 2/3, 5/6, 1, 6/5, 3/2 and 2 and $e_y = 1$ and vice versa, while in the second case e_x values are 1/2, 3/5, 3/4, 1, 4/3, 5/3 and 2 and $e_y = 1/e_x$. The orientation of the ellipsoid with respect to x-axis β is varied at 15^0 interval between $0^0 - 90^0$. For analytical studies, the axes sizes are varied with ellipticity ratios e_x as 1/4, 2/7, 1/3, 2/5, 1/2, 2/3, 4/5, 1, 5/4, 3/2, 2, 5/2, 3, 7/2, 4 and the orientation β varied at 7.5° interval between $0^0 - 90^0$ for the same cases.

3.1 Computational method

The MPM based ploughing model is used to simulate ploughing using an ellipsoidal asperity. The ellipsoidal asperity is made up of a triangulated mesh with mesh size varying from 5-20 μm. These triangles have no self-interaction which makes the asperity perfectly rigid. The substrate is made up of particles which interact with each other following the 'linear-MPM pair-wise' interaction algorithm. The interaction between the ellipsoidal asperity and the substrate follows from the 'triangle-MPM pair-wise' interaction algorithm as mentioned in [32]. The substrate is modelled as a half cylinder in order to optimize the number of particles and hence the computational time. The size of the MPM particles are varied from 5-20 μm for studying the convergence of the model-results with particle resolution. The parameters for the MPM based ploughing model are listed in Table 1. The MPM-based ploughing model has been shown in Figure 7.

The deformation in the substrate is modelled by using the material model composed of the linear elastic equation of state and the Bergström van Liempt material model [33] as given in equation 9.1 and 9.2 respectively. The total stress is computed from the hydrostatic and deviatoric components. The hydrostatic stress σ_{hyd} is computed using the equation of state model from the bulk modulus $K$and volumetric strain αI where I is the identity matrix. The deviatoric stress is computed from the deviatoric strain using a 'radial return' plasticity algorithm [32]. For validating the MPM-based ploughing model with the analytical model, a perfect-plastic material behaviour is chosen for the substrate whose parameters are listed in Table 2. In order to compare the results of MPM-based ploughing model with the experiments, the Bergström van Liempt material model (yield stress: σ_y^{BL}) for DX56 steel is chosen with its parameters as listed in table 3.

$$\sigma_{\text{hyd}} = \text{K}\alpha\text{I} \tag{9.1}$$

$$\sigma_y^{\text{BL}} = \sigma_{f0} + d\sigma_m \left(\beta_0 \left(\varepsilon + \varepsilon_0\right) + \left\{1 - \exp\left[-\omega\left(\varepsilon + \varepsilon_0\right)\right]\right\}^g\right) + \sigma_{v0}\left(1 + \frac{kT}{\Delta G_0}\ln\frac{\dot{\varepsilon}}{\dot{\varepsilon}_0}\right)^h \tag{9.2}$$

Table 1: MPM ploughing model parameters.

Parameters	Symbol	Values/ expression
Rigid spherical indenter radius for validation	R_i	0.2 mm and 0.5 mm
Semi-cylindrical DX 56 steel substrate radius	R_s	0.25 mm
Sliding distance of indenter	l	0.6 mm
Semi-cylindrical DX 56 steel substrate length	l_s	1 mm
Substrate's MPM particle cell size	r_p	5, 10, 15 and 20 μm
Indenter's triangulated mesh element size	r_t	5, 10 and 20 μm
Sliding velocity of indenter	v_i	0.1 mm/s
Mass scaling factor	m_s	1e6

Table 2: MPM material model (linear elastic- plastic) parameters for analytical validation.

Parameters	Symbol	Values/ expression
Substrate and indenter material density	ρ	7900 kg/m^3
Substrate and indenter specific heat capacity	c_p	502 J/(kg K)
Substrate and indenter thermal conductivity	κ	502 W/(m K)
Young's Modulus of substrate	E	210 GPa
Poisson's ratio of the substrate	ν	0.3
Initial yield stress of the substrate	σ_y	150.02 MPa
Hardness of the substrate	H	$3\sigma_y$ [34]
Interfacial friction factor	f	0.45
Ambient temperature	T_{room}	294 K

Further the interfacial shear stress is modelled using either of the two models that have been developed using experimental fitting and characterization [32]. (1) A theoretical model is used for validation of the MPM-based ploughing model with the analytical model. The first interfacial friction model takes the interfacial shear stress τ_{sh} as a fraction, f (interfacial friction factor), of the bulk shear stress of the substrate (equation 10.1). The bulk shear stress κ is taken as $\sigma_y/\sqrt{3}$ based on von Mises yield criterion where σ_y is the yield stress. (2) An empirical model

is used to compare the results from the MPM based ploughing model with the experimental results. The second interfacial friction model takes the interfacial shear stress as a power-law function of the contact pressure between the triangles of the indenter in contact with the MPM particles of the substrate (equation 10.2). Based on the experimental characterization of the interfacial shear strength of DX56 steel sheet lubricated with 'Quaker Ferrocoat N136' lubricant under varying loads (contact pressure P_c) and fitting of results, coefficient $C_p = 1.34$ and exponent $n_p = 0.88$ are obtained [32] and [35].

$$\tau_{sh}{=}f\kappa \tag{10.1}$$

$$\tau_{sh} = C_p P_c^{n_p} \tag{10.2}$$

Table 3: Bergström-van Liempt material model parameters for DX56 steel [32].

Parameters	Symbols	Value
Initial static stress	σ_{f0}	82.988 MPa
Stress increment parameter	$\mathrm{d}\sigma_\mathrm{m}$	279.436 MPa
Linear hardening parameter	β_0	0.482
Remobilization parameter	ω	6.690
Strain hardening exponent	g	0.5
Initial strain	ε_0	0.005
Initial strain rate	$\dot{\varepsilon}_0$	$10^8 s^{-1}$
Maximum dynamic stress	σ_{v0}	1000 MPa
Dynamic stress power	h	3.182
Activation energy	$\Delta\mathrm{G}_0$	0.8
Boltzmann's constant	k	$8.617{\times}10^{-5}$ eV

3.2 Experimental procedure

The experimental procedure consisted of ploughing experiments using indenters with ellipsoidal tips on a DX-56 steel sheet lubricated using 'Quaker Ferrocoat N136' forming lubricant. The section elaborates on the design of the ellipsoidal pin specimens with different ellipticity ratios, preparation of sheet specimens and the test set-up used for the ploughing experiments. The experiments were done 3 times for repeatability.

3.2.1 Material

The material used for making indenters is D2 tool steel DIN 1.2379, obtained by heat treatment in vacuum. The pin is heat treated to a hardness of 62±2 HRC (746HV or 7.316 GPa). The elastic modulus of the pin is 210 GPa and its Poisson's ratio is 0.3. After heat treating the D2 tool steel cylinders, the outside base diameter is ground followed by high precision milling and polishing to obtain the ellipsoidal shape at the tip to validate the numerical model. Ten different ellipticity ratios were chosen. Seven of the designs, B1 to B7 have ellipticity ratios changing along one of the ellipsoids axis a while the size of the other axis b remained constant. Three of the pins A1-A3 had the size of the axis such that the ellipticity ratio of one axis was reciprocal of the other axis. The reference radius of the ellipsoidal pins was kept at 0.5 mm.

Table 4: Design of ellipsoidal pins ($a_d \pm a_m$: design length $\pm$ deviation) and the surface roughness parameters: R_a and R_q.

Pin type	$a_d \pm a_m$ $[\mu m]$	$b_d \pm b_m$ $[\mu m]$	S_a $[\mu m]$	S_q $[\mu m]$
A1	1000±55.8	375±24.1	0.828	0.428
A2	833.3±21.8	300±1	0.823	0.481
A3	666.7±32.4	250±6.9	0.774	0.120
B1	250±12.2	500±10.3	0.844	0.153
B2	333.3±2.2	500±4.3	0.716	0.909
B3	417.5±10	500±5.5	1.007	0.333
B4	500±4	500±5.5	0.629	0.530
B5	600±11.2	500±6.7	0.710	0.542
B6	750±7.1	500±7.2	1.38	0.581
B7	1000±32	500±7.3	0.969	0.527

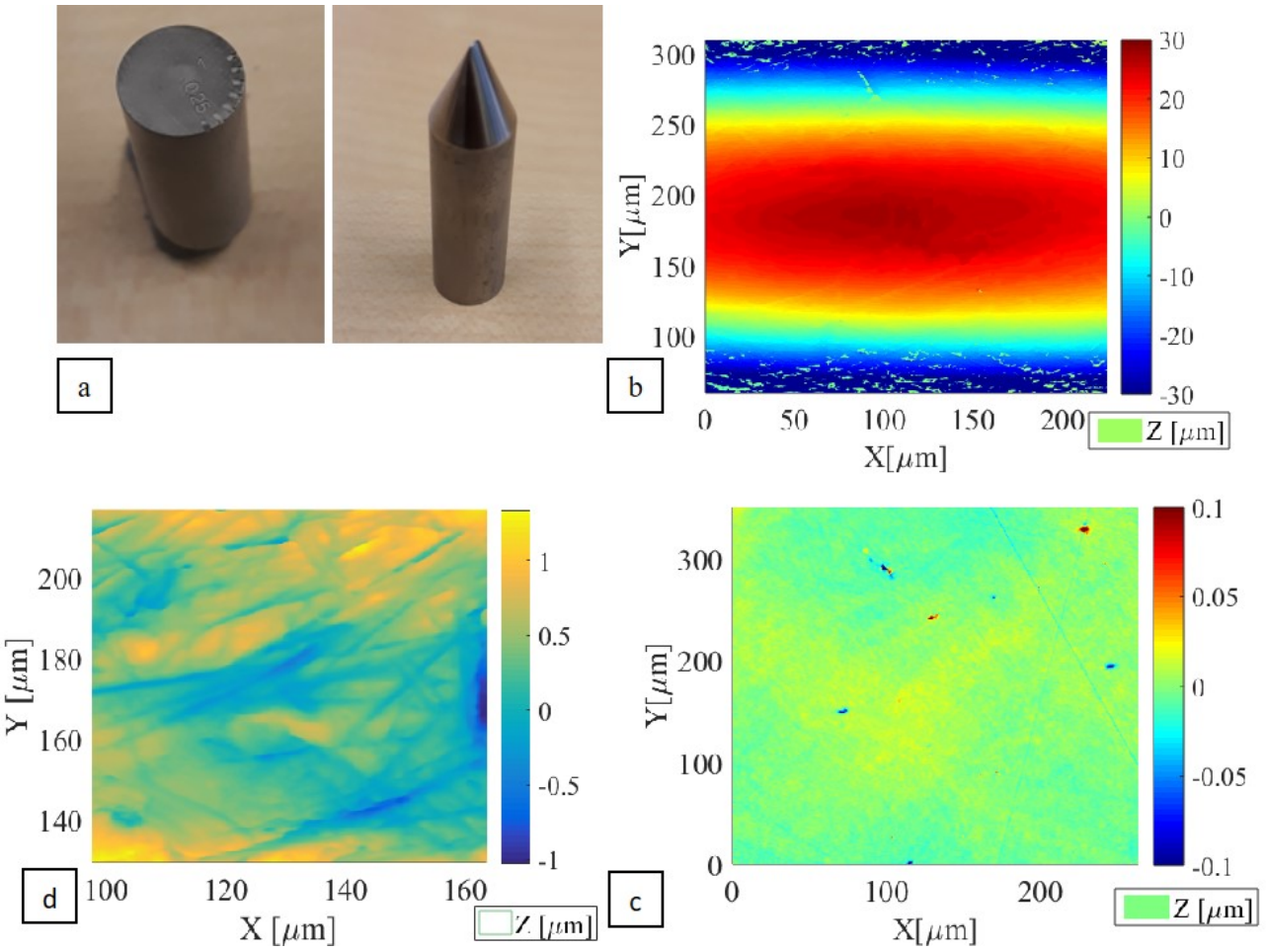

Figure 5: The design of an ellipsoidal pin with (a) axes size 1 mm and 0.25 mm showing orientation slots at 15^0 interval and (d) surface roughness after removing the (b) surface profile from the measured confocal image and (c) surface of the polished DX56 sheet as seen under confocal microscope at 50x magnification.

The designed pins were marked with slots with 15^0 intervals for aligning the pins at the desired orientation with respect to the sliding direction as shown in Figure 5a. The surface of the pin was measured using a confocal microscope to verify for the axes size and surface roughness as

shown in Figure 5b. The axes sizes a and b were within the design limits $a_d \pm a_m$ and $b_d \pm b_m$ as shown in table 4. The mean roughness R_a of the pin tips were about 0.5-1 μm as polishing the tips was challenging (Figure 5d). The root mean squared roughness R_q and average surface roughness R_a of the pins are listed in table 4. The sheet, made up of DX 56 steel, was hot mounted on 50 mm diameter bakelite resin disc and polished using a lapping machine. Initially sandpaper grit P220 was used to grind out the unevenness and 1, 3 and 9 μm size diamond suspensions were used for mirror polishing. A final R_a of 5nm was obtained on the DX56 steel sheets prior to the ploughing experiments, see Figure 5c. The polished sheet was then lubricated with $2g/m^2$of 'Quaker Ferrocoat N136' lubricant.

3.2.2 Method

The ploughing experiments were carried out using the designed ellipsoidal pins in the Bruker's UMT-2 tribometer. The tribometer has been adapted to be a scratch test set-up as shown in Figure 6a. The UMT-2 scratch set-up consisted of three stages for motion in all three directions. The z-carriage was used to adjust the height of the ellipsoidal pin while also applying the given load on the contact. The pin was slid along the x axis using the x-slider. The y-stage was used to mount the specimen to be tested and was also for any sliding required for the purpose of ploughing or offsetting. The z-carriage, x-slider and y-stage were moved using a stepper motor drive by translating rotational into linear motion using a lead screw and guide rails. The y-stage consisted of an eccentric screw which along with two other screws was used to clamp the disc specimen onto the stage. The y-stage was connected to the motor using a lead screw with 2 mm pitch.

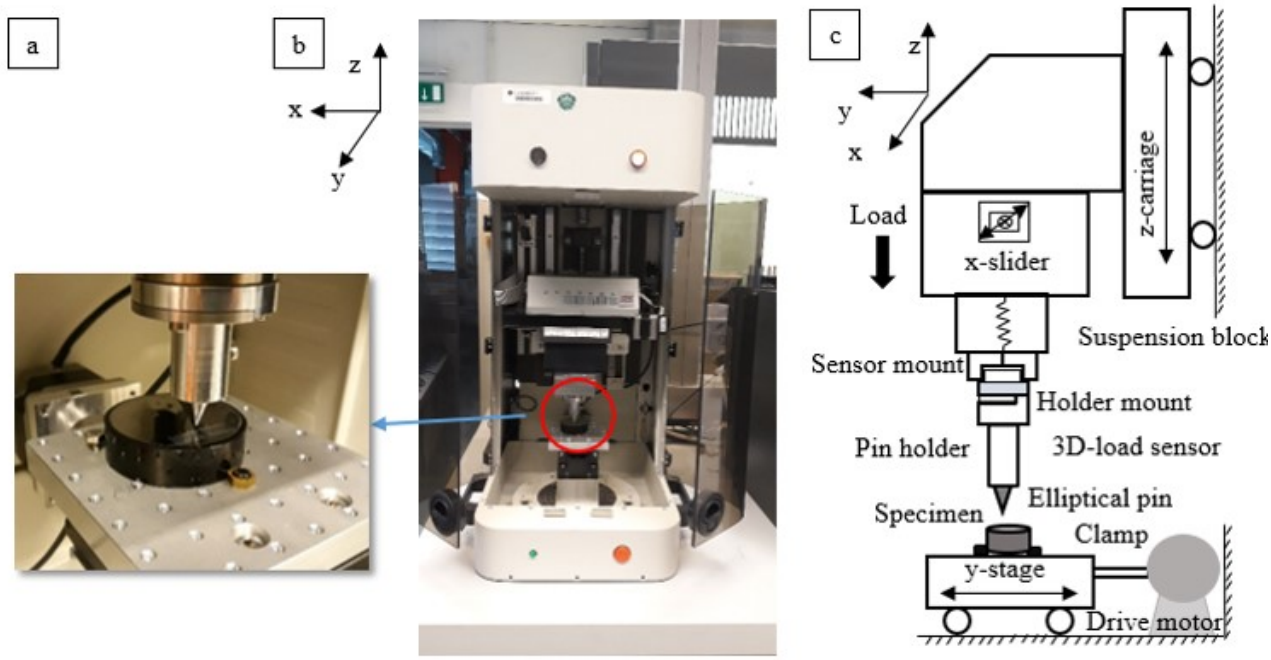

Figure 6: (a) The image of the UMT-2 tribometer used as a scratch test-set up using ellipsoidal pin on a lubricated DX56 steel sheet showing (b) scratch tests and its (c) corresponding schematic diagram.

The load applied on the pin and the friction in both x and y direction were measured using the ATI F/T mini 40 (3D) load sensor with a load range of 0-60 N and 0.01 N resolution in the

z-axis and a load range of 0-20 N and 0.05N resolution in the x- and y-axis. In this way, all the force components involved in ploughing with an elliptical indenter can be measured. The 3D load sensor was connected to the pin holder using a mount and to the upper drive stage using a suspension block as shown in Figure 6b. The suspension block with its spring plates helped in adjusting for possible shock loads. The pin holder consisted of a hole with inner diameter same as that of the base of the pin and a marking along the x-axis, i.e. direction of x-slider to adjust the orientation of the ellipsoidal pin. Load controlled tests were performed at 7 N and 16 N, normal loads for the different pin sizes and orientation along the sliding direction as shown in Figure 6a.

4 Results and discussion

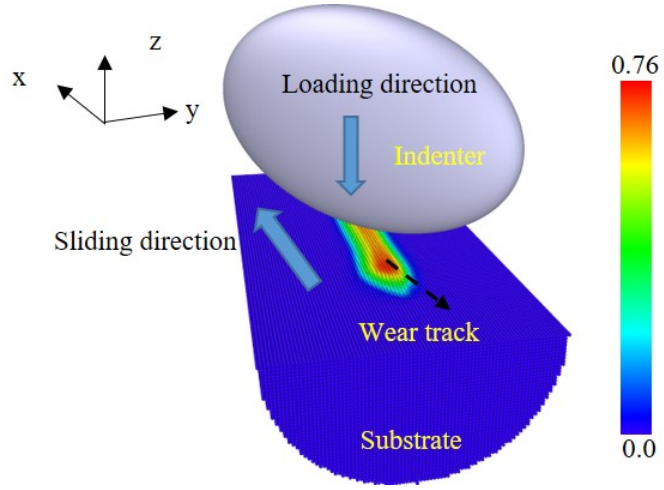

Figure 7: MPM simulation of an ellipsoidal indenter with ellipticity ratios $e_x = 2$ and $e_y = 0.5$ ploughing through a substrate oriented at $\beta = 30°$ with respect to sliding x-direction with plastic strain being shown.

MPM-based ploughing simulations have been performed on a rigid-plastic substrate and DX56 steel sheet in order to compare and validate the results with the analytical model and the ploughing experiments as elaborated in section 4.1 and 4.2 respectively. An ellipsoidal indenter has been loaded in the $-z$-axis and slid along the x-axis as seen in Figure 7 based on the ploughing model parameters listed in table 1, 2 and 3.

4.1 Comparison of analytical results with numerical results

Fitting factors p and q (section 2.1) are used to calculate the change in ploughing depth in front and at the periphery of the asperity-substrate contact respectively, due to the change in asperity size and orientation relative to sliding. Values of p and q change with the asperity shape (ellipticity ratio) and applied load. The change in ploughing depth due to interfacial shear is measured using $w = 1$ in equation 5 for all cases. Incorporating the depth corrections due to the plastic flow and interfacial shear, the forces acting on an asperity were recalculated using equation 8.1-8.6. The results were compared with the results obtained from the MPM-based ploughing simulation of ellipsoidal asperity on a rigid-plastic substrate. The modelling parameters are listed in Table 1 and 2. The superscripts of 's', 'p' represent interfacial shear and plastic deformation respectively. The subscripts 'ex', 'ey' and 'exy'

represent the changing ellipticity ratio along only x-direction, only y-direction, both x-and y-direction such that $e_x e_y = 1$. The subscript '1N', '2N' represent the applied load. The subscript 'x', 'y', 'z' represent the corresponding axis.

4.1.1 Comparison of friction results

The coefficient of friction plot was resolved into the components in the x and y axis due to plastic deformation and interfacial shear and plotted for different axis size and load in Figure 8. The coefficient of friction in x-direction due to plastic deformation μ_x^p increased with β from 0^0 to 90^0 due to increase in projected area along the plane perpendicular to the x-axis as shown in equation 8.1. The coefficient of friction in the y-axis due to plastic deformation μ_y^p increases to its maximum at 30^0 due to the difference in the net projected area perpendicular to the y-axis for positive plastic flow from equation 8.2 and is 0 at 0^0 and 90^0 due to the symmetry of the ellipsoid along the x-axis. The coefficient of friction due to interfacial shear along x and y axis, i.e. μ_x^s and μ_y^s remain constant and close to zero respectively. Following equations 8.3 and 8.4, the projected area in the horizontal plane dominates μ_x^s while the net projected area perpendicular to the x-axis for net positive shear flow dominates μ_y^s. The increase in applied load increases the ploughing depth and hence the (projected) contact area resulting in an increase in the components of the coefficient of friction, μ_x^p and μ_y^p as shown in Figure 8b. The decrease in ellipticity ratio (a/b) decreases the difference in the projected contact area in the yz plane at 0^0 and 90^0 orientation and also the difference in the projected contact area in the xz plane in $+y$ and $-y$ direction with orientation β. Hence the increase in μ_x^p and the change in μ_y^p decreases with β for a decrease in the ellipticity ratio a/b (asymmetry) of the asperity (compared to Figure 8a) as shown in Figure 8c. For an ellipsoidal asperity with major axis perpendicular to the sliding direction, the trends in the coefficient of friction with β are reversed as shown in Figure 8d. The results obtained from the numerical ploughing simulation for a rigid-plastic substrate are in good agreement with that obtained from the analytical model, taking into account the modified ploughed profile including e.g. pile up as discussed in section 2.1.

The effect of asperity size and applied load on the coefficient of friction due to plastic deformation and interfacial shear has been shown for three different cases in Figure 9. For the case where the ellipticity ratio e_x is increased while keeping e_y as 1, the coefficient of friction due to ploughing decreases. This is because the ploughing depth decreases with increase in asperity size to maintain the same contact area for a given load. However if the ellipticity ratio e_x is increased as the reciprocal of e_y, the coefficient of friction due to plastic deformation decreases due to the decrease in projected area perpendicular to the sliding direction. The depth also increases with e_x as explained in 4.1.2., which combined with the change in projected area results in the friction plots in Figure 9a. On the third case, as the ellipticity ratio e_y increases keeping e_x as 1, the ploughing depth decreases while the projected area perpendicular to the sliding direction increases. This decreases the coefficient of friction due to plastic deformation with increase in e_y, although at a lower rate compared to the previous two cases. The coefficient of friction due to plastic deformation increases with load while that due to interfacial shear remains mostly constant as shown in Figure 9b. However for low values of e_y, μ^s increases with e_y due to the faster increase in projected area perpendicular to the x-axis due to an increase in ploughing depth. The analytical model shows good agreement with the numerical model except for small e_y, where large deformation due to cutting increases the numerical friction force.

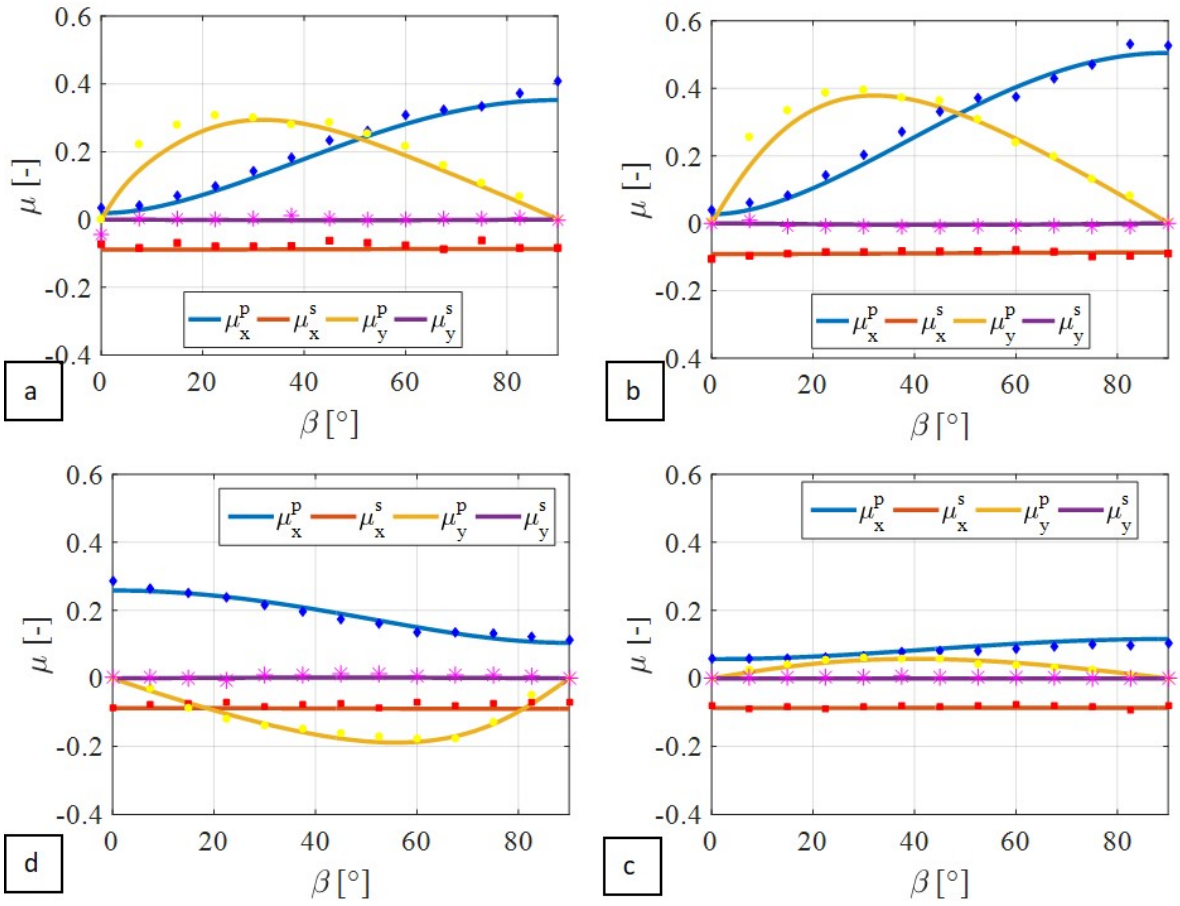

Figure 8: Effect of orientation and load on forces acting on an ellipsoidal asperities of axes size $a = 500\mu m$, $b = 80\mu m$, $c = 200\mu m$ at a load of (a) 1N and (b) 2N; axes size (c) $a = 250\mu m$, $b = 160\mu m$, $c = 200\mu m$ and (d) $a = 100\mu m$, $b = c = 200\mu m$ at a load of 1N, ploughing through a rigid-plastic substrate with interfacial friction factor $f = 0.45$. Factors $p = 0.2$ and $q = 2.5$ for case (a), (b) $q = 1.25$ for case (c) and $q = 1$ for case (d) are taken (marks: MPM model, lines: analytical model).

4.1.2 Comparison of ploughed profile

In order to study the ploughed profile, and compare the numerically simulated ploughing depths, a section of the substrate material surface was chosen as shown in Figure 10. The section comprised of different regions with size of a unit particle volume and the average position of each of the region was plotted as a function of the sliding distance. Figure 10a shows the average position of the particle in the region under the central axis of the asperity in the sliding direction over the whole sliding distance, shown as black mark in Figure 10b. It can be said that as the orientation of the asperity changes towards 90^0 the pile up increase rapidly initially with a small decrease in ploughing depth as further discussed in the previous and upcoming sections. The ploughing depth d_p is calculated as the sum of the pile-up height and groove depth (see Figure 2) in the ploughed profile. The ploughed profile is obtained from the final average position of the particles in the ploughed cross section as shown in Figure 10a and 10b.

Following equation 2, the ploughing depth should remain constant irrespective of the orientation of the asperity. However, the developed model has accounted for the plastic and shear flow behaviour to develop fitting factors to compute the ploughing depth as a function of asperity orientation. Figure 11 shows the ploughing depth obtained from the analytical and numerical

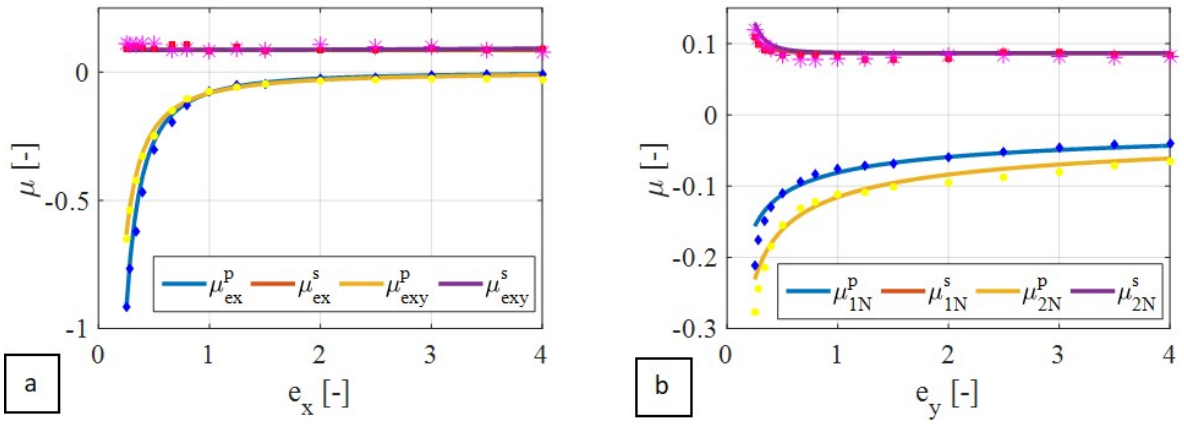

Figure 9: Effect of asperity size and load on forces acting on ellipsoidal asperities with ellipticity ratio (a) e_x changing such that $e_y = 1$ and $e_x e_y = 1$ at a load of 1N (b) and e_y changing such that $e_x = 1$ at loads of 1N and 2N, ploughing through a rigid-plastic substrate with interfacial friction factor $f = 0.45$. Factors $q = 1$ and $p = 0.154$ for case (a) and $p = 0.038$ for case (b) are taken (marks: MPM model, lines: analytical model).

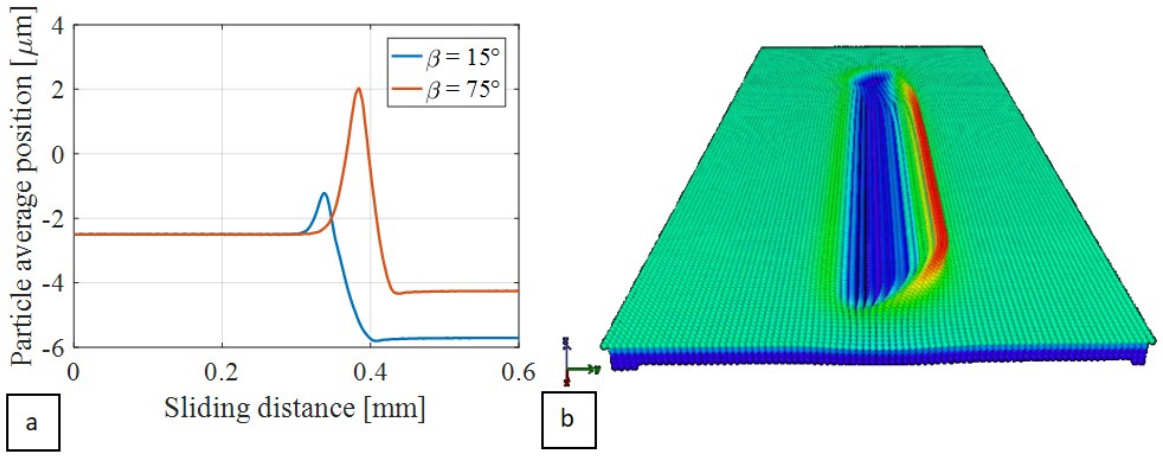

Figure 10: The asymmetry in pileup/ ploughing depth for an ellipsoidal asperity sliding through a rigid-plastic substrate along with the corresponding (a) particle position-time plot (b) ploughed track simulated using MPM (OVITO) for at $\beta = 30°$ orientation showing the studied surface cross-section in the black box.

model for various orientation, size and ellipticity ratio of the ellipsoidal asperity. It can be seen from Figure 11a that the total ploughing depth in front (at point C shown in Figure 3a) of an ellipsoidal asperity ($a = 100\mu m, \quad b = c = 200\mu m$) during ploughing decreases with increase in β. This is due to the decrease in A_{yz} and the resistance to plastic flow, which increases the pile-up height in front of the sliding asperity (see section 2.1.1). The change in ploughing depth in Figure 11a corresponds to the change in friction force due to plastic deformation in the Figure 8d. The interfacial shear stress aids to the yielding of the substrate and marginally increases the ploughing depth as shown for $f = 0.45$ in Figure 11a (see section 2.1.2). The decrease in (pile-up height) ploughing depth in front of the asperity with β in Figure 11a corresponds to an increase in the groove depth of the ploughed profile to balance the load shared deformed substrate (see section 2.1). Hence the depth of the ploughed track (sum of groove depth and pile-up height of the peripherical ridges of the ploughed track), given as the average of d_{+y} and d_{-y} in Figure 11b, increases with increase in β for the same asperity.

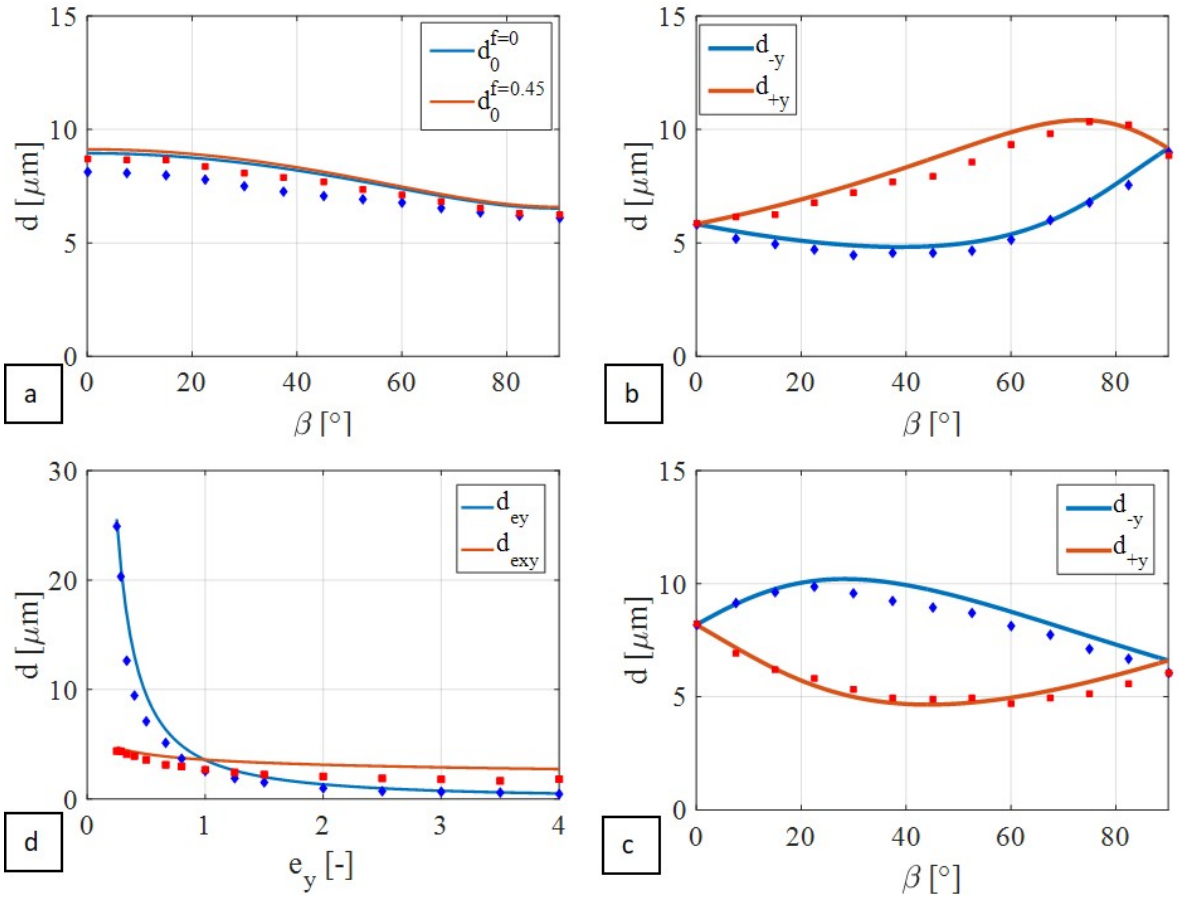

Figure 11: (a) The effect of orientation β and interfacial shear f on ploughing by an ellipsoidal asperity with axes size $a = 100\mu m,\ b = c = 200\mu m$ at 1N load on ploughing depth d_0 along the (x-) sliding axis ($y = 0$) ($p = 0.2$). (b) The effect of β on the ploughing depth $d_{\pm y}$ at the periphery of the ploughed profile ($p = -0.33,\ q = 0.6$). (c) The effect of β on $d_{\pm y}$ for ploughing by ellipsoidal asperity with axis size $a = 250\mu m,\ b = 160\mu m,\ c = 200\mu m$ ($p = -0.25,\ q = 2$) at 2N load. (d) The effect of asperity size on ploughing depth with ellipticity ratio e_y changing such that $e_x = 1$ ($p = -0.4$) and $e_x e_y = 1$ ($p = -0.1$) at 1N load. (marks: MPM model, line: analytical model). Fitting factors p and q are given.

The asymmetric separation of flow due to asymmetry in the ploughing asperity results in a variable ploughing depth on either ends of the ploughed track (points S and N shown in Figure 3), as given in Figure 11b and 11c. The change in asperity orientation from 0^0 to 90^0 results in an rapid divergence in ploughing depths d_{+y} and d_{-y} on either side of ploughed wear track followed by their steady convergence resulting as shown in Figure 11b and 11c. This behaviour is explained by the variation in distribution of piled-up substrate material in front of the asperity to its periphery with β, as shown in section 2.1 using equations 4.2 and 4.3. The depth profiles are reversed as the major axis of the asperity is perpendicular to sliding direction as shown in Figure 11c. The ploughing depths for ellipsoidal asperity increases with decrease in e_y only following load balance and plastic flow correction as shown in Figure 11d. However the ploughing depth increases with e_y, which increases as reciprocal of e_x, due to increase in the resistance to plastic flow. The numerical ploughing depth does agree fairly well with the analytical ploughing depths.

4.2 Experimental validation of numerical results

The overall coefficient of friction along the sliding direction and perpendicular to the sliding direction was measured from the experiments and compared with the MPM-based ploughing simulations. The ploughed profile of the DX-56 sheet was obtained from the observed cross-section of the wear track after the ploughing experiments. These cross-sections will be compared to the MPM-based simulation results. The effect of ellipsoid size, orientation and applied load on the coefficient of friction and deformation are explained as a part of the effect of asperity geometry on the ploughing behaviour.

4.2.1 Validation of friction results

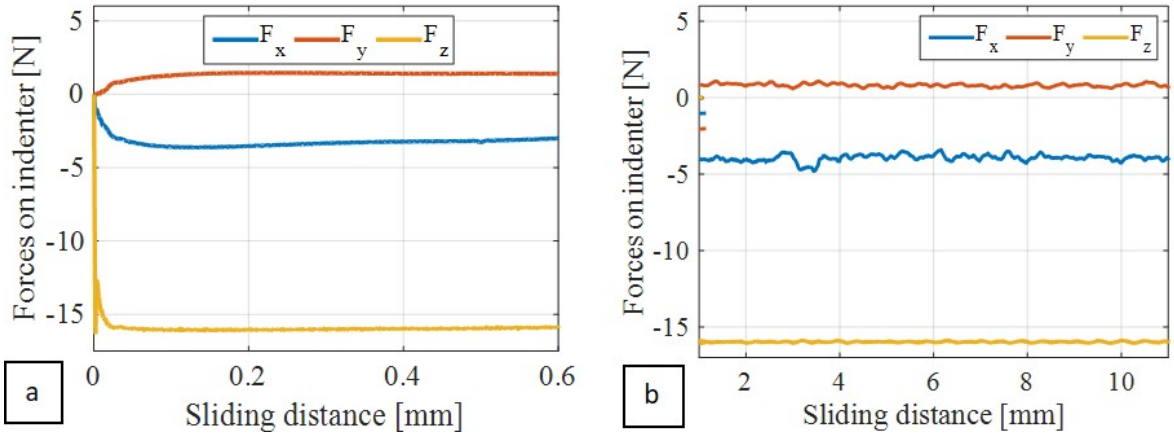

Figure 12: Components of forces along x, y and z axis acting on an indenter of axes sizes $a = 667\mu m$, $b = 375\mu m$ and $c = 500\mu m$ sliding at an orientation of $\beta = 30°$ with respect to the x axis under an applied load of $16N$ as obtained from (a) MPM-based ploughing simulation and (b) ploughing experiments.

In order to obtain the coefficient of friction from the ploughing experiments and ploughing simulations, the force components acting on the indenter were plotted over the sliding distance as shown in Figure 12. The sliding distance of the numerical simulations was kept small to reduce computational cost. The average friction force was taken in the steady state of friction in the last one-third of the sliding distance. The friction force in the x and y direction was divided by the applied load to obtain the coefficient of friction in the x and y direction as μ_x and μ_y. The coefficient of friction values obtained from the numerical simulation were converged for particle and mesh sizes of 5,10 and 20 μm for the substrate and indenter respectively to obtain the final result (see [32] for convergence study background). It can be seen in Figure 12 that the orientation of the asperity results in friction force acting on the indenter in both x and y direction.

Loads of 7N and 16N were applied to the indenters B1-B7 with their reference axis either along or perpendicular to the sliding direction leading to the case with varying ellipticity ratio e_x and e_y. The coefficient of friction was plotted against the asperity size increasing from 250-2000μm both along the sliding direction and perpendicular to the sliding direction as shown in Figure 13. It can be seen that the coefficient of friction is only measured along the sliding direction due to the axis symmetry in the sliding ellipsoidal indenter. As it can be seen from Figure 13a that for the case μ vs e_x of axis size the agreement between the experiment and the numerical

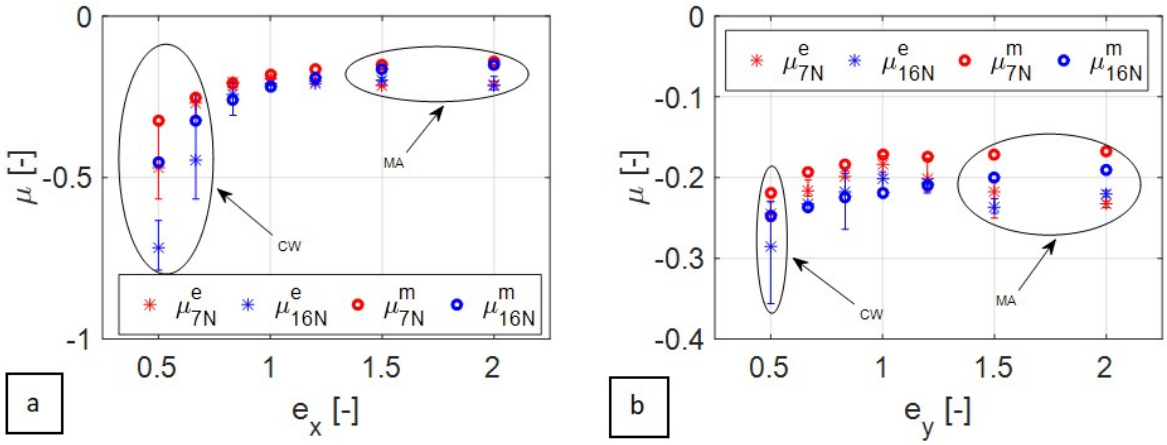

Figure 13: Comparison of coefficient of friction μ for applied loads of $7N$ and $16N$ (subscript) obtained from MPM-based ploughing simulation (superscript: 'm') and ploughing experiments (superscript: 'e') for varying ellipticity ratio along the (a) x- axis (sliding direction) and (b) y-axis. (CW: cutting wear, MA: misalignment).

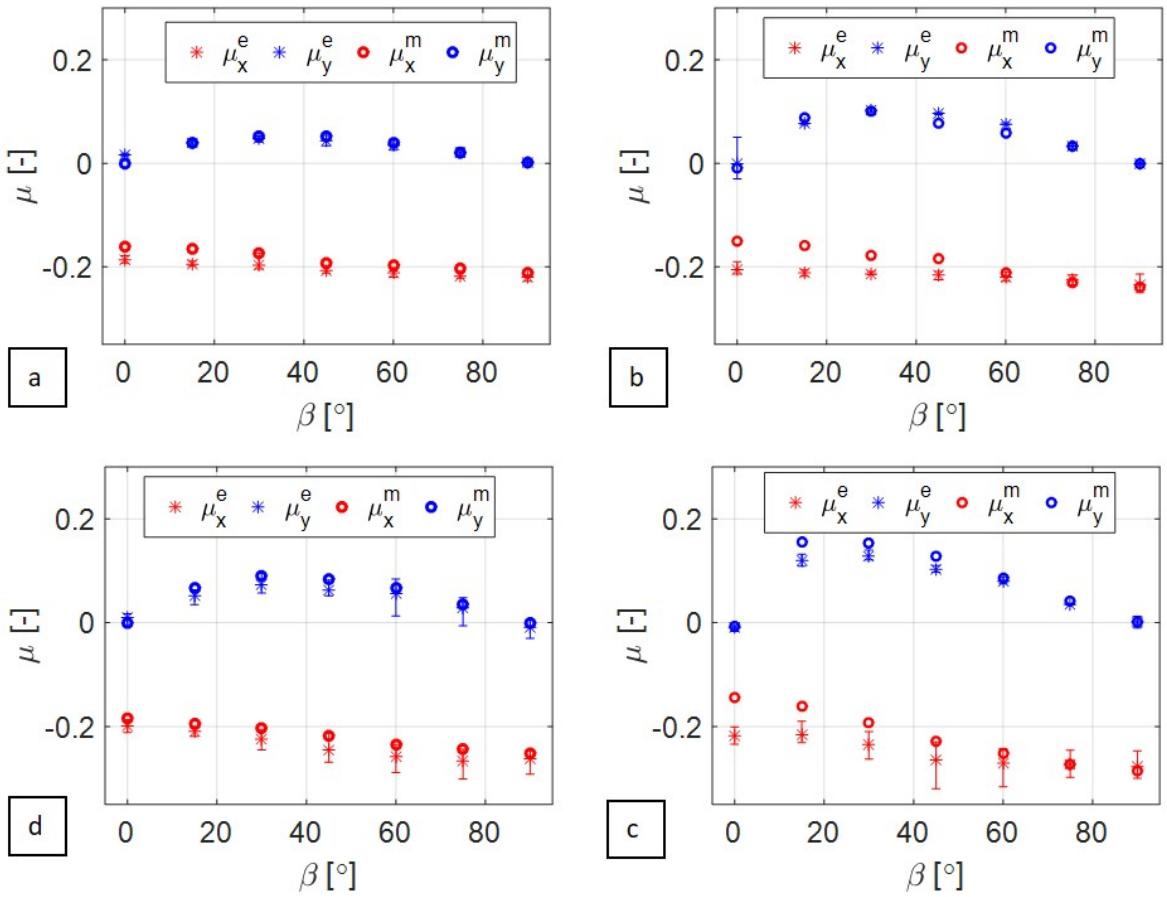

Figure 14: Comparison of coefficient of friction μ along x and y direction (subscript) obtained from MPM-based ploughing simulation (superscript: 'm') and ploughing experiments (superscript: 'e') for varying angle of ellipsoid orientation β at $7N$ load for axes size (a) $a = 667\mu m$, $b = 375\mu m$ (b) $a = 833\mu m$, $b = 300\mu m$ (c) $a = 1000\mu m$, $b = 250\mu m$ and (d) $a = 667\mu m$, $b = 375\mu m$ at $16N$ load.

results is shown for ellipsoidal indenters which are less skewed and have ellipticity ratio closer to unity. The results obtained from ploughing experiments with smaller ellipsoidal tips with e_x of 0.5 and 0.33 deviate largely from numerical results at high loads as cutting wear sets instead of ploughing and friction becomes unstable. For large ellipsoidal tips with e_x of 0.75 and 1 the friction results obtained from the ploughing experiments exceed those obtained from the numerical model. The measured friction for indenters with large axis size are highly sensitive to alignment with respect to both loading and sliding direction. The regions in the μ vs e_x and μ vs e_y plots with the aforementioned effects of cutting wear and misalignment, are marked as CW and MA respectively in Figure 13.

The coefficient of friction was studied as a function of the angle of orientation with respect to the sliding direction β for ellipsoidal pins with varying ellipticity ratio and applied load. The ellipticity ratio of the axes e_x/e_y in the sliding plane was varied from 1.8, 2.8 to 4 such that the product $e_x e_y$ was 1 and the coefficient of friction was plotted in Figure 14a, 14b and 14c respectively. A load of 7N was applied to avoid any cutting effects and maintain ploughing wear. The load was changed to 16N for ellipticity ratio of 1.8 and the coefficient of friction was plotted in Figure 14d. For lower ellipticity ratio of 1.8 the coefficient of friction plots both in the x and y axis 7N and 16N as shown in Figure 14a and 14d. However, as the ellipticity ratio of the pins were increased to 2.8 and 4, the coefficient of friction plots both in x and y axis obtained from the ploughing experiments exceeded than that obtained from the numerical simulations for lower β values. The spread in values of the measured coefficient of friction can be attributed to the high sensitivity of the friction force with respect to misalignment for highly skewed and long indenters. A small forward tilt in the indenter in the x and y axis could lead to an increase in the friction force experienced by the indenter. Although theoretically the coefficient of friction for angle $\beta = 0^0$ should reduce with increasing ellipticity ratio due to decrease in projected area in the sliding x direction, the observed increase in friction with increasing ellipticity ratio could be explained due to a minor misalignment and subsequent increase in contact area and friction due to interfacial shear.

4.2.2 Validation of ploughed profile

The ploughing depth d was obtained as the sum of the maximum groove depth, d_g and the maximum pile-up height h_{pu} on either side of the ploughed wear track for both the experiments as well as the simulations. The ploughing depth on the $+y$ axis was given as d_{+y} and on the $-y$ axis was termed as d_{-y}. The ploughed track that was observed under the confocal microscope for experiments done at different orientations for a ellipsoidal asperity with ellipticity ratio e_{xy} of 4 are shown in Figure 15. It can be clearly seen particularly in Figure 15a and somewhat in Figure 15d that for orientation of 0^0 and 90^0 the ploughing depths on either side of the wear track are more or less similar. Any possible difference in the ploughing depth can be due to the sliding misalignment in clamping the ellipsoidal pin mark with the pin holder marking to set the require orientations of 0^0 and 90^0. As the ellipsoid is oriented at an angle of 30^0 or 60^0 there is a difference in the ploughing height on either side of the ploughed wear track as seen in Figure 15b and 15c. It can also be seen that the ploughing depth reduces while the contact width increases from Figure 15a to 15d which follows the asperity geometry.

The total ploughing depths obtained from ploughing experiments and simulation has been plotted as a function of the ellipsoid size in x and y direction for applied loads of 7N and 16N as shown in Figure 17. It can be seen in Figure 17a and 17b that the ploughing depth decreases with increase in size of the ellipsoidal pin tip as also follows from the load balance

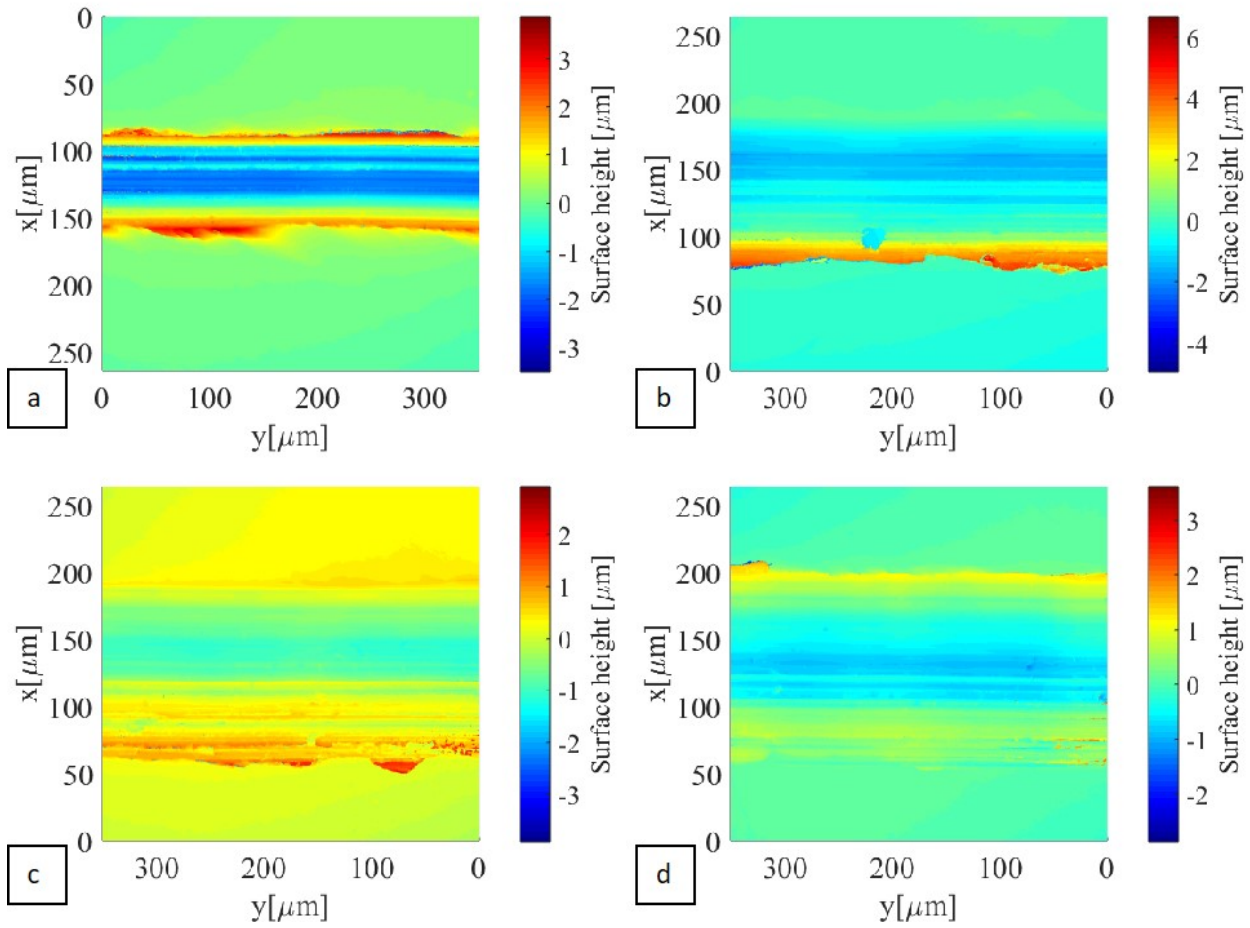

Figure 15: Confocal image at $50x$ magnification of the ploughed track showing surface height distribution of a substrate ploughed by a load of $7N$ using an ellipsoidal asperity of axes size $a = 1000\mu m$, $b = 250\mu m$ orientated at angle with respect to sliding direction (a) $\beta = 0°$, (b) $\beta = 30°$ (c) $\beta = 60°$ and (d) $\beta = 90°$.

given in equation 2.1 and 2.2, The ploughing depths for pins with e_y between 0.5 to 1 is higher as compared to the pins with e_x between 0.5 to 1 as shown in Figure 17. This follows from equation 3.1 and 3.2 where a smaller axes size in the y-direction results in a lower resistance to plastic flow, and hence a higher penetration of the pin into the substrate. However, both the numerical and experimental ploughing depths decreases as e_x and e_y increase from 1 to 2, the experimental ploughing depth in fact marginally increases as the ellipticity ratio e_x increases from 1 to 2. The increase in ploughing depth could be due to misalignment of the ellipsoidal pins in the vertical plane which results in deeper penetration of the pin into the substrate. As discussed previously, an ellipsoidal pin with its major axis in the sliding direction is sensitive to misalignment in the x or y axis. The increase in ploughing depth for larger pins in Figure 17a also explains the increase in their corresponding coefficient of friction as shown in Figure 13a.

It can also be seen that the ploughing depths for the ellipsoidal pins in experiments are smaller than those obtained from the simulations. The difference in penetration can be attributed to the high surface roughness of the pins as listed in table 4. To compare the effect of roughness on penetration, when a highly polished reference spherical ball of 0.5mm radius was used instead of pin 'B4' of radius 0.5mm, the ploughing depth obtained was about 1.5 - 2 times higher as seen in Figure 16a. The effect of roughness is mostly prominent for ellipsoids with low ellipticity

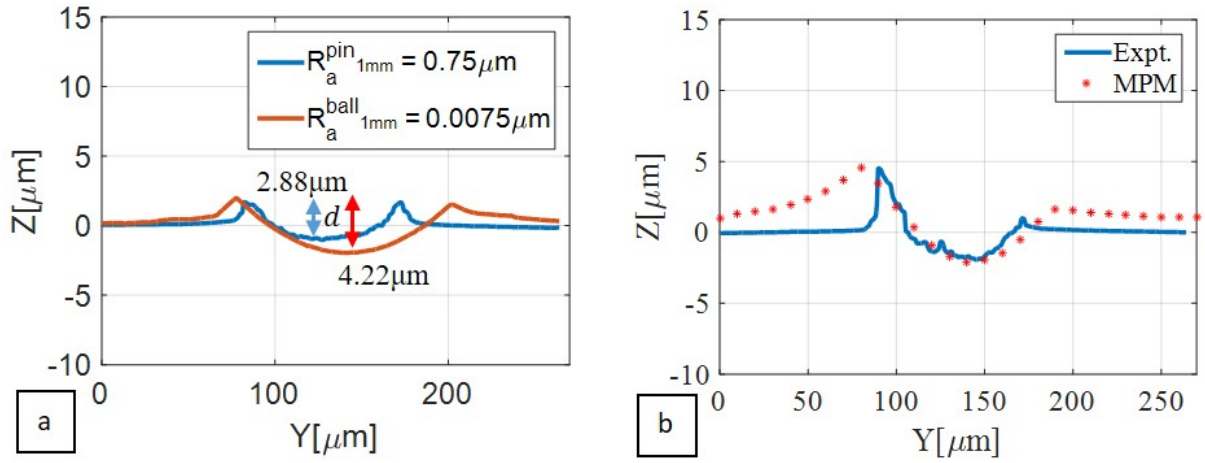

Figure 16: (a) The effect of indenter roughness of ploughed profile shown using pins with spherical tips of 1mm diameter with varying roughness R_a and (b) the comparison of the ploughed profile obtained from numerical simulation and experiments all ploughing the lubricated steel substrate at an applied load of 7N.

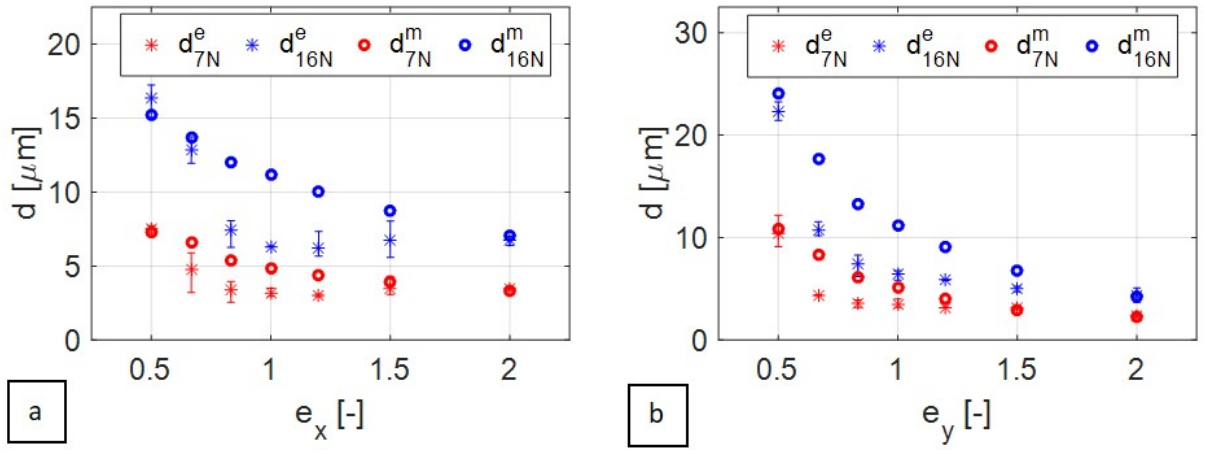

Figure 17: Comparison of ploughing depth d for applied loads of $7N$ and $16N$ (subscript) obtained from MPM-based ploughing simulation (superscript: 'm') and ploughing experiments (superscript: 'e') for varying ellipticity ratio along the (a) x- axis (sliding direction) and (b) y-axis.

ratio and large size where the geometry of the ellipsoid doesn't allow for deeper penetration and the surface roughness affects the ploughing depths. However, for high ellipticity ratio the numerical and the experimental wear profile compare very well as shown in Figure 16b. The ploughing depth obtained from experiments and simulations for either side of the ploughed track are plotted for applied loads of 7N using ellipsoidal pins of ellipticity ratios 4, 2.8 and 1.8 and applied load of 16N for ellipticity ratio 4 as shown in Figure 18. It can be seen from Figure 18a and 18d that for high ellipticity ratio of 4, the ploughing depths obtained on the +y and -y axis of the ploughed tracks are in good agreement for both experiments and simulation for both applied loads of 7N and 16N. However, as the ellipticity ratio decreases and the ellipsoidal pin is closer to a spherical shape, the roughness effects sets in and the experimental ploughing depths decreases on either side of the ploughed track (see Figure16a). This results in experimental ploughing depth being lower as compared to the simulated ploughing depth for ellipsoidal pins with ellipticity ratio of 1.8 and 2.8 at 16N load as shown in Figure 18b and 18c.

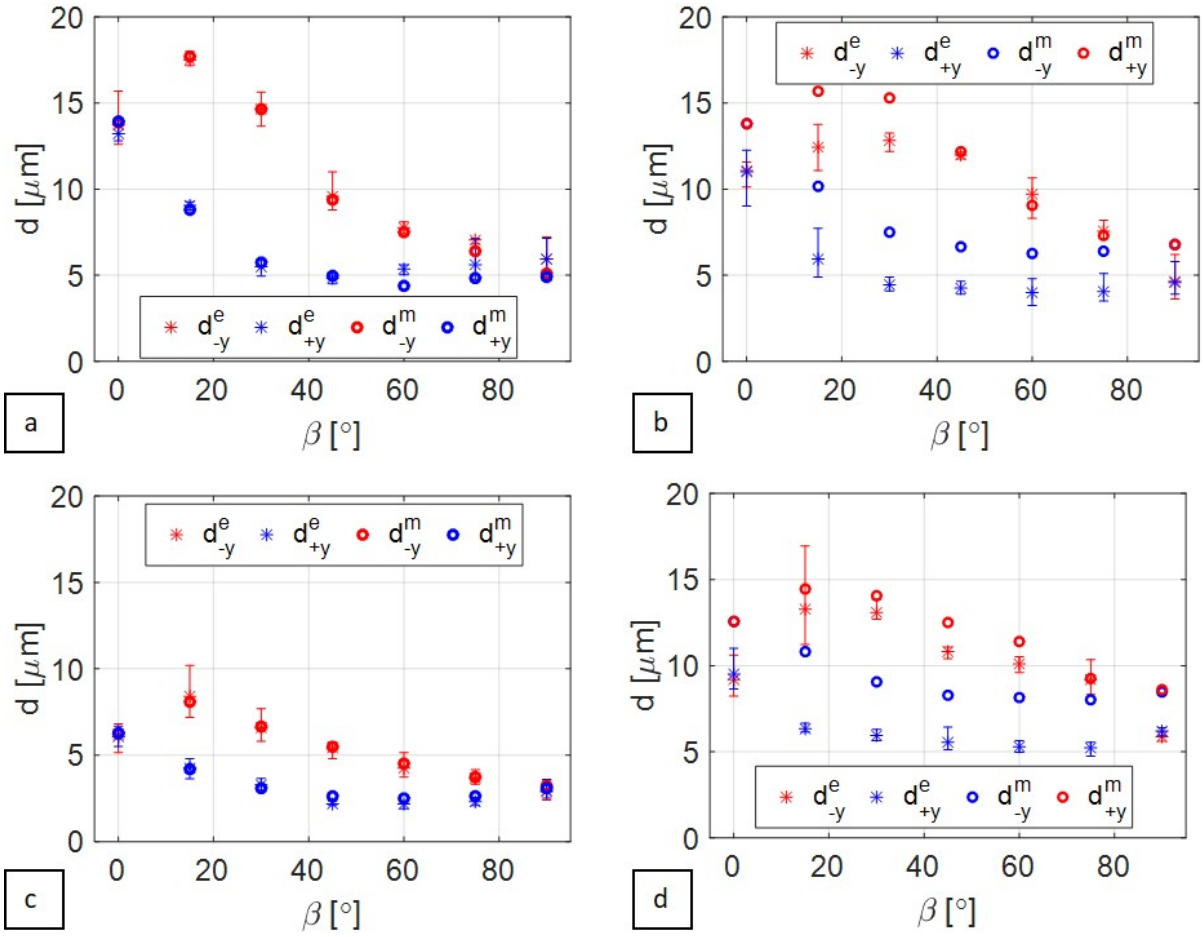

Figure 18: Comparison of ploughing depths d along the periphery at $+y$ and $-y$ axis (subscript) obtained from MPM-based ploughing simulation (superscript: 'm') and ploughing experiments (superscript: 'e') for varying angle of ellipsoid orientation β at $16N$ load for axes sizes (a) $a = 1000\mu m$, $b = 250\mu m$, (b) $a = 833\mu m$, $b = 300\mu m$, (c) $a = 667\mu m$, $b = 375\mu m$ and (d) $a = 1000\mu m$, $b = 250\mu m$ at $7N$ load.

The models have been successfully validated for forces and penetration depths in ploughing of an elliptical asperity through a lubricated steel sheet. In the transition to cutting wear, in ploughing experiments for smaller ellipsoidal pin sizes, unstable and high friction is observed along with the formation of wear debris (chips). Modelling of friction and material removal in cutting wear requires inclusion of robust damage models in the numerical model, which is beyond the scope of the current paper. However, the effect of the size, orientation relative to the sliding direction, of the elliptical asperity and the applied load on the ploughing forces and the ploughed profile have been studied using both the analytical and the numerical models. The forces for each asperity size and orientation can be combined to calculate the ploughing forces in a multi-asperity sliding contact. Hence, by describing the contact between a (anisotropic) rough, hard tool surface and a soft, smooth sheet as a set of elliptic contact patches [11], the forces in ploughing of the sheet by the tool asperities and the ploughed profile of the sheet can be computed by the developed models.

5 Conclusion

An analytical model to compute the ploughed profile and forces in ploughing by ellipsoidal asperities of varying size, ellipticity ratio and orientation has been extended and compared to the numerical model for a rigid-plastic substrate. The effect of asymmetry in asperity geometry on the ploughing depths and ploughing friction has been discussed through results of the numerical model. The MPM-based ploughing model has further been validated with ploughing experiments using ellipsoidal pins on lubricated steel sheets. The results are in good agreement for most asperity geometries. The comparison between the analytical model, simulations and experiments have been done for both the forces involved in ploughing as well as the profile of the ploughed track. A good agreement has been found between the approaches. The deviation in the experimental and numerical results are described through roughness and alignment effects.

Acknowledgment

This research was carried out under project number S22.1.14520a in the framework of the Partnership Program of the Materials innovation institute M2i (www.m2i.nl) and the Technology Foundation TTW (www.stw.nl), which is part of the Netherlands Organization for Scientific Research (www.nwo.nl). The authors would like to acknowledge ing. Erik de Vries from University of Twente for his support in designing the UMT2 test set-up for ploughing. The authors would also like to thank G.S.M.b.v., Haaksbergen for their help in machining the ellipsoidal pins and TATA steel Europe R&D, Ijmuiden for the provision of Bergström van Liempt material model parameters for DX56 steel sheets.

Bibliography

[1] J.M. Challen and P.L. Oxley. "An explanation of the different regimes of friction and wear using asperity deformation models". In: Wear 53 (1979), pp. 229–243. DOI: 10.1016/0043-1648(79)90080-2.

[2] J.M. Challen and P.L. Oxley. "Slip-line fields for explaining the mechanics of polishing and related processes". In: International Journal of Mechanical Sciences 26 (1984), pp. 403–418. DOI: 10.1016/0020-7403(84)90030-4.

[3] N. Tayebi, T.F. Conry, and A.A. Polycarpou. "Determination of hardness from nanoscratch experiments: Corrections for interfacial shear stress and elastic recovery". In: Journal of materials research 18 (2003), pp. 2150–2162. DOI: 10.1557/JMR.2003.0301.

[4] G. van der Linde, M.B. de Rooij, and D.J. Schipper. "Stability criteria for a pyramidal shaped asperity ploughing through a plastically deforming substrate". In: Wear 300 (2013), pp. 96–104. DOI: 10.1016/j.wear.2013.01.119.

[5] M.B. de Rooij, G. van der Linde, and D.J. Schipper. "Modelling material transfer on a single asperity scale". In: Wear 307 (2013), pp. 198–208. DOI: 10.1016/j.wear.2013.09.006.

[6] F.P. Bowden, A.J. Moore, and D. Tabor. "The ploughing and adhesion of sliding metals". In: Journal of Applied Physics 14 (1943), pp. 80–91. DOI: 10.1063/1.1714954.

[7] A.P. Green. "The plastic yielding of metal junctions due to combined shear and pressure". In: Journal of the Mechanics and Physics of Solids 2 (1954), pp. 197–211. DOI: 10.1016/0022-5096(54)90025-3.

[8] K. Hokkirigawa and K. Kato. "An experimental and theoretical investigation of ploughing, cutting and wedge formation during abrasive wear". In: Tribology international 21 (1988), pp. 51–57. DOI: 10.1016/0301-679X(88)90128-4.

[9] J.A. Greenwood and J.P. Williamson. "Contact of nominally flat surfaces". In: Proceedings of the royal society of London. Series A. Mathematical and physical sciences 295 (1966), pp. 300–319. DOI: 10.1098/rspa.1966.0242.

[10] P.R. Nayak. "Random process model of rough surfaces in plastic contact". In: Wear 26 (1973), pp. 305–333. DOI: 10.1016/0043-1648(73)90185-3.

[11] X. Ma, M.B. De Rooij, and D.J. Schipper. "A load dependent friction model for fully plastic contact conditions". In: Wear 269 (2010), pp. 790–796. DOI: 10.1016/j.wear.2010.08.005.

[12] A.W. Bush, R.D. Gibson, and T.R. Thomas. "The elastic contact of a rough surface". In: Wear 35 (1975), pp. 87–111. DOI: 10.1016/0043-1648(75)90145-3.

[13] J.I. McCool. "Comparison of models for the contact of rough surfaces". In: Wear 107 (1986), pp. 37–60. DOI: 10.1016/0043-1648(86)90045-1.

[14] J.A. Williams. "Analytical models of scratch hardness". In: Tribology international 29 (1996), pp. 675–694. DOI: 10.1016/0301-679X(96)00014-X.

[15] G. Van der Linde. "Predicting galling behaviour in deep drawing processes". PhD thesis. University of Twente, The Netherlands, 2011. ISBN: 978-90-365-3284-6.

[16] T. Mishra, M. de Rooij, M. Shisode, J. Hazrati, and D.J. Schipper. "An analytical model to study the effect of asperity geometry on forces in ploughing by an elliptical asperity". In: Tribology international 137 (2019), pp. 405–419. DOI: 10.1016/j.triboint.2019.05.015.

[17] D. Meng, Y.G. Li, Z.T. Jiang, and M.K. Lei. "Scratch behavior and FEM modelling of Cu/Si (100) thin films deposited by modulated pulsed power magnetron sputtering". In: Surface and Coatings Technology 263 (2019), pp. 25–33. DOI: 10.1016/j.surfcoat.2019.02.008.

[18] G. Kermouche, J.L. Loubet, and J.M. Bergheau. "A 3D finite element pocedure for modelling scratch test". In: In Proceedings of the 10th International Conference Metrology and Properties of Engineering Surfaces. Ed. by International Conference Metrology and Properties of Engineering Surfaces. Accessed from https://www.researchgate.net/publication/273256479_A_3D_finite_element_procedure_for_modeling_scratch_test. Saint-Etienne, France, 2005, pp. 311–320.

[19] R. Komanduri, N. Chandrasekaran, and L.M. Raff. "MD simulation of indentation and scratching of single crystal aluminum". In: Wear 240 (2000), pp. 113–143. DOI: 10.1016/s0043-1648(00)00358-6.

[20] T. Junge and J.F. Molinari. "Molecular dynamics nano-scratching of aluminium: a novel quantitative energy-based analysis method". In: Procedia IUTAM 3 (2012), pp. 192–204. DOI: 10.1016/j.piutam.2012.03.013.

[21] K.E. Avila, S. Küchemann, I.A. Alhafez, and H.M. Urbassek. "Nanoscratching of metallic glasses-An atomistic study". In: Tribology international 139 (2019), pp. 1–11. DOI: 10.1016/j.triboint.2019.06.017.

[22] J.L. Bucaille, E. Felder, and G. Hochstetter. "Mechanical analysis of the scratch test on elastic and perfectly plastic materials with the three-dimensional finite element modeling". In: Wear 249 (2001), pp. 422–432. DOI: 10.1016/S0043-1648(01)00538-5.

[23] G. Kermouche, N. Aleksy, J.L. Loubet, and J.M. Bergheau. "Finite element modeling of the scratch response of a coated time-dependent solid". In: Wear 267 (2009), pp. 1945–1953. DOI: 10.1016/j.wear.2009.05.005.

[24] K. Holmberg, A. Laukkanen, H. Ronkainen, K. Wallin, S. Varjus, and J. Koskinen. "Tribological contact analysis of a rigid ball sliding on a hard coated surface: Part I: Modelling stresses and strains". In: Surface and Coatings Technology 200 (2006), pp. 3793–3809. DOI: 10.1016/j.surfcoat.2005.03.0405.

[25] F. Elwasli, F. Zemzemi, A. Mkaddem, S. Mzali, and S. Mezlini. "A 3D multi-scratch test model for characterizing material removal regimes in 5083-Al alloy". In: Materials & Design 87 (2015), pp. 352–362. DOI: 10.1016/j.matdes.2015.07.121.

[26] D.A. Doman, R. Bauer, and A. Warkentin. "Experimentally validated finite element model of the rubbing and ploughing phases in scratch tests". In: Proceedings of the Institution of Mechanical Engineers, Part B: Journal of Engineering Manufacture 223 (2009), pp. 1519–1527. DOI: 10.1243/09544054JEM1520.

[27] Z. Wang, H. Zhang, Z. Li, G. Li, J. Zhang, J. Zhang, H. ul Hassan, Y. Yan, A. Hartmaier, and T. Sun. "Crystal plasticity finite element simulation and experiment investigation of nanoscratching of single crystalline copper". In: Wear 430 (2019), pp. 100–107. DOI: 10.1016/j.wear.2019.04.024.

[28] Y. Gao, C. Lu, N.N. Huynh, G. Michal, H.T. Zhu, and A.K. Tieu. "Molecular dynamics simulation of effect of indenter shape on nanoscratch of Ni". In: Wear 267 (2009), pp. 1998–2002. DOI: 10.1016/j.wear.2009.06.024.

[29] X. Zheng, H. Zhu, A.K. Tieu, and B. Kosasih. "Molecular dynamics simulation of effect of indenter shape on nanoscratch of Ni". In: Tribology international 67 (2013), pp. 217–221. DOI: 10.1016/j.triboint.2013.07.015.

[30] S. Solhjoo and A.I. Vakis. "Single asperity nanocontacts: Comparison between molecular dynamics simulations and continuum mechanics models". In: Computational Materials Science 99 (2015), pp. 209–220. DOI: 10.1016/j.commatsci.2014.12.010.

[31] S. Leroch, M. Varga, S.J. Eder, A. Vernes, M.R. Ripoll, and G. Ganzenmüller. "Single asperity nanocontacts: Comparison between molecular dynamics simulations and continuum mechanics models". In: International Journal of Solids and Structures 81 (2016), pp. 188–202. DOI: 10.1016/j.ijsolstr.2015.11.025.

[32] T. Mishra, G.C. Ganzenmüller, M.B. de Rooij, M. Shisode, J. Hazrati, and D.J. Schipper. "Modelling of ploughing in a single-asperity sliding contact using material point method". In: Wear 418 (2019), pp. 180–190. DOI: 10.1016/j.wear.2018.11.020.

[33] P. Van Liempt. "Workhardening and substructural geometry of metals". In: Journal of Materials Processing Technology 45 (1994), pp. 459–464. DOI: 10.1016/0924-0136(94)90382-4.

[34] D. Tabor. The hardness of metals. London: Oxford University Press, 1951. ISBN: 0-521-29183-6.

[35] T. Mishra, M.B. de Rooij, M. Shisode, J. Hazrati, and D.J. Schipper. "Characterization of interfacial shear strength and its effect on ploughing behaviour in single-asperity sliding". In: Wear 436-437 (2019), p. 203042. DOI: 10.1016/j.wear.2019.203042.

Paper D

Characterization of interfacial shear strength and its effect on ploughing behaviour in single-asperity sliding

Tanmaya Mishra[1*], Matthijn de Rooij[1], Meghshyam Shisode[2], Javad Hazrati[2], and Dirk J. Schipper[1]

[1]Surface Technology and Tribology, Faculty of Engineering Technology, University of Twente, 7500 AE Enschede, the Netherlands
[2]Nonlinear Solid Mechanics, Faculty of Engineering Technology, University of Twente, 7500 AE Enschede, the Netherlands

Abstract

The shear strength at the interface contributes to the overall friction force experienced by the contacting bodies sliding against each other. In this article, an experimental technique to characterize the shear strength at the interface of metallic bodies in sliding contact has been developed. The boundary layers formed at interface in a lubricating contact have been varied by using two different types of lubricants in combination with both zinc coated and uncoated steel sheets. The empirical relations between the experimental parameters such as contact pressure and sliding velocity and the interfacial shear strength have been expressed by fitting the experimental results. These expressions have been incorporated in the Material Point Method (MPM) based ploughing model. The coefficient of friction and ploughing depth obtained from the numerical simulations have been validated relative to the experimental results with a good agreement for both lubricated and unlubricated substrates, different loads and spherical indenter sizes. Furthermore, the interfacial shear strength has been varied in the MPM-based ploughing model and ploughing experiments to study the contribution of interfacial shear strength to overall friction, deformation and wear.

Keywords: Friction model, Boundary layer, Ploughing, Interfacial shear, Material Point Method.

Nomenclature of symbols

A_c	Contact area of the asperity with substrate	a	Contact radius (for point contact)
A	Constant (unit J/s)	b	Contact width (for line contact)
C	Proportionality constant for interfacial shear	b_0	Initial guess for contact width
D	Proportionality constant	b^*	Corrected contact width
E	Height of energy barrier	c_0	Lattice constant
E^*	Effective elastic/Young's modulus	d	Total ploughing depth
E_{in}	Young's modulus of indenter	d_g	Groove depth
E_s	Young's modulus of substrate	d_0	Ploughing depth without interfacial shear
F_{sh}	Force on the asperity due to interfacial shear	d_μ	Ploughing depth with interfacial shear
F_f	Total friction force	$\overline{d}$	Ratio of d_μ and d_0
F_a	Friction force due to adhesion	f_{hk}	Interfacial friction factor (ratio of τ and κ)
F_p	Friction force due to ploughing	h	Thickness of boundary layer
F	Constant in logarithmic shear stress term	h_{pu}	Pile-up height
F_n	Applied normal load	i	Coating layer position, $i = 1, 2, \ldots, n$
G	Proportionality constant	l	Uncrowned/contact length of roller
H_s	Hardness of substrate	n	Number of coating layers
H_c	Hardness of coating	n_0	Proportionality constant for visco-elastic term
I_0	First influence factor	n_P	Exponent of pressure
I_1	Second influence factor	n_v	Exponent of sliding velocity
K	Strain rate term	n_T	Exponent of temperature
$K^{'}$	Antilog of constant C	p	Proportionality constant of log of pressure
P	Pressure	q	Proportionality constant of log of velocity
$\overline{P}$	Effective pressure in visco-elastic effect	r	Radius of tool (cylinder/sphere)
P_0	Maximum constant pressure	u_0	Reference molecular velocity
P_{nom}	Nominal contact pressure	u	Average molecular velocity
R	Gas constant	v_0	Reference sliding velocity
R_a	Mean surface roughness	v	Sliding velocity
$Q^{'}$	Activation energy	$t^{'}$	Average time to overcome energy barrier
Q	Potential barrier	t_i	Thickness of i^{th} coating layer
T	Temperature	$\overline{t}_i$	Cumulative thickness up to i^{th} coating layer

Nomenclature of symbols

Φ	Stress activation volume	κ	Bulk shear strength of the substrate
Ω	Pressure activation volume	μ	Overall coefficient of friction
σ_y	Yield stress (uniaxial)	μ_b	Ratio of F_{sh} and F_n
α_0	Visco-elastic term	μ_p	Ratio of F_p and F_n
α	Proportionality constant for pressure	$\overline{\mu}$	Ratio of μ_b and μ
β	Proportionality constant for sliding velocity	$\overline{\mu}_{3mm}^{UL}$	$\overline{\mu}$ of unlubricated contact with ball, $2r$ =3mm
ψ	Proportionality constant for temperature	$\widetilde{\mu}$	Ratio of F_a and F_f
$\dot{\gamma}$	Shear rate	γ_s	Angle of attack for spherical asperity
ω_0	Molecular vibration frequency	γ_{pl}^{wd}	γ_s for transition from ploughing to wedging
τ/τ_{BL}	Shear strength of the interface/ boundary layer	γ_{UL}^{SP}	γ_{pl}^{wd} in unlubricated shine-polished sheet
τ_{GI}^{Q}	τ of zinc coated steel with Quaker lubricant	$\overline{\nu}$	Average Poisson's ratio of all coating layers
τ_I^A	τ of steel sheet with Anticorit lubricant	ν	Poisson's ratio
τ_0	Intrinsic shear strength for pressure	ν_{cs}	Poisson's ratio of the coated system
τ_1	Intrinsic shear strength for sliding velocity	ν_i	Poisson's ratio of the i^{th} coating layer
τ_2	Intrinsic shear strength for temperature	φ	Characteristic frequency for strain rate term
$\tau_0^{'}$	Intrinsic shear strength for strain rate	θ	Characteristic frequency for visco-elastic term
$\tau_0^{''}$	Intrinsic shear strength for temperature	η_{40^0C}	Dynamic viscosity of lubricant at 40^0C

1 Introduction

Most metallic surfaces are naturally covered by an oxide layer as well as a boundary layer when lubricated. Shear takes place at these surface layers when a tangential load is applied. The stress required to shear off these layers at the sliding contact interface is defined as the 'interfacial shear strength' or specifically 'boundary layer shear strength' for boundary layers. In the absence of a lubricating boundary layer, metallic oxide films are typically formed at the contact which contributes to a higher interfacial shear strength. In the absence of any interfacial layer, direct contact between sliding bodies results in a very high interfacial shear strength which might almost equal the bulk shear strength of the deforming substrate. The interfacial shear strength along with the resistance of the substrate to plastic deformation of the substrate contributes to the overall friction and wear in sliding of a rigid asperity through a metallic substrate [1].

Initial work on functioning of lubricated boundary layer was done in [1], [2] and [3]. The presence of lubricant between two bodies sliding against each other prevents direct contact of the metallic asperities, thereby greatly reducing friction and wear. The lubricant does so by forming boundary layers [4] of low shear strength, either by physical or chemical adsorption on the surface of the contacting body(s) in boundary lubrication regime. A non-polar lubricant adsorbs (attaches) itself to the inactive metallic surfaces by weak Van der Waals forces. In the presence of functional groups such as acids, amines or esters, the lubricant's polar head adsorbs itself on the metallic surface while the long hydrocarbon tail forms parallel chains which shear during loading and sliding of the contacting bodies [5]. The polar functional heads in the physically-adsorbed boundary layers might further react and chemically bond with the activated metallic surfaces to form metal-hydrocarbon based chemically-adsorbed boundary layers. The boundary layers typically fail as the severity of contact increases at high contact pressure and temperature. Boundary layers have been studied using Langmuir-Blodgett (LB) films by depositing them on surfaces of metals, glass and mica as vertically adsorbed monolayers [6].

Typically, the shear strength of the lubricant boundary layer has been measured by sliding large spheres at low loads on smooth-lubricated surfaces to avoid plastic deformation. By eliminating the friction due to plastic deformation of the substrate, the shear strength of the boundary layer is given as the ratio of the measured friction force and the real area of contact. In elastic deformation, the contact area is a function of the applied load. Hence, the boundary layer shear strength is typically load-dependent. It has been shown to be directly proportional to the applied load [7], in the sliding experiments using glass spheres on LB mono- and multilayers of stearic acid and calcium stearate deposited on glass plates under a range of contact pressures [8]. The shear strength of the lubricant monolayers of fluorides and metal soaps (stearates) with long chain fatty acids, polymeric films and anthracene deposited on glass, mica and platinum [7], [8] and [9] have also shown a linear relationship with applied load, above a critical value of contact pressure. The boundary layer shear strength remains constant at low loads due to the constraining of the contact pressure by the Van der Waals attraction between the contacting surfaces and/or due to the gradual orientation of the adsorbed molecular chains along the direction of sliding under the critical contact pressure [9]. Hence, for the shear strength to increase with load, the contact pressure must exceed the energy barrier (activation energy) required to cause shear [10]. For higher contact pressures, the increase in shear strength is due to squeezing of the molecular chains and consequent hardening of the boundary layers [9]. The 'hardening' of the boundary layers has been also associated with the increase in activation

energy with contact pressure [10].

In certain lubricants like calcium carbonate in dodecane colloidal films boundary layer shear strength increased linearly within two given pressure ranges, while staying constant for the pressures in between [11]. The boundary layer shear strength has been shown to decrease exponentially with temperature in [8] and [9]. The slope of the plot of logarithmic boundary layer shear strength and temperature is the activation energy. For low loads and sliding velocities, the boundary layer shear stress has been shown to linearly decrease with temperature. Initial studies in [12] and [13] with lubricants such as stearic acid have showed an increase in the boundary layer shear strength with sliding velocity. This has been explained due to the increase in strain rate of the boundary layers with sliding velocity and its subsequent 'hardening'. However, other studies [9], [14] and [15] with lubricants such as calcium stearate have observed a decrease in boundary layer shear strength with the sliding velocity [9]. This has been explained by the visco-elastic behaviour, where the response time to an applied load, i.e. the apparent pressure felt by the boundary layer over a given time period, decreases with sliding velocity. The shear strength of boundary layers has also been shown to marginally decrease with increasing film thickness with multiple monolayers in [15] and [16]. However, since shear only occurs at the surface of boundary layers, the shear strength is often assumed to be unchanged with additional layers.

Challen and Oxley [17] have shown, using slip line field solutions, the effect of interfacial shear strength on the friction and wear behaviour of two-dimensional wedge shaped asperity. The theoretical solutions to compute friction and wear in two dimensional asperities have been extended for three dimensional spherical asperities by single-asperity sliding experiments on lubricated and unlubricated metallic contacts by Hokkirigawa and Kato [18]. The various wear regimes have been mapped in a wear mode diagram as 'ploughing', where substrate material is displaced to the sides of the track due to the sliding asperity, 'wedging', where substrate material is removed and accumulated in front of the sliding asperity and 'cutting', where substrate material is removed as chips. The increase in interfacial shear strength e.g. by absence of boundary layers in the contact can result in a transition from ploughing to wedging. The wedging wear mode results in formation of wedges of deformed substrate material stacked in front of the sliding asperity and subsequently, a possible transfer of the stacked substrate material to the surface of the asperity due to high adhesive forces. The slip-line field theory has also been used to study the influence of pressure and boundary layer shear strength for rigid cylindrical asperities ploughing through a soft substrate in [19].

Friction and wear in boundary lubrication regime have been modelled using particle-based, molecular dynamics (MD) simulations for rough surfaces in contact during loading and sliding [20, 21, 22, 23]. The effect of applied load, lubricant amount and chain length of molecules for different long chain-alkanes on friction has been studied in [22] for boundary lubrication, while their effect on contact area has been studied in [20] for different lubricated conditions. Polarisable lubricant such as polyethylene oxide polymer has been shown in [21] to form films in the contact between charged, oxidised metallic surfaces, thereby preventing direct asperity contact and reducing friction force. Recently, MD simulation has also been used to investigate the reduction in friction and wear in water lubricated contact between inert polymers and metals compared to dry contact in [23]. While MD simulations of boundary layers has been helpful in understanding of friction mechanisms in boundary lubrication at an atomistic scale, the up-scaling of the MD results can be challenging.

So far the characterization of boundary layer shear strength has been done for long chain fatty acid based lubricants on smooth glass and mica substrates. The boundary layer shear strength for mineral oils on metallic substrates has been determined for aluminium and gold coated glass and steel in [24], [25] and [26] respectively. Moreover, the effect of boundary layer shear strength on ploughing friction has not been investigated using numerically models so far. Most manufacturing systems use coated metallic tools and workpiece, working in the boundary lubrication regime where the shearing of boundary layers occurs under varying operating conditions. The presence of a coated system adds to the complexity of deformation behaviour of the substrate in measuring boundary layer shear strength. Furthermore, the use of large spherical balls to characterize the boundary layer shear strength also poses challenges in designing the required experimental set up.

Hence, the research has focussed on characterizing the boundary layer shear strength of both lubricated and unlubricated zinc coated and uncoated steel sheets under varying loads and sliding velocities using an in-house developed experimental set up. The effect of interfacial shear strength in overall friction and wear modes of a single-asperity ploughing through metallic substrate is investigated by the material point method (MPM)-based numerical ploughing model developed by [27]. The MPM model [27] is used to investigate the effect of the interfacial shear strength on the ploughing behaviour of a single asperity sliding through a steel substrate. By incorporating experimentally determined relationships for the interfacial shear strength in the ploughing model, the numerical results have been validated and are found to be in good agreement with the ploughing experiments using spherical tip pins.

2 Calculation of friction due to interfacial shear strength

The current section elaborates on the theory behind calculation of the interfacial shear strength τ and the contact area A_c whose product results in the interfacial friction force $F_{sh} = \tau A_c$. The section also introduces on an algorithm to calculate the contact area in loading of a roller on a zinc-coated steel sheet.

2.1 Calculation of interfacial shear strength

The activation energy based Eyring model describes boundary layer shear with discrete movement (dislocation) of a small number of molecules [10]. The dislocation movement is resisted by the neighbouring molecules due to a potential barrier, which must be overcome with shear and/or thermal stresses. The height of the barrier increases linearly with applied pressure as shown schematically in figure 1. Figure 1 describes the energy of the potential barrier Q affected by pressure P and shear stress τ. The average time reciprocal, $1/t^{'}$ to overcome this barrier, for a mobile unit of molecules, is the product of their effective vibration frequency ν and the Boltzmann factor, $\exp(-E/kT)$ as given in equation 1.1. Here E is the height of the energy barrier, k is the Boltzmann constant and T is the temperature. Chugg and Chaudri [28] have expressed (equation 1.1) the average time reciprocal as the shear rate $\dot{\gamma}$ and the effective vibration frequency as AkT where constant A is $\sim 5 \times 10^{32}/Js$. The Boltzmann factor shows the probability of a system being in a state with energy E, where E/kT is the entropy per molecule. Here $E = Q + P\Omega - \tau\Phi$ is the height of the barrier, kT is the heat required for increasing thermodynamic entropy of system. In macroscopic system with large number of molecules, RT is used instead of kT with units J/mol (R is the gas constant).

In equation 1.1, Ω and Φ are used for dimension correction with units of volume in the order of $0.1 - 1nm^3$. Ω can be physically interpreted as the pressure activation volume, causing a local increase in volume at a given lattice, permitting molecular motion. Physically, Φ is the stress activation volume, which is the change in molecular/dislocation volume due to unit shear. The energy barriers are periodically separated by a distance c with allowable transition in both directions. Taking the ratio of the sliding velocity v and a reference sliding velocity v_0 equal to the ratio of the average molecular velocity $u = c_0/t^{'}$and u_0 which is the product of molecular vibration frequency $\omega_0 = 10^{11}/s$ and lattice constant $c_0 = 0.2nm$, equation 1.2 is written as equation 1.3. In equation 1.3, we approximate $2\sinh\tau\Phi/kT \approx \exp\tau\Phi/kT$ taking $\tau\Phi/kT > 1$ for low temperatures. The shear stress τ is then expressed in equation 1.4 as a function of P, T and v where the values of Q, Φ and Ωcan be obtained using experiments with given values of v, P and T for various lubricant monolayers [9]. At high temperatures, $(\tau\Phi/kT < 1)$, we approximate $\sinh\tau\Phi/kT \approx \tau\Phi/kT$ by expanding power series of hyperbolic sine and neglecting its higher order terms. The values of Q, Ω, Φ and v/v_0 range between 1-100 kJ/mol, 0.01-1 nm^3, 1-10 nm^3 and 10^{-6}- 10^{-4} respectively for long chain hydrocarbon based lubricants [9]. Hence, the value of $vkT/v_0\Phi$ doesn't vary largely with temperature and remains nearly constant. Rearranging terms in equation 1.2 and 1.3 would lead to an exponential temperature dependence of the shear strength as shown in equation 1.5 [9].

$$\frac{1}{t'} = \omega_0 \exp\left\{-\frac{Q + P\Omega - \tau\Phi}{kT}\right\} \tag{1.1}$$

$$u = 2u_0 \exp\left(-\frac{Q + P\Omega}{\mathrm{kT}}\right) \sinh\frac{\tau\Phi}{\mathrm{kT}} \tag{1.2}$$

$$v = v_0 \exp\left\{-\frac{Q + P\Omega - \tau\Phi}{\mathrm{kT}}\right\} \tag{1.3}$$

$$\tau = \frac{kT}{\Phi}\ln\frac{v}{v_0} + \frac{Q + P\Omega}{\Phi} \tag{1.4}$$

$$\tau = \frac{kT}{\Phi}\frac{v}{v_0}\exp\left(\frac{Q + \Omega P}{\mathrm{kT}}\right) \tag{1.5}$$

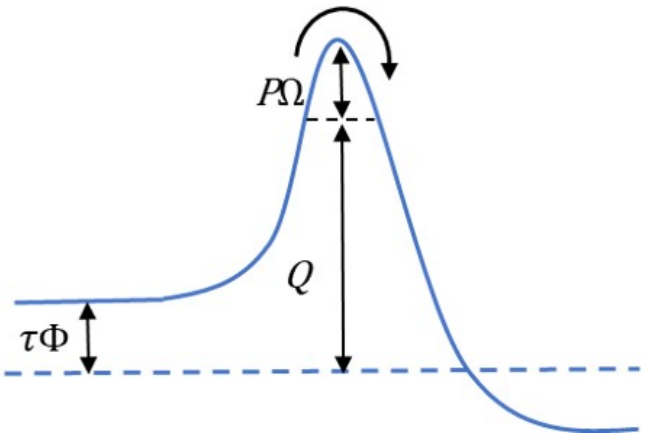

Figure 1: Energy barrier for dislocation movement during shearing of a boundary layer [10].

Based on the observations and fitting of experimental data, empirical linear-relationships between boundary layer shear strength and contact pressure, temperature and logarithmic sliding velocity have been proposed as shown in equation 2.1, 2.2 and 2.3 respectively [9], [29].

In the work of Briscoe and Evans [9] and Chugg and Chaudri [28], the expressions of shear stress obtained from the Eyring model (equation 1.4) have been compared with the empirical relations in equations 2.1-2.3 to obtain the values of intrinsic shear strength τ_0, τ_1 and τ_2 and the proportionality constants $\alpha,\ \beta$ and ψ in equation 2.4 [9].

$$\tau = \tau_0 + \alpha P \tag{2.1}$$

$$\tau = \tau_1 - \beta T \tag{2.2}$$

$$\tau = \tau_2 + \psi \ln v \tag{2.3}$$

$$where, \tau_0 = \frac{kT \ln \frac{v}{v_0} + Q}{\Phi}, \alpha = \frac{\Omega}{\Phi}, \tau_1 = \frac{Q + P\Omega}{\Phi}, \beta = \frac{k}{\Phi} \ln \frac{v}{v_0}, \tau_2 = \frac{Q + P\Omega - kT \ln v_0}{\Phi}, \psi = \frac{kT}{\Phi} [9] \tag{2.4}$$

$$\tau_0 = K \exp\left(-\frac{Q^{'}}{RT}\right), K = \tau_0^{'} \ln\left(\frac{v}{h\varphi}\right) and\ \alpha = n_0 \exp\left(-\frac{v}{a\theta}\right) [15] \tag{2.5}$$

Earlier work of Briscoe and Tabor [15] have shown the shear strength of organic and polymeric films to decrease exponentially with temperature as given in equation 2.5 taking gas constant R and activation energy $Q^{'}$. Further, under isothermal and isobaric conditions, the shear strength is given to increase with increase in strain rate of the boundary layer (of thickness h) i.e. v/h. Hence the intrinsic shear strength term τ_0, which is independent of contact pressure, can be expressed as a function of strain rate (sliding velocity) and temperature. However, the boundary layer shear strength for some lubricants have been shown to decrease with increase in sliding velocity v. The increase in v reduces the mean contact time $t_c = v/2a$ for compression of the boundary layer. Here, a is the contact radius. This effect, termed as 'visco-elastic retardation in compression' [15], reduces the response time of the boundary layer to applied pressure, thereby reducing α. Equation 2.5 corrects the value of α taking the 'visco-elastic' effect into account [15].

The characteristic frequencies φ and θ in equation 2.5 corresponds to high strain rate and low strain rate processes respectively [15]. Hence the 'strain rate effect' dominates the boundary layer shear strength at high sliding velocity while the viscoelastic effect dominates boundary layer shear strength at reduced sliding velocity. The 'strain rate term' K corresponds to shear strength at high sliding velocity and varies between 0 to $\tau_0^{'}$ for velocities ranging from $(v_k,\ ev_k)$ where $v_k = h\varphi$ and $e \cong 2.72$. Similarly, the visco-elastic term $\alpha = \alpha_0$ corresponds to shear strength at low sliding velocity and varies between n_0 to 0 for velocity ranging between $(0,\ \infty)$. It can be seen that for high sliding velocity, the 'visco-elastic' term diminishes while for low sliding velocity the 'strain rate term' diminishes.

Based on experimental data from [8] and [9] it has been observed that for large pressure ranges, the boundary layer shear strength doesn't vary linearly with contact pressure. Hence a more general power-law relationship between shear strength and contact pressure can be used for fitting the experimental data. Similarly, by taking positive and negative exponents in the power-law relationship between shear strength and sliding velocity the effect of visco-elastic retardation due to compression and strain rate can be accounted for. Taking these observations into account, Westeneng [30] proposed a power law relationship between τ-P and τ-v, where D and G are proportionality constants and p and q are exponents. The exponential relation between τ and T is used in equation 3.3, where $\tau_0^{''}$ is a constant. Assuming the shear stress in equations 3.1, 3.2 and 3.3 to be independent of each other and taking the natural logarithm of

τ in all the equations, the logarithmic τ is combined to obtain equation 3.4.

$$\tau = DP^p \Longrightarrow \ln\tau \ = \ln D \ + p\ln P \tag{3.1}$$

$$\tau = Gv^q \Longrightarrow \ln\tau \ = \ln E \ + q\ln v \tag{3.2}$$

$$\tau = \tau_0^{''} \exp\frac{Q^{'}}{RT} \ \Longrightarrow \ln\tau \ = \ln\tau_0^{''} \ + \frac{Q^{'}}{RT} \tag{3.3}$$

$$\ln\tau \ = F + \frac{Q^{'}}{RT} + p\ln P \tag{3.4}$$

In equation 3.4, F can be taken as equivalent to the parameter K in equation 2.5 which is influenced by the 'strain rate' effect of sliding velocity v. Similarly p can be taken as equivalent to the parameter α in equation 2.5 which is influenced by the 'visco-elastic' effect of the sliding velocity v. Expanding the expressions for F and p, logarithmic shear stress is expressed in equation 4.1. Taking $Q^{'}/R$ as n_T, α as n_p, τ_0 as n_v and $-\tau_0 \ln h\varphi$ combined with other constants as $K^{'}$ in equation 4.2, boundary layer shear strength is given as a function of contact pressure, sliding velocity and temperature in equation 4.3.

$$\ln\tau \ = \tau_0^{'} \ln\frac{v}{h\varphi} \ + \frac{Q^{'}}{RT} + n_0 \exp\left(-\frac{v}{a\theta}\right) \ln P \tag{4.1}$$

$$\ln\tau \ = n_v \ln v \ + \frac{n_T}{T} + n_p \ln P \ + K^{'} \tag{4.2}$$

$$\tau\,(P,\ T,\ v) = CP^{n_p} v^{n_v} \exp\frac{n_T}{T} \tag{4.3}$$

In order to measure the interfacial shear strength, experiments can be done where the shear strength will be calculated from the measured friction force and calculated contact area. The details about the procedure for calculation of contact area are explained in section 2.2 below.

2.2 Calculation of contact area and contact pressure for a coated line contact

The contact width b for a cylinder of radius r and length l pressing into an uncoated flat surface is given in equation 5.1 in terms of its normal load F_n and effective modulus of elasticity E^* for the substrate and the tool. In order to improve friction and wear behaviour, materials can be coated with surface layers. The effective elastic modulus E^* in then defined by the Young's modulus and the Poisson's ratio of the coated system E_{cs} and ν_{cs}, and of the indenter E_{in} and ν_{in} as given in equation 5.2. The effective Young's modulus E_{cs} for a multilayered system with the substrate 's' covered with n number of layers is given in equation 5.3, see [31] and [32]. Equation 5.3 uses influence factors I_0 and I_1, given in equation 5.4 and 5.5 respectively with $i = 1$ as the bottom layer and $i = n$ as the top layer. The relative depth of the layer i $\bar{t}_i$ in equation 5.6 is the ratio of the total layer thickness up to layer i $(t_1,\ t_2, \ldots t_i)$ and the contact radius a. The average Poisson's ratio $\overline{\nu}$ of all the layers is given in equation 5.7.

The equations to estimate the effective modulus of a coated system is based on spherical indentation of the multi-layered substrate. The influence factors I_0 and I_1 are functions of the contact width (radius for point contact) a used in the expression of $\bar{t}_i$. The contact width is typically computed from the effective elastic modulus as shown in equation 5.1.

In order to compute the contact width in a line contact for the case of a cylindrical roller in contact with a flat surface, using the effective elastic modulus of the coated system, an initial

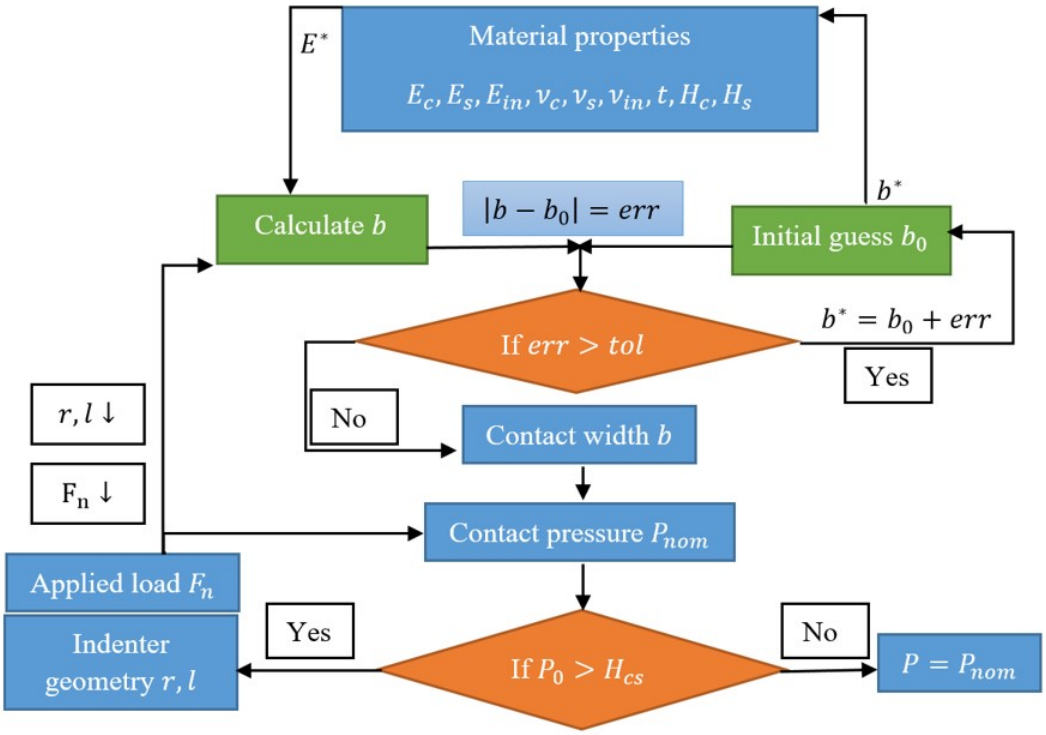

Figure 2: Flow chart to calculate contact width and nominal contact pressure in coated systems.

guess for the contact width b_0, is used to calculate the line contact width b. The calculated contact width b is then corrected by adding the difference $|b - b_0|$ to b_0 and using the new value of contact width b^* to recalculate b. The steps are iterated until the difference $|b - b_0|$ is minimized below a given tolerance as shown by the algorithm in figure 2. The algorithm calculates the line contact area for a single layer of (hot dip galvanized) zinc-coated steel sheet using the effective Young's modulus E_{cs} computed by the equation 5.8, deduced from equation 5.3 for $n = 1$ and $\nu_s = \nu_c$.

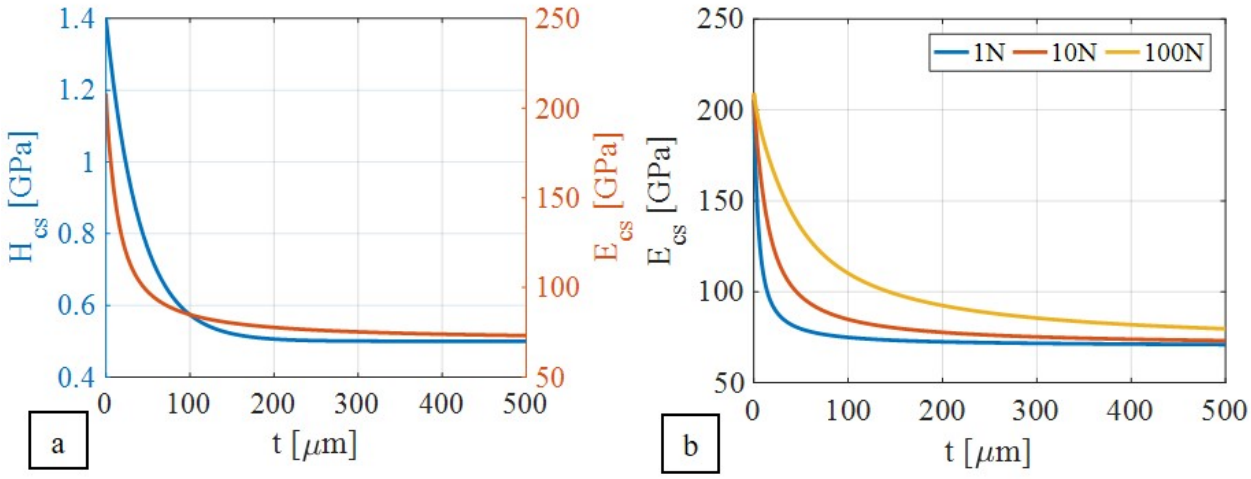

Figure 3: (a) The effect of coating thickness t on effective hardness H_{cs} and Young's modulus E_{cs} of a coated system and (b) the effect of applied load on E_{cs} obtained using equation 5.8 and equation 6.1 and material data from table 1 ($H_c = 0.5GPa,\ H_s = 1.4GPa,\ E_c = 70GPa,\ E_s = 210GPa$).

The mean nominal contact pressure, for a Hertzian line contact, is calculated using equation 6.2 from the normal load F_n and the Hertzain contact area $A_c = 2bl$ where b is the contact half width and l is the contact length. The maximum nominal contact pressure $P_0 = 4P_{nom}/\pi$ should be maintained below the yield stress of the substrate sheet to avoid any plastic deformation [12]. The yield strength for perfectly plastically deforming substrate can be approximated by $\sigma_y = H_{cs}/2.8$ as per [33]. The effective hardness H_{cs} of the coated system is given based on the experimental fit relations by [34] and [35]. For a soft zinc coating of thickness t on a hard steel substrate the H_{cs} is expressed in equation 6.1. The applied loads should be chosen such that $P_0 < \sigma_y$.

$$b = \sqrt{\frac{4F_n r}{\pi l E^*}} \tag{5.1}$$

$$\frac{1}{E^*} = \frac{1-\nu_{cs}^2}{E_{cs}} + \frac{1-\ \nu_{in}^2}{E_{in}} \tag{5.2}$$

$$\frac{1-\nu_{cs}^2}{E_{cs}} = \frac{\left(1-\nu_s-\sum_{i=1}^{n-1} I_1\left(\nu_i-\nu_{i+1}\right)-I_1\left(\nu_n-\nu_s\right)\right)}{\frac{E_s}{1+\nu_s}+\sum_{i=1}^{n-1} I_0\left(\frac{E_i}{1+\nu_i}-\frac{E_{i+1}}{1+\nu_{i+1}}\right)+I_0\left(\frac{E_n}{1+\nu_n}-\frac{E_s}{1+\nu_s}\right)} \tag{5.3}$$

$$I_0 = \frac{2}{\pi}\arctan\bar{t}_{\ i} + \frac{\left((1-2\overline{\nu})\,\bar{t}_i \ln\left(\frac{1+\bar{t}_i^2}{\bar{t}_i^2}\right)\ +\frac{\bar{t}_i}{1+\bar{t}_i^2}\right)}{2\pi(1-\overline{\nu})} \tag{5.4}$$

$$I_1 = \frac{2}{\pi}\arctan\bar{t}_i\ + \frac{\bar{t}_i}{\pi}\ln\left(\frac{1+\bar{t}_i^2}{\bar{t}_i^2}\right) \tag{5.5}$$

$$\bar{t}_i = \sum_{k=1}^{i}\frac{t_k}{b} \tag{5.6}$$

$$\overline{\nu} = \frac{1}{n}\sum_{i=1}^{n}\nu_i \tag{5.7}$$

$$E_{cs} = E_s + (E_c - E_s)I_0/, \forall n = 1,\ \nu_s = v_c \tag{5.8}$$

$$E_{cs} = E_s + (E_c - E_s)I_0/, \forall n = 1,\ \nu_s = v_c \tag{5.9}$$

Figure 3a shows the variations in effective hardness and Young's modulus of the zinc coated steel sheet with the coating thickness that is calculated using equation 5.8 and equation 6 and material data from table 1. The indentation hardness of the bulk zinc, zinc coating and the steel sheets were measured Berkovich indenters at 100mN load. Both the hardness and Young's modulus of the zinc coated steel sheet decrease with increase in coating thickness from that of the steel substrate to that of the zinc coating. The effective hardness of the coated system is independent of the applied load. However, the effective Young's modulus of the coated system increasingly approaches towards the Young's modulus of zinc with increase in coating thickness for lower applied loads. For high loads the Young's modulus of the stiffer substrate's dominates the effective Young's modulus. The effective Young's modulus E_{cs} ranges between 92.5-135.1 GPa and the effective hardness H_{cs} is 1.046 GPa is obtained from equation 5.8 and 6.1 for the given zinc coating thickness of $20\mu m$ and applied load of 1 to 16N.

$$H_{cs} = H_s + (H_s - H_c)\exp\left(-125\frac{t}{r}\right) \tag{6.1}$$

$$\overline{P}_{nom} = \frac{N}{A_c} = \frac{N}{2bl} \tag{6.2}$$

3 Experimental method

This section describes the design of the experimental set up for determining the boundary layer shear strength. The preparation of the sheets specific to characterize the boundary layer shear strength and ploughing experiments have been explained. The experimental set-up has also been elaborated.

3.1 Design of experiments

The friction in sliding of a rigid asperity through a soft substrate is attributed to the resistance to plastic deformation of the substrate and the shearing of the interface. The key to experimentally characterize the interfacial shear strength is to eliminate the component of friction due to plastic deformation of the sheet. Hence, the measured friction solely results from shearing of the interface. Typically, large glass spheres have been slid on smooth (glass, mica, metal coated) surfaces in experiments pertaining to characterize the boundary layer shear strength [8]. Since a line contact distributes the load over a larger contact area compared to a point contact using pins of similar dimensions, it is easier to limit the generated nominal contact pressures below the yield stress of the sheet. This helps to avoid any macro-scale plastic deformation of the substrate. Hence, the curved surface of a hard cylindrical roller pin is slid against a soft, flat sheet in a lubricated line contact to characterize the interfacial shear strength.

Further, flattening and polishing of the substrate (sheet) is done to maximize the real contact area, avoid unwanted friction and formation of wear particles due to asperity interlocking. However, at the micro-scale, the local pressure on the asperities in the line contact exceeds the yield point. To prevent the local plastic deformation of the asperities and optimize the conformity of contact, multiple traverses are performed on the sliding track until a steady state friction is obtained. During the initial sliding traverses, the harder asperities on the pin tool plastically deforms the surface of the polished sheet during the 'running-in' phase. During the subsequent traverses, repeated re-loading and unloading of the sheet results in metal work hardening of the sheet surface thereby increasing its yield strength. As the surface of the sheet work hardens, the surface of the sheet deforms elastically during sliding and a 'steady state' friction is reached. The friction measured in the 'steady-state' is predominantly due to shearing of the boundary layers. Subsequently lower applied loads are applied during sliding of the roller.

The pressure distribution under the cylindrical roller is determined by the shape of the roller and its surface roughness. The discontinuity in contact at the edge of the cylindrical roller results in high stress concentration. The roller acts like a punch along the length of its contact with the sheet. The stress concentration at edges combined with bending of the sheet localizes the roller-sheet contact and results in ploughing instead of shearing on the sheet surface. Typically, the edges of cylindrical rollers are crowned with different geometries to avoid the punching (edge) effect leading to stress concentration at the edges. In the experiments for the current study, the cylindrical roller has been provided with a logarithmic crowned profile towards the edges [36].

3.2 Preparation of experimental specimen

Mirror polishing of rough DX46 steel sheets, shown in figure 4a, with roughness of 1.24 μm was done. For mirror-polishing, the sheets are laser cut into 46 mm diameter circles and mounted on bakelite discs of 50 mm diameter either by hot mounting or by using the Loctite industrial

glue. Using an automatic lapping/polishing machine, initial coarse grinding of the mounted sheet specimens is performed with 320 ($46\mu m$ size) grade sandpaper under 30N load to remove any unevenness. The specimens are then fine-polished using diamond suspension of different particle sizes on metal disc in 3 steps, each lasting for 3 minutes under a load of 30N. The size of the diamond particles at each step is reduced from $9\mu m$ to $3\mu m$ to $1\mu m$. Finally, an OPS (oxide polishing suspension) with $0.04\mu m$ grain size is used to obtain a scratch free surface. A final mean surface roughness of 6-8 nm is obtained and the sheet is degreased using ethanol. The polished sheet is shown in figure 4b with a clear view of its grain boundaries.

Figure 4: Surface of mounted sheet before (a) polishing R_a= 1.24 μm (b) after mirror polishing R_a= 0.006μm and (c) shine polishing R_a= 0.028μm seen under confocal microscope at 50x magnification.

A set of sheet specimens with substrate roughness of 20-30 nm, shown in figure 4c, were also prepared by 'shine polishing', where the final polishing steps of $3\mu m$, $1\mu m$ size diamonds suspension and OPS in 'mirror polishing' were skipped. The polished sheet specimen was degreased and stored at room temperature for 1000 hours to allow formation of a stable oxide film on the surface. The presence of an oxide film and higher surface roughness of the specimens helped prevent material transfer to the surface of the pin during characterization of the interfacial shear strength of unlubricated steel sheets. The fresh, mirror polished specimen with surface roughness of 6-8 nm had higher possibility of material transfer due to the high interfacial shear strength resulting from direct contact between the metallic asperities.

3.3 Experimental set up

The shear experiments on DX56 steel sheet lubricated with 2 different lubricants were done using the linear friction tester, shown in figure 5, with 3 repetitions. The linear friction tester consists of a XY linear positioning stage driven separately by actuators as shown in figure 5c. A horizontal beam supports the loading tip and moves the Z-stage using a linear and piezo actuator for coarse and fine displacement respectively while applying a normal load. The normal load is applied using a force controlled piezo actuator, connected to a PID control loop feedback system so the system can operate load controlled. The friction forces are measured by a piezo sensor along the loading tip as shown in figure 5b. An example of the friction signal divided by the normal load, the coefficient of friction, is shown as a function of the sliding distance in figure 9a.

A cylindrical roller of diameter 10mm and length 10mm is mounted on a self-aligning pin as shown in figure 5b and 5c. The pin holder consists of a joint which allows for rotation of the roller in the axis along the sliding direction such that proper alignment of the roller over a slightly titled surface results in a continuous line contact. Different loads were applied on these

Table 1: Material parameters

Parameters	Substrate	Coating	Tool/Pin
Geometry	Circular sheet of thickness 1mm and diameter 50mm		Logarithmic crowned cylindrical roller
Radius at the centre of roller r	-		5 mm
Uncrowned/contact length of roller l	-		5 mm
Total length of roller	-		10 mm
Material	DX56 steel	Zinc coated /galvanized steel	AISI 52100 bearing steel
Coating thickness t	uncoated	20 μm	uncoated
Mean surface roughness R_a	8 nm	10 nm	100 nm
Young's modulus, E	210 GPa	70 GPa [37]	210 GPa
Hardness of sheet H	1.4 GPa	0.5 GPa [38]	8.2 GPa
Poisson's ratio ν	0.3	0.3	0.3
Lubricant A	Viscosity: η_{40^0C}	Lubricant B	Viscosity: η_{40^0C}
Quaker FERROCOAT N6130	23 mPas	Fuchs Anticorit PLS100T	90 mPas

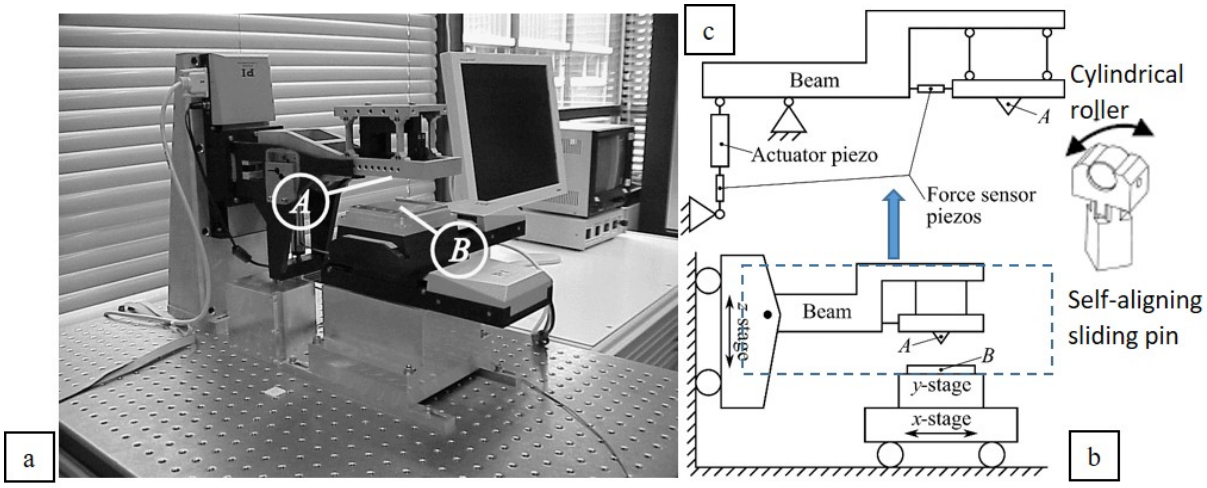

Figure 5: (a) Linear friction tester for boundary shear characterization and ploughing experiments with (b) its (figure 5a) schematic showing substrate specimen (B), (c) the loading set-up and sliding tool (A).

rollers to perform load controlled shear experiments. The plots for forces on the roller pin were obtained from the linear sliding tester and the average coefficient of friction for the steady state was obtained for all applied loads. The wear track was studied under both optical and confocal microscopes to measure the contact area on the wear track. The applied loads for characterizing the interfacial shear strength were 1, 2, 4, 7, 11 and 16 N.

4 Computational method

The ploughing of asperities in the substrate is modelled using material point method (MPM) which has been introduced and implemented in Mishra et al. in [27]. The MPM-based ploughing simulation models the MPM particles in the substrate using the 'mpm-linear pair style' code which has been further explained in [27]. The indenter/asperity has been modelled using triangular mesh as an STL file with no self-interaction. The asperity interacts with the substrate using contact algorithm defined in the 'tri-smd-pair style' code [27] which includes the contact and friction algorithm between the triangular mesh and MPM particles. The friction algorithm computes the contact area and the overall friction using the interfacial shear strength which will be measured in section 5.2. Figure 6 shows the MPM-ploughing model set up.

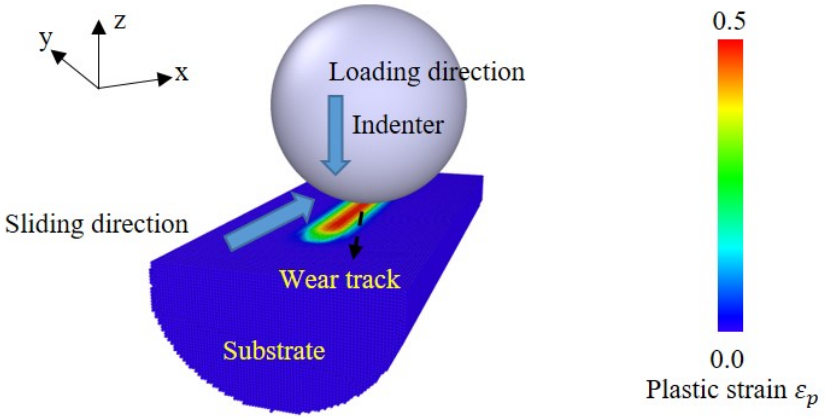

Figure 6: MPM simulation of an spherical indenter (asperity) with radius 0.1 mm ploughing through a substrate along sliding x-direction with equivalent plastic strain being shown.

Table 2: Material parameters for DX56 steel substrate in MPM model.

Parameters	Symbol	Values/ expression
Substrate and indenter material density	ρ	7900 kg/m^3
Substrate and indenter specific heat capacity	c_p	502 J/(kg K)
Substrate and indenter thermal conductivity	κ	502 W/(m K)
Young's Modulus of substrate	E	210 GPa
Poisson's ratio of the substrate	ν	0.3
Ambient temperature	T_{room}	294 K

The flow stress is computed from the physically based isothermal Bergström van Liempt hardening relation [39]. The relation was modified by Vegter for sheet metal forming processes [40], leading to the following formulation where the flow stress σ_y^{BL} is decomposed into a static-work/strain hardening stress σ_{wh} and dynamic stress σ_{dyn} which takes into account the strain-rate and the thermal effects as shown in equation 7.1. This flow stress model has been included in the current MPM numerical set up to account for the interaction processes between dislocations in cell structures including the changing shape of dislocation structures. The Bergström van Liempt material model constants are listed in table 3 with their characteristic values obtained for the DX56 steel sheet [27]. The model parameters ε, $\dot{\varepsilon}$ and T represent the strain, strain rate and working temperature respectively.

Table 3: Bergström-van Liempt material model parameters for DX56 steel [27].

Parameters	Symbols	Value
Initial static stress	σ_{f0}	82.988 MPa
Stress increment parameter	$\mathrm{d}\sigma_{\mathrm{m}}$	279.436 MPa
Linear hardening parameter	β	0.482
Remobilization parameter	ω	6.690
Strain hardening exponent	c	0.5
Initial strain	ε_0	0.005
Initial strain rate	$\dot{\varepsilon}_0$	$10^8 s^{-1}$
Maximum dynamic stress	σ_{v0}	1000 MPa
Dynamic stress power	m	3.182
Activation energy	$\Delta \mathrm{G}_0$	0.8
Boltzmann's constant	k	8.617×10^{-5} eV

A power-law expression for boundary-layer shear stress as a function of the nominal pressure P_c, sliding velocity v_s and the contact temperature T_c has been implemented in the triangles-particles interaction pair style following from equation 4.3, as given in equation 7.2 [27].

$$\begin{aligned}\sigma_y^{\mathrm{BL}} &= \sigma_{wh} + \sigma_{dyn} \\ &= \sigma_{f0} + d\sigma_m \left(\beta \left(\varepsilon + \varepsilon_0\right) + \left\{1 - \exp\left[-\omega \left(\varepsilon + \varepsilon_0\right)\right] \right\}^c\right) + \sigma_{v0}\left(1 + \frac{kT}{\Delta G_0}\ln\frac{\dot{\varepsilon}}{\dot{\varepsilon}_0}\right)^m \end{aligned} \tag{7.1}$$

$$\tau = C_p P_c^{n_p} C_v v_s^{n_v} C_T \exp - \frac{n_T}{T_c} \; = C P_c^{n_p} v_s^{n_v} \exp - \frac{n_T}{T_c} \tag{7.2}$$

where C_p is the pressure constant, C_v is the velocity constant, n_p is the pressure exponent, n_v is the velocity exponent and n_T is the temperature exponent. The constant term C the product of C_p, C_p and C_T. The C's and n's are experimentally fitting factors. The contact pressure for experiments is taken as the nominal contact pressure $P_{nom} = F_n/A_c$. In the MPM model, contact pressure is obtained between each indenter's triangular mesh in contact with the MPM particle of the sheet. The coefficients and exponents in the equation 7.2 can be arranged to reduce the expression to the Coulomb friction law. In equation 7.2, the contact temperature is obtained from the simulations for sliding as the wall temperature of indenter T_c. The relative tangential velocity of the indenter's triangle with respect to the MPM particle in contact v_{tan}, is taken locally as v_s. The coefficients C_p and C_v and exponents n_p, n_v and n_T can be obtained through experiments in a linear sliding friction experiments by varying the contact pressure, sliding velocity and temperature.

5 Results and discussion

The interfacial shear strength of both lubricated and unlubricated, zinc coated and uncoated steel sheet have been determined by the experimental method, discussed in this section. The subscripts UL and QL correspond to unlubricated (no lubricant applied on the shine polished sheet) and Quaker lubricated sheets while the superscripts MP and SP correspond to mirror polished and shine polished sheets (specimen preparation explained in section 3.2) respectively. Firstly, the contact area in the line contact has been calculated for varying loads based on the model discussed in section 2.2. Using the calculated contact area, the interfacial shear strength has been measured for the range of applied loads and sliding velocities and expressed

as empirical equations. The equations have been implemented in the MPM-based numerical model described in section 4. Further, the effect of interfacial shear strength on the friction forces and wear mode in the sliding of the asperity/indenter is highlighted using results from MPM-based ploughing simulation.

5.1 Calculation of contact area and contact pressure

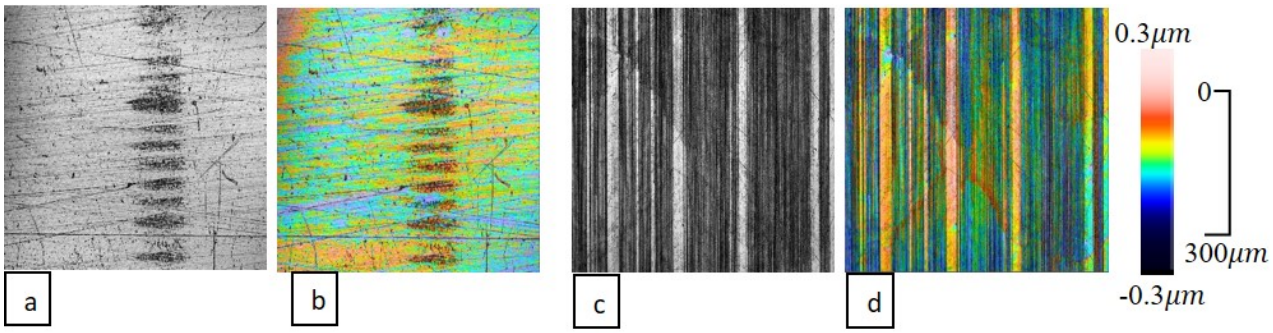

Figure 7: (a) Surface of the cylindrical pin, (b) its surface height profile ($R_a = 0.016\mu m$) (c) surface of the sheet ($R_a = 0.073\mu m$) after sliding experiments and (d) its surface height profile. Length scale and colour bar for surface heights are shown on the right side for all the images.

The sliding of the cylindrical pin on the lubricated, mirror polished sheet surface at an applied load of 16N increases its roughness from 6 nm to 93nm as shown in figure 7b and 7d. As the asperities on the surface of the pin slide (plough) through the polished sheet, there is transfer of roughness from the pin to the surface of the smooth sheet. Now, with increased conformity between the contacting surfaces, the boundary shear characterization experiments are performed on the same wear track with lower applied loads. On the other hands, the surface of the pin remains unchanged for most lubricated experiments. However, there is transfer of material from sheet to tool due to galling/adhesive wear for some unlubricated experiments on steel and lubricated experiments on zinc coated steel specimen at high loads as shown in figure 7a. Results pertaining to experiments with material transfer are avoided in calculation of boundary layer shear strength.

Table 4: Contact width and contact pressure for line contact on zinc coating

Load (N)	Contact width b (Analytical) (μm)	Contact width b (FEA) (μm)	Nominal contact pressure (Analytical) P_{nom} (MPa)
1	8.44	11.8	23.7
2	11.68	13	34.4
4	16.01	17.2	30.3
7	20.40	23	68.3
11	25.32	28.8	87.3
16	30.02	34.2	106.7

The apparent contact width and the nominal contact pressure for the coated system are calculated from the algorithm in figure 2, and validated against a finite element model (MSC Marc) as listed in table 4. An element size of 0.2 μm is taken in the FE model for line

contact. Both the analytical model and the finite element model give good agreement in calculation of Hertzian line contact and hence contact pressure for coated systems. For lower loads the finite element method requires a very fine mesh resolution to give an accurate line contact width. The layer hardness of 800.141 MPa with a standard deviation of 18.788 MPa is obtained for the zinc coating using Berkovich indentation at 100mN load.

5.2 Calculation of boundary layer shear strength

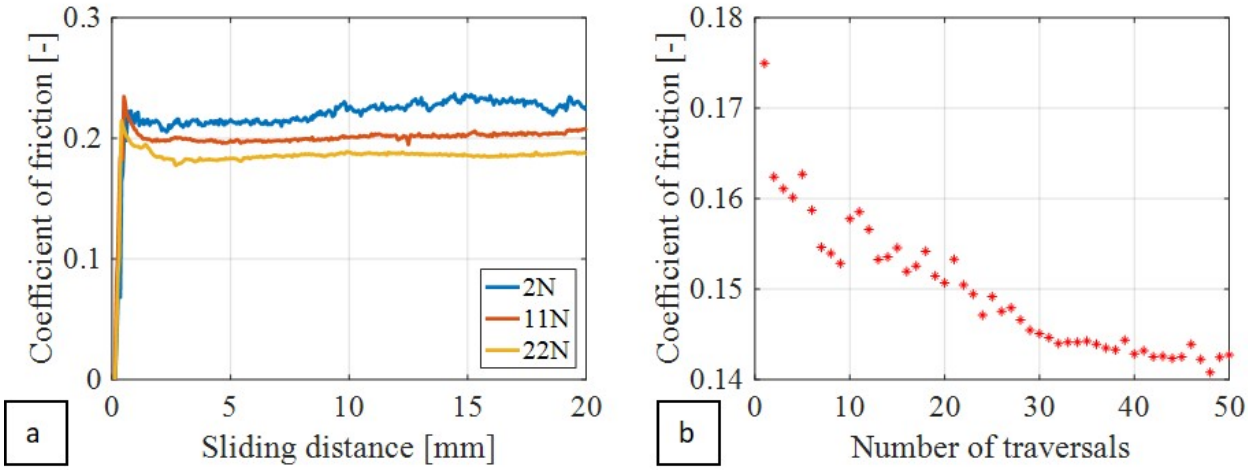

Figure 8: (a). Friction measurements with the linear sliding friction tester for various normal loads F_n= 2, 11 and 22N. (b) Coefficient of friction with each traverse and running-in of the sheet to obtain friction due to boundary layer shear at 16 N load.

The coefficient of friction vs sliding distance plots, obtained for different loads, are given in figure 8a. The mean friction force is calculated over a sliding length of 14mm after the first 3mm of sliding for a total sliding distance of 20mm. The coefficient of friction due to shearing of the boundary layer decreases with increasing load. The steady state friction force is obtained after multiple traverses as shown in the steadying of the average coefficient of friction after initial decline due to running-in with each traverse in figure 8b. The mean steady state friction forces measured from the sliding experiments are divided by the computed Hertzian contact area to obtain the boundary layer shear strength.

The mean coefficient of friction for the shear experiments are plotted against various sliding velocities in figure 9. It can be seen that the boundary layer shear strength is not greatly affected by the change in sliding velocity v. The boundary layer shear strength τ, for the Quaker lubricant marginally increases with sliding velocity while that for the Anticorit lubricant marginally decreases with sliding velocity, as shown in figure 9a and 9b respectively. For experiments done with Quaker lubricant, the effect of shear strain rate, i.e. $\dot{\gamma} = dv/dt$ for boundary layer thickness t seems to dominate, as a result of which τ increases with v. For experiments done with Anticorit lubricant, the visco-elastic effect seems to dominate, where the effect contact pressure $\overline{P} \propto P/exp(v/a)$ in response to application to normal stress (contact radius a) reduces with v as a result of which τ decreases with v [15]. The relationship between the interfacial shear strength and sliding velocity is given in equation 8.1 and 8.2 for both the lubricants. The experiments were done at constant load of 7N and at room temperature.

Corresponding to equations 4.3 and 7.2, $n_p = 0$ and $n_T = 0$ are taken for equations 8.1 and 8.2.

$$\tau_I^Q = 13.13 \times 10^7 v^{0.018} \tag{8.1}$$

$$\tau_I^A = 9.32 \times 10^6 v^{-0.053} \tag{8.2}$$

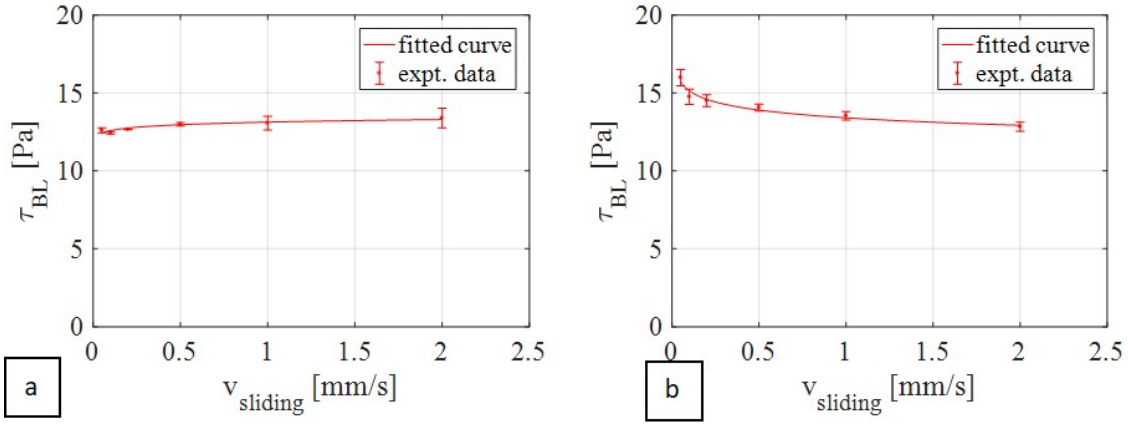

Figure 9: Variation of boundary layer shear strength with nominal contact pressure at a sliding velocity of $1mm/s$ for (a) Quaker Ferrocoat N136, (b) Fuchs Anticorit PLS100T lubricated (c) unlubricated DX56 sheet and (d) their comparison.

The characterization of boundary layer shear strength for 'Quaker Ferrocoat N136' and 'Fuchs Anticorit PLS100T' lubricated and unlubricated -DX56 steel sheets with varying contact pressures was done using the linear sliding friction experimental set-up, shown in figure 4. Figure 10 shows the variation of boundary layer shear strength with (applied load) nominal contact pressure for both lubricated and unlubricated steel sheets. As explained in the literature [9] and [11], a higher contact pressure increases the potential barrier for the shearing of the boundary layers, thereby increasing the interfacial shear strength. It can be seen from figure 10a, 10b and 10c that the slope of the boundary layer shear strength plots decreases with increase in nominal contact pressure. Hence, the boundary layer shear strength (at constant sliding velocity of 1 mm/s and at room temperature) has been plotted against the contact pressure by fitting the experimental data with the power law relation (based on equation 7.2) in equations 9.1-9.3. Both the lubricants seem to result in boundary layers with different shear strengths. The shear strength of the Quaker lubricated interface is slightly lower than that of the Anticorit lubricated interface. The shear strength of the unlubricated interface has been measured for experiments with stable friction behaviour where galling is absent. The absence of a lubricant boundary layer results in formation of stronger metallic junctions with high shear strength. So the unlubricated contact has a higher interfacial shear strength than the lubricated contact, see figure 10d. Corresponding to equations 4.3 and 7.2, $n_v = 0$ and $n_T = 0$ are taken for equations 9.1, 9.2 and 9.3 and equations 10.1 and 10.2.

$$\tau_I^Q = 1.34 P_{nom}^{0.88} \tag{9.1}$$

$$\tau_I^A = 0.64 P_{nom}^{0.93} \tag{9.2}$$

$$\tau_I^U = 2.05 P_{nom}^{0.88} \tag{9.3}$$

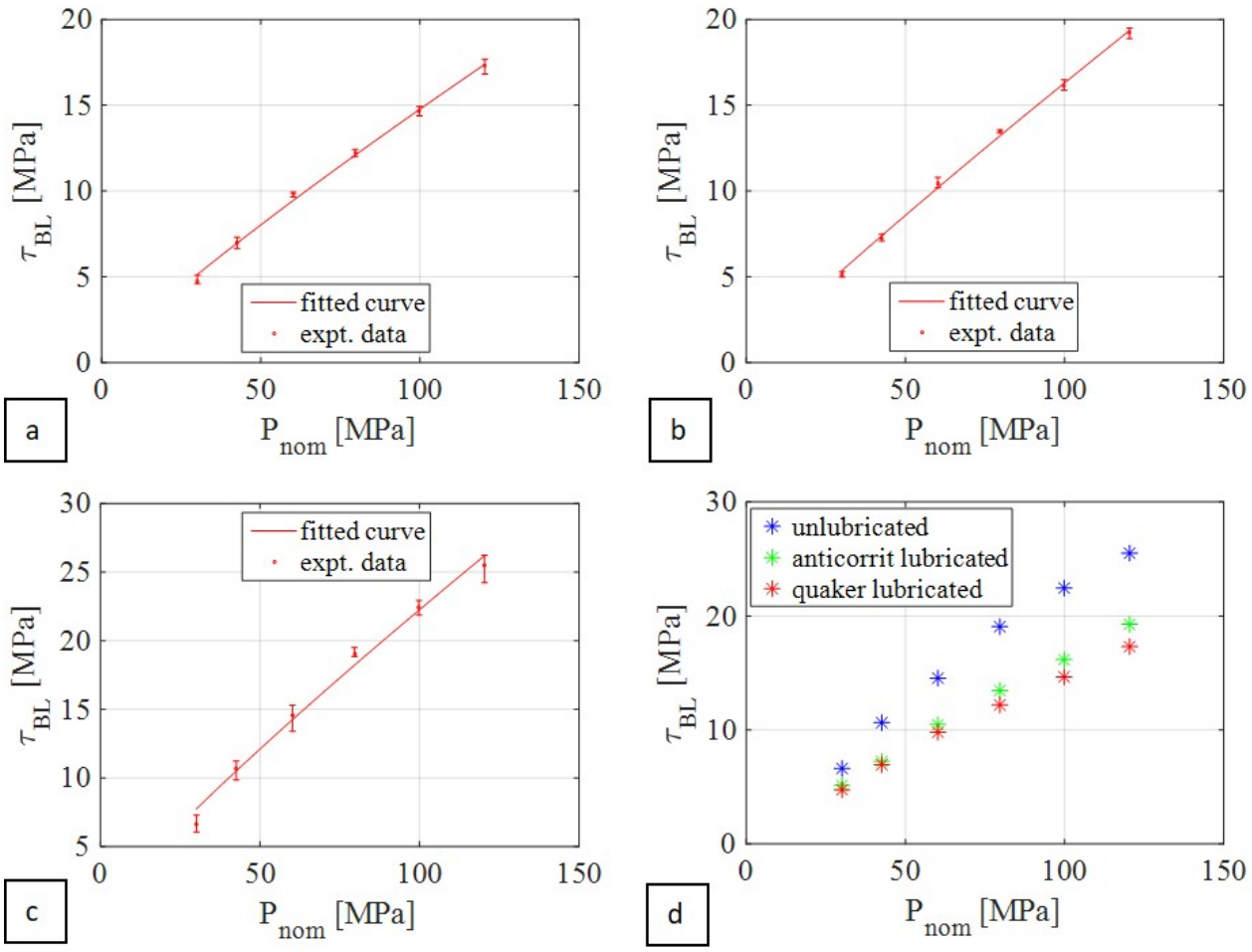

Figure 10: Variation of boundary layer shear strength with nominal contact pressure at a sliding velocity of 1mm/s for (a) Quaker Ferrocoat N136, (b) Fuchs Anticorit PLS100T lubricated (c) unlubricated DX56 sheet and (d) their comparison.

The characterization of the boundary layer shear strength for experiments done with zinc coated DX-56 steel was also carried out with sheets lubricated with Quaker and Anticorit lubricants. The unlubricated shear experiments done with zinc coated steel were avoided as steel pins sliding through zinc coated sheets have shown a higher affinity for material transfer or galling. The mean friction forces obtained from the shear experiments were divided by the contact area calculated for the coated system in section 5.1. The boundary layer shear strengths were plotted against the applied nominal pressure for experiments done with lubricated GI sheets (at constant temperature and velocity) and fitted with power law expressions derived in equation 8.1 in figure 11a and11b. The curve fit expressions for both the lubricants are listed in equation 10.1 and 10.2.

$$\tau_{GI}^{Q} = 0.32 P_{nom}^{0.95} \tag{10.1}$$

$$\tau_{GI}^{A} = 7.34 P_{nom}^{0.78} \tag{10.2}$$

5.3 Effect of boundary layer shear stress on single asperity sliding behaviour

The effect of the boundary layer shear strength on the friction and wear in sliding of a rigid asperity has been studied in this section. Both experiments and simulations have been performed using “asperities” of 1mm and 3mm diameter under Quaker lubricated and

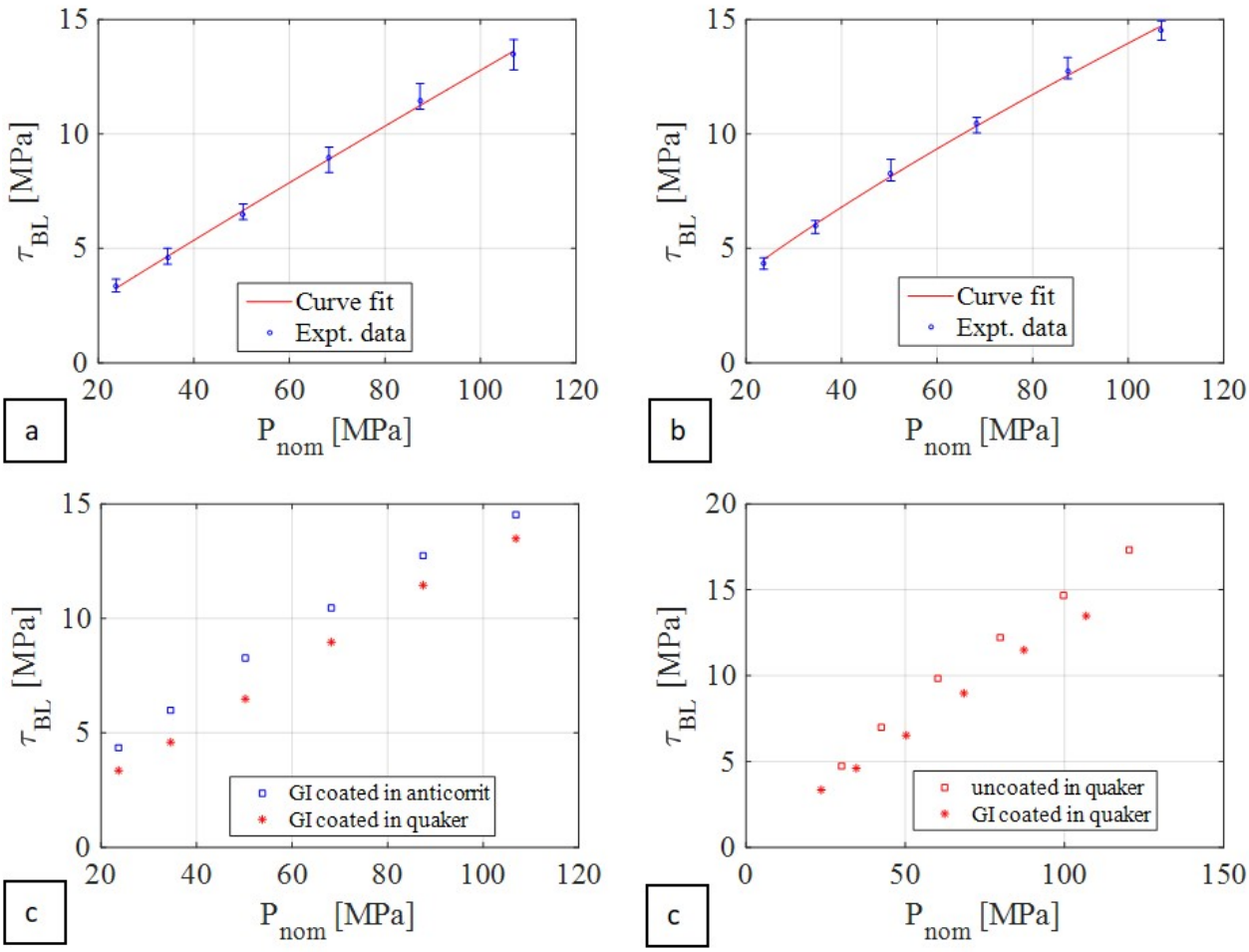

Figure 11: Variation of boundary layer shear strength with nominal contact pressure at a sliding velocity of $1mm/s$ for zinc-coated GI sheet lubricated with (a) Quaker Ferrocoat N136 (b) Fuchs Anticorit PLS100T and (c) their comparison with each other and (d) with uncoated steel sheet.

unlubricated contact. The MPM-based ploughing model incorporates the relationship between the boundary layer shear strength and the contact pressure given in equations 9.2 and 9.3 for lubricated and unlubricated steel sheets to compute the interfacial friction. The ploughing model also uses material model (equation 7.1) parameters listed in table 2 and 3 to compute the substrate deformation. The change in wear regime and wear volume in the presence and absence of a lubricant is highlighted using ploughing experiments and simulations.

5.4 Effect on friction in ploughing.

The shear strength of the interface is varied by using a clean, unlubricated or lubricated 'shine polished' substrate prepared as per the method explained in section 3.2. Indenters having tips fitted with spherical balls of 3mm diameter are used to plough the substrate. MPM-based ploughing simulations are done using same parameters as the experimental set-up. The MPM-ploughing simulations have incorporated interfacial friction models from equation 9.1 and 9.3 for the 'Quaker' lubricated and unlubricated contact respectively. The coefficient of friction is plotted against the sliding distance for ploughing experiments and ploughing simulations on both unlubricated and lubricated substrates in figure 12a and 12b respectively. The mean value

of the coefficient of friction is measured at the steady state and plotted against applied loads ranging from 1N to 46 N. MPM-based ploughing simulations are also performed for applied loads of 1 to 46N and for particle-cell sizes of 5, 10 and 20 μm. The coefficient of friction for different resolutions are interpolated to 0 cell size to obtain the converged coefficient of friction.

The mean coefficient of friction obtained from MPM-based ploughing simulations with 'Quaker' lubricated and unlubricated substrate are validated against the ploughing experiments for the applied load range. The MPM-based ploughing simulation results are in good agreement with the experimental results for sliding of indenter of 3mm diameter through the lubricated substrate. Previous results [27] have also shown agreement between MPM-based ploughing simulation and ploughing experiments for an indenter of 1mm and 3mm diameter (figure 13). The MPM-based ploughing simulations on unlubricated substrate also show good agreement with the ploughing experiments on unlubricated substrate for loads ranging from 4 to 29N (figure 13a). For loads on either side of the range 4-29N, the experimental coefficient of friction is higher than that numerical ones. Since the substrate is not mirror polished (see section 3.2) and the roughness of the substrate is kept at 20 to 30 nm, which is close to the roughness of the spherical indenter, the asperities of the indenter and substrate may interlock while sliding at low penetration depth. The asperity interlocking (AI) results in the additional coefficient of friction for ploughing experiments at low loads. Also, at high loads, the substrate-material is transferred onto the indenter-surface resulting in increased wear and friction in the ploughing experiments. This phenomena, termed 'wedging' is further explained in section 5.3.3.

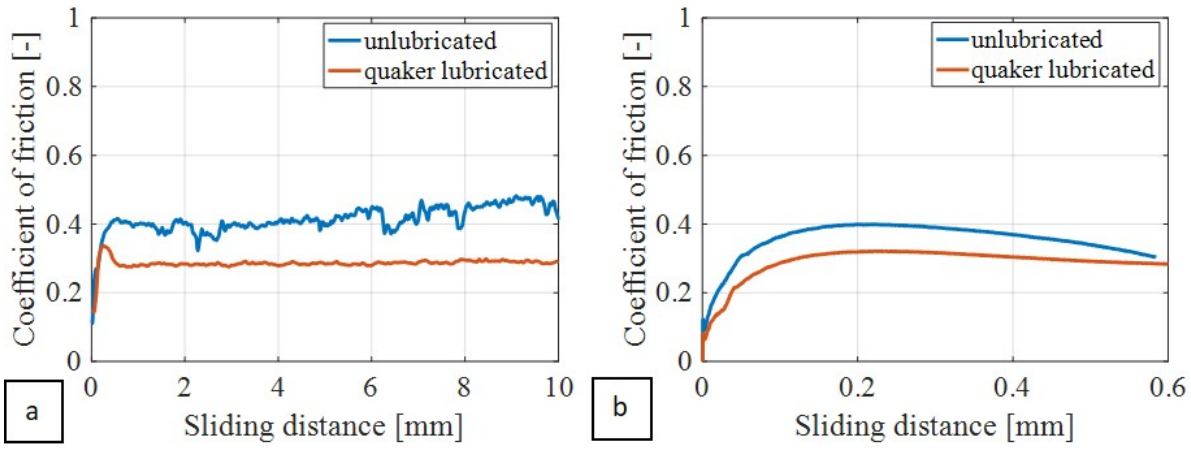

Figure 12: Coefficient of friction vs sliding distance for a 3mm diameter spherical tip indenter sliding through 'Quaker' lubricated and unlubricated DX-56 steel substrate for (a) ploughing experiments and (b) MPM-based ploughing simulations at an applied load of 16N (smaller sliding distance in ploughing model is to reduce the computation time).

Having validated the numerical coefficient of friction results for various loads, indenter size and interfaces, MPM-based ploughing simulations have been used to study the contribution of interfacial shear strength to the total coefficient of friction. The ratio of the coefficient of friction due to interfacial shear strength and the total coefficient of friction $\overline{\mu} = \mu_b/\mu$, for various loads is shown in equation 11.1. The friction force due to ploughing has been calculated by running MPM simulations without any interfacial shear. This had been done theoretically by taking the coefficients of expressions in equation 9.1 and 9.3 as zero. The resulting friction force has been attributed to the plastic deformation of the substrate only and termed as 'ploughing

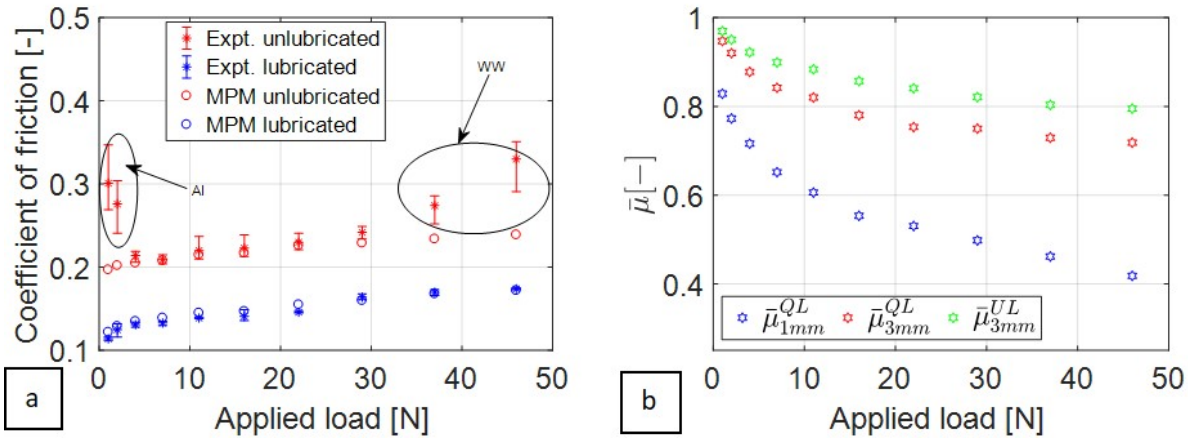

Figure 13: (a) The validation of coefficient of friction obtained from MPM-based ploughing simulations with ploughing experiments for various loads in ploughing of lubricated and unlubricated substrates using a DX-56 steel sheet by 3mm diameter indenter (AI: asperity interlocking, WW: wedging wear). (b) The analysis of component of coefficient of friction due to shearing of the interface from MPM-based ploughing simulation of indenters of 1mm and 3mm diameter sliding through 'Quaker' lubricated and unlubricated substrates.

friction'. The coefficient of ploughing friction μ_p has been subtracted from the total coefficient of friction μ and then normalized by μ to obtain $\overline{\mu}$ as shown in equation 11.1. It can be seen from figure 10b that the interfacial shear strength is a major contributor to the total friction force for larger indenter shapes. The effect of interfacial shear on total friction acting on a sliding asperity reduces with the applied load. As the penetration of the asperity into the substrate increases with the applied load, the plastic deformation of the substrate increases. This conversely diminishes the effect of the friction due to interfacial shear. The shape of the plot in figure 10b corresponds to the flow stress curve with material hardening under increased loading based on the Bergström van Liempt material model in equation 7.

$$\overline{\mu} = \frac{\mu_b}{\mu} = 1 - \frac{\mu_p}{\mu} \Rightarrow \mu_p = (1 - \overline{\mu})\,\mu \tag{11.1}$$

$$\overline{d} = \frac{d_\mu}{d_0} \tag{11.2}$$

$$F_f = F_a + F_p = \widetilde{\mu} F_f + F_p \Rightarrow F_f = \frac{F_p}{1 - \widetilde{\mu}} \tag{11.3}$$

5.4.1 Effect on deformation of substrate.

The substrate deformation due to ploughing also depends on the interfacial shear strength. The wear track on the substrate is observed under the confocal microscope to obtain the ploughed profile as shown in figure 14a. The cross-section of the ploughed profile is plotted in figure 14b in the zy-plane where the sliding direction of the indenter is along x-axis. It can be seen that the increase in interfacial shear strength, in the absence of lubricant, increases the deformation of the substrate and hence the ploughing depth. The ploughing depth d is calculated as the sum of the groove depth d_g and the pile-up height h_{pu} as shown in figure 14b. The ploughing depths are then computed for loads ranging from 1 to 46N for both lubricated and unlubricated substrates. The ploughing depth for numerical simulations are converged for particle-cell resolutions of 5-20μm.

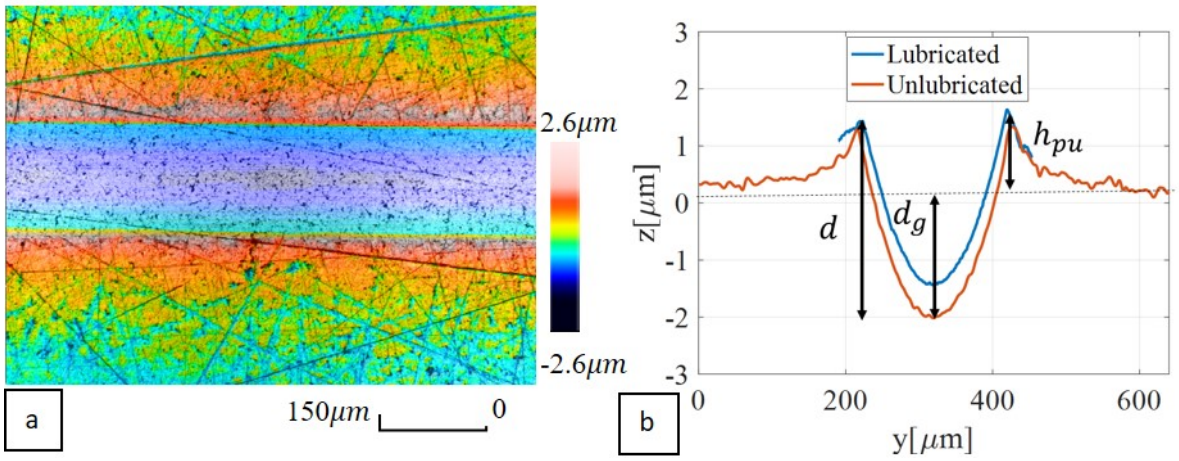

Figure 14: (a) Ploughed profile of unlubricated DX-56 steel substrate ploughed using an indenter of 1mm diameter under an applied load of 16N as seen under confocal microscope at 20x magnification (colour bar for heights given). (b) Comparison of the cross-section of the ploughed profile in figure 14a with the ploughed profile of the lubricated steel substrate at the 16N load by 1mm diameter indenter.

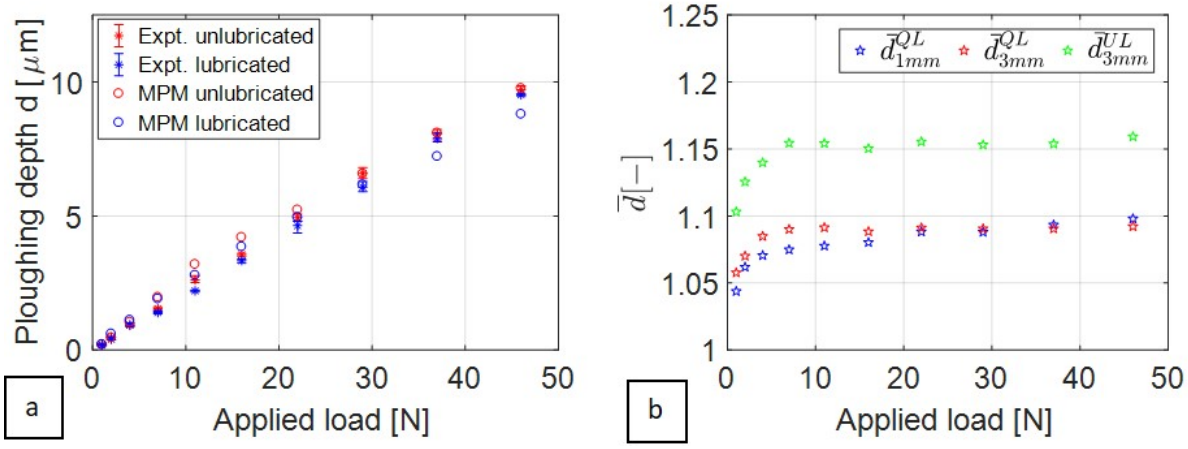

Figure 15: (a) The validation of ploughing depths obtained from MPM-based ploughing simulations with ploughing experiments for various loads, ploughing of lubricated and unlubricated substrates using a DX-56 steel sheet by 3mm diameter indenter. (b) The analysis of change in normalized ploughing depths due to shearing of the interface from MPM-based ploughing simulation of indenters of 1mm and 3mm diameter sliding through 'Quaker' lubricated and unlubricated substrates.

The ploughing depths obtained from the MPM-based ploughing simulations for ploughing of lubricated and unlubricated steel substrate by a 3mm diameter indenter have been validated against ploughing experiments in figure15a. The ploughing simulation results agree well with the experimental results for the given range of loads both in lubricated and unlubricated conditions. The agreement also extends the validation of ploughing depths in [27] for different interfaces and indenter sizes. An increase in ploughing depth increasing with increasing the applied load can also be seen in the absence of lubricant.

The MPM-ploughing simulations done in the absence of interfacial shear strength by taking coefficients in equation 9.1 and 9.3 as zero have been used to compute contribution of the deformation in the substrate to the ploughing depth. The increase in ploughing depth due to

interfacial shear has been characterized by normalizing the ploughing depth for (lubricated and unlubricated) substrates with interfacial shear d_μ to the ploughing depth of substrate without interfacial friction d_0, given as $\overline{d}$ in equation 11.2 and shown in figure 15b. The ratio for all loads, indenter sizes and interfaces exceeds unity. An additional component of force acts on the substrate, due to shearing at the interface, in the direction opposite to the direction of plastic flow. For plastic flow beneath the indenter, the interfacial friction force on the substrate also has components acting in the z direction. This component of interfacial friction along with the applied load in $-z$ direction, causes a biaxial stress state on the substrate elements in contact which assists the deformation of the substrate and increases the ploughing depth of the substrate. Also, the resistance of friction force due to interfacial shear to the plastic flow of the deformed substrate around the indenter which acts reduces the ploughing depth.

Both the effects of interfacial friction force in resulting in 'biaxial stress-state' and 'resistance to plastic flow' act against each other. However, the increase in ploughing depth with increasing interfacial shear indicates the dominance of the 'multiaxial stress-state' effect. As the contact area increases with the applied load, the magnitude of interfacial friction force increases and hence the ploughing depth ratio increases. At higher loads the substrate not only flows underneath the indenter, but also piles up and flow around the indenter. The section of piled up substrate experiences interfacial friction force along the (loading) $-z$ direction. Hence the 'biaxial stress-state' effect diminishes for the piled-up substrate at higher loads and the rate of increase of $\overline{d}$ decreases and becomes almost constant at higher loads (figure 15b). The initial rate of increase of $\overline{d}$ is higher for 3mm diameter indenter where the interfacial shear strength is a major contributor to total friction force as shown in figure 13b. However, for the smaller indenter of 1mm diameter, $\overline{d}$ reaches a constant value (steady-state) slower compared to larger 3mm diameter indenter.

Considering the depth factor $\overline{d}$ for larger indenters becomes constant at higher loads, the ploughing depth d_μ can be calculated as a factor ($k_d = \overline{d}$) of the friction less ploughing depth d_0. Since the coefficient of friction due to plastic deformation μ_p is a function of the frictionless ploughing depth d_0, it becomes constant for higher loads as can also be seen in figure 15b. The total coefficient of friction μ is calculated as a factor k_μ of μ_p, i.e. $\mu = k_\mu \mu_p, \forall k_\mu = (1 - \overline{\mu})^{-1}$ as shown in equation 11.1. Hence the total friction force is given as a factor of the total friction force due to plastic deformation of the substrate (ploughing), i.e. $F_f = k_\mu F_p$. This corresponds to the theory in Bowden and Tabor [1] where the friction force due to adhesion F_a, given using factor $\widetilde{\mu}$ as $\widetilde{\mu} F_f$, and ploughing F_p are independent of each other and their sum is the total friction force. Hence, the Bowden and Tabor relation for total friction force holds for large indenters at large loads. Thus the total friction force for large indenters at high loads is given in equation 11.3. So, the factors k_μ and $\widetilde{\mu}$ are related as $k_\mu = (1 - \widetilde{\mu})^{-1}$ and $\widetilde{\mu} = \overline{\mu}$.

5.4.2 Effect on the wear behaviour.

The increase in interfacial shear strength results in transition of the wear mode from 'ploughing' to 'wedging' based on the 'wear mode diagram' for sliding of a single-asperity [18]. The absence of lubricant at the sliding metallic interface can result 'wedging' and possible material transfer [41]. The wear mode diagram plots the wear modes as a function of the 'angle of attack' and the 'interfacial friction factor'. The angle of attack for a spherical asperity is defined as the angle made by the tangent to the sphere at the point of contact with the substrate in the xz plane with the sliding x-direction. The angle of attack γ_s for a sphere of radius r and ploughing depth d is computed from the equation 12.1. The 'interfacial friction factor' f_{hk} is the ratio of the

interfacial shear strength τ to the bulk shear strength of the substrate κ. If the angle of attack exceeds the critical value of γ_{pl}^{wd} (see equation 12.2) for $f_{hk} \in (0.5,\ 1)$ there is transition from ploughing to the 'wedging' wear mode. The transition to the cutting wear mode is achieved for an angle of attack $\gamma_{pl,wd}^{cu}$ are approximated by equation 12.3 [42].

$$\tan\gamma_s = \frac{a}{r-d} = \frac{\sqrt{d\,(2r-d)}}{r-d} \tag{12.1}$$

$$\gamma_{pl}^{wd} = \arccos f_{hk} \quad \forall f_{hk} \in (0.5,\ 1) \tag{12.2}$$

$$\gamma_{pl,\ \ wd}^{cu} = \frac{(\pi - \arccos f_{hk}\ )}{4} \tag{12.3}$$

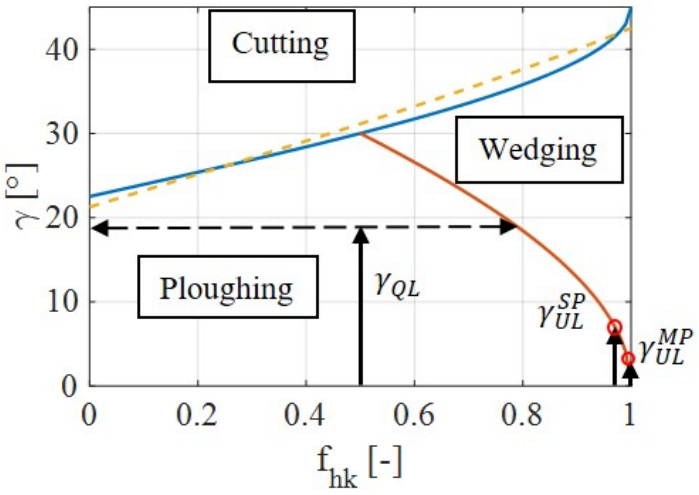

Figure 16: Wear mode diagram for ploughing experiments done on Quaker lubricated (QL) and unlubricated (UL) steel substrate which has been prepared by shine polishing (SP) and mirror polishing (MP) (see section 3.2). The arrows indicate the change in angle of attack with ploughing depth/applied loads with their end points marking the transition into wedging wear mode from ploughing.

The surface of the spherical tip of the indenter was observed under the confocal microscope after each experiment to check for material transfer. For lubricated ploughing experiments, the value of the interfacial friction factor is less than 0.5 which is why the wear mode is generally ploughing or cutting. The maximum ploughing depth obtained was 30 μm, for an (maximum) applied load of 46N on the 1mm diameter indenter. The corresponding maximum angle of attack computed was $\gamma_{QL} = 19.6°$. From the wear mode diagram in figure 16, it can be seen that the interfacial friction factor corresponding to the maximum angle of attack for ploughing on a lubricated surface γ_{QL} corresponds to $f_{hk} < 0.8$ (figure 16). Ploughing experiments on unlubricated substrate has been done on steel sheets prepared by shine polishing and by mirror polishing as explained in section 3.2. The shine polished substrate formed a stable oxide film which prevents direct metal-metal contact during ploughing. Hence transition into the wedging wear mode occurs at a ploughing depth of 8.6μm which corresponds to an attack angle γ_{UL}^{SP} of 6.6°. The interfacial friction factor corresponding to the transition attack angle γ_{UL}^{SP} for shine polished substrate is $f_{hk} = 0.95$. For a mirror polished substrate, the transition to wedging occurs almost immediately at low ploughing depth of 1.6μm. This transition corresponds to an attack angle $\gamma_{UL}^{MP} = 1.3°$ and an interfacial friction factor of $f_{hk} = 0.99$. This implies that the interfacial shear strength for a fresh, clean 'mirror polished' substrate (defined in section 3.2) is close to its bulk shear strength.

The surface of the 3mm spherical pins, for experiments done using the mirror polished and shine polished substrate after the transition to wedging wear mode has been shown in figure 17. The material transferred from the groove of the substrate is stacked and hardened as wedges on the surface of pins as shown in figure 17a and 17c. It can be seen that the transition to the wedging wear mode occurs at a low ploughing depth of $1.1\mu m$ for an unlubricated, clean mirror polished substrate as compared to a high ploughing depth of 9.8 μm for a shine polished substrate (defined in section 3.2) which has been used approximately after 1000 hours of the polishing process. The ploughing depths of $1.1\mu m$ and $9.8\mu m$ correspond to the applied loads of 4N and 46N respectively. This transition in wear mode corresponds to the computed attack angle and interfacial friction factor mapped in figure 16.

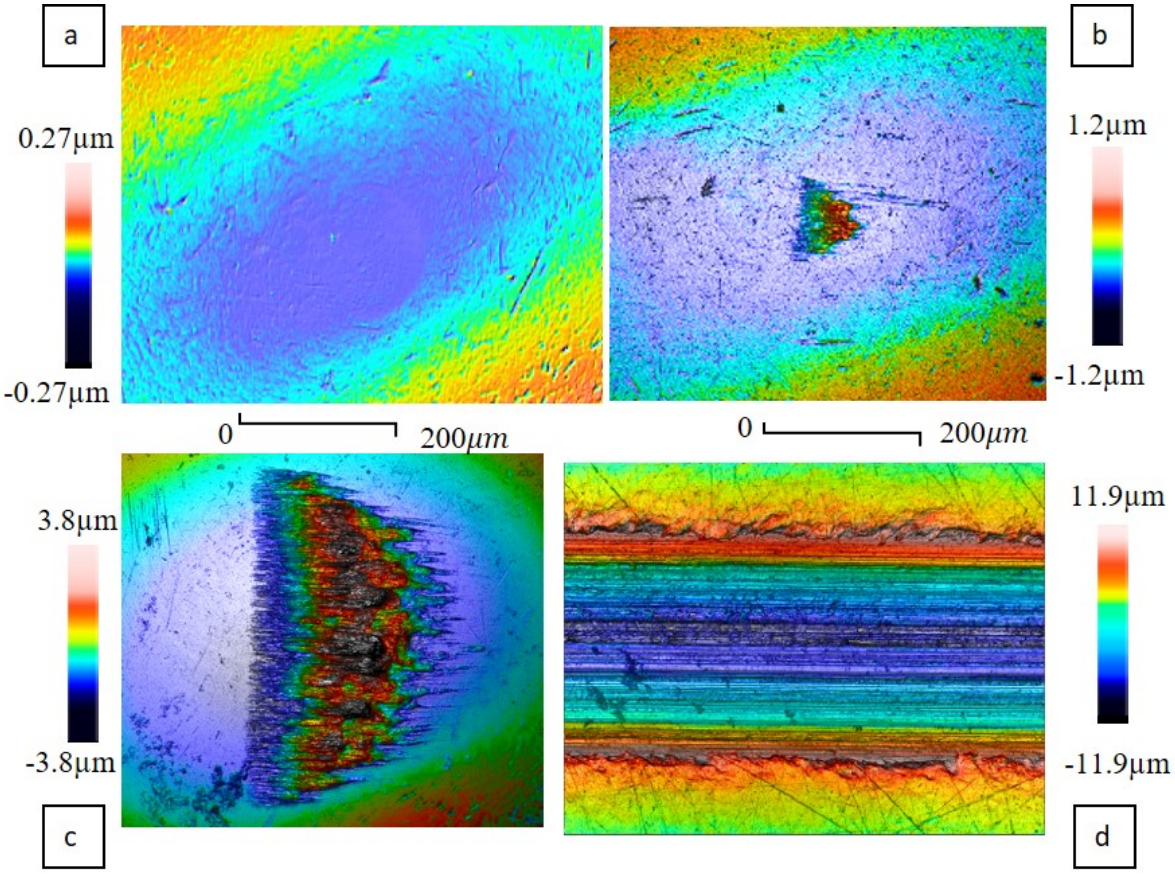

Figure 17: Wear mode diagram for ploughing experiments done on Quaker lubricated (QL) and unlubricated (UL) steel substrate which has been prepared by shine polishing (SP) and mirror polishing (MP) (see section 3.2). The arrows indicate the change in angle of attack with ploughing depth/applied loads with their end points marking the transition into wedging wear mode from ploughing.

The modelling of the wedging wear mode is challenging using the MPM-based ploughing model. This is because, to model material removal from the substrate, its transfer and adhesion onto the surface of the asperity on unloading requires a robust damage model and adhesion model. Such models have not been implemented in the current MPM-based ploughing model. However, the friction and deformation of the substrate in the MPM-based ploughing model has been compared to the experiments for the same experimental parameters resulting in wedging as shown in figure 18. The friction plot in figure 18a shows the fluctuations in the friction with sliding distance due to pile-up and stacking of the wedges (lumps of substrate material) in

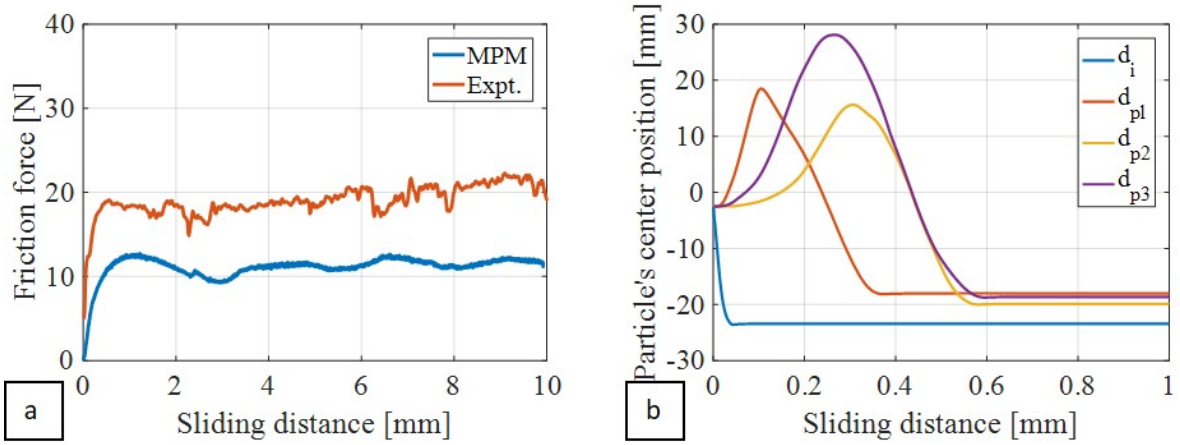

Figure 18: (a) The friction plots obtained from experiments and MPM based simulations and (b) the mean position of MPM particles in four regions along the sliding track for an applied load of 22N by 0.4mm diameter indenter ($f_{hk} = 1$), corresponding to wedging in sliding on an unlubricated substrate.

front of the indenter during wedging. This pile-up of the substrate material can be also seen by checking the mean position of groups of particles along the sliding length of the ploughed track as shown in figure 18b. It can be seen that the particle pile-up to subsequently higher height (mean $+z$ coordinate) as the asperity moves along the substrate. However, due to absence of adhesion between the asperity and substrate the MPM particles do not stick to the asperity as in case of wedging in experiments. Thus the MPM-based ploughing model can be used to compute friction and ploughing depth for various interfaces given their interfacial shear strength. The MPM-based ploughing model can also be used to develop a deeper understanding on the effect of boundary layer shear strength on friction and deformation due to ploughing of a single-asperity.

6 Conclusion

An experimental method to characterize the interfacial shear strength of lubricated and unlubricated contacts (coated and uncoated) has been developed. The interfacial shear strength has been fitted with empirical relations to express it as a function of contact pressure and sliding velocity. The fitted relations have been successfully implemented in the MPM-based ploughing model and the results have been validated against ploughing experiments with good agreement. The MPM-based ploughing model has been further used to understand the effect of interfacial shear strength of the friction and wear behaviour of a single asperity sliding through a steel substrate. The Bowden and Tabor [1] relationship for friction in sliding contacts has been shown to hold for large indenters at large applied loads. In these cases, the contribution of the interfacial shear strength and plastic deformation to the total friction force and the ploughing depth is shown to be independent and additive. An experimental study on the transition from ploughing to wedging wear mode has been carried out by varying the interfacial shear strength and the transition has been explained using the wear mode diagram for spherical indenters [18].

Acknowledgments

This research was carried out under project number S22.1.14520a in the framework of the Partnership Program of the Materials innovation institute M2i (www.m2i.nl) and the Technology Foundation TTW (www.stw.nl), which is part of the Netherlands Organization for Scientific Research (www.nwo.nl).

Bibliography

[1] F.P. Bowden, A.J.W. Moore, and D. Tabor. "The Ploughing and Adhesion of Sliding Metals". In: Journal of Applied Physics 14 (1943), pp. 80–91. DOI: 10.1063/1.1714954.

[2] F.P. Bowden and L. Leben. "The friction of lubricated metals". In: Philosophical Transaction of the Royal Society of London A. Mathematical and Physical Sciences 239 (1940), pp. 1–27. DOI: 10.1098/rsta.1940.0007.

[3] S. Jahanmir and M. Beltzer. "Effect of additive molecular structure on friction coefficient and adsorption". In: Journal of Tribology 108 (1986), pp. 109–116. DOI: 10.1115/1.3261129.

[4] D. Godfrey. "Boundary Lubrication". In: Interdisciplinary Approach to Friction and Wear. Ed. by P.M. Ku. Washington DC: NASA SP-181, 1968, pp. 335–384.

[5] F.P. Bowden and D. Tabor. The friction and lubrication of solids. Oxford University press, 1954. ISBN: 9780198507772.

[6] K.B. Blodgett. "Films built by depositing successive monomolecular layers on a solid surface". In: Journal American Chemical Society 57 (1935), pp. 1007–1022. DOI: 10.1021/ja01309a011.

[7] B.J. Briscoe and D. Tabor. "Rheology of thin organic films". In: ASLE Transactions 17 (1973), pp. 158–165. DOI: 10.1080/05698197408981452.

[8] B.J. Briscoe, B. Scruton, and R.F. Willis. "The Shear Strength of Thin Lubricant Films". In: Proceedings of the Royal Society A: Mathematical, Physical and Engineering Sciences 333 (1973), pp. 99–114. DOI: 10.1098/rspa.1973.0050.

[9] B.J. Briscoe and D.C.B. Evans. "The Shear Properties of Langmuir-Blodgett Layers". In: Proceedings of the Royal Society A: Mathematical, Physical and Engineering Sciences 380 (1982), pp. 389–407. DOI: 10.1098/rspa.1982.0048.

[10] H. Eyring. "Viscosity, plasticity, and diffusion as examples of absolute reaction rates". In: Journal of Chemical Physics 4 (1936), pp. 283–291. DOI: 10.1063/1.1749836.

[11] J.M. Georges and D. Mazuyer. "Pressure effects on the shearing of a colloidal thin film". In: Journal Physics: Condensed Matter 3 (1991), pp. 9545–9550. DOI: 10.1088/0953-8984/3/47/026.

[12] C.M. Pooley and D. Tabor. "Friction and molecular structure: the behaviour of some thermoplastics". In: Proceedings of the Royal Society A: Mathematical, Physical and Engineering Sciences 329 (1972), pp. 251–274. DOI: 10.1098/rspa.1972.0112.

[13] C.M. Pooley and D. Tabor. "Transfer of PTFE and Related Polymers in a Sliding Experiment". In: Nature Physical Science 237 (1972), pp. 88–90. DOI: 10.1038/physci237088a0.

[14] B.J. Briscoe and A.C. Smith. "Time dependence effects in the shear of thin polymeric films". In: Journal of Physics D: Applied Physics 15 (1982), pp. 579–594. DOI: 10.1088/0022-3727/15/4/010.

[15] B.J. Briscoe and D. Tabor. "Shear properties of thin polymeric films". In: The Journal of Adhesion 9 (1978), pp. 145–155. DOI: 10.1080/00218467808075110.

[16] A.S. Akhmatov. Molecular physics of boundary friction. Vol. 2108. Israel program for scientific translations, 1966. ISBN: 0706505484.

[17] J.M. Challen and P.L.B Oxley. "An explanation of different friction and wear using asperity deformation models". In: Wear 53 (1979), pp. 229–243. DOI: 10.1016/0043-1648(79)90080-2.

[18] K. Hokkirigawa and K. Kato. "An experimental and theoretical investigation of ploughing, cutting and wedge formation during abrasive wear". In: Tribology International 21 (1988), pp. 51–57. DOI: 10.1016/0301-679X(88)90128-4.

[19] J.D. Bressan, G. Genin, and J.A. Williams. "The Influence of Pressure, Boundary Film Shear Strength and Elasticity on the Friction between a Hard Asperity and a Deforming Softer Surface". In: Tribology Series 36 (1999), pp. 79–90. DOI: 10.1016/S0167-8922(99)80030-3.

[20] X. Zheng, H. Zhu, A.K. Tieu, and B. Kosasih. "A molecular dynamics simulation of 3D rough lubricated contact". In: Tribology International 67 (2013), pp. 217–221. DOI: 10.1016/j.triboint.2013.07.015.

[21] H.T. Zhu, X. Zheng, P.B. Kosasih, and A.K. Tieu. "Tribo-surface charge and polar lubricant molecules on friction and lubrication under multiple 3D asperity contacts". In: Wear 332 (2015), pp. 1248–1255. DOI: 10.1016/j.wear.2015.02.045.

[22] X. Zheng, H. Zhu, B. Kosasih, and A.K. Tieu. "A molecular dynamics simulation of boundary lubrication: The effect of n-alkanes chain length and normal load". In: Wear 301 (2013), pp. 62–69. DOI: 10.1016/j.wear.2013.01.052.

[23] J. Song and G. Zhao. "A molecular dynamics study on water lubrication of PTFE sliding against copper". In: Tribology International 136 (2019), pp. 234–239. DOI: 10.1016/j.triboint.2019.03.070.

[24] R.S. Timsit and C.V. Pelow. "Shear strength and tribological properties of stearic acid films -Part I: On glass and aluminium-coated glass". In: Journal of Tribology 114 (1992), pp. 150–158. DOI: 10.1115/1.2920854.

[25] R.S. Timsit and C.V. Pelow. "Shear strength and tribological properties of stearic acid films -Part II: On gold-coated glass". In: Journal of Tribology 114 (1992), pp. 159–166. DOI: 10.1115/1.2920855.

[26] D.K. Karupannasamy. "Modelling of contact and friction in deep drawing processes". PhD thesis. University of Twente, The Netherlands, 2013. ISBN: 978-94-91909-01-6.

[27] T. Mishra, G.C. Ganzenmüller, M.B. de Rooij, M. Shisode, J. Hazrati, and D.J. Schipper. "Modelling of ploughing in a single-asperity sliding contact using material point method". In: Wear 418-419 (2019), pp. 180–190. DOI: 10.1016/j.wear.2018.11.020.

[28] K.J. Chugg and M.M. Chaudhri. "Boundary lubrication and shear properties of thin solid films of dioctadecyl dimethyl ammonium chloride (TA 100)". In: Journal of Physics D: Applied Physics 26 (1993), pp. 1993–2000. DOI: 10.1088/0022-3727/26/11/023.

[29] L. Chang, H. Zhang, and J. Lococo. “Effects of boundary films on the frictional behaviour of rough-surface contacts in incipient sliding”. In: Proceedings of the Institution of Mechanical Engineers, Part J: Journal of Engineering Tribology 220 (2006), pp. 385–394. DOI: 10.1243/13506501JET120.

[30] A. Westeneng. “Modelling of contact and friction in deep drawing processes”. PhD thesis. University of Twente, The Netherlands, 2001. ISBN: 90-365-1549-1.

[31] H. Gao, C.H. Chiu, and J. Lee. “Elastic contact versus indentation modelling of multi-layered materials”. In: International Journal of Solids and Structures 29 (1992), pp. 2471–2492. DOI: 10.1016/0020-7683(92)90004-D.

[32] M.V. Swain and J. Meník. “Mechanical property characterization of thin films using spherical tipped indenters”. In: Thin Solid Films 253 (1994), pp. 204–211. DOI: 10.1016/0040-6090(94)90321-2.

[33] D. Tabor. The Hardness of Metals. Clarendon Press, 1951. ISBN: 0198507763.

[34] J. Halling and R.D. Arnell. “Ceramic Coating in the war on wear”. In: Wear 100 (1984), pp. 367–380. DOI: 10.1016/0043-1648(84)90022-X.

[35] J. Malzbender, G. de With, and J.M.J den Toonder. “Determination of the Elastic Modulus and Hardness of Sol-Gel Coatings on Glass: Influence of Indenter Geometr”. In: Thin Solid Films 372 (2000), pp. 134–143. DOI: 10.1016/S0040-6090(00)01025-7.

[36] H. Fujiwara and T. Kawase. “Logarithmic profile of rollers in roller bearing and optimization of the profile”. In: Nippon Kikai Gakkai Ronbunshu C Hen (Transactions of the Japan Society of Mechanical Engineers Part C 18 (2006), pp. 3022–3029. DOI: 10.1299/kikaic.72.3022.

[37] G.M. Song, W.G. Sloof, Y.T. Pei, and J.T.M De Hosson. “Interface fracture behavior of zinc coatings on steel: Experiments and finite element calculations”. In: Surface and Coatings Technology 201 (2006), pp. 4311–4316. DOI: 10.1016/j.surfcoat.2006.08.046.

[38] G. van der Linde. “Predicting galling behaviour in deep drawing processes”. PhD thesis. University of Twente, The Netherlands, 2011. ISBN: 978-90-365-3284-6.

[39] P. van Liempt. “Work hardening and sub structural geometry of metals”. In: Journal of Materials Processing Technology 45 (1994), pp. 459–464. DOI: 10.1016/0924-0136(94)90382-4.

[40] H. Vegter. “On the plastic behaviour of steel during sheet forming”. PhD thesis. University of Twente, The Netherlands, 1991. ISBN: 9789090043739.

[41] E. Rabinowicz and D. Tabor. “Metallic Transfer between Sliding Metals: An Autoradiographic Study”. In: Proceedings of the Royal Society A: Mathematical, Physical and Engineering Science 208 (1951), pp. 455–475. DOI: 10.1098/rspa.1951.0174.

[42] M.B. de Rooij. “Tribological aspects of unlubricated deep drawing processes”. PhD thesis. University of Twente, The Netherlands, 1998. ISBN: 90-3651218-2.

Paper E

Characterization of yield criteria for zinc coated steel sheets using Nano-indentation with Knoop indenter

Tanmaya Mishra[1*], Matthijn de Rooij[1], Meghshyam Shisode[2], Javad Hazrati[2], and Dirk J. Schipper[1]

[1]Surface Technology and Tribology, Faculty of Engineering Technology, University of Twente, 7500 AE Enschede, the Netherlands
[2]Nonlinear Solid Mechanics, Faculty of Engineering Technology, University of Twente, 7500 AE Enschede, the Netherlands

Abstract

An indentation based method to characterize the yield locus for steel sheets is developed and implemented. Knoop hardness based indentation experiments have been performed on the surface as well as on the cross sections of an uncoated steel sheet to obtain the corresponding yield locus in the deviatoric and plane-stress situation. Stress ratios following the indenter's geometry are used to plot the yield locus from indentation data. The stress ratios have been corrected for the anisotropy of the material by an optimization algorithm. Points are then plotted in the plane-stress plane using the corrected stress ratios, the strain increment vectors and indentation hardness data. The parameters for the Hill's quadratic yield criteria are obtained from the indentation data based on a curve fitted yield locus. The results obtained using nano-indentation have been compared with those obtained from the standard characterization tests for steel sheet and shown to have good agreement. The method is also applied to the yield locus characterization of zinc coatings on steel sheet for multi-scale modelling of friction in deep drawing.

Keywords: Knoop indentation, Anisotropy, Yield locus, Zinc coating, Galvanized steel.

1 Introduction

The plastic deformation (yielding) in metals results from shear stress which causes the formation and movement of dislocations at the slips systems in the crystals. The deformation modes in most crystals are directional resulting in anisotropic yielding of the metals on loading. In sheet metal forming processes like deep-drawing, metallic sheets are typically cold rolled a priori which induces a deformation texture in the sheet [1]. The textures, i.e. preferred orientations of crystals along direction of applied stress, are oriented along the rolling, transverse and normal directions. Hence most sheet metals exhibit anisotropic yielding which is described by a yield function and is represented by the corresponding yield surface in a three-dimensional principal stress space.

Of the available criteria, Hill's quadratic yield criterion has been most commonly used to describe the anisotropic yielding in most metals [2]. Further, the von Mises and Tresca yield criterions [3] and [4] for isotropic materials have been generalized and given a non-quadratic model defined in the principal stress space by Hosford in [5]. Likewise, an anisotropic extension of the Hosford model has been proposed by Hill in [6]. The yield criterions have been typically plotted as yield loci in the octahedral π-plane with deviatoric stresses along the axis. Since in sheet metal forming processes, the out-of-plane stresses are neglected, the yield loci can also be plotted in the plane-stress plane. Anisotropic yield criteria specific to sheet metals have also been developed in the principal stress space in [7], [8] and [9]. Among them, the Vegter yield criterion [7] and [8] has been used to develop and characterize the yield loci for sheet metals in the plane-stress plane.

The measurement of anisotropic yield parameters (Lankford coefficients: R values) is typically done by uniaxial testing (tensile loading) of sheet material with varying orientations relative to the rolling direction. For planar isotropic materials the R values are obtained by bulk loading methods such as pure shear, uniaxial tensile, plane strain tensile or an equi-biaxial tensile test. Each of these experiments are combined to measure the stress points on the plane-stress plane, between which the Bezier curve has been used to describe the yield locus independent of R values, in the Vegter yield criteria [10], [7] and [8]. Also virtual field methods (VFM) have been used in combination with digital image correlation of strain fields to obtain parameters for anisotropic yield criteria [11]. However, VFM has been applied successfully for characterizing only certain types of yield criteria mostly for uncoated sheet metals [12]. Indentation based characterization techniques have also been modelled and designed to estimate the anisotropic plastic properties [13], [14] and [15] from measured results. Using the load-depth curve and the pile-up height modelled utilizing spherical indenters, the yield stress ratio has been derived for planar isotropy [14] and [15]. FE models involving indentation near free edge, free corner, interface of bonded samples and linear and circular scratch tests have also been used to characterize anisotropic yield parameters [13]. However, a rigorous development of a measurement and characterization method based on such indentation techniques is unavailable.

Among the pyramidal shaped indenters commonly used for hardness measurements [16], the use of an asymmetric Knoop indenter [17] with a rhombic base having diagonals of lengths in ratio $7:1$ has been used to measure the anisotropy in plastic deformation of metals. The dependence of the measured hardness on orientation of the long diagonal of the Knoop indenter relative to the crystal planes has been observed and explained using the resolved shear stress of the slip systems for hexagonal single crystal of WC, zinc and zircalloy-2 in [18], [19] and [20]. However, for larger indentations over multiple grains, a flow surface theory relating the deviatoric shear

stress to the indentation hardness and the geometry of the Knoop indenter was first proposed by Wheeler and Ireland [21]. By aligning the diagonals of the Knoop indenter along the principal axes of stress (axes of anisotropy), six indentations were performed on zircalloy-2 specimens. The Knoop hardness number (KHN) specific to each indentation was plotted in the octahedral (deviatoric stress) plane by taking the ratio of the corresponding deviatoric stress as equal to the ratio of the diagonal lengths of the Knoop indenter, i.e. $7:1$. The yield locus was plotted using the points on the plane and the strain ratios were compared with those obtained from bulk tensile tests along the anisotropic axes to good agreement.

This technique of characterizing the yield loci from KHN data of anisotropic metals was modified by relating the hardness number to plane-stress yield loci and implemented in [22] for two titanium alloys. By relating the ratio of plastic strain underneath the indenter to the ratio of its diagonal lengths and using constancy of volume of deformed substrate and the Lévy-Mises equations, the strain ratios could be related to the stress ratios in the plane-stress plane. The yield loci were plotted by equating the KHN with the equivalent stress for Hosford yield criteria [22] and compared with the yield loci obtained by tensile tests [23] at various strains to give the best agreement at 0.01 strain. The KHN-based yield loci of highly anisotropic single magnesium crystal, polycrystalline magnesium sheets and magnesium alloys in plane-stress plane were also compared with conventional yield loci for small strains in [24] but did not show good agreement. Wonsiewicz and Wilkening [24] also observed the insensitivity of the KHN-based yield loci to capture the difference in compression and in tension as well as the excessive bulk of the KHN-yield locus into plane-stress plane's quadrants for the stress ratios computed using the techniques in [22]. Hence, the R value was included in the calculation of the stress ratios from the strain ratios in [24]. Using the initial methods to plot a yield locus from KHN [21], [22] and [24], the yield loci of pure polycrystalline titanium [25], titanium alloys [26] and zircalloys [27], [28] have been determined.

Although the yield loci plotted from the indentation hardness seems convenient for bulk polycrystalline metals and alloys as has been discussed above, micro-hardness indentation of a coating along the anisotropic axes (surface and cross-section) is challenging. Hence, attempts to utilize depth-sensing Nano indentation techniques with a Knoop indenter are made in [29] and [30]. The hardness of the indent is measured from the maximum penetration depth in the load-depth curve or the long diagonal lengths. However, compared to the standard Berkovich tip, the elastic recovery along the shorter diagonal of the residual impression by the Knoop indenter is accounted for. In order to express the elastic modulus, the ratio of the short and the long diagonals of the residual impression by the Knoop indenter is used [30]. Knoops indentation has also been analysed by modelling the indentation response of substrate with elastic and elastoplastic material behaviour without [31] and with strain hardening effects [32]. Numerical simulation of the depth-sensing indentation tests with a Knoop indenter on substrates with various hardening and material properties were also done recently using 3D finite element models to measure the area function, hardness and the elastic modulus [33] and [34]. Knoop indentations have been also performed on ductile metals and brittle ceramics and the results have been compared to other pyramidal shaped indenters (Berkovich and Vickers) [35] and [36]. The slip anisotropy has been determined from the indentation anisotropy by Knoop nano-indentation of SiC-6H single crystals [37].

The available research to measure the yield criteria for anisotropic material has mostly focussed on bulk metals and alloys and not on surfaces and coatings. Thus far, experimental techniques to characterize the parameters for yield criteria or yield locus for coated systems

have not been investigated. Moreover, zinc coatings applied on steel sheets used in deep-drawing have a high degree of anisotropy [38] and [39] due to orientation of the zinc grains during the prior galvanization and temper rolling processes. However, the yield criterion for zinc layer in galvanized steel sheets is unavailable in the literature. Among the available characterization techniques for coating, nano-indentation using depth sensing indentation has been mostly focussed upon [40]. Nano-indentation of zinc coating has been done to quantify the elastic anisotropy by measuring the elastic modulus and hardness for various grain orientations in [41]. Furthermore, yield loci have been plotted for various anisotropic materials using Knoop indentation [42] and have shown fair agreement with conventional yield loci.

Knoop indenter has not been used in Nano-indentation to plot obtain the yield locus of zinc coating on steel sheet so far. With the current advances in technology, modelling and analysis of Nano-indentation using the Knoop indenters, the Knoop indentation of both the surface and cross-section of zinc coating on steel substrate has been performed in the current research. A methodology to determine the parameters for Hill '48 yield criteria [32] from Knoop hardness number is designed. The current method accounts for the anisotropic behaviour of the coating by measuring the stress ratios induced by asymmetric Knoop indenter. The yield parameters are compared with those obtained by standard tests for a cold-rolled DC04 steel sheet, thereby validating the methodology. The same method is then implemented for measuring the yield parameters for the zinc coating in the temper-rolled, galvanized steel sheets as modelled by the Hill '48 yield criterion.

2 Calculation of yield parameters from KHN

A systematic procedure to derive the yield criteria for the zinc coating through indentation hardness data has been laid out in this section. Hill's quadratic yield function [2] is chosen for its ability of being expressed in matrix vector product form and hence the ease of implementation in numerical codes. Hills yield parameters have been related to the Lankford coefficients. Accounting for the anisotropy, the stress ratios in plane-stress condition have been expressed in terms of the Lankford coefficients and the strain ratio corresponding to each (six) Knoop indentation as explained in [21].

Some of the key assumptions as obtained from the literature and used in the method described below to obtain the yield parameters using Knoop indentation hardness are as follows:

1. The Knoop hardness number KHN in kgf/mm^2 is approximated to be equal to the equivalent flow stress, i.e. KHN is taken proportional to the shearing stress on the octahedral plane and (uniaxial) yield strength in plane stress [22] and [43].

2. The ratio of the deviatoric strain along the long and short diagonals of the Knoop indenter is assumed to be 1/7 [21].

3. The loading (strain) path of the Knoop indentation resulting in the intersection of the KHN based stress points with the yield locus is assumed to be linear [21] and [22].

4. The contact between the Knoop indenter and the experimental specimen is assumed to be frictionless and adhesionless.

2.1 Hill's Yield criterion and flow rule.

The quadratic Hill's yield function $f(\sigma_{ij})$ also named as the Hill 48 yield criterion [2] has been used in the current work to quantify the anisotropy in sheet metals, see equation 1.1. The Hill 48 yield criterion assumes no difference between the tensile and compressive yield stresses in a particular stress direction. The yield criterion depends on the deviatoric stresses and is pressure independent. Hence, σ_{ij} are deviatoric stresses where $i, j \, \epsilon \, 1, 2, 3$ being the anisotropic axes and $F,\ G,\ H,\ L,\ M$ and N are constants which are experimentally determined. For a rolled sheet metal, 1 is the rolling direction RD, 2 is the transverse direction TD and 3 is the normal direction ND. Typically, the constants $F,\ G$ and H are determined from uniaxial yield stresses with respect to the axes of anisotropy $\sigma^y_{11},\ \ \sigma^y_{22}$ and σ^y_{33} while the constants $L,\ M$ and N are determined from shear yield stresses associated to the same directions $\sigma^y_{23},\ \ \sigma^y_{31}$ and σ^y_{12} as shown in equation 1.2. The Hill's 48 yield criterion is expressed in equation 1.3 for the principal stresses $\sigma_1,\ \sigma_2$ and σ_3 aligned with the directions of anisotropy, $k \, \epsilon \, 1, 2, 3$ being the principal stress axes. Further assuming associated flow for plasticity in metals, the associated flow rule is expressed in equation 1.4 using $\dot{\lambda}$ which is the rate of the plastic multiplier. The flow rule represents the coincidence between the plastic potential and the yield surface and gives the plastic deformation rate $\dot{\varepsilon}^p$ as orthogonal to the yield surface.

$$f(\sigma_{ij}) \equiv F(\sigma_{22} - \sigma_{33})^2 + G(\sigma_{33} - \sigma_{11})^2 + H(\sigma_{11} - \sigma_{22})^2 + 2L\sigma_{23}^2 + 2M\sigma_{31}^2 + 2N\sigma_{12}^2 = 1 \quad (1.1)$$

$$\begin{aligned} F &= \frac{1}{2}\left[\frac{1}{(\sigma^y_{22})^2} + \frac{1}{(\sigma^y_{33})^2} - \frac{1}{(\sigma^y_{11})^2}\right],\ G = \frac{1}{2}\left[\frac{1}{(\sigma^y_{33})^2} + \frac{1}{(\sigma^y_{11})^2} - \frac{1}{(\sigma^y_{22})^2}\right], \\ H &= \frac{1}{2}\left[\frac{1}{(\sigma^y_{11})^2} + \frac{1}{(\sigma^y_{22})^2} - \frac{1}{(\sigma^y_{33})^2}\right],\ L = \frac{1}{2(\sigma^y_{23})^2},\ M = \frac{1}{2(\sigma^y_{31})^2},\ N = \frac{1}{2(\sigma^y_{12})^2} \end{aligned} \quad (1.2)$$

$$f(\sigma_k) \equiv F(\sigma_2 - \sigma_3)^2 + G(\sigma_3 - \sigma_1)^2 + H(\sigma_1 - \sigma_2)^2 = 1 \quad (1.3)$$

$$\dot{\varepsilon}^p_k = \dot{\lambda}\frac{\partial f}{\partial \sigma_k} \Rightarrow \frac{\partial \varepsilon^p}{\partial \lambda} = \frac{\partial f}{\partial \sigma_k} \quad (1.4)$$

2.2 Relationship between yield parameters and Lankford coefficients

Typically, for thin rolled sheets, a plane-stress condition is assumed where $\sigma_3 = 0$. The yield criteria in plane-stress condition, i.e. for a planar anisotropic material is given in terms of principal stresses, uniaxial yield stress in rolling direction σ^y_1 and Lankford coefficients in equation 2.1. The Lankford coefficients or the plastic strain ratios $R_0,\ R_{90}$ and R_{45} are the ratios of in-plane plastic strain to out of plane (through thickness) plastic strain due to loading under uniaxial stress $\sigma_1,\ \sigma_2$ and σ_{12} (at an angle $\theta = 0°,\ 90°$ and $45°$ relative to the rolling direction) respectively as defined in equation 2.2. The relationship between the Lankford coefficients and the Hill's parameter in equation 2.2 has been derived from the flow rule in equation 1.4. The Hill's yield criterion is written for plane-stress condition in the anisotropic axes taking $\sigma_{13}, \sigma_{23},\ \sigma_{33} = 0$ in equation 2.3. Hill's yield criteria in plane-stress is written in terms of the Lankford coefficients in equation 2.4 [44]. By comparing the individual terms in equation 2.3 and 2.4, the relationships between Hill's yield parameters and the Lankford coefficients are obtained in equation 2.5. For planar isotropy, the plastic strain ratio R_0 is independent of θ and $R_{90} = R_{45} = 1$. By substituting values of the yield parameters $F,\ G$ and H in equation 1.4, the equivalent flow stress is expressed in the principal stresses as given in equation 2.6.

$$f(\sigma_k) = \sigma_1^2 - \frac{2R_0}{R_0+1}\sigma_1\sigma_2 + \frac{R_0(R_{90}+1)}{R_{90}(R_0+1)}\sigma_2^2 = (\sigma_y)^2 \;\forall\; \sigma_3 = 0 \tag{2.1}$$

$$R_0 = \frac{d\varepsilon_2}{d\varepsilon_3} = \frac{H}{G}\forall(\theta=0)\,;\; R_{90} = \frac{d\varepsilon_1}{d\varepsilon_3} = \frac{H}{F}\forall\left(\theta=\frac{\pi}{2}\right)\,;\; R_{45} = \frac{d\varepsilon_{12}}{d\varepsilon_3} = \frac{H}{F+G} - \frac{1}{2}\forall\left(\theta=\pm\frac{\pi}{4}\right) \tag{2.2}$$

$$2f(\sigma_{ij}) = (G+H)\sigma_{11}^2 - 2H\sigma_{11}\sigma_{22} + (F+H)\sigma_{22}^2 + 2N\sigma_{12}^2 \;= 1 \;\forall\; \sigma_{13},\sigma_{23},\; \sigma_{33} = 0 \tag{2.3}$$

$$f(\sigma_{ij}) = \sigma_{11}^2 - \frac{2R_0}{R_0+1}\sigma_{11}\sigma_{22} + \frac{R_0(R_{90}+1)}{R_{90}(R_0+1)}\sigma_{22}^2 + \frac{(R_0+R_{90})(2R_{45}+1)}{R_{90}(R_0+1)}\;\sigma_{12}^2 \;= 1 \tag{2.4}$$

$$F = \frac{R_0}{R_{90}(R_0+1)},\; G = \frac{1}{R_0+1},\; H = \frac{R_0}{R_0+1},\; N = \frac{(R_0+R_{90})}{R_{90}(R_0+1)}\left(R_{45}+\frac{1}{2}\right),\; M = \frac{3}{2},\; L = \frac{3}{2} \tag{2.5}$$

$$\sigma_f^2 = \frac{R_0(\sigma_1-\sigma_2)^2 + R_0R_{90}(\sigma_2-\sigma_3)^2 + R_{90}(\sigma_3-\sigma_1)^2}{R_0R_{90}+R_{90}} \tag{2.6}$$

2.3 Derivation of stress ratio's using anisotropy constants

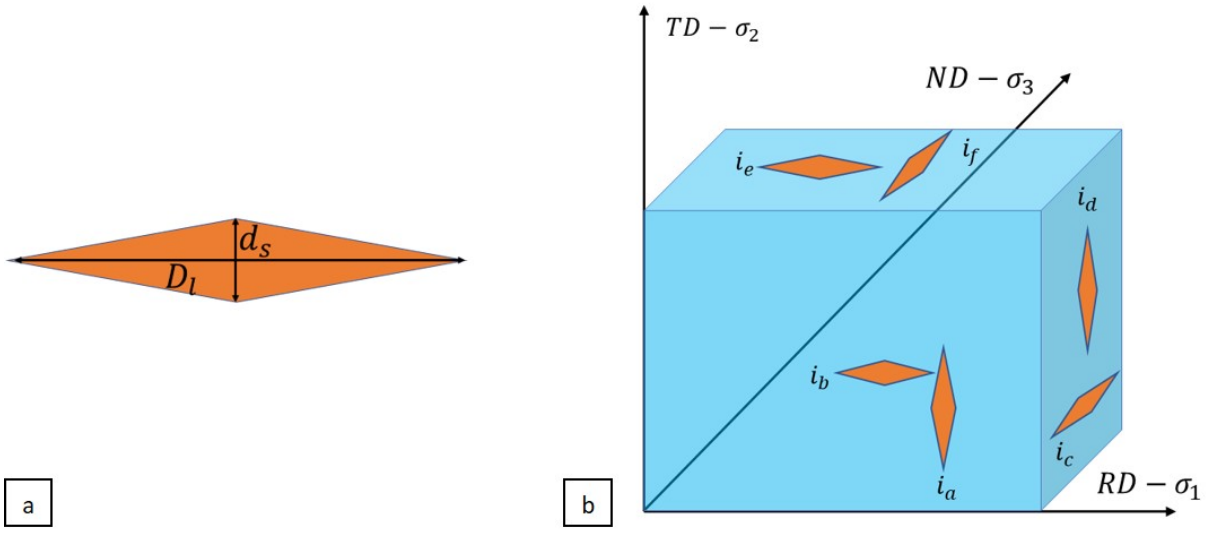

Figure 1: (a) The geometry of a Knoop indent showing lengths of short diagonal d_s and long diagonal D_l and (b) the orientation of six Knoop indentations i_a, i_b, i_c, i_d, i_e and i_f with D_l and d_s along RD (Rolling direction), TD (Transverse direction) and ND (Normal direction).

The ratio of plastic strain underneath the Knoop indenter along the long and short diagonal is assumed proportional to the inverse of the ratio of the length of the diagonals, i.e. $d\varepsilon^p_{D_l}/d\varepsilon^p_{d_s} = d_s/D_l = 1/7$ as shown in figure 1a. This results from the plastic deformation (displacement of substrate) along the diagonals of a penetrating Knoop indenter follows the projected length the edges of the faces of the indenter in contact with the substrate. Following the work done in [21], the diagonals of the Knoop indenters are oriented along the principal coordinate direction which are also aligned along the axes of anisotropy (RD, TD and ND). In the analysis, the axes of anisotropy for the measured specimen are supposed to be known in advance. So, the sides of the Knoop indenter can be aligned with the anisotropy direction. This is the case for six possible indentations namely i_a, i_b, i_c, i_d, i_e and i_f as shown in figure 1b. In plane-stress condition the yield criterion is expressed in terms of principal

stresses σ_1 and σ_2. Hence the strain ratios of the indentations i_a and i_b corresponding to the $\sigma_1 - \sigma_2$ plane are taken as 1/7 and 7. The other strain ratios corresponding to the indentations i_c, i_d, i_e and i_f are obtained from volume constancy, i.e. $d\varepsilon_1^p + d\varepsilon_2^p + d\varepsilon_3^p = 0$. The strain ratios on the $\sigma_1 - \sigma_2$ plane are given in equation 3.1 as a vector $\boldsymbol{B}$ using the ratio $\delta = 7$. By using the associated flow rule the expression for the strain ratio vector $\boldsymbol{B}$ has been expanded in equation 3.2 following which the stress ratio vector, i.e. the ratio of principal stresses in plane stress-plane $\boldsymbol{\alpha} = \sigma_2/\sigma_1$ for each indentation $(i_a - i_f)$ has been expressed in terms of Lankford coefficients, and strain ratio vector $\boldsymbol{B}$. The expression of $\boldsymbol{\alpha}$ in equation 3.3 accounts for the anisotropy in the specimen characterized for its yield criterion parameters.

$$\boldsymbol{B} = \frac{d\boldsymbol{\varepsilon_2}}{d\boldsymbol{\varepsilon_1}} = \begin{bmatrix} B_a & B_b & B_c & B_d & B_e & B_f \end{bmatrix} = \begin{bmatrix} \frac{1}{\delta} & \delta & -\frac{\delta}{1+\delta} & -\frac{1}{1+\delta} & -\delta - 1 & -\frac{1+\delta}{\delta} \end{bmatrix} \tag{3.1}$$

$$B = \frac{d\varepsilon_2}{d\varepsilon_1} = \frac{\frac{\partial f}{\partial \sigma_2}}{\frac{\partial f}{\partial \sigma_1}} = \frac{\frac{2R_0(R_{90}+1)}{R_{90}(R_0+1)}\sigma_2 - \frac{2R_0}{R_0+1}\sigma_1}{2\sigma_1 - \frac{2R_0}{R_0+1}\sigma_2} \tag{3.2}$$

$$\Rightarrow \boldsymbol{\alpha} = \frac{\sigma_1}{\sigma_2} = \frac{R_0}{R_{90}} \frac{\boldsymbol{B}R_{90} + R_{90} + 1}{\boldsymbol{B}R_0 + \boldsymbol{B} + R_0} \tag{3.3}$$

2.4 Plotting points on $\sigma_1 - \sigma_2$ plane from KHN data.

The Knoop hardness number is taken proportional to the deviatoric shearing stress on the octahedral plane. Therefore, the KHN is assumed to be equivalent to the equivalent flow stress (uniaxial yield stress) in plane stress as explained in [22] and is in agreement with [43]. For the Hill's 48 yield criterion the equivalent stress in plane stress condition is given as the uniaxial yield stress in the (rolling direction) principal axis 1, σ_1^y. By equating the Knoop hardness number with uniaxial yield stress ($KHN \sim \sigma_1^y$), equation 4.1 can be obtained. By expressing equation 4.1 in terms of ratios of σ_1 and σ_2, i.e. α for each indentation i_a, i_b, i_c, i_d, i_e and i_f the expressions for the points (coordinates) on the KHN yield locus are obtained in the $\sigma_1 - \sigma_2$ plane as given in equation 4.2.

$$KHN \sim \sqrt{\sigma_1^2 - \frac{2R_0}{R_0+1}\sigma_1\sigma_2 + \frac{R_0\,(R_{90}+1)}{R_{90}\,(R_0+1)}\sigma_{\,2}^{\,2}} \tag{4.1}$$

$$\begin{aligned} &\sigma_1 \sim \frac{\alpha_i KHN_i}{\sqrt{(C_1 - C_2\alpha_i + \alpha_i^2)}}, \sigma_2 \sim \pm\frac{KHN_i}{\sqrt{(C_1 - C_2\alpha_i + \alpha_i^2)}}\ \forall\ i\ \epsilon\ i_a, i_b, i_c, i_d, i_e, i_f\ \forall \\ &C_1 = \frac{R_0\,(R_{90}+1)}{R_{90}\,(R_0+1)},\ C_2 = \frac{2R_0}{R_0+1} = 2C_0 \end{aligned} \tag{4.2}$$

The Knoop hardness number (KHN) is measured using the dimensions of the indentation mark as shown in figure 1a. The KHN is given as the ratio of the applied load P and the area of the indentation A_c. The area of the indent is given is terms of the major diagonal length D_l of the indentation mark and a constant factor $C_K = 0.070279$. For the Knoop indenter, the contact area is given in terms of the indentation depth h as $A = 64.55h^2$. Using the relationship between the indentation depth h and major diagonal length as $D = 30.514h$, KHN is given in terms of h in equation 5.1 in Kgf/mm^2 units and in terms of h and D in equation 5.2 in GPa units [29]. The Young's modulus E of the specimen is calculated from the elastic recovery of the indented material during unloading of the indenter [45]. However, the elastic recovery along the shorter diagonal of the Knoop indenter is higher compared to that of the longer diagonal of the Knoop indenter [30]. The difference in the recovered (final) contact length ratio and the

maximum contact length 7.114 is proportional to the ratio $KHN[GPa]/E$. Hence, the Young's modulus of the specimen can be calculated by equation 5.3 using a geometry factor of 0.45 [30] and [46].

$$KHN = \frac{P}{A_c} \Rightarrow KHN = 14.229\frac{P\,[Kgf]}{D_l^2\,[mm^2]} \tag{5.1}$$

$$\Rightarrow KHN\,[GPa] = 0.13944\frac{P\,[N]}{D_l^2\,[mm^2]} = 0.015492\frac{P\,[mN]}{h^2\,[\mu m^2]} \tag{5.2}$$

$$\frac{d_s}{D_l} = \frac{1}{7.114} - 0.45\frac{KHN}{E} \tag{5.3}$$

2.5 Optimizing the yield parameters based on KHN-data points

The yield parameters R_0, R_{90} and σ_y obtained for the yield locus fitting the KHN based points for all six orientations plotted in the $\sigma_1 - \sigma_2$ plane (equation 4.2) is optimized by minimizing the distance between the yield locus and the KHN based points in the $\sigma_1 - \sigma_2$ plane. The distance between the KHN data points ($\sigma_1,\ \sigma_2$) and the yield locus is measured along a straight line using either of the two methods described below. In both the methods, a linear strain path is assumed for the Knoop indentation to find the intersection of the KHN data points with yield locus as shown in figure 2.

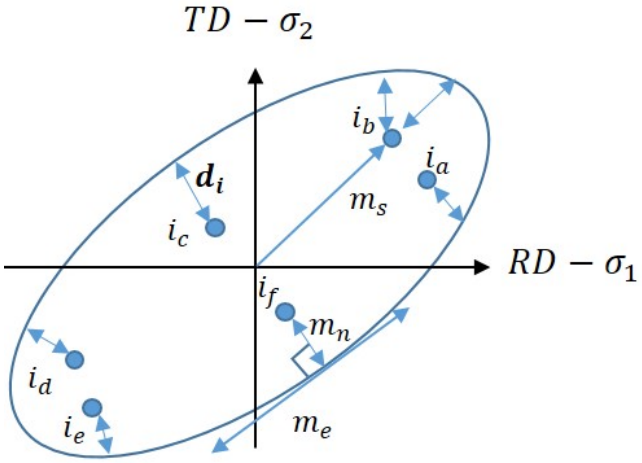

Figure 2: Minimization of distance between the points plotted in the plane-stress plane and the yield locus obtained from the values of R_0, R_{90} and σ_y.

The distance between the points plotted using equation 4.2 from the KHN-data ($\sigma_1,\ \sigma_2$) and the yield locus plotted from R_0 and R_{90} values obtained by solving the equation for the ellipse in the $\sigma_1 - \sigma_2$ plane for the plotted KHN-data points is calculated by two methods. In the first method the shortest distance between the points and the yield locus is calculated taking the perpendicular line from the points and the intersection with the yield locus. The slope of the perpendicular line to the ellipse is given as m_n and the slope of the ellipse (yield locus) at the point of intersection is given as m_e as shown in figure 2. In the second method, the distance between the KHN points and the yield locus along the line through the origin and the KHN points intersecting the yield locus is minimized. The slope of the line passing through the origin of the plane-stress plane and the measured points using KHN data points is given as m_s as shown in figure 2. The point of intersection ($\sigma_1^{'},\ \sigma_2^{'}$) for the normal to the yield locus,

passing through the KHN-data point is given by solving equations 6.1 and 6.2. The point of intersection $(\sigma_1^{'},\ \sigma_2^{'})$ along the line from the origin to the KHN-data points by solving equations 6.2 and 6.3. The total distance $\boldsymbol{d}$ between the KHN-data points and the intersecting points on the yield locus is given as the norm of distance between the individual KHN points $d_i\ (\sigma_1,\ \sigma_2)$ and the points of intersection $(\sigma_1^{'},\ \sigma_2^{'})$.

$$m_n m_e = -1\ \forall m_n = \frac{\sigma_2^{'} - \sigma_2}{\sigma_1^{'} - \sigma_1},\quad m_e = \frac{d\sigma_2^{'}}{d\sigma_1^{'}} = -\frac{\frac{\partial f}{\partial \sigma_1^{'}}}{\frac{\partial f}{\partial \sigma_2^{'}}} = -\frac{2\sigma_1^{'} - \frac{2R}{R+1}\sigma_2^{'}}{\frac{2R(P+1)}{P(R+1)}\sigma_2^{'} - \frac{2R}{R+1}\sigma_1^{'}} = -\frac{\sigma_1^{'} - C_0\sigma_2^{'}}{C_1\sigma_2^{'} - C_0\sigma_1^{'}}$$
$$\Rightarrow C_1\left(\sigma_1^{'2} - \sigma_2^{'2}\right) + (1 - C_1)\,\sigma_1^{'}\sigma_2^{'} + \left(C_1\sigma_2^{'}\sigma_1 - \sigma_1^{'}\sigma_2\right) + C_0\left(\sigma_2^{'}\sigma_2 - \sigma_1^{'}\sigma_1\right) = 0 \tag{6.1}$$

$$\sigma_1^{'2} - 2C_0\sigma_1^{'}\sigma_2^{'} + C_1\sigma_2^{'2} - \sigma_1^{y2} = 0 \tag{6.2}$$

$$m_s = \frac{\sigma_2}{\sigma_1} = \frac{\sigma_2^{'}}{\sigma_1^{'}} \Rightarrow \sigma_2^{'} = m_s\sigma_1^{'} \tag{6.3}$$

$$d_i = \sqrt{\left(\sigma_1^{'} - \sigma_1\right)^2 + \left(\sigma_2^{'} - \sigma_2\right)^2} \Rightarrow \boldsymbol{d} = \|d_i\| = \sqrt{\sum_{i=1}^{6} d_i^2} \tag{6.4}$$

The values of $R_0,\ R_{90}$ and σ_y are chosen and changed such that the distance between the KHN-data points and the yield locus is minimized in the $\sigma_1 - \sigma_2$ plane as shown in figure 2. The optimization function selects various values of $R_0,\ R_{90}$ and σ_y using an objective function where distance d is minimized as further explained in figure 2. The KHN data for all 6 orientations are used to measure the coordinates in the $\sigma_1 - \sigma_2$ plane by taking an initial values of $R_0 = 1$ and $R_{90} = 1$. The initial value of R_0 and R_{90} are varied across a range of values until the distance between the points and the yield locus is minimized.

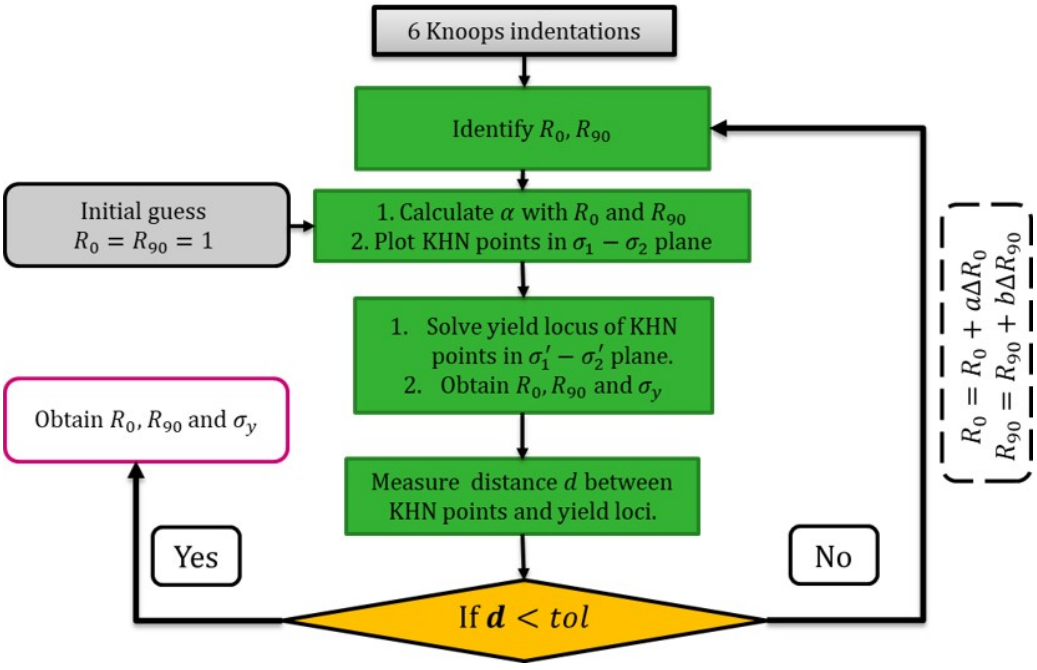

Figure 3: Flowchart showing the optimization algorithm to obtain values of $R_0,\ R_{90}$ and σ_y.

To further analyse the data, an algorithm to plot the yield locus from the KHN data and to calculate $R_0,\ R_{90}$ and σ_y has been developed and shown in figure 3. Initially, points are

plotted in the deviatoric plane from KHN, using equation 3.1 ($\alpha = \boldsymbol{B}$) and 3.3 ($R_0 = R_{90} = 1$) respectively. However, the yield locus obtained in the deviatoric plane or for that matter in the plane-stress plane with an isotropic assumption of $R_0 = R_{90} = 1$ is not accurate for anisotropic material. Also, typically sheet metal processes have used plane stress assumptions in expressing anisotropic material behaviour. Hence, an algorithm has been developed to optimize the value of R_0 and R_{90} and use the optimized values to plot the yield locus in the plane-stress plane. The algorithm minimizes the distance between the points plotted in the plane-stress plane using KHN-data. Then, the yield locus plotted in the plane stress plane using the optimized values of R_0, R_{90} and the value of σ_y.

3 Experimental procedure

Anton Paar's NHT^3 nano-indentation set-up along with the Knoop indenter is used to perform nano-indentation of both zinc coated and uncoated steel sheets. For higher loads Lecco's LM100 micro hardness test set up was used with a Knoop indenter. The geometry of the Knoop indenter is explained in the current section. Also metallographic preparation of steel sheets has been done prior to the indentation as explained in this section. The polished sheets are also used for EBSD (electron backscatter diffraction) analysis in SEM (scanning electron microscopy) to study the grain size and grain orientation in the sheets. The surface of the specimen is measured using a confocal microscope for its roughness after polishing.

3.1 Preparation of specimens

Knoop indentation based characterization has been done on low carbon DC04 steel sheets and zinc coating on steel sheets. Prior to characterization polishing of the sheets is done which serves a two-fold purpose. The effect of friction on the maximum resolved deviatoric stress on the surface of the Knoop indenter is minimised by polishing. The aim is to equate the Knoop hardness to the deviatoric stress resulting in plastic flow of the sheet due to indentation. By comparing the size of the indent with the grain size the indentation loads are adjusted such that the indentation measurements are done for multiple grains.

Both the DC04 steel sheet and the zinc coated steel sheets have been obtained from cold rolling mills with a marked rolling direction. They have been cut into rectangular sheets of different sizes for polishing of the surface and the cross-section. Rectangular sheets of length $10mm$ and with $15mm$ with the rolling direction along the length have been laser cut from the rolled sheets and used for polishing the surface. The cross section of rectangular sheets of length $10mm$ cut along transverse direction of length 15mm cut along rolling direction and width 2.5 mm width have been polished as well. The surface of the 10×15 mm sheets and the cross-section of the 10×2.5 mm and 15×2.5 mm are hot mounted using a bakelite disc of 25 mm diameter for the metallographic preparation.

An automatic polishing machine was used to polish the mounted bakelite discs. The following polishing steps are used for the surface and cross-section of the DC04 steel sheets. Grinding of the steel sheets is done initially using 220 grade silicon carbide paper at 25N load and 300rpm for 3 minutes using water as lubricant. Further grinding was done using diamond suspension of $9\mu m$ particle size at 40N load and 150rpm for 5 minutes. The grinding steps removed unevenness on the surface of the steel sheet. Further polishing was done in three steps. Diamond suspensions with $3\mu m$ and $1\mu m$ particle sizes were used at 20N load 150rpm

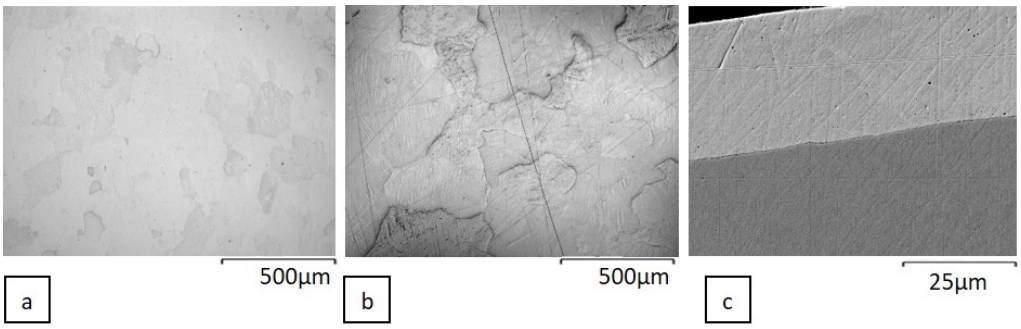

Figure 4: Surface of the polished and etched (a) DC04 steel sheet and (b) zinc coating on steel sheet at 20x magnification seen using confocal microscopy and (c) cross-section of the zinc coated steel sheet at 1900x magnification seen using SEM.

for 4 minutes. For the final etching step, a silica suspension of 0.04 μm was used at 15N load 150rpm for 3 minutes. This results in a surface roughness of 20nm on the steel surface as shown in figure 4a.

The polishing of the zinc coating using similar steps is challenging due to the softness of the coating, the shrinkage gap between the coating and the bakelite resin mount and the reaction of water with the coating resulting in discoloration. Hence water and water based lubricants are only used in the initial grinding of the zinc coating cross-section using 320 grade sandpaper at 300 rpm and 9μm particle size diamond suspension at 150rpm both at 30N load for 4 minutes respectively. To avoid the reaction of water, an alcohol based lubricant with diamond slurries of 3μm and 1μm are applied at 25N and 20N at 150rpm for 4-6 minutes respectively. The final etching of the zinc coating was done using de-agglomerated gamma alumina powder of 0.05μm mixed with Ethanol denatured with iso-propyl alcohol at 15N and 150rpm for 2 minutes. In order to polish the surface of the zinc coating on the steel sheet without removing the soft zinc coating, the grinding steps are avoided and only polishing and etching steps are followed similar to that of the zinc coating cross-section. The polished surface and cross-section of the zinc coating is shown in figure 4b and 4c respectively. The size and thickness of the zinc grains can be estimated to be around 100-200μm and 10-20μm from figure 4b and 4c respectively. The slip deformation marks due to rolling process can be seen on the zinc grains in figure 4b.

3.2 Indentation test set-up

Anton Paar's NHT^3 nano-indentation set up has been used to perform indentation based characterization of the DC04 and zinc coated specimen as shown in figure 5a. Nano indentation is a depth sensing indentation technique where the applied load and the penetration depth of the indenter into the specimen are recorded and used to determine the mechanical properties of the test specimen [47]. The force is applied during indentation by a piezo-electric actuator with a feedback control. In the current work, the Nano-indentation tester can apply a load up to a maximum force of 500 mN at a resolution of 0.02 μN and a maximum penetration depth of 200 μm at a resolution of 0.01nm. The Nano-indentation tester used, has a noise floor value of $\pm 0.5 \mu N$ for load controlled indentation which indicates the maximum resolution by which noise is precisely measured [48]. The schematic of the Nano-indentation test set-up and the Knoop indenter tip is shown in figure 5a and 5b.

In a depth sensing nano-indentation technique [45] the hardness and the elastic modulus of the specimen are measured using the loading and unloading curves respectively as shown in figure

6b. During loading the load is increased to the set load P_m for a time duration of $30s$. At maximum load P_m the load is kept constant for a dwell time duration of $10s$ to avoid creep effects. The unloading is done at a similar rate as loading for a duration of $30s$. The loading and unloading sequence and the corresponding penetration depth is plotted in figure 7.1. The hardness of the specimen H_i is measured from the ratio of the applied load to the indentation area A_c which corresponds to the maximum penetration depth h_m as given in equation 7.1 for Knoop indenter. The unloading of the indenter is followed by elastic recovery of the substrate. The stiffness of the substrate system can be given as the slope of the unloading curve in figure 6b. The residual elastic modulus of the indenter substrate system E_r is calculated by equation 7.2. The elastic modulus of the substrate E_s is calculated from equation 7.3, given the elastic modulus value of the indenter E_i.

$$H_i = \frac{P_m}{A_c} \; \forall A_c = 65.44 h_m^2 \tag{7.1}$$

$$E_r = \frac{\sqrt{\pi}}{2}\frac{S}{A} \; \forall S = \frac{dP}{dh} \tag{7.2}$$

$$\frac{1}{E_r} = \frac{1-\nu_i^2}{E_i} + \frac{1-\nu_s^2}{E_s} \tag{7.3}$$

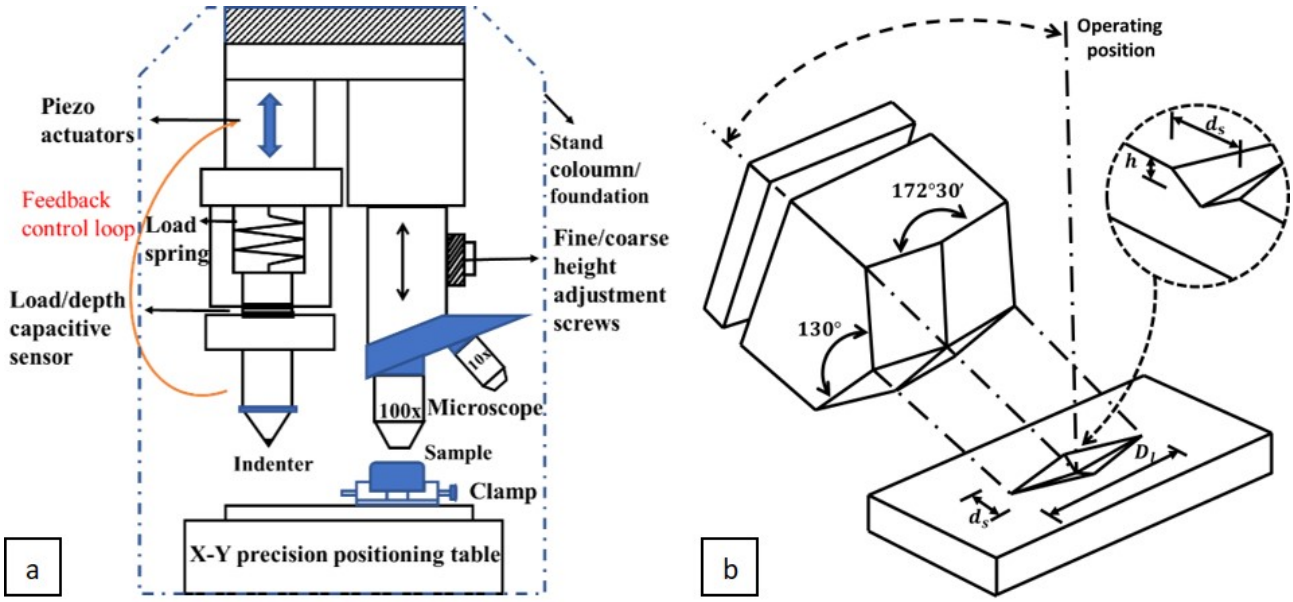

Figure 5: Schematic of the (a) the nano-indenter set up, (b) the Knoop indenter and the indent.

3.3 Calibration of indenter shape function

The schematic of an indent on the cross section of a coating is given in figure 7a. The applied load is maintained such that the size of the indent is less than the coating thickness ($20\mu m$). However, prior to indentation experiments the tip of the Knoop indenter must be calibrated for its tip shape by a shape function. The shape function of the indenter gives the projected area of the indentation at the contact depth h_c and is approximated by fitting polynomial function to the experimentally calibrated data. The shape function takes into account the curvature of the indenter tip in measurement of the projected contact area. By indenting the calibrated fused silica specimen and curve-fitting the experimental data as shown in figure 7b, the shape function of the Knoop indenter in nano-indentation was obtained with equation 8 and implemented in the calibration file of the nano-indenter for Knoop indentation.

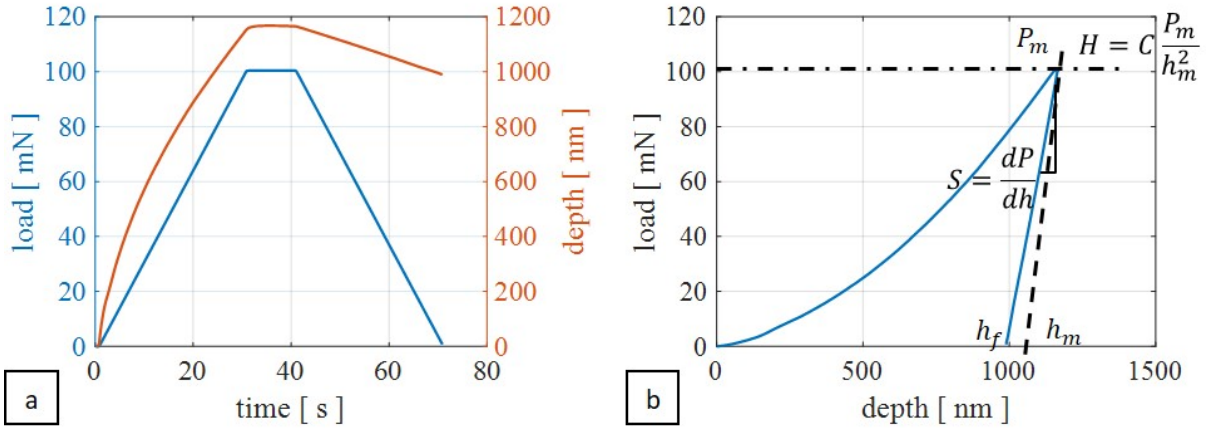

Figure 6: (a) Loading and penetration curves for Nano-indentation using Knoop indentation (b) to obtain hardness and stiffness from the load-depth curve [47].

For very large loads in micro-hardness measurement methods, where the elastic recovery is negligible compared to the indent size, the hardness can be measured by the final indent size after indentation. However, the KHN is measured with the depth sensing method at loads of 10-100mN by equation 7.1.

$$A_c = 97.77h_c^2 + 5.57 \times 10^{-6}h_c + 5 \times 10^{-14} \tag{8}$$

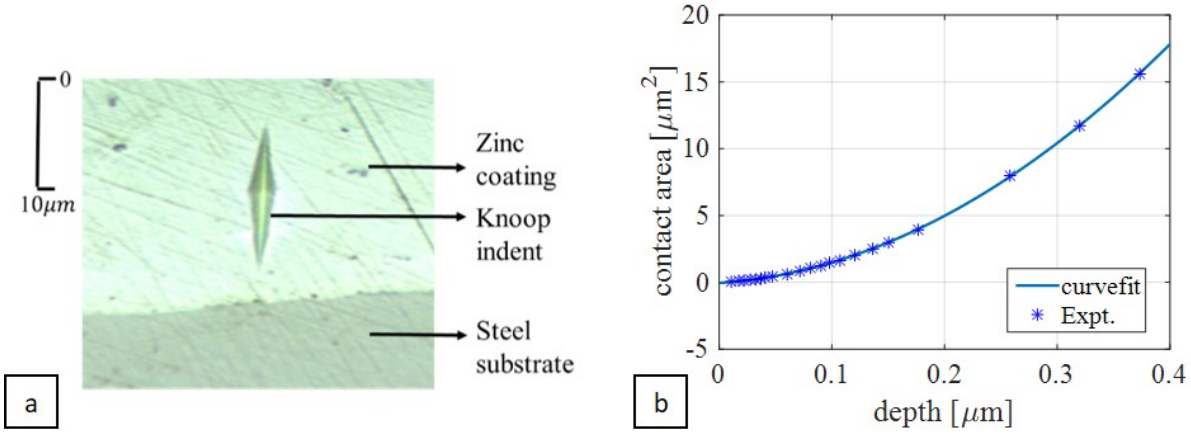

Figure 7: (a) Schematic of Knoop indent in the coated cross-section. (b)Fitting of the contact areas obtained for various penetration depths in calibration of shape function of the tip of the Knoop indenter.

4 Results and discussion

The grain size and orientations of the DC04 steel sheet and zinc coated steel sheet have been studied using SEM with EBSD analysis. Based on the grain size, the loads and distribution of in the Knoop indentations has been varied such that the anisotropy at the crystal scale is minimized. The grain orientations are also helpful in understanding the slip systems and the anisotropy in the grains with respect to rolling process.

The Knoop hardness number is measured for all 6 orientations for both the DC04 steel sheet and the zinc coating on the steel sheet. The six orientation namely i_a, i_b, i_c, i_d, i_e and i_f correspond to the orientation of the longer diagonal D_l and the shorter diagonal d_s along the anisotropy axes rolling direction RD, transverse direction TD and normal direction ND. Hence a given orientation, for instance can be written as $ND-rd$ where the long diagonal D_l is oriented along the normal direction ND and the shorter diagonal d_s is oriented along the rolling direction rd (RD). The results are plotted in the plane-stress plane. The distance between the plotted points and the yield locus $\boldsymbol{d}$ is minimized along the slope m_s. Then the anisotropy parameters are optimized using the algorithm in section 2.5 and used to plot the yield locus in plane stress plane. The KHN-based yield curve and anisotropic parameters have been validated with the yield curve and anisotropic parameters obtained using bulk tests.

4.1 Grain size and orientation of DC04 steel and zinc coating

The cross section of the zinc coated steel substrate and surface of the zinc coating showing the individual grains is given in figure 8. The average grain size of the zinc coating can be estimated to be around 100-200μm. It can be seen that the zinc grains are aligned as pancakes with a thickness of 20μm. It can be deduced from figure 8a and 8b that the size of the grains is typically in the order of the size of the Knoop indent (see figure 7a). If the grain size is larger than the indentation size, then the grain size and orientation has a major effect on the properties obtained from the indentation [41]. Hence larger loads are chosen for Nano-indentation keeping in mind the coating thickness for zinc coated specimens. Furthermore, multiple indentations (20-50 in number) have been performed as a matrix spread out over a region of the specimen and the average of the data obtained from the indentation is taken. This helps in averaging the effect of local grain orientation and size on the data obtained from the Knoop indentation.

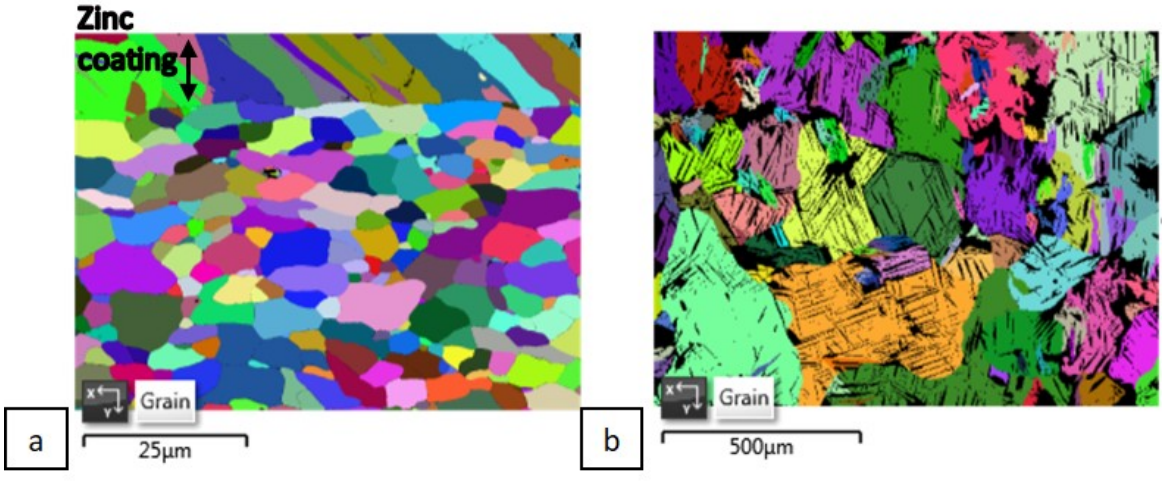

Figure 8: (a) Image of the grains in the (a) cross section of the zinc coating and (b) surface of the zinc coating on steel sheet after polishing and etching as seen in the backscattered image in EBSD analysis.

Figure 9b shows the Euler angles in the inverse pole figure (IPF Z) map of the SEM scan of the area shown in figure 8b. The zinc grains are mostly oriented along their (*hcp* crystals) c axis almost normal to the sheet plane. However certain grains can be seen elongated and aligned along the rolling direction in figure 9b. Multiple pyramidal slips and twins can be seen throughout the grain matrix as well. The deformation of the zinc grains during the

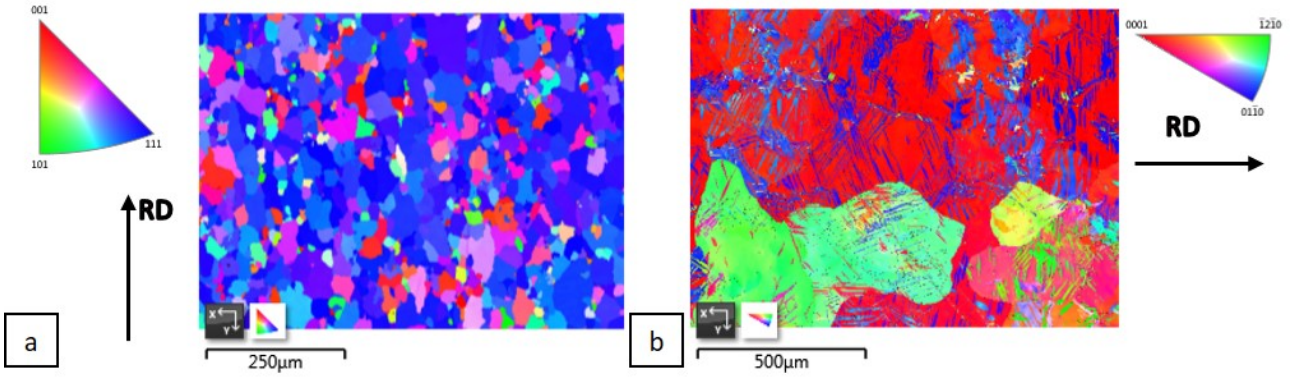

Figure 9: Image of the inverse pole figures (IPF Z) of the grains in the surface of the (a) DC04 steel sheet and the (b) zinc coating on steel sheet after polishing and etching as seen in the EBSD analysis.

(temper/cold) rolling process orients the zinc grains in a preferred direction as can be seen in figure 8a and IPF figure in figure 9b. The grain size of the steel substrate and the DC04 steel is much smaller around 10-20μm from figure 8a and 9a. The DC04 steel grains (*bcc* (body centred cubic) crystals) are predominantly aligned with their axis along the 111 direction.

4.2 Yield locus of DC04 steel

The hardness of the DC04 steel sheet specimen was measured for each of the six orientations using 20 measurements. The average values of the Knoop hardness numbers for each six indentations were plotted for 50g load in figure 10a. A maximum load of 50g equivalent to 490.05mN was applied using a Knoop indenter to avoid any grain effects on yield behaviour of the DC04 steel. Multiple indentations have been done, in an indentation matrix shown in figure 10b. The size of the Knoop indentation has been measured by observing them under a confocal microscope. The length of the long diagonal D_l, short diagonal d_s and indentation depth h of the Knoop indent mark is measured from the height profile of the indent as shown in figure 10c. The symbols in the bar plots below represent the orientation of the longer and shorter diagonals of the Knoop indenter along the axis of anisotropy, e.g. the $ND - rd$ represents the longer diagonal D_l along the normal direction (N) and shorter diagonal d_s along the rolling direction (r).

The yield locus of the DC04 steel sheet is initially plotted in the deviatoric plane as shown in figure 11. By assuming the Levy's Mises criteria for isotropic materials, the stress ratio is taken equal to the strain ratios from equation 3.1 ($\alpha = \boldsymbol{B}$). The six points i_a, i_b, i_c, i_d, i_e and i_f corresponding to six indentation orientations are scaled according to the Knoop hardness number given in table 1. However, the anisotropic parameters obtained from the deviatoric yield locus are typically the same as those obtained from bulk tests for DC04 steel sheet [49]. Hence, the yield locus is plotted in the plane-stress plane and optimised to obtain the anisotropic parameters.

The initial KHN-data points are plotted in the plane-stress plane by taking initial values of $R_0 = \mathrm{R}_{90} = 1$. The yield locus is solved for the plotted points from which values of R_0, R_{90} and σ_y are obtained. The values of R_0 and R_{90} are used to correct and re-plot the yield locus until the difference in the distance between iterated KHN-data points and the yield loci from the values of modified R_0, R_{90} and σ_y is below a specified tolerance. The optimized KHN-yield

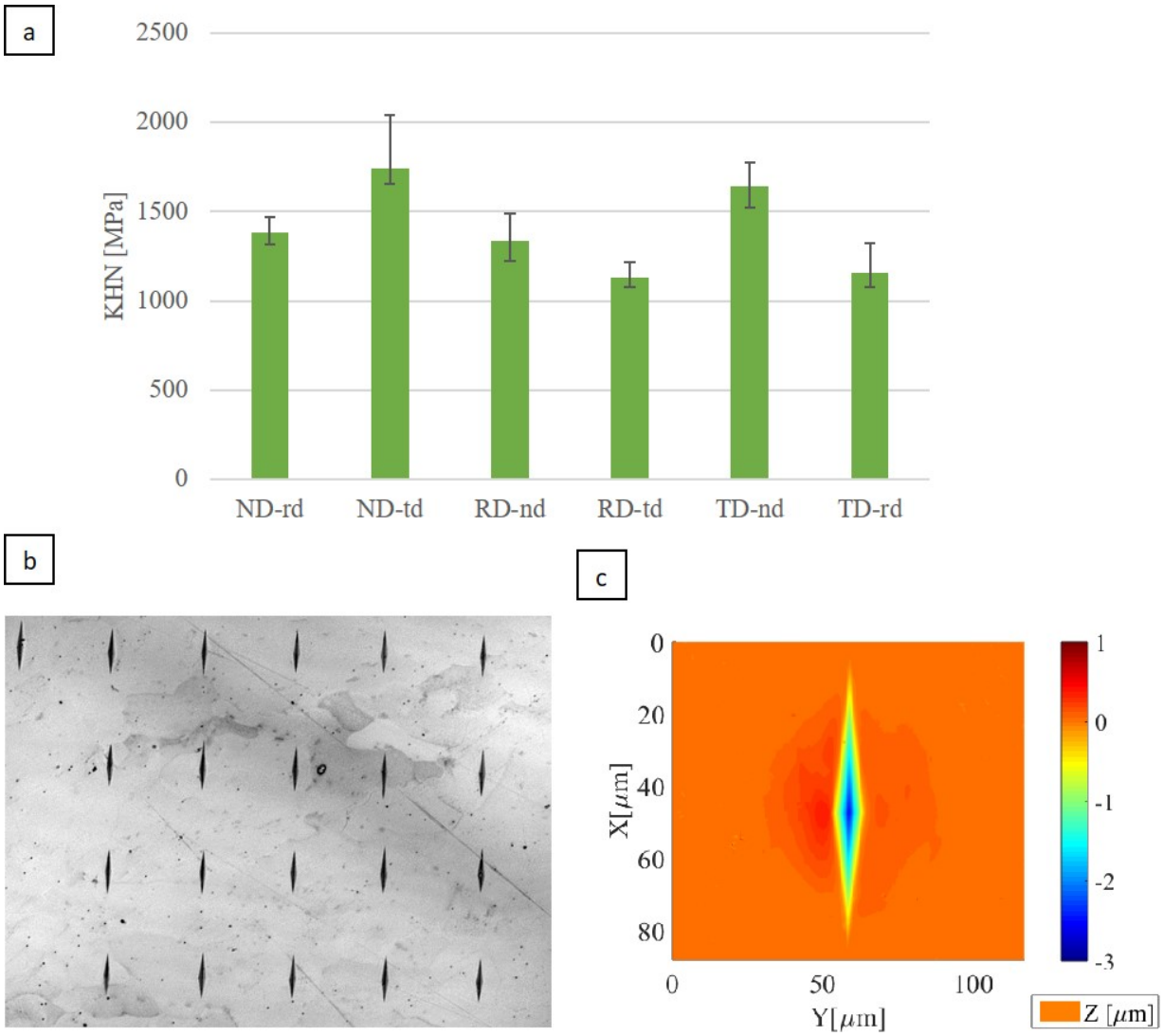

Figure 10: (a) Mean Knoop hardness number for indentations with six different orientations on DC04 steel sheet at 491mN load. (b) Image of matrix of Knoop indents at 20 mN load and (c) the height profile and size of the Knoop indent at 50mN load.

locus is plotted in the plane-stress plane in figure 12 and its optimized R_0, R_{90} and σ_y are listed in table 1 and compared with those obtained from the bulk loading tests of DC04 steel [49]. The close agreement in both the methods, sets the possibility of using Knoop (Nano-) indentation with the developed algorithm given in figure 12 to characterize the yield locus for thin, zinc coatings of galvanized steel sheets [41].

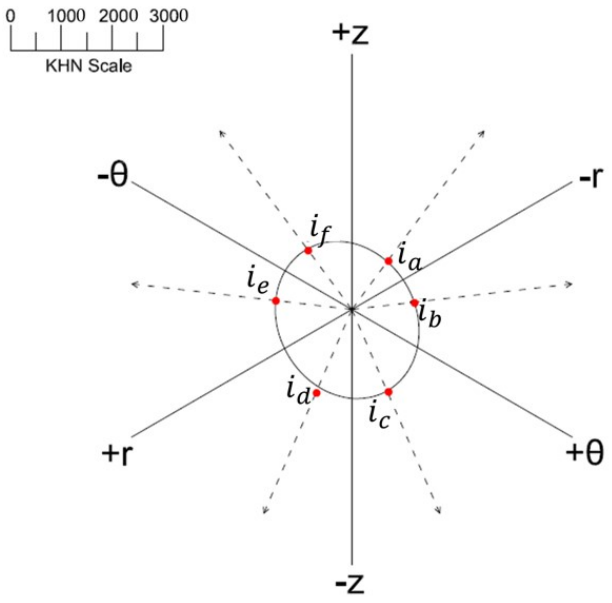

Figure 11: Yield locus for DC04 steel sheet in the deviatoric plane in the rolling direction z, transverse direction θ and normal direction r with KHN scale in MPa.

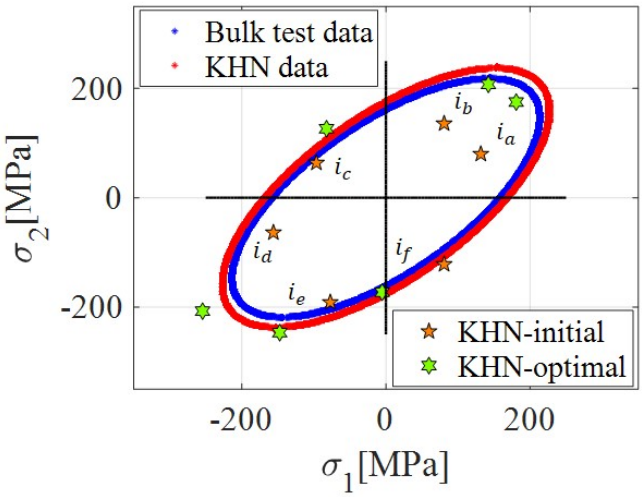

Figure 12: The yield loci obtained from KHN data on the plane-stress plane optimised for anisotropy and compared with that obtained with bulk tests on DC04 steel sheet.

Table 1: Knoop hardness number and Yield criteria parameters for DC04 steel sheet [49].

KHN-orientation	Value[$\boldsymbol{kgf/mm^2}$]	Yield criteria parameters	Value
KHN_{i_a}	118.25	R_0^{bulk}	1.93
KHN_{i_b}	115.1	R_{90}^{bulk}	2.21
KHN_{i_c}	177.35	σ_y^{bulk}	157.8 MPa
KHN_{i_d}	167.4	R_0^{KHN}	1.8
KHN_{i_e}	136.55	R_{90}^{KHN}	2.34
KHN_{i_f}	141.35	σ_y^{KHN}	168.5 MPa

4.3 Yield locus of Zinc coating

Multiple indentations have also been performed on the cross-sections of the zinc coating as shown in the figure 13b and 13c. The size of the indents for indentation along the cross-section of coating at higher loads ($> 50\ mN$) exceeds the thickness of the coating cross-section. Hence, the indentation load is taken as 20mN in order to keep the indentation size well within the coating thickness of 20 μm as shown in figure 13b. The length of the longer diagonal for the 20mN load can be seen as 10-12μm in figure 13c which is lower than the average coating thickness of 20μm. This corresponds to a penetration depth of $h = D_l/30$ which is approximately 0.4μm. For such low penetration depth, the plastic flow along the coating thickness direction which is also along the longer diagonal is minimal. The plastic flow occurs along the short diagonal which is along the coating. Therefore, it can be concluded that for indentations with 20mN loads along the coating cross section, the effect of substrate mechanical properties is minimal. Furthermore, the plastic flow component under the indenter along the penetration direction does not feel substrate effect for indentation along the coating cross section.

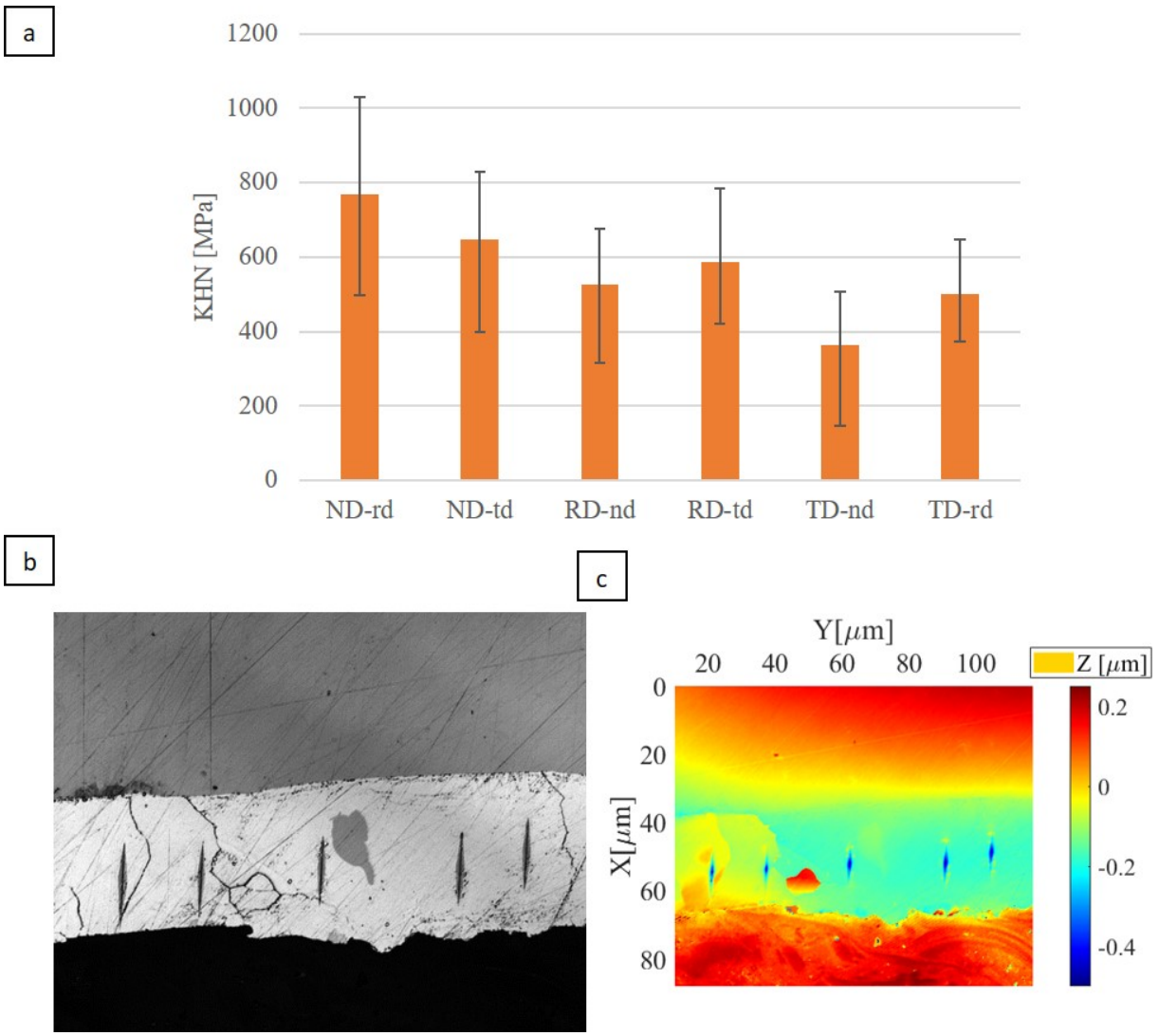

Figure 13: (a) Mean Knoop hardness number for indentations with six different orientations on zinc coated steel sheet at two different loads. (b) Image of matrix of Knoop indents and (c) the height profile and size of the Knoop indents at the cross section of the zinc coating at 50 mN load.

The value of Knoop hardness value for all six orientations is plotted for three different loads in figure 13a. A large deviation in the hardness values is obtained for each of the six indentation orientation resulting from the effect of the orientation of the zinc grains on indentation hardness (see figure 13a). The average value of the measurements of the indents at the same orientation are taken to reduce the local effects of anisotropy due to grain size and orientation. The average of the hardness values (KHN) obtained from indents with an applied load of 20 mN is used to calculate the yield locus of the zinc coating in order to avoid effects of coating-substrate interface, properties of the steel substrate, individual grain orientation and grain boundaries (see figure 13b and 13c). The anisotropy determined using Knoop indentation accounts for the anisotropy in the zinc coating attributed to the hcp crystal structure of the zinc as well as the deformation textures induced in the zinc coating by the temper rolling of the galvanized steel sheet.

Initially the yield locus for the KHN data is plotted in the deviatoric plane as shown in figure 14. The points on the deviatoric plane are plotted along the lines following the stress ratios from equation 3.1 ($\alpha = \boldsymbol{B}$) and scaled according to the KHN data. Comparing the yield locus of the DC04 steel and the zinc coating from figure 11 and figure 14, it can be said the zinc coating has higher induced anisotropy compared to the DC04 steel sheet. The anisotropy in the plastic deformation of the zinc coating and the steel is induced from the rolling process. The difference in the size and amount of zinc along the thickness and surface plane could also be attributed to the anisotropy in the mechanical properties of zinc coatings. Additional anisotropy is inherent to the zinc grains due to their hcp (hexagonal closed pack) crystal structure. The difference in the critical resolved shear stress for the various slip systems in the zinc grains, e.g. basal slip, pyramidal slip and twinning results in its anisotropy [41] and [50].

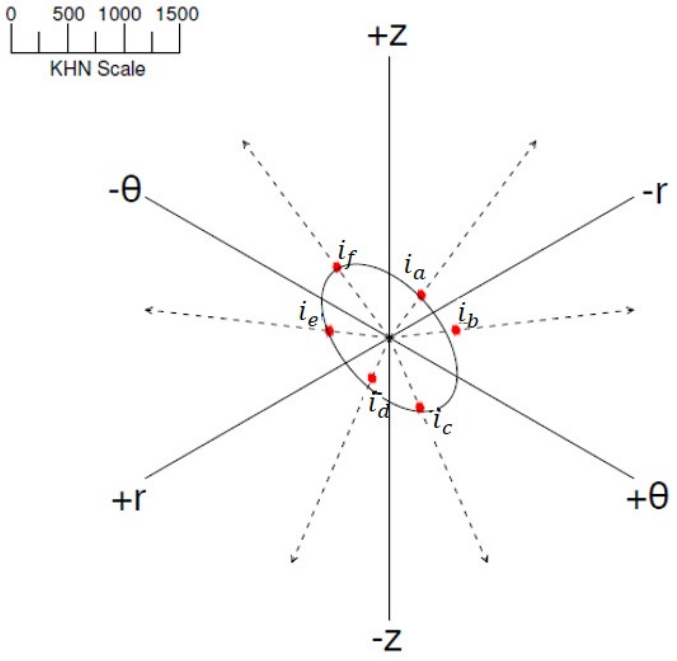

Figure 14: Yield locus for zinc coating in the deviatoric plane in the rolling direction z, transverse direction θ and normal direction r with KHN scale in MPa.

After validating the yield locus obtained from the Knoop indentations of DC04 steel sheet with the bulk tests, the yield locus of zinc coating on steel sheets has been characterised by Knoop

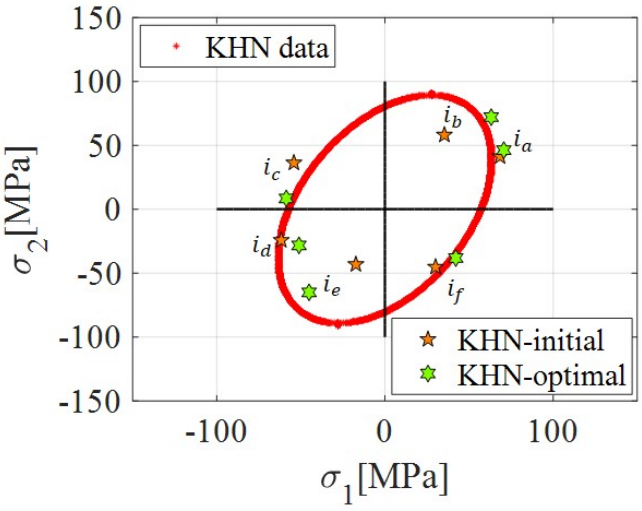

Figure 15: The yield loci obtained from KHN data on the plane-stress plane optimised for anisotropy on zinc coating on steel sheet.

indentation. The KHN data has been listed for the 6 orientations in table 2. The points are plotted in the plane stress $\sigma_1 - \sigma_2$ plane taking initial values of $R_0 = R_{90} = 1$ in figure 15. The values of R_0, R_{90} and σ_y are then varied (increased/decreased) using constants a and b as shown in the algorithm in figure 3. The distance d between the measured KHN-data points on the plane stress plane and the yield locus based on R_0, R_{90} and σ_y is computed. Finally, the optimized yield locus for the zinc coating on the steel sheet is plotted by optimizing the KHN-data points in figure 15. The parameters of the yield locus obtained using the procedure above are listed in table 2.

Table 2: Yield criteria parameters for zinc coating on steel sheet

KHN-orientation	Value $[\boldsymbol{kgf/mm^2}]$	Yield criteria parameters	Value
KHN_{i_a}	44.7	R_0^{bulk}	-
KHN_{i_b}	68.2	R_{90}^{bulk}	-
KHN_{i_c}	68.0	σ_y [41] and [51]	55-115 MPa
KHN_{i_d}	43.9	R_0^{KHN}	0.45
KHN_{i_e}	64.9	R_{90}^{KHN}	1.56
KHN_{i_f}	83.4	σ_y^{KHN}	57.7-81.7 MPa

Using equation 2.2 and 2.5 the parameters for the Hill's quadratic yield criteria of the zinc coating can be obtained from the R values as $F = 0.2$, $G = 0.69$, $H = 0.31$. The values of F, G and H are implemented in the Hill's quadratic equation in principal stress coordinates given in equation 1.3. The constants of the shear stress in the Hill's quadratic equation in equation 1.1 are taken $N = 1.5$, $M = 1.5$ and $L = 1.5$ assuming isotropy. As of now the value of R_{45} (Lankford coefficient/strain ratio at 45° orientation) is required to obtain the value of N has not been obtained from the Knoop indentation method listed above.

The objective of the current work is developing a new indentation based method to characterize the yield locus for metallic coatings with rolling induced anisotropy. To elaborate on this method, as an example hot dip galvanized, temper rolled zinc coating have been used. The

yield locus of the zinc coating has been successfully plotted from Knoop hardness data using the above method after an initial validation of the yield locus by Knoop indentation with the yield locus by standard tests for an uncoated cold rolled DC04 steel specimen.

5 Conclusion

To conclude, a method to obtain the yield parameters and to plot the anisotropic yield locus based on Knoop indentation has been developed. The yield parameters are optimized to plot the best fit yield locus from the KHN data. The method has been implemented to plot the yield locus for DC04 steel sheet and validated against bulk tests. Both experimental characterization procedures have been shown to be in good agreement. The method has been extended to plot the yield locus of the zinc coating on steel sheet. The parameters for the Hill's quadratic yield criteria have been derived from the plotted yield locus of the zinc coating and can be used in modelling of material deformation behaviour in various numerical simulations.

Acknowledgment

This research was carried out under project number S22.1.14520a in the framework of the Partnership Program of the Materials innovation institute M2i (www.m2i.nl) and the Technology Foundation TTW (www.stw.nl), which is part of the Netherlands Organization for Scientific Research (www.nwo.nl). The authors would also like to thank ing. Erik de Vries from the University of Twente for setting the Knoop indenter in the indentation set-ups, Dr. ir. Mohammad Bazrafshan from University of Twente for discussions on the optimization algorithm and TATA steel Europe R&D, Ijmuiden for the provision of the data and parameters for the yield loci of the DC04 steel sheets.

Bibliography

[1] S. Suwas and R.K. Ray. "Deformation Textures". In: Crystallographic Texture of Materials. Springer, London, 2014, pp. 95–141. DOI: 10.1007/978-1-4471-6314-5_5.

[2] R. Hill. "A theory of the yielding and plastic flow of anisotropic metals". In: Proceedings of the Royal Society of London. Series A. Mathematical and Physical Sciences 193 (1948), pp. 281–297. DOI: 10.1098/rspa.1948.0045.

[3] R.V. Mises. "Mechanik der festen Körper im plastisch-deformablen Zustand". In: Nachrichten von der Gesellschaft der Wissenschaften zu Göttingen, Mathematisch-Physikalische Klasse 1913 (1913). Retrieved from http://eudml.org/doc/58894, pp. 582–592.

[4] H. Tresca. Mémoire sur l'écoulement des corps solides soumis à de fortes pressions. Imprimerie de Gauthier-Villars, Paris, 1864.

[5] W.F. Hosford. "A generalized isotropic yield criterion". In: Journal of Applied Mechanics 39 (1972), pp. 607–609. DOI: 10.1115/1.3422732.

[6] R. Hill. "Theoretical plasticity of textured aggregates". In: Mathematical Proceedings of the Cambridge Philosophical Society 85 (1979), pp. 179–191. DOI: 10.1017/S0305004100055596.

[7] H. Vegter, P. Drent, and H. Huetink. "A planar isotropic yield criterion based on mechanical testing at multi-axial stress states". In: In Proceedings of the fifth international conference on numerical methods in industrial forming processes. Ed. by International conference on numerical methods in industrial forming processes. 1995.

[8] H. Vegter and A.H. van den Boogaard. "A plane stress yield function for anisotropic sheet material by interpolation of biaxial stress states". In: International journal of plasticity 22 (2006), pp. 557–580. DOI: 10.1016/j.ijplas.2005.04.009.

[9] F. Barlat, J.W. Yoon, and O. Cazacu. "On linear transformations of stress tensors for the description of plastic anisotropy". In: International Journal of Plasticity 23 (2007), pp. 876–896. DOI: 10.1016/j.ijplas.2006.10.001.

[10] H. Vegter, C.H.L.J Ten Horn, Y. An, E.H. Atzema, H.H. Pijlman, T.H. van den Boogaard, and H. Huétink. "Characterisation and modelling of the plastic material behaviour and its application in sheet metal forming simulation". In: In Proceedings of VII International Conference on Computational Plasticity COMPLAS VII. Ed. by E. Oñate VII International Conference on Computational Plasticity COMPLAS VII and D.R.J. Owen. 2003.

[11] M. Rossi, F. Pierron, and M. tamborská. "Application of the virtual fields method to large strain anisotropic plasticity". In: International Journal of Solids and Structures 97 (2016), pp. 322–335. DOI: 10.1016/j.ijsolstr.2016.07.015.

[12] F. Pierron and M. Grédiac. The virtual fields method: extracting constitutive mechanical parameters from full-field deformation measurements. Springer, New York, NY, 2012. DOI: 10.1007/978-1-4614-1824-5.

[13] S.M. Kalkhoran. "Characterization of Anisotropic Plasticity in Material Systems Using Modified Indentation-Based Techniques". PhD thesis. Northeastern University, 2013. ISBN: 9781267835628.

[14] A. Yonezu, Y. Kuwahara, K. Yoneda, H. Hirakata, and K. Minoshima. "Estimation of the anisotropic plastic property using single spherical indentation–An FEM study". In: Computational Materials Science 47 (2009), pp. 611–619. DOI: 10.1016/j.commatsci.2009.10.003.

[15] A. Yonezu, K. Yoneda, H. Hirakata, M. Sakihara, and K. Minoshima. "A simple method to evaluate anisotropic plastic properties based on dimensionless function of single spherical indentation-Application to SiC whisker-reinforced aluminum alloy". In: Materials Science and Engineering: A 527 (2010), pp. 7646–7657. DOI: 10.1016/j.msea.2010.08.014.

[16] D. Tabor. The Hardness of Metals. Oxford university press, 2000. ISBN: 9780198507765.

[17] F. Knoop, C.G. Peters, and W.B. Emerson. "A sensitive pyramidal-diamond tool for indentation measurements". In: Journal of Research of the National Bureau of standards 23 (1939), p. 39.

[18] D.N French and D.A. Thomas. "Hardness anisotropy and slip in WC crystals". In: Transactions of the Metallurgical Society of AIME 233 (1965), pp. 950–952.

[19] F.W. Daniel and C.G Dunn. "The effect of orientation on Knoop hardness of single crystals of zinc and silicon ferrite". In: Transactions: American Society of Metals 41 (1949). NAID: 10016191481, pp. 419–442.

[20] P.L. Rittenhouse and M.L. Picklesimer. Comparison of Pole Figure Data Obtained by X-ray Diffraction and Microhardness Measurements on Zircaloy-2. Tech. rep. Oak Ridge National Lab., TN, 1965.

[21] R.G. Wheeler and D.R. Ireland. "Multiaxial plastic flow of Zircaloy-2 determined from hardness data". In: Electrochemical Technology (U.S.) Absorbed by J. Electrochem. Soc. 4 (1966), pp. 313–317.

[22] D. Lee, S. Jabara, and W.A. Backofen. "The Knoop-hardness yield loci for two titanium alloys". In: Transactions of the Metallurgical Society of AIME 115 (1967), pp. 172–175.

[23] D. Lee and W.A. Backofen. "An experimental determination of the yield locus for titanium and titanium-alloy sheet". In: Transactions of the Metallurgical Society of AIME 236 (1966), pp. 1077–1084.

[24] B.C. Wonsiewicz and W.W. Wilkening. "A Comparison of Conventional and Knoop-Hardness Yield Loci for Magnesium and Magnesium Alloys". In: Transactions of the Metallurgical Society of AIME 245 (1969), pp. 1313–1319.

[25] F. Larson and A. Zarkades. Properties of textured titanium alloys. Tech. rep. Retrieved from: https://apps.dtic.mil/dtic/tr/fulltext/u2/781884.pdf. Metals and ceramics information center Columbus OH, 1974.

[26] M.F. Amateau and W.D. Hanna. "Comparison of first quadrant yield loci for Ti-6Al-4V with those predicted by knoop hardness measurements". In: Metallurgical and Materials Transactions A 6 (1975), pp. 417–419. DOI: 10.1007/BF02667299.

[27] K.L. Murty and I. Charit. "Texture development and anisotropic deformation of zircaloys". In: Progress in nuclear energy 48 (2006), pp. 325–359. DOI: 10.1016/j.pnucene.2005.09.011.

[28] M. Nakatsuka and M. Nagai. "Reduction of plastic anisotropy of zircaloy cladding by neutron irradiation, (I) Yield loci obtained from Knoop hardness". In: Journal of Nuclear Science and Technology 24 (1987), pp. 832–838. DOI: 10.1080/18811248.1987.9735886.

[29] L. Riester, P.J. Blau, E. Lara-Curzio, and K. Breder. "Nanoindentation with a Knoop indenter". In: Thin Solid Films 377 (2000), pp. 635–639. DOI: 10.1016/S0040-6090(00)01298-0.

[30] L. Riester, T.J. Bell, and A.C. Fischer-Cripps. "Analysis of depth-sensing indentation tests with a Knoop indenter". In: Journal of Materials Research 16 (2001), pp. 1660–1667. DOI: 10.1557/JMR.2001.0230.

[31] A.E. Giannakopoulos and T. Zisis. "Analysis of Knoop indentation". In: International journal of Solids and Structures 48 (2011), pp. 175–190. DOI: 10.1016/j.ijsolstr.2010.09.014.

[32] T. Zisis and A.E. Giannakopoulos. "Analysis of Knoop indentation strain hardening effects". In: International journal of Solids and Structures 48 (2011), pp. 3217–3231. DOI: 10.1016/j.ijsolstr.2011.07.014.

[33] M.I Simões, A.X. Martins, J.M. Antunes, N.A. Sakharova, and M.C. Oliveiraand J.V. Fernandes. "Numerical Simulation Study of the Knoop Indentation Test". In: In Proceedings of the XI International Conference on Computational Plasticity. Fundamentals and Applications. Ed. by XI International Conference on Computational Plasticity. Fundamentals, E. Oñate Applications (COMPLAS XI), D.R.J. Owen, D. Peric, and B. Suárez. Accessed from https://www.researchgate.net/profile/M$_O$*liveira*3/*publication*/.

[34] M. Simões, J. Antunes, J. Fernandes, and N. Sakharova. "Numerical Simulation of the Depth-Sensing Indentation Test with Knoop Indenter". In: Metals 8 (2018), p. 885. DOI: 10.3390/met8110885.

[35] J. Zhang and M. Sakai. "Geometrical effect of pyramidal indenters on the elastoplastic contact behaviors of ceramics and metals". In: Materials Science and Engineering: A 381 (2004), pp. 62–70. DOI: 10.1016/j.msea.2004.04.015.

[36] G.B.Ghorbal, A. Tricoteaux, A. Thuault, G. Louis, and D. Chicot. "Mechanical characterization of brittle materials using instrumented indentation with Knoop indenter". In: Mechanics of Materials 108 (2017), pp. 58–67. DOI: 10.1016/j.mechmat.2017.03.009.

[37] A. Datye, L. Li, W. Zhang, Y. Wei, Y. Gao, and G.M. Pharr. "Extraction of anisotropic mechanical properties from nanoindentation of SiC-6H single crystals". In: Journal of Applied Mechanics 83 (2016), p. 091003. DOI: 10.1115/1.4033790.

[38] G. Li, X.Y. Long, S.S. Cui, Q.W. Huang, Z.P. Chen, and S.H. Tan. "Influence of zinc coating on anisotropic mechanical properties of hot dip galvanized steel sheet DP600". In: Journal of Physics: Conference Series 1063 (2018), p. 012164. DOI: 10.1088/1742-6596/1063/1/012164.

[39] N. Coni, M.L. Gipiela, A.S.C.M. D'Oliveira, and P.V.P. Marcondes. "Study of the mechanical properties of the hot dip galvanized steel and galvalumeő". In: Journal of the Brazilian Society of Mechanical Sciences and Engineering 31 (2009), pp. 319–326. DOI: 10.1590/S1678-58782009000400006.

[40] W. Wen, A.A. Becker, and W. Sun. "Determination of material properties of thin films and coatings using indentation tests: a review". In: Journal of Materials Science 52 (2017), pp. 12553–12573. DOI: 10.1007/s10853-017-1348-3.

[41] Y.T. Pei, G.M. Song, W.G. Sloof, and J.T.M. De Hosson. "A methodology to determine anisotropy effects in non-cubic coatings". In: Surface and Coatings Technology 201 (2007), pp. 6911–6919. DOI: 10.1016/j.surfcoat.2006.11.044.

[42] K. Ikegami. "Experimental plasticity on the anisotropy of metals". In: Mechanical Behavior of Anisotropic Solids/Comportment Méchanique des Solides Anisotropes. Springer, Dordrecht, 1982, pp. 201–242. DOI: 10.1007/978-94-009-6827-1/_14.

[43] W.F. Hosford. "Texture strengthening". In: Metals Eng Quart 6 (1966). ISSN 0026-0967, pp. 13–19.

[44] D. Banabic. "Anisotropy of sheet metal". In: Formability of metallic materials: plastic anisotropy, formability testing, forming limits. Springer, Berlin, 2000, pp. 119–172. DOI: 10.1007/978-3-662-04013-3_4.

[45] W.C. Oliver and G.M. Pharr. "An improved technique for determining hardness and elastic modulus using load and displacement sensing indentation experiments". In: Journal of materials research 7 (1992). 10.1557/JMR.1992.1564, pp. 1564–1583.

[46] D.B. Marshall, T. Noma, and A.G. Evans. "A Simple Method for Determining Elastic-Modulus–to-Hardness Ratios using Knoop Indentation Measurements". In: Journal of the American Ceramic Society 65 (1982), pp. c175–c176. DOI: 10.1111/j.1151-2916.1982.tb10357.x.

[47] A.C. Fischer-Cripps. "Depth-Sensing Indentation Testing". In: Introduction to Contact Mechanics. Springer, Boston, MA, 2007, pp. 189–199. DOI: 10.1007/978-0-387-68188-7_11.

[48] A.C. Fischer-Cripps. "Nanoindentation Test Instruments". In: Nanoindentation. Springer, New York, NY, 2004, pp. 178–194. DOI: 10.1007/978-0-387-22462-6_9.

[49] Y.G. An, E. Atzema, M. Workel, H. Vegter, L. Elliott, and J. Moerman. "A Comparison of Yield loci measured with mechanical tests and calculated from crystal plasticity for steel sheets". In: In Proceedings of the 1st International Conference on Super-high Strength Steels. Ed. by 1st International Conference on Super-high Strength Steels. Rome, 2005.

[50] R. Parisot, S. Forest, A.F. Gourgues, A. Pineau, and D. Mareuse. "Modeling the mechanical behavior of a multicrystalline zinc coating on a hot-dip galvanized steel sheet". In: Computational Materials Science 19 (2000), pp. 189–204. DOI: 10.1016/S0927-0256(00)00155-5.

[51] G.M. Song, J.T.M. De Hosson, W.G. Sloof, and Y.T. Pei. "Evaluation of interface adhesion of hot-dipped zinc coating on TRIP steel with tensile testing and finite element calculation". In: WIT Transactions on Engineering Sciences 91 (2015). 10.2495/SECM150011, pp. 3–14.

Paper F

Modelling of ploughing behaviour in soft metallic coatings using material point method

Tanmaya Mishra[1*], Matthijn de Rooij[1], Meghshyam Shisode[2], Javad Hazrati[2], and Dirk J. Schipper[1]

[1]Surface Technology and Tribology, Faculty of Engineering Technology, University of Twente, 7500 AE Enschede, the Netherlands
[2]Nonlinear Solid Mechanics, Faculty of Engineering Technology, University of Twente, 7500 AE Enschede, the Netherlands

Abstract

A coating layer is often present on engineering surfaces. An example is a zinc coating on steel sheet, this being a soft metallic coating on a hard substrate. To characterize the tribological behaviour of these engineered surfaces, it is necessary to understand the mechanical behaviour of the coating during ploughing. The material point method (MPM)-based ploughing model has been used to compute friction and the ploughed profile when an asperity is ploughing through a coated surface. An analytical ploughing model has also been used to study the effect of the thickness and hardness of the coating relative to the substrate on coefficient of friction using rigid-plastic material behaviour and its results have been compared with the MPM-model results. The MPM-based ploughing model has been experimentally validated and is shown to agree well with the ploughing experiments using rigid spherical indenters sliding through lubricated- zinc coated steel, uncoated steel and bulk zinc over a range of applied loads.

Keywords: Friction model, Galvanized steel, Ploughing, Coating, Material point method.

Nomenclature of symbols

A_{xy}	Projected contact area in the xy plane	a	Total contact radius
A_{yz}	Projected contact area in the yz plane	c	Related to the coating (subscript)
C_0	Proportionality constant for interfacial shear	d_p	Total ploughing depth
C_p	Proportionality constant for contact pressure	d_g	Groove depth
E	Young modulus	d	Penetration depth
F_n	Normal load/force on the indenter	f	Ratio of interfacial to bulk shear strength
H_{cs}	Effective hardness of the coated substrate	h_{pu}	Pile up height
H_c	Hardness of the coating	k_1	Fitting factor for effective hardness
H_s	Hardness of the substrate	k_0	Ratio of interfacial strength to hardness
$\tilde{H}$	Relative hardness of coating, H_c/H_s	m	Mass of particle
I	Identity matrix	n_P	Exponent of pressure
K	Bulk Modulus	n_v	Exponent of sliding velocity
P_{pl}	Contact pressure due to plastic deformation	n_T	Exponent of temperature
$\overline{P}$	Mean nominal contact pressure	q	Heat generated
R_a	Mean surface roughness	r	Radius of the indenter/asperity
R_q	Root mean squared surface roughness	s	Related to substrate (subscript)
T_0	Contact/ambient temperature	t	Thickness of the coating
V	Volume of particle	t_c	Coating thickness for transition in ploughing
ρ	Density of the material	v_i	Sliding velocity of the indenter
κ	Shear strength of the substrate (bulk)	x	Related to x axis (sub/superscript)
κ_t	Thermal conductivity	y	Related to y axis (sub/superscript)
τ_{sh}	Shear strength of the interface	z	Related to z axis (sub/superscript)
τ_{bl}	Shear strength of the boundary layer	cs	Related to coated-substrate (subscript)
σ_y	Yield/flow stress	pl	Related to plastic deformation (subscript)
σ_h	Hydrostatic stress	sh	Related to interfacial shear (subscript)
μ	Coefficient of friction	M	Volumetric change

1 Introduction

Zinc coatings are often applied on steel sheets in a molten zinc bath using continuous hot-dip galvanizing to improve their corrosion resistance and paintability. The presence of a zinc coating also affects the friction and wear behaviour of the galvanized sheets which are further used in deep-drawing, stamping and other forming processes [1], [2] and [3]. Both the thickness and the hardness of the zinc coating are critical for the tribological performance of the galvanized products [1]. In the production process, the thickness of the zinc coating is controlled by using air knives to remove the excess of zinc from the sheets drawn out from the zinc bath [4], while the hardness of the galvanized sheets is varied by alloying the zinc bath with various elements or by annealing the galvanized sheets [5].

During the loading and sliding of the forming tools and galvanized sheets against each other, the harder tool surface flattens the asperities of the softer sheet surface, while the hard tool asperities plough through the flattened sheet surface [6]. The friction force is therefore due to the plastic deformation of the substrate as well as the shearing of the interface [7]. The thickness of the coating and the hardness of the coating relative to the substrate determines the friction and wear mechanisms in a coated system [8]. Furthermore, soft metallic coatings have large scale localised plastic deformation resulting in coating fracture and abrasive wear, these phenomena studied using scratch testing at [9] and [10]. Hence, numerical ploughing models are critical in computing and understanding friction and wear.

The effect of the properties of the substrate and the coating on the plastic deformation in coated systems have been studied by modelling both indentation and scratching using finite element (FE) models [11] and [8]. The effect of the ratio of the yield strength of the coating relative to the substrate, on the plastic deformation in the coating has been studied by indenting at different penetration depths [11]. The critical depth, defined as the penetration depth below which the substrate had negligible effect on the deformation in the coating, was shown to decrease with the increase in coating-substrate yield strength ratio and size of the indenter tip [11]. For a coating-substrate yield strength ratio less than 0.1-0.2, the measured critical depth was 0.3 times the coating thickness [11] and [12]. Harder substrates promote initiation and propagation of plastic deformation in the coating with increased pile-up of the coating material around the indenter [11]. The critical penetration depth was given as a function of the ratios of yield strength and stiffness of the coating and the substrate in [13]. Experimental studies on the effect of coating thickness in single and multi-layer metallic coatings have been done in combination with FE-based indentation models in [14], [15] and [16]. The contribution of coating and substrate to ploughing and shear components of friction were also studied experimentally in [17] while considering elastic recovery in hard coatings on steel. Experimentally validated theories have shown the effect of coating thickness, surface roughness and material properties of the coating and the substrate on friction and wear due to shearing in soft thin coating in [18], [19], [20] and [21].

Although FE models for different coated systems have provided a good overview of the deformation response of coatings to indentation, numerical ploughing models are required to understand the dynamic deformation response of coating subjected to ploughing by an asperity. Typically scratch models and experiments are used to study the coating-substrate adhesion and coating damage mechanisms [9]. The scratch behaviour in both hard and soft polymeric coatings has been studied using FE models [22], where the principal stresses along the wear track have been analysed to explain the failure and damage in the coatings. The

effects of coating thickness and hardness on deformation and damage have been studied by FE models for scratching in multilayer polymeric coatings [23]. The stresses, strains, damage and friction has been modelled for spherical indenters sliding through hard coated surface using FE models in [24]. Similarly, critical loads, friction, deformation and damage in coatings and coating-substrate adhesion are also studied for both hard and soft coatings using FE models in [25] and [26]. Typically, a linear-elastic material model is used for hard coatings while elastic-plastic material model is used for soft coatings in these FE models. The FE models use adaptive re-meshing techniques to avoid element distortion in modelling large scale plastic deformation which makes these models inefficient. Moreover, constant (Coulomb's law) coefficient of friction is used in the simulation for the shearing of the indenter-coating interface [25] and [26].

Recently, particle-based, molecular dynamics (MD) models have been used to study nano-indentation and nano-scratch behaviour of multi-layered films [27] and [28]. The effect of indentation size and coating thickness on the indentation hardness [29] and the effect of indentation depth on adhesion and plastic deformation during loading and unloading has been observed and explained using the slip systems and plastic energy in MD simulations of indentation [27]. MD simulation of scratching processes have been used to explain coating-asperity adhesion, coating-substrate adhesion, plastic deformation, work-hardening, pile-up, stick-slip and wear phenomenon in multi-layer films [28] and [30] at an atomistic scale. However, the correct choice of interatomic potentials, scaling up and physical validation of results are challenging in MD models.

In modelling of coated systems, it is critical to accurately characterize the material and contact behaviour of the coating. Typically, the hardness and the Young's modulus of a thin coating is measured by nano-indentation considering the properties of the coating with respect to the substrate in [31], [32] and [33]. Initial work to measure the effective hardness for single layered coatings was done by [34] for soft coatings and by [32] for hard coatings. The effect of indentation size and coating thickness was accounted for in estimating the intrinsic hardness of both hard and soft coated systems using theoretical and FE models and experiments in [35]. Furthermore, the Young's modulus of thin films can be characterized by the approach given in [36] and [37]. Also, the shear strength of the asperity-coating interface needs to be characterized accurately to model friction during ploughing. In the presence of a boundary layer on the coated surface, e.g. aluminium and gold coating on glass [38] and [39], the interfacial shear strength is characterized as a function of applied load [40].

The elastic and plastic properties of zinc coating on steel sheets have been characterized by tensile tests in [41] and [42] and by nano-indentation in [43]- [44]. However, there is still lack of sufficient data on the material, contact and interfacial properties of galvanized steel sheets. Moreover, the numerical models available for coated systems have mostly studied either indentation or scratching behaviour for hard-metallic or polymeric coatings relevant to their damage and failure mechanisms. The available FE and MD based numerical scratch/ploughing models for coated systems lack accurate experimental validation of the ploughing friction. Also, specific numerical ploughing models for zinc coatings, in the galvanized steel sheets, are absent in the literature to the knowledge of the authors.

Recently, the material point method (MPM) has been successfully used to model ploughing in steel for various loads and indenter sizes [45]. The MPM-based ploughing model combines features of both particle and mesh based numerical methods to measure friction and wear

in lubricated steel sheets with experimental validation. Also the interfacial shear strength of lubricated zinc coating has been measured for a range of loads in [46]. The current research has focussed on extending the MPM-based ploughing model for lubricated, zinc coated steel sheets. A theoretical study on the effect of the coating thickness and hardness of the coating relative to the substrate on ploughing friction and ploughing depth has been done and compared with the MPM-based ploughing model for coated-systems with a rigid-plastic (negligible elastic recovery and work hardening) material behaviour. The size of the indenter, thickness of the zinc coating and applied load have been varied to study their effect on ploughing friction and wear. The MPM model results for zinc coated steel sheets are experimentally validated and compared with ploughing experiments of uncoated steel sheets and zinc blocks. The results have been explained using the available literature on characterization of soft, thin coatings.

2 Calculation of friction in ploughing of coated systems.

Before the MPM simulations of ploughing is discussed, an approximate analytical model has been developed to investigate the expected effect of parameters such as coating thickness and hardness on the frictional behaviour in ploughing of the coatings. The analytical model is based on the concept of load sharing in a coated system in contact with a rigid-counter face, given in [20], [47], and [21]. Rigid-plastic material behaviour is chosen for the coated system. The analytical model will consist of a contact model to compute the contact area between the asperity sliding through the coated substrate. Using the calculated contact area and the hardness of coating, substrate and coated system the ploughing friction will be calculated. As mentioned, the analytical model will be used to understand the factors contributing to ploughing friction and to compare and explain the results obtained from the numerical (MPM) ploughing model and ploughing experiments on coated systems respectively.

A rigid spherical indenter sliding through a rigid-plastic coated system could result in two contacting conditions. In the first case, the spherical indenter is only in contact with the coating, i.e. the ploughing depth d_p is less than the coating thickness t. In the second case, the spherical indenter is in contact with both the coating and the substrate, i.e. the ploughing depth is more than the coating thickness.

The response to loading (indentation) of a coated system is determined from its effective hardness H_{cs}. The effective hardness of a coated system H_{cs} is given by combining the hardness of the substrate (H_s) and the hardness of the coating (H_c) typically by using a rule of mixtures. The hardness H_{cs} is obtained as a function of coating thickness t from the indentation response to a spherical indenter. For thin, soft coatings on hard substrates the effective hardness is given using equation 1 [48]. The value $k_1 = 125$ was obtained by experimentally fitting the indentation response of spheres of various radii (r) on a coated substrate, where $H_{cs} \approx H_c$ for values of $t/r \geq 0.04$ [48].

$$H_{cs} = H_c + (H_s - H_c)\, exp\left(-k_1 \frac{t}{r}\right) \tag{1}$$

2.1 Calculation of contact area in ploughing of a coated substrate

For a spherical indenter of radius r, ploughing through the coated substrate with ploughing depth less than or equal to the coating thickness ($d_p \leq t$), the contact radius is taken as a. Considering the frontal half of the indenter in contact during ploughing through the coating in

a rigid-plastic coated-substrate (see figure 1a), the horizontal projection A_{xy} of the total contact area is determined. By dividing the applied load F_n by the mean contact pressure P_{pl} (due to plastic deformation), the horizontal projection (in the 'xy plane') of the contact area A_{xy} is obtained, see equation 2.1. For normal loading of a plastically deforming coated substrate, the contact pressure P_{pl} equals the effective indentation hardness H_{cs} of the coated system. The ploughing depth d_p for a spherical indenter of radius r is obtained from its contact radius as given in equation 2.2. The (vertical) cross-sectional contact area A_{yz} for a spherical indenter ploughing in x direction is given as the area of the segment formed by the intersection of the contact plane on the indenter's 'mid yz-plane' and is expressed in equation 2.3 [45] (see figure 1b).

$$A_{xy} = \frac{\pi a^2}{2} = \frac{F_n}{H_{cs}} \tag{2.1}$$

$$d_p = r - \sqrt{r^2 - a^2} \tag{2.2}$$

$$A_{yz} = r^2 \text{atan}\frac{a}{r - d_p} \; - a\,(r - d_p) \tag{2.3}$$

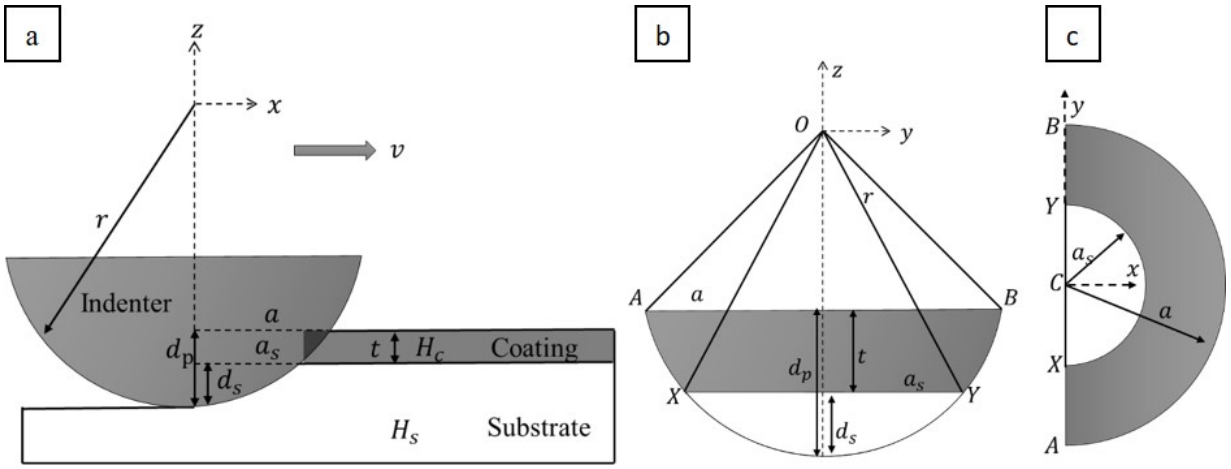

Figure 1: (a) Schematic of a spherical indenter of radius r ploughing through a rigid-plastic coated substrate, with coating thickness t, coating hardness H_c, substrate hardness H_s. (b) The frontal projection of the contact area of the indenter showing total ploughing depth d_p, ploughing depth into the substrate d_s. (c) The horizontal projection of the contact area showing total contact radius a and contact radius with the substrate a_s. (Coating in grey and substrate in white).

Figure 1 shows the case of a rigid spherical indenter ploughing through both the coating and the substrate. So, $d_p > t$. The total ploughing depth d_p is given as the sum of ploughing depth in the substrate d_s and ploughing depth in the coating d_c. In this case $d_c = t$, as $d_p > t$. The applied normal load F_n is now carried by both the coating and the substrate over the total contact area $A_{xy} = A_{xy_s} + A_{xy_c}$ where A_{xy_s} is the contact area of the substrate and A_{xy_c} is the contact area of the coating, (see figure 1c). It is assumed that the contact pressure generated in the coating equals the effective hardness of the coated system H_{cs}, while the contact pressure in the substrate equals hardness of the substrate H_s. The contact area of the coating with the indenter A_{xy_c} (the area of the annular semi-circle in figure 1c) is given in equation 3.1 in terms of the ploughing depth in the substrate d_s, indenter radius r and coating thickness t (using equation 2.2 for $d_p = d_s + t$). By equating the applied load to the contact pressure in the contact area with the coating and the substrate and substituting expression of A_{xy_c} from

equation 3.1, the expression of d_s can be calculated by solving the resulting quadratic equation in equation 3.2, and choosing the one feasible solution of d_s (the $d_s < r$). The horizontal and vertical projections of the contact area with the substrate A_{xy_c} and A_{yz_s}, are given in equation 3.3 and 3.4 respectively. The total horizontal projection A_{yz} of the indenter with the coated substrate is now given by substituting $d_p = d_s + t$ in equation 2.3. The vertical projection of the contact area of the indenter with the coating A_{yz_c} is given as the difference between A_{yz} and A_{yz_s} in equation 3.5 (see figure 1b).

$$\begin{aligned} &A_{xy_c} = A_{xy} - A_{xy_s} = 0.5\pi\left(a^2 - a_s^2\right) = 0.5\pi\left(r^2 - (r-d_p)^2 - \left(r^2 - (r-d_s)^2\right)\right) \\ &\Rightarrow A_{xy_c} = 0.5\pi t\left(2\left(r-d_s\right) - t\right) \end{aligned} \tag{3.1}$$

$$\begin{aligned} &H_s A_{xy_s} + H_{cs} A_{xy_c} = F_n \Rightarrow 0.5\pi\left(r^2 - (r-d_s)^2\right) H_s = F_n - 0.5\pi t\left(2\left(r-d_s\right) - t\right) H_{cs} \\ &\Rightarrow 0.5\pi H_s d_s^2 + \pi\left(H_{cs}t - H_s r\right) d_s + F_n - 0.5\pi t\left(2r - t\right) H_{cs} = 0 \\ &\Rightarrow d_s = -\frac{B + \sqrt{B^2 - 4AC}}{2A} \forall\ A = 0.5\pi H_s,\ B = \pi\left(H_{cs}t - H_s r\right),\ C = F_n - 0.5\pi t(2r-t)H_{cs} \end{aligned} \tag{3.2}$$

$$A_{xy_s} = 0.5\pi\left(r^2 - (r-d_s)^2\right) \tag{3.3}$$

$$A_{yz_s} = r^2 \text{atan}\frac{a_s}{r-d_s} - a_s\left(r-d_s\right)\ \forall a_s = \sqrt{r^2 - (r-d_s)^2} \tag{3.4}$$

$$A_{yz_c} = A_{yz} - A_{yz_s}\ \forall A_{yz} = r^2 \text{atan}\frac{a}{r-d_s-t} - a\left(r-d_s-t\right) and a = \sqrt{r^2 - (r-d_s-t)^2} \tag{3.5}$$

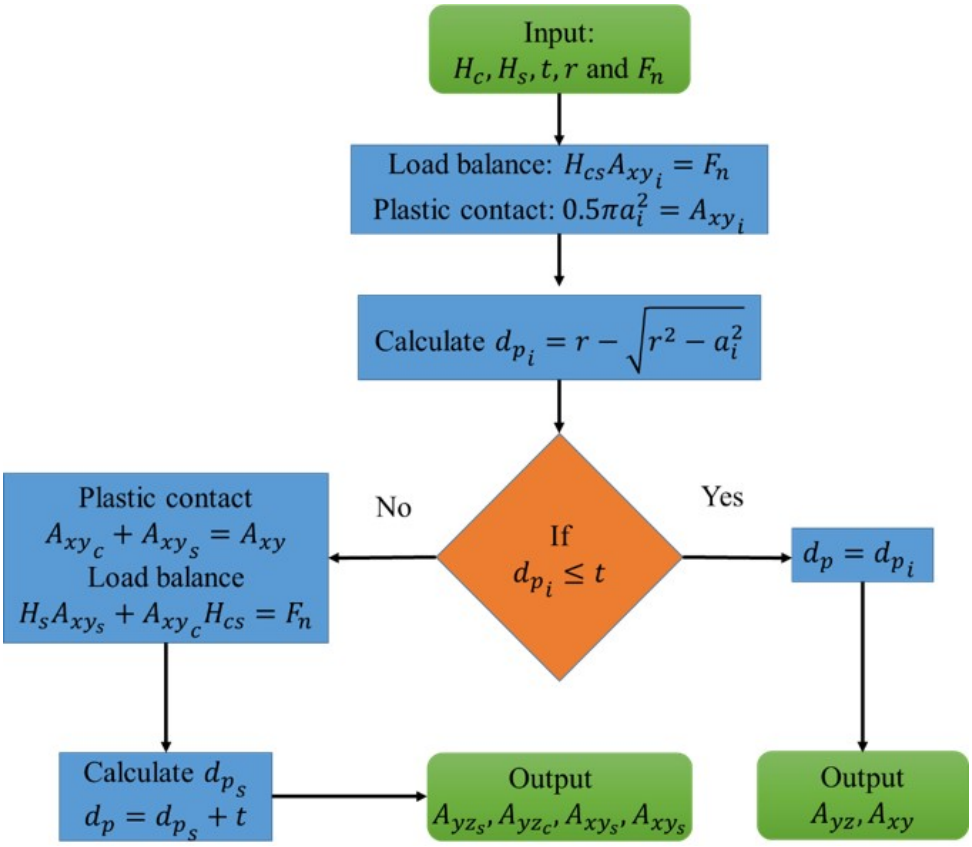

Figure 2: Algorithm to calculate the projected contact areas in the horizontal xy plane A_{sh} and vertical xz plane A_{pl} for a rigid-sphere ploughing through a rigid plastic coated system in x direction.

An algorithm to compute the projection of contact area of the indenter sliding through a coated substrate is shown in figure 2. The algorithm accounts for both the cases of contact between the indenter and the coated substrate, i.e. indenter with the coating and the indenter with both the coating and the substrate. An initial prediction of the ploughing depth of the spherical indenter is made by equating the applied load with the effective indentation hardness H_{cs}. The ploughing depth is compared with the coating thickness to categorize the contact condition amongst the two cases described above. Following the set of equations 2.1-2.3 and 3.1- 3.5 the algorithm computes the contact areas for each of the cases.

2.2 Calculation of components of ploughing friction force

The ploughing friction is calculated as the sum of the friction force due to plastic deformation of the ploughed specimen and the friction force due to shearing of the interface [7]. The friction force F_f acting on a spherical asperity ploughing through a specimen is given in equation 4.1. The friction force due to ploughing is given as the product of the contact pressure due to the plastic deformation of the substrate P_{pl} and the area of the ploughed cross section A_{yz}. The friction force due to shearing of the interface is given as the product of the interfacial shear strength τ_{sh} and the contact area between the indenter and the specimen at the surface A_{xy}. The overall coefficient of friction μ is calculated using equation 4.2.

$$F_f = F_{pl} + F_{sh} = p_{pl}A_{yz} + \tau_{sh}A_{xy} \tag{4.1}$$

$$\mu = \frac{F_f}{F_n} = \mu_{pl} + \mu_{sh} = \frac{p_{pl}A_{yz} + \tau_{sh}A_{xy}}{F_n} \tag{4.2}$$

$$\mu_{pl} = \frac{F_{pl}}{F_n} = \frac{H_s A_{yz_s} + H_c A_{yz_c}}{F_n} \tag{4.3}$$

$$\mu_{sh} = \frac{F_{sh}}{F_n} = \frac{f_s H_s A_{xy_s} + f_c H_c A_{xy_c}}{3\sqrt{3}F_n} \tag{4.4}$$

In ploughing through a rigid-plastic coated substrate, the stress acting on the ploughed cross section p_{pl} are taken as the hardness of the coating H_c or hardness of the substrate H_s. The coefficient of friction due to plastic deformation of the coated system μ_{pl} is obtained using equation 4.3, where the friction force due to ploughing is shared by the vertical projected areas of the coating A_{yz_c} and the substrate A_{yz_s}. The shear stresses at the indenter-coating contact and the indenter-substrate contact are taken as fractions (f), f_c and f_s of the maximum shear strength of the coating τ_{shc} and the substrate τ_{shs} respectively. Typically for very clean surfaces, $f = 1$. For a rigid-plastic material, its shear strength τ_{sh} is given as a factor $1/k_0$ of its hardness H. Typically for metals $k_0 = 3\sqrt{3}$ [10] and [49]. The interfacial friction due to shearing of the substrate and the coating is given by $f_s\tau_{sh_s}$ and $f_c\tau_{sh_c}$ respectively distributed over the horizontal projected areas A_{xy_s} and A_{xy_c} respectively. The coefficient of friction due to shearing of the interface μ_{sh} in a coated system is given in equations 4.4. If $d_p < t$, the coefficient of friction is given by substituting $A_{yz_s} = 0$ and $A_{xy_s} = 0$ in equation 4.3 and 4.4 respectively. The variations in μ_{pl}, μ_{sh} and μ with coating thickness t for a soft and a hard coating and with relative coating hardness (hardness ratio) $\tilde{H} = H_c/H_s$ are illustrated in figure 3a, 3b and 3c respectively.

The shearing of the contact interface (on the vertical plane in the yz plane) also results in a component for force F^z_{sh} along the loading z direction. Hence the shear stress is carried by vertical contact areas of the substrate A_{yz_s} and the coating A_{yz_c}. In ploughing using an applied load of F_n in $-z$ direction, F^z_{sh} acts on the indenter in the z direction. The ratio of F^z_{sh} and F_n

is given for a coated system as a factor of μ^z_{pl} in equation 5.1. The total normal load $F_n^{'}$ acting on the indenter in z direction is now corrected by adding the force due to shear stress F^z_{sh} to applied load F_n. The contact area deformation and hence the ploughing depth of the coated system is corrected using the load F_n in equation 2.1-2.3 and equation 3.1-3.5 [50]. Also the friction forces are computed with the new contact areas in equation 4.1-4.4.

$$\mu^z_{sh} = \frac{F^z_{sh}}{F_n} = \frac{\tau_s A_{yz_s} + \tau_c A_{yz_c}}{F_n} = \frac{1}{k_0}\mu_{pl} \tag{5.1}$$

$$F_n^{'} = F_n - F^z_{sh} = F_n\left(1 + \frac{1}{k_0}\right)\mu_{pl} \tag{5.2}$$

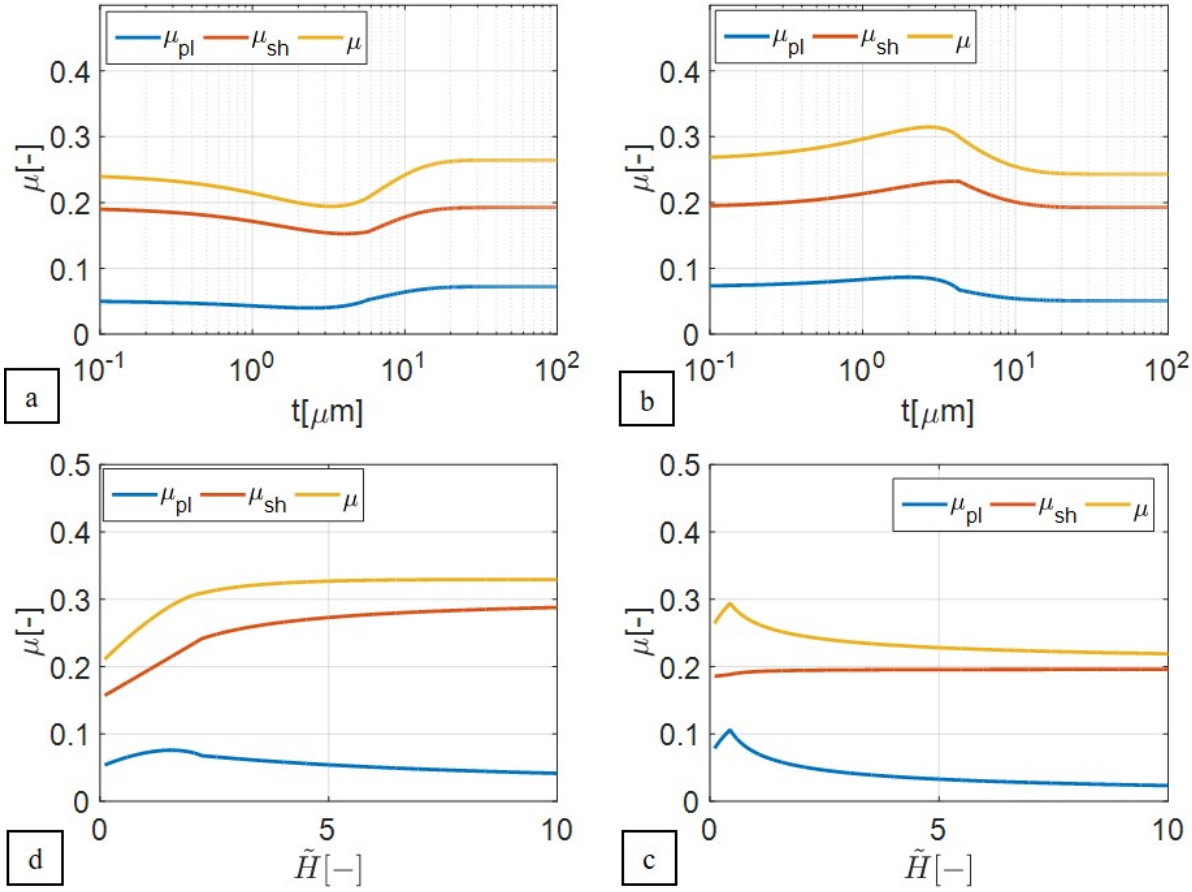

Figure 3: Coefficient of friction due to ploughing of rigid-plastic coated substrate by 1mm diameter indenter at F_n= 5N as a function of (a) coating thickness for a soft coating ($\tilde{H}$ = 0.5, $H_s = 900MPa$) and (b) hard coating ($\tilde{H} = 2$, $H_s = 450MPa$) ($k_1 = 12.5$). (c) Effect of relative coating hardness $\tilde{H}$ ($H_s = 450MPa$) on ploughing coefficient of friction for coating thickness $t = 4\mu m$ and (d) $t = 16\mu m$.

The ploughing depths calculated using equation 2.2 and 3.2 is plotted in figure 4a and 4b as a function of the coating thickness for a hard coating and a soft coating and as a function of coating hardness with and without including the including the shear force F^z_{sh} in the z direction respectively. It can be seen from figure 4b, that μ^z_{sh} has a small contribution on the ploughing depth. The results obtained from the analytical model will be discussed further in comparison with the numerical MPM- ploughing model and ploughing experiments in section 4.1 and section 4.2 respectively. As the results shown in figures 3a and 4a are calculated over a

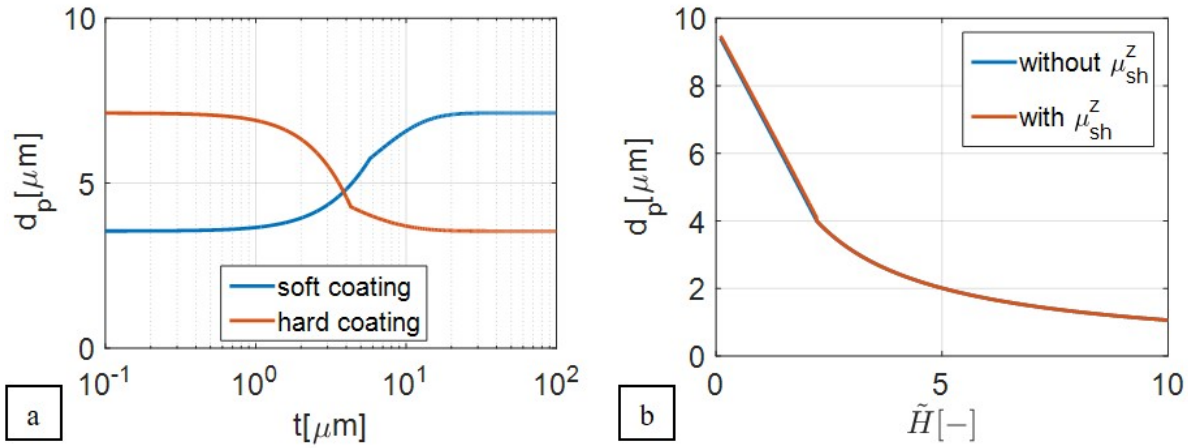

Figure 4: Ploughing depth of rigid-plastic coated substrate by 1mm diameter indenter at F_n= 5N as a function of the (a) coating thickness t for a soft coating ($\tilde{H} = 0.5,\ \ H_s = 900MPa$) and hard coating ($\tilde{H} = 2,\ \ H_s = 450MPa$) ($k_1 = 12.5$) and (b) relative coating hardness $\tilde{H}$ ($H_s = 450MPa,\ t = 4\mu m$) with and without correction of F_n using μ^z_{sh}.

large range of coating thickness t, the value of the fitting factor k_1 is varied (from 125 to 12.5) to avoid scaling effects and obtain smoother results.

3 Experimental and computational method

The current section describes the set-up used to perform the ploughing experiments and the MPM-based ploughing simulation. The parameters of the material models and the interfacial friction models used in the ploughing simulations are also plotted and listed in this section.

3.1 Experimental method

The preparation of both the zinc block and the zinc coated specimen for the ploughing experiments is explained below. Also the ploughing experimental set-up is described.

3.1.1 Preparation of specimen

The zinc coated steel sheets are prepared by hot dip galvanizing 210mm long and 300mm wide rectangular sheets in molten zinc bath. The surface of the (unrolled) zinc coating is characterized by dendritic growth and spangles (snowflake) formed during solidification of the molten zinc on surface of the steel sheet after hot dip galvanization as shown in figure 5a [51]. The surface roughness R_a of the galvanized sheets is measured to be $0.5\mu m$. The mean thickness of the zinc coating is maintained within 20-55μm by blowing off the excess zinc melt from the sheet using air knives. The thickness of the zinc coating on the steel is measured using the magnetic induction probe of Fisher's FMP 40 Dualscope.

Mirror polishing of rough galvanized steel sheets is done by hot mounting circular galvanized sheets of 46mm diameter on 50mm diameter bakelite disc. Polishing is done using an automatic polishing machine. The galvanized sheets were polished using a diamond suspension with $9\mu m$ particle size at 30N load, 150rpm for 90seconds. The fine polishing of the sheets was done using a (water-less) alcohol-based yellow lubricant, as the softness of zinc and its reaction with water can leave the coatings discoloured and with scratches. Firstly, the zinc coated surface was

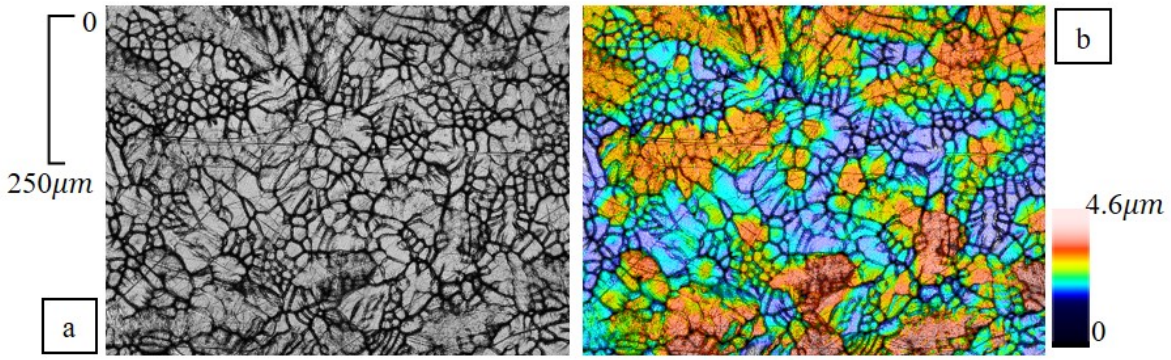

Figure 5: Surface of mounted (zinc coated) galvanized sheet before polishing, (a) as seen under confocal microscope at 20x magnification with its (b) surface height profile, R_a= 0.5μm and $R_q = 0.75\mu m$.

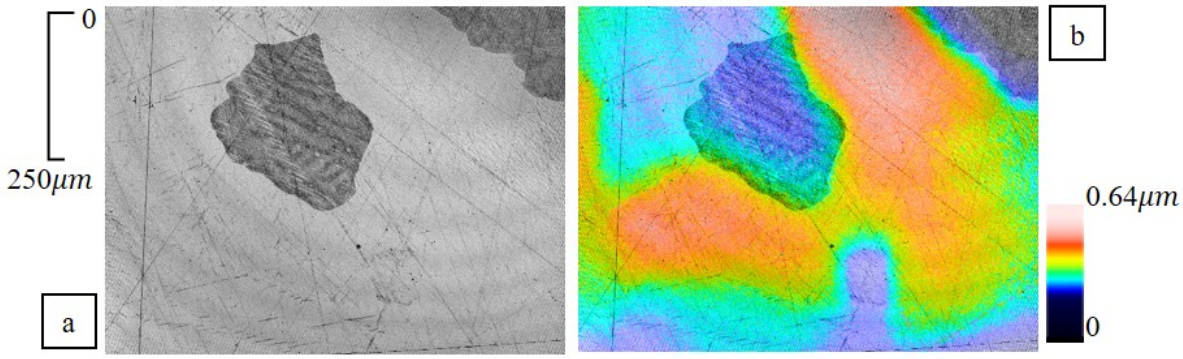

Figure 6: Surface of mounted (zinc coated) polished galvanized sheet, (a) as seen under a confocal microscope at 20x magnification with its (b) surface height profile, R_a= 0.05μm and $R_q = 0.1\mu m$.

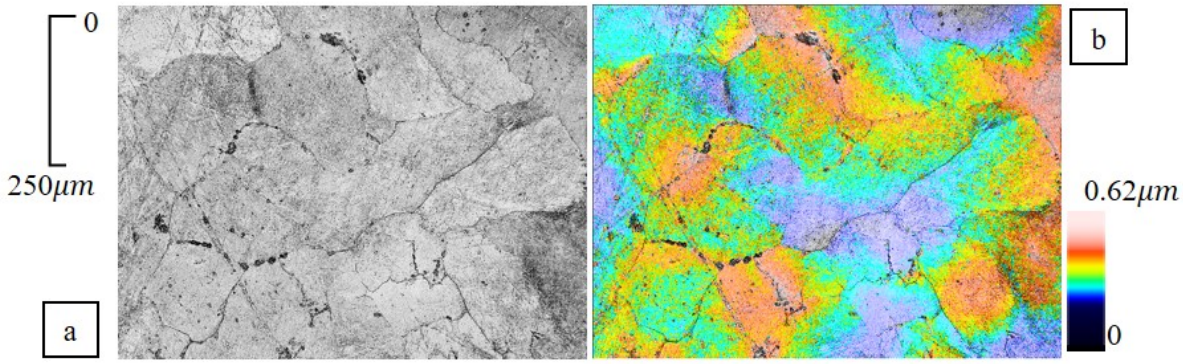

Figure 7: Surface of mounted polished zinc block, (a) as seen under confocal microscope at 20x magnification with its (b) surface height profile, R_a= 0.55μm and $R_q = 0.7\mu m$.

polished with a poly-crystalline diamond slurry suspension of $3\mu m$ particle size at 25N load, 150rpm for 90 seconds. Then a diamond slurry suspension of $1\mu m$ particle size was used at 20N load, 150rpm for 90seconds. Finally, the sheets were polished using de-agglomerated gamma alumina powder of $0.05\mu m$ particle size mixed with ethanol denatured with iso-propyl alcohol at 15N and 150rpm for 60seconds. The polished sheet is shown in figure 6a where the grain boundaries can be clearly seen. The resulting mean surface roughness was $0.05\mu m$ as shown in figure 6b. The resulting mean coating thickness post polishing was measured to be 30 μm.

For reducing the coating thickness, the duration and loads in the polishing steps were increased. Zinc coated specimens were also polished up to 10 and 15μm coating thickness. Zinc coated samples with a mean coating thickness of 40 and 55μm in an unpolished state were also used in the ploughing experiments as specimens high coating thickness. To simulate a very high zinc coating thickness, a zinc block was used. The rectangular zinc block was also mounted and polished to obtain a mean surface roughness of 0.05μm as shown in figure 7.

3.1.2 Experimental set-up

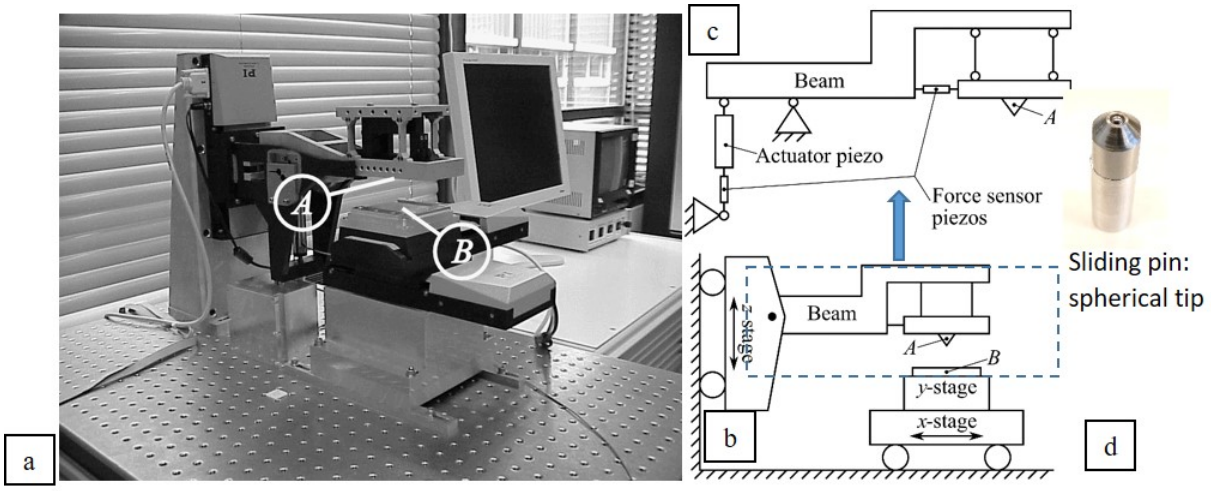

Figure 8: (a) Linear friction tester for ploughing experiments with schematic of (b) A: loading set-up (c) B: sliding set up and (d) the indenter/pin with 3mm diameter spherical tip.

The ploughing experiments on zinc coated DX56 steel sheet and zinc block lubricated with Quaker FERROCOAT N6130 lubricant were done using the linear friction tester, shown in figure 8, with 3 repetitions. The linear friction tester consists of an XY linear positioning stage driven separately by actuators as shown in figure 8c. A horizontal beam supports the loading tip and moves the Z-stage using a linear and piezo actuator for coarse and fine displacement respectively while applying a normal load. The normal load is applied using a force controlled piezo actuator, connected by PID control loop feedback system, so the system can operate load-controlled. The friction forces are measured by a piezo sensor along the loading tip as shown in figure 8b. Spherical balls of 1mm and 3mm diameter were mounted on the pin holder as shown in figure 8d. In the experiments, the sliding distance was 10mm and the sliding velocity was set equal to 1mm/s.

3.2 Computational method

The material point method (MPM), a particle-in-cell based modelling tool, has been used to simulate ploughing. The MPM-based ploughing model has been introduced and implemented successfully for ploughing of a steel sheet in [45]. In that paper, the model-set up, the material model and the interfacial friction model used in the MPM-based ploughing simulations have been elaborated. Further, the parameters for the material model and the interfacial friction model have been listed using the data from tensile and compression tests, obtained from the supplier, the literature on bulk zinc and zinc coatings [52], [53] and [54] and the experiments done for interfacial shear characterization in [46].

3.2.1 Model set-up

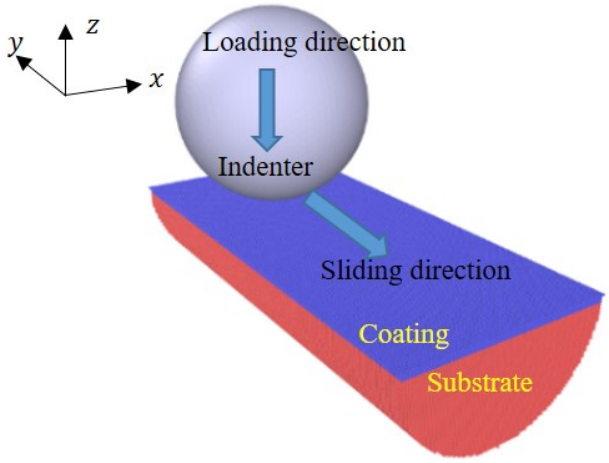

Figure 9: MPM simulation of an spherical indenter (asperity) with radius 0.2 mm ploughing through a coated-substrate along sliding x-direction.

The MPM-based ploughing model results are obtained by extrapolating and converging the results for decreasing particle/element sizes towards $0\mu m$ size, where the size of the particles in coated-substrate is varied from 2.5, 5 to $10\mu m$ and the size of the triangles in the indenter is varied from 5,10 and 20 μm. Indenters of radii 200, 500 to $1500\mu m$ are used for analytical and experimental validation. The coating thickness is varied from 10-$55\mu m$, comparable to the measured coating thickness of the zinc coated specimen. The particles in the coated-substrate are grouped in the half cylindrical domain of radius $200\mu m$ and length 1mm. A scratch length of $600\mu m$ is made using a spherical indenter sliding at a velocity of 0.1m/s. A mass scaling factor of 1e6 is used to increase computation speed. Figure 9 shows the MPM-ploughing model set-up. Table 1 list the MPM model set-up parameters.

The material model computes the total stress as a sum of the hydrostatic stress and the deviatoric stress. The hydrostatic stress is computed using a linear equation of state as given in equation 6.1. The bulk modulus K is obtained from the Young's modulus E and the Poissons ratio ν while the hydrostatic strain is obtained from the volumetric change $\mathbf{M}$ and identity matrix I. The deviatoric stress is obtained by updating the flow stress using a radial return plasticity algorithm [45]. Assuming, adiabatic conditions, the heat generated -q due to plastic deformation results in a temperature change -T which is calculated in equation 6.2 using the specific heat capacity c_p and the mass of the particle $m = \rho V$ (material density ρ and cell volume V). The heat transfer is calculated using thermal conductivity κ_t. The parameters for heat transfer in zinc and steel are listed in table 3 and 4.

$$\sigma_h = K\mathbf{M}I \;\forall\; K = \frac{E}{3(1-2\nu)} \tag{6.1}$$

$$\text{-}T = \frac{\text{-}q}{mc_p} \tag{6.2}$$

The flow stress σ_y is taken as constant for a rigid-plastic material. In the model, the flow stress is computed for materials using physically based material models. The isothermal Bergström van Liempt hardening relation [55], modified by Vegter for sheet metal forming processes [56], is used for the DX56 steel substrate where the flow stress σ_y^{BL} is decomposed into a static-strain

Table 1: MPM ploughing model parameters.

Parameters	Symbol	Values/ expression
Rigid spherical indenter radii	R_i	0.2, 0.5 and 1.5 mm
Semi-cylindrical substrate radius	R_s	0.2 mm
Sliding distance of indenter	l	0.6 mm
Semi-cylindrical substrate length	l_s	1 mm
Coating thickness	t	15 and 30 μm
MPM particle cell size	r_p	2.5, 5 and 10 μm
Indenter's mesh element size	r_t	5, 10 and 20 μm
Sliding velocity of indenter	v_i	0.1 mm/s
Sliding distance	d_s	0.6 mm
Mass scaling factor	m_s	1e6

hardening stress σ_{wh} and dynamic stress σ_{dyn}. It takes into account the strain ε, strain-rate $\dot{\varepsilon}$ and thermal (temperature) T effects as shown in equation 7.1. The Bergström van Liempt material model parameters for the DX56 steel sheet are listed in table 3 [45]. The Johnson-Cook material model is used for modelling the flow stress σ_y^{JC} of the bulk zinc specimen [57] as shown in equation 7.2 where ε is strain, $\dot{\varepsilon}$ is strain-rate and T is temperature. The flow stress σ_y^S for the zinc coating is computed from the initial yield stress σ_{y_0}using the material model in equation 7.3. The model is taken from [43] and [52], and has similarities with the Swift strain hardening law [58]. Table 4 lists the material model parameters for bulk zinc and zinc coating, given in equations 8.2 and 8.3.

$$\begin{aligned}\sigma_y^{\mathrm{BL}} &= \sigma_{wh} + \sigma_{dyn} \\ &= \sigma_{f0} + d\sigma_m \left(\beta \left(\varepsilon + \varepsilon_0\right) + \left\{1 - \exp\left[-\omega \left(\varepsilon + \varepsilon_0\right)\right]\right\}^c\right) + \sigma_{v0}\left(1 + \frac{kT}{\Delta G_0}\ln\frac{\dot{\varepsilon}}{\dot{\varepsilon}_0}\right)^m \end{aligned} \tag{7.1}$$

$$\sigma_y^{JC} = \left(A + B\varepsilon^p\right)\left(1 + C\ln\frac{\dot{\varepsilon}}{\dot{\varepsilon}_0}\right)\left(1 - \left(\frac{T - T_0}{T_m - T_0}\right)^q\right) \tag{7.2}$$

$$\sigma_y^S = \sigma_{y_0}\left(1 + \frac{E}{\sigma_{y_0}}\varepsilon\right)^n \tag{7.3}$$

The interfacial friction algorithm is used to calculate the friction force due to shearing of the interface as the product of the interfacial shear strength τ_{bl} and contact area A_c. For rigid-plastic materials, the interfacial shear strength can be given as a fraction f of the bulk shear strength κ in equation 8.1 (model parameters listed in table 2 and used in section 4.1). The boundary-layer shear strength at the interface of the indenter and the metallic coating/substrate (lubricated) is given as a function of the nominal contact pressure $\overline{P}$, sliding velocity v_i and the contact temperature T_0 in equation 8.2 [43], where, C_0 is the proportionality constant, n_p is the pressure exponent, n_v is the velocity exponent and n_T is the temperature exponent, obtained by fitting experimental data. For a constant v_i and T_0, a power-law relationship between τ_{bl} and $\overline{P}$ can be deduced in equation 8.3. This interfacial friction model is used in ploughing simulation of zinc coated steel in section 4.2 (model parameters are given in table 5).

$$\tau_{bl} = f\kappa \tag{8.1}$$

$$\tau_{bl} = C_0\overline{P}^{n_p} v_i^{n_v} \exp - \frac{n_T}{T_0} \tag{8.2}$$

$$\tau_{bl} = C_p\overline{P}^{n_p} \tag{8.3}$$

3.2.2 Model parameters

The material model parameters for bulk specimens of DX56 steel sheets are obtained by uniaxial tensile tests. Tensile tests are done at various strain rates and temperatures up to a true strain of 1. The resulting stress-strain curves are fitted with equation 7.3 to obtain the model parameters, listed in table 3. The strain hardening parameters (A, B and p) of the zinc block are obtained by fitting the stress-strain data from the uniaxial compression tests pependicular to the rolling plane with equation 7.2. The strain rate hardening and thermal softening parameters (C and q) are obtained by fitting the results from Kolsky bar experiments done on commercially pure zinc in [54] with equation 7.2. The material model parameters for the zinc coating on steel in [43] and [52] are obtained from the load-depth curves of nanoindention experiments measured on various zinc grains in [53]. The material parameters for bulk zinc and the zinc coating are listed in table 4.

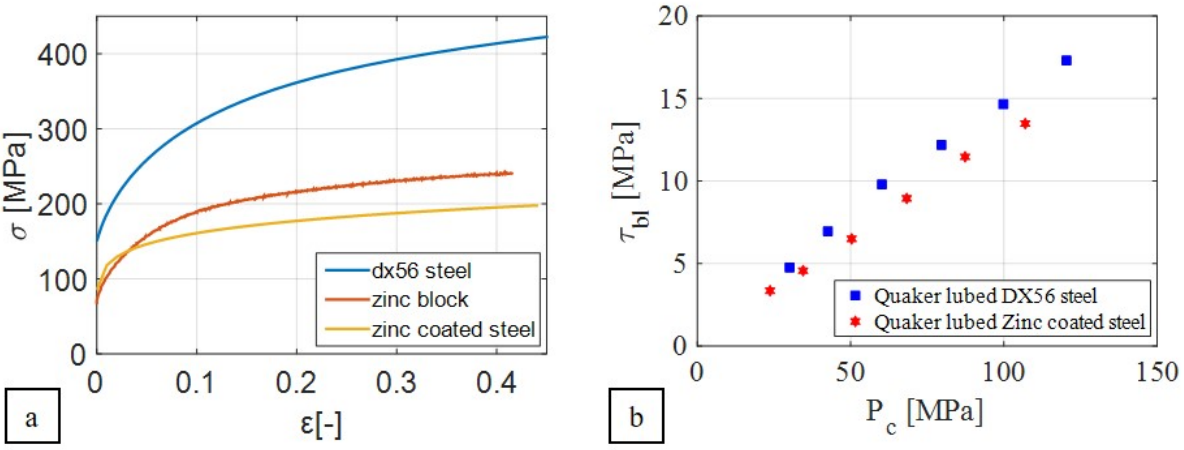

Figure 10: Comparison of (a) the true flow stress-strain curves for DX56 steel sheet, zinc coated steel sheet and zinc block obtained by uniaxial compression test and (b) of the boundary layer shear stress against applied nominal pressure of DX56 steel sheet and zinc coated steel sheet lubricated with Quaker FERROCOAT N136 lubricant [46].

Table 2: Material parameters for rigid-plastic material

Parameters	Symbol	Value/expression
Elastic modulus of the substrate	E_s	210GPa
Poisson's ratio (coating and substrate)	ν	0.3
Elastic modulus of the coating	E_c	80GPa
Reference hardness of the coating	H_{0_c}	225/450MPa
Reference hardness of the substrate	H_{0_s}	450/900MPa
Reference coating thickness	t_0	$25\mu m$
Relative hardness of coating	$\tilde{H}$	$0.1 - 10$
Coating thickness	t	$0 - 200\mu m$
Interfacial shear stress	τ_{sh}	$H/3\sqrt{3}$

The true stress-strain curves of the DX56 steel, bulk zinc and zinc coating are plotted in figure 10a [52] and [53]. The DX56 steel shows highest flow stress (hardness) compared to both the bulk zinc and zinc coating. The pure zinc block shows higher strain hardening, although

low yield strength compared to the zinc coating. The interfacial friction model parameters for Quaker lubricated zinc coated steel sheet and uncoated steel sheet have been obtained by performing boundary layer shear experiments in a linear friction tester [46]. Likewise, the boundary layer shear stress of the Quaker lubricated steel sheet and Quaker lubricated zinc coated steel sheet are plotted as a function of the applied nominal pressure in figure 10b. The boundary layer shear strength results are used to calibrate the interfacial friction model given in equation 8.2. The model parameters obtained are listed in table 5. The boundary layers at the interface of the zinc coating and the sliding pin have a lower shear strength compared to those formed at the interface of the DX56 steel sheet and the sliding pin.

Table 3: Parameters for DX56 steel substrate [45].

Parameters	Symbols	Value
Heat transfer		
Material density	ρ	7850 kg/m^3
Specific heat capacity	c_p	502 J/(kg K)
Thermal conductivity	κ_t	50 W/(m K)
Equation of state		
Young's modulus	E	210GPa
Poisson's ratio	ν	0.3
Material model		
Initial static stress	σ_{f0}	82.988 MPa
e Stress increment parameter	$\mathrm{d}\sigma_\mathrm{m}$	279.436 MPa
Linear hardening parameter	β	0.482
Remobilization parameter	ω	6.690
Strain hardening exponent	c	0.5
Initial strain	ε_0	0.005
Initial strain rate	$\dot{\varepsilon}_0$	$10^8 s^{-1}$
Maximum dynamic stress	σ_{v0}	1000 MPa
Dynamic stress power	m	3.182
Activation energy	$\mathrm{-G_0}$	0.8
Boltzmann's constant	k	8.617×10^{-5} eV

The material parameters, listed in table 2 are for rigid-plastic material behaviour. The relative hardness of the coating to the substrate $\tilde{H} = H_c/H_s$ is varied from 0.1 to10 to study the effect of coating hardness on ploughing friction and ploughing depth. The coating thickness t is varied from 0 (uncoated substrate) to ∞ (bulk coating) to study the effect of coating thickness on ploughing friction and ploughing depth. To simulate rigid-plastic behaviour, hardness is taken as $H = 3\sigma_y$ [49] and shear strength of the bulk is taken as $\kappa = \sigma_y/\sqrt{3}$ [10]. The interfacial friction factor is taken to be $f = 1$ assuming a very clean surface. A high value of (maximum) interfacial shear in the analytical study can help highlight its effect on the overall ploughing friction. The interfacial friction model given in equation 8.3 is used to determine the interfacial shear strength.

Table 4: Parameters for zinc [52], [53] and [54].

Parameters	Symbols	Value
Heat transfer		
Material density	ρ	7140 kg/m^3
Specific heat capacity	c_p	377 J/(kg K)
Thermal conductivity	κ_t	116 W/(m K)
Equation of state (bulk)		
Young's modulus	E	108GPa
Poisson's ratio	ν	0.25
Material model (bulk)		
Initial yield stress	A	82.51MPa
Strain hardening exponent	p	0.1786
Strain hardening constant	B	288.34
Strain rate hardening constant	C	0.0202
Reference strain rate	$\dot{\varepsilon}_0$	1s^{-1}
Thermal softening constant	q	0.843
Reference temperature	T_0	298 K
Melting point temperature	T_m	692.68 K
Equation of state (coating)		
Young's modulus	E	80GPa
Poisson's ratio	ν	0.3
Material model (coating)		
Initial yield stress	σ_{y_0}	85MPa
Strain hardening exponent	n	0.14

Table 5: Interfacial friction model parameters [46].

Parameters	Symbols	Value
Quaker lubricated DX56 steel sheet		
Pressure constant	C_p	1.34
Pressure exponent	n_p	0.88
Quaker lubricated Zinc coated steel sheet		
Pressure constant	C_p	0.32
Pressure exponent	n_p	0.95

4 Results and discussion

The coefficient of friction and ploughing depths obtained from the MPM-based ploughing simulations of the coated systems have been compared with those obtained from the analytical model in section 2. The coating thickness and relative material hardness has been varied to study their effect on friction and ploughing depths for rigid-plastic material behaviour. Ploughing experiments have been performed on bulk zinc and zinc coatings on a steel substrate over a range of coating thicknesses and applied loads using spherical indenters of two different sizes. The coefficient of friction and the ploughing depths obtained from the experiments are used to validate the results obtained from the MPM-based ploughing model and thereby to study the effects of applied load, indenter size, coating thickness and substrate material properties on the ploughing behaviour of (soft) coated system such as galvanized steel. The MPM results obtained for particle sizes of 5 and 10μm are extrapolated to

converge to infinitesimal particle sizes.

4.1 Analytical validation of the MPM-based ploughing model

In the following, the ploughing depths and the coefficient of friction obtained from the theory given in section 2 has been plotted and compared with those obtained from the ploughing simulations of rigid-plastic coated-substrates in section 4.1.1 and 4.1.2 respectively. The effects of relative hardness of the coating with respect to the substrate $\tilde{H}$ and the coating thickness t on the coefficient of friction and the ploughing depths have been studied. The material parameters used in the MPM-simulations of the rigid-plastic coated-substrates to be compared with the analytical model in this section are listed in table 2.

The ploughing depth and coefficient of friction, are obtained for the ploughing simulations utilize a 0.4mm diameter indenter at 3N load. A coating thickness of $t = 25\mu m$ is taken in the first study where the relative hardness of the coating $\tilde{H}$ is varied from 0.1 to 10 and the interfacial shear strength is varied for two different cases. In the first case, the interfacial shear strength of the coating τ_c and the substrate τ_s is kept constant at H_0/k_0 where $H_0 = 450MPa$ and $k_0 = 3\sqrt{3}$. In the second case, the interfacial shear strength of the coating and the substrate is taken as per $\tau = H/k_0$ where $H = H_s$ for the substrate and $H = H_c$ for the coating. In the second study, the coating thickness is varied from $0\mu m$ for uncoated substrate to $200\mu m$ for the coating material as bulk. The relative coating hardness is varied for two different cases. In first case, $\tilde{H} = 0.5$ ($H_c = 450MPa$, $H_s = 900MPa$) and in the second case, $\tilde{H} = 2$ ($H_s = 900MPa$, $H_c = 450MPa$).

4.1.1 Comparison of ploughing depth

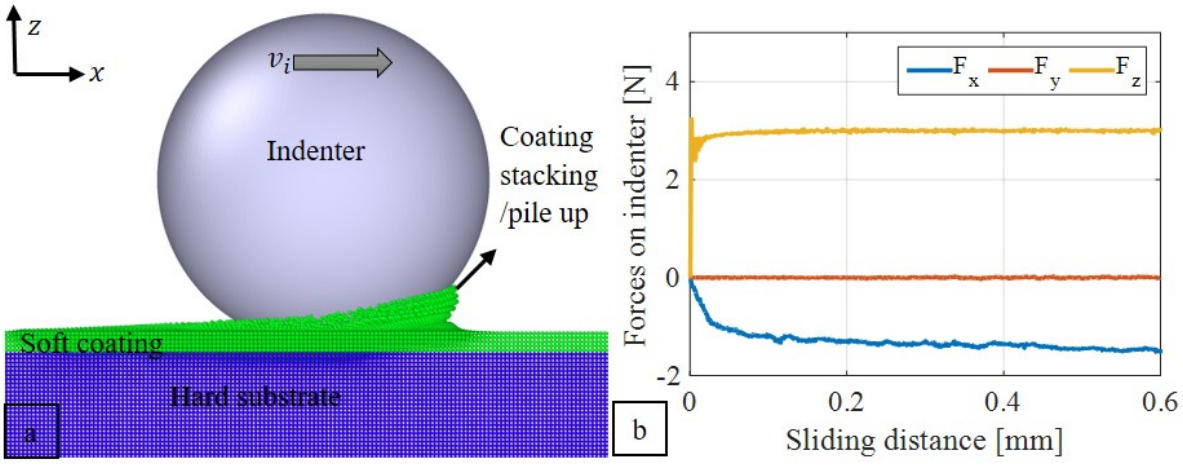

Figure 11: Ploughing of a spherical indenter through a soft coating on a hard substrate ($\tilde{H} = 0.25$, $t = 25\mu m$) resulting in pile up, stacking and eventual peeling off of the coating. (b) The corresponding plot of components forces acting on the indenter.

The total ploughing depth obtained from the ploughing simulations is compared with that obtained by the analytical model in figure 12 using equations 2.2 and 3.2 which calculate the ploughing depths with and without considering the interfacial friction force in the z direction. The ploughing depths obtained by the analytical model agree well for those obtained from the ploughing simulations for both studies.

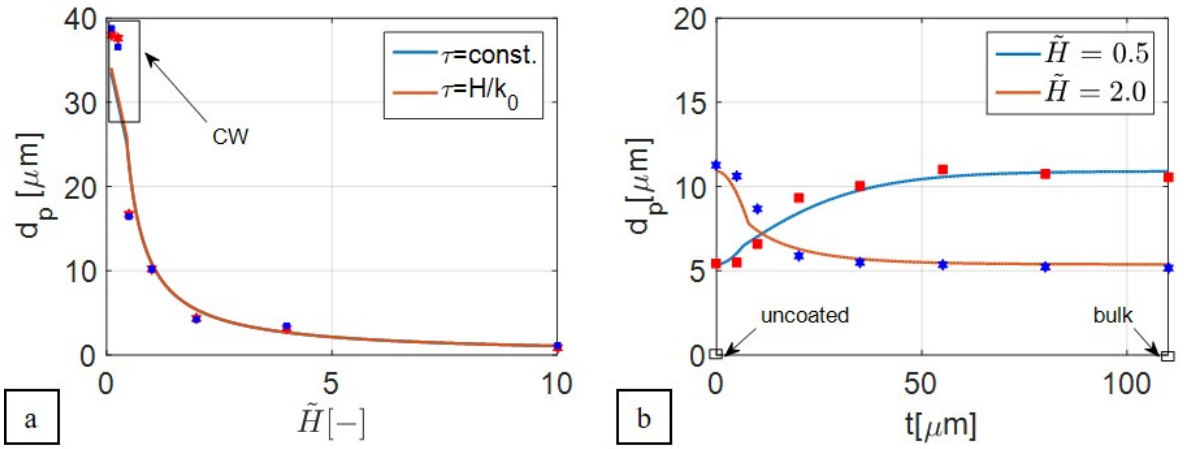

Figure 12: Simulated ploughing of rigid-plastic coated substrate by 0.4 mm diameter ball at 3N load. (a) Effect of relative coating hardness $\tilde{H}$ ($t = 25\mu m$) on the total ploughing depth with a constant interfacial shear and with interfacial shear $\tau = H/k_0$. (b) Effect of coating thickness on the total ploughing depth for a hard coating ($\tilde{H} = 2$) and a soft coating ($\tilde{H} = 0.5$). (Marks: MPM model, Lines: Analytical model). CW: Coating wear/degradation.

In the first study, where the relative hardness $\tilde{H}$ is varied from 0.1 to 10, the ploughing depths obtained using the analytical model and the MPM simulations decrease with $\tilde{H}$ and are shown to agree for $\tilde{H} \geq 0.5$ in figure 12a. For low values of $\tilde{H}$ (coating hardness), the ploughing depths obtained from the MPM model exceed those calculated by the analytical model. Also for low values of $\tilde{H}$, the indenter penetrates more into the coating and the simulated ploughing depths exceed the coating thickness resulting in the wear of the coating material as shown in the corresponding MPM ploughing simulations in figure 11a. The coating material piles up in front of the indenter as layers and wears out which can be related to degradation mechanisms such as peeling and delamination of thin soft coatings, as also shown in [22]. The results in figure 12a show that ploughing depth d_p is not affected by the interfacial shear strength.

In the second study, the total ploughing depths for a hard coating ($\tilde{H} = 2$) and for a soft coating ($\tilde{H} = 0.5$) are studied as a function of the coating thickness t as shown in figure 12b. The ploughing depths obtained from the MPM ploughing simulations agree well with those obtained from the analytical model. The ploughing depth for the soft coated system increases with coating thickness, as the effective hardness of the soft coated system decreases with the increase in coating thickness. Consequently, the ploughing depth for the hard coated system decreases with coating thickness as the effective hardness increases with the coating thickness (equation 1). The slope of the ploughing depth plots changes at a coating thickness $t_c = 5.75\mu m$ for the soft coating and $t_c = 4.3\mu m$ for the hard coating where $d_p = t$ after which increase in t results in transition of the contact of the indenter from both the substrate and the coating to the coating only. So, the ploughing depths are calculated accurately by MPM for all cases.

4.1.2 Comparison of coefficient of friction

The overall coefficient of friction μ, obtained from the MPM ploughing simulations is also compared with the values obtained by the analytical model using equations 4.2 which combines μ_{pl} and $\mu_{sh}$for a coated substrate. The results are shown to agree well in both the case studies depicted in figure 13. The mean coefficient of friction is calculated from the friction plots given in figure 11b. The steady increase in friction force can be seen over the sliding distance in figure

11b which corresponds to the piling up of material in front of the coating as shown in figure 11a.

The calculated coefficient of friction plotted against $\tilde{H}$ for a constant interfacial shear stress (figure 13a) shows a good agreement with the simulated coefficient of friction. The ploughing depth at $\tilde{H} = 0.46$ corresponds to the coating thickness $t = 25\mu m$ as shown in figure 12a. Hence, at lower $\tilde{H}$ and for $d_p > t$, there is coating wear, resulting in the difference in friction computed by the MPM model and the analytical ploughing model. As $\tau_{sh_c} = \tau_{sh_s}$ is constant, and d_p and consequently A_{pl} and A_{sh} decrease with $\tilde{H}$, thereby decreasing μ_{pl} and μ_{sh}. However in the case where $\tau_{sh_c} = H_c/k_0$, $\mu_{sh} = \tau_{shc}A_{sh}$ increases with as H_c $(\tilde{H})$, in spite of the decrease in A_{pl} and A_{sh}. Therefore the simulated coefficient of friction increases with $\tilde{H}$ is also shown in figure 3c, and agrees with the simulated coefficient of friction.

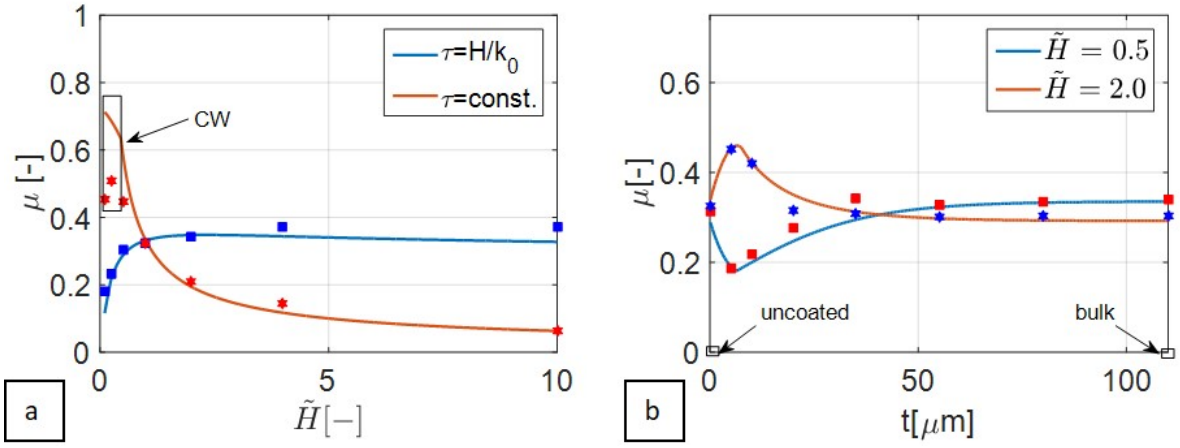

Figure 13: Simulated ploughing of rigid-plastic coated substrate by 0.4 mm diameter ball at 3N load. (a) Effect of relative coating hardness ($t = 25\mu m$) on the overall coefficient of friction with a constant interfacial shear and with interfacial shear $\tau = H/k_0$. (b) Effect of coating thickness on the total ploughing depth for a hard coating ($\tilde{H} = 2$) and a soft coating ($\tilde{H} = 0.5$). ($r = 200\mu m$, $k_1 = 12.5$) (Marks: MPM model, Lines: Analytical model). CW: Coating wear/degradation.

The coefficient of friction has been plotted as a function of the coating thickness t for a hard coating ($\tilde{H} = 2$) and a soft coating ($\tilde{H} = 0.5$) in figure 13b. The coefficient of friction obtained from the MPM simulations agrees well with the values obtained from the analytical model. For a low coating thickness, the indenter is in contact with both the coating and the substrate. In figure 13b, μ is shown to initially increase and then decrease with t for the hard coating. The initial increase in μ corresponds to the increase in contact area due to increase of the (hard) coating thickness which require more friction force to shear and plough. However once the indenter is in contact with the coating only ($t > 7.8\mu m$), the coefficient of friction plot follows the ploughing depth plot, and decreases with increase in t for the hard coating. Therefore, with the same analogy, the coefficient of friction first decreases and then increases ($t > 6.5\mu m$) with coating thickness for a soft coating. The plots in figure 13b resembles the coefficient of friction versus thickness plots in figure 3a and 3b. A fitting factor of $k_1 = 12.5$ is used to calculate H_{cs} for $r = 0.2$mm. It can be concluded that the MPM accurately predicts the coefficient of friction for ploughing in a coated substrate.

4.2 Experimental validation of ploughing friction and depths

The friction and ploughing depths are obtained from the MPM-based ploughing model over a range of applied loads (1-46 N) and indenter sizes of 1mm and 3mm. The coefficient of friction and ploughing depths were calculated for MPM particle sizes of 2.5, 5 and 10μm and extrapolated to 0μm to obtain a resolution independent result. The plots for the friction force and the ploughed profile obtained from the ploughing simulation are compared with those obtained from the ploughing experiments. The material parameters listed in table 3, 4 and 5 are used in the MPM ploughing model in this section. So the actual material behaviour has been implemented.

4.2.1 Comparison of ploughed profile

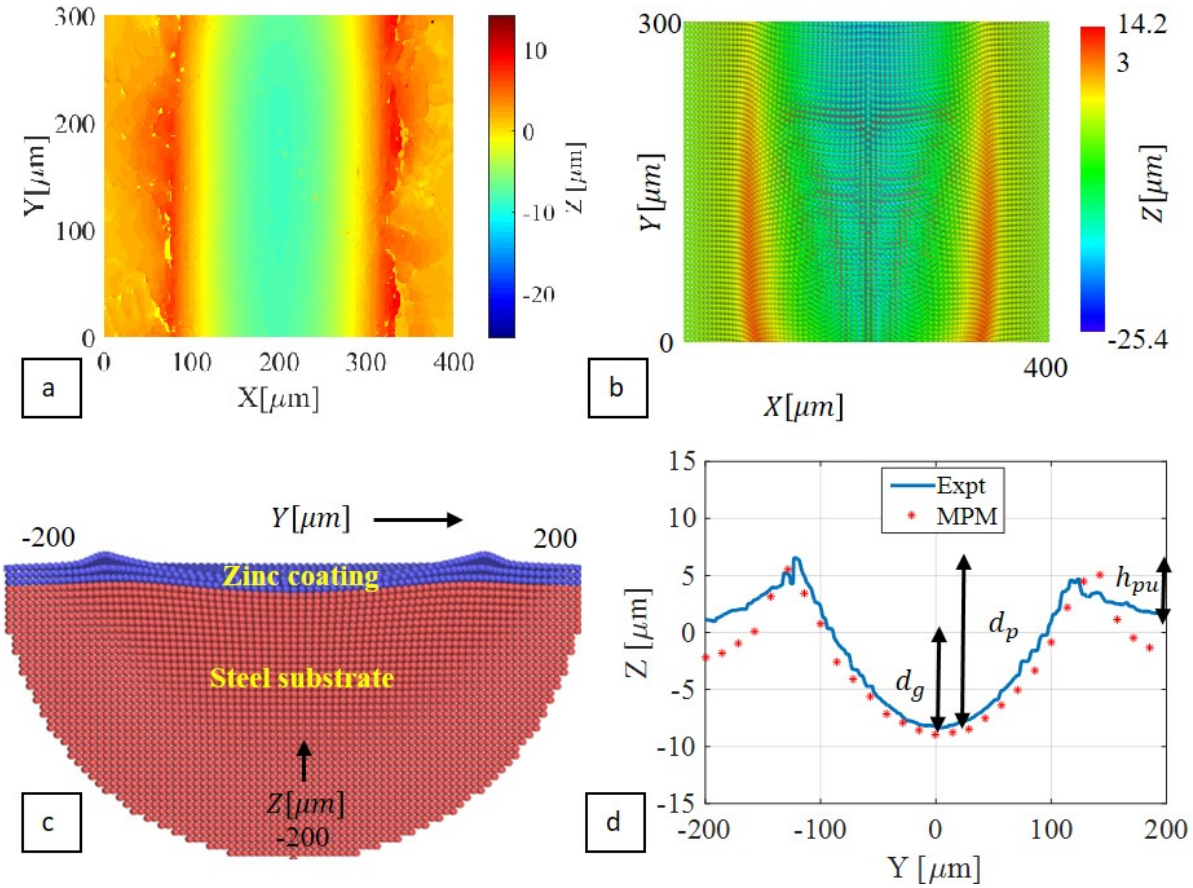

Figure 14: Surface profile of zinc coating on steel ploughed at 22N load by 1mm dia. sphere in (a) ploughing experiments as seen using confocal microscope at 20x magnification and from (b) MPM-simulations as seen using OVITO visulization tool. (c) Cross-section of the zinc coated specimen specimen during ploughing. (d) Comparision of the ploughed cross-section obtained from MPM-simulation and eperiments by 1mm dia. ball at 22N load. (MPM model parameters: table 3, 4 and 5).

The height profile of the ploughed surface in the sliding xy plane obtained from the ploughing experiments and the MPM simulations are shown in figure 14a and 14b respectively. The ploughed profiles are plotted over the cross-section (yz plane) in figure 14d. The MPM particles along the cross-section of the wear track (see figure 14c) were grouped and their positions at the end of the simulation were plotted in figure 14d. The cross-section of the ploughed

profile obtained from both the ploughing experiments and the MPM simulations showed good agreement in figure 14d. The total ploughing depth d_p is calculated as the sum of the groove depth d_g and the pile-up height h_{pu} in figure 14d.

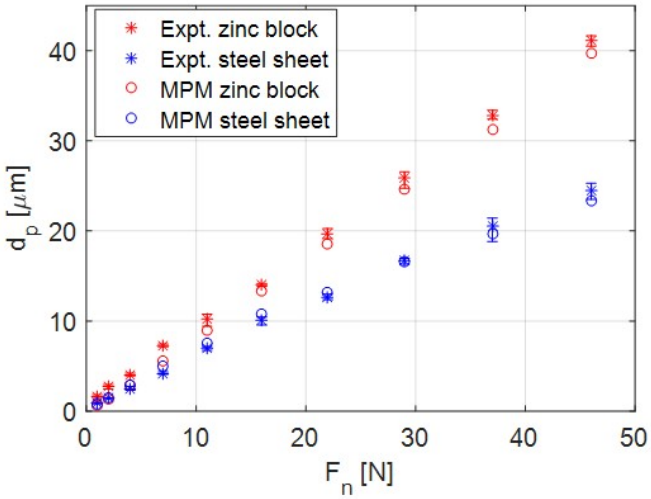

Figure 15: Comparison of the ploughing depths obtained from MPM model and ploughing experiments on Quaker lubricated zinc block and DX56 steel sheet by a 1mm diameter ball [46]. (MPM model parameters: table 3, 4 and 5).

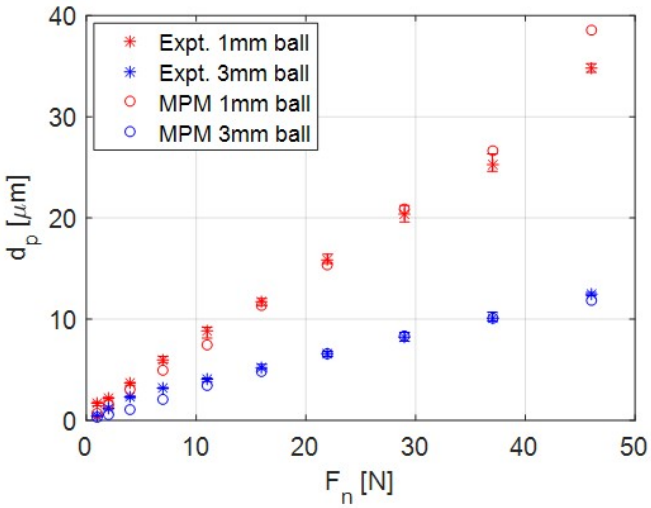

Figure 16: Ploughing depths for load controlled test carried out with indenters of diameter 1mm and 3mm on lubricated zinc coated steel sheet (zinc coating thickness of $15\mu m$) with the linear sliding friction tester and MPM-ploughing model that includes the material model parameters from table 3 and 4 and interfacial friction model parameters in table 5. (MPM model parameters: table 3, 4 and 5).

The total ploughing depths obtained from the uncoated steel sheet [45] and the zinc block both lubricated by Quaker lubricant and ploughed by a 1mm diameter ball were compared and found to be in good agreement (figure 15). The zinc block having a lower yield stress compared to the DX56 steel sheet (see figure 10a) resulted in a higher ploughing depth for all the loads. The ploughing depth for the zinc blocks also increased faster than that of the DX56 steel sheets due

to the lower strain hardening of the zinc block at high loads compared to the DX56 steel sheet (see figure 10, table 3 and table 4). Having validated the ploughing depth for bulk zinc and steel, the numerically calculated ploughing depths will be also validated using zinc coated steel sheet.

The total ploughing depth obtained from the ploughing experiments and simulations on the zinc coated steel sheet for a load range of 1-46N were compared for spherical indenters of 1mm and 3mm diameters and found to agree well as shown in figure 16. It is obvious that the larger 3mm diameter indenter penetrates less compared to the 1mm indenter owing to its larger contact area to carry the applied load.

Ploughing experiments and MPM simulations were also done for zinc coated steel sheets with a coating thickness ranging from 0-55μm including the zinc block (bulk zinc). The ploughed profile of the zinc coated steel sheets was compared with the ploughed profile of the zinc block at the zinc surface and at 15μm beneath the surface, see figure 17. For a zinc coated steel sheet with 15μm coating thickness, the deformation of the (surface of the steel substrate) bulk steel is significantly lower than the bulk zinc due to its higher hardness as shown in figure 17a and 17b. Also, the higher hardness of the steel substrate results in a lower ploughing depth at the surface of the zinc coating as compared to that of the zinc block as shown in figure 17a and 17b.

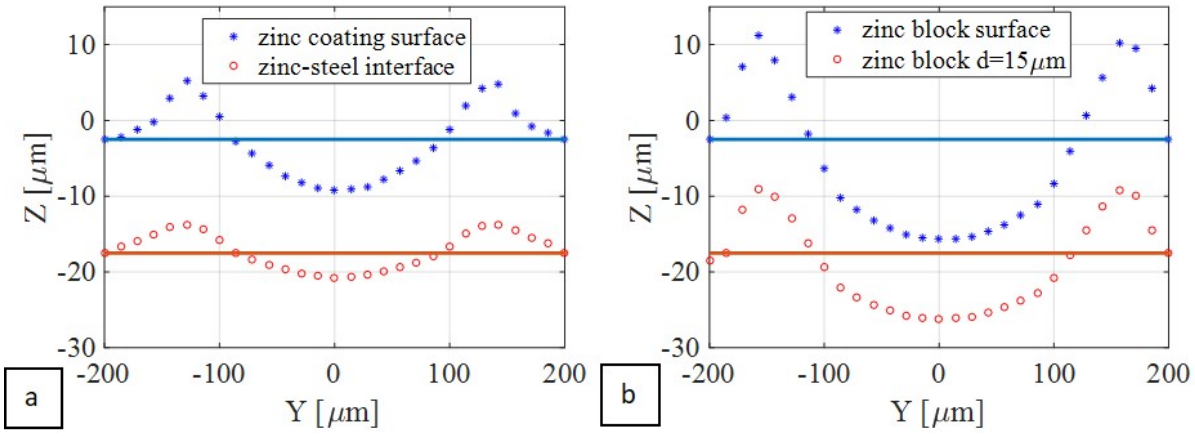

Figure 17: Comparison of deformation in the ploughed specimen (ploughed cross-section profile) at the surface (blue) and the interface 15μm depth (red) (a) in presence of 15 μm zinc coating on steel substrate and (b) with pure zinc block under 22N load by 1mm diameter indenter (MPM model parameters given : table 3, 4 and 5).

The differences in the ploughing depths obtained from experiments with steel sheet, zinc coated steel sheet and the zinc block are summarised over loads ranging from 1-46N in figure 18a. As the thickness of the zinc coating is increased from 10 to 15, 30, 40 and 55 μm, the ploughing depths are also shown to increase for three different loads in figure 18b. The increase in ploughing depth with coating thickness is due to the decrease in the effective hardness for the soft zinc coated system with increase in coating thickness (see equation 1). The rate of increase in ploughing depth with respect to the coating thickness increases with increase in the applied load. The MPM simulations have a larger increase in ploughing depth compared to that of the experiments with coating thickness above 30μm, as shown in figure 18b. The lower penetration

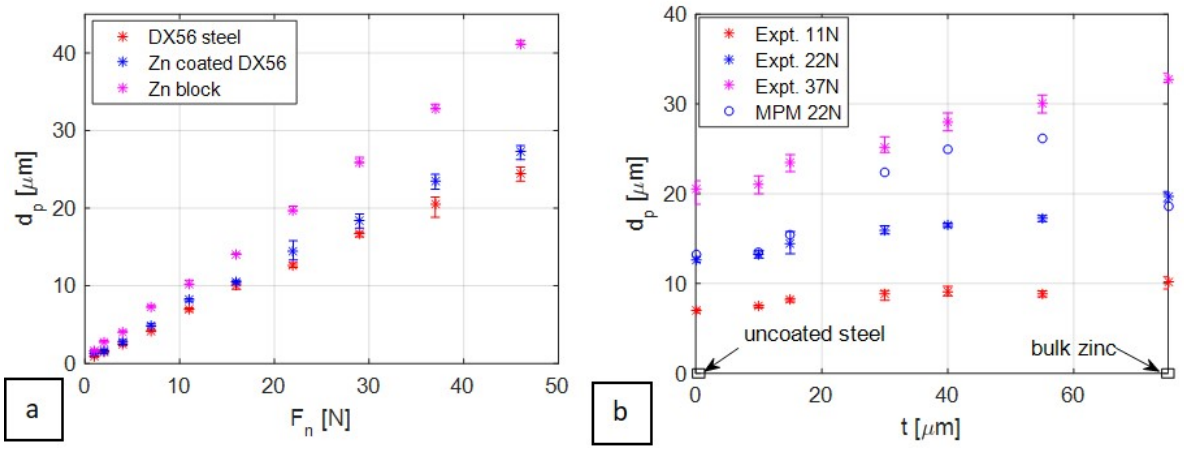

Figure 18: (a) Comparison of ploughing depths obtained from ploughing experiments by 1mm indenter with Quaker lubricated DX56 steel sheet, $15\mu m$ thick zinc coated steel sheet, and pure zinc block. (b) Effect of coating thickness on ploughing depth for applied loads of 11, 22 and 37N obtained from ploughing experiments and compared with MPM simulations for 22N load with 1mm diameter ball. (MPM model parameters: table 3, 4 and 5).

depths obtained from the ploughing experiments for large coating thickness can be explained by the rougher surface of thicker (unpolished) zinc coatings which could result in higher surface hardness of the zinc coatings. Further the yield strength of the zinc coating used in the MPM simulations is measured by Nano-indentation for a coating thickness of $10\mu m$ [53]. For higher coating thickness, the size and orientation of the zinc grains could have significant effect on the measured yield strength and hardness. The mechanical properties of the thicker zinc coatings are unknown in the current analysis to be used in the MPM model.

4.2.2 Comparison of coefficient of friction

The forces acting on the indenter were plotted over the sliding distance as obtained from the ploughing experiments and simulations in figure 19. The pin was slid over a distance of 0.6 mm in the MPM simulations. The friction force F_x due to ploughing in x direction is divided by the normal force F_z to obtain the overall coefficient of friction μ. The average coefficient of friction was measured during steady state from 3mm to 9mm sliding distance in the ploughing experiments and from 0.3mm to 0.6mm sliding distance in MPM simulations.

The coefficient of friction is obtained for the MPM ploughing simulations on the zinc block and the DX56 steel substrate lubricated with Quaker oil by a 1mm diameter ball is shown to be in good agreement over the load range of 1-46N in figure 20. The coefficient of friction for ploughing of the zinc block is slightly higher than for the DX56 steel sheet at normal loads larger than 7N. The higher coefficient of friction results from the larger plastic deformation of the bulk zinc during ploughing as can be seen from the higher ploughing depths for the bulk zinc in figure 15. However, in spite of a large difference in the ploughing depths between bulk zinc and steel sheet, resulting in a large component of coefficient of friction μ_{pl}, the difference in the overall coefficient of friction is minimized. This is due to the large contribution of the coefficient of friction due to interfacial shear μ_{sh} to the overall μ [46], where the boundary layer shear strength τ_{bl} of lubricated zinc is also lower than that of the lubricated steel sheet (see figure 10b). The coefficient of friction at lower loads is higher for the ploughing experiments compared to the MPM simulation due to the possible asperity interlocking at low d_p.

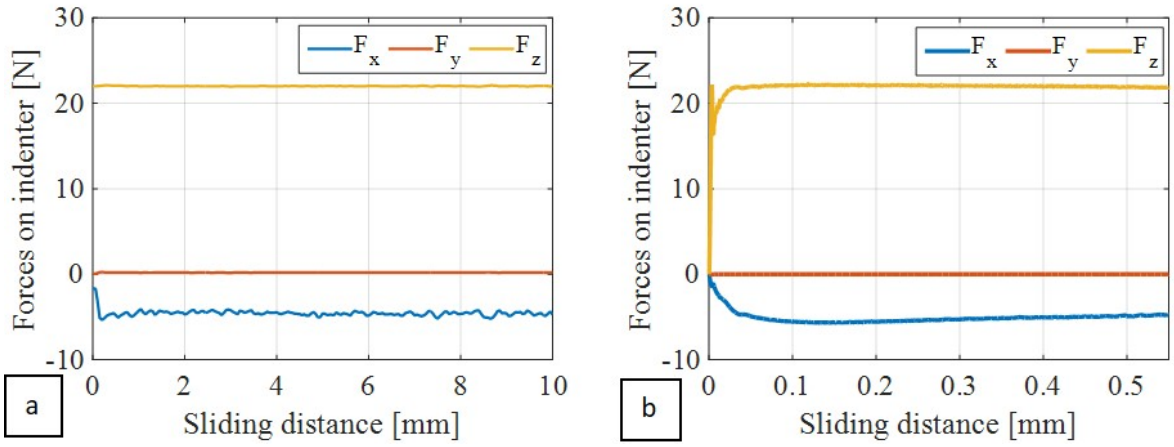

Figure 19: Forces acting on a 1mm diameter spherical indenter ploughing in x direction on a lubricated, 15μm thick, zinc coated steel sheet at 22N normal load in (a) experiments and (b) MPM simulations.

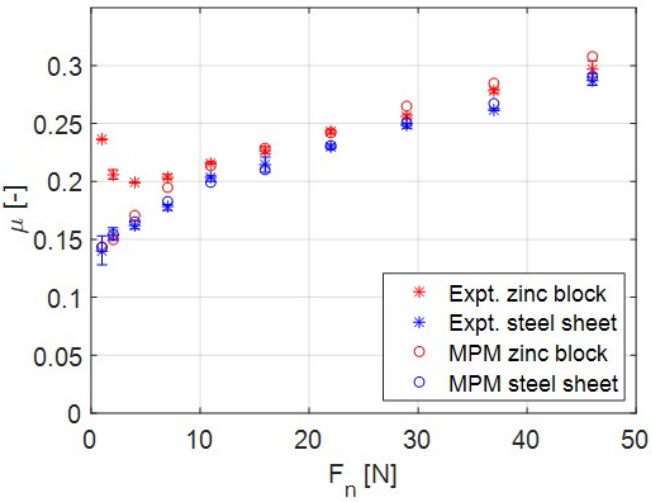

Figure 20: Comparison of the coefficient of friction obtained from MPM model and ploughing experiments on Quaker lubricated zinc block and DX56 steel sheet by 1mm diameter ball [45]. (MPM model parameters: table 3, 4 and 5).

The mean coefficient of friction obtained from both ploughing experiments and MPM simulations was plotted over a range of loads (1-46N) for spherical indenters of 1mm and 3mm diameters sliding over zinc coated steel sheet in figure 21. The coefficient of friction obtained from the MPM ploughing model is very close to that obtained from the ploughing experiments. The coefficient of friction obtained for ploughing with 1mm diameter ball increases steadily with the applied load range of 1-46N. However, as the diameter of the indenter is increased to 3mm, the coefficient of friction drops significantly compared to ploughing with 1mm ball. The increase in indenter size reduces the penetration of the indenter into the coating required to balance the applied load. The effective hardness of the coated system in response to penetration by a larger indenter is also higher as shown in figure 1a [48]. Furthermore, the increase in indenter size also increases the relative contribution of interfacial shear strength to the coefficient of friction as shown in [46]. Consequently, the coefficient of friction due to interfacial shear reduces with increase in applied load. However, for large indenters although the coefficient of friction due to ploughing increases with load.

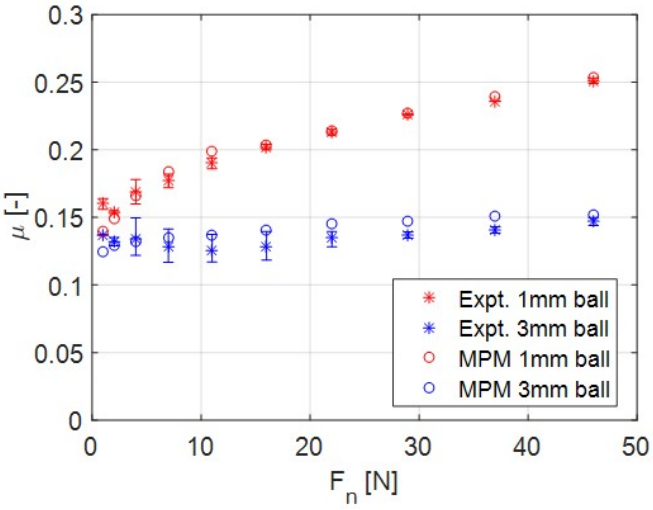

Figure 21: Coefficient of friction for load controlled tests carried out with indenters of diameter 1mm and 3mm on lubricated zinc coated steel sheet (zinc coating thickness of $15\mu m$) with the linear sliding friction tester and MPM-ploughing model that includes the material model parameters from table 3 and 4 and interfacial friction model parameters in table 5. (MPM model parameters: table 3, 4 and 5).

The later counterbalances the decreasing coefficient of friction due to interfacial shear. This results in almost constant overall coefficient of friction over the range of applied loads.

The effect of asperity size on ploughing friction is explained below using the analytical ploughing model and power law curve fitting of experimental data in equations 9.1-9.2 for their mathematical simplicity. The ploughing depth here is taken to be less than the coating thickness. The relationship between the ploughing depth and applied load for the 1mm and 3mm diameter indenters is obtained by power law fitting of figure 16. Taking $d_p = a_1 F_n^{x_1}$, we have $a_1 = 8.6 \times 10^{-6}$, $x_1 = 0.95$ for 1mm dia. ball and $a_1 = 4.7 \times 10^{-6}$, $x_1 = 0.85$ for 3mm dia. ball. By curve fitting the relationship between A_{yz} and the ploughing depth d_p from equation 2.3 to a power law $A_{yz} = b_1 d_p^{y_1}$, the coefficients $b_1 = 1.51$, $y_1 = 0.96$ and $b_1 = 0.15$, $y_1 = 1.5$ are obtained for 1mm and 3mm dia. balls respectively. Assuming a constant hardness $H_c = 3\sigma_{y_0}$ where σ_{y_0} for zinc is taken $85MPa$ [44], an analytical expression of μ_{pl} in given in terms of F_n in equation 9.1. By curve fitting the relationship between A_{xy} and the ploughing depth d_p from equation 2.2 to a power law $A_{yz} = c_1 d_p^{z_1}$, the coefficients $c_1 = 0.0015$, $z_1 = 0.997$ and $c_1 = 0.0046$, $z_1 = 0.999$ are obtained for 1mm and 3mm dia. balls respectively. Also, from equation 8.2, $\tau_{bl} = C_p \overline{P}^{n_p}$ where, $C_p = 0.32$, $n_p = 0.95$ and $\overline{P} = F_n/A_{xy}$ (see table 5). By substituting the power law relations, μ_{sh} is given as a function of applied load F_n in equation 9.2. The total coefficient of friction μ is taken as the sum of μ_{sh} and μ_{pl}.

$$\mu_{pl} = H_c \frac{A_{yz}}{F_n} = \frac{H_c}{F_n} b_1 d_p^{y_1} = \frac{H_c}{F_n} b_1 (a_1 F_n^{x_1})^{y_1} \tag{9.1}$$

$$\mu_{sh} = \tau_{sh} \frac{A_{xy}}{F_n} = C_p \left(\frac{F_n}{A_{xy}}\right)^{n_p} \left(\frac{A_{xy}}{F_n}\right) = C_p \left(\frac{c_1 d_p^{z_1}}{F_n}\right)^{1-n_p} = C_p \left(c_1 (a_1 F_n^{x_1})^{z_1 - 1}\right)^{1-n_p} \tag{9.2}$$

The analytical coefficient of friction relations obtained by curve fitting are plotted in figure 22. A good agreement is shown for the 3 mm diameter indenter in figure 22b. The increase in μ_{pl} for the 3mm ball is smaller than the 1mm ball as expected from the lower plastic deformation

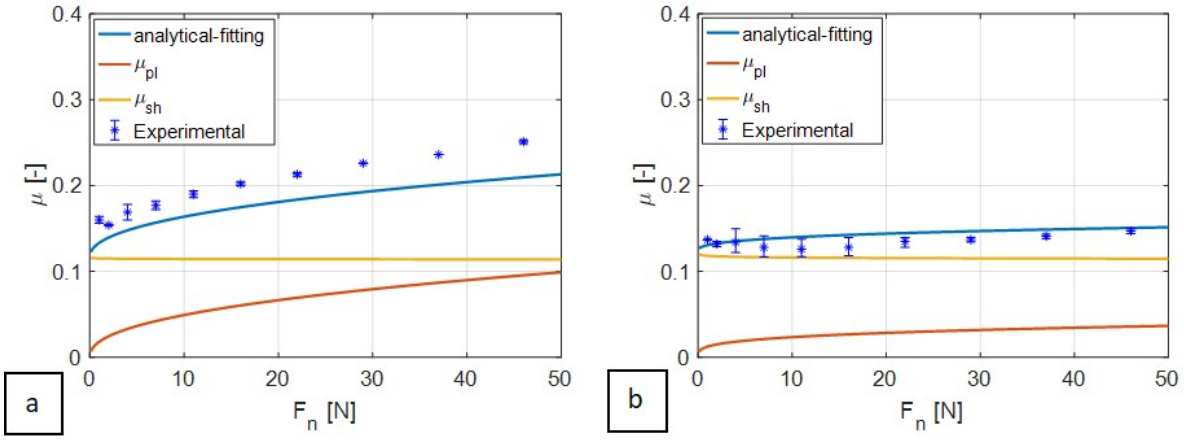

Figure 22: Effect of asperity shape on ploughing coefficient of friction studied using analytical model and curve fitting for (a) 1mm diameter indenter (b) 3mm diameter indenter sliding on zinc coated steel.

with the larger indenter. The analytical under predicts the coefficient of friction for 1mm ball in figure 22a. Although a constant hardness is assumed, the increase in hardness due to strain hardening is ignored in the simple analysis shown in figure 22. In reality, the increase in hardness is higher for 1mm ball where higher ploughing depths result in higher hardening and higher hardness. From the results in figure 22a, the analytical model can be used to predict ploughing friction given the experimental data on the ploughing depths in a substrate.

The presence of zinc coating on the steel substrate results in a reduced coefficient of friction in ploughing as compared to both the zinc block and the steel substrate (see figure 23a). This is because the presence of hard steel substrate underneath the zinc reduces the ploughing depth in the zinc (see figure 17) and hence μ_{pl}. Furthermore, the interfacial shear strength of Quaker lubricant on zinc coating is lower as compared to that on DX56 steel substrate as shown in figure 10b. As interfacial shear has a major contribution to the overall coefficient of friction for large indenters [46], the lower boundary layer shear strength of the zinc coating combined with its low plastic deformation during ploughing contribute to a lower coefficient of friction in the zinc coating compared to bulk zinc and steel. At low normal loads, both the bulk zinc and the zinc coating have higher coefficient of friction. This could be due to asperity interlocking and high interfacial shear strength (see figure 4a) for the rough zinc surface.

The effect of coating thickness on the overall coefficient of friction for the soft zinc coating on the steel substrate is shown in figure 23b. The coefficient of friction was measured from ploughing experiments on zinc coatings with coating thickness of 10, 15, 30, 40 and 55μm for 11, 22 and 37N loads and MPM simulations for the same coating thickness at 22N load. The coefficient of friction decreases with increase in coating thickness up to 15μm and then increases with the coating thickness until the bulk zinc (infinite coating thickness). The change in coefficient of friction with zinc coating thickness resembles the theoretical relation between the coefficient of friction and the coating thickness for soft coatings shown in figure 4a. A higher coefficient of friction for thicker coatings, obtained with the MPM simulation could be explained due to the increase in ploughing depth and the higher μ_{sh}, for a perfectly smooth zinc coated surface with $R_q = 0\mu m$ (see figure 4c).

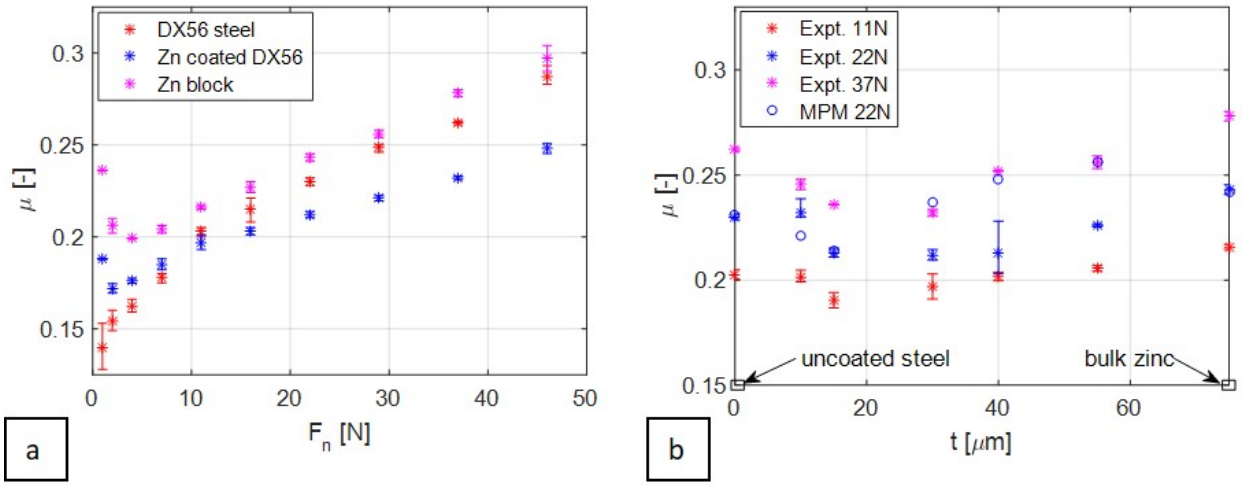

Figure 23: (a) Comparison of coefficient of friction obtained from ploughing experiments by 1mm indenter with Quaker lubricated DX56 steel sheet, 15 μm thick zinc coated steel sheet, and pure zinc block. (b) Effect of coating thickness t on coefficient of friction at loads of 11, 22 and 37N obtained from ploughing experiments and compared with MPM model for 22N load with 1mm diameter ball. (MPM model parameters: table 3, 4 and 5).

5 Conclusion

The coating thickness, substrate material properties and applied load have been varied to study their effect on the ploughing friction and ploughing depth. An analytical model is developed to predict the coefficient of friction and wear track depth of a single asperity ploughing through a coated or uncoated substrate and also validated using the using the MPM based-ploughing model. The ploughing behaviour of a zinc coating on a steel substrate has been numerically modelled and validated to good agreement using the MPM-based ploughing model and ploughing experiments. The analytical model is calibrated relative to the experimental data and then used to explain the variation in coefficient of friction with applied load and indenter size in ploughing experiments. The analytical model is also able to predict the effect of the coating thickness and substrate hardness on the coefficient of friction and ploughing depth for various normal loads in the ploughing experiments. Therefore, it can be concluded that friction in ploughing of a coated system is a function of the material properties (flow/yield curve) of the coating and the substrate, the shear strength of the contacting interfaces and the coating thickness.

Acknowledgments

This research was carried out under project number S22.1.14520a in the framework of the Partnership Program of the Materials innovation institute M2i (www.m2i.nl) and the Technology Foundation TTW (www.stw.nl), which is part of the Netherlands Organization for Scientific Research (www.nwo.nl). The authors would like to greatly acknowledge Dr.ir. Jeroen van Beeck from Tata Steel Europe R&D for their technical guidance and provision of Bergström-van Liempt material model parameters for DX56 steel and the stress-strain curves for the zinc block.

Bibliography

[1] R. ter Haar. "Friction in sheet metal forming, the influence of (local) contact conditions and deformation". PhD thesis. University of Twente, The Netherlands, 1996. ISBN: 90-9009296-X.

[2] H.C. Shih. "Friction of Coated Automotive Steels in Stamping". In: Encyclopedia of Tribology. Ed. by Q.J. Wang and Y.W. Chung. Boston, MA: Springer, 2013, pp. 1359–1365. DOI: 10.1007/978-0-387-92897-5_623.

[3] Y. Kim, H. Kim, and Y.T. Keum. "Evaluation of frictional characteristic for Zinc-coated steel sheet". In: Metals and Materials 6 (2000), pp. 323–329. DOI: 10.1007/BF0302807.

[4] Y. Zhang, Q.P. Cui, F.Q. Shao, J.S. Wang, and H.Y. Zhao. "Influence of air-knife wiping on coating thickness in hot-dip galvanizing". In: Journal of Iron and Steel Research International 19.4 (2012), pp. 70–78. DOI: 10.1016/S1006-706X(12)60130-7.

[5] S. Lee, M. Joun, D. Kim, and J. Lee. "Effect of elastic-plastic behavior of coating layer on drawability and frictional characteristic of galvannealed steel sheets". In: Journal of Mechanical Science and Technology 30.7 (2016), pp. 3313–3319. DOI: 10.1007/s12206-016-0640-5.

[6] A.J.D Westeneng. "Modelling of contact and friction in deep drawing process". PhD thesis. University of Twente, The Netherlands, 2001. ISBN: 90-365-1549-1.

[7] F.P. Bowden, A.J.W. Moore, and D. Tabor. "The Ploughing and Adhesion of Sliding Metals". In: Journal of Applied Physics 14.2 (1943), pp. 80–91. DOI: 10.1063/1.1714954.

[8] K. Holmberg, H. Ronkainen, and A. Matthews. "Tribology of thin coatings". In: Ceramics international 26.7 (2000), pp. 787–795. DOI: 10.1016/S0272-8842(00)00015-8.

[9] S.J. Bull and E.G. Berasetegui. "An overview of the potential of quantitative coating adhesion measurement by scratch testing". In: Tribology International 39.2 (2006), pp. 99–114. DOI: 10.1016/j.triboint.2005.04.013.

[10] M.B de Rooij. "Tribological aspects of unlubricated deep-drawing process". PhD thesis. University of Twente, The Netherlands, 1998. ISBN: 90-3651218-2.

[11] N. Panich and Y. Sun. "Effect of penetration depth on indentation response of soft coatings on hard substrates: a finite element analysis". In: Surface and Coatings Technology 182.2-3 (2004), pp. 342–350. DOI: 10.1016/j.surfcoat.2003.07.002.

[12] C. Gamonpilas and E.P. Busso. "On the effect of substrate properties on the indentation behaviour of coated systems". In: Materials Science and Engineering: A 380.1-2 (2004), pp. 52–61. DOI: 10.1016/j.msea.2004.04.038.

[13] Z.H. Xu and D. Rowcliffe. "Finite element analysis of substrate effects on indentation behaviour of thin films". In: Thin Solid Films 447 (2004), pp. 399–405. DOI: 10.1016/S0040-6090(03)01071-X.

[14] Z. Liu, A. Neville, and R.L. Reuben. "The effect of film thickness on initial friction of elastic-plastically rough surface with a soft thin metallic film". In: Journal of tribology 124.3 (2002), pp. 627–636. DOI: 10.1115/1.1454103.

[15] J. Lackner, L. Major, and M. Kot. "Microscale interpretation of tribological phenomena in Ti/TiN soft-hard multilayer coatings on soft austenite steel substrates". In: Bulletin of the Polish Academy of Sciences: Technical Sciences 59.3 (2011), pp. 343–355. DOI: 10.2478/v10175-011-0042-x.

[16] J. Cao, Z. Yin, H. Li, and G. Gao. "Tribological studies of soft and hard alternated composite coatings with different layer thicknesses". In: Tribology International 110 (2017), pp. 326–332. DOI: 10.1016/j.triboint.2017.02.039.

[17] J.D. Kamminga and G.C.A.M. Janssen. "Experimental discrimination of plowing friction and shear friction". In: Tribology Letters 25.2 (2007), pp. 149–152. DOI: 10.1007/s11249-006-9135-3.

[18] M.A. Sherbiney and J. Halling. "Friction and wear of ion-plated soft metallic films". In: Wear 45.2 (1977), pp. 211–220. DOI: 10.1016/0043-1648(77)90075-8.

[19] J. Halling. "Surface coatings materials conservation and optimum tribological performance". In: Tribology international 12.5 (1979), pp. 203–208. DOI: 10.1016/0301-679X(79)90189-0.

[20] J. Halling. "The tribology of surface films". In: Thin Solid Films 108.2 (1983), pp. 103–115. DOI: 10.1016/0040-6090(83)90496-0.

[21] W.R. Chang. "An elastic-plastic contact model for a rough surface with an ion-plated soft metallic coating". In: Wear 212.2 (1997), pp. 229–237. DOI: 10.1016/S0043-1648(97)00148-8.

[22] H. Jiang, R. Browning, J.D. Whitcomb, M. Ito, M. Shimouse, T.A. Chang, and H.J. Sue. "Mechanical modeling of scratch behavior of polymeric coatings on hard and soft substrates". In: Tribology letters 37.2 (2010), pp. 159–167. DOI: 10.1007/s11249-009-9505-8.

[23] M.M. Hossain, S. Xiao, H.J. Sue, and M. Kotaki. "Scratch behavior of multilayer polymeric coating systems". In: Materials Design 128 (2017), pp. 143–149. DOI: 10.1016/j.matdes.2017.05.012.

[24] K. Holmberg, A. Laukkanen, H. Ronkainen, K. Wallin, S. Varjus, and J. Koskinen. "Tribological contact analysis of a rigid ball sliding on a hard coated surface: Part I: Modelling stresses and strains". In: Surface and Coatings Technology 200.12-13 (2006), pp. 3793–3809. DOI: 10.1016/j.surfcoat.2005.03.040.

[25] D. Meng, Y.G. Li, Z.T. Jiang, and M.K. Lei. "Scratch behavior and FEM modelling of Cu/Si (100) thin films deposited by modulated pulsed power magnetron sputtering". In: Surface and Coatings Technology 363 (2019), pp. 35–33. DOI: 10.1016/j.surfcoat.2019.02.008.

[26] G. Kermouche, N. Aleksy, J.L. Loubet, and J.M. Bergheau. "Finite element modeling of the scratch response of a coated time-dependent solid". In: Wear 367.11 (2009), pp. 1945–1953. DOI: 10.1016/j.wear.2009.05.005.

[27] T.H. Fang, C.H. Liu, S.T. Shen, S.D. Prior, L.W. Ji, and J.H. Wu. "Nanoscratch behavior of multi-layered films using molecular dynamics". In: Applied Physics A 90.4 (2008), pp. 753–758. DOI: 10.1007/s00339-007-4351-8.

[28] T.H. Fang and J.H. Wu. "Molecular dynamics simulations on nanoindentation mechanisms of multilayered films". In: Computational Materials Science 43.4 (2008), pp. 785–790. DOI: 10.1016/j.commatsci.2008.01.066.

[29] A.V. Bolesta and V.M. Fomin. "Molecular dynamics simulation of sphere indentation in a thin copper film". In: Physical Mesomechanics 12.3-4 (2009), pp. 117–123. DOI: 10.1016/j.physme.2009.07.003.

[30] T. Akabane, Y. Sasajima, and J. Onuki. "Coating adhesion evaluation by nanoscratching simulation using the molecular dynamics method". In: Japanese journal of applied physics 46.5R (2007), p. 3024. DOI: 10.1143/JJAP.46.3024.

[31] J. Malzbender, G. de With, and J.M.J. Den Toonder. "Determination of the elastic modulus and hardness of sol–gel coatings on glass: influence of indenter geometry". In: Thin Solid Films 372.1-2 (2000), pp. 134–143. DOI: 10.1016/S0040-6090(00)01025-7.

[32] R. Saha and W.D. Nix. "Effects of the substrate on the determination of thin film mechanical properties by nanoindentation". In: Acta materialia 50.1 (2002), pp. 23–38. DOI: 10.1016/S1359-6454(01)00328-7.

[33] R. Saha, Z. Xue, Y. Huang, and W.D. Nix. "Indentation of a soft metal film on a hard substrate: strain gradient hardening effects". In: Journal of the Mechanics and Physics of Solids 49.9 (2001), pp. 1997–2014. DOI: 10.1016/S0022-5096(01)00035-7.

[34] J.M. Challen and P.L.B. Oxley. "An explanation of the different regimes of friction and wear using asperity deformation models". In: Wear 53.2 (1979), pp. 229–243. DOI: 10.1016/0043-1648(79)90080-2.

[35] Z.S. Ma, Y.C. Zhou, S.G. Long, and C. Lu. "On the intrinsic hardness of a metallic film/substrate system: Indentation size and substrate effects". In: International journal of plasticity 34 (2012), pp. 1–11. DOI: 10.1016/j.ijplas.2012.01.001.

[36] H. Gao, C.H. Chiu, and J. Lee. "Elastic contact versus indentation modeling of multi-layered materials". In: International Journal of Solids and Structures 29.20 (1992), pp. 2471–2492. DOI: 10.1016/0020-7683(92)90004-D.

[37] M.V. Swain and J. Meník. "Mechanical property characterization of thin films using spherical tipped indenters". In: Thin Solid Films 253.1-2 (1994), pp. 204–211. DOI: 10.1016/0040-6090(94)90321-2.

[38] R.S. Timsit and C.V. Pelow. "Shear strength and tribological properties of stearic acid films-Part I: on glass and aluminum-coated glass". In: Journal of tribology 114.1 (1992), pp. 150–158. DOI: 10.1115/1.2920854.

[39] R.S. Timsit and C.V. Pelow. "Shear Strength and Tribological Properties of Stearic Acid Films-Part II: On Gold-Coated Glass". In: Journal of tribology 114.1 (1992), pp. 159–166. DOI: 10.1115/1.2920855.

[40] B.J. Briscoe and D.C.B. Evans. "The shear properties of Langmuir-Blodgett layers". In: Proceedings of the Royal Society of London. A. Mathematical and Physical Sciences 380.1779 (1982), pp. 389–407. DOI: 10.1098/rspa.1982.0048.

[41] N. Coni, M.L. Gipiela, A.S.C.M. D'Oliveira, and P.V.P. Marcondes. "Study of the mechanical properties of the hot dip galvanized steel and galvalumeő". In: Journal of the Brazilian Society of Mechanical Sciences and Engineering 31.4 (2009), pp. 319–326. DOI: 10.1590/S1678-58782009000400006.

[42] R. Parisot, S. Forest, A.F. Gourgues, A. Pineau, and D. Mareuse. "Modeling the mechanical behavior of a multicrystalline zinc coating on a hot-dip galvanized steel sheet". In: Computational Materials Science 19.1-4 (2000), pp. 189–204. DOI: 10.1016/S0927-0256(00)00155-5.

[43] G.M. Song, W.G. Sloof, Y.T. Pei, and J.T.M De Hosson. "Interface fracture behavior of zinc coatings on steel: Experiments and finite element calculations". In: Surface and Coatings Technology 201.7 (2006), pp. 4311–4316. DOI: 10.1016/j.surfcoat.2006.08.046.

[44] R.R. Tohid and S.J. Bull. "Getting accurate nanoindentation data from time-dependent and microstructural effects of zinc". In: International journal of materials research 98.5 (2007), pp. 353–359. DOI: 10.3139/146.101477.

[45] T. Mishra, G.C. Ganzenmüller, M.B. de Rooij, M. Shisode, J. Hazrati, and D.J. Schipper. "Modelling of ploughing in a single-asperity sliding contact using material point method". In: Wear 418-419 (2019), pp. 180–190. DOI: 10.1016/j.wear.2018.11.020.

[46] T. Mishra, M.B. de Rooij, M. Shisode, J. Hazrati, and D.J. Schipper. "Characterization of interfacial shear strength and its effect on ploughing behaviour in single-asperity sliding". In: Wear 436-437 (2019), p. 203042. DOI: 10.1016/j.wear.2019.203042.

[47] J. Halling and M.A. Sherbiney. "The role of surface topography in the friction of soft metallic films". In: Tribology 1978: Materials Performance and Conservation IMechE. Tribology Convention. Swansea, 1978. ISBN: 0852984006.

[48] J. Halling and R.D. Arnell. "Ceramic coatings in the war on wear". In: Wear 100.1-3 (1984), pp. 367–380. DOI: 10.1016/0043-1648(84)90022-X.

[49] D. Tabor. The Hardness of Metals. Oxford university press, London, 2000. ISBN: 9780198507765.

[50] T. Mishra, M.B. de Rooij, M. Shisode, J. Hazrati, and D.J. Schipper. "A material point method based ploughing model to study the effect of asperity geometry on the ploughing behaviour of an elliptical asperity". In: International journal of materials research 142 (2019), p. 106017. DOI: 10.1016/j.triboint.2019.106017.

[51] J. Strutzenberger and J. Faderl. "Solidification and spangle formation of hot-dip-galvanized zinc coatings". In: Metallurgical and Materials Transactions A 29.2 (1998), pp. 631–646. DOI: 10.1007/s11661-998-0144-8.

[52] G.M. Song, J.T.M De Hosson, W.G. Sloof, and Y.T. Pei. "Evaluation of interface adhesion of hot-dipped zinc coating on TRIP steel with tensile testing and finite element calculation". In: WIT Transactions on Engineering Sciences 91 (2015), pp. 3–14. DOI: 10.2495/SECM150011.

[53] Y.T. Pei, G.M. Song, W.G. Sloof, and J.T.M De Hosson. "A methodology to determine anisotropy effects in non-cubic coatings". In: Surface and Coatings Technology 201.16-17 (2007), pp. 6911–6916. DOI: 10.1016/j.surfcoat.2006.11.044.

[54] P.E. Senseny, J. Duffy, and R.H. Hawley. "Experiments on strain rate history and temperature effects during the plastic deformation of close-packed metals". In: Journal of Applied Mechanics 45.1 (1978), pp. 60–66. DOI: 10.1115/1.3424274.

[55] P. Van Liempt. "Workhardening and substructural geometry of metals". In: Journal of Materials Processing Technology 45.1-4 (1994), pp. 459–464. DOI: 10.1016/0924-0136(94)90382-4.

[56] H. Vegter. “On the plastic behaviour of steel during sheet forming”. PhD thesis. University of Twente, The Netherlands, 1993. ISBN: 9789090043739.

[57] G.R. Johnson and W.H. Cook. “Fracture characteristics of three metals subjected to various strains, strain rates, temperatures and pressures”. In: Engineering fracture mechanics 21.1 (1985), pp. 31–48. DOI: 10.1016/0013-7944(85)90052-9.

[58] H. Swift. “Plastic instability under plane stress”. In: Journal of the Mechanics and Physics of Solids 1.1 (1952), pp. 1–18. DOI: 10.1016/0022-5096(52)90002-1.